Bioinspired Model Complexes of Non-Heme Iron Enzymes

Modelling the 2-His-1-Carboxylate Facial Triad with a Family of *N,N,O* Phenolate Ligands

Emily C. Monkcom

Bioinspired Model Complexes of Non-Heme Iron Enzymes

Modelling the 2-His-1-Carboxylate Facial Triad
with a Family of *N,N,O* Phenolate Ligands

Bio-geïnspireerde Modellen van Niet-Heem IJzer-Enzymen

Het Modellen van de 2-His-1-Carboxylaat Faciale Triade
met een Familie van *N,N,O* Fenolaat Liganden

(met een samenvatting in het Nederlands en in het Frans)

Proefschrift

ter verkrijging van de graad van doctor aan de Universiteit Utrecht op gezag van de rector magnificus, prof. dr. H. R. B. M. Kummeling, ingevolge het besluit van het college voor promoties in het openbaar te verdedigen
op 20 juni 2022 des middags te 12.15 uur

door

Emily Charlotte Monkcom

geboren op 17 maart 1992 te Brussel, België

Promotor:

prof. dr. Robertus J. M. Klein Gebbink

The work described in this thesis was financially supported by the European Union Horizon 2020 funding programme under the “NoNoMeCat” Marie Sklodowska-Curie ITN Network grant agreement (675020-MSCA-ITN-2015-ETN).

Bioinspired Model Complexes of Non-Heme Iron Enzymes

Modelling the 2-His-1-Carboxylate Facial Triad
with a Family of *N,N,O* Phenolate Ligands

Je dédie cette thèse à mes très chers parents
et à la mémoire de ma bobonne adorée.

Monkcom, Emily Charlotte

Bioinspired Model Complexes of Non-Heme Iron Enzymes: Modelling the 2-His-1-Carboxylate Facial Triad with a Family of *N,N,O* Phenolate Ligands

ISBN: 978-94-6458-342-7
Cover design: Emily C. Monkcom
Print: Ridderprint | www.ridderprint.nl

The work described in this doctoral thesis was carried out in the Organic Chemistry and Catalysis (OCC) group, Debye Institute for Nanomaterials Science, Faculty of Science, Utrecht University, The Netherlands.

Contents

Preface

Aim and Scope of the Thesis

In the face of climate change and the growing world population, mankind is faced with unprecedented humanitarian and environmental challenges. As such, there is a pressing need to achieve a circular economy and a more sustainable, less wasteful society. Many of the processes necessary for maintaining a sustainable existence on this planet are already built into the fundamental biological mechanisms of living organisms, thanks to billions of years of evolution. Indeed, nature holds tremendous potential as a source of inspiration for more sustainable innovations in the domains of engineering, architectural and chemical design. For instance, buildings can be made more energy-efficient by imitating the ventilation systems found in termite and ant nests. Similarly, wind turbine blades can be made more aerodynamic by imitating the tubercles found on humpback whale flippers. The practise of looking to nature for inspiration and direction in order to sustainably solve our most pressing challenges is termed biomimicry – i.e. the imitation of life.

In this thesis, biomimicry is put into practise chemically through the imitation of metalloenzyme active sites using small synthetic coordination compounds. More particularly, the aim of this thesis to develop bioinspired model complexes of non-heme iron enzymes that feature the 2-His-1-Carboxylate facial triad (2H1C) at their active site. This superfamily of enzymes employs O_2 to mediate a diverse set of challenging C–H bond oxidation reactions under ambient conditions and with exquisite regio- and stereocontrol. Isopenicillin N synthase (IPNS) is a particularly fascinating member of this enzyme family, as it utilises O_2 to activate two aliphatic C–H bonds and form two new C–X bonds (X = S, N). Developing synthetic iron-based catalysts that mimic IPNS reactivity is an attractive means with which to increase the green credentials of today's chemical industry. In this thesis, tridentate, bis-imidazole phenolate ligands have been developed that provide a tripodal, anionic *N,N,O* coordination motif that models the 2H1C.

In **Chapter 1**, the structure and mechanism of IPNS is discussed alongside those of six other mononuclear iron enzymes that also feature a single iron-sulfur bond at their active site. The role of iron-sulfur bonds in the structure and reactivity of these mononuclear iron enzymes is discussed, and an overview of their related model iron complexes is provided.

In **Chapter 2**, two new bis-imidazole phenolate ligands, **BenzImNNO** and **Im^{Ph2}NNO**, are synthesized, which contain 1-methylbenzimidazole and 1-methyl-4,5-diphenylimidazole groups, respectively. Their coordination chemistry with iron and zinc is explored, and the resulting mononuclear and dinuclear complexes reveal that the phenolate coordination mode is dependent on the steric bulk of the imidazole groups.

In **Chapter 3**, mononuclear iron and zinc complexes are synthesised using a bulky *N,N,O* phenolate ligand, **Im^{Ph2}NNO^{tBu}**, which features *tert*-butyl substituents on its phenolate ring. A detailed solid- and solution-state study is presented that delimits the conditions under which the complexes retain their biomimetic *N,N,O*-bound structure. In addition, the ligand is shown to retain its *N,N,O* coordination in the presence of a thiolate co-ligand.

Chapter 4 expands on the methodology developed in Chapter 3 and describes the synthesis, structure and reactivity of a family of mononuclear, *N,N,O*-bound iron and zinc complexes with thiolate co-ligands of varying steric and electronic properties. These complexes can be regarded as some of the closest structural models of IPNS to date.

In **Chapter 5**, ligand **Im^{Ph2}NNO^{tBu}** is used to prepare the first example of a mononuclear, pentacoordinate *N,N,O*-bound iron(II) benzoylformate complex. Exposing this complex to O_2 leads to the rapid decarboxylation of the benzoylformate ligand, which reflects important mechanistic aspects of α-ketoglutarate-dependent iron enzyme reactivity.

Finally, **Chapter 6** closes this thesis with a short perspective on the evolution of bioinspired, bis-imidazole-derived *N,N,O* ligand design, where a carboxylate, ester, amide or phenolate group is incorporated as O-donor. Trends in the coordination chemistry of these different ligands are discussed in detail, with pro's and con's highlighted in all cases.

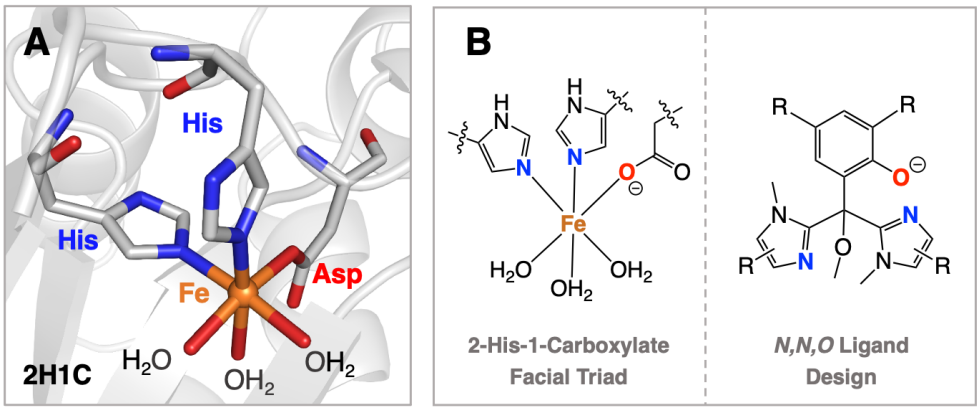

Figure 1. A: The 2-His-1-Carboxylate facial triad. B: bioinspired *N,N,O* phenolate ligand design.

Chapter 1

Mononuclear Sulfur-Ligated Iron Enzymes and their Model Non-Heme Iron Thiolate Complexes

Abstract

Mononuclear iron enzymes that contain a single Fe–S bond constitute a small but select class of enzymes that employ the soft, malleable electronic nature of sulfur to mediate a diverse and challenging scope of reactions. In this review, we examine the influence of the sulfur-rich thiolate ligand on the different structures and reactivities of seven well-studied enzymes: cytochrome P450 (CyP450), superoxide reductase (SOR), nitrile hydratase (NHase), isopenicillin N synthase (IPNS), ethymalonic encephalopathy protein 1 (ETHE1), cysteine dioxygenase (CDO) and ergothioneine sulfoxide synthase (EgtB). Bioinspired non-heme iron thiolate complexes relevant to these enzymes are highlighted and inter-comparisons are made between complexes designed to model different aspects of these unique enzyme active sites. This provides a molecular "tool-kit" with which to better understand and predict the structure and reactivity of sulfur-ligated iron complexes and enzymes.

E. C. Monkcom, S. J. Van Dijk, R. J. M. Klein Gebbink*, manuscript in preparation*

1.1 General Concepts

1.1.1 Bioinorganic Chemistry

Bioinorganic chemistry is a vibrant and flourishing field, poised at the interface of chemistry and biology. Its primary focus is the study of the inorganic matter of life – that is to say, the metal-containing proteins and enzymes, as well as the biologically relevant metal complexes that enable metabolic processes to occur. Indeed, metal sites in biology enable some of the most challenging and consequential reactions on Earth, ranging from oxygen transport in animals to photosynthesis in plants and nitrogen-fixation in bacteria. This astounding breadth of reactivity involves attractive features such as small molecule activation and late-stage functionalisation, all of which are achieved under physiological conditions and with exquisite stereo- and regioselectivity. For bioinorganic chemists, the direct deployment, engineering or mimicry of metalloenzymes and metal-containing biomolecules in research and commercial applications holds great potential for improving the green credentials of today's chemical industry.

Although it has long been known that metals play a central role in biological function, it was not until the mid-20th century that bioinorganic chemistry emerged as an independent field, fuelled by advancements in enzymology, protein crystallography, spectroscopy, bioinformatics and computational chemistry.[1–4] Combined, these techniques enabled scientists to adopt a molecular approach in their analysis of the structural and electronic factors dictating the function of a biologically relevant metal site (also known as the "structure-function relationship"). This is perhaps best exemplified by iron. For over 300 years, iron has been known to be a key component of mammalian blood, but it was not until the late 1950s, thanks to the pioneering work of Kendrew and Perutz,[5–7] that the molecular structure of haemoglobin was elucidated, thereby revealing the exact coordination chemistry involved in the uptake of oxygen by iron in this metalloprotein.

Gaining a molecular perspective on the active sites of metalloproteins and metalloenzymes is perhaps the most important and revolutionary concept in the development of bioinorganic chemistry. Indeed, site structure elucidation has injected renewed vigour and stimulated novel approaches in the field of coordination chemistry as a direct consequence of metal-containing biomolecules now being regarded as elaborate inorganic metal complexes.[3] Using this molecular perspective, bioinorganic chemists continue to extract the general principles underlying catalysis by metalloenzymes, and marry them with the known coordination chemistry of synthetic transition metal complexes. As a result, a multitude of different disciplines now exists within the field of bioinorganic chemistry, ranging from the incorporation of abiotic metals in artificial metalloenzymes, to the development of medical imaging agents, and the design of synthetic biomimetic complexes as novel industrial catalysts.

Overall, it is estimated that approximately half of all structurally characterised enzymes require one or more metal centres to carry out their function.[8] Furthermore, most metalloenzymes function with only a specific metal ion or cluster, embedded within the protein scaffold by a complex assembly of ligands whose electronic properties are tuned to hosting that particular metal ion. Too little of a particular metal can deprive a metalloenzyme of its active metal centre; too much can force metal promiscuity in other metal-dependent biomolecules, blocking their function. This stringent metal selectivity and the accompanying ligand architecture is closely linked to the evolution of metalloenzymes from the primordial soup, dictated by the response of species to massive environmental changes such as shifts in ocean acidity and metal solubility. Consequently, one of the central challenges of bioinorganic chemistry is the delineation of the biosynthetic mechanisms through which metalloenzymes arose, as these are fundamental to the understanding of our origins.

1.1.2 Iron-Sulfur Bonds in Nature

Sulfur is the fifth most abundant element, forming approximately 3% of the Earth's mass, and is mostly found in the core. Both elemental sulfur (a pyrophoric yellow solid) and H_2S (a pungent, malodorous gas) are emitted by volcanoes and undersea smoker vents, prompting sulfur's archaic name of brimstone meaning "burning stone". Sulfur forms part of the chalcogen group of elements, located under oxygen in the periodic table. Much of its chemistry is therefore similar to that of oxygen, although dramatic differences arise due to its electronic configuration ([Ne]$3s^2 3p^4$), which comprises filled 3p orbitals and low-lying empty 3d orbitals. By hybridising its s, p and d atomic orbitals to form new molecular orbitals (up to sp^3d^2), sulfur has access to many oxidation states, –2 to +6 (Figure 1).

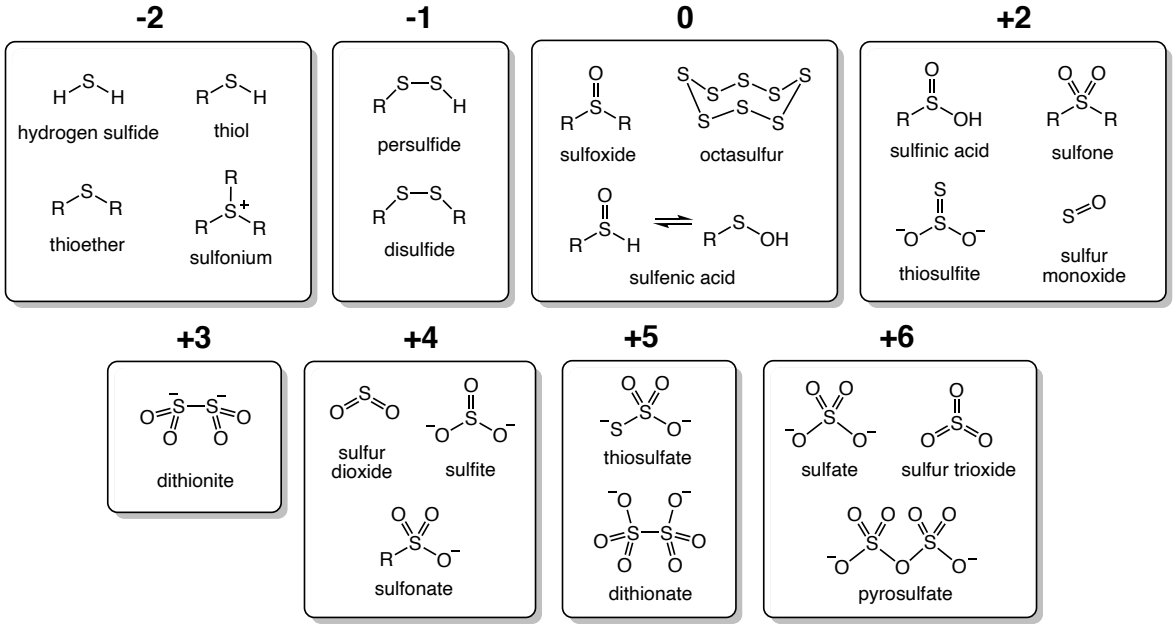

Figure 1. Examples of different sulfur-containing compounds, accessible through sulfur's many different oxidation states (highlighted in bold).

This chemical versatility means that sulfur is ubiquitously found across all living organisms and plays an essential role in metabolic, catalytic and structural biochemical processes.[9–11] For example: cysteine (Cys) and methionine (Met) are essential sulfur-containing amino acids, disulfide bridges (RS–SR) are often required for protein tertiary structure, and a wide range of important biomolecules (*e.g.* cofactor A, biotin, insulin) contain sulfur. Indeed, many scientists believe that life emerged from the presence of sulfur in the primordial soup. This has been extensively covered in other reviews.[12–15]

Fe–S bonds are abundantly found in Nature and are essential to biological function.[12,15,16] The binding affinity of iron and sulfur derives from the relatively small energy gap between the Fe 3d and the S 3p valence orbitals, which enables them to mix well upon formation of an Fe–S bond.[17] This results in a high degree of electron delocalisation across the bonds, giving them strong covalent character.[12,18] The electronic properties of the Fe–S bonds can be modulated by changing the properties of the constituent iron and sulfur atoms. Thiols, thiolates and sulfides are typical examples of electron-rich, easily polarisable "soft" ligands that have a high affinity for a "soft" Lewis acid such as Fe^{2+} (ferrous) ions. However, upon increased oxidation or oxygenation, the sulfur becomes less easily polarisable, qualifying it as a "harder" ligand that will tend to show a greater affinity for the more Lewis acidic Fe^{3+} (ferric) ions. From a structural point of view, sulfur ligands are capable of coordinating in a monodentate (*e.g.* a terminal cysteinate ligand) or bridging fashion (*e.g.* a sulfide dianion). Iron-sulfur complexes therefore encompass an enormous diversity of electronic and structural properties that can be tailored for specific biological requirements. Three different categories can be defined according to their nuclearity: mononuclear sites, dinuclear sites, or polynuclear clusters. Selected examples are given in Figure 2.

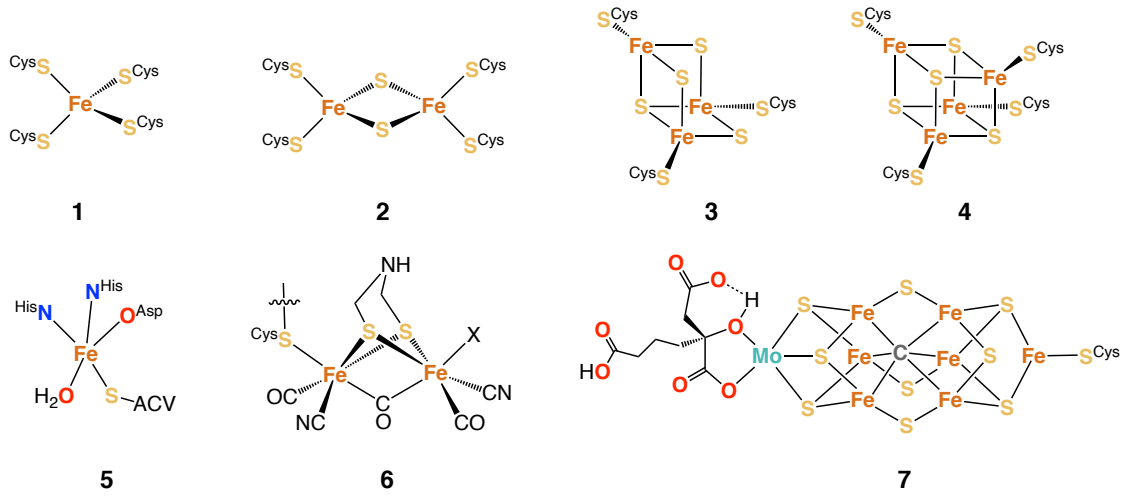

Figure 2. Examples of iron-sulfur complexes containing one (**1**), two (**2**), three (**3**) and four (**4**) iron centres. The mononuclear substrate-bound active site of isopenicillin N synthase (**5**) contains a single Fe–S bond. The dinuclear non-heme iron "H-cluster" from [FeFe] hydrogenase (**6**) contains two bridging thiolate ligands. The large "M-cluster" (FeMoco) from Mo-dependent nitrogenase consists of a [$MoFe_7S_9C$] cluster with a central carbide (**7**).

The most well-known examples of iron-sulfur proteins are those containing Fe–S clusters. These clusters (also referred to as prosthetic groups or cofactors) have a structure that is based on a rhomboid arrangement of two iron centres and two "naked" bridging sulfides, [2Fe–2S], which serves as a basic building block for larger structures of greater complexity.[19] One of the most common structures is the [4Fe–4S] cubane form composed of four iron and four sulfides, linked to the protein scaffold by terminal cysteinate ligands. Larger and more complex clusters are also found in enzymes such as [FeFe]-hydrogenase[20] and Mo-nitrogenase.[21] These clusters are perhaps most well-known for their ability to mediate electron transfer through changes in the iron oxidation state between +2 and +3, effectively giving them the function of biological "wires". Their high conductivity is linked to the fact that no structural changes occur as the iron changes oxidation state, resulting in an almost negligible energy barrier for electron transfer.[19] Typical examples of electron transfer proteins are ferredoxin and rubredoxin. The field of Fe–S clusters is extremely well established and has been extensively summarised elsewhere.[22–24]

In recent years, a small but rapidly growing number of mononuclear iron metalloenzymes has been identified whose active sites involve a single iron-sulfur interaction. The sulfur ligand takes the form of either an endogenous cysteine ligand (from the protein scaffold) or an exogenous sulfur ligand (such as a substrate molecule). This has prompted a greater examination of the role that the sulfur might play in promoting and directing enzyme reactivity or selectivity.

1.1.3 Scope

This review will examine the role of the single Fe–S bond found at the mononuclear iron active sites of seven different mononuclear heme or non-heme iron enzymes: cytochrome P450 (CyP450), superoxide reductase (SOR), nitrile hydratase (NHase), isopenicillin N synthase (IPNS), ethymalonic encephalopathy protein 1 (ETHE1), cysteine dioxygenase (CDO) and ergothioneine sulfoxide synthase (EgtB). A schematic representation of their active sites is given in Figure 3. These seven enzymes have been selected because they encompass a wide variety of active site structures and diverse reactivities. For instance, the iron centres of CyP450, SOR and NHase are bound axially to an endogenous cysteinate ligand, which imparts a *trans* effect that is crucial for determining enzyme reactivity. In contrast, IPNS, ETHE1, CDO and EtgB all form Fe–S bonds with an exogenous sulfur-rich substrate, which undergoes an oxidative transformation as the enzyme reacts with O_2. However, the nature of this transformation differs drastically depending on the enzyme. For example, CDO mediates sulfur dioxygenation whereas IPNS mediates C–N and C–S bond formation through H-atom abstraction. These seven enzymes encompass several different bioinorganic motifs at their active sites, including the heme porphyrin group in CyP450, the 2-His-1-Carboxylate facial triad (2H1C) in IPNS and ETHE1 and the 3-His facial triad (3His) in CDO and EgtB.

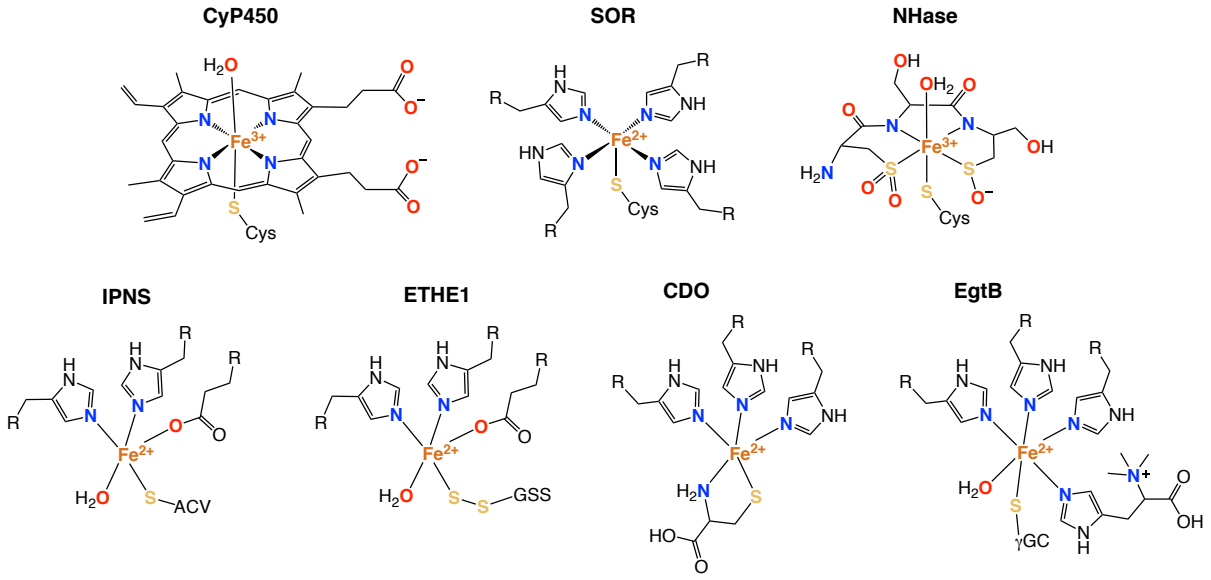

Figure 3. Active site structures of the CyP450, SOR, NHase, IPNS, ETHE1, CDO, and EgtB enzymes. The active sites of CDO and IPNS are depicted in their substrate-bound form. To date, no crystal structure of ETHE1 in complex with its substrate has been obtained, so the crystal structure of its resting state is given (Cys = cysteine; ACV = δ-(L-α-aminoadipoyl)-L-cysteine-D-valine; GSS = glutathione persulfide; γGC = γ-glutamyl cysteine).

In Section 1.2, key structural, mechanistic, electronic and spectroscopic considerations for each enzyme active site will be summarised. Particular emphasis will be given to the role of the sulfur ligand throughout. In Section 1.3, focus will be given to the structure and reactivity of relevant examples of bioinspired non-heme iron thiolate complexes that have been designed to probe the role of the sulfur ligand in enzyme catalysis. Their relevance to the parent enzyme active site will be discussed and a comparison of the different types of complexes will be provided in order to better understand why Nature utilises different bioinorganic motifs for different enzymes. Finally, the last section of this review (section 1.4) provides a summary of the over-arching trends and concepts underlying these iron-sulfur metalloenzymes and their respective biomimetic complexes. In this way, a conceptual "toolbox" is provided for better understanding and predicting sulfur-ligated enzyme reactivity and designing future non-heme iron catalysts.

1.2 Mononuclear Sulfur-Ligated Iron Enzymes

1.2.1 Cytochrome P450 (CyP450)

Cytochrome P450s (CyP450; EC.1.14) are a superfamily of monooxygenase heme iron enzymes found in bacteria and fungi as well as eukaryotic organisms, including mammals. To date more than 18,000 different CyP450 enzymes have been identified.[25] In humans, CyP450 enzymes are responsible for the hydroxylation of xenobiotic drugs, an important step in catabolic and detoxification processes.[26,27] CyP450s are also capable of mediating numerous other transformations including epoxidation, deformylation, sulfoxidation, dehalogenation, N-oxygenations, and N-/O-dealkylation. Due to their chemical versatility and biological importance, CyP450 enzymes have become the target of intense biochemical, medicinal, spectroscopic and computational research. CyP450s draw their name from the distinct Soret absorption band at 450 nm that arises in the presence of CO.

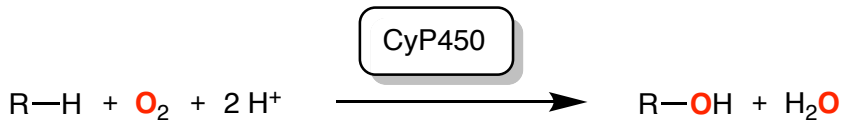

Scheme 1. General scheme for a hydroxylation reaction catalysed by CyP450 (R = organic substituent).

Structure. CyP450s active sites contain a low-spin ($S = {}^{1}/_{2}$) iron(III) ion coordinated to a porphyrin (heme) unit, which forms a dianionic N_4 tetradentate chelate in the equatorial plane of the iron coordination sphere. The iron centre is ligated to an anionic cysteinate at the proximal axial position, which links it to the protein scaffold. During the enzyme resting state, the site *trans* to the cysteinate ligand (the distal position) is typically populated by a water ligand, although it can also remain vacant, giving the iron centre a

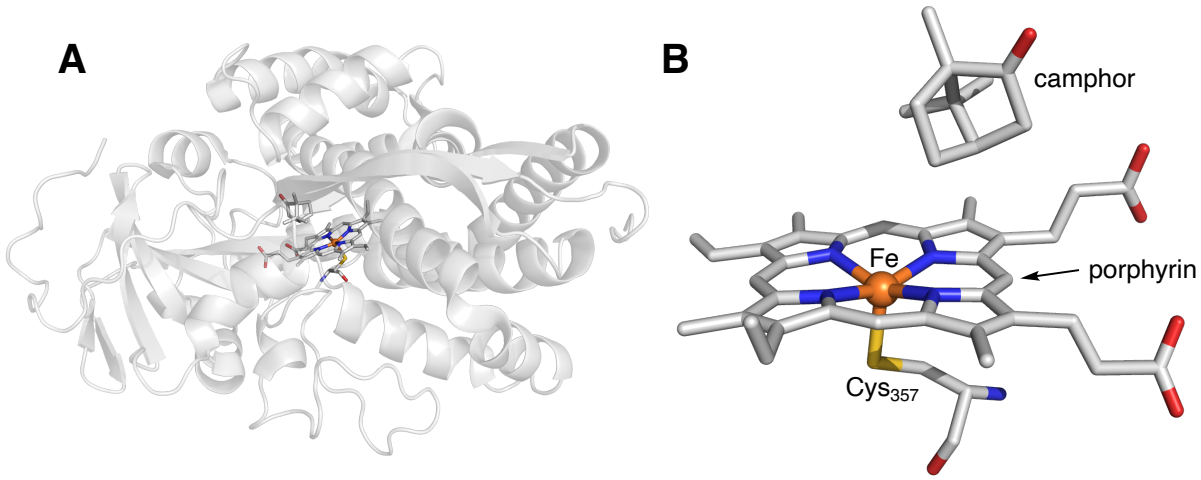

Figure 4. A: Protein crystal structure of CyP450cam from *Pseudomonas putida* (PDB 2CPP).[28] **B:** First coordination sphere of the active site in CyP450cam, depicted without the surrounding protein scaffold and with the substrate bound in close proximity. Carbon, iron, nitrogen, oxygen and sulfur are depicted in grey, orange, blue, red, and yellow, respectively.

(pseudo)octahedral geometry. Upon binding of the hydrophobic substrate, this water molecule is displaced and a pentacoordinate high-spin (S = $^5/_2$) iron(III) complex is generated, as exemplified by the crystal structure of CyP450cam (CYP101A1) in complex with its substrate, camphor (Figure 4).[28] This coordinatively unsaturated species is primed for reaction with O_2. The active site of CyP450s is buried deep within the protein scaffold, far from the enzyme's solvent boundary. The substrate (and product) therefore enters or leaves the active site cavity through specific access channels, typically gated by phenylalanine residues.[29,30]

Mechanism. In this review, a general mechanism for hydroxylation by CyP450 will be discussed.[25,27,31] Catalysis begins with the binding of the substrate (*e.g.* a hydrocarbon) to the active site cavity, within the vicinity of the low-spin (S = $^1/_2$) iron(III) centre (Scheme 2). This displaces the labile water molecule and initiates spin-crossover, generating a pentacoordinate high-spin (S = $^5/_2$) iron(III) centre (**A**). Its higher reduction potential triggers an electron transfer from a reductase redox partner, yielding a high-spin (S = 2) ferrous complex (**B**). O_2 binds readily with this species, forming an low-spin Fe^{3+}–OO^- complex (**C**).[25,26] The end-on superoxide ligand is further stabilised through H-bonding interactions with a water molecule and the hydroxyl side-chain of a threonine residue (Thr-252).[32] A second electron transfer event reduces the superoxide ligand to the peroxide dianion, forming a Fe^{3+}–OO^{2-} species (**D**). Protonation of the distal oxygen atom yields an Fe^{3+}–OOH intermediate (*Compound 0*). A second protonation of the distal oxygen atom triggers heterolytic O–O bond cleavage, releasing a water molecule with the concomitant formation of *Compound I*, a high-valent iron-oxo intermediate with a formal oxidation state of +5.[33] The oxidation state is assigned partly to the iron as Fe(IV) and partly to the

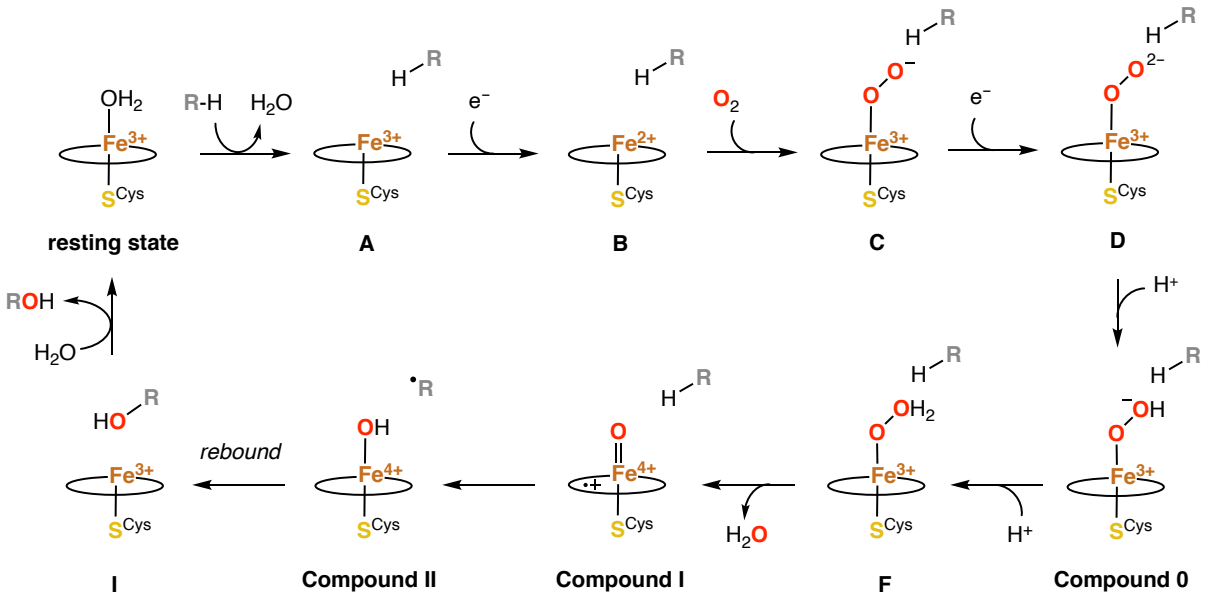

Scheme 2. Schematic representation of the general mechanism for hydroxylation catalysed by CyP450 enzymes. R-H is the substrate. The equatorial N_4 coordination of the porphyrin is depicted by an ellipsoid.

porphyrin ring as a π-cation radical. This gives rise to a pair of almost degenerate spin states, one being a quartet ($S = {}^3/_2$) and one being a doublet ($S = {}^1/_2$) with a spin-flip in the singly occupied porphyrin-based orbital. *Compound I* is the species responsible for H-atom abstraction,[34,35] which generates an Fe^{4+}–OH complex (*Compound II*) and a substrate radical. Recombination of the organic radical with the hydroxo ligand forms the final hydroxylated product and generates a low-spin pentacoordinate ferric complex (**I**), whose vacant site is swiftly repopulated by a H_2O molecule. For CyP450 enzymes, the electron donor is NADH or NADPH, and electron transfer is mediated by electron transfer proteins such as putidaredoxin reductase (PdR) and putidaredoxin (Pd).

Role of the thiolate. Reaching a consensus as to the role of the thiolate in Cy450 reactivity has been challenging due to the sheer number of reported CyP450 enzymes, whose reactivity depends not only on the thiolate but also on the size and nature of the substrate molecule, the second coordination sphere residues and the size of the binding pocket. The exact role of the thiolate therefore remains highly debated. In general, two principal factors are believed to underly the role of the thiolate ligand in CyP450 catalysis: (1) the covalency of the Fe–S bond, and (2) the thiolate's negative charge.

S K-edge XAS results from the Solomon group have shown that the Fe–S bond is highly covalent, with a total covalency of approximately 69% in the low-spin water-bound ferric resting state and 41% in the high-spin pentacoordinate substrate-bound intermediate (**A**).[36] The high covalency of the Fe–S bond correlates with a significant ligand-to-metal charge transfer (LMCT), also termed the thiolate "push-effect",[37] that raises the reduction potential of the ferric ion by approximately 130 mV. However, the one-electron reduction of the iron centre only takes place upon water dissociation and after spin-crossover of the iron has occurred.[38] The thiolate can therefore be considered a redox "switch" that is only activated upon substrate binding. As well as being a covalent ligand, the negative charge of the thiolate ligand introduces an electrostatic component to its "push-effect" that is important for raising the pK_a of *Compound 0*. Additionally, a mutagenesis study by Auclair *et al*. showed that substitution of the axial Cys for a neutral His residue reduces the electrostatic binding affinity of the PdR protein to the CyP450 enzyme, thereby significantly lowering the rate at which electron transfer can occur.[39] The role of the thiolate ligand therefore extends beyond simple first-coordination sphere electronic considerations.

DFT calculations have shown that the covalency of the Fe–S bond can be modulated by NH…S hydrogen bonds between the axial thiolate and peptidic amide groups in the secondary coordination sphere.[28,40] This is referred to as the "pull-effect", as the π-donicity of the thiolate is lowered. This has been proposed to help reduce the rotational barriers of the π-donor ligands coordinated *trans* to the thiolate. For *Compound 0*, this enables the hydroperoxide ligand to more easily engage in H-bonding with Thr-252, which is necessary for protonation of the distal oxygen atom.[27,36] For *Compound II*, faster reorientation of the hydroxide to a S–Fe–O–H *syn* conformation leads to a faster rate of hydroxyl rebound.[36] For *Compound I*, modulation of the Fe–S covalency has an effect on the extent of mixing

between the thiolate and the singly occupied porphyrin a_{2u} orbital,[26] which gives it the chameleonic character necessary to mediate a broad range of reactivity and selectivity patterns.[41,42] For CyP450cam, a single NH…S interaction is present involving the Gly-359 residue (Figure 5), although other CyP450 enzymes have been reported that have two such interactions.

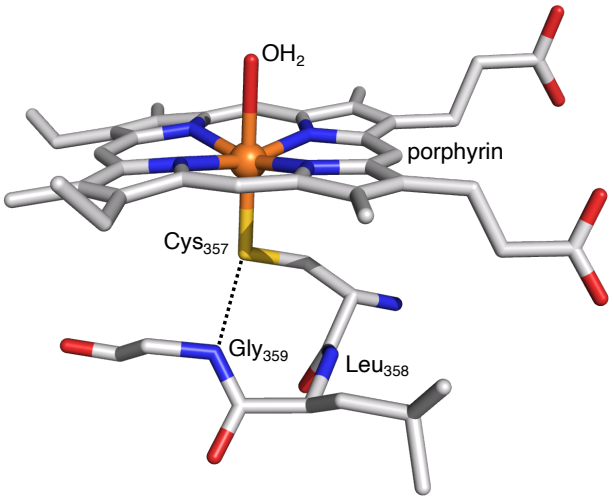

Figure 5. The low-spin six-coordinate active site of CyP450cam (PDB 1PHC),[43] depicted with the Cys-Leu-Gly tripeptidic unit. The NH…S hydrogen bond between glycine and cysteine is depicted with a dashed line.

Finally, the positioning of the active site cavity deep within the protein structure means that the access of water molecules is gated by a highly organised network of amino acid residues. This means that protonation of the proximal oxygen atom of *Compound 0* is kinetically unfavourable, which therefore promotes O–O bond cleavage and loss of a water molecule atom instead of Fe–O bond cleavage and loss of H_2O_2 as is observed in SOR enzymes (*vide infra*).

1.2.2 Superoxide Reductase (SOR)

Superoxide reductase (SOR; EC.1.15.1.2) enzymes are vital antioxidant agents that combat oxidative stress in microaerophilic and anaerobic microorganisms.[44–47] They catalyse the one-electron reduction of superoxide (O_2^-), a product of partial O_2 reduction, to H_2O_2 (Scheme 3). This prevents the superoxide radical from reacting in an undesired and uncontrolled manner with hydrogen peroxide or other biological radicals in the cell such as nitric oxide (NO), which would otherwise form toxic by-products such as peroxynitrite or hydroxyl radicals. SORs are distinct from superoxide dismutase (SOD) enzymes, as they do not catalyse the partitioning of the superoxide to molecular oxygen and hydrogen peroxide, which would be toxic to their anoxic host organisms. The electron donor required for superoxide reduction is widely accepted as being a reduced rubredoxin protein (Rbr). H_2O_2 produced by SORs is, in turn, reduced to H_2O by rubrerythrin.[48]

Scheme 3. General scheme for the reduction of superoxide by SOR.

Structure. To date, crystal structures have been obtained for two types of SOR, the 1Fe-SOR and 2Fe-SOR enzymes.[47,49,50] Both share a common domain, harbouring a mononuclear, high-spin (S = 2) iron(II) centre of square pyramidal geometry (centre II), ligated by four equatorial histidyl nitrogens and an axial cysteinate.[51] An open coordination site is available *trans* to the cysteinate ligand for superoxide to bind directly to the iron centre. The crystal structure of 1Fe-SOR from *Pyrococcus furiosus* is organised as a homotetramer, whose four subunits each contain a catalytic site close to the protein's solvent edge (Figure 6). The availability of protons at the active site is believed to be one of the principal factors favouring superoxide reduction rather than oxidation.[52] Additionally, the presence of four catalytic sites per enzyme ensures high catalytic activity, which enables SOR to successfully compete with the rate of spontaneous dismutation of O_2^- (~5 x 10^5 M^{-1} s^{-1} in H_2O at pH 7).[53] The 2Fe-SOR enzymes contain a second domain with a rubredoxin-like [Fe(Cys)$_4$] prosthetic group (centre I), whose function is not yet fully understood. For the purpose of this review, focus is given to the structure and reactivity of centre II.

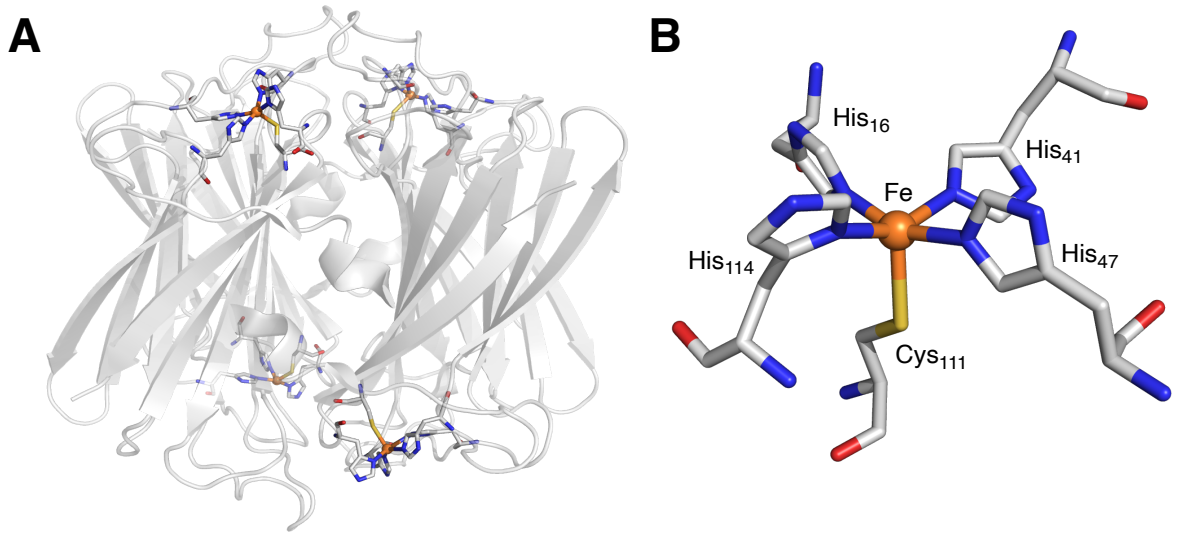

Figure 6. A: Protein crystal structure of SOR in its reduced state, from *Pyrococcus furiosus* (PDB 1DQK).[49] **B:** Structure of centre II from *Pyrococcus furiosus*, shown without the surrounding protein scaffold. Carbon, iron, nitrogen, oxygen and sulfur are depicted in grey, orange, blue, red, and yellow, respectively.

Mechanism. The reaction mechanism of SOR, involving the transfer of an electron and two protons to superoxide, has been the focus of many kinetic, spectroscopic and computational studies, and important contributions have been made by the groups of

Kurtz,[45,51,54,55] Nivière,[56–59] and Solomon.[60] A general mechanistic proposal has been agreed upon and will be discussed here (Scheme 4). For a more comprehensive review of the enzyme mechanism, the reader is referred to other reviews.[46,47,56]

The oxidised resting state (**R**) comprises a six-coordinate (6C) high-spin ($S = {}^5/_2$) octahedral ferric ion, featuring four equatorial histidine residues, an axial cysteinate, and a glutamate *trans* to the cysteinate.[49,61] An intense $S_{Cys} \rightarrow Fe^{3+}$ charge transfer (CT) band at 645 nm ($\varepsilon \sim 2000\ M^{-1}\ cm^{-1}$) is responsible for its distinct blue colour.[45] Catalysis begins with the one-electron reduction of **R** by rubredoxin, which induces a protein conformational change that displaces the glutamate away from the iron centre and creates a vacant site *trans* to the cysteinate.[46,47] This five-coordinate (5C) reduced resting state (centre II) is catalytically active. Next, superoxide binds end-on to centre II (at a rate of $\sim 1.2 \times 10^9\ M^{-1}\ s^{-1}$)[45] and is reduced *via* an inner-sphere mechanism to form a first intermediate, **T1**, with a CT band at 600 nm ($\varepsilon \sim 3500\ M^{-1}\ cm^{-1}$).[45,55,56] The nature of this intermediate is generally accepted as being an Fe^{3+}–OOH species, although there is some debate as to whether it forms directly by means of a proton-coupled mechanism or sequentially through superoxide protonation by a highly conserved lysine residue in the active site cavity.[49,54,56,57,62]

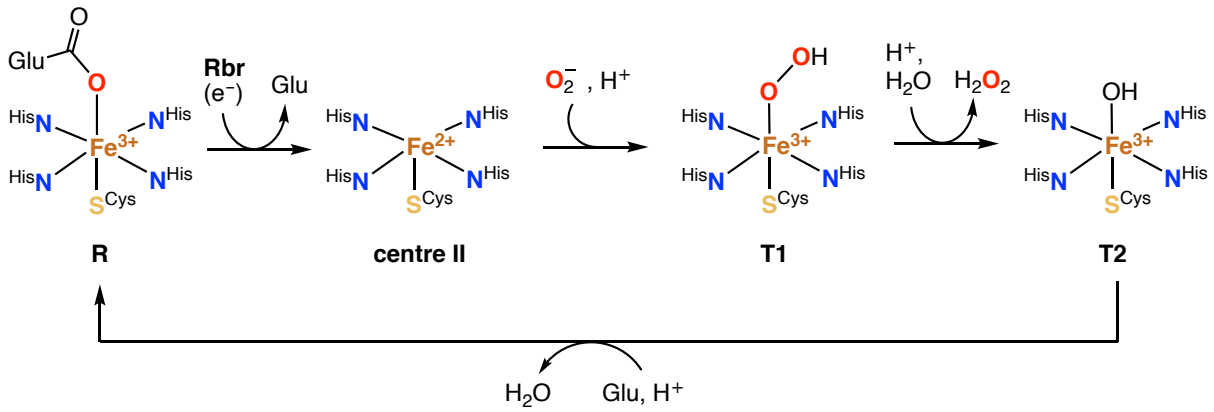

Scheme 4. Proposed general mechanism with which SORs catalyse the reduction of superoxide to hydrogen peroxide.

Both these proposals are supported by theoretical analysis.[45,58] Experiments by Clay *et al.* involving NO as a substrate analogue and DFT calculations by Dey *et al.* support the assignment of **T1** as a high-spin ($S = {}^5/_2$) Fe^{3+}–OOH species, although it should be noted that definitive assignment of the spin state has yet to be made.[60,62] **T1** decays through pH-dependent protonation of the hydroperoxide ligand's proximal oxygen atom, releasing H_2O_2 and generating the second intermediate, **T2**.[59] This intermediate is widely believed to be an iron(III)-hydroxo species, on the basis of its absorbance maximum at 580 nm.[47] Depending on the pH, this hydroxide ligand can undergo protonation to form a labile water ligand, enabling the glutamate residue to repopulate the coordination site and regenerating the catalytically inactive ferric resting state, **R**.

Role of the thiolate. Similar to CyP450, the iron centre in reduced SOR is square pyramidal in geometry, bound by an N_4S donor set. Both enzymes are also proposed to form an end-on Fe^{3+}–OOH intermediate, with the hydroperoxide ligand bound *trans* to the axial cysteinate. However, SOR subsequently undergoes Fe–O bond cleavage instead of O–O cleavage, with the consequence that its iron centre never exceeds the +3 oxidation state. This unique reactivity is proposed to derive principally from the anionic, covalent nature of the axial thiolate ligand that helps determine the redox potential, Lewis acidity and spin state of the iron centre. Indeed, S→Fe CT at SOR's active site ensures a Fe^{3+}/Fe^{2+} redox potential of ~250–300 mV, which is high enough to prevent autooxidation of the Fe^{2+} resting state in air but low enough to enable the one-electron reduction of the 6C Fe^{3+} state to the 5C Fe^{2+} state by Rbr during catalysis.[45] The covalent anionic nature of the thiolate ligand was also calculated to raise the pK_a of the Fe^{3+}–OOH intermediate, thereby lowering the energy of protonation of the hydroperoxide ligand by 7.5 kcal/mol relative to a non-covalent anionic ligand such as F^-.[60] Importantly, the axial thiolate in SOR participates in H-bonding with two amide NH groups of a conserved Cys–Asn–Leu/Ile–His tetrapeptide unit that links the cysteine to one of the histidine ligands in centre II (Figure 7).[51,63] These NH…S hydrogen bonds modulate the covalency of Fe–S bonds and make the anionic thiolate a weaker σ-donor.[40,64] This stabilises the 5C Fe^{2+} resting state and increases the Lewis acidity of the iron centre.[60] One of the major consequences thereof is that the 5C Fe^{3+} site formed upon H_2O_2 release has a greater affinity for binding of an anionic ligand (Glu or -OH) at the sixth coordination site than a superoxide ligand, which helps prevent superoxide dismutase activity in SOR.[45,60]

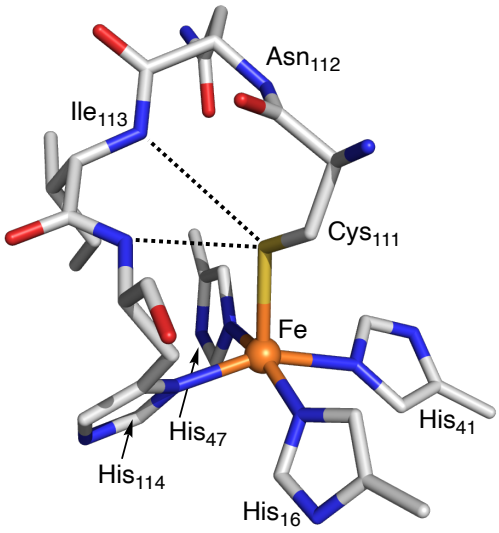

Figure 7. Reduced ferrous active site of SOR from *Pyrococcus furiosus* (PDB 1DQK)[49] including the Cys-Asn-Ile-His tetrapeptide unit. NH…S hydrogen bonding interactions are represented with dashed lines. Iron, carbon, nitrogen, oxygen, and sulfur are depicted in grey, orange, blue, red, and yellow, respectively.

Finally, the high-spin ($S = {}^5/_2$) electronic configuration of SOR's Fe^{3+}–OOH intermediate is believed to be a key factor in determining SOR's unique reactivity, as sulfur-to-iron CT

is therefore more readily donated into the σ^*(Fe–O) antibonding orbitals, labilising the Fe–O bond rather than the O–O bond.[46] SOR's high-spin state is generally believed to derive from the weak ligand field of its N_4S donor set. To elaborate, the four neutral histidine ligands are significantly twisted out of the equatorial N4 plane and the thiolate participates in H-bonding, whereby the donor strength of each group is reduced.[60] Moreover, O–O bond heterolysis analogous to that observed in CyP450 would result in the formation of an iron(IV)-oxo histidine cation radical, which has been calculated as being ~+250 kcal mol^{-1} uphill in energy, and is therefore highly unlikely.[45,46,60]

1.2.3 Nitrile Hydratase (NHase)

Nitrile hydratases (NHase; EC.4.2.1.84) are a class of metalloenzymes that catalyse the hydration (or partial hydrolysis) of nitriles to their respective primary amides under mild conditions (pH 7.5, ambient temperature). They occur in a variety of soil bacteria that are thought to exploit nitriles as their only source of carbon and nitrogen. Because amides are generally more susceptible to hydrolysis than their parent nitriles, it is extremely difficult to mediate the chemoselective hydration of nitriles by non-enzymatic means.[65] Currently, NHases are used industrially for the production of amides, including acrylamide,[66] nicotinamide,[67] and 5-cyanovaleramide[68], making them one of the most relevant metalloenzymes in biocatalysis.[46,67,69,70] Furthermore, NHase enzymes are also used for the removal of anthropogenic nitriles such as the herbicide bromoxynil in waste water remediation processes.[71–73]

Scheme 5. General scheme for the hydration of nitriles to amides, catalysed by nitrile hydratase (NHase).

Structure. NHases consist of two non-homologous subunits, α and β, that forms $\alpha_1\beta_1$ dimers or $\alpha_2\beta_2$ heterotetramers. The active site is located in the α subunit, at the interface with the β subunit. There are two different classes of NHases, harbouring either a low-spin ($S = {}^1/_2$) non-heme iron(III) ion or a low-spin ($S = 0$) non-corrinoid cobalt(III) ion at their active site (Figure 8). In both cases, the metal ion is bound by an identical N_2S_3 ligand set derived from the protein scaffold as well as a water molecule, resulting in an overall octahedral geometry.[74–76] The five ligands provided by the protein scaffold comprise two deprotonated peptidic amides and three cysteine-derived sulfur ligands, two of which have been post-translationally modified to the sulfenic ($CysSO^-$) and sulfinic ($CysSOO^-$) states.[77,78] The amide, sulfenic and sulfinic ligands are contained within a rigid 11-atom chelate that folds into an N_2S_2 equatorial plane, superimposable on the N_4 plane of a heme group.[75] The unmodified thiolate ($CysS^-$) ligand occupies the axial position *trans* to the

substrate binding site, similar to the axial coordination of the cysteine ligand in CyP450 and SOR. When stored in the dark, whole-cell samples of Fe-NHase become inhibited by nitric oxide (•NO), produced by the enzyme NO synthase, which displaces the axial water molecule at the active site.[79] The ^{113}SerOH, ^{114}CysSO^{-} and ^{112}CysSO$_2$ groups provide an axially orientated "claw setting" within which the NO ligand can reside.[74,80] Light exposure reactivates the enzyme by homolytically cleaving the Fe–NO bond and reinstating a H_2O/OH ligand.[79,81]

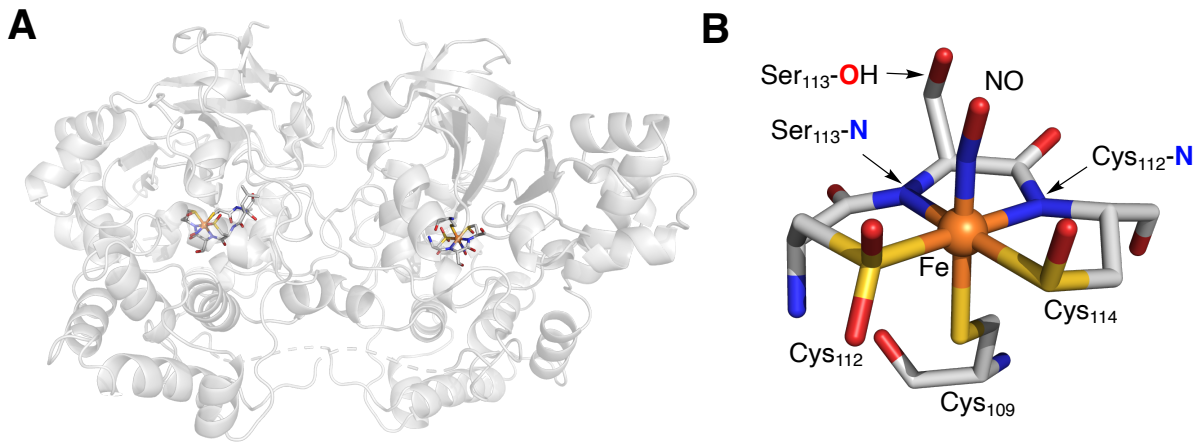

Figure 8. A. Full protein crystal structure of the (inactive) nitrosylated Fe-NHase from *Rhodococcus* sp. N771 (PDB 2AHJ).[80] **B.** First coordination sphere of the active site of nitrosylated Fe-NHase. Carbon, iron, nitrogen, oxygen, and sulfur are depicted in grey, orange, blue, red, and yellow, respectively.

Mechanism. Recent crystallographic, spectroscopic and computational studies from the groups of Holtz,[82–84] Odaka,[85,86] and Solomon[78,87] have shown that methylacrylonitrile, *tert*-butyl-isonitrile, butyric acid and alkylboronic acids coordinate directly to the iron centre in Fe-NHase, supporting the proposal that the native nitrile substrate is activated through direct coordination to the Lewis-acidic metal centre. These studies also invoke the role of the sulfenate as a catalytic nucleophile during the reaction. This has resulted in several mechanistic proposals, *Paths I*, *II*, *III* and *IV*, summarised in Scheme 6.

All mechanistic proposals start with the displacement of the labile axial water ligand by the nitrile substrate.[83,87] Light *et al*. have shown computationally that nitrile coordination is dependent on the low-spin ($S = {}^{1}/_{2}$) state of the iron centre and does not occur when the iron is in a higher spin state.[87] Next, nucleophilic attack on the nitrile carbon atom by an oxygen-rich group takes place. It was initially proposed that an outer-sphere water molecule, H-bonded to the sulfenate ligand, could perform this nucleophilic attack (*Path I*).[85,88] However, DFT calculations have shown that the transition state for this reaction lies much higher in energy compared to that of the nucleophilic attack by the equatorial sulfenate oxygen atom (*via* an inner-sphere mechanism), which forms a five-membered cyclic intermediate (*Path II*, *III*, *IV*).[78,89]

Following sulfenate attack, the S–O bond of the cyclic intermediate must be cleaved in order to generate an iron-bound iminol structure. Several mechanistic possibilities have been considered for this transformation, including the nucleophilic attack of an activated water molecule on either the C-atom or the S-atom of the cyclic intermediate (*Path II* and *Path III*, respectively). Experiments using labelled water ($H_2{}^{18}O$) have confirmed that the product amide oxygen takes its source from the NHase protein, supporting *Path III*.[90] Light *et al*. also showed that *Path II* is unlikely to occur due to an unfavourable transition state energy.[78] Alternatively, Hopmann *et al*. envisaged that nucleophilic attack on the sulfur atom of the cyclic intermediate by the axial thiolate ligand could occur, rather than by a water molecule (*Path IV*). This pathways produces a disulfide-bound iron-iminol intermediate,[89] after which a series of protonation and hydrolysis steps are proposed to regenerate the water-bound NHase active site. However, the theoretical spectroscopic parameters calculated for the disulfide-bound intermediate are not consistent with empirical spectroscopic data, therefore making *Path IV* unlikely.[83,87] Based on these studies, *Path III* is the most likely mechanism for NHase, although further experimental and computational studies are required for a definite mechanistic description to be made.

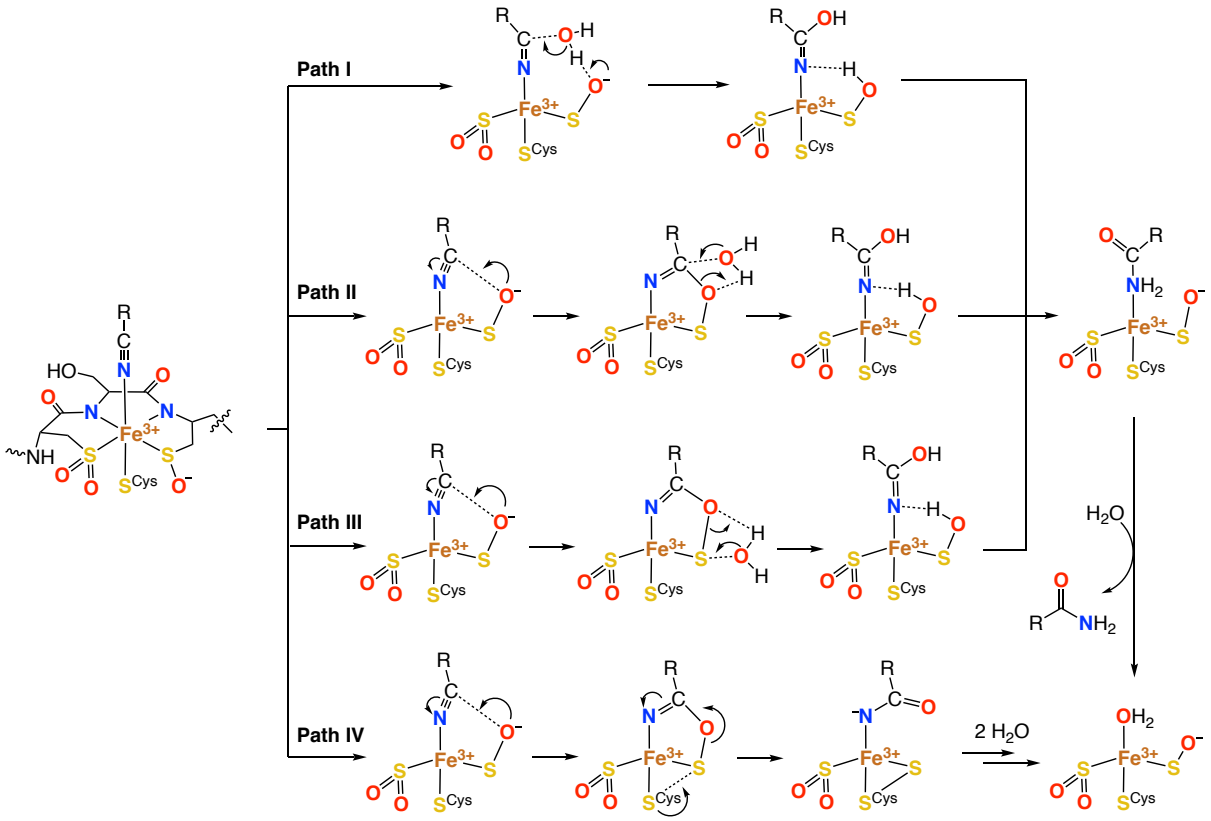

Scheme 6. Proposed mechanistic pathways by which Fe-NHase operates.

Role of the thiolate. NHase enzymes comprise an assembly of unusual coordination features that have long fascinated the bioinorganic community. Amongst these is the presence of three anionic sulfur-rich ligands that exist in different oxygenation states as well as two deprotonated amido groups. The coordination of five anionic ligands at the

NHase active site should, in principle, make the environment about the metal centre electron-rich.[46] However, DFT calculations indicate that charge neutrality is retained at the active site and that the iron centre is even moderately positively charged.[91] One of the ways in which electron density is diverted away from the metal centre is through the post-translational oxygenation of the equatorial cysteine residues, which decreases their donicity and increases the Lewis acidity of the metal centre.[46,73,78] Indeed, it was shown that the absence of S-oxygenation causes a loss in NHase catalytic activity.[77] Intriguingly, the "over-oxygenation" of the equatorial sulfur positions to a symmetric bis-sulfinate state was also shown to cause a loss in activity, demonstrating the mechanistic relevance of the sulfenate moiety.[77,92] Charge neutrality at the NHase active site is also ensured through the presence of two positively charged arginine residues (Arg-56 and Arg-141) in the active site cavity, which lie close enough to participate in H-bonding with the sulfinate and sulfenate moieties.[80,93]

The most electron-rich cysteinate ligand (Cys-109) is bound *trans* to the substrate binding site. EPR, MCD, and DFT data suggest that this ligand is the strongest π-donor and controls the orientation of the half-occupied t_{2g} d_{xy} orbital. Light *et al*. estimate that the axial cysteinate has a *trans*-labilising effect, promoting the dissociation of the water and amide molecules bound to the iron at the beginning and at the end of the catalytic cycle, respectively. However, it is not believed to participate to any significant degree in the activation of the nitrile substrate. From modelling studies in the group of Kovacs, the axial cysteinate has been described as being an electronic buffer that helps maintain a relatively constant Lewis acidity of the metal centre (*vide infra*). In EPR spectroscopy, the low-spin ($S = {}^1/_2$) ferric centre of photoactivated Fe-NHase has g values of $g_x = 2.27$, $g_y = 2.13$ and $g_z = 1.97$,[94] which are significantly lower than those of low-spin Fe^{3+} heme complexes ($g_{max} = 2.45$). This indicates a higher degree of covalency between the metal centre and the axial cysteinate ligand in Fe-NHase.

1.2.4 Isopenicillin N Synthase (IPNS)

Isopenicillin N synthase (IPNS; EC.1.21.3.1) is a mononuclear non-heme iron enzyme that belongs to a superfamily of enzymes containing the 2-His-1-Carboxylate (2H1C) facial triad at their active site. It catalyses the oxidative bicyclisation of δ-(L-α-aminoadipoyl)-L-cysteine-D-valine (ACV) to isopenicillin N (IPN), using molecular oxygen as the oxidant (Scheme 7). Strikingly, none of the constituent atoms of dioxygen are incorporated within the final product. Instead, two aliphatic C–H bonds are activated to form a new C–N and C–S bond, closing the β-lactam and thioazolidine rings of IPN, respectively, and O_2 undergoes a four-electron reduction to two equivalents of water. IPNS is therefore classified as a cofactor-independent oxidase enzyme. Its unique reactivity and its relevance to the production of β-lactam antibiotics has long fascinated the bioinorganic community, making it one of the most well-studied non-heme iron enzymes of all time.

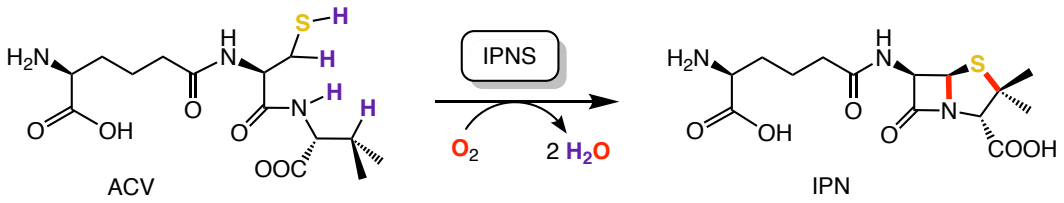

Scheme 7. The oxidative bicyclisation of ACV to IPN, catalysed by IPNS.

Structure. At its active site, IPNS contains a mononuclear high-spin ($S = 2$) iron(II) centre, facially capped by two histidine residues (His) and an aspartate (Asp) residue that constitute the 2H1C (Figure 9). In the resting state, a loosely bound glutamine residue (Gln) and two water molecules occupy the coordination sites *trans* to the 2H1C.[95] The tertiary structure of IPNS consists of a double-stranded β-helix ("jelly roll") core, very similar to that observed in many α-ketoglutarate-dependent mononuclear non-heme iron enzymes. Important structural and spectroscopic studies conducted in the Baldwin group showed that ACV binds directly to the iron centre as a monodentate thiolate trans to the His-270 residue, displacing two of the labile water ligands.[96] The sulfur-to-iron charge transfer as well as the decrease in coordination number also give rise to a more electron-rich environment around the iron centre, which is manifested spectroscopically by a decrease of the ^{57}Fe Mössbauer isomer shift from 1.30 mm s^{-1} for the resting state to 1.10 mm s^{-1} for the substrate-bound complex.[97] On the basis of experiments using NO as an O_2 surrogate, it was shown that the dioxygen binding site is likely to be *trans* to the Asp-216 residue, *cis* to the substrate's ligated thiolate.[96]

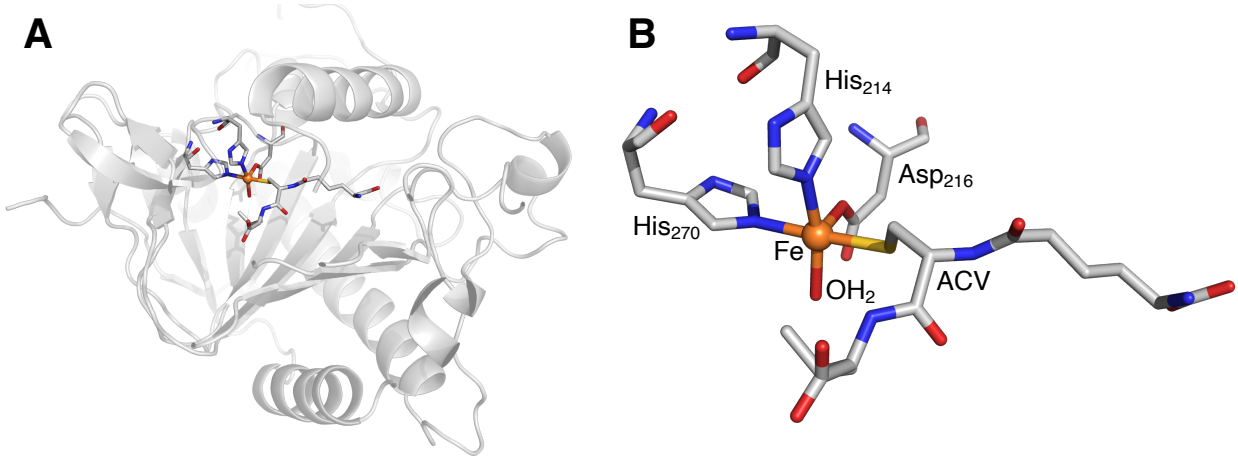

Figure 9. A: Full protein X-ray crystal structure of substrate-bound IPNS from *Aspergillus nidulans* (PDB 1BK0).[96] **B:** Structure of the substrate-bound active site of IPNS from *Aspergillus nidulans*, shown without the surrounding protein scaffold. Carbon, iron, nitrogen, oxygen and sulfur are depicted in grey, orange, blue, red and yellow, respectively.

Mechanism. The mechanism of IPNS (Scheme 8) has been extensively investigated since the early 1980s by the group of Baldwin, by means of enzymological, spectroscopic, kinetic and substrate analogue studies.[98] Catalysis is initiated by the binding of the ACV substrate to the enzyme's iron centre through its anionic cysteinyl sulfur atom *trans* to the His-270

residue (**A**). This displaces the glutamine residue (Gln-330) and one of the water molecules and, in doing so, triggers a conformational change in the protein's tertiary structure that encloses ACV rigidly within the active site cavity. Next, end-on O_2 binding to the coordinatively unsaturated iron centre, *trans* to the Asp-216 residue, leads to the formation of an high-spin (S = 2) iron(III)-superoxide intermediate (**B**), which was recently detected spectroscopically.[99] DFT calculations suggest that this intermediate consists of a high-spin (S = $^5/_2$) Fe^{3+} centre antiferromagnetically coupled to $O_2^{\bullet-}$ (S = $^1/_2$).[96,100,101] This intermediate is responsible for the first aliphatic C–H bond activation, where the *pro-3-S* hydrogen of ACV's cysteinyl residue is abstracted and an iron(II)-hydroperoxo species is formed (**C**). Subsequent electron transfer from the bound thioalkyl radical to the iron(III) centre yields an iron(II)-hydroperoxo intermediate with a thioaldehyde ligand (**D**). Deprotonation of the amide by the hydroperoxide's distal oxygen atom leads to O–O heterolysis and loss of water, in concert with the nucleophilic attack of the amide on the thiocarbonyl. This generates a high-spin (S = 2) iron(IV)-oxo complex with a *cis*-coordinated thiolate from the monocyclic β-lactam intermediate (**E**). This highly oxidising intermediate, which was recently detected spectroscopically,[99] performs the second H-atom abstraction at the tertiary valinyl *β*-carbon, forming a high-spin (S = $^5/_2$) Fe^{3+}–OH intermediate bound to a valinyl radical (**F**). Attack of the radical on the thiolate closes the thiazolidine ring, completing the formation of the bicyclic IPN product, which binds to the iron(II) centre through its thioether moiety (**G**).[102]

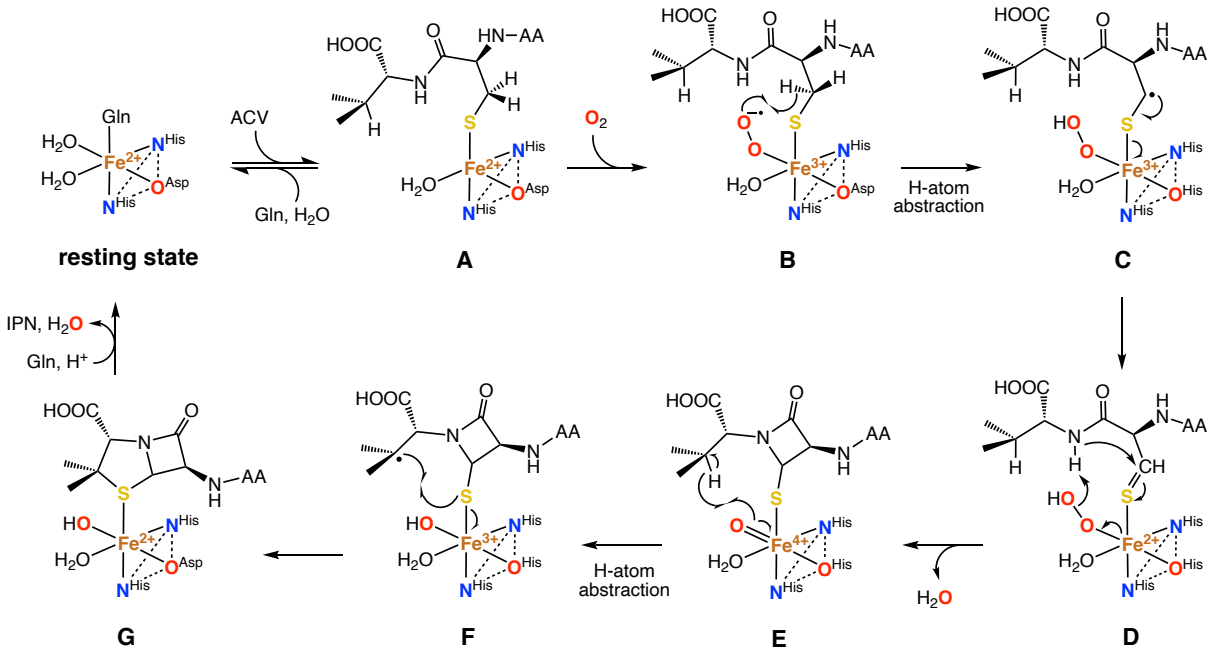

Scheme 8. Generally accepted mechanism for the oxidative bicyclisation of ACV to IPN, catalysed by IPNS.

Role of the thiolate. The selectivity of IPNS for H-atom abstraction rather than sulfur oxygenation remains a very open and active discussion, particularly when contrasted to the S-oxygenation reactivities of ETHE1 and CDO (*vide infra*). It appears to be linked to

three principal factors. The first is the enzyme's substrate specificity to ACV,[103] whose steric and electronic properties are optimally tuned to activate bicyclisation activity. Indeed, the valine's hydrophobicity helps keeps the iron centre coordinatively unsaturated and free of excess water molecules.[98,104–106] The valine's steric bulk also helps prevent the formation of a bridged Fe–O–O–S intermediate, making S-oxygenation kinetically unfavourable (calculated as being energetically uphill by ~4 kcal mol^{-1} compared to native H-atom abstraction).[100,104] Moreover, the steric bulk helps install a particular substrate conformation within the active site cavity, enabling ACV to bind as a monodentate ligand and ensuring that the NH group points towards the iron centre. Secondly, ACV's thiolate-to-metal charge transfer and the accompanying decrease in coordination number upon ACV binding generates a significantly more covalent environment around the iron nucleus, which modulates the iron redox potential in favour of dioxygen binding and promotes the correct Fe^{3+}–$O_2^{\bullet-}$ π^* orbital for H-atom abstraction at the cysteinyl Cβ–H bond.[101] Finally, the site of O_2 binding *trans* to the anionic O-donor of the Asp-216 residue is believed to be a key factor determining subsequent reactivity of IPNS. Indeed, mutagenesis showed that an almost complete loss in enzymatic activity occurs when substituting the Asp for a neutral His residue.[107] The coordination of O_2 *trans* to the Asp residue ensures good proximity between the terminal oxygen atom of an η^1-$OO^{\bullet-}$ ligand and the cysteinyl Cβ–H bonds, which are orientated away from the coordination site *trans* to the His-214 residue.[108] Coordination *trans* to the anionic Asp residue also means that the superoxo ligand experiences a greater *trans* effect than it would from a histidine residue. As previously discussed for SOR, this could aid the labilisation of the Fe–O bond rather than the O–O bond.

1.2.5 Ethylmalonic Encephalopathy Protein 1 (ETHE1)

Ethylmalonic encephalopathy protein 1 (ETHE1; 1.13.11.18) is a persulfide dioxygenase (PDO) enzyme found in the mitochondria of bacterial and eukaryote organisms.[109] It catalyses the dioxygenation of glutathione persulfide (GSSH), producing glutathione (GSH) and sulfite (SO_3^{2-}) (Scheme 9). In humans, its malfunction is closely tied to ethymalonic encephalopathy, a rare autosomal recessive disorder that causes severe neurological and gastrointestinal symptoms, ultimately leading to fatal sulfide toxicity.[110] ETHE1 belongs to the metallo-β-lactamase superfamily of enzymes and is similar in sequence to the glycolase II proteins, although it does not exhibit glycolase II activity.[111]

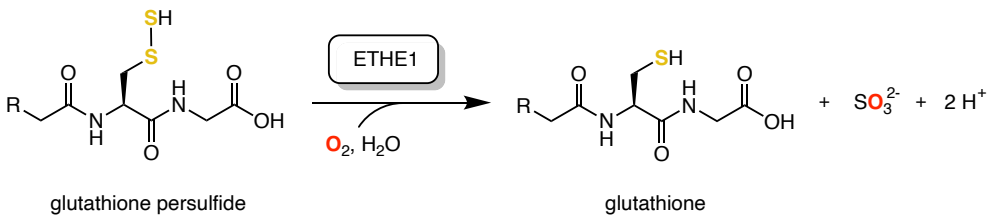

Scheme 9. The conversion of glutathione persulfide to glutathione and sulfite by ETHE1.

Structure. The overall protein structure of ETHE1 is dimeric and each monomer features a mononuclear high-spin (S = 2) non-heme iron(II) centre, facially capped by the 2H1C.[111,112] During its resting state, three water molecules populate the opposite face of the iron's octahedral coordination sphere. Recent spectroscopic efforts by Goudarzi *et al.* suggest that persulfide binding displaces one or two labile water ligands to yield a five- or six-coordinate substrate-bound complex.[100] To date, no crystal structure of ETHE1 in complex with its substrate has been obtained, due to the instability of the persulfide. However, DFT calculations predict the persulfide to bind as a monodentate anionic persulfide ligand *trans* to the neutral His-79 residue, with the dioxygen binding site located *trans* to the anionic O-donor of Asp-154 (Figure 10). The strong similarities between the substrate-bound active sites of IPNS and ETHE1 have stimulated investigations into the factors determining sulfur oxidation versus sulfur oxygenation.[100]

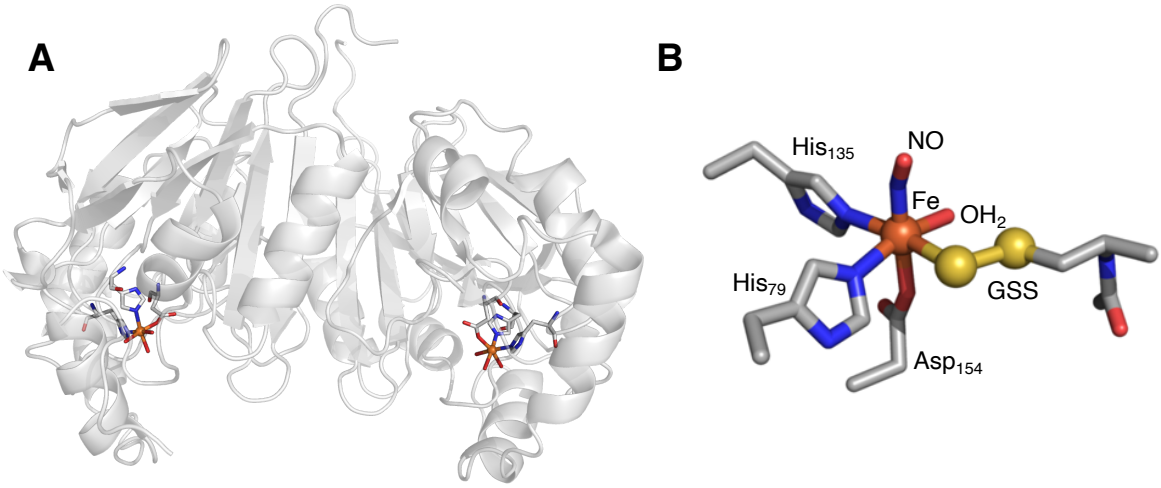

Figure 10. A: Protein crystal structure of ETHE1 in its resting state from *Homo sapiens* (PDB 4CHL). **B:** The truncated DFT-optimised substrate-bound active site structure of ETHE1. Figure reprinted with permission from Goudarzi, S.; Babicz, J. T.; Kabil, O.; Banerjee, R.; Solomon, E. I., *J. Am. Chem. Soc.* **2018**, 140, 44, 14887-14902. Copyright 2018 American Chemical Society. Carbon, iron, nitrogen, and oxygen are depicted in grey, orange, blue, and red, respectively.

Mechanism. Many biomedical studies have focused on the impact of specific gene sequence mutations on the development of ethylmalonic encephalopathy. However, spectroscopic, kinetic and computational studies investigating the mechanism that takes place at the iron active site remain, to date, rather scarce. In general, the mechanism for ETHE1 is believed to be similar to that of thiolate dioxygenase enzymes (see section 1.2.7), as the terminal sulfur atom of the persulfide substrate is dioxygenated. However, an additional hydrolysis step occurs in ETHE1 that cleaves the S–S bond to yield sulfite and glutathione. This final hydrolysis step is essential to avoid enzyme inhibition by the oxygenated persulfide.[113] A general mechanism has been proposed by the groups of Liu and Solomon, shown in Scheme 10.

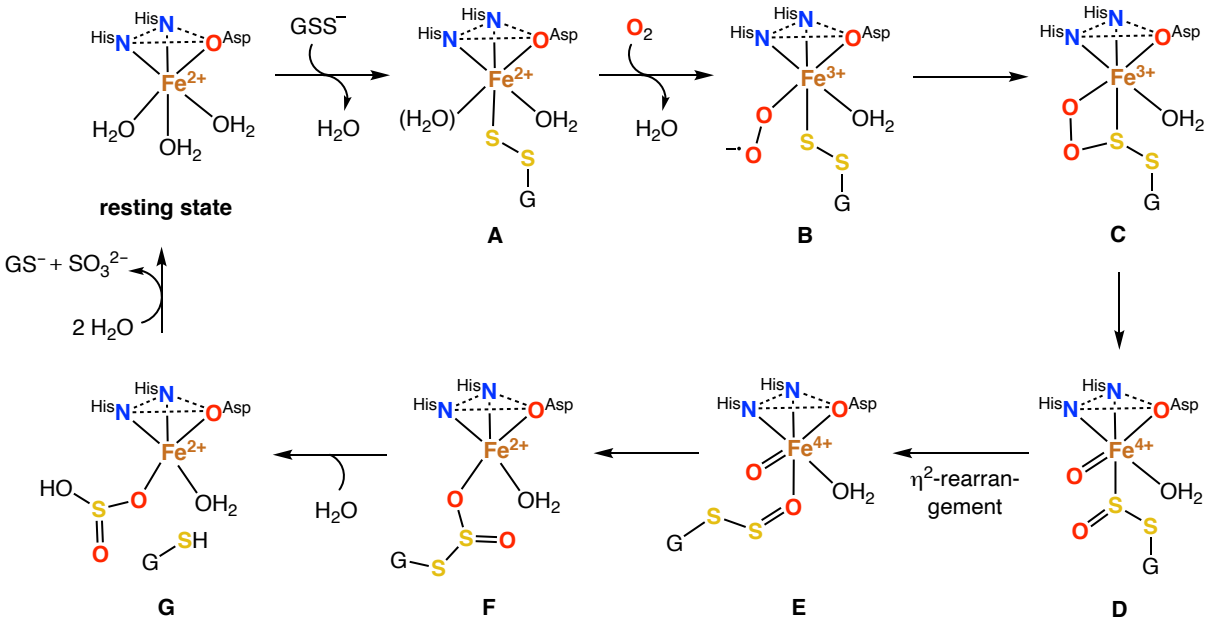

Scheme 10. Proposed mechanism for ETHE1, which catalyses the dioxygenation of glutathione disulfide (GSSH), forming glutathione (GSH) and sulfite.

Catalysis begins with the binding of the sulfur-rich substrate directly to the iron centre, *trans* to His-79, displacing one or more labile water molecules from the resting state. Near-IR, MCD (magnetic circular dichroism), and VTVH MCD (variable temperature variable field MCD) spectroscopies have shown that substrate binding yields a 5- or 6-coordinate substrate-bound ferrous complex (**A**) that is "primed" for dioxygen binding.[100] Computational docking studies predict a monodentate binding mode for the GSS^- substrate due its relatively large size and the constraints imposed by the active site pocket. An electrostatic interaction between the glycinyl carboxylate group and Arg-214 and a hydrogen bonding interaction between the cysteinyl amide and Tyr-197 are alsobelieved to promote monodentate binding for the persulfide.[100,112] Dioxygen subsequently binds end-on to the iron, *trans* to Asp-154, forming an (S = 2) iron(III)-superoxide intermediate (**B**) that consists of a high-spin (S = 5/2) Fe^{3+} centre antiferromagnetically coupled to the $O_2^{\bullet-}$ ligand (S = $^1/_2$), as was the case for IPNS.

Computational modelling of the enzyme's spectroscopy suggests the persulfide is likely to be orientated with a O^{O2}–Fe–S–S dihedral angle of approximately 90°, with respect to the dioxygen binding site (see Figure 10B), ensuring optimal orbital overlap between $O_2^{\bullet-}$ and GSS. Next, electrophilic attack of the superoxide's distal oxygen atom on the coordinated sulfur atom of the persulfide substrate is proposed to occur, forming a cyclic Fe–O–O–S peroxy-bridged ferric intermediate (**C**) that parallels the CDO reaction coordinate (see section 1.2.7).[100,114] Cleavage of the O–O bond subsequently occurs, yielding a high-valent iron(IV)-oxo intermediate with a sulfur-coordinated persulfenate moiety (**D**). A geometric rearrangement of the η^2–S=O coordination mode is proposed to take place, resulting in a high-valent iron(IV)-oxo species with an oxygen-coordinated persulfenate moiety (**E**). This rearrangement is necessary to make the remaining oxidisable sulfur orbitals available for

oxygen atom transfer (OAT).[100] OAT occurs by means of a stepwise, 2-electron transfer from the sulfur to the oxo ligand, thereby breaking the Fe–O bond, creating the new S–O bond and reducing the iron to its ferrous state, (**F**). Finally, hydrolysis of the deoxygenated persulfide's S–S bond occurs (**G**), releasing sulfite and glutathione from the active site.

Role of the thiolate. A persulfide is a weaker donor than a thiolate due to the delocalisation of its π* HOMO orbital across two sulfur atoms rather than one.[100] Spectroscopically, this is manifested by a weaker and lower-energy persulfide LMCT band in the [Fe·ETHE1·GSS·NO] spectrum compared to the intense thiolate LMCT band in the [Fe·IPNS·ACV·NO] spectrum.[100,101] Similarly, the DFT-calculated Fe–S bond length of the [Fe·ETHE1·GSS·NO] complex is longer than than that of the [Fe·IPNS·ACV·NO] complex (2.55 Å versus 2.33 Å, respectively).[96] Nonetheless, charge donation from glutathione persulfide to iron is sufficient to modulate the redox potential of the iron centre in favour of O_2 binding ($\Delta G = -1.5$ kcal mol^{-1}). For comparison, O_2 binding directly to the resting state without the persulfide is calculated as being significantly endergonic ($\Delta G = +8.9$ kcal mol^{-1}).[100] In fact, DFT calculations suggest that GSS charge donation to the iron centre in ETHE1 promotes the same π* FMO in the $O_2^{\bullet-}$ ligand in ETHE1 as the ACV charge donation does in IPNS. However, unlike IPNS, sulfur dioxygenation occurs in ETHE1. This discrepancy is believed to derive from a combination of several factors. Firstly, the first available C–H bond in the GSS substrate is separated from the iron centre by an extra sulfur atom, placing it significantly further away from the superoxide ligand. Secondly, the second sphere interactions holding GSS in place in the active site cavity are not located near the persulfide moiety, making the local environment around the Fe less constrained than in IPNS. The formation of a bridged peroxy intermediate is therefore more favourable in ETHE1. Lastly, DFT calculations show optimal overlap between the $O_2^{\bullet-}$ FMO and the persulfide HOMO, making sulfur dioxygenation the most thermodynamically favourable reactivity.

1.2.6 Cysteine Dioxygenase (CDO)

Cysteine dioxygenase (CDO; EC.1.13.11.20) is a mononuclear non-heme iron enzyme that catalyses the dioxygenation of L-cysteine to its cysteine sulfinic acid (CSA) using molecular oxygen (Scheme 11).[115–117] It is a highly regulated enzyme that plays an important role in cysteine catabolism, as high levels of cysteine are linked to cytotoxic and neurological disorders, including cancer and Alzheimer's disease.[118,119] CDO is a member of an emerging class of iron enzymes known as the thiol dioxygenases (TDO),[120] which include aminothiol dioxygenase (ADO),[121,122] 3-mercaptopropionate dioxygenase (3MDO),[123,124] and mercaptosuccinate dioxygenase (MSDO).[125] As CDO is the most well-studied of these enzymes to date, this review will restrict the discussion to CDO.

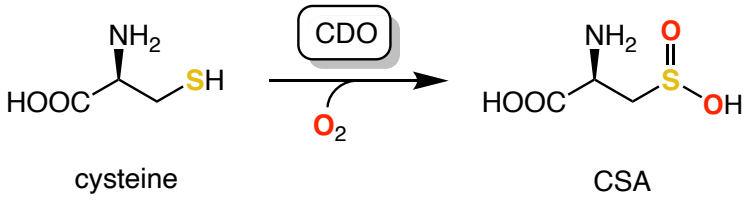

Scheme 11. The conversion of cysteine to cysteine sulfinic acid by CDO.

Structure. CDO contains a mononuclear high-spin (S = 2) iron(II) centre at its active site, facially capped by three neutral histidine residues, which together are better known as the 3-His facial triad (3His).[117,126,127] During the enzyme's resting state, the three remaining coordination sites are occupied by labile water molecules and sometimes a chloride ion.[128] CDO from rat,[129,130] mouse,[126] and human[117,131] have been isolated and purified, and crystal structures have been reported in all cases. Another important structural feature is the presence of a conserved sequence of second-sphere residues (Ser-His-Tyr) within 3.3 Å of the iron centre. In mammalian CDO, the tyrosine (Tyr-157) residue of this sequence has undergone a post-translational modification and is covalently crosslinked with a cysteine (Cys-93), forming a Y157-C93 pair.[117] Bacterial CDO, on the other hand, utilises an unmodified Tyr residue at this position.[132] Catalysis in CDO begins with the bidentate coordination of cysteine to the iron through its amine and thiolate groups, which displaces all water molecules and generates a pentacoordinate, high-spin (S = 2) iron(II) species primed for O_2 binding (Figure 11).[131] Additionally, cysteine's carboxylate group engages in a salt bridge with Arg-60 from CDO's protein scaffold, which ensures correct substrate orientation within the active site cavity.[128]

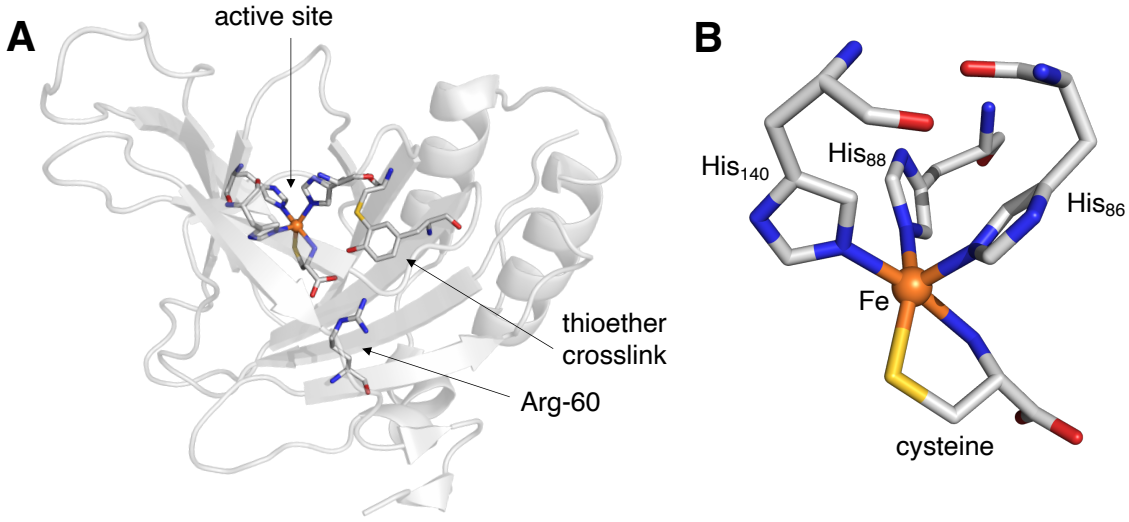

Figure 11. A: Protein crystal structure of CDO from *Homo sapiens* (PDB 4IEV).[131] **B:** Structure of the first coordination sphere in the cysteine-bound active site of CDO from *Homo sapiens*. Carbon, iron, nitrogen, oxygen, and sulfur are depicted in grey, orange, blue, red, and yellow, respectively.

Mechanism. The mechanism of CDO has been extensively studied through enzymology,[132–134] kinetics,[135–137] and spectroscopy,[127,136–139] supported by computational work,[114,139–142] and substrate analogue studies.[127,143,144] One of the most intriguing research questions is why CDO mediates the dioxygenation of its cysteine substrate while IPNS (*vide supra*) or EgtB (*vide infra*) exhibit oxidase and mono-oxygenase reactivity with their cysteine-derived substrates, respectively. However, owing to the difficulty in isolating reactive intermediates, the mechanism has been surprisingly difficult to elucidate and no single consensus mechanism for CDO has yet been reached. Two mechanistic proposals have been put forward in previous literature, shown in Scheme 12.

Both mechanisms start with the bidentate coordination of the cysteine ligand to iron, followed by the formation of an low-spin ($S = {}^1/_2$) iron(III)-superoxo complex (**A**) as O_2 binds end-on at the site *trans* to the His-86 residue. From this point on, the two mechanisms diverge. In *Path I*, spin-crossover occurs from the singlet to the quintet state as the distal oxygen atom of the superoxo ligand attacks the iron-bound sulfur atom to form a cyclic Fe–O–O–S iron(III) intermediate (**B'**).[100,114,141] Homolytic cleavage of the O–O bond generates a high-valent oxoiron(IV) species with a bound sulfenate moiety (**C'**). Next, a geometric η^2-rearrangement of the S=O bond occurs such that the sulfenate's oxygen atom is ligated to the iron, making the sulfur atom more prone to oxidation (**D'**).[100,141] After this, OAT can occur to the sulfur atom, forming the sulfinic acid product. In *Path II*, the proximal atom of the superoxo ligand attacks the iron-bound sulfur atom, forming a three-membered

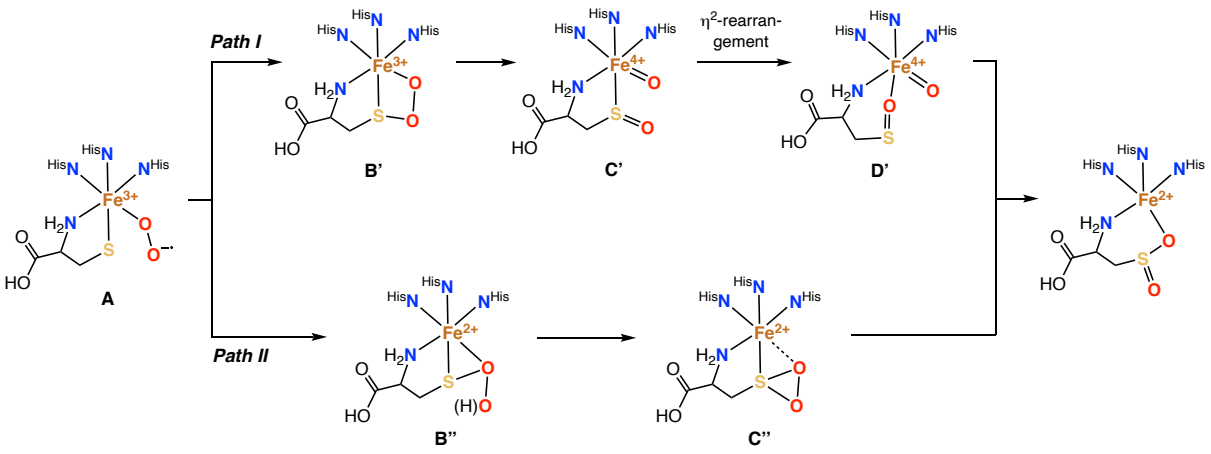

Scheme 12. Mechanistic proposals for the dioxygenation of cysteine by CDO.

Fe–S–O cyclic persulfenate intermediate (**B"**). This species then converts into an thiadioxirane intermediate (**C"**) before release of the sulfinic acid product.[131] In this mechanism, no high-valent iron intermediate is invoked and the sulfur undergoes direct dioxygenation rather than two independent mono-oxygenation steps. This proposal is supported by the crystal structures of an iron-persulfenate CDO complex that was obtained upon soaking crystals of CDO with substrate in aerobic conditions at varying pH values.[131,145] However, the stability of these crystals has been argued to be indicative of an

off-cycle species rather than a catalytically relevant intermediate.[146] Moreover, another study showed these crystals to be incapable of forming the expected sulfinate product.[144] *Path I* and *Path II* have been investigated computationally by means of DFT and QM/MM calculations.[114,139–141] These calculations predict that much higher energy barriers are required to form the persulfenate intermediate, making *Path I* the most likely mechanism for CDO.[114]

Currently, the catalytic role of the thioether cross-link remains unknown. Eukaryotic forms of CDO have been shown to remain active in the absence of this cross-link, albeit with a 5–20-fold decrease in activity under physiological conditions.[133] Davies *et al.* postulated that the cross-link has a protective role, removing labile thiol from the active site and expanding the pH range for CDO activity.[147] It has also been proposed that the Ser-His-Tyr "triad" acts as a proton relay network and helps gate substrate denticity upon coordination to the iron centre.[147,148] Indeed, CDO was shown to exhibit a solvent KIE of ~1.45, which suggests a proton-sensitive rate determining step following O_2 activation.[135] The Tyr-157 residue in particular has been proposed as playing a potential role in acid-base catalysis during CDO activity,[147] possibly engaging in hydrogen-bonding with the superoxo ligand following O_2 binding to the iron centre.[148] The presence of a tyrosyl radical has been excluded experimentally.[137] However, the exact manner in which the second sphere residues influence catalysis remains unknown. More experimental and theoretical work is required to fully elucidate the mechanistic intricacies of CDO and other thiol dioxygenases.

Role of the thiolate. The binding of cysteine to the iron centre in CDO results in a more covalent iron ligand environment as well as a decrease in coordination number. This is observed spectroscopically by a drop in the ^{57}Fe Mössbauer isomer shift (δ) from 1.22 mm s^{-1} for the resting state to 0.80 mm s^{-1} for the substrate-bound complex.[127] Analogously to other enzymes discussed so far, the thiolate-to-metal charge transfer is responsible for lowering the redox potential of CDO's iron site, rendering it susceptible to O_2 binding. However, the iron site in CDO appears to be slightly less oxidisable than that of IPNS. Experimentally, this is manifested by the low-spin ($S = {}^1/_2$) electronic configuration of the substrate-bound $\{FeNO\}^7$ complex for CDO, which was assigned as a low-spin ($S = 0$) iron(II) centre coupled to $NO^{\bullet}$ ($S = {}^1/_2$).[137,138] For comparison, the analogous substrate-bound $\{FeNO\}^7$ complex for IPNS has $S = {}^3/_2$ and consists of a high-spin ($S = {}^5/_2$) iron(III) centre antiferromagnetically coupled to the NO^- anion.[97,100] Thus, nitric oxide cannot oxidise the iron centre in CDO as easily as it can in IPNS. This discrepancy is believed to arise, in part, from the neutral coordination environment provided by the 3-His facial triad compared to the anionic 2H1C. Calculations have also shown that the charge transfer from the thiolate promotes the correct π^* FMO in the iron(III)-superoxide intermediate for S-oxygenation and the formation of the cyclic Fe–O–O–S structure.

1.2.7 Ergothioneine Sulfoxide Synthase (EgtB)

Ergothioneine sulfoxide synthase (EgtB; EC.1.14.99.50) is a mononuclear non-heme enzyme found in fungi and bacteria that catalyses the O_2-dependent sulfoxidation and C–S bond formation between *N*-α-trimethyl histidine (TMH) and either γ-glutamyl cysteine (γGC) or L-cysteine (on the EgtB enzyme) as a central step in the biosynthesis of ergothioneine.[149] Together with the ovothiol A biosynthesis enzyme, OvoA (Scheme 13),[150] EgtB represents an emerging class of mononuclear non-heme iron enzymes, known as the sulfoxide synthases, which distinguish themselves from other sulfur-oxidising enzymes such as IPNS or CDO.[151]

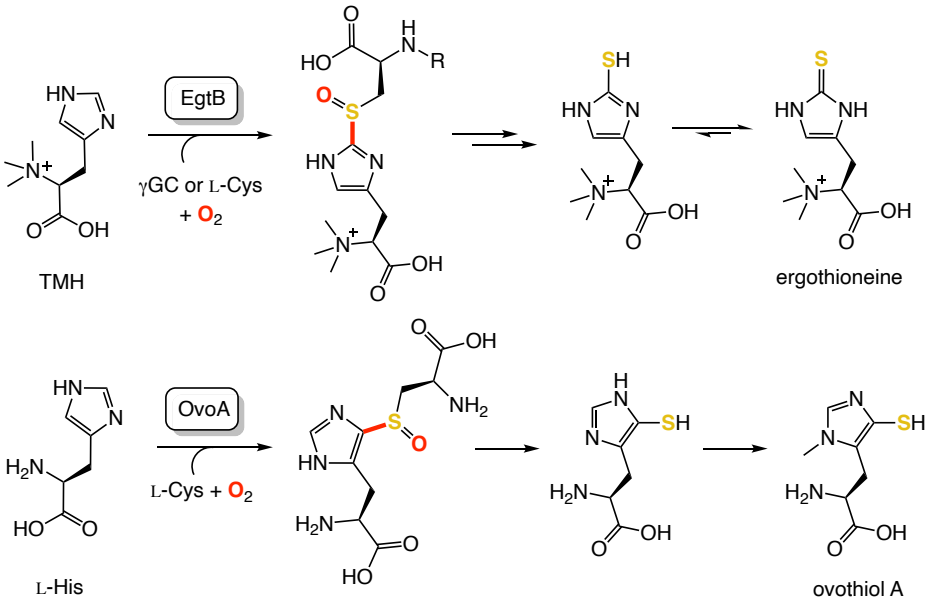

Scheme 13. The O_2-dependent C–S bond forming reactions catalysed by the EgtB and OvoA enzymes. New C–S bonds are highlighted in red. The C–S bonds are formed at the imidazole's *ε*– and *δ*–position during ergothioneine and ovothiol A biosynthesis, respectively.

Ergothioneine and ovothiol A are thiohistidine amino acids that exist in their thione and thiolate forms, respectively, at physiological pH.[149,150,152–154] They both have the unique attribute of having a relatively high thiol-disulfide redox couple (E^o = –0.06 V and –0.09 V *vs.* SHE, respectively)[150,153] compared to other naturally occurring thiols such as cysteine or glutathione, making them more stable to oxidation. Indeed, both ergothioneine and ovothiol A are believed to play vital roles as radical scavengers and metal chelators, protecting organisms against oxidative stress. They therefore hold great therapeutic potential as antioxidants in treatments against inflammatory, neurodegenerative, and cardiovascular disorders.[53,152,153] Owing to the lack of structural data currently available for OvoA, this review will restrict further discussion to the coordination chemistry of EgtB.

Structure. In 2010, the group of Seebeck identified the genetic sequence responsible for ergothioneine biosynthesis,[155] and the protein X-ray crystal structure of EgtB from *Mycolicibacterium thermoresistibile* (*Mth*EgtB, also known as EgtB type I) was first reported in 2015 by the same group.[149]

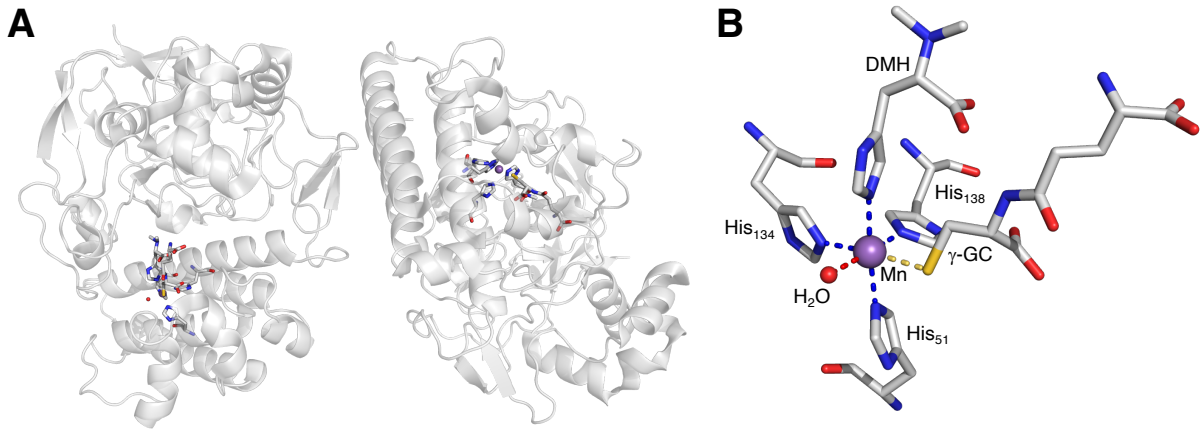

Figure 12. A: Full protein X-ray crystal structure of *Mth*EgtB, reconstituted with Mn (PDB 4X8D). **B:** Structure of the DMH- and γ-GC-bound active site of *Mth*EgtB (PDB 4X8D), shown without the surrounding protein scaffold. Carbon, manganese, nitrogen, oxygen and sulfur are depicted in grey, orange, blue, red and yellow, respectively.

The crystal structure of the Fe-bound EgtB in the presence of TMH revealed that the non-heme iron(II) site is located at the bottom of a large channel (15 Å deep, 10 Å wide) and is coordinated by the 3-His facial triad (His-134, His-51 and His-138), similarly to the active site of CDO.[149] TMH and two water molecules bind to the iron on the opposite sites of the octahedral coordination sphere, with TMH coordinated through its Nτ atom *trans* to the His-51 residue. The substrate is held tightly in place within the large channel by means of a water-assisted H-bonding network as well as salt bridge interactions in the secondary coordination sphere. In the crystal structure of Mn-bound EgtB in the presence of γ-GC and *N,N*-dimethylhistidine (DMH), the γ-GC substrate was observed to displace a water molecule in order to bind directly to the metal centre, *cis* to DMH and *trans* to His-134 (Figure 12). The sixth coordination site is populated by a water molecule that H-bonds to the phenolic side-chain of a nearby Tyr-377 residue, which has been proposed as being mechanistically relevant. Indeed mutation of Tyr-377 to phenylalanine produced an enzyme that catalyses the dioxygenation of γ-GC to its corresponding sulfinic acid instead of the native sulfoxidation.[156] Analogous attempts to obtain the Fe-bound *Mth*EgtB in complex with both substrates have been unsuccessful, to date.[149] More recently in 2019, the crystal structure of EgtB from *Chloracidobacterium thermophilium* (*Cth*EgtB, also known as EgtB type II) was resolved.[157] The structure reveals an overall protein structure and sequence that differs significantly from that of *Mth*EgtB, although the mononuclear iron centre remains facially capped by the 3-His facial triad. Two tyrosine residues (Tyr-93 and Tyr-94) lie in close proximity to the oxygen binding site in *Cth*EgtB instead of one. As was observed for *Mth*EgtB, mutation of Tyr-93 in *Cth*EgtB to phenylalanine caused cysteine sulfinic acid to become the major product, while mutation of Tyr-94 caused a significant decrease in L-Cys consumption, suggesting that Tyr-94 may affect O_2 binding.[157]

Mechanism. The understanding of EgtB's mechanism is still in its infancy but is rapidly growing. Two of the most pressing research questions are: how does EgtB prevent the dioxygenation of its thiolate substrate, and does C–S bond formation occur before or after

sulfoxidation? Several mechanistic investigations have been conducted using enzymological and computational methods, with notable contributions from the groups of Seebeck,[149,156,158] Liu,[159–162] and De Visser.[163] Two mechanistic pathways, *Path I* and *Path II*, have been proposed in the literature (Scheme 14). In both of them, the first steps of the mechanism involve the sequential coordination of the TMH and the thiolate substrates, followed by end-on dioxygen binding the iron's last available coordination site, forming a high-spin (S = 2) iron(III)-superoxo intermediate.

Path I proceeds similarly to the mechanistic pathway defined for CDO, with initial attack of the distal superoxide oxygen atom on the iron-bound sulfur atom, forming a bridged Fe–O–O–S peroxide intermediate.[164,165] Homolytic cleavage of the O–O bond produces an iron(IV)-oxo intermediate, with a bound sulfenate moiety, after which C–S bond formation occurs through a proton-coupled electron transfer (PCET) mechanism. However, the major shortcoming of *Path I* is that it does not take the effect of the tyrosine into account, and the proposed rate-determining step, involving proton transfer from the TMH substrate, does not agree with the lack of a KIE that was observed experimentally upon use of a deuterated TMH analogue.[156]

Path II was postulated on the basis of QM/MM calculations and predicts that C–S bond formation occurs prior to sulfoxidation. The superoxo ligand is proposed to deprotonate the tyrosine residue (*via* a Grotthus mechanism), and a proton-coupled electron transfer back to the tyrosinate forms an iron(III)-hydroperoxo intermediate. Next, the iron-bound thiolate attacks the C2 position of the imidazole ring, resulting in the formation of the new C–S bond. Simultaneously, a proton is relayed back to the tyrosinate and an electron is transferred from the sulfur to the iron, resulting in an iron(II)-superoxo intermediate coordinated to the de-aromatised-TMH-γ-GC sulfide. Finally, the distal oxygen atom of the superoxide ligand deprotonates the TMH moiety, and subsequently oxygenates the sulfide.

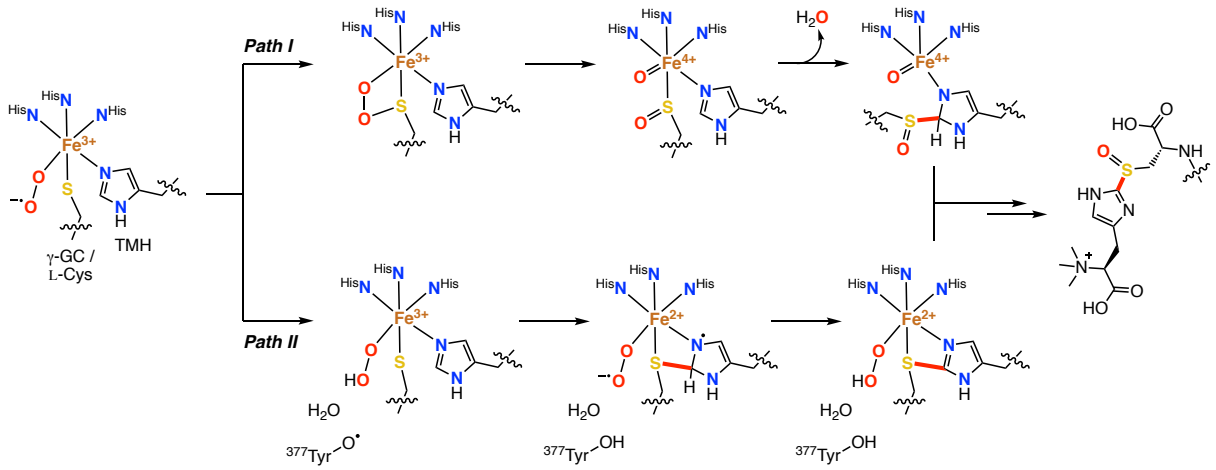

Scheme 14. Proposed mechanistic pathways (either *Path I* or *Path II*) with which EgtB operates.

Role of the thiolate. Similarly to IPNS, ETHE1, and CDO, the anionic sulfur-rich substrate binds directly to the iron centre in EgtB. Presumably, sulfur-to-iron charge transfer has a similar effect of reducing the iron's redox potential and rendering it prone to oxidation. However, spectroscopic studies of EgtB are extremely limited and data corroborating current mechanistic proposals involving iron-oxygen intermediates are almost exclusively based on computational studies. More experimental, spectroscopic and computational work is therefore required to assign the dioxygen coordination modes and metal spin states in order to understand how EgtB activates O_2 and mediates C–S bond formation and sulfoxidation. Thus far, it is believed that the redox involvement of the tyrosinate (through proton delivery and electron relay) and the accompanying H-bonding network are key to modulating the electron density of the terminal oxygen atom of the superoxide ligand, directing its attack on the sulfide's sulfur atom and likely having an impact on the oxidation state of the iron centre.[142]

1.3 Synthetic Non-Heme Iron Thiolate Model Complexes

1.3.1 Overview

In the previous section, seven different mononuclear heme and non-heme iron enzymes were described, whose active sites contain a single Fe–S(thiolate) bond: CyP450, SOR, NHase, IPNS, ETHE1, CDO, and EgtB. In all cases, this iron-sulfur interaction has a significant impact on their respective reactivities. Over the last decade, many synthetic iron thiolate model complexes have been developed, whose steric, electronic or geometric parameters have been systematically varied in order to correlate spectroscopic properties and trends in enzyme reactivity with the local environment of the iron centre. This section presents an overview of selected examples of mononuclear non-heme iron thiolate complexes designed to model sulfur-ligated enzyme active sites. Heme complexes will not be discussed, in order to limit the scope of this review. As well as show-casing the diversity of complex design, this review aims to highlight the importance of this chemistry given the current interest in performing challenging chemical transformations (*e.g.* C–X cross-coupling reactions) using iron as a catalyst.

The synthesis of iron thiolate complexes can be quite challenging due to the ease with which low-valent iron and anionic thiolate moieties can be oxidised, as well as the tendency for sulfur ligands to engage in bridging coordination modes. Two principal strategies can be identified for creating well-defined iron thiolate complexes. The first involves the use of a bioinspired supporting ligand with a tethered (pendant) sulfur-rich moiety (*e.g.* a thiolate or a thioether). The second strategy involves the use of a bioinspired supporting ligand in combination with an exogenous thiolate co-ligand. For the former, the principal advantage is that the thiolate and the rest of the ligand's donor groups are guaranteed to be simultaneously present, and, depending on where it has been integrated in the ligand architecture, the thiolate can be directed to a specific coordination site. For

the latter, the main advantage is that spectroscopic trends can easily be probed by varying the nature of the exogenous thiolate without requiring any further (often exhaustive) synthetic modifications of the supporting ligand.

Another important distinction in biomimetic complexes is whether they are considered as functional or structural model complexes. Functional model complexes are designed to replicate important mechanistic aspects of the enzyme's native reactivity, without necessarily incorporating all structural parameters strictly observed at the enzyme's active site. Structural model complexes aim to faithfully reproduce all structural aspects of the enzyme's active site, including the nature of the donor groups and the geometry of the iron centre. A schematic overview of the complexes discussed in this section is given in Figures 13 and 14 for complexes featuring sulfur-tethered ligands or exogenous thiolate co-ligands, respectively.

1.3.2 General Structural and Electronic Considerations

A broad and diverse family of ligands have been developed to model the different structural and functional aspects of the active sites of CyP450, SOR, NHase, IPNS, ETHE1, CDO and EgtB. These include tripodal anionic or neutral N3 ligands, meridional N3 ligands, tripodal N4 ligands, equatorial N4 ligands, or polydentate mixed N,S-donor ligands.[146] Common to them all is the presence of relatively weak-field nitrogen and/or sulfur donor groups, which generally give rise to high-spin iron(II) complexes ($S = 2$). However, a few examples of low-spin ($S = 0$) iron(II) thiolate complexes are also known, where a strong-field ligand (*e.g.* an acetonitrile or thiocyanato ligand) is present.

In general, Fe–S bond properties are dependent on three different factors. The first is the nature of the sulfur ligand itself. Typically, aliphatic thiolates or thiolates with an electron-rich organic substituent produce shorter Fe–S bond lengths than thiolates with an electron-poor substituent (*e.g.* the Fe–S bond length of 2.286(1) Å is reported for propylthiolate-bound complex $[Fe^{II}(cyclam\text{-}PrS)]^+$ compared to 2.3316(11) for complex thiophenolate-bound complex $[Fe^{II}([15]aneN_4)(SPh)]$, both high-spin).[166,167] Similarly, a thiolate will typically produce a longer Fe–S bond length than an S-bound sulfinato ligand, since oxygenation of the sulfur contracts the size of the sulfur atom (as a result of the increase in formal oxidation state) and eliminates the repulsive interaction between the iron's filled *d*-orbitals and the lone pairs on the thiolate donor.[168] For example, an Fe–S bond length of 2.3018(4) Å is reported for complex $[Fe^{II}(N_3PyS)(MeCN)]$ compared to 2.1812(9) Å for complex $[Fe^{II}(N3PySO_2)(SCN))]$, both low-spin).[168] Another factor that affects Fe–S bonds is the coordination number of the iron centre, where lower coordination numbers typically produce shorter Fe–S bonds due to the more electron-poor nature of the iron, for a given spin-state. Finally, the spin-state of the metal also has an influence, where low-spin iron will typically produce shorter Fe–S bonds than high-spin complexes due to the lesser extent of antibonding orbital population.

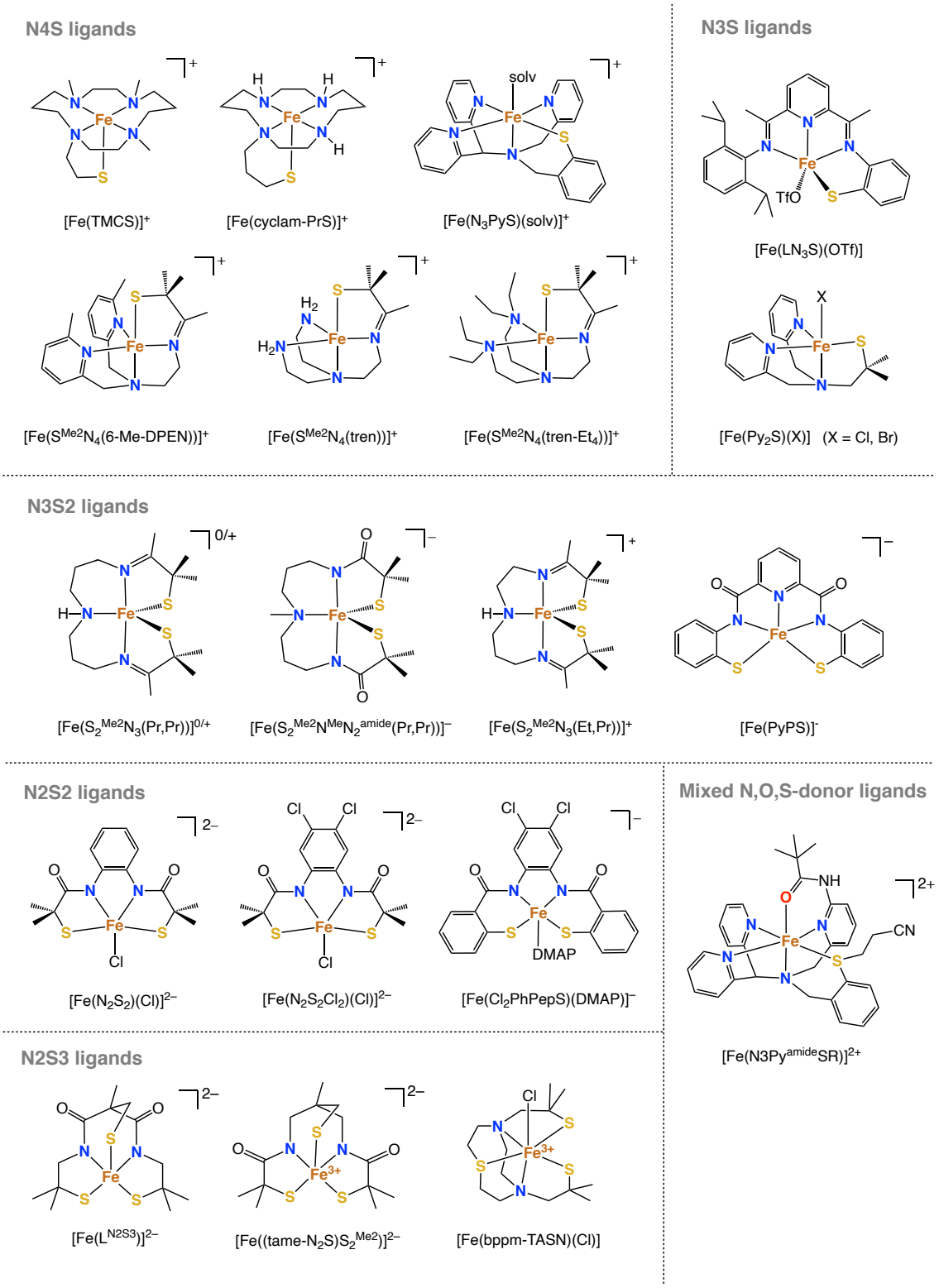

Figure 13. Selected examples of mononuclear, monoligated non-heme iron thiolate complexes featuring bioinspired ligands with a tethered sulfur donor.

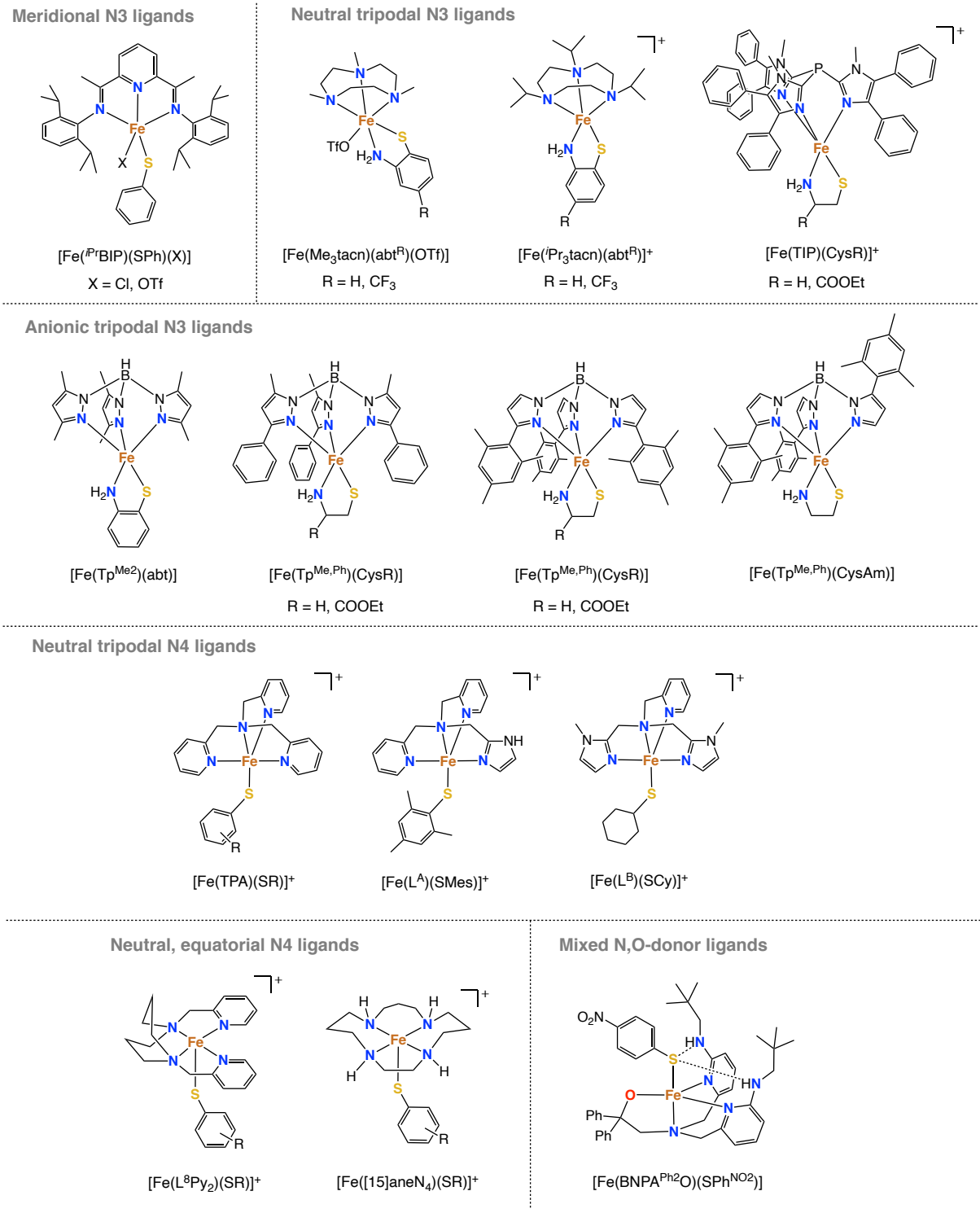

Figure 14. Selected examples of mononuclear non-heme iron thiolate complexes featuring a bioinspired supporting ligand and an exogenous thiolate co-ligand.

1.3.3 Model Complexes of CyP450 and SOR

In this section, complexes relevant to the active sites of CyP450 and SOR will be discussed jointly since, with the exception of their differing heme and non-heme natures, these enzymes share many structural features, including a nitrogen-rich N4 equatorial plane, an iron-bound thiolate at the apical site of the complex, and a vacant site *trans* to the thiolate.

Early SOR modelling work was conducted by the group of Halfen. The pyridyl-appended diazacyclooctane ligand $\mathbf{L^8Py_2}$ was used to prepare a series of pentadentate, high-spin (S = 2) iron(II) thiolate complexes, $[Fe^{II}(L^8Py_2)(SR)]^+$, where R = *p*-Tol (**1a**), *m*-Tol (**1b**), Cy (**1c**) (Figure 15). The complexes are square pyramidal in geometry, comprising a basal plane of four nitrogen donors from the tetradentate $\mathbf{L^8Py_2}$ ligand and the thiolate at the apical site.[169] The Fe–S bond lengths were shown to be dependent on the approximate donicity of the thiolate ligand: complex **1c**, which bears an alkylthiolate ligand, has the shortest bond length of the series (2.259(2) Å) while **1a** has the longest (2.323(2) Å). Electrochemical studies by cyclic voltammetry showed that the complexes undergo an irreversible oxidation event at approximately +0.6 V in MeCN, rendering them inert to aerobic oxidation. However, the irreversibility of this event shows that the electrochemically generated iron(III) complex decomposes in solution, likely to the disulfide and an unidentified ferrous complex.

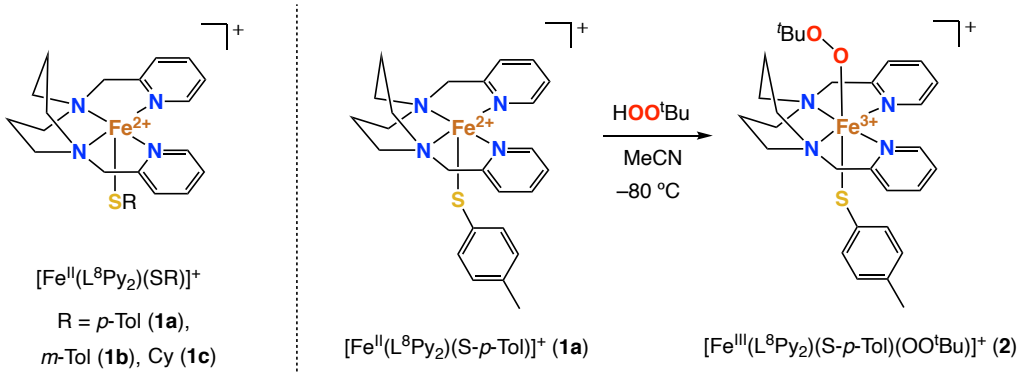

Figure 15. $[Fe^{II}(L^8Py_2)(SR)]$ complexes reported by the group of Halfen.

Reacting complex **1a** with ^{t}BuOOH at –80 °C affords a deep purple species, identified spectroscopically as a six-coordinate high-spin ($S = {}^5/_2$) iron(III) alkylperoxo intermediate, $[Fe^{III}(L^8Py_2)(S\text{-}p\text{-Tol})(OO^tBu)]^+$ (**2**) (Figure 15).[170] Interestingly, the authors observe that the arylthiolate ligand prolongs the lifetime of the hydroperoxo intermediate, which is opposite to the general trend seen for low-spin ($S = {}^1/_2$) iron(III) alkylperoxo intermediates, where Lewis bases typically accelerate their decay to Fe^{IV}=O species.[171] These results support the hypothesis that SOR contains a high-spin centre because this gives rise to a weaker Fe–O bond and a stronger O–O bond upon superoxide binding, which favours H_2O_2 release rather than O–O bond cleavage.[172] Charge donation from the axial thiolate to the iron thus lowers the $Fe^{III/II}$ redox potential and promotes the one-electron reduction of the superoxide. In contrast, CyP450 contains a low-spin centre, as this gives rise to a

stronger Fe–O bond and weaker O–O bond upon O_2 binding. Charge donation from the axial thiolate therefore promotes O–O bond cleavage *via* the "push effect" and accelerates formation of an iron(IV) oxo species.

In later studies, the group of Goldberg synthesised a series of complexes $[Fe^{II}([15]aneN_4)(SAr)]^+$ derived from the **[15]aneN$_4$** ligand (Figure 16), where Ar = Ph (**3a**), *p*-OMe-Ph (**3b**), *p*-Cl-Ph (**3c**), *p*-NO_2-Ph (**3d**), and C_6F_4-*p*-SC_6F_5 (**3e**).[166,173] These complexes are all pentacoordinate, and have a distorted square pyramidal geometry defined by the basal plane of the macrocyclic tetraaza ligand and the exogenous thiolate at the apical site. The Fe–S bond distances range from 2.3197(12) Å to 2.3426(8) Å, consistent with high-spin (S = 2) iron(II). Reacting complexes **3a-3e** with ^{t}BuOOH at –78 °C produces dark red species, assigned as six-coordinate, low-spin (S = $^1/_2$) alkylperoxoiron(III) intermediates (**4a-4e**) on the basis of UV-vis, EPR, resonance Raman, and EXAFS spectroscopy. Interestingly, the vibrational signatures and the bond distances obtained by EXAFS for these alkylperoxo intermediates show that the Fe–O bonds are weak,[173,174] which is in sharp contrast to many other low-spin Fe^{III}–OOR complexes. The authors speculate that the *trans* effect of the thiolate is responsible for the Fe–O bond elongation and propose that a low-spin intermediate may in fact be formed during SOR's mechanism.

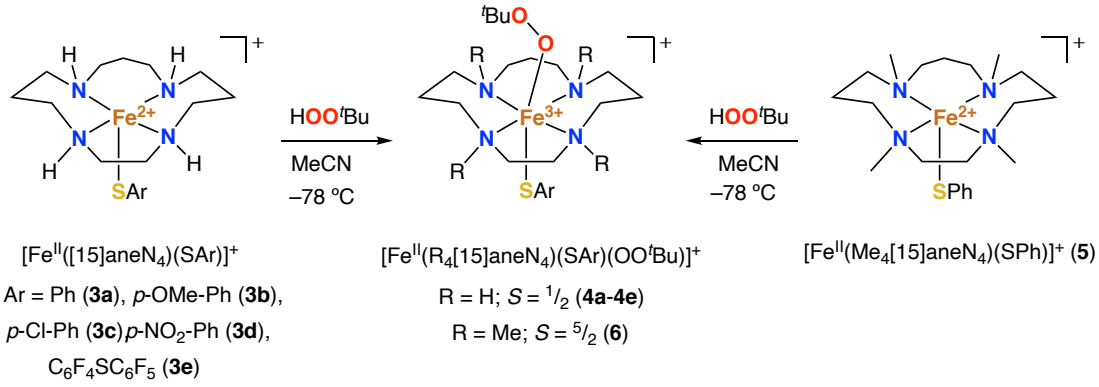

Figure 16. SOR model complexes reported by the group of Goldberg.

In a related study, Goldberg and co-workers observed that analogous complex $[Fe^{II}(Me_4[15]aneN_4)(SPh)]^+$ (**5**), which features a tetramethylated tetraaza ligand, forms a turquoise-coloured high-spin (S = $^5/_2$) alkylperoxoiron(III) intermediate (**6**).[175] The high-spin state and the strongly red-shifted UV-vis absorption of this complex compared to the non-methylated analogues are attributed to the less donating nature of the tertiary amines in the ligand framework. Overall, these results of this study are in line with those obtained by Halfen and co-workers for the **L^{8}Py$_2$** complex series.

At approximately the same period, the group of Kovacs employed an propylthiolate-tethered tetraaza macrocyclic ligand, **cyclam-PrS**, to synthesise one of the first functional models of SOR, complex $[Fe^{II}$(cyclam-PrS)$]^+$ (**7**) (Figure 17).[167] The pentacoordinate complex has a distorted square pyramidal geometry, with the pendant thiolate occupying

the apical position. The complex is high-spin ($S = 2$), with an Fe–S bond length of 2.286(1) Å. Reacting **7** with KO_2 at −78 °C in the presence of a crown ether and a protic solvent affords a high-spin ($S = {}^5/_2$) iron(III)-hydroperoxide species, $[Fe^{II}(cyclam\text{-}PrS)(OOH)]^+$ (**8**). This contrasts somewhat with the low-spin alkylperoxoiron(III) **[15]aneN$_4$** complexes, which are structurally very similar as they also feature secondary amine groups in the equatorial plane. A comparative study by Halfen and co-workers proposed that ligands with a tethered alkylthiolate moiety (*e.g.* [15]aneN4 or TMCS) produce complexes that more accurately model the electronic properties of SOR, largely due to the constrained orientation of the pendant thiolate. This leads to a highly covalent Fe–S σ-bonding interaction and limits the thiolate's π-bonding interaction to a single Fe d_π-orbital.[176] Kovacs and co-workers observed a very low Fe–O stretch for **8** in resonance Raman spectroscopy (400 cm^{-1}), reflecting the *trans* effect of the thiolate. Importantly, addition of HOAc to **8** at −78 °C releases H_2O_2 and generates a low-spin iron(III)-acetate complex, $[Fe^{III}(cyclam\text{-}PrS)(OAc)]^+$ (**9**), which models the glutamate-bound active site of SOR. Finally, reduction of the iron centre in **9** using a sacrificial oxidant regenerates **7**.

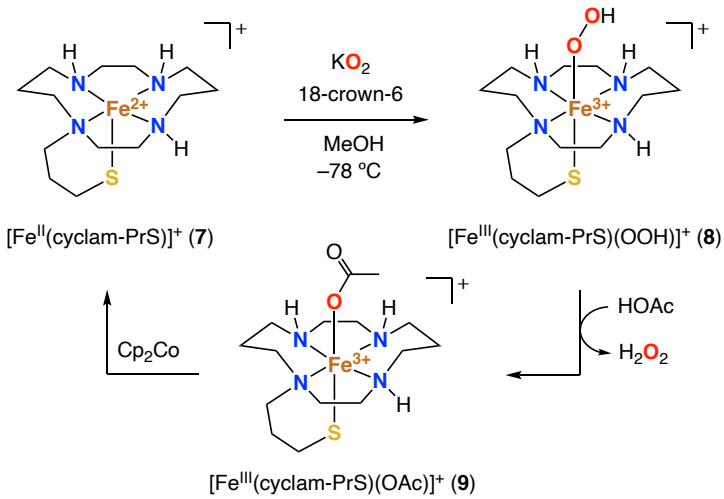

Figure 17. The SOR functional model complex reported by the group of Kovacs.

The first example of a non-heme thiolate-ligated iron(IV)-oxo complex relevant to CyP450 was reported by the groups of Halfen, Nam and Que, employing the tetraaza macrocyclic ethylthiolate-tethered ligand, **TMCS** (Figure 18).[177] Pentacoordinate complex $[Fe^{II}(TMCS)]^+$ (**10**) has a distorted square pyramidal geometry with an Fe–S bond length of 2.297(3) Å, consistent with high-spin (S = 2) iron(II).[176] Treatment of this square pyramidal complex with 1 equiv. of *m*-CPBA in the presence of excess base affords the low-spin (S = 1) iron(IV)-oxo complex, $[Fe^{IV}(O)(TMCS)]^+$ (**11**), where the oxo atom is coordinated to the iron centre *trans* to the thiolate.[177] In contrast, reacting **10** with 2 equiv. of *m*-CPBA in slightly acidic conditions resulted in the direct oxygenation of the sulfur atom instead of the iron, forming the corresponding iron(II) sulfinate complex, $[Fe^{II}(TMC\{SO_2\})]^+$ (**12**).[178] Complex **12** is converted to oxoiron(IV)-sulfinate complex $[Fe^{IV}(O)(TMC\{SO_2\})]^+$ (**13**) through treatment with an additional equivalent of *m*-CPBA.

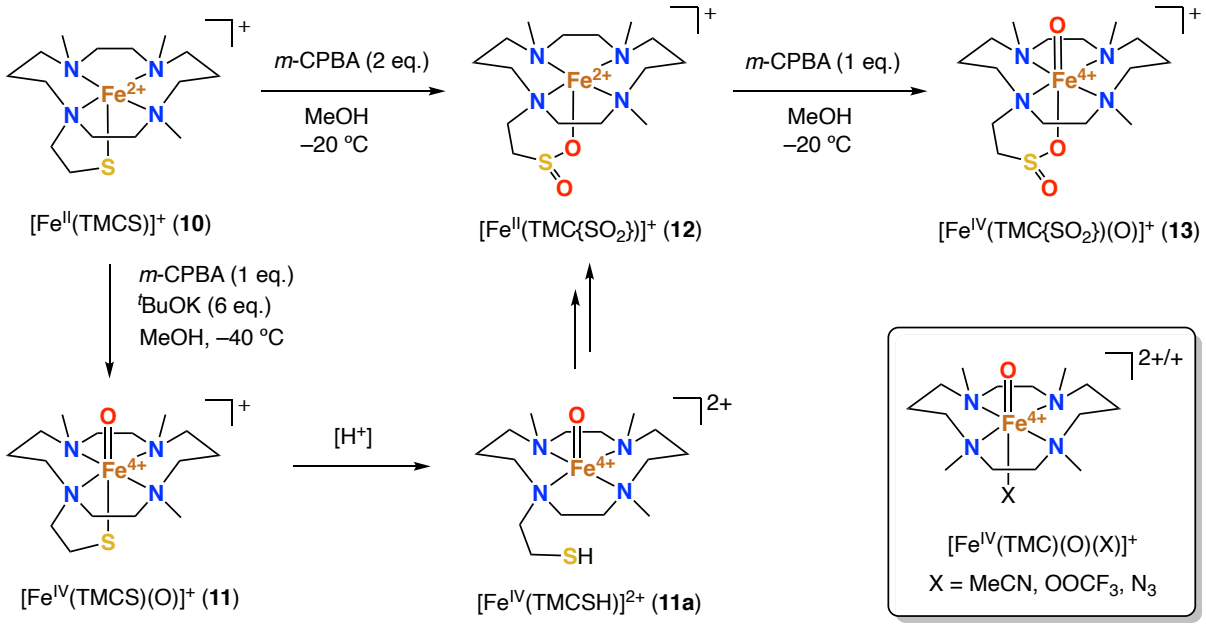

Figure 18. The CyP450 model complexes reported by the group of Halfen, Nam and Que.

Investigations into the hydrogen atom transfer (HAT) and oxygen atom transfer (OAT) reactivities of **11** and related $[Fe^{IV}(O)(TMC)(X)]^{2+/+}$ complexes (X = MeCN, $OOCF_3$, or N_3) showed that these are significantly affected by the nature of the axial X-ligand *trans* to the oxo group.[179,180] A reactivity order of MeCN > CF_3COO^- > N_3^- > RS^- was observed for OAT to PPh_3, reflecting a decrease in the electrophilicity of the iron(IV)-oxo unit as the electron donating ability of the X-ligand increases. In contrast, the opposite reactivity order of RS^- > N_3^- > CF_3COO^- > MeCN was observed for the oxidation of alkyl- and aromatic C–H bonds and phenolic O–H bonds.[179]

This counterintuitive anti-electrophilic effect is rationalised by taking two different factors into account. The first is the so-called "two-state reactivity" (TSR) hypothesis,[181] where increasing electron donation of the X-ligand decreases the energy gap (ΔE_{TQ}) between the triplet ground state (^{3}TS, S = 1) and the low-lying quintet excited state (^{5}TS, S = 2),[179,182] ultimately leading to a higher spin-inversion probability (SIP) and a lower energy barrier *en-route* to the S = 2 transition state (Figure 19A).[182,183] The second important factor is quantum mechanical tunnelling of the H atom. Hydrogen tunnelling is regarded as the propagation of a hydrogen atom through an energy barrier, at a point that depends on the temperature of the reaction and that requires the de Broglie wavelength of the H atom to match the width of the energy barrier. Quantum tunnelling lowers the semiclassical transition state energy barrier ($\Delta E^{\ddagger}$) by a quantity ($\Delta\Delta E^{\ddagger}_{tun}$), to yield an effective barrier ($\Delta E^{\ddagger}_{eff}$). This is represented in Figure 19B. The thiolate in **10** has been described as having a privileged role in enabling quantum tunnelling due to its charge transfer, which provides greater electrostatic stabilisation to the H-atom and increases the symmetry of the transition state.[184]

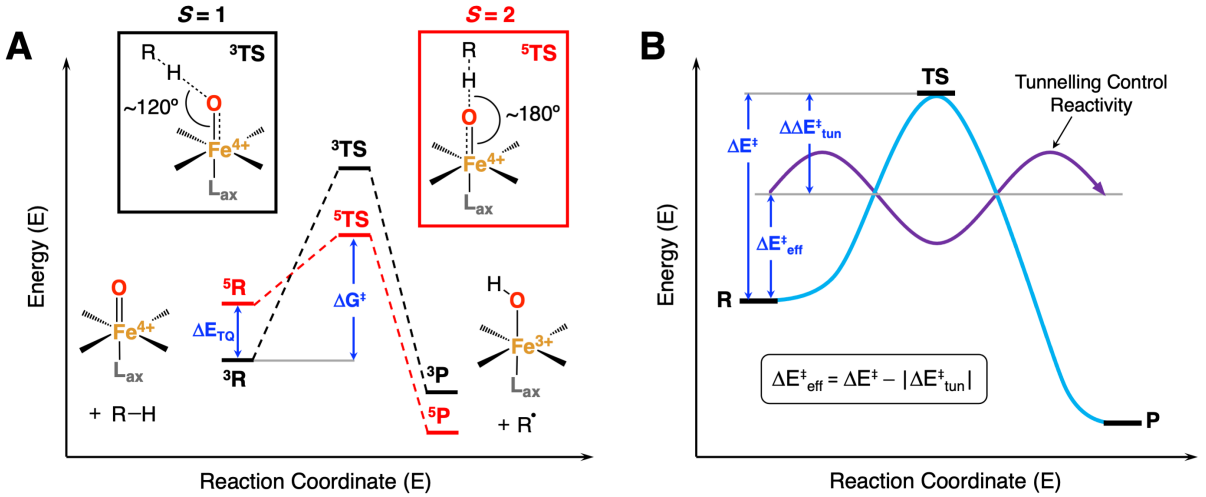

Figure 19. A: Generic two-state reactivity (TSR) scenario for low-spin (S = 1), non-heme iron(IV)-oxo complexes during H-atom abstraction reactions (adapted from Klein *et al.*)[184]. B: Schematic representation of how quantum tunnelling lowers the observed energy barrier ($\Delta E^{\ddagger}_{eff}$) relative to the semiclassical TS energy barrier ($\Delta E^{\ddagger}$) for H-atom abstraction (adapted from Mandal *et al.*).[185]

Using the tripodal thiolate-tethered amine ligand **$S^{Me2}N_4$(tren)**, the group of Kovacs synthesised complex $[Fe^{II}(S^{Me2}N_4(tren)]^+$ (**14**), which was investigated as a functional model of SOR (Figure 20, *vide infra*).[52,186] The complex has a distorted trigonal bipyramidal geometry, with three equatorial nitrogens, an axial amine and a tethered thiolate provided by the pentadentate supporting ligand. Like the reduced SOR active site, the complex is high-spin (S = 2), although unlike SOR, the remaining vacant site is located *cis* to the thiolate rather than *trans*, as demonstrated by the isolation of various ferric complexes featuring an additional anionic ligand bound *cis* to the thiolate, $[Fe^{III}(S^{Me2}N_4(tren)(X)]^{2+}$, where X = Cl (**17a**),[187] OAc (**17b**),[188] N_3 (**17c**),[188] CN (**17d**)[188] NO_2 (**17e**),[189] and NO (**17f**)[189].

Complex **14** reacts with KO_2 in the presence of a proton source to afford a short-lived burgundy-coloured species, identified as a low-spin (S = $^1/_2$) iron(III)-hydroperoxo intermediate, $[Fe^{III}(S^{Me2}N4(tren))(OOH)]^+$ (**15**), using UV-vis, EPR, IR, and EXAFS spectroscopies.[190] The Fe–O(peroxo) bond is cleaved through addition of a second, more acidic proton donor, releasing H_2O_2 and affording solvent-bound complex $[Fe^{III}(S^{Me2}N_4(tren)(solv)]^+$ (**16**). The rate of H_2O_2 release was shown to be dependent on the pK_a of the proton donor.[191] Reduction of **16** using cobaltacene regenerates ferrous complex **14**, thereby closing the "catalytic" cycle. This stepwise process is reproducible for approximately 8 cycles before degradation of **14**, likely through oxidation of the thiolate by H_2O_2.[192] Overall, these results demonstrate that achieving SOR reactivity is possible using biomimetic complexes that incorporate a *cis*-thiolate rather than a *trans*-thiolate. On this basis, Kovacs and co-workers propose that sulfur-to-iron charge transfer is essential for SOR activity regardless of the relative positioning of the thiolate within the iron's first coordination sphere.[52] Nonetheless, the *trans* effect of the thiolate in SOR is likely to contribute significantly to the labilisation of H_2O_2, encouraging fast product release and ensuring high turnover rates.

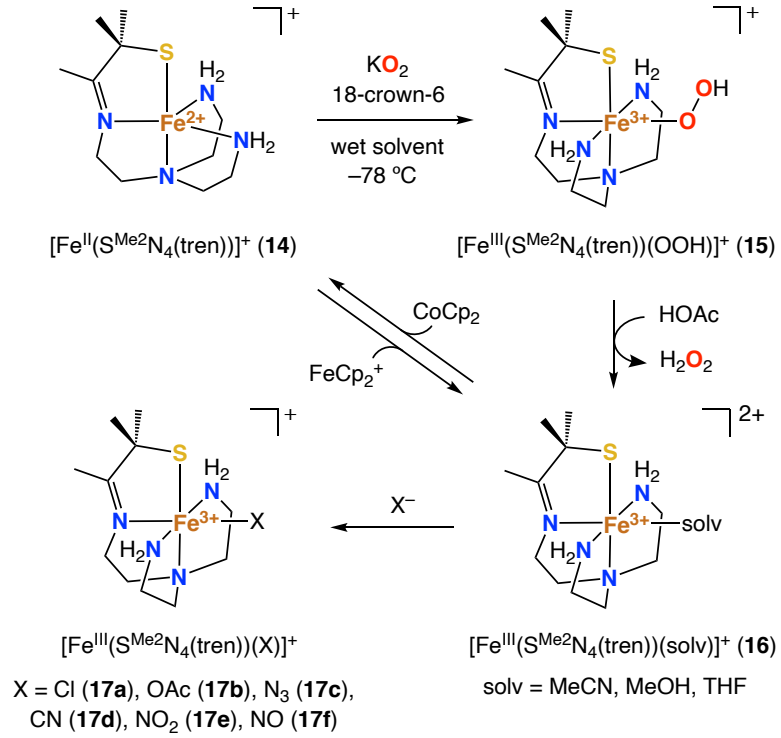

Figure 20. The superoxide reduction reactivity exhibited by $[Fe^{II}(S^{Me2}N_4(tren)]^+$ (**14**).

Other studies by the Kovacs group have shown that **14** displays interesting O_2 reactivity (Figure 21, *vide infra*). Complex **14** reacts with O_2 at room temperature to afford a μ-oxo-bridged diiron(III) complex, $[Fe^{III}_2(S^{Me2}N_4(tren))_2(\mu\text{-}O)]^{2+}$ (**18**), which can be reversibly cleaved using strong or weak acids (HX) to afford the corresponding monomeric complexes $[Fe^{III}(S^{Me2}N_4(tren))(X)]^+$ (X = Cl (**17a**), OAc (**17b**), CN (**17c**), N_3 (**17d**)).[193] In contrast, reacting **14** with O_2 at –130 °C in a EtOH/MeOH mixture affords a putative intermediate, assigned as a low-spin (S = $^1/_2$) iron(III)–superoxo complex, $[Fe^{III}(S^{Me2}N_4(tren)(O_2)]^+$ (**19**), by means of UV-vis and EPR spectroscopies.[187] Warming this complex slightly to –115 °C results in O_2 evolution and the regeneration of ferrous complex **14**. Coordinating anions such as Cl and OAc were shown to inhibit the oxidation of superoxide to O_2. Superoxide complex **19** was also obtained upon reacting ferric complex $[Fe^{III}(S^{Me2}N_4(tren))(THF)]^{2+}$ (**16**$^{\mathbf{THF}}$) with KO_2 at –80 °C in dry THF.[187]

Finally, it is important to note that the complex topology associated to ligand **$S^{Me2}N_4$(tren)** is of high relevance to other enzymes such as CDO, EgtB or IPNS, where O_2 binds to the vacant coordination site *cis* to the thiolate group. Indeed, Kovacs and co-workers have also investigated complex **16**$^{\mathbf{MeCN}}$ and its cobalt(III) analogue as functional models of NHase (*vide infra*), demonstrating the ease with which many biomimetic iron thiolate complexes can be interchangeably examined in the context of different enzymes.

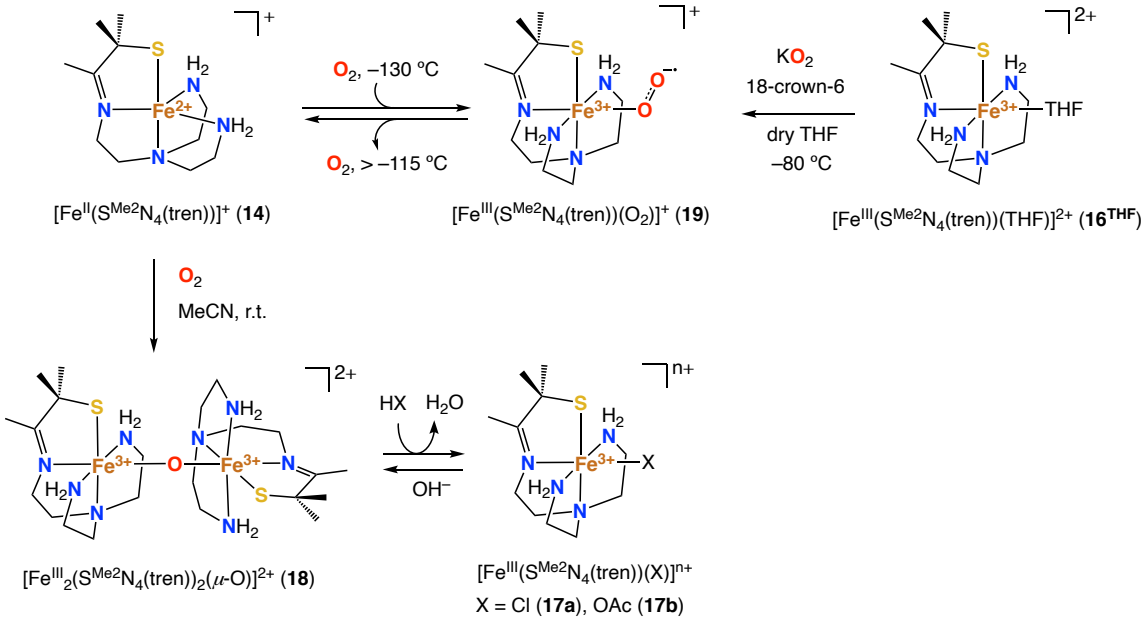

Figure 21. The superoxide oxidation reactivity exhibited by complexes $[Fe^{II}(S^{Me2}N_4(tren)]^+$ (**14**) and $[Fe^{III}(S^{Me2}N_4(tren)(THF)]^{2+}$ (**16**^{THF}).

1.3.4 Model Complexes of NHase

The unique coordination environment at the active site of nitrile hydratase (NHase) has inspired the development of many polydentate, mixed N,S-donor ligands and their corresponding metal complexes. Although NHase does not formally activate O_2 during its catalytic cycle, the post-translational oxygenation of the equatorial thiolates to their sulfenate and sulfinate forms is crucial to the proper functioning of the enzyme and has been a key focus of many NHase modelling studies. In this section, we will primarily focus on synthetic iron model complexes and any sulfur oxygenation reactivity. Notable examples of functional cobalt complexes will also be mentioned, although the reader is referred to other sources for more complete coverage of cobalt complexes.[46,73,194,195]

In early NHase modelling studies, the groups of Kovacs and Mascharak synthesised low-spin ($S = {}^1/_2$), octahedral iron(III) complexes (Figure 22), each bisligated by two tridentate N_2S imino or carboximido thiolate ligands.[196–198] These complexes exhibit a maximum absorption at approximately 700 nm and rhombic EPR signals, that well-reproduce those of the iron NHase enzyme. However, the coordinatively saturated nature of these complexes prevents the direct coordination of nitriles, O_2 or NO to the metal centre. Nonetheless, these studies were important for establishing the appropriate synthetic strategies with which to create NHase model complexes, including the incorporation of *gem*-dimethyl substituents *ortho* to an alkylthiolato S-donor to prevent disulfide formation, or alternatively, making sure the carboximido and thiolato moieties are comprised within a conjugated ligand system to prevent undesired ligand oxidation from occurring.[199] Additionally, Mascharak and co-workers demonstrated that the basicity of the deprotonated carboximido moieties is decreased upon coordination to iron(III), rendering them stable in protic media.[200,201]

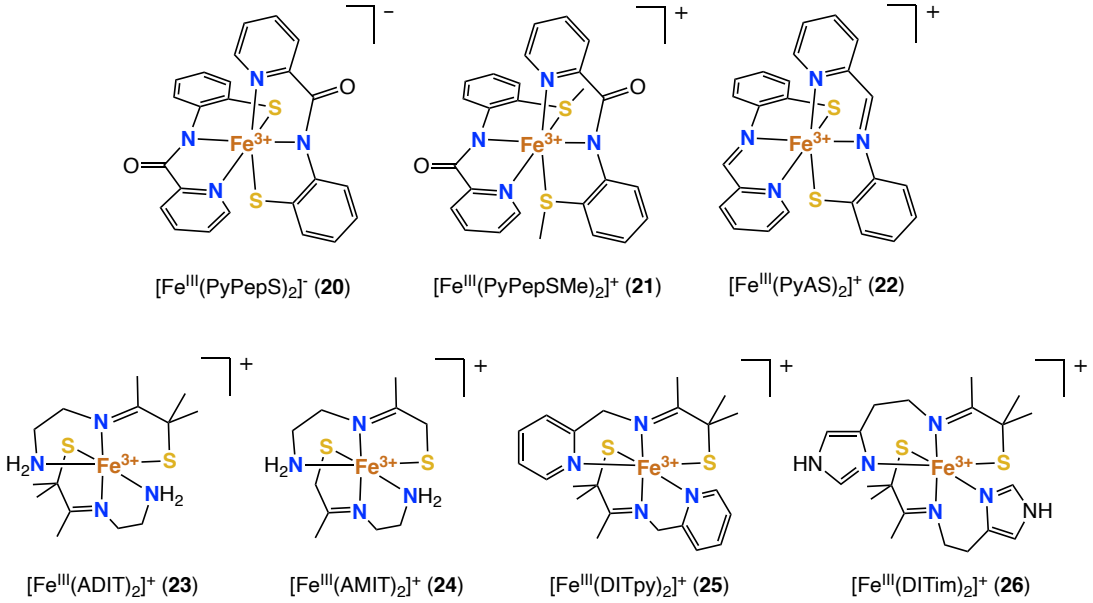

Figure 22. Early NHase model iron(III) complexes of octahedral geometry.

In related studies, the reactions of complexes $[Fe^{III}(PyPepS)_2]^-$ (**20**) and $[Fe(ADIT)_2]^+$ (**23**) with oxygen atom transfer agents were explored in an attempt to model the post-translational modification of the equatorial NHase cysteinates. The reaction of $[Fe^{III}(PyPepS)_2]^-$ (**20**) with excess H_2O_2 in DMF at low temperature affords the green-coloured bis-sulfinato complex $[Fe^{III}(PyPepSO_2)_2]^-$ (**27**).[201] Similarly, the reaction of green complex $[Fe^{III}(ADIT)_2]^+$ (**23**) with 1.4 equiv. *tert*-butyl N-sulfonyloxaziridine in MeOH results in a colour change to purple, associated to the formation of mono-sulfenate complex $[Fe^{III}(ADIT)(ADIT\text{-}O)]^+$ (**28**).[202] These studies demonstrate that the thiolates are prone to oxidation when coordinated to the Lewis acidic iron(III), but that the degree of oxygenation can be controlled by adjusting the quantities and the nature of the oxidant.

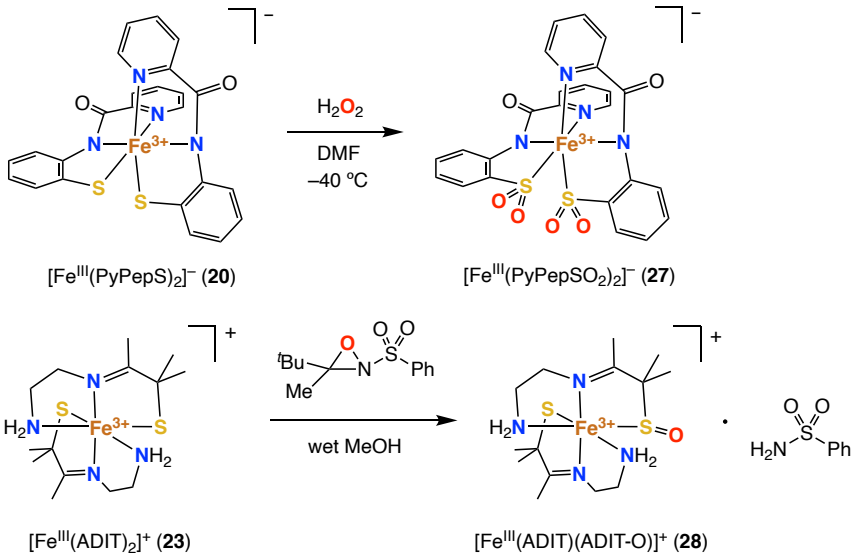

Figure 23. The oxygenation of complexes $[Fe^{III}(PyPepS)_2]^-$ (**20**) and $[Fe^{III}(ADIT)_2]^+$ (**23**).

In order to create coordinatively unsaturated complexes, the group of Kovacs developed the linear, pentadentate **$S_2^{Me2}N_3$(Pr,Pr)** ligand, which comprises two thiolato sulfurs, two imino nitrogen donors and an amine group. A pentacoordinate, low-spin ($S = {}^1/_2$) complex $[Fe^{III}(S_2^{Me2}N_3(Pr,Pr))]^+$ (**29**) was obtained by ferrocenium oxidation of the corresponding divalent complex.[203–205] The X-ray crystal structure of **29** shows that the ligand wraps itself around the iron(III) centre in a helical fashion, giving the complex a distorted trigonal bipyramidal geometry with the thiolato and amine groups occupying the equatorial plane and both imino nitrogens occupying the axial positions. Complex **29** was shown to accommodate azide (a NHase inhibitor) and NO (a NHase inactivator) binding *cis* to one of the thiolates and *trans* to the second thiolate (Figure 24).

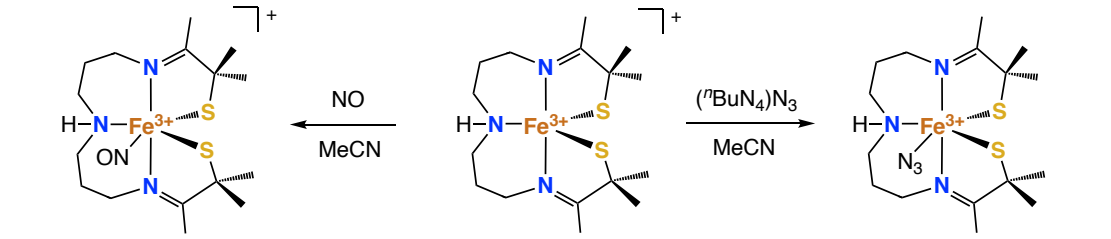

$[Fe^{III}(S_2^{Me2}N_3(Pr,Pr))(NO)]^+$ (**31**) $[Fe^{III}(S_2^{Me2}N_3(Pr,Pr))]^+$ (**29**) $[Fe^{III}(S_2^{Me2}N_3(Pr,Pr))(N_3)]$ (**30**)

Figure 24. Synthesis of $[Fe^{III}(S_2^{Me2}N_3(Pr,Pr))]^+$ (**29**) and its reactivity to azide and NO.

The six-coordinate azide complex $[Fe^{III}(S_2^{Me2}N_3(Pr,Pr))(N_3)]^+$ (**30**) exhibits a strong absorption band at 708 nm and a rhombic EPR signal at low temperature (g = 2.23, 2.16, 1.99), consistent with low-spin ($S = {}^1/_2$) iron(III) and very similar to the spectroscopic parameters of the azide-inhibited Fe-NHase enzyme.[203,204] Nitrosyl complex $[Fe(S_2^{Me2}N_3(Pr,Pr))(NO)]$ (**31**) is best described as a $\{FeNO\}^6$ species where the Fe^{3+} and NO radicals couple.[206] The X-ray crystal structure of this complex shows that NO is coordinated in a linear fashion (Fe–N–O angle of 172.2(3)°). It was proposed that lack of any sulfenic or sulfinic groups in this model complex may result in greater backbonding to the Fe–NO unit, compared to the Fe-NHase(dark) active site where the NO is slightly more bent (Fe–N–O angle of 158.6°). Illuminating **31** with strong UV-light resulted in NO photolysis, although the resulting metal complex was observed to undergo irreversible decomposition. Interestingly, coordination of nitriles to **29** was not observed under any circumstances.

In order to increase the affinity of this complex type to nitriles, the group of Kovacs developed a ligand variant, **$S_2^{Me2}N_3$(Et,Pr)**, whose modified alkyl chain length distorts the coordination environment further towards square pyramidal in pentacoordinate complex $[Fe^{III}(S_2^{Me2}N_3(Et,Pr)]^+$ (**32**).[207] This has the effect of increasing the size of the binding pocket at the iron centre, reflected by the much higher rate at which **32** reacts with azide compared to **$S_2^{Me2}N_3$(Pr,Pr)**-bound **29**. Complex **32** was also shown to bind to thiocyanate and a variety of nitriles, including MeCN, EtCN, ^{i}PrCN, ^{t}BuCN, and PhCN (Figure 25).[208]

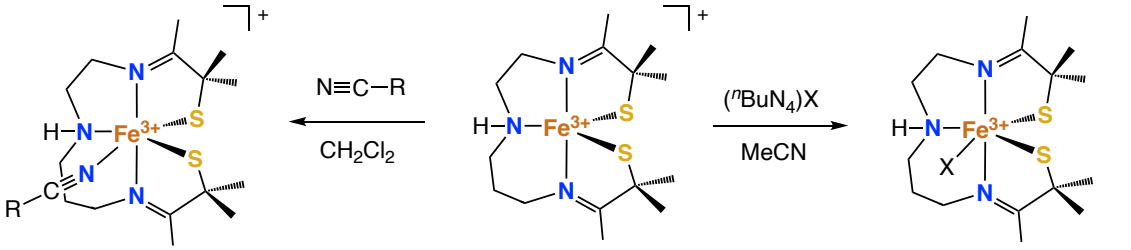

Figure 25. Reactivity of $[Fe^{III}(S_2{}^{Me2}N_3(Et,Pr))]^+$ (**32**) and its reactivity to azide, thiocyanate and nitriles.

More recently, Kovacs and co-workers showed that reacting **29** with an oxo atom donor such as iodosylbenzene (PhIO) affords the singly oxygenated low-spin ($S = {}^1/_2$) ferric complex, $[Fe^{III}(\eta^2\text{-}S^{Me2}O)(S^{Me2}N_3(Pr,Pr))]]^+$ (**35**), which features a side-on coordinated sulfenate group (Figure 26).[209] A metastable green intermediate is observed *en-route* to **35** with a maximum absorption at 675 nm. The authors hypothesise that this species could either be an iron(IV)-oxo or an iron(III)-iodosoaryl adduct, and that oxygenation of the sulfur is therefore dependent on the presence of a vacant site at the iron centre, since azide complex **30** was shown to be unreactive to PhIO.

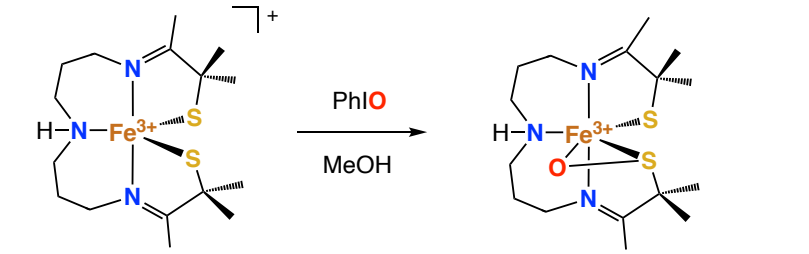

Figure 26. The conversion of $[Fe^{III}(S_2{}^{Me2}N_3(Pr,Pr))]^+$ (**29**) to its sulfenate form (**35**) using PhIO.

The group of Mascharak published several important NHase modelling studies involving the pentadentate N_3S_2 ligand **PyPSH$_4$**, which features a 2,6-bis(amido)pyridine backbone and two tethered thiophenolato groups.[210] Pentacoordinate, low-spin ($S = {}^1/_2$) iron(III) complex $[Fe^{III}(PyPS)]^-$ (**36**) was obtained by reacting the deprotonated, tetra-anionic ligand with $[FeCl_4](Et_4N)$ in DMF. The complex has a pseudo trigonal bipyramidal geometry and can reversibly bind to a variety of Lewis bases (including CN, SPh, N-methylimidazole, H_2O), which populate the site *trans* to one of the thiolato groups (Figure 27).[211] In all cases, the resulting six-coordinate iron(III) complexes (**37a-37d**) exhibit a low-spin ($S = {}^1/_2$) EPR signal almost identical to that of the Fe-NHase enzyme.

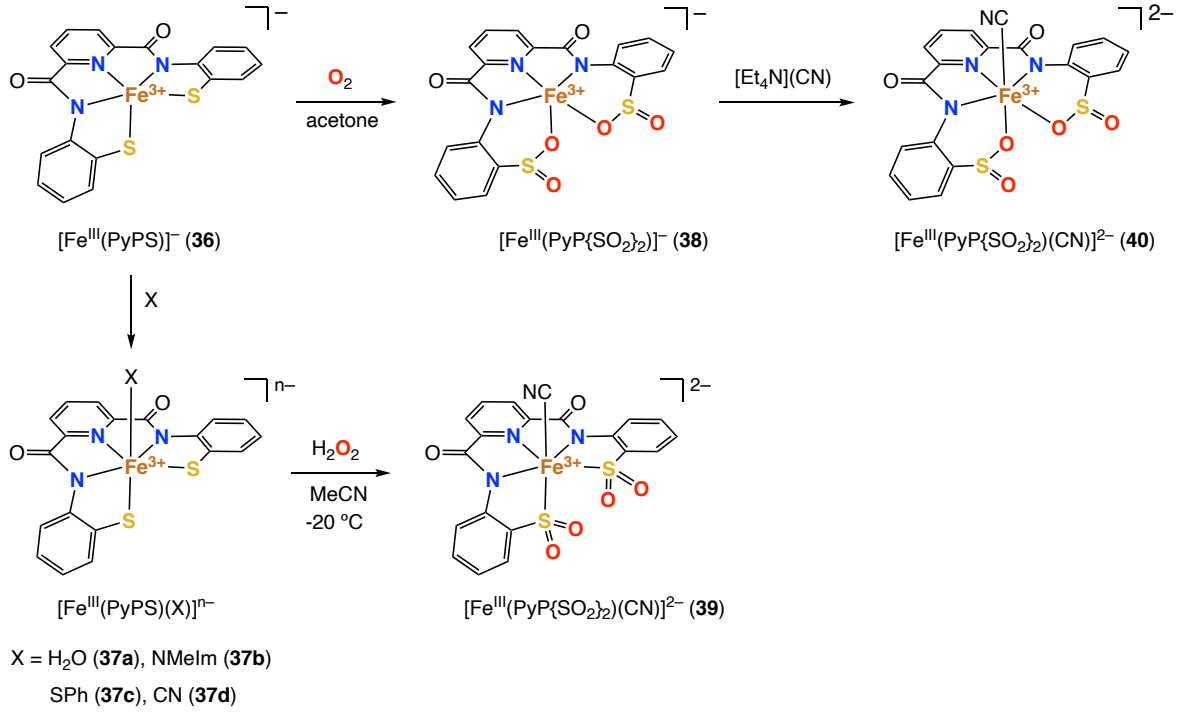

Figure 27. NHase model complexes supported by the pentadentate, tetra-anionic **PyPS^{4-}** ligand.

Stirring complex **36** in air for a period of several days affords the corresponding O-bound bis-sulfinato complex $[Fe^{III}(PyP\{SO_2\}_2]^-$ (**38**). In contrast, reacting $[Fe^{III}(PyPS)(CN)]^{2-}$ (**37d**) with H_2O_2 or O_2 affords the S-bound bis-sulfinato complex $[Fe^{III}(PyP\{SO_2\}_2(CN)]^{2-}$ (**39**). This discrepancy is likely due to the lack of vacant site in **37d**, which prevents the sulfinato groups from isomerising and adopting an O-bound coordination mode.[73]

The group of Artaud explored the use of carboxamido-containing tetradentate N_2S_2 ligands for NHase modelling studies (Figure 28). Pentacoordinate complex $[Fe^{III}(N_2S_2)(Cl)]^{2-}$ (**41**) has a distorted square pyramidal geometry and produces an EPR spectrum with features at g = 4.5 and 2, consistent with intermediate-spin ($S = {}^3/_2$) iron(III).[212] This contrasts to the typically low-spin nature of complexes obtained with the N_3S_2 ligands previously described. Electrochemical investigations showed that the chloride ligand can be substituted with water, hydroxide, and various solvents. The air-stable $\{FeNO\}^6$ adduct, $[Fe(N_2S_2)(NO)]^{2-}$ (**42**), was synthesised and its X-ray crystal structure shows that the NO is bound at the axial site with an almost linear configuration (Fe–N–O angle of 177.5°). However, unlike Fe-NHase, **42** is not photosensitive, which the authors attribute to the absence of any S-oxygenated moieties in the ligand framework. The same group showed that reacting related complex $[Fe^{III}(S_2N_2Cl_2)(Cl)]^{2+}$ (**43**) with two equivalents of cyanide in the presence of O_2 affords a low-spin ($S = {}^1/_2$), six-coordinate iron(III) complex where CN ligands occupy the axial positions of the complex and the equatorial thiolato groups are oxidised to their sulfinate forms.[213] The sulfinates are S-bound, as was the case for related complex $[Fe^{III}(PyP\{SO_2\}_2(CN)_2]^-$ (**31**), reported by Mascharak and co-workers. The NO reactivity of this complex was not investigated.

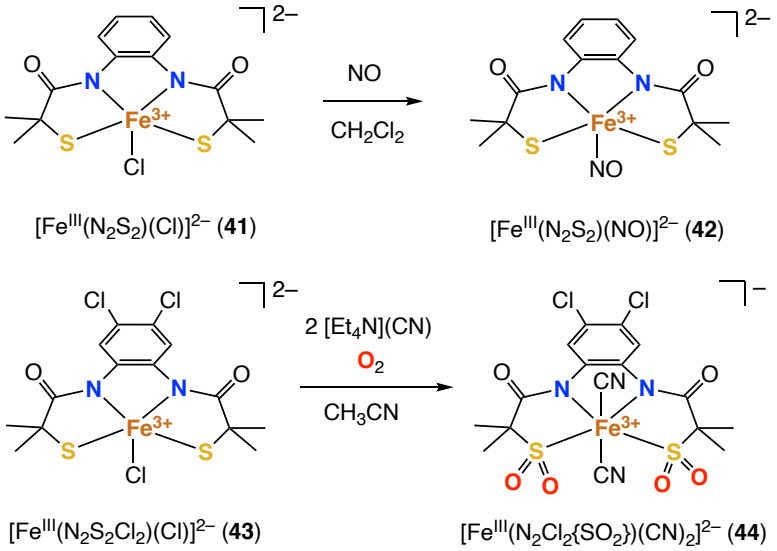

[Fe^{III}(N$_2$S$_2$)(Cl)]$^{2-}$ (**41**) [Fe^{III}(N$_2$S$_2$)(NO)]$^{2-}$ (**42**)

[Fe^{III}(N$_2$S$_2$Cl$_2$)(Cl)]$^{2-}$ (**43**) [Fe^{III}(N$_2$Cl$_2${SO$_2$})(CN)$_2$]$^{2-}$ (**44**)

Figure 28. NHase model complexes supported by the tetradentate **N$_2$S$_2$** and **N$_2$S$_2$Cl$_2$** ligands.

In a complementary study, the group of Mascharak prepared complex [Fe^{III}(Cl$_2$PhPepS)(DMAP)]$^-$ (**45**), supported by an equatorial, tetradentate N$_2$S$_2$ ligand that contains thiophenolate moieties rather than alkylthiolate groups (Figure 29).[214] Similarly to **41** and **43**, complex **45** is square pyramidal and exhibits an intermediate-spin (S = $^3/_2$) EPR signal with features at g = 4.39 and 1.98. Interestingly, the complex reacts readily with NO at –40 °C to form the {FeNO}^{6} adduct, [Fe(Cl$_2$PhPepS)(DMAP)(NO)] (**46**). The NO is coordinated axially with an almost linear configuration, *trans* to the DMAP ligand. The NO was shown to be labile in the absence of light, both under vacuum and in coordinating solvents such as MeCN. Oxygenation of **46** by 4 equivalents of (1*S*)-(+)-(10-camphorsulfonyl)oxaziridine affords the corresponding bis-sulfinato complex [Fe(Cl$_2$PhPep{SO$_2$}$_2$)(DMAP)(NO)]$^-$ (**47**) which, interestingly, does not show any NO lability in the dark. Upon exposure to light, NO was photo-released from X with a quantum yield of 0.55, similar to the NO-inactivated Fe-NHase value of 0.48. These studies strongly support the general hypothesis that S-oxygenation serves as a chemical "switch" with which to allow photolability of NO, thereby facilitating NHase activation.

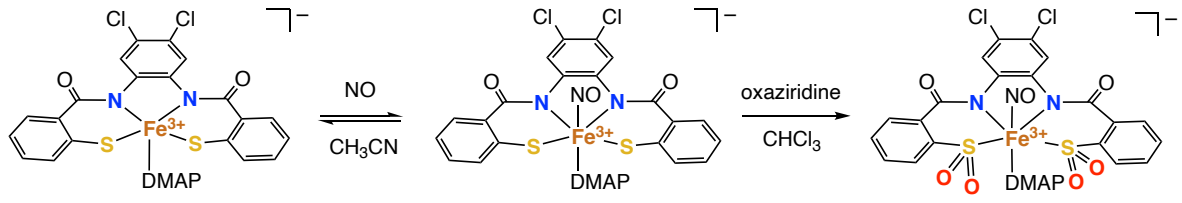

[Fe^{III}(Cl$_2$PhPepS)(DMAP)]$^-$ (**45**) [Fe^{III}(Cl$_2$PhPepS)(DMAP)(NO)]$^-$ (**46**) [Fe^{III}(Cl$_2$PhPep{SO$_2$}$_2$)(DMAP)(NO)]$^-$ (**47**)

Figure 29. Synthesis of a photolabile nitrosyl sulfinato complex that models the NHase active site.

Several groups have developed N$_2$S$_3$ ligand systems in an effort to more accurately structurally model the N$_2$S$_3$ coordination sphere of the NHase active site. The groups of Kovacs and Chottard developed the structurally isomeric **((tame-N$_2$S)S$_2$^{Me2})** and **L^{N2S3}**

ligands, whose dicarboxamide-trithiolate structures differ only in the relative arrangement of the carboxamide moieties (Figure 30). Chottard and co-workers synthesised an intermediate-spin iron(III) complex using $\mathbf{L}^{\mathbf{N2S3}}$, although the complex was so air-sensitive that it could only be isolated as the square pyramidal, monosulfinic complex, $[Fe^{III}(L^{N2S3}\text{-}O_2)]^{2-}$ (**48**). The O-bound sulfinate occupies the apical position and the equatorial plane is defined by the remaining N_2S_2 donors of the ligand scaffold.[215] In a similar study, Kovacs and co-workers were able to isolate and fully characterise the square pyramidal, intermediate-spin iron(III) trithiolate complex $[Fe^{III}((tame\text{-}N_2S)S_2^{Me2})]^{2-}$ (**49**).[216] Exposing this complex to air resulted in the selective dioxygenation of the apical thiolate moiety, yielding an O-bound sulfinate derivative, $[Fe^{III}((tame\text{-}N_2SO_2)S_2^{Me2})]^{2-}$ (**50**). The structural and electronic properties of **50** are similar to those reported by Chottard for **48**. All attempts at binding additional ligands to **50** were unsuccessful and no NHase reactivity was observed. The authors hypothesis that NHase enzyme activity is therefore dependent on the presence of the non-oxygenated cysteinate residue at the apical position of its active site. The authors further argue that regioselective oxygenation of the equatorial cysteinates in NHase increases the Lewis acidity of the ferric ion and strengthens the Fe–S interaction to the apical thiolate, resulting in the low-spin state ($S = {}^1/_2$) of the iron(III) centre.

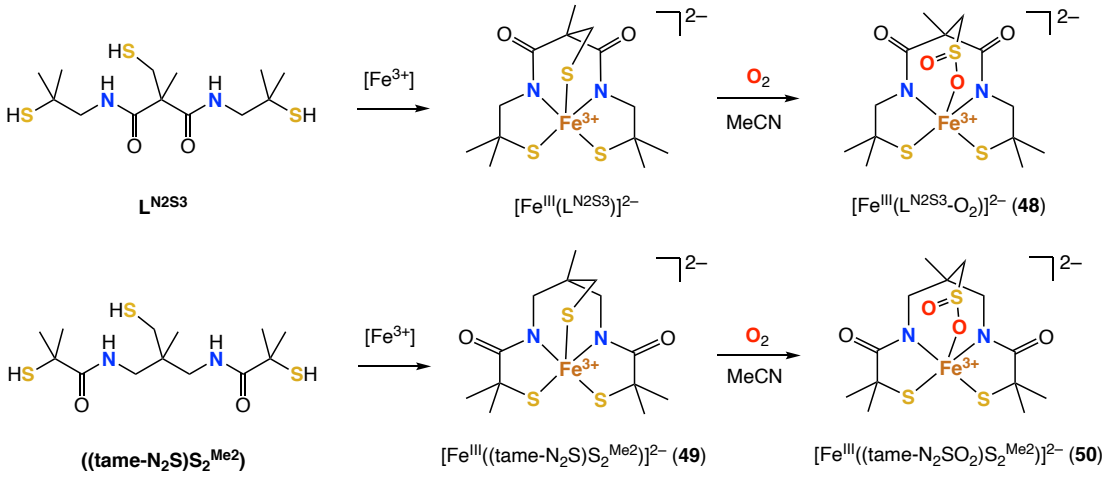

Figure 30. Selected examples of NHase model complexes featuring an N_2S_3 ligand.

Grapperhaus and co-workers employed the macrocyclic [9]aneS2 **(bmmp-TASN)$^{2-}$** ligand to synthesise complexes $[Fe^{III}(bppm\text{-}TASN)(Cl)]$ (**51**) and $[Fe^{III}(bmmp\text{-}TASN)(CN)]$ (**52**), depicted in Figure 31.[217,218] The reactivities of these complexes to O_2 was shown to differ significantly as a function of their different spin states.[218] High-spin ($S = {}^5/_2$) chloride complex **51** reacts with O_2 to produce ligand-derived disulfide and a mixture of insoluble iron-oxo clusters. In contrast, low-spin ($S = {}^1/_2$) cyano complex **52**, reacts with O_2 to produce the corresponding O-bound bis-sulfonato complex. Metathesis of the chloride in **51** with thallium triflate affords complex $[Fe^{III}(bppm\text{-}TASN)(OTf)]$ (**53**), which is low-spin ($S = {}^1/^2$) in non-coordinating solvents.[219] The complex was shown to bind reversibly to MeCN and PhCN, producing low-spin, six-coordinate nitrile complexes with EPR parameters very similar to those reported for Fe-NHase. Further binding studies also

showed that the triflate ligand in **53** is easily displaced by coordinating solvents such as DMF, H_2O, pyridine, MeOH, and DMSO, affording high-spin iron(III) species in all cases. Thus, complex **53** is the first structural model complex of NHase that binds to nitrile, water, and amide moieties.

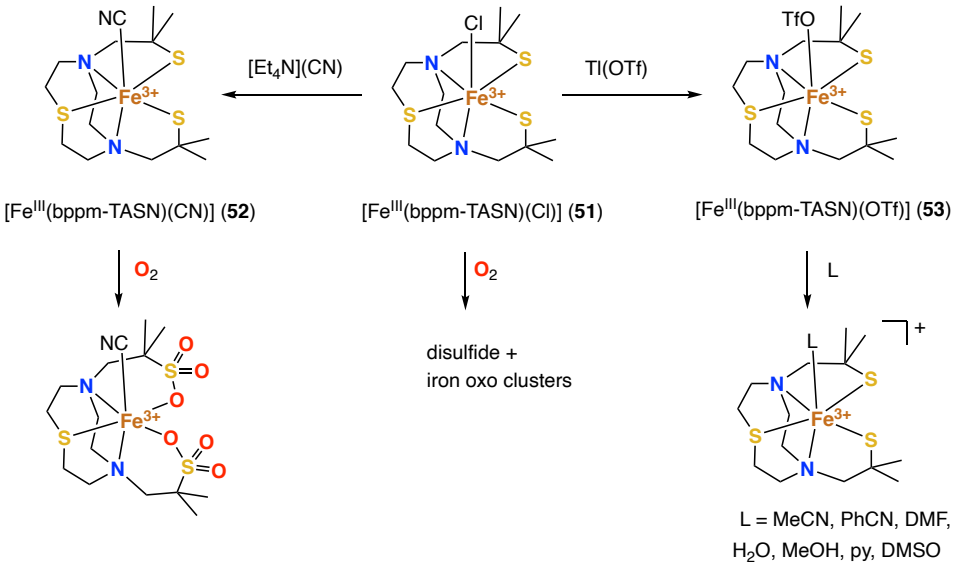

Figure 31. Selected examples of NHase model complexes featuring a N_2S_3 ligand.

Finally, it is worth noting that other NHase modelling studies have been reported using ligands or complexes that have classically been regarded as platforms with which to model other enzymes. The most notable examples are complexes $[Fe^{III}(S^{Me2}N_4(tren))(MeCN)]^{2+}$ (**16**^{MeCN}) and $[Co^{III}(S^{Me2}N_4(tren))]^{2+}$ (**54**) reported by Kovacs and co-workers, both of which are supported by a N_4S ligand that is typically used to model SOR or CDO reactivity (Figure 32). Acetonitrile-bound iron complex **16**^{MeCN} was first reported in 2001 and has so far only been investigated in the context of SOR modelling (*vide supra*).[186] The complex is low-spin ($S = {}^1/_2$) and produces an axial EPR spectrum with features at $g = 2.12$ and 1.98. The analogous cobalt complex **54** was reported in 2011 and can be regarded as one of the closest functional models of NHase to date as it is able to convert acetonitrile to its corresponding amidate in the presence of hydroxide.[220] To the best of our knowledge examples of iron NHase model complexes that can successfully activate and hydrate nitriles are still lacking.

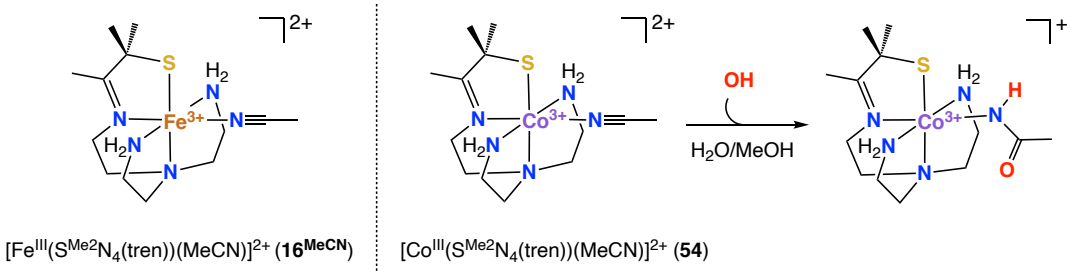

Figure 32. NHase models reported by the group of Kovacs, supported by an atypical N_4S ligand.

1.3.5 Model Complexes of CDO and EgtB

The 3-His facial triad (3His) bioinorganic motif, found at the active sites of CDO and EgtB, is typically modelled using tridentate, facially coordinating, nitrogen-rich ligands that ensure the availability of mutually-*cis* vacant sites at the iron centre for substrate and O_2 binding. Alternatively, tripodal, tetradentate N4 ligands can also be used to model CDO and EgtB. From a functional modelling point of view, the increased denticity of N4 ligands can help stabilise the formation of mononuclear, high-spin iron(II) complexes, whose structural integrity often suffers from ligand lability. From a structural modelling point of view, these ligands can be regarded as mimicking the additional nitrogen group present at these active sites (i.e. the cysteine amine group in CDO and the trimethyl histidine (TMH) in EgtB). Thiolate-tethered tripodal ligands such as **N3PyS**, **N3PySR**, **$S^{Me2}N_4$(6-Me-DPEN)** and **$S^{Me2}N_4$(tren)** (*vide infra*) provide N3S or N4S donor sets that are also relevant to CDO and EgtB modelling.

The first CDO modelling study was published in 2010 by the group of Goldberg (Figure 33). In this study, a bis-iminopyridine-derived ligand with a pendant thiolate, **LN_3S** was used to synthesise a high-spin ($S = 2$) iron(II) complex, [$Fe^{II}(LN_3S)(OTf)$] (**55**).[221] Contrary to the facial arrangement of amino acids observed in the 3His, the three nitrogen donors of **LN_3S** coordinate in a planar, meridional fashion to the iron centre. The pendant thiolate coordinates *cis* to the labile triflate anion.[222] Reacting **55** with O_2 initially forms a sulfinato complex, which subsequently oxidises to its sulfonate form, [$Fe^{II}(LN3SO_2)(OTf)$] (**56**). Isotopic labelling studies using both $^{18}O_2$ and $H_2{}^{18}O$ confirm that all oxygen atoms incorporated in the sulfonate product derive from O_2 gas. DFT studies performed in

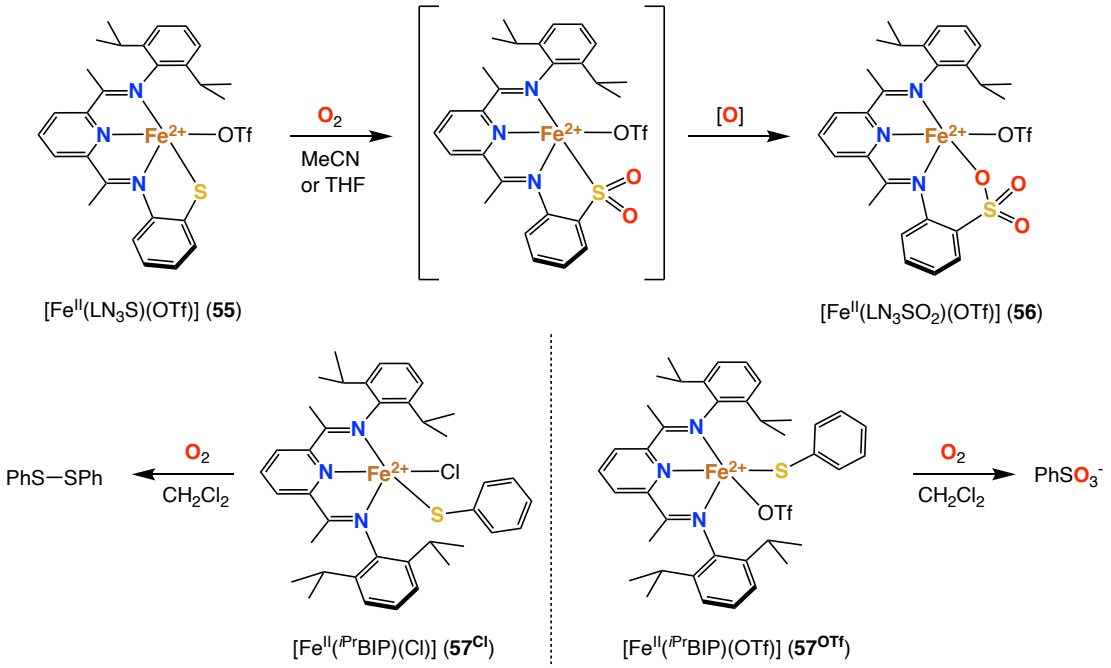

Figure 33. The O_2 reactivity of [$Fe^{II}(LN_3S)(OTf)$] (**55**) and $Fe^{II}(^{iPr}BIP)(SPh)(X)$] (**57**), X = Cl, OTf .

collaboration with the De Visser group suggest that dioxygen binds *cis* to the thiolate group, forming an iron(III) superoxo intermediate, similar to the mechanism with which thiol dioxygenase enzyme reactivity takes place.[223] The zinc analogue of **55** did not exhibit any O_2 reactivity, enabling the authors to conclude that iron is essential for O_2 activation.

In a related study, Goldberg and co-workers used tridentate bis-iminopyridine ligand **^{iPr}BIP** in conjunction with an exogenous thiophenolate ligand to synthesise high-spin (S = 2) iron(II) complexes [Fe^{II}(^{iPr}BIP)(SPh)(Cl)] (**57^{Cl}**) and [Fe^{II}(^{iPr}BIP)(SPh)(OTf)] (**57^{OTf}**).[224] Interestingly, the positioning of the thiolate was seen to be dependent on the nature of the anion present in the iron's coordination sphere. The weakly coordinating triflate anion in **57^{OTf}** causes the thiolate to occupy the pseudo-equatorial position, *cis* to the remaining vacant site. In contrast, the strongly coordinating chloride anion in **57^{Cl}** forces the thiolate to occupy the pseudo- axial position, *trans* to the remaining vacant site. Both complexes are reactive to O_2 but differ significantly in their product outcomes (Figure 33). By means of DFT calculations, it was proposed that O_2 binds *cis* to SPh in **57^{OTf}**, forming an iron(III)-superoxo intermediate whose distal oxygen atom can attack the bound thiolate, forming a new S–O bond and ultimately leading to sulfonate production.[225] In contrast, O_2 binds *trans* to SPh in **57^{Cl}**, preventing S-oxygenation and generating disulfide instead.[226]

In order to more accurately model the facial coordination of the 3His bioinorganic motif, Goldberg and co-workers developed the thiolate-tethered **N_3PyS** ligand, which provides a square pyramidal N_4S coordination environment (Figure 34).[168] A low-spin (S = 0), octahedral iron(II) complex was prepared, [Fe^{II}(N_3PyS)(MeCN)](BF_4) (**58**), that is unreactive to O_2 in MeCN solution. The crystal structure of the complex revealed the presence of a potentially labile MeCN ligand bound *cis* to the ligand's thiolate moiety. Reacting **58** with NO in MeCN generates a low-spin (S = $^1/_2$) {FeNO}^{7} complex, [Fe(N_3PyS)(NO)]$^+$ (**59**), whose spectroscopy is comparable to the low-spin {FeNO}^{7} species formed when exposing CDO to NO. Interestingly, dissolving **58** in methanol induces crossover to the high-spin (S = 2) state, likely through displacement of the bound MeCN for MeOH. This high-spin complex is reactive to O_2 and forms a green solution from which brown crystals of a sulfinic product complex, [Fe^{II}(N_3PySO_2)(NCS)] (**60**), were grown after addition of KSCN. The nature of the metastable green intermediate could not be determined.

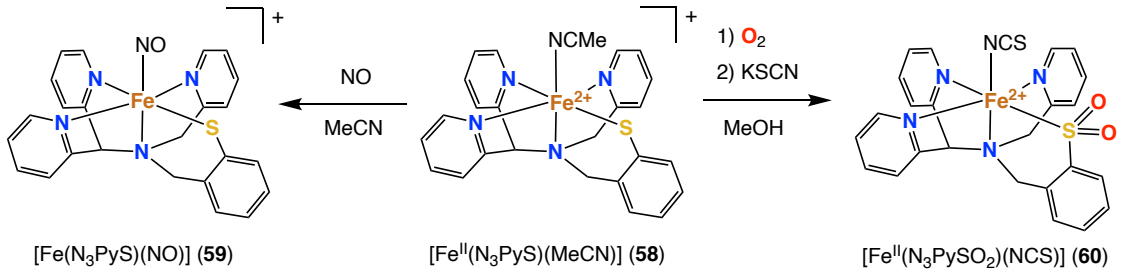

Figure 34. Reactivity of complex [Fe^{II}(N_3PyS)(MeCN)]$^+$ (**58**) to NO and O_2.

The group of Limberg reported complexes [$Fe^{II}(Tp^{Ph,Me})$(CysOEt)] (**61**) and [$Fe^{II}(Tp^{Ph,Me})$(CysAm)] (**62**), which were shown not only to be close structural models of the CDO and ADO active sites, respectively, but also some of the most realistic functional models of thiol dioxygenase enzyme reactivity (Figure 35).[227,228] Both complexes are pentacoordinate, featuring a facial, tridentate **$Tp^{Ph,Me}$** ligand and an exogenous L-cysteine-derived co-ligand, which coordinates through both its anionic thiolate and neutral amine groups. Exposing **61** or **62** to O_2 in dichloromethane under anhydrous conditions affords the corresponding sulfinic product exclusively, with no observable formation of either the disulfide or sulfonate products. Isotopic labelling studies confirm that both oxygen atoms incorporated within the sulfinic products originate from O_2 gas, although no Fe-O_2 intermediates were detected spectroscopically. DFT analysis, performed in collaboration with the De Visser group,[229] suggests that O_2 activation by **61** is only possible upon dissociation of one of the supporting **$Tp^{Ph,Me}$** pyrazole groups, due to the limited accessibility of the iron centre within its binding pocket. This not only disrupts the supporting N3 coordination motif but also enables O_2 to bind *trans* to the amine group of the cysteine co-ligand, deviating somewhat from native thiol dioxygenase reactivity.

In a later study, Limberg and co-workers employed mesityl-substituted ligands **Tp^{Mes}** and **Tp^{Mes*}** to prepare complexes [$Fe^{II}(Tp^{Mes})$(CysOEt)] (**63**), [$Fe^{II}(Tp^{Mes})$(CysAm)] (**64**) and [$Fe^{II}(Tp^{Mes*})$(CysAm)] (**65**).[230] The increased steric repulsion between the pyrazole mesityl substituents was shown to provide larger binding cavities for the iron centres, causing their reaction with O_2 to proceed much faster and without any ligand dissociation needing to occur. This kinetic enhancement enabled a short-lived iron(III)-superoxo intermediate to accumulate sufficiently for spectroscopic analysis. Moreover, this study presented the first examples of structurally characterised iron(II) η^2-*O,O*-sulfinate product complexes.

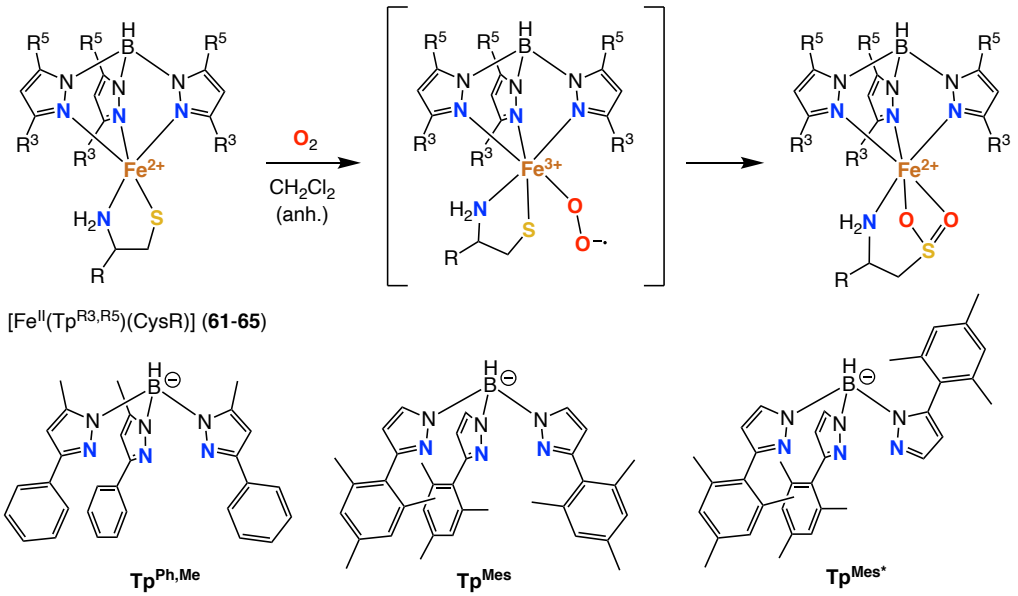

Figure 35. The reaction of complexes [$Fe^{II}(Tp^{R3,R5})$(CysR)] (**61-65**) with O_2, affording the corresponding sulfinic products. $Tp^{R3,R5}$ = $Tp^{Ph,Me}$, Tp^{Mes}, Tp^{Mes*}; R = COOEt (CysOEt), H (CysAm).

In a related study, Fiedler and co-workers synthesised pentacoordinate complexes $[Fe^{II}(^{Ph2}TIP)(CysOEt)]^+$ (**66**) and $[Fe^{II}(^{Ph2}TIP)(CysAm)]^+$ (**67**), supported by the neutral, tridentate tris(imidazolyl)phosphine ligand ^{Ph2}**TIP** (Figure 36).[231] Exposing **66** or **67** to O_2 results in the exclusive formation of the corresponding sulfinic products, thus mirroring the reactivity previously observed by Limberg for Tp-bound complexes **61**-**65**. From a steric point of view, ligands ^{Ph2}**TIP** and **Tp**^{Ph,Me} are similar as their imidazole- or pyrazole-derived phenyl substituents help encapsulate the iron within the ligand's binding pocket. Indeed, kinetic studies do not reveal any particular influence of either ligand on the rate of reaction of the complexes with O_2. However, DFT calculations suggest that the anionic **Tp**^{Ph,Me} ligand promotes greater charge transfer from the iron to dioxygen (i.e. O_2 binding is thermodynamically more favourable), while the neutral ^{Ph2}**TIP** ligand promotes a greater degree of radical thiyl character on the ligated sulfur atom, thereby lowering the energy barrier for S–O bond formation. Reacting **66** and **67** with NO affords six-coordinate, intermediate-spin ($S = {}^3/_2$) $\{FeNO\}^7$ adducts, with only minor contributions from a low-spin ($S = {}^1/_2$) species observed at low temperature.[231]

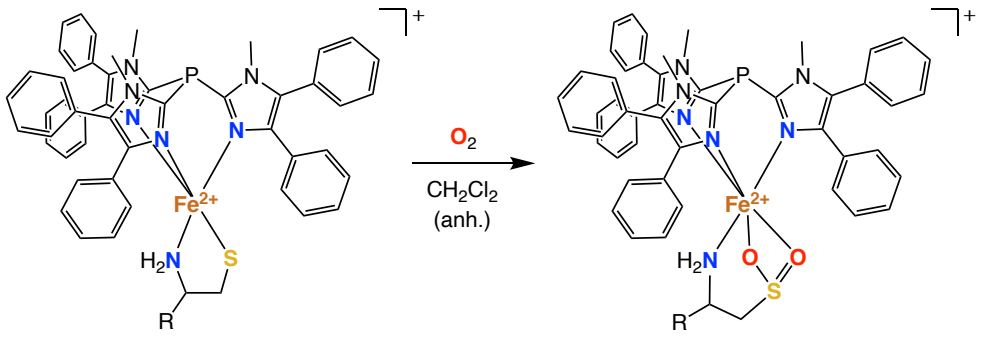

Figure 36. The reaction of $[Fe^{II}(^{Ph2}TIP)(CysOEt)]$ (**66**) and $[Fe^{II}(^{Ph2}TIP)(CysAm)]$ (**67**) with O_2.

In recent years, the group of Goldberg has explored the reactivity of iron(II) 2-aminobenzenethiolate (abt) complexes as models of the CDO active site, supported by facial, tridentate 1,4,7-tris(alkyl)-1,4,7-triazacyclononane (R_3tacn) ligands.[232] Complexes $[Fe^{II}(Me_3tacn)(abt)(OTf)]$ (**68**) and $[Fe^{II}(Me_3tacn)(abt^{CF3})(OTf)]$ (**69**) are six coordinate, with the bidentate abt ligand coordinated *cis* to the potentially labile triflate anion (Figure 37). In contrast, complexes $[Fe^{II}(^iPr_3tacn)(abt)](OTf)$ (**70**) and $[Fe^{II}(^iPr_3tacn)(abt^{CF3})](OTf)$ (**71**) are pentacoordinate as a result of the increased steric bulk of the ligand's ^{i}Pr substituents, which force the triflate anion to become non-coordinating (Figure 38).

Reacting complexes **68** and **69** with O_2 at –95 °C in MeOH produces deep blue solutions in both cases and oxygenation of abt to its sulfinic form is observed. For the reaction of **68**, the methyl sulfinate ester is isolated after work-up. For the reaction of **69**, a dinuclear oxo-bridged diiron(III) product complex was crystallographically characterised, featuring bridging sulfinato ligands. In contrast, letting the reaction between complex **68** and O_2

proceed at 23 °C results in 2-aminophenyl disulfide production. For these reactions, the authors propose a common iron(III) superoxide intermediate, although no Fe-O_2 species were detected spectroscopically.

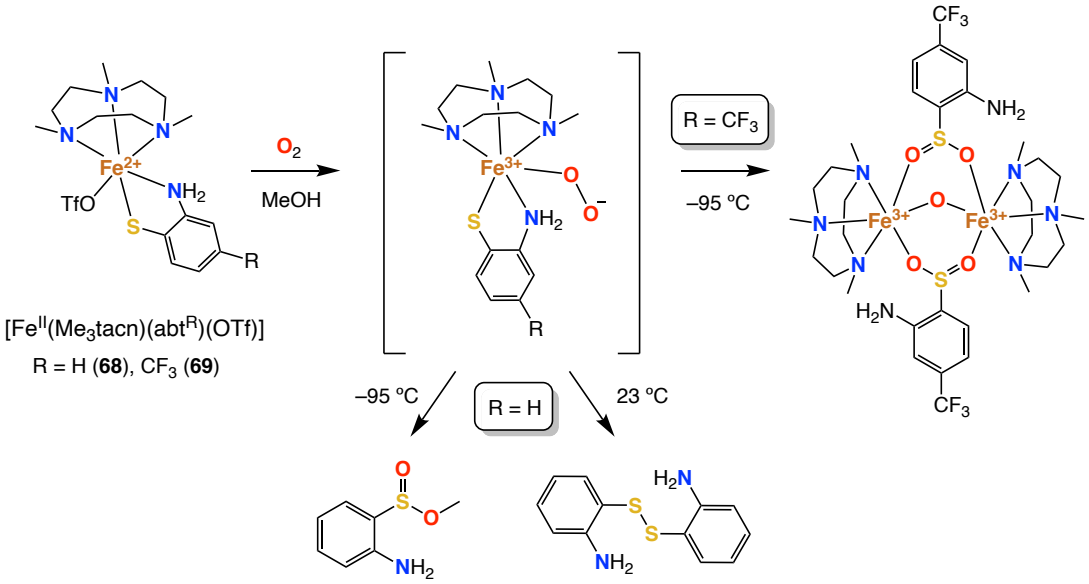

Figure 37. The reaction of [Fe^{II}(Me_3tacn)(abt)] (**68**) and [Fe^{II}(Me_3tacn)(abt^{CF3})] (**69**) with O_2.

In contrast, ^{i}Pr-substituted complexes **70** and **71** decompose rapidly in MeOH solution and are only stable in aprotic solvents such as acetonitrile.[232] Their reaction with O_2 in the presence of a base quantitatively affords the corresponding iron(III)-iminobenzenethiolate (ibt) complexes, [Fe^{III}($^{i}Pr_3$tacn)(ibt^{R})]$^{+}$ (R = H (**72**), CF_3 (**73**)), in line with proton-coupled electron transfer (PCET) reactivity (Figure 38).[233] In the absence of a base, oxidation of **70** or **71** with O_2 generates the corresponding aminobenzene disulfide product. These results indicate that iron or sulfur oxidation in these complexes is determined by the protonation state of the aniline.

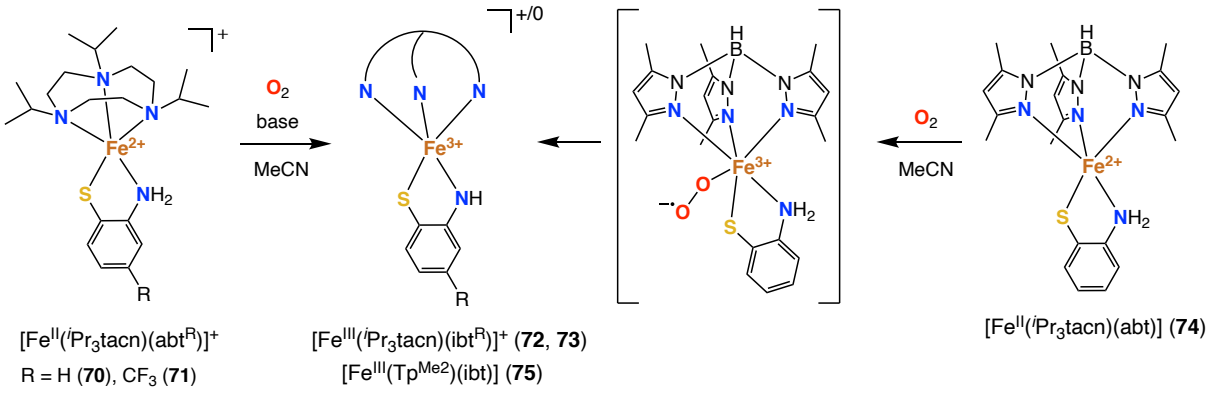

Figure 38. The reaction of complexes [Fe^{II}($^{i}Pr_3$tacn)(abt)]$^{+}$ (**70**), [Fe^{II}($^{i}Pr_3$tacn)(abt^{CF3})]$^{+}$ (**71**) and [Fe^{II}(Tp^{Me2})(abt)] (**74**) with O_2, forming iron(III) iminobenzenethiolate complexes (**72**, **73**, **75**).

Fiedler and co-workers described a similar phenomenon for related complex [$Fe^{II}(Tp^{Me2})$(abt)] (**74**), depicted in Figure 38.[234] Exposing **74** to O_2 at –80 °C forms a short-lived purple intermediate, assigned as an iron(III)-superoxo complex on the basis of UV-vis, MCD and resonance Raman spectroscopies and isotopic $^{18}O_2$ labelling studies. This intermediate decays to form a green EPR-active ferric iminobenzenethiolate complex, [$Fe^{III}(Tp^{Me2})$(ibt)] (**75**). A PCET mechanism was proposed on the basis of DFT analysis, which suggests that proton transfer from the aniline donor to the η^1-superoxide is ~4 kcal/mol lower in energy than S–O bond formation.

Biomimetic complexes that are of relevance to CDO and EgtB may also be found in past studies that were either targeting different enzyme active sites or that were not focused on any particular enzyme at all. A good example is complex [$Fe^{II}(S^{Me2}N_4$(tren-R_4))]$^+$ (R = H (**14**), Et (**76**)), first reported by the group of Kovacs for SOR modelling studies (*vide supra*).[186,193] The supporting ligands in these complexes provide a trigonal bipyramidal N_4S coordination environment reminiscent of that of **N_3PyS** (Figure 39). Another example is complexes [$Fe^{II}(Py_2S)$(X)], where X = Cl (**77^{Cl}**) and X = Br (**77^{Br}**), reported by the group of Rheingold, which were investigated in the context of Fe–S cluster nuclearity control and whose O_2 reactivity has not been investigated (Figure 39).[235]

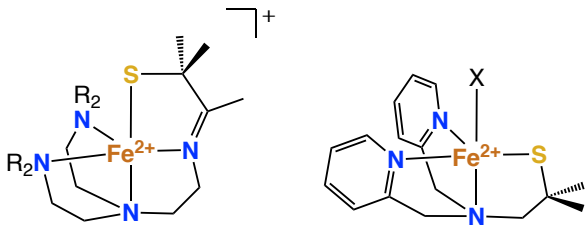

[$Fe^{II}(S^{Me2}N_4$(tren-R_4))]$^+$ R = H (**14**), Et (**76**)

[$Fe^{II}(Py_2S)$(X)] X = Cl (**77^{Cl}**), Br (**77^{Br}**)

Figure 39. Examples of iron(II) thiolate complexes relevant to CDO and EgtB modelling.

Conversely, new biomimetic studies have been conducted with the intention of investigating CDO reactivity using complexes that were classically used for modelling other enzymes. For instance, Kovacs and co-workers investigated the oxidation chemistry of iron complexes supported by ligand **$S_2^{Me2}N_3$(Pr,Pr)**, which was initially developed to model NHase (*vide supra*).[203] This pentadentate N_3S_2 ligand ensures the presence of a vacant site *cis* to one of its alkylthiolate donors. Reacting ferrous complex [$Fe^{II}(S_2^{Me2}N_3$(Pr,Pr))] (**78**) with O_2 in THF at –73 °C generates a red-coloured, metastable intermediate, assigned as an iron(III)-superoxo species, [$Fe^{III}(S_2^{Me2}N_3$(Pr,Pr))(O_2)] (**79**), on the basis of UV-vis, NMR and resonance Raman spectroscopies and $^{18}O_2$ labelling studies.[236] This intermediate is capable of abstracting a H-atom from the THF solvent, likely forming an iron(III) hydroperoxo intermediate (**80**) that collapses to yield the singly oxygenated low-spin (S = $^1/_2$) iron(III) complex, [$Fe^{III}(\eta^2$-$S^{Me2}O)(S^{Me2}N_3$(Pr,Pr))]]$^+$ (**35**), which features a side-on coordinated sulfenate group. As previously mentioned, complex **35** is also obtained

through treatment of complex $[Fe^{III}(S_2{}^{Me2}N_3(Pr,Pr))]^+$ (**29**) with iodosylbenzene.[209] The oxidation of sulfur in this manner was shown to be dependent on the availability of an iron coordination site *cis* to the alkylthiolate.

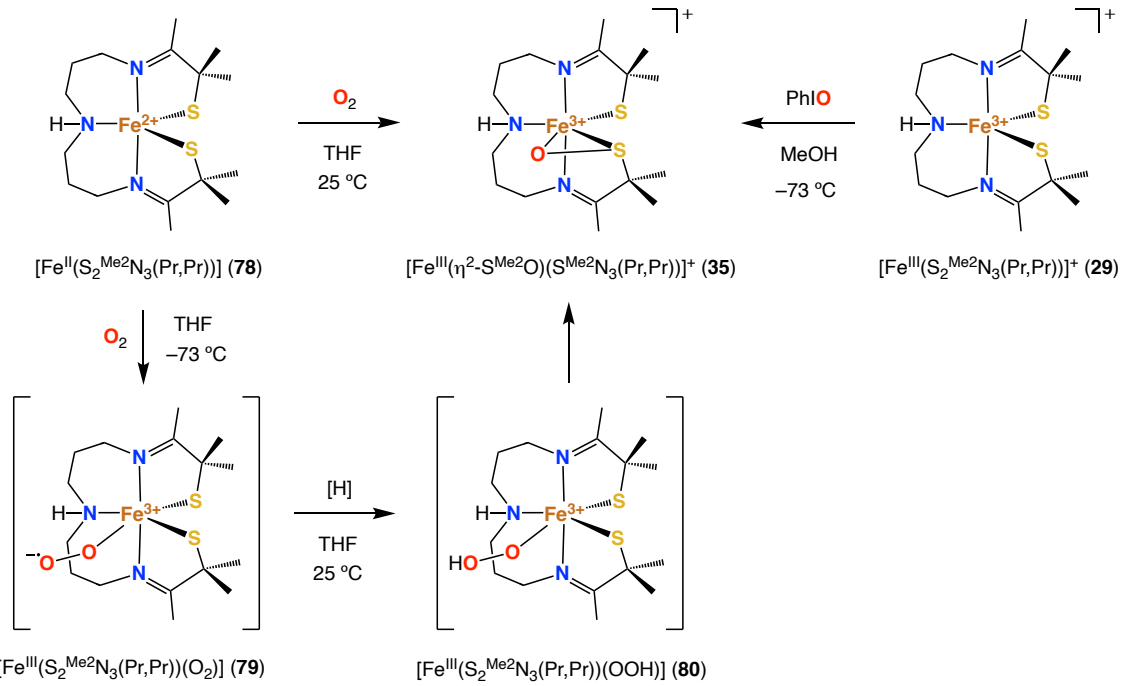

Figure 40. The oxidation chemistry of $[Fe^{II}(S_2{}^{Me2}N_3(Pr,Pr))]$ (**78**) and $[Fe^{III}(S_2{}^{Me2}N_3(Pr,Pr))]^+$ (**29**).

Very recently, the group of Fiedler reported complexes $[Fe^{II}(L^A)(SMes)]^+$ (**81**) and $[Fe^{II}(L^B)(SCy)]^+$ (**82**), specifically designed to model sulfoxide synthase enzyme active sites (Figure 41). Ligands $\mathbf{L^A}$ and $\mathbf{L^B}$ have tripodal TPA-like designs that have been adapted to include pendant imidazole groups in order to structurally model TMH coordination.[237] The trigonal bipyramidal N4S coordination sphere of these complexes ensures that the remaining vacant site is positioned *cis* to the thiolate, reminiscent of Goldberg's **N_3PyS**-based complexes. The reported Fe–S bond lengths of 2.3616(7) Å for **81** and 2.3048(7) for **82** reflect the aromatic and aliphatic natures of the exogenous thiolates, respectively.

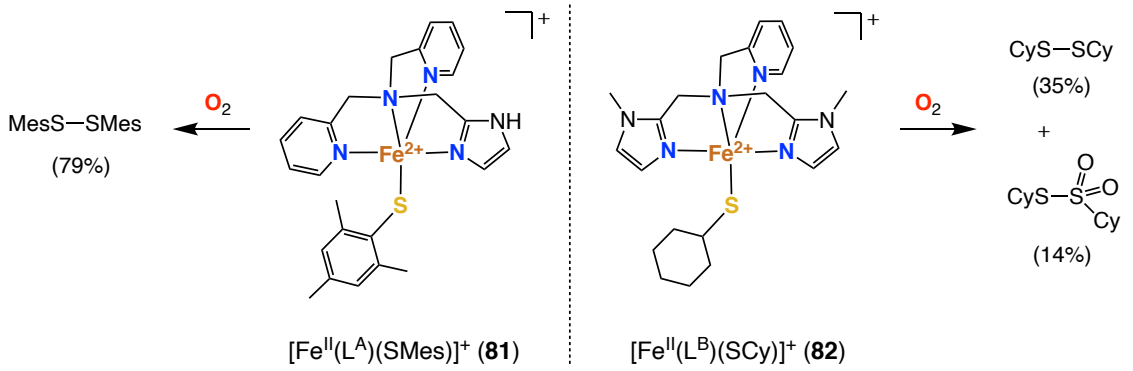

Figure 41. Reactions of $[Fe(L^A)(SMes)]^+$ (**81**) and $[Fe(LB)(SCy)]^+$ (**82**) with O_2.

NO reactivity studies showed that NO could bind directly to the iron centre, forming a $S = {}^{3}/_{2}$ $\{FeNO\}^{7}$ species. However, no sulfoxide product formation was observed upon exposure of the complexes to O_2. Instead, disulfide was produced, with small amounts of thiosulfonate ester also detected in the case of **82**. The lack of any sulfinic product is somewhat surprising given the results of Goldberg and co-workers, where oxygenation of the sulfur was observed in complexes where O_2 could bis *cis* to the thiolate.

A related study was published in the mid-1990s by the group of Que, which described the structure and reactivity of high-spin ($S = 2$) $[Fe^{II}(TPA)(SR)]^{+}$ complexes, where R = Ph (**83a**), *p*-Tol (**83b**), *p*-Cl-Ph (**83c**), Mes (**83d**), depicted in Figure 42.[238] Interestingly, this family of complexes was originally published with the aim of modelling the substrate-bound IPNS active site rather than sulfoxide synthase enzymes. However, the tetradentate, tripodal N_4 ligand architecture of **TPA** is very similar to the $\mathbf{L}^{A}$ and $\mathbf{L}^{B}$ ligands reported by the Fiedler group and is, arguably, structurally closer to the 3His bioinorganic motif found in CDO and EgtB than it is to the 2H1C.

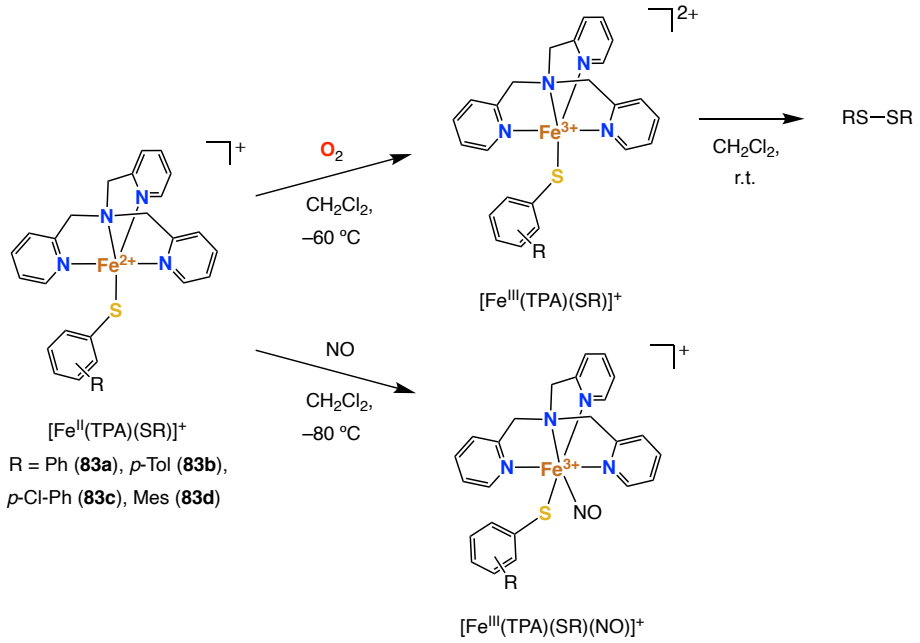

Figure 42. The reaction of $[Fe(TPA)(SR)]^{+}$ with O_2 and NO (R = Ph, *p*-Tol, *p*-Cl-Ph, Mes).

The X-ray crystal structure of $[Fe(TPA)(SMes)]^{+}$ (**83d**) reveals the Fe–S bond length to be 2.345(1) Å, which is similar (albeit slightly shorter) than that of related complex $[Fe(L^{A})(SMes)]^{+}$ (**81**), reported by the group of Fiedler (*vide supra*). Reacting complexes $[Fe(TPA)(SR)]^{+}$ with O_2 at –60 °C lead to the formation of metastable green species corresponding to the one-electron oxidised iron(III) derivatives. Warming to room temperature caused a rapid decay of these species to (μ-oxo)diiron(III) complexes and thiolate oxidation to the corresponding disulfide products. Reacting the complexes with NO gas at –80 °C produced $S = {}^{3}/_{2}$ $\{FeNO\}^{7}$ adducts.

1.3.6 Model Complexes of IPNS and ETHE1

The active sites of IPNS and ETHE1 share a common bioinorganic motif: the 2-His-1-Carboxylate facial triad (2H1C). The anionic O-donor of the 2H1C is proposed to play a crucial role in enzyme reactivity. Rather strikingly, enzymes that contain the 2H1C at their active site have frequently been modelled using synthetic iron complexes that feature tripodal nitrogen-rich N_3 or N_4 ligands such as the **TPA** or **Tp** ligand families. This is largely due to the well-established coordination chemistry of these ligands as well as the characteristic spectroscopic traces associated to their complexes, which aid the identification of crucial intermediates during reactivity studies. However, these ligands are arguably closer in structure to the 3-His facial triad than the 2H1C, as they do not provide any anionic O-donor.

In recent years, the group of Goldberg has explored the coordination chemistry of mixed *N,O*-donor ligands related to the **N_3PyS** ligand scaffold, which was initially developed to model CDO. One such example is thioether ligand **$N_3Py^{amide}SR$**, which provides a neutral N_4SO coordination sphere, as seen in low-spin (S = 0) complex $[Fe^{II}(N_3Py^{amide}SR)]^{2+}$ (**84**) (Figure 43).[239] The ligand's pendant *tert*-butyl amide binds to the iron centre through its carbonyl oxygen atom, *cis* to the thioether group. Reactivity studies demonstrated that the amide is readily displaced by alky- or hydroperoxo ligands, affording low-spin ($S = {}^1/_2$) complexes $[Fe^{III}(N_3Py^{amide}SR)(OOR)]^{2+}$ at –40 °C (R = H (**85a**), ^{t}Bu (**85b**)).[240] Similarly, complex **84** reacts with PhIO at –40 °C to afford a metastable high-valent iron(IV)-oxo complex, $[Fe^{IV}(N_3Py^{amide}SR)(O)]^{2+}$ (**86**), with the oxo ligand bound *cis* to the thioether.[239] In all cases, ligand's pendant amide moiety acts as a H-bond donor to the iron-bound oxygen atom.

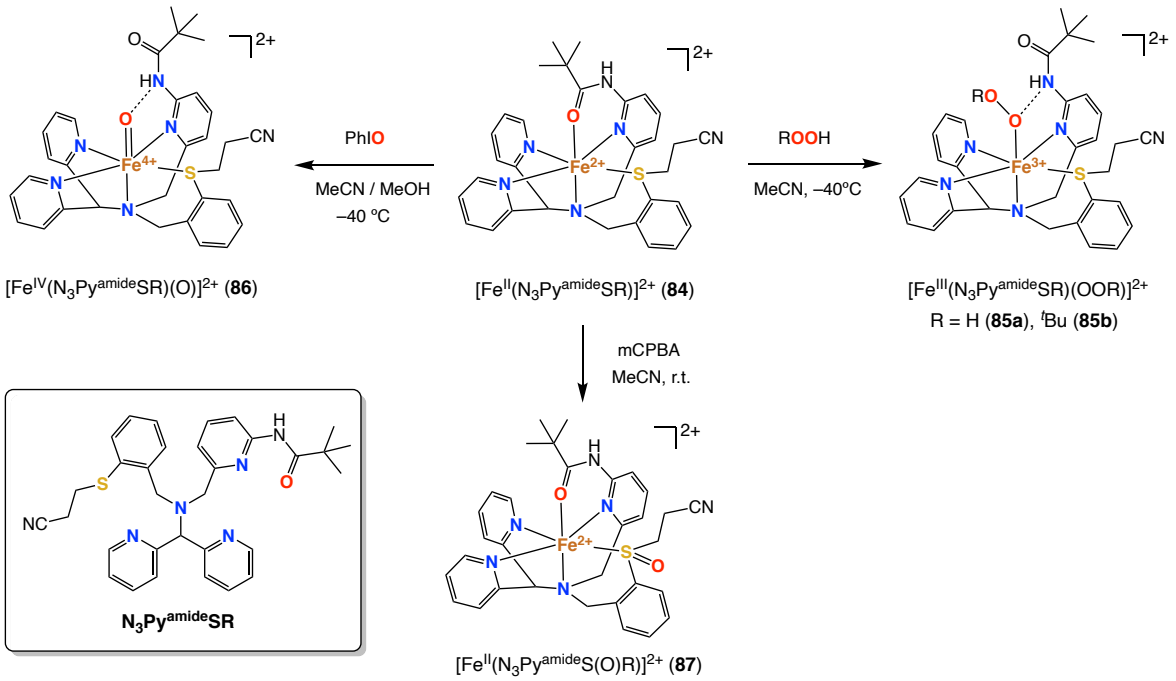

Figure 43. Complex $[Fe^{II}(N_3Py^{amide}SR)]$ (**84**) and its reactivity to a variety of oxidants, including ROOH (R = H, ^{t}Bu), PhIO and mCPBA (*meta*-chloroperbenzoic acid).

Complex **86** is further demonstrated to perform S-oxygenation by OAT to external thioether substrates. Interestingly, the ligand thioether bound *cis* to the oxo atom does not undergo any oxygenation. In contrast, reacting **84** with a more powerful oxidant such as mCPBA does result in oxygenation of the ligand thioether moiety, affording $[Fe^{II}(N_3Py^{amide}S(O)R)]^{2+}$ (**87**). Overall, ligand these studies by Goldberg provide a nice example of how ligand design can be tuned to incorporate O-donors, approaching the active site structure of IPNS to a greater extent. However, **$N_3Py^{amide}SR$**'s high denticity and the coordination lability exhibited by its amide group make it more suitable for modelling second sphere coordination effects than IPNS modelling.

Very recently, the group of Goldberg reported an interesting IPNS model complex, $[Fe^{II}(BNPA^{Ph2}O)(SPh^{NO2})]$ (**88**), which features a tripodal, tetradentate mixed *N,O*-donor ligand with an anionic alkoxide O-donor.[241] Reacting this complex with O_2 produced an iron(III) hydroxide complex, $[Fe^{III}(BNPA^{Ph2}O)(SPh^{NO2})(OH)]$ (**89**), whose terminal OH ligand is bound *cis* to the thiophenolate co-ligand. This octahedral complex showed temperature dependent reactivity to tertiary carbon radicals, where OH transfer was observed at room temperature and C–S bond formation was observed at –35 °C, in line with IPNS reactivity.

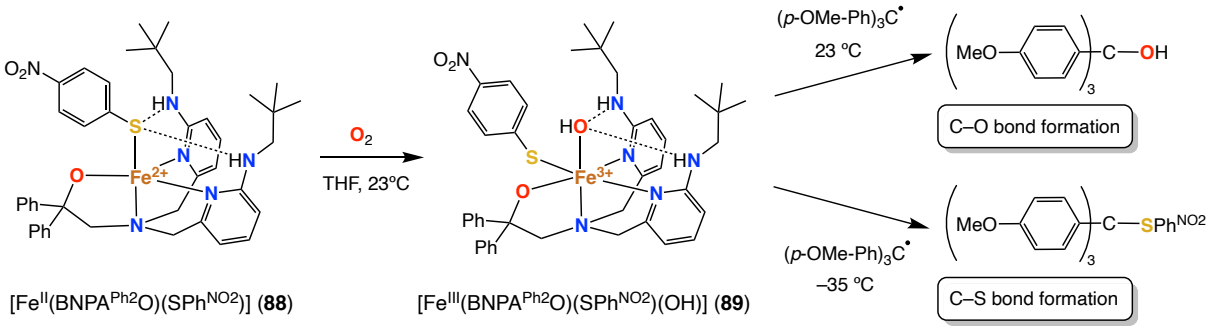

Figure 44. Complexes $[Fe^{II}(BNPA^{Ph2}O)(SPh^{NO2})]$ (**88**) and $[Fe^{III}(BNPA^{Ph2}O)(SPh^{NO2})(OH)]$ (**89**) reported by the group of Goldberg. The temperature-dependent reactivity of **89** to tertiary carbon radicals is also shown.

In order to more accurately model the structural aspects of the 2H1C, several groups have focused on the development of so-called "*N,N,O* ligands" that provide a facial, tridentate coordination motif comprising two N-donors and one O-donor. Notable *N,N,O* ligand contributions have been made by the groups of, amongst others, Que,[242,243] Burzlaff,[244–246] Otero, Carrano,[247,248] Paine,[249] Otte,[250] and Klein Gebbink.[251–255] In general, difficulties in obtaining mononuclear, monoligated *N,N,O*-bound iron complexes with these ligands have typically been encountered due to the formation of homoleptic, bisligated complexes, the bridging coordination of an anionic O-donor, or the coordinative lability of a neutral N- or O-donor. A few examples of mononuclear *N,N,O*-bound zinc thiolate complexes have been reported (Figure 45). However, no iron counterparts have been reported and, to the best of our knowledge, investigations on the spectroscopy and reactivity of *N,N,O*-bound iron thiolate complexes are still lacking.

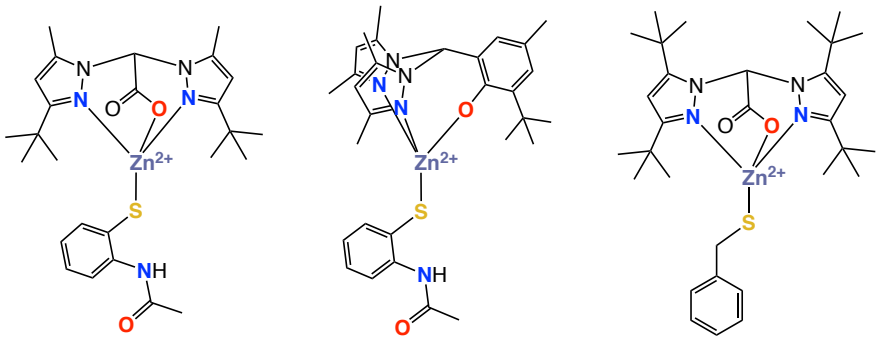

[Zn^{II}(L1)(*o*-*N*-Ac-SPh)] (**91**) [Zn^{II}(L2)(*o*-*N*-Ac-SPh)] (**92**) [Zn^{II}(bdtbpza)(SBn)] (**93**)

Figure 45. Mononuclear *N,N,O*-bound zinc(II) thiolate complexes relevant to IPNS modelling.

A rare example of an non-heme iron persulfide complex, [Fe^{III}($S_2^{Me2}N_3$-(Et,Pr))-S^{pers})]$^+$ (**94**), was reported by the group of Kovacs in the early 2000s as part of their NHase modelling studies.[207] The complex was stable enough to grow crystals suitable for X-ray diffraction, and the resulting crystal structure reveals a side-on coordinated persulfide group within the octahedral coordination sphere of the low-spin ($S = {}^1/_2$) iron(III) centre. Complex **94** was able to cleanly transfer its terminal sulfur atom to PEt_3 during the synthesis of NHase model complex **32** (*vide supra*). Reactivity studies of **94** in relation to the recently discovered ETHE1 have not been attempted to date. This complex presents itself as a highly attractive entry point into the biomimetic oxidation chemistry of persulfide dioxygenases. Indeed, the side-on coordination of the persulfide could be an attractive means with which to examine which iron-bound sulfur atom is most likely to be oxygenated first in the presence of an oxidant. To date, no examples of *N,N,O*-bound iron persulfide complexes relevant to ETHE1 modelling have been reported.

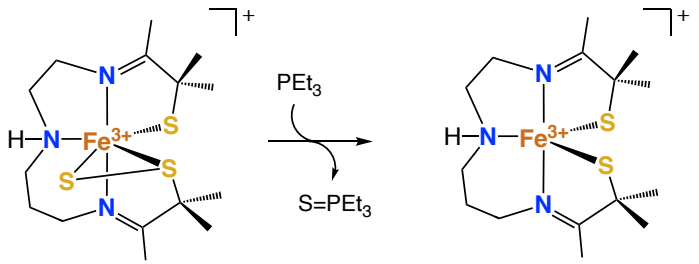

[Fe^{III}($S_2^{Me2}N_3$(Et,Pr)-S^{pers})]$^+$ (**94**) [Fe^{III}($S_2^{Me2}N_3$(Et,Pr))]$^+$ (**32**)

Figure 46. Persulfide-bound complex [Fe^{III}($S_2^{Me2}N_3$(Et,Pr)-S^{pers}))]$^+$ (**94**), formed en-route to **32**.

In conclusion, biomimetic complexes related to IPNS and ETHE1 are still extremely rare, and the field holds much potential for future exploration, both in terms of coordination chemistry and spectroscopic investigation, as well as the fine-tuning of conditions suitable for catalytic applications such as C–X cross-coupling reactions. Of particular interest would be the development of *N,N,O* ligands that model the 2H1C to a high degree of structural fidelity, in order to better understand the factors governing enzyme selectivity for S-oxygenation or H-atom abstraction.

1.4 Lessons Learned: The Effect of Thiolate Ligands

1.4.1 Overview

The previous sections have described the structure and function of seven different mononuclear heme and non-heme iron enzymes bearing single iron-sulfur bonds, as well as their associated biomimetic non-heme complexes. In this section, we dissociate the properties of the thiolate ligands from their specific biological or biomimetic contexts and provide an analysis of the general, over-arching influence of thiolate ligands on the electronic properties of the iron (i.e. Fe–S bond covalency, redox potential, Lewis acidity and spin state) as well as the reactivity of the complexes (i.e. H-atom abstraction, sulfur oxygenation or oxidation). In this way, we aim to provide a "tool-kit" with which to better predict and understand the structure and reactivity of sulfur-ligated non-heme iron complexes and enzymes.

1.4.2 Sulfur-to-Iron Charge Transfer

Thiolates generally form highly covalent bonds with iron due to the soft, malleable nature of their electron structure, which enables a greater degree of charge donation towards the iron centre. This is commonly observed spectroscopically by the manifestation of intense sulfur-to-ligand CT bands. Sulfur-to-iron charge transfer is responsible for modulating many of the electronic properties at the iron centre that govern proper enzyme function. The first is the modulation of the iron centre's redox potential and its Lewis acidity. Higher sulfur-to-iron charge transfer affords electron-rich, Lewis basic iron centres that are more prone to electrochemical oxidation (*e.g.* by Rubredoxin) or dioxygen binding. Lower sulfur-to-iron charge transfer increases the Lewis acidity of the metal, which can promote the binding of additional ligands (*e.g.* glutamate binding in the oxidised active site of SOR). Sulfur-to-iron charge transfer also has a significant influence on the iron spin state. Stronger sulfur-to-iron charge transfer increases the overall ligand field of the iron's first coordination sphere, which can promote a low spin state. In the case of ETHE1, IPNS and CDO, S→Fe charge transfer is not only responsible for promoting O_2 binding to the iron(II) centre, but also helps generate an important $O_2^{\bullet-}$ π^* frontier molecular orbital (FMO) in the resulting Fe^{III}–superoxo intermediate, which helps direct enzyme reactivity and selectivity.

Sulfur-to-iron charge transfer can be modulated by external factors. In enzymatic systems, the extent of sulfur-to-iron charge transfer is typically modulated by the participation of the thiolate in H-bonding interactions with second coordination sphere residues of the active site cavity. Alternatively, oxygenation of the sulfur to a sulfenate or sulfinate group renders the sulfur atom a poorer electron donor, thereby reducing its charge transfer to the iron centre. The former case is particularly relevant to CyP450 and SOR, while the latter case is relevant to NHase. Synthetically, sulfur-to-iron charge transfer can be modulated by changing the nature of the organic substituent of the sulfur atom, which is reflected by the

different Fe-S bond lengths obtained across complex families bearing a range of different thiolate ligands. Other synthetic strategies for modifying the donicity of the sulfur atom include the use of sulfides instead of thiolates, or oxygenation of the sulfur atom.

1.4.3 Spin States and H-Tunnelling

Spin states play a major role in metalloenzymes and their biomimetic complexes. The spin state determines the structure, spectroscopy, bonding interactions (orbital population) and reactivity of these enzymes and complexes. Of particular interest is the difference in reactivity between SOR and CyP450, both of which feature an equatorial arrangement of four nitrogen donors and a thiolate at the apical position with a vacant site available *trans* to the thiolate for superoxide or dioxygen binding, respectively. In these enzymes, spin state is key for determining the orbitals to which charge donation from the thiolate is directed upon formation of end-on peroxo-bound iron(III) intermediates. Computational studies by Que have demonstrated that a low-spin iron state strengthens the Fe–O interaction and promotes O–O bond homolysis, leading to the formation of a high-valent Fe^{IV}=O intermediate. In contrast, high-spin iron typically leads to a weaker Fe–O interaction, which promotes Fe–O heterolysis and the release of H_2O_2 from the SOR active site.

One of the key properties of oxo-iron complexes is the presence of close-lying spin-states. Indeed, two-state reactivity (TSR) and multiple-state reactivity (MSR) are reaction pathways that invoke spin-crossover between two or more spin states, respectively. Because of this phenomenon, many DFT studies conduct mechanistic investigations by calculating several different spin states of the same intermediates. These studies also show that sulfur-to-iron charge transfer decreases the energy gap between orbitals of different spin-states, thereby promoting TSR or MSR. The thiolate ligand in CyP450 and related model complexes is also responsible for promoting H-atom quantum tunnelling,[182] which gives rise to the so-called "anti-electrophilic" trend experimentally observed,[179] where electron-rich thiolate-ligated iron(IV)-oxo compounds exhibit the highest rates for H-atom abstraction.

1.4.4 Sulfur versus Iron Oxidation

The soft, electronically malleable nature of sulfur means sulfur can adopt a variety of different oxidation (and oxygenation) states. Similarly, the typically electron-rich nature of iron(II) and the Lewis-acidic nature of iron(III) means these ions can readily interact with dioxygen. These properties have been successfully exploited by Nature for achieving the diverse reactivities exhibited by the seven different enzymes discussed in this review. However, the factors governing sulfur or iron oxidation are still not fully understood and are the subject of very active and thriving discussions in the field.

In general, there are few examples of enzymes or biomimetic complexes where sulfur oxygenation occurs without any involvement of the iron centre. Typically, oxygen

activation always occurs through coordination to the iron centre, after which sulfur oxidation or oxygenation may occur. Throughout the enzymes and related complexes discussed in this review, iron has been shown to oxidise the sulfur to a variety of different forms, including sulfonate, sulfinate, sulfenate, sulfoxide and disulfide. While the degree of oxygenation is known to be dependent on the nature and amount of oxidant used, the selectivity for some model complexes towards disulfide formation versus S-oxygenation is not well understood.

One of the most important aspects that directs iron or sulfur oxygenation is the positioning of the thiolate within the coordination sphere of the iron centre. When the sulfur is coordinated *trans* to the oxygen binding site, it is overall less likely to be oxygenated due to its positioning directly opposite and away from the O_2 ligand. Indeed, enzymes CyP450, SOR and NHase all contain a thiolate *trans* to the O_2 or substrate coordination site, and the thiolate does not undergo any oxidative transformation. Highly oxidising iron(IV)-oxo complexes with thiolate ligands bound *trans* to the oxo group have also been successfully isolated and characterised. When the sulfur is coordinated *cis* to the O_2 binding site, sulfur-oxygenation typically occurs. This is exemplified by enzymes CDO, EgtB, and EHTE1, all of which exhibit S-oxygenation following O_2 coordination *cis* to their sulfur-rich substrate and the formation of a peroxy-bridged Fe–O–O–S intermediate.

1.4.5 Steric Considerations

The influence of sterics on substrate ligation and substrate orientation to metal-containing active sites should not be underestimated, especially at the active site of metalloenzymes that are often buried deep within the protein structure. This is of particular relevance for IPNS, whose unique oxidase reactivity is, in part, dictated by the orientation of the substrate within the active site cavity, which prevents water molecules from repopulating the iron's coordination sphere upon substrate binding and raises the energy for S-oxygenation relative to H-atom abstraction.

Steric effects are also very significant for determining the structure and reactivity of synthetic model complexes. Ligand size often determines the nuclearity of the complex, leading to cluster formation if the ligand is too small, or unwanted bridging coordination modes if the ligand is too big to for all its donor groups to coordinate simultaneously to a single iron centre. The size of the supporting ligand scaffold and the nature of any co-ligands (including counter anions) can also influence the orientation of the thiolate ligand within the complex architecture. As has been demonstrated in the group of Goldberg, thiolate orientation can have a dramatic influence on the outcome of oxidation, where either iron or sulfur oxidation are promoted. Yet, for modelling studies in general the ability to model a particular enzymatic reactivity that is based on a specific substrate orientation enforced by the protein envelope is amongst the most challenging aspects in bioinorganic chemistry.

1.5 Concluding Remarks

Mononuclear heme and non-heme enzymes featuring single Fe–S bonds have emerged as an important, diverse and mechanistical complex group of enzymes. They share several structural and mechanistic features, such as an axial thiolate ligand located *trans* to the substrate binding site in CyP450, SOR and NHase, or the binding of a sulfur-rich substrate *cis* to the dioxygen binding site in CDO, EgtB, IPNS and ETHE1. Yet, the overall reactivity exhibited by these enzymes is markedly different. Identifying how these mechanisms diverge is not only important for a better understanding of the individual enzymes as stand-alone catalytic entities, but is also crucial for the development of synthetic iron complexes for challenging catalytic applications.

Elucidating the structure-function relationship of iron enzymes continues to rely on structural information obtained from protein X-ray crystal structures. The development of more advanced spectroscopic methods such as stopped-flow or freeze-quench Mössbauer spectroscopy have also enabled great advancements to be made in the investigations of enzyme mechanisms. Theoretical studies are also key to better understanding the electronic and structural properties of short-lived, highly reactive intermediates that cannot be structurally characterised by means of X-ray crystallography. Synthetic biomimetic complexes have greatly contributed to the mechanistic understanding of sulfur-ligated iron enzymes by enabling systematic variation of the first coordination sphere around the iron centre and enabling spectroscopic identification of important intermediates where their enzymatic counterparts could not easily be identified using conventional enzyme spectroscopy. As the number of known metalloenzymes containing a single Fe–S bond increases and the library of related biomimetic iron thiolate complexes grows, broader comparisons can be made and a more refined understanding of each enzyme can be gained.

In this review, we have shown that newly discovered enzymes such as ETHE1 or EgtB share structural features with other more well-understood such as IPNS or CDO. Modelling these newly discovered enzymes may, in some cases, simply be a question of re-examining certain known biomimetic complexes in the presence of alternative substrate models and exploiting the existing knowledge associated to their structural and spectroscopic properties. Conversely, IPNS has long been investigated mechanistically and is very well-understood, but modelling efforts lag far behind with the number of complexes able to reproduce aspects of its structure and reactivity. In this case, major challenges present themselves not only with respect to modelling the structural aspects of its active site but also synthetically modelling the important mechanistic influence of its secondary coordination sphere. Thus, many new challenges and interesting questions await bioinorganic chemists exploring how and why the reactivities of sulfur-ligated iron enzymes diverge.

1.6 Author Contributions

E.C.M. and B.K.G. devised the aim, scope and structure of this review. E.C.M. and S.J.D. wrote the manuscript. B.K.G. provided input on the manuscript during its creation.

1.7 References and Notes

(1) Kaim, W.; Schwederski, B.; Klein, A. In *Bioinorganic Chemistry: Inorganic Elements in the Chemistry of Life*; Wiley, 1994; pp. 1–426.
(2) Costas, M.; Mehn, M. P.; Jensen, M. P.; Que Jr., L. *Chem. Rev.* **2004**, *104*, 939–986.
(3) Holm, R. H.; Kennepohl, P.; Solomon, E. I. *Chem. Rev.* **1996**, *96*, 2239–2314.
(4) Bruijnincx, P. C. A.; van Koten, G.; Klein Gebbink, R. J. M. *Chem. Soc. Rev.* **2008**, *37*, 2716–2744.
(5) Kendrew, J. C.; Bodo, G.; Dintzis, H. M.; Parrish, R. G.; Wyckoff, H. *Nature* **1958**, *133*, 794–795.
(6) Perutz, M. F. *Science (80-.).* **1963**, *140*, 863–869.
(7) Perutz, M. F.; Rossmann, M. G.; Cullis, A. F.; Muirhead, H.; Will, G.; North, A. C. T. *Nature* **1960**, *185*, 416–422.
(8) Waldron, K. J.; Rutherford, J. C.; Ford, D.; Robinson, N. J. *Nature* **2009**, *460*, 823–830.
(9) Jacob, C.; Giles, G. I.; Giles, N. M.; Sies, H. *Angew. Chemie Int. Ed.* **2003**, *42*, 4742–4758.
(10) Huxtable, R. *The Biochemistry of Sulfur*; Springer, 1986.
(11) Francioso, A.; Baseggio Conrado, A.; Mosca, L.; Fontana, M. *Oxid. Med. Cell. Longev.* **2020**, *2020*, 1–27.
(12) Wächtershäuser, G. In *Bioinspired Catalysis*; Weigand, W.; Schollhammer, P., Eds.; Wiley-VCH Verlag GmbH & Co. KGaA: Weinheim, Germany, 2014; pp. 1–20.
(13) Parker, E. T.; Cleaves, H. J.; Dworkin, J. P.; Glavin, D. P.; Callahan, M.; Aubrey, A.; Lazcano, A.; Bada, J. L. *Proc. Natl. Acad. Sci.* **2011**, *108*, 5526–5531.
(14) Miller, S. L. *Science (80-.).* **1953**, *117*, 528–529.
(15) Wächtershäuser, G. *Prog. Biophys. Mol. Biol.* **1992**, *58*, 85–201.
(16) Walker, J. C. G.; Brimblecombe, P. *Precambrian Res.* **1985**, *28*, 205–222.
(17) Harris, T. V.; Szilagyi, R. K. *J. Comput. Chem.* **2014**, *35*, 540–552.
(18) Thiel, J.; Byrne, J. M.; Kappler, A.; Schink, B.; Pester, M. *Proc. Natl. Acad. Sci.* **2019**, *116*, 6897–6902.
(19) Rouault, T. A. *Nat. Rev. Mol. Cell Biol.* **2015**, *16*, 45–55.
(20) Wittkamp, F.; Senger, M.; Stripp, S. T.; Apfel, U.-P. *Chem. Commun.* **2018**, *54*, 5934–5942.
(21) Van Stappen, C.; Decamps, L.; Cutsail, G. E.; Bjornsson, R.; Henthorn, J. T.; Birrell, J. A.; DeBeer, S. *Chem. Rev.* **2020**, *120*, 5005–5081.
(22) Venkateswara Rao, P.; Holm, R. H. **2003**.
(23) Johnson, D. C.; Dean, D. R.; Smith, A. D.; Johnson, M. K. *Annu. Rev. Biochem.* **2005**, *74*, 247–281.
(24) Cardenas-Rodriguez, M.; Chatzi, A.; Tokatlidis, K. *JBIC J. Biol. Inorg. Chem.* **2018**, *23*, 509–520.
(25) Poulos, T. L. *Chem. Rev.* **2014**, *114*, 3919–3962.
(26) Shaik, S.; Cohen, S.; Wang, Y.; Chen, H.; Kumar, D.; Thiel, W. *Chem. Rev.* **2010**, *110*, 949–1017.
(27) Denisov, I. G.; Makris, T. M.; Sligar, S. G.; Schlichting, I. *Chem. Rev.* **2005**, *105*, 2253–2277.
(28) Poulos, T. L.; Finzel, B. C.; Howard, A. J. *J. Mol. Biol.* **1987**, *195*, 687–700.
(29) Urban, P.; Lautier, T.; Pompon, D.; Truan, G. *Int. J. Mol. Sci.* **2018**, *19*, 1617–1638.
(30) Fishelovitch, D.; Shaik, S.; Wolfson, H. J.; Nussinov, R. *J. Phys. Chem. B* **2009**, *113*, 13018–13025.
(31) Davydov, R.; Makris, T. M.; Kofman, V.; Werst, D. E.; Sligar, S. G.; Hoffman, B. M. *J. Am. Chem. Soc.* **2001**, *123*, 1403–1415.
(32) Schlichting, I.; Berendzen, J.; Chu, K.; Stock, A. M.; Maves, S. A.; Benson, D. E.; Sweet, R. M.; Ringe, D.; Petsko, G. A.; Sligar, S. G. *Science (80-.).* **2000**, *287*, 1615–1622.
(33) Newcomb, M.; Zhang, R.; Chandrasena, R. E. P.; Halgrimson, J. A.; Horner, J. H.; Makris, T. M.; Sligar, S. G. *J. Am. Chem. Soc.* **2006**, *128*, 4580–4581.
(34) Rittle, J.; Green, M. T. *Science (80-.).* **2010**, *330*, 933–937.
(35) Rittle, J.; Younker, J. M.; Green, M. T. *Inorg. Chem.* **2010**, *49*, 3610–3617.
(36) Dey, A.; Jiang, Y.; Ortiz de Montellano, P.; Hodgson, K. O.; Hedman, B.; Solomon, E. I. *J. Am. Chem. Soc.* **2009**, *131*, 7869–7878.

(37) Ogliaro, F.; de Visser, S. P.; Shaik, S. *J. Inorg. Biochem.* **2002**, *91*, 554–567.
(38) Suzuki, H.; Inabe, K.; Shirakawa, Y.; Umezawa, N.; Kato, N.; Higuchi, T. *Inorg. Chem.* **2017**, *56*, 4245–4248.
(39) Auclair, K.; Moënne-Loccoz, P.; Ortiz de Montellano, P. R. *J. Am. Chem. Soc.* **2001**, *123*, 4877–4885.
(40) Dey, A.; Okamura, T.; Ueyama, N.; Hedman, B.; Hodgson, K. O.; Solomon, E. I. *J. Am. Chem. Soc.* **2005**, *127*, 12046–12053.
(41) de Visser, S. P.; Ogliaro, F.; Sharma, P. K.; Shaik, S. *Angew. Chemie Int. Ed.* **2002**, *41*, 1947–1951.
(42) Bernadou, J.; Fabiano, A.-S.; Robert, A.; Meunier, B. *J. Am. Chem. Soc.* **1994**, *116*, 9375–9376.
(43) Poulos, T. L.; Finzel, B. C.; Howard, A. J. *Biochemistry* **1986**, *25*, 5314–5322.
(44) Jenney, F. E.; Verhagen, M. F. J. M.; Cui, X.; Adams, M. W. W. *Science (80-.).* **1999**, *286*, 306–309.
(45) Kurtz, D. M. *Acc. Chem. Res.* **2004**, *37*, 902–908.
(46) Kovacs, J. A. *Chem. Rev.* **2004**, *104*, 825–848.
(47) Sheng, Y.; Abreu, I. A.; Cabelli, D. E.; Maroney, M. J.; Miller, A. F.; Teixeira, M.; Valentine, J. S. *Chem. Rev.* **2014**, *114*, 3854–3918.
(48) Sztukowska, M.; Bugno, M.; Potempa, J.; Travis, J.; Kurtz, D. M. *Mol. Microbiol.* **2002**, *44*, 479–488.
(49) Yeh, A. P.; Hu, Y.; Jenney, F. E.; Adams, M. W. W.; Rees, D. C. *Biochemistry* **2000**, *39*, 2499–2508.
(50) Lucchetti-Miganeh, C.; Goudenège, D.; Thybert, D.; Salbert, G.; Barloy-Hubler, F. *BMC Microbiol.* **2011**, *11*, 1–12.
(51) Clay, M. D.; Emerson, J. P.; Coulter, E. D.; Kurtz, D. M.; Johnson, M. K. *J. Biol. Inorg. Chem.* **2003**, *8*, 671–682.
(52) Kovacs, J. A.; Brines, L. M. *Acc. Chem. Res.* **2007**, *40*, 501–509.
(53) Halliwell, B.; Gutteridge, J. M. C. *Free Radicals in Biology and Medicine*; Halliwell, B.; Gutteridge, J. M. C., Eds.; Oxford University Press, 2015.
(54) Clay, M. D.; Yang, T. C.; Jenney, F. E.; Kung, I. Y.; Cosper, C. A.; Krishnan, R.; Kurtz, D. M.; Adams, M. W. W.; Hoffman, B. M.; Johnson, M. K. *Biochemistry* **2006**, *45*, 427–438.
(55) Silaghi-Dumitrescu, R.; Silaghi-Dumitrescu, I.; Coulter, E. D.; Kurtz, D. M. *Inorg. Chem.* **2003**, *42*, 446–456.
(56) Katona, G.; Carpentier, P.; Nivière, V.; Amara, P.; Adam, V.; Ohana, J.; Tsanov, N.; Bourgeois, D. *Science (80-.).* **2007**, *316*, 449–453.
(57) Lombard, M.; Houée-Levin, C.; Touati, D.; Fontecave, M.; Nivière, V. *Biochemistry* **2001**, *40*, 5032–5040.
(58) Bonnot, F.; Molle, T.; Ménage, S.; Moreau, Y.; Duval, S.; Favaudon, V.; Houée-Levin, C.; Nivière, V. *J. Am. Chem. Soc.* **2012**, *134*, 5120–5130.
(59) David, R.; Jamet, H.; Nivière, V.; Moreau, Y.; Milet, A. *J. Chem. Theory Comput.* **2017**, *13*, 2987–3004.
(60) Dey, A.; Jenney, F. E.; Adams, M. W. W. W.; Johnson, M. K.; Hodgson, K. O.; Hedman, B.; Solomon, E. I. *J. Am. Chem. Soc.* **2007**, *129*, 12418–12431.
(61) Clay, M. D.; Jenney, F. E.; Hagedoorn, P. L.; George, G. N.; Adams, M. W. W.; Johnson, M. K. *J. Am. Chem. Soc.* **2002**, *124*, 788–805.
(62) Clay, M. D.; Cosper, C. A.; Jenney, F. E.; Adams, M. W. W.; Johnson, M. K. *Proc. Natl. Acad. Sci. U. S. A.* **2003**, *100*, 3796–3801.
(63) Ascenso, C.; Rusnak, F.; Cabrito, I.; Lima, M. J.; Naylor, S.; Moura, I.; Moura, J. J. G. *J. Biol. Inorg. Chem.* **2000**, *5*, 720–729.
(64) Zheng, P.; Takayama, S. I. J.; Mauk, A. G.; Li, H. *J. Am. Chem. Soc.* **2012**, *134*, 4124–4131.
(65) Goswami, A.; Stewart, J. D. *Organic Synthesis Using Biocatalysis*; Goswami, A.; Stewart, J. D., Eds.; Elsevier, 2016.
(66) Yamada, H.; Kobayashi, M. *Biosci. Biotechnol. Biochem.* **1996**, *60*, 1391–1400.
(67) Martinkova, L.; Mylerova, V. *Curr. Org. Chem.* **2003**, *7*, 1279–1295.
(68) Hann, E. C.; Eisenberg, A.; Fager, S. K.; Perkins, N. E.; Gallagher, F. G.; Cooper, S. M.; Gavagan, J. E.; Stieglitz, B.; Hennessey, S. M.; DiCosimo, R. *Bioorg. Med. Chem.* **1999**, *7*, 2239–2245.
(69) Martínková, L. In *Green Biocatalysis*; Patel, R. N., Ed.; John Wiley & Sons, Inc: Hoboken, NJ, 2016; pp. 331–349.
(70) Cheng, Z.; Xia, Y.; Zhou, Z. *Front. Bioeng. Biotechnol.* **2020**, *8*, 1–18.
(71) Wyatt, J. M.; Knowles, C. J. *Int. Biodeterior. Biodegradation* **1995**, *35*, 227–248.
(72) Knossow, N.; Siebner, H.; Bernstein, A. *J. Agric. Food Chem.* **2020**, *68*, 1546–1554.
(73) Mascharak, P. K. In *Molecular Design in Inorganic Chemistry*; Rabinovich, D., Ed.; Springer, 2014; Vol. 160, pp. 89–114.

(74) Miyanaga, A.; Fushinobu, S.; Ito, K.; Wakagi, T. *Biochem. Biophys. Res. Commun.* **2001**, *288*, 1169–1174.
(75) Huang, W.; Jia, J.; Cummings, J.; Nelson, M.; Schneider, G.; Lindqvist, Y. *Structure* **1997**, *5*, 691–699.
(76) Jin, H.; Turner, I. M.; Nelson, M. J.; Gurbiel, R. J.; Doan, P. E.; Hoffman, B. M. *J. Am. Chem. Soc.* **1993**, *115*, 5290–5291.
(77) Murakami, T.; Nojiri, M.; Nakayama, H.; Dohmae, N.; Takio, K.; Odaka, M.; Endo, I.; Nagamune, T.; Yohda, M. *Protein Sci.* **2000**, *9*, 1024–1030.
(78) Dey, A.; Chow, M.; Taniguchi, K.; Lugo-Mas, P.; Davin, S.; Maeda, M.; Kovacs, J. A.; Odaka, M.; Hodgson, K. O.; Hedman, B.; Solomon, E. I. *J. Am. Chem. Soc.* **2006**, *128*, 533–541.
(79) Odaka, M.; Fujii, K.; Hoshino, M.; Noguchi, T.; Tsujimura, M.; Nagashima, S.; Yohda, M.; Nagamune, T.; Inoue, Y.; Endo, I. *J. Am. Chem. Soc.* **1997**, *119*, 3785–3791.
(80) Nagashima, S.; Nakasako, M.; Dohmae, N.; Tsujimura, M.; Takio, K.; Odaka, M.; Yohda, M.; Kamiya, N.; Endo, I. *Nat. Struct. Biol.* **1998**, *5*, 347–351.
(81) Noguchi, T.; Hoshino, M.; Tsujimura, M.; Odaka, M.; Inoue, Y.; Endo, I. *Biochemistry* **1996**, *35*, 16777–16781.
(82) Stein, N.; Gumataotao, N.; Hajnas, N.; Wu, R.; Lankathilaka, K. P. W.; Bornscheuer, U. T.; Liu, D.; Fiedler, A. T.; Holz, R. C.; Bennett, B. *Biochemistry* **2017**, *56*, 3068–3077.
(83) Gumataotao, N.; Kuhn, M. L.; Hajnas, N.; Holz, R. C. *J. Biol. Chem.* **2013**, *288*, 15532–15536.
(84) Martinez, S.; Wu, R.; Sanishvili, R.; Liu, D.; Holz, R. *J. Am. Chem. Soc.* **2014**, *136*, 1186–1189.
(85) Hashimoto, K.; Suzuki, H.; Taniguchi, K.; Noguchi, T.; Yohda, M.; Odaka, M. *J. Biol. Chem.* **2008**, *283*, 36617–36623.
(86) Yamanaka, Y.; Kato, Y.; Hashimoto, K.; Iida, K.; Nagasawa, K.; Nakayama, H.; Dohmae, N.; Noguchi, K.; Noguchi, T.; Yohda, M.; Odaka, M. *Angew. Chemie Int. Ed.* **2015**, *54*, 10763–10767.
(87) Light, K. M.; Yamanaka, Y.; Odaka, M.; Solomon, E. I. *Chem. Sci.* **2015**, *6*, 6280–6294.
(88) Mitra, S.; Holz, R. C. *J. Biol. Chem.* **2007**, *282*, 7397–7404.
(89) Hopmann, K. H. *Inorg. Chem.* **2014**, *53*, 2760–2762.
(90) Nelp, M. T.; Song, Y.; Wysocki, V. H.; Bandarian, V. *J. Biol. Chem.* **2016**, *291*, 7822–7829.
(91) Nowak, W.; Ohtsuka, Y.; Hasegawa, J.; Nakatsuji, H. *Int. J. Quantum Chem.* **2002**, *90*, 1174–1187.
(92) Prejanò, M.; Marino, T.; Rizzuto, C.; Madrid Madrid, J. C.; Russo, N.; Toscano, M. *Inorg. Chem.* **2017**, *56*, 13390–13400.
(93) Piersma, S. R.; Nojiri, M.; Noguchi, T.; Yohda, M.; Inoue, Y.; Endo, I. *J. Inorg. Biochem.* **2000**, *80*, 283–288.
(94) Popescu, V.-C.; Münck, E.; Fox, B. G.; Sanakis, Y.; Cummings, J. G.; Turner, I. M.; Nelson, M. J. *Biochemistry* **2001**, *40*, 7984–7991.
(95) Roach, P. L.; Clifton, I. J.; Fülöp, V.; Harlos, K.; Barton, G. J.; Hajdu, J.; Andersson, I.; Schofield, C. J.; Baldwin, J. E. *Nature* **1995**, *375*, 700–704.
(96) Roach, P. L.; Clifton, I. J.; Hensgens, C. M. H.; Shibata, N.; Schofield, C. J.; Hajdu, J.; Baldwin, J. E. *Nature* **1997**, *387*, 827–830.
(97) Chen, V. J.; Orville, A. M.; Harpel, M. R.; Frolik, C. A.; Surerus, K. K.; Münck, E.; Lipscomb, J. D. *J. Biol. Chem.* **1989**, *264*, 21677–21681.
(98) Baldwin, J. E.; Bradley, M. *Chem. Rev.* **1990**, *90*, 1079–1088.
(99) Tamanaha, E.; Zhang, B.; Guo, Y.; Chang, W.; Barr, E. W.; Xing, G.; St. Clair, J.; Ye, S.; Neese, F.; Bollinger, J. M.; Krebs, C. *J. Am. Chem. Soc.* **2016**, *138*, 8862–8874.
(100) Goudarzi, S.; Babicz, J. T.; Kabil, O.; Banerjee, R.; Solomon, E. I. *J. Am. Chem. Soc.* **2018**, *140*, 14887–14902.
(101) Brown, C. D.; Neidig, M. L.; Neibergall, M. B.; Lipscomb, J. D.; Solomon, E. I. *J. Am. Chem. Soc.* **2007**, *129*, 7427–7438.
(102) Burzlaff, N. I.; Rutledge, P. J.; Clifton, I. J.; Hensgens, C. M.; Pickford, M.; Adlington, R. M.; Roach, P. L.; Baldwin, J. E. *Nature* **1999**, *401*, 721–724.
(103) Huffman, G. W.; Gesellchen, P. D.; Turner, J. R.; Rothenberger, R. B.; Osborne, H. E.; Miller, F. D.; Chapman, J. L.; Queener, S. W. *J. Med. Chem.* **1992**, *35*, 1897–1914.
(104) Long, A. J.; Clifton, I. J.; Roach, P. L.; Baldwin, J. E.; Rutedge, P. J.; Schofield, C. J. *Biochemistry* **2005**, *44*, 6619–6628.
(105) Howard-Jones, A. R.; Elkins, J. M.; Clifton, I. J.; Roach, P. L.; Adlington, R. M.; Baldwin, J. E.; Rutledge, P. J. *Biochemistry* **2007**, *46*, 4755–4762.
(106) Blackburn, J. M.; Sutherland, J. D.; Baldwin, J. E. *Biochemistry* **1995**, *34*, 7548–7562.

(107) Kreisberg-Zakarin, R.; Borovok, I.; Yanko, M.; Frolow, F.; Aharonowitz, Y.; Cohen, G. *Biophys. Chem.* **2000**, *86*, 109–118.
(108) Ge, W.; Clifton, I. J.; Stok, J. E.; Adlington, R. M.; Baldwin, J. E.; Rutledge, P. J. *J. Am. Chem. Soc.* **2008**, *130*, 10096–10102.
(109) Tiranti, V.; D'Adamo, P.; Briem, E.; Ferrari, G.; Mineri, R.; Lamantea, E.; Mandel, H.; Balestri, P.; Garcia-Silva, M. T.; Vollmer, B.; Rinaldo, P.; Hahn, S. H.; Leonard, J.; Rahman, S.; Dionisi-Vici, C.; Garavaglia, B.; Gasparini, P.; Zeviani, M. *Am. J. Hum. Genet.* **2004**, *74*, 239–252.
(110) Tiranti, V.; Viscomi, C.; Hildebrandt, T.; Di Meo, I.; Mineri, R.; Tiveron, C.; D Levitt, M.; Prelle, A.; Fagiolari, G.; Rimoldi, M.; Zeviani, M. *Nat. Med.* **2009**, *15*, 200–205.
(111) McCoy, J. G.; Bingman, C. A.; Bitto, E.; Holdorf, M. M.; Makaroff, C. A.; Phillips, G. N. *Acta Crystallogr. Sect. D Biol. Crystallogr.* **2006**, *62*, 964–970.
(112) Pettinati, I.; Brem, J.; McDonough, M. A.; Schofield, C. J. *Hum. Mol. Genet.* **2015**, *24*, 2458–2469.
(113) Kabil, O.; Motl, N.; Strack, M.; Seravalli, J.; Metzler-Nolte, N.; Banerjee, R. *J. Biol. Chem.* **2018**, *293*, 12429–12439.
(114) Kumar, D.; Thiel, W.; de Visser, S. P. *J. Am. Chem. Soc.* **2011**, *133*, 3869–3882.
(115) Ewetz, L.; Sörbo, B. *Biochim. Biophys. Acta - Enzymol. Biol. Oxid.* **1966**, *128*, 296–305.
(116) Yamaguchi, K.; Hosokawa, Y. In *Methods in Enzymology*; Jakoby, W. B.; Griffith, O. W., Eds.; 1987; pp. 395–403.
(117) Ye, S.; Wu, X.; Wei, L.; Tang, D.; Sun, P.; Bartlam, M.; Rao, Z. *J. Biol. Chem.* **2007**, *282*, 3391–3402.
(118) Stipanuk, M. H.; Ueki, I.; Dominy, J. E.; Simmons, C. R.; Hirschberger, L. L. Cysteine dioxygenase: A robust system for regulation of cellular cysteine levels. *Amino Acids*, 2009, *37*, 55–63.
(119) Griffith, O. W. In *Methods in Enzymology*; Jakoby, W. B.; Griffith, O. W., Eds.; 1987; pp. 366–376.
(120) Stipanuk, M. H.; Simmons, C. R.; Karplus, P. A.; Dominy, J. E.; Jr. *Amino Acids* **2011**, *41*, 91–102.
(121) Dominy, J. E.; Simmons, C. R.; Hirschberger, L. L.; Hwang, J.; Coloso, R. M.; Stipanuk, M. H. *J. Biol. Chem.* **2007**, *282*, 25189–25198.
(122) Richerson, R. B.; Ziegler, D. M. In *Methods in Enzymology*; Jakoby, W. B.; Griffith, O. W., Eds.; 1987; pp. 410–415.
(123) Bruland, N.; Wübbeler, J. H.; Steinbüchel, A. *J. Biol. Chem.* **2009**, *284*, 660–672.
(124) Tchesnokov, E. P.; Fellner, M.; Siakkou, E.; Kleffmann, T.; Martin, L. W.; Aloi, S.; Lamont, I. L.; Wilbanks, S. M.; Jameson, G. N. L. *J. Biol. Chem.* **2015**, *290*, 24424–24437.
(125) Brandt, U.; Schürmann, M.; Steinbüchel, A. *J. Biol. Chem.* **2014**, *289*, 30800–30809.
(126) McCoy, J. G.; Bailey, L. J.; Bitto, E.; Bingman, C. A.; Aceti, D. J.; Fox, B. G.; Phillips, G. N. *Proc. Natl. Acad. Sci.* **2006**, *103*, 3084–3089.
(127) Tchesnokov, E. P.; Wilbanks, S. M.; Jameson, G. N. L. *Biochemistry* **2012**, *51*, 257–264.
(128) Aloi, S.; Davies, C. G.; Karplus, P. A.; Wilbanks, S. M.; Jameson, G. N. L. *Biochemistry* **2019**, *58*, 2398–2407.
(129) Chai, S. C.; Jerkins, A. A.; Banik, J. J.; Shalev, I.; Pinkham, J. L.; Uden, P. C.; Maroney, M. J. *J. Biol. Chem.* **2005**, *280*, 9865–9869.
(130) Simmons, C. R.; Liu, Q.; Huang, Q.; Hao, Q.; Begley, T. P.; Karplus, P. A.; Stipanuk, M. H. *J. Biol. Chem.* **2006**, *281*, 18723–18733.
(131) Driggers, C. M.; Cooley, R. B.; Sankaran, B.; Hirschberger, L. L.; Stipanuk, M. H.; Karplus, P. A. *J. Mol. Biol.* **2013**, *425*, 3121–3136.
(132) Dominy, J. E.; Simmons, C. R.; Karplus, P. A.; Gehring, A. M.; Stipanuk, M. H. *J. Bacteriol.* **2006**, *188*, 5561–5569.
(133) Siakkou, E.; Rutledge, M. T.; Wilbanks, S. M.; Jameson, G. N. L. *Biochim. Biophys. Acta - Proteins Proteomics* **2011**, *1814*, 2003–2009.
(134) Blaesi, E. J.; Fox, B. G.; Brunold, T. C. *Biochemistry* **2015**, *54*, 2874–2884.
(135) Crowell, J. K.; Li, W.; Pierce, B. S. *Biochemistry* **2014**, *53*, 7541–7548.
(136) Tchesnokov, E. P.; Faponle, A. S.; Davies, C. G.; Quesne, M. G.; Turner, R.; Fellner, M.; Souness, R. J.; Wilbanks, S. M.; de Visser, S. P.; Jameson, G. N. L. *Chem. Commun.* **2016**, *52*, 8814–8817.
(137) Pierce, B. S.; Gardner, J. D.; Bailey, L. J.; Brunold, T. C.; Fox, B. G. *Biochemistry* **2007**, *46*, 8569–8578.
(138) Blaesi, E. J.; Gardner, J. D.; Fox, B. G.; Brunold, T. C. *Biochemistry* **2013**, *52*, 6040–6051.
(139) Blaesi, E. J.; Fox, B. G.; Brunold, T. C. *Biochemistry* **2014**, *53*, 5759–5770.
(140) Aluri, S.; de Visser, S. P. *J. Am. Chem. Soc.* **2007**, *129*, 14846–14847.
(141) de Visser, S. P.; Straganz, G. D. *J. Phys. Chem. A* **2009**, *113*, 1835–1846.
(142) de Visser, S. P. *Chem. – A Eur. J.* **2020**, *26*, 5308–5327.

(143) Gardner, J. D.; Pierce, B. S.; Fox, B. G.; Brunold, T. C. *Biochemistry* **2010**, *49*, 6033–6041.
(144) Souness, R. J.; Kleffmann, T.; Tchesnokov, E. P.; Wilbanks, S. M.; Jameson, G. B.; Jameson, G. N. L. *Biochemistry* **2013**, *52*, 7606–7617.
(145) Simmons, C. R.; Krishnamoorthy, K.; Granett, S. L.; Schuller, D. J.; Dominy, J. E.; Begley, T. P.; Stipanuk, M. H.; Karplus, P. A. *Biochemistry* **2008**, *47*, 11390–11392.
(146) Gordon, J. B.; Goldberg, D. P. In *Reference Module in Chemistry, Molecular Sciences and Chemical Engineering*; Elsevier, 2020.
(147) Davies, C. G.; Fellner, M.; Tchesnokov, E. P.; Wilbanks, S. M.; Jameson, G. N. L. *Biochemistry* **2014**, *53*, 7961–7968.
(148) Sardar, S.; Weitz, A.; Hendrich, M. P.; Pierce, B. S. *Biochemistry* **2019**, *58*, 5135–5150.
(149) Goncharenko, K. V.; Vit, A.; Blankenfeldt, W.; Seebeck, F. P. *Angew. Chemie Int. Ed.* **2015**, *54*, 2821–2824.
(150) Braunshausen, A.; Seebeck, F. P. *J. Am. Chem. Soc.* **2011**, *133*, 1757–1759.
(151) Stampfli, A. R.; Blankenfeldt, W.; Seebeck, F. P. *Curr. Opin. Struct. Biol.* **2020**, *65*, 1–8.
(152) Halliwell, B.; Cheah, I. K.; Tang, R. M. Y. *FEBS Lett.* **2018**, *592*, 3357–3366.
(153) Cheah, I. K.; Halliwell, B. *Biochim. Biophys. Acta - Mol. Basis Dis.* **2012**, *1822*, 784–793.
(154) Castellano, I.; Seebeck, F. P. *Nat. Prod. Rep.* **2018**, *35*, 1241–1250.
(155) Seebeck, F. P. *J. Am. Chem. Soc.* **2010**, *132*, 6632–6633.
(156) Goncharenko, K. V.; Seebeck, F. P. *Chem. Commun.* **2016**, *52*, 1945–1948.
(157) Stampfli, A. R.; Goncharenko, K. V.; Meury, M.; Dubey, B. N.; Schirmer, T.; Seebeck, F. P. *J. Am. Chem. Soc.* **2019**, *141*, 5275–5285.
(158) Goncharenko, K. V.; Flückiger, S.; Liao, C.; Lim, D.; Stampfli, A. R.; Seebeck, F. P. *Chem. – A Eur. J.* **2020**, *26*, 1328–1334.
(159) Chen, L.; Naowarojna, N.; Song, H.; Wang, S.; Wang, J.; Deng, Z.; Zhao, C.; Liu, P. *J. Am. Chem. Soc.* **2018**, *140*, 4604–4612.
(160) Naowarojna, N.; Irani, S.; Hu, W.; Cheng, R.; Zhang, L.; Li, X.; Chen, J.; Zhang, Y. J.; Liu, P. *ACS Catal.* **2019**, *9*, 6955–6961.
(161) Chen, L.; Naowarojna, N.; Chen, B.; Xu, M.; Quill, M.; Wang, J.; Deng, Z.; Zhao, C.; Liu, P. *ACS Catal.* **2019**, *9*, 253–258.
(162) Naowarojna, N.; Cheng, R.; Chen, L.; Quill, M.; Xu, M.; Zhao, C.; Liu, P. *Biochemistry* **2018**, *57*, 3309–3325.
(163) Faponle, A. S.; Seebeck, F. P.; De Visser, S. P. *J. Am. Chem. Soc.* **2017**, *139*, 9259–9270.
(164) Bushnell, E. A. C.; Fortowsky, G. B.; Gauld, J. W. *Inorg. Chem.* **2012**, *51*, 13351–13356.
(165) Wei, W.-J.; Siegbahn, P. E. M.; Liao, R.-Z. *Inorg. Chem.* **2017**, *56*, 3589–3599.
(166) Krishnamurthy, D.; Kasper, G. D.; Namuswe, F.; Kerber, W. D.; Narducci Sarjeant, A. A.; Moënne-Loccoz, P.; Goldberg, D. P. *J. Am. Chem. Soc.* **2006**, *128*, 14222–14223.
(167) Kitagawa, T.; Dey, A.; Lugo-Mas, P.; Benedict, J. B.; Kaminsky, W.; Solomon, E.; Kovacs, J. A. *J. Am. Chem. Soc.* **2006**, *128*, 14448–14449.
(168) McQuilken, A. C.; Jiang, Y.; Siegler, M. A.; Goldberg, D. P. *J. Am. Chem. Soc.* **2012**, *134*, 8758–8761.
(169) Halfen, J. A.; Moore, H. L.; Fox, D. C. *Inorg. Chem.* **2002**, *41*, 3935–3943.
(170) Bukowski, M. R.; Halfen, H. L.; van den Berg, T. A.; Halfen, J. A.; Que, L. *Angew. Chemie Int. Ed.* **2005**, *44*, 584–587.
(171) Kaizer, J.; Costas, M.; Que, L. *Angew. Chemie* **2003**, *115*, 3799–3801.
(172) Lehnert, N.; Ho, R. Y. N.; Que Jr., L.; Solomon, E. I. *J. Am. Chem. Soc.* **2001**, *123*, 12802–12816.
(173) Namuswe, F.; Kasper, G. D.; Sarjeant, A. A. N.; Hayashi, T.; Krest, C. M.; Green, M. T.; Moënne-Loccoz, P.; Goldberg, D. P. *J. Am. Chem. Soc.* **2008**, *130*, 14189–14200.
(174) Stasser, J.; Namuswe, F.; Kasper, G. D.; Jiang, Y.; Krest, C. M.; Green, M. T.; Penner-Hahn, J.; Goldberg, D. P. *Inorg. Chem.* **2010**, *49*, 9178–9190.
(175) Namuswe, F.; Hayashi, T.; Jiang, Y.; Kasper, G. D.; Sarjeant, A. A. N.; Moënne-Loccoz, P.; Goldberg, D. P. *J. Am. Chem. Soc.* **2010**, *132*, 157–167.
(176) Fiedler, A. T.; Halfen, H. L.; Halfen, J. A.; Brunold, T. C. *J. Am. Chem. Soc.* **2005**, *127*, 1675–1689.
(177) Bukowski, M. R.; Koehntop, K. D.; Stubna, A.; Bominaar, E. L.; Halfen, J. A.; Münck, E.; Nam, W.; Que, L. *Science (80-.).* **2005**, *310*, 1000–1002.
(178) McDonald, A. R.; Bukowski, M. R.; Farquhar, E. R.; Jackson, T. A.; Koehntop, K. D.; Seo, M. S.; De Hont, R. F.; Stubna, A.; Halfen, J. A.; Münck, E.; Nam, W.; Que, L. *J. Am. Chem. Soc.* **2010**, *132*, 17118–17129.
(179) Sastri, C. V.; Lee, J.; Oh, K.; Lee, Y. J.; Lee, J.; Jackson, T. A.; Ray, K.; Hirao, H.; Shin, W.; Halfen,

J. A.; Kim, J.; Que, L.; Shaik, S.; Nam, W. *Proc. Natl. Acad. Sci.* **2007**, *104*, 19181–19186.
(180) Jackson, T. A.; Rohde, J.-U.; Seo, M. S.; Sastri, C. V.; DeHont, R.; Stubna, A.; Ohta, T.; Kitagawa, T.; Münck, E.; Nam, W.; Que, L. *J. Am. Chem. Soc.* **2008**, *130*, 12394–12407.
(181) Schröder, D.; Shaik, S.; Schwarz, H. *Acc. Chem. Res.* **2000**, *33*, 139–145.
(182) Mandal, D.; Ramanan, R.; Usharani, D.; Janardanan, D.; Wang, B.; Shaik, S. *J. Am. Chem. Soc.* **2015**, *137*, 722–733.
(183) Hirao, H.; Kumar, D.; Que, L.; Shaik, S. *J. Am. Chem. Soc.* **2006**, *128*, 8590–8606.
(184) Klein, J. E. M. N.; Mandal, D.; Ching, W.-M.; Mallick, D.; Que, L.; Shaik, S. *J. Am. Chem. Soc.* **2017**, *139*, 18705–18713.
(185) Mandal, D.; Mallick, D.; Shaik, S. *Acc. Chem. Res.* **2018**, *51*, 107–117.
(186) Shearer, J.; Nehring, J.; Lovell, S.; Kaminsky, W.; Kovacs, J. A. *Inorg. Chem.* **2001**, *40*, 5483–5484.
(187) Dedushko, M. A.; Pikul, J. H.; Kovacs, J. A. *Inorg. Chem.* **2021**, *60*, 7250–7261.
(188) Shearer, J.; Fitch, S. B.; Kaminsky, W.; Benedict, J.; Scarrow, R. C.; Kovacs, J. A. *Proc. Natl. Acad. Sci.* **2003**, *100*, 3671–3676.
(189) Villar-Acevedo, G.; Nam, E.; Fitch, S.; Benedict, J.; Freudenthal, J.; Kaminsky, W.; Kovacs, J. A. *J. Am. Chem. Soc.* **2011**, *133*, 1419–1427.
(190) Shearer, J.; Scarrow, R. C.; Kovacs, J. A. *J. Am. Chem. Soc.* **2002**, *124*, 11709–11717.
(191) Nam, E.; Alokolaro, P. E.; Swartz, R. D.; Gleaves, M. C.; Pikul, J.; Kovacs, J. A. *Inorg. Chem.* **2011**, *50*, 1592–1602.
(192) Theisen, R. M.; Kovacs, J. A. *Inorg. Chem.* **2005**, *44*, 1169–1171.
(193) Theisen, R. M.; Shearer, J.; Kaminsky, W.; Kovacs, J. A. *Inorg. Chem.* **2004**, *43*, 7682–7690.
(194) Mascharak, P. K. *Coord. Chem. Rev.* **2002**, *225*, 201–214.
(195) Kumar, D.; Grapperhaus, C. A. In *Bioinspired Catalysis*; Wiley-VCH Verlag GmbH & Co. KGaA: Weinheim, Germany, 2014; pp. 325–348.
(196) Noveron, J. C.; Olmstead, M. M.; Mascharak, P. K. *Inorg. Chem.* **1998**, *37*, 1138–1139.
(197) Jackson, H. L.; Shoner, S. C.; Rittenberg, D.; Cowen, J. A.; Lovell, S.; Barnhart, D.; Kovacs, J. A. *Inorg. Chem.* **2001**, *40*, 1646–1653.
(198) Shoner, S. C.; Barnhart, D.; Kovacs, J. A. *Inorg. Chem.* **1995**, *34*, 4517–4518.
(199) Harrop, T. C.; Olmstead, M. M.; Mascharak, P. K. *Inorg. Chem.* **2005**, *44*, 9527–9533.
(200) Marlin, D. S.; Olmstead, M. M.; Mascharak, P. K. *Inorg. Chem.* **1999**, *38*, 3258–3260.
(201) Tyler, L. A.; Noveron, J. C.; Olmstead, M. M.; Mascharak, P. K. *Inorg. Chem.* **1999**, *38*, 616–617.
(202) Lugo-Mas, P.; Dey, A.; Xu, L.; Davin, S. D.; Benedict, J.; Kaminsky, W.; Hodgson, K. O.; Hedman, B. H.; Solomon, E. I.; Kovacs, J. A. *J. Am. Chem. Soc.* **2006**, *128*, 11211–11221.
(203) Ellison, J. J.; Nienstedt, A.; Shoner, S. C.; Barnhart, D.; Cowen, J. A.; Kovacs, J. A. *J. Am. Chem. Soc.* **1998**, *120*, 5691–5700.
(204) Shearer, J.; Kung, I. Y.; Lovell, S.; Kaminsky, W.; Kovacs, J. A. *J. Am. Chem. Soc.* **2001**, *123*, 463–468.
(205) Shoner, S. C.; Nienstedt, A. M.; Ellison, J. J.; Kung, I. Y.; Barnhart, D.; Kovacs, J. A. *Inorg. Chem.* **1998**, *37*, 5721–5726.
(206) Schweitzer, D.; Ellison, J. J.; Shoner, S. C.; Lovell, S.; Kovacs, J. A. *J. Am. Chem. Soc.* **1998**, *120*, 10996–10997.
(207) Schweitzer, D.; Shearer, J.; Rittenberg, D. K.; Shoner, S. C.; Ellison, J. J.; Loloee, R.; Lovell, S.; Barnhart, D.; Kovacs, J. A. *Inorg. Chem.* **2002**, *41*, 3128–3136.
(208) Shearer, J.; Jackson, H. L.; Schweitzer, D.; Rittenberg, D. K.; Leavy, T. M.; Kaminsky, W.; Scarrow, R. C.; Kovacs, J. A. *J. Am. Chem. Soc.* **2002**, *124*, 11417–11428.
(209) Villar-Acevedo, G.; Lugo-Mas, P.; Blakely, M. N.; Rees, J. A.; Ganas, A. S.; Hanada, E. M.; Kaminsky, W.; Kovacs, J. A. *J. Am. Chem. Soc.* **2017**, *139*, 119–129.
(210) Noveron, J. C.; Olmstead, M. M.; Mascharak, P. K. *J. Am. Chem. Soc.* **1999**, *121*, 3553–3554.
(211) Noveron, J. C.; Olmstead, M. M.; Mascharak, P. K. *J. Am. Chem. Soc.* **2001**, *123*, 3247–3259.
(212) Chatel, S.; Chauvin, A.-S.; Tuchagues, J.-P.; Leduc, P.; Bill, E.; Chottard, J.-C.; Mansuy, D.; Artaud, I. *Inorganica Chim. Acta* **2002**, *336*, 19–28.
(213) Galardon, E.; Giorgi, M.; Artaud, I. *Chem. Commun.* **2004**, 286.
(214) Rose, M. J.; Betterley, N. M.; Mascharak, P. K. *J. Am. Chem. Soc.* **2009**, *131*, 8340–8341.
(215) Heinrich, L.; Li, Y.; Vaissermann, J.; Chottard, G.; Chottard, J.-C. *Angew. Chemie Int. Ed.* **1999**, *38*, 3526–3528.
(216) Lugo-Mas, P.; Taylor, W.; Schweitzer, D.; Theisen, R. M.; Xu, L.; Shearer, J.; Swartz, R. D.; Gleaves, M. C.; DiPasquale, A.; Kaminsky, W.; Kovacs, J. A. *Inorg. Chem.* **2008**, *47*, 11228–11236.

(217) Grapperhaus, C. A.; Patra, A. K.; Mashuta, M. S. *Inorg. Chem.* **2002**, *41*, 1039–1041.
(218) O'Toole, M. G.; Kreso, M.; Kozlowski, P. M.; Mashuta, M. S.; Grapperhaus, C. A. *JBIC J. Biol. Inorg. Chem.* **2008**, *13*, 1219–1230.
(219) O'Toole, M. G.; Bennett, B.; Mashuta, M. S.; Grapperhaus, C. A. *Inorg. Chem.* **2009**, *48*, 2300–2308.
(220) Swartz, R. D.; Coggins, M. K.; Kaminsky, W.; Kovacs, J. A. *J. Am. Chem. Soc.* **2011**, *133*, 3954–3963.
(221) Jiang, Y.; Widger, L. R.; Kasper, G. D.; Siegler, M. A.; Goldberg, D. P. *J. Am. Chem. Soc.* **2010**, *132*, 12214–12215.
(222) Widger, L. R.; Jiang, Y.; Siegler, M. A.; Kumar, D.; Latifi, R.; de Visser, S. P.; Jameson, G. N. L.; Goldberg, D. P. *Inorg. Chem.* **2013**, *52*, 10467–10480.
(223) Kumar, D.; Sastry, G. N.; Goldberg, D. P.; de Visser, S. P. *J. Phys. Chem. A* **2012**, *116*, 582–591.
(224) Badiei, Y. M.; Siegler, M. A.; Goldberg, D. P. *J. Am. Chem. Soc.* **2011**, *133*, 1274–1277.
(225) Gonzalez-Ovalle, L. E.; Quesne, M. G.; Kumar, D.; Goldberg, D. P.; de Visser, S. P. *Org. Biomol. Chem.* **2012**, *10*, 5401.
(226) Che, X.; Gao, J.; Zhang, D.; Liu, C. *J. Phys. Chem. A* **2012**, *116*, 5510–5517.
(227) Sallmann, M.; Siewert, I.; Fohlmeister, L.; Limberg, C.; Knispel, C. *Angew. Chemie Int. Ed.* **2012**, *51*, 2234–2237.
(228) Sallmann, M.; Braun, B.; Limberg, C. *Chem. Commun.* **2015**, *51*, 6785–6787.
(229) Sallmann, M.; Kumar, S.; Chernev, P.; Nehrkorn, J.; Schnegg, A.; Kumar, D.; Dau, H.; Limberg, C.; de Visser, S. P. *Chem. - A Eur. J.* **2015**, *21*, 7470–7479.
(230) Müller, L.; Hoof, S.; Keck, M.; Herwig, C.; Limberg, C. *Chem. – A Eur. J.* **2020**, *26*, 11851–11861.
(231) Fischer, A. A.; Stracey, N.; Lindeman, S. V.; Brunold, T. C.; Fiedler, A. T. *Inorg. Chem.* **2016**, *55*, 11839–11853.
(232) Gordon, J. B.; McGale, J. P.; Prendergast, J. R.; Shirani-Sarmazeh, Z.; Siegler, M. A.; Jameson, G. N. L.; Goldberg, D. P. *J. Am. Chem. Soc.* **2018**, *140*, 14807–14822.
(233) Gordon, J. B.; McGale, J. P.; Siegler, M. A.; Goldberg, D. P. *Inorg. Chem.* **2021**, *60*, 6255–6265.
(234) Fischer, A. A.; Lindeman, S. V.; Fiedler, A. T. *Chem. Commun.* **2018**, *54*, 11344–11347.
(235) Krishnamurthy, D.; Sarjeant, A. N.; Goldberg, D. P.; Caneschi, A.; Totti, F.; Zakharov, L. N.; Rheingold, A. L. *Chem. - A Eur. J.* **2005**, *11*, 7328–7341.
(236) Blakely, M. N.; Dedushko, M. A.; Yan Poon, P. C.; Villar-Acevedo, G.; Kovacs, J. A. *J. Am. Chem. Soc.* **2019**, *141*, 1867–1870.
(237) Ekanayake, D. M.; Fischer, A. A.; Elwood, M. E.; Guzek, A. M.; Lindeman, S. V.; Popescu, C. V.; Fiedler, A. T. *Dalt. Trans.* **2020**, *49*, 17745–17757.
(238) Zang, Y.; Que, L. *Inorg. Chem.* **1995**, *34*, 1030–1035.
(239) Widger, L. R.; Davies, C. G.; Yang, T.; Siegler, M. A.; Troeppner, O.; Jameson, G. N. L.; Ivanović-Burmazović, I.; Goldberg, D. P. *J. Am. Chem. Soc.* **2014**, *136*, 2699–2702.
(240) Widger, L. R.; Jiang, Y.; McQuilken, A. C.; Yang, T.; Siegler, M. A.; Matsumura, H.; Moënne-Loccoz, P.; Kumar, D.; De Visser, S. P.; Goldberg, D. P. *Dalt. Trans.* **2014**, *43*, 7522–7532.
(241) Yadav, V.; Siegler, M. A.; Goldberg, D. P. *J. Am. Chem. Soc.* **2021**, *143*, 46–52.
(242) Oldenburg, P. D.; Shteinman, A. A.; Que, L. J. *J. Am. Chem. Soc.* **2005**, *127*, 15672–15673.
(243) Oldenburg, P.; Que, L. J. *Catal. Today* **2006**, *117*, 15–21.
(244) Hegelmann, I.; Beck, A.; Eichhorn, C.; Weibert, B.; Burzlaff, N. *Eur. J. Inorg. Chem.* **2003**, *2003*, 339–347.
(245) Beck, A.; Barth, A.; Hübner, E.; Burzlaff, N. *Inorg. Chem.* **2003**, *42*, 7182–7188.
(246) Beck, A.; Weibert, B.; Burzlaff, N. *Eur. J. Inorg. Chem.* **2001**, 521–527.
(247) Smith, J. N.; Shirin, Z.; Carrano, C. J. *J. Am. Chem. Soc.* **2003**, *125*, 868–869.
(248) Higgs, T. C.; Carrano, C. J. *Inorg. Chem.* **1997**, *36*, 298–306.
(249) Paria, S.; Halder, P.; Paine, T. K. *Inorg. Chem.* **2010**, *49*, 4518–4523.
(250) Bete, S. C.; Otte, M. *Angew. Chemie Int. Ed.* **2021**, *60*, 18582–18586.
(251) Bruijnincx, P. C. A.; Lutz, M.; Spek, A. L.; Hagen, W. R.; Weckhuysen, B. M.; van Koten, G.; Klein Gebbink, R. J. M. *J. Am. Chem. Soc.* **2007**, *129*, 2275–2286.
(252) Bruijnincx, P. C. A.; Lutz, M.; Spek, A. L.; van Faassen, E. E.; Weckhuysen, B. M.; van Koten, G.; Klein Gebbink, R. J. M. *Eur. J. Inorg. Chem.* **2005**, *2005*, 779–787.
(253) Moelands, M. A. H.; Schamhart, D. J.; Folkertsma, E.; Lutz, M.; Spek, A. L.; Klein Gebbink, R. J. M. *Dalt. Trans.* **2014**, *43*, 6769.
(254) Moelands, M. A. H.; Nijsse, S.; Folkertsma, E.; de Bruin, B.; Lutz, M.; Spek, A. L.; Klein Gebbink, R. J. M. *Inorg. Chem.* **2013**, *52*, 7394–7410.

(255) Folkertsma, E.; de Waard, E. F.; Korpershoek, G.; van Schaik, A. J.; Solozabal Mirón, N.; Borrmann, M.; Nijsse, S.; Moelands, M. A. H.; Lutz, M.; Otte, M.; Moret, M.-E.; Klein Gebbink, R. J. M. *Eur. J. Inorg. Chem.* **2016**, *2016*, 1319–1332.

Chapter 2

2H1C Mimicry: Bioinspired Iron and Zinc Complexes Supported by *N,N,O* Phenolate Ligands

Abstract

In pursuit of mimicking the ubiquitous 2H1C motif in mononuclear non-heme iron enzymes, two new bioinspired *N,N,O* phenolate ligands, **BenzImNNO** and **Im^{Ph2}NNO**, are synthesised and their coordination chemistry with zinc(II) and iron(II) is explored. **BenzImNNO** coordinates by means of an anionic κ_3-*N,N,O* donor set and readily forms homoleptic bisligated complexes, also in the presence of equimolar amounts of metal salt. In contrast, the increased steric bulk of **Im^{Ph2}NNO** promotes the formation of dinuclear complexes, $[M_2(Im^{Ph2}NNO)_2(OTf)_2]$ (M = Fe, Zn), with facially opposing metal sites, as a result of its unique bridging μ_2:κ_2-*N,N*:κ_1-*O* coordination mode. We investigate the robustness of the ligand's dinucleating coordination mode during oxidative transformations and demonstrate that its coordination mode is retained upon triflate substitution for a biorelevant thiophenolate co-ligand.

This chapter is based on:
E. C. Monkcom, H. A. Negenman, E. Masferrer-Rius, M. Lutz, S. Ye, E. Bill, R. J. M. Klein Gebbink, *European Journal of Inorganic Chemistry*, **2022**, 9, e202101046.

2.1 Introduction

The 2-His-1-Carboxylate facial triad (2H1C) is a bioinorganic motif that has been identified at the active site of a superfamily of mononuclear non-heme iron oxygenase and oxidase enzymes (Figure 1).[1–3] It comprises two neutral histidine (His) residues and one anionic carboxylate group, typically an aspartate (Asp) or a glutamate (Glu), that coordinate in a facial, tripodal arrangement to a single metal ion. As well as anchoring the metal site in place within the protein scaffold, the 2H1C ensures that three mutually *cis* vacant sites are available for substrate, co-substrate or dioxygen binding during catalysis. Typically, loosely bound water molecules occupy these sites in the enzyme's resting state. The 2H1C is so ubiquitous at the active sites of mononuclear, O_2-activating, non-heme iron enzymes that it can be regarded as an entity almost independent of any host protein scaffold and is considered one of the most versatile structural motifs with which nature carries out oxidative transformations. The 2H1C has served as a founding architectural model for a wide variety of bioinspired ligands, developed by the bioinorganic community to synthetically model enzyme active sites and better understand the mechanistic pathways underlying enzyme function.[4–7]

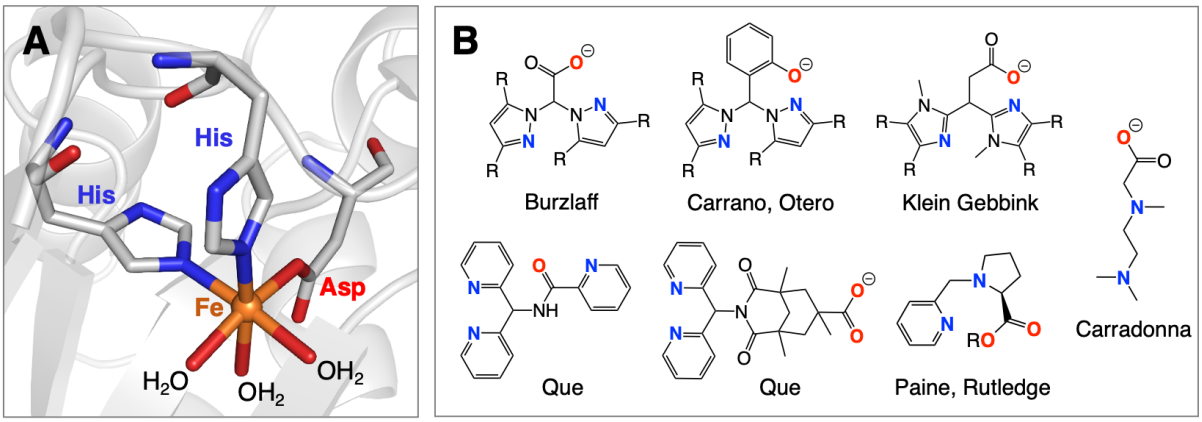

Figure 1. A: The 2-His-1-Carboxylate facial triad (2H1C) at the active site of deacetoxycephalosporin C synthase (DAOCS, PDB 1RXF).[8] B: Notable examples of *N,N,O* ligand designs in the literature.

Over the years, many efforts have been made towards the development of so-called "*N,N,O* ligands", designed to model the structural aspects of the 2H1C as faithfully as possible by incorporating two N-donors and an O-donor within a facial, tridentate coordination motif. However, obtaining mononuclear, monoligated iron complexes with such ligands is challenging due to their low denticity as well as the inherent ligand lability exhibited by high-spin iron centres. Notable examples of *N,N,O* ligands include the bis-pyrazolyl acetate ligand family developed in the group of Burzlaff,[9–12] the bis-pyrazolyl phenolate ligand family developed in the groups of Carrano and Otero,[13–15] the carboxylate-tethered ethylenediamine ligands reported by Caradonna and co-workers,[16,17] the amide- or carboxylate-tethered bis-pyridyl ligands developed in the group of Que,[18,19] and the L-proline-derived ligands reported in the groups of, amongst others, Paine and Rutledge.[20,21]

Our group has focused on the development of bis-imidazole derived *N,N,O* ligands, since imidazoles are of particular bio-relevance to the histidyl imidazole side-chain found in enzymatic systems (see Chapter 6 for a full overview of these efforts).[22–27] Our studies show that achieving monoligated, *N,N,O*-bound iron complexes is highly dependent on the steric bulk of the imidazole groups as well as the nature of the O-donor (Figure 2).[28] While anionic carboxylates are the most biologically relevant O-donor, these have the tendency to engage in bridging coordination modes that can disrupt the ligand's *N,N,O* coordination and lead to the formation of coordination oligomers.[23] Esters and amides, on the other hand, have the advantage that their solubility and steric properties can easily be tuned by varying the nature of their tethered organic substituent.[24,26] However, the neutral charge of these O-donors deviates somewhat from the electronic properties of the 2H1C and is associated to a greater degree of coordination lability.[27]

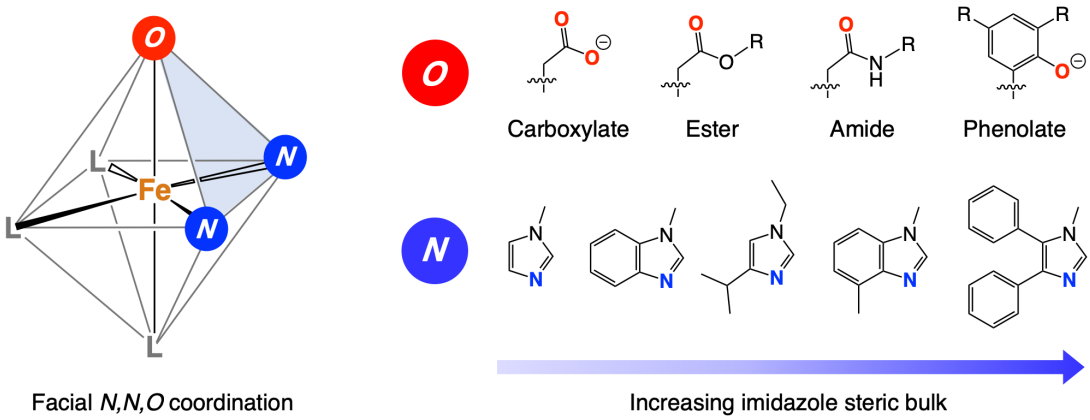

Figure 2. The variation in bis-imidazole-derived *N,N,O* ligand design.

Phenolates are an attractive means with which to incorporate an anionic O-donor into the *N,N,O* ligand design that can be tuned both sterically and electronically. However, phenolates can also engage in mono- or dinucleating (bridging) coordination modes, due to the availability of two lone pairs on the anionic oxygen atom.[29] Control of this nuclearity is typically dependent on the size and positioning of substituents on the phenolate ring. Previously, our group demonstrated that bis-imidazole-derived phenolate ligand **ImNNO** (Figure 3) can coordinate facially to an iron(III) centre by means of its *N,N,O* donor set.[30] However, the small size of its constituent imidazole groups enables two ligand molecules to bind simultaneously to the ferric ion, producing a homoleptic, bisligated complex $[Fe(ImNNO)_2]^+$. A monoligated iron complex was successfully synthesised by including one equivalent of tetrachlorocatecholate (tcc) as an exogenous co-ligand, which could block the coordination of a second ligand equivalent. No further efforts have since been undertaken to explore the coordination chemistry of bis-imidazole phenolate ligands.

In this study, we expand the family of bis-imidazole-derived phenolate ligands by incorporating the bulkier 1-methyl-*1H*-benzimidazole and 1-methyl-4,5-diphenyl-*1H*-imidazole heterocycles into the ligand architectures of **BenzImNNO** and **Im^{Ph2}NNO**, respectively. Our aim is to create new bioinspired *N,N,O* ligands that structurally model

the 2H1C and support the formation of facially capped, monoligated complexes without the need for any additional co-ligand. We show that the steric properties of the imidazole groups have a drastic impact on the coordination mode of the phenolate, and therefore also on the structure and nuclearity of the resulting metal complexes. The structure of these complexes in both their solid and solution states is investigated using X-ray crystal structure determination and NMR spectroscopy. The electronic and magnetic properties of the iron complexes are analysed by means of Mössbauer spectroscopy and SQUID magnetometry. Finally, we examine the robustness of the ligand coordination modes during oxidative transformations and ligand exchange studies involving a thiophenolate co-ligand.

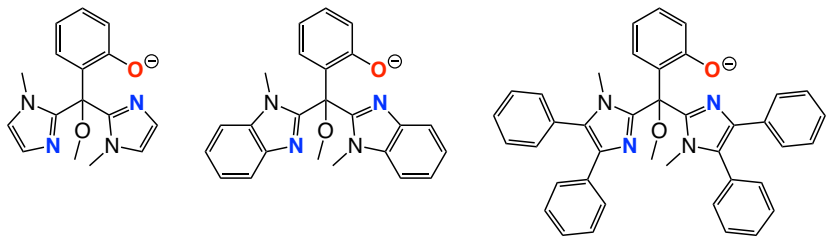

Figure 3. Bis-imidazole phenolate ligands with a *N,N,O* donor set.

2.2 Results and Discussion

2.2.1 Ligand Synthesis

The ligands **H-BenzImNNO** and **H-Im^{Ph2}NNO** can be readily synthesized on a multigram scale, using a procedure adapted from Jameson *et al.*[31] that incorporates 1-methyl-*1H*-benzimidazole or 1-methyl-4,5-diphenyl-*1H*-imidazole into the ligand design, respectively (Scheme 1). The synthesis begins with the methoxymethyl ether (MOM) protection of methyl salicylate, affording **LS1** in 89% yield. Next, two equivalents of the desired imidazole are deprotonated with *n*-BuLi, and the resulting imidazolium salt is reacted with **LS1**. For 1-methylbenzimidazole, it is essential to perform this step in anhydrous diethyl ether in order to generate **LS2** cleanly in 71% yield. For 1-methyl-4,5-diphenylimidazole, this reaction proceeds cleanly in anhydrous THF, affording **LS3** in 96% yield. Due to their sterically encumbered nature, the subsequent methylation of **LS2** and **LS3** is kinetically slow and requires a large excess of NaH and MeI as well as overnight stirring to form **LS4** and **LS5** in 98% and 95% yields, respectively. Protection of the tertiary alcohol in this manner prevents any ambiguity in the potential donor set of the ligand. Finally, the MOM-group is cleaved under acidic conditions, affording the phenols **H-BenzImNNO** and **H-Im^{Ph2}NNO** in 83% and 85% yield, respectively. In ^{1}H NMR spectroscopy, the phenolic proton for both ligands manifests itself as broad singlets at 10.35 ppm. For both ligands, a relatively sharp O–H vibration is also observed at approximately 3390 cm^{-1} by solid-state IR spectroscopy.

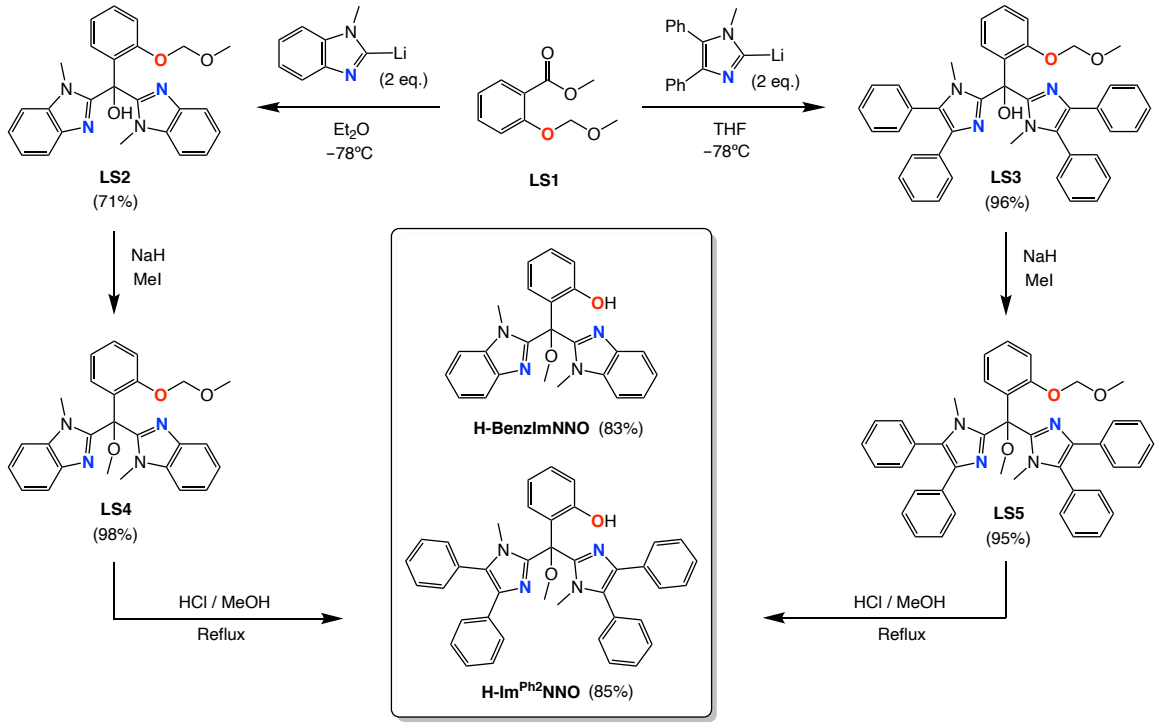

Scheme 1. Synthetic pathway towards ligand precursors **H-BenzImNNO** and **H-Im^{Ph2}NNO**.

H-Im^{Ph2}NNO crystallises overnight as small colourless blocks from the slow vapour diffusion of hexane into a THF solution of the compound at room temperature. The resulting X-ray crystal structure confirms the structure of **H-Im^{Ph2}NNO** and reveals the presence of an intramolecular hydrogen bond between the methoxy group and the phenolic proton, analogous to that observed by Bruijnincx *et al.* for **H-ImNNO**,[30] which orientates the phenol away from the potential metal coordination site (Figure 4). From this, it can already be deduced that deprotonation of this ligand precursor to its phenolate form could promote the facial, anionic *N,N,O* coordination of this bulky ligand scaffold by eliminating the H-bonding interaction and creating a more strongly donating phenolate O-donor.

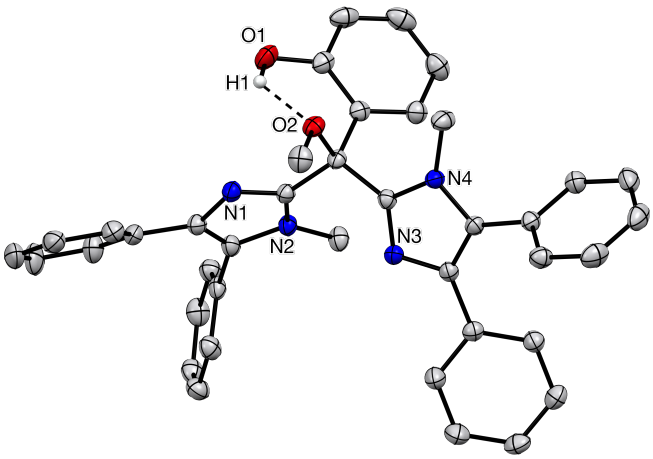

Figure 4. Displacement ellipsoid plot (50% probability level) for **H-Im^{Ph2}NNO** in the solid state. All C–H hydrogen atoms are omitted for clarity. The intramolecular H-bond is depicted by a dashed line.

2.2.2 The Coordination Chemistry of BenzImNNO

2.2.2.1 Reaction with $ZnCl_2$

H-BenzImNNO was dissolved in THF and deprotonated using a slight excess of KH. After stirring for 1 h, the bright yellow solution was filtered and one equivalent of $ZnCl_2$, suspended in THF, was added to the mixture. The reaction was stirred for another 3 h, after which the solvent was removed under vacuum. The residual brown solid was extracted with MeCN, the solution filtered, and the solvent removed under vacuum. The resulting complex, $[Zn(BenzImNNO)_2ZnCl_2]$ (**1**), was obtained in 54% yield (Scheme 2).

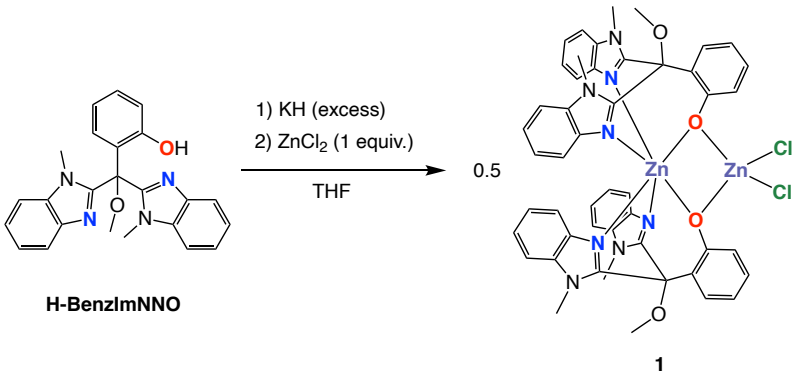

Scheme 2. The synthesis of $[Zn(BenzImNNO)_2ZnCl_2]$ (**1**).

Single crystals suitable for X-ray diffraction were obtained from the slow vapour diffusion of diethyl ether into an MeCN solution of the complex at room temperature. The X-ray crystal structure (Figure 5) reveals that **1** is a dinuclear complex. The first zinc ion (Zn1) has a distorted octahedral geometry, facially capped by the anionic κ_3-*N,N,O* donor set of two **BenzImNNO** molecules. The second zinc ion (Zn2) has a distorted tetrahedral geometry, coordinated by two chloride ions and the μ_2-bridging phenolic oxygen atoms of

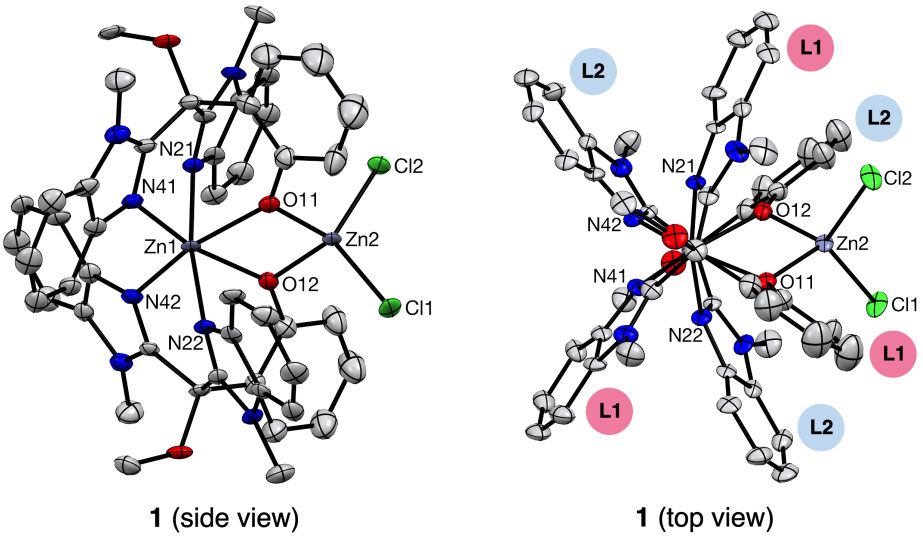

Figure 5. Displacement ellipsoid plot (50% probability level) for **1**. All H-atoms are omitted for clarity. L1 and L2 indicate the phenolate and imidazole groups belonging to two different ligand molecules.

Table 1. Selected bond lengths (Å) and bond angles (º) for $[Zn(BenzImNNO)_2ZnCl_2]$ (**1**).

$[Zn(BenzImNNO)_2ZnCl_2]$ (**1**)					
Bond	Length	Bond Angle	Degrees	Bond Angle	Degrees
Zn1–N21	2.097(4)	N21–Zn1–N41	85.2(2)	Cl1–Zn2–Cl2	117.01(6)
Zn1–N41	2.044(5)	N21–Zn1–O11	82.45(17)	C31–O11–Zn1	142.6(4)
Zn1–N22	2.096(4)	N41–Zn1–O11	90.22(18)	C31–O11–Zn2	118.2(4)
Zn1–N42	2.047(5)	N22–Zn1–N42	85.3(2)	Zn1–O11–Zn2	95.71(18)
Zn1–O11	2.220(4)	N22–Zn1–O12	82.80(18)	Zn1–O12–Zn2	95.00(18)
Zn1–O12	2.234(4)	N42–Zn1–O12	89.87(18)	C32–O11–Zn1	143.0(4)
Zn2–O11	1.977(4)	O11–Zn1–O12	78.59(13)	C32–O12–Zn2	118.3(4)
Zn2–O12	1.987(4)	O11–Zn2–O12	90.70(15)		

both ligand molecules. The zinc centres are comprised within a Zn_2O_2 diamond core and are separated by an intermetallic distance of 3.1162(8) Å. The longer Zn1–O and shorter Zn2–O distances reflect the more electron-rich and poor natures of the octahedral and tetrahedral zinc ions, respectively. In both cases, the Zn–O bond lengths are slightly longer than those typically reported for mononuclear zinc complexes of similar geometries, which we attribute to the bridging coordination mode of the phenolate.

This structure demonstrates that the reaction between equimolar amounts of **BenzImNNO** and $ZnCl_2$ does not produce a mononuclear, monoligated complex. Instead, the coordination of two ligand molecules to one zinc ion appears to be thermodynamically favoured, generating a homoleptic, bisligated complex to which the remaining equivalent of $ZnCl_2$ co-ligates *via* the distal lone pairs of the phenolic O-donors. The co-ligation of $ZnCl_2$ in this manner causes the phenolates to orientate themselves *cis* to each other, which results in a staggered arrangement of both ligand molecules about Zn1 that gives the complex a "butterfly" structure in its solid state (Figure 5, top view). A similar dinuclear nickel(II) complex was reported by Higgs *et al.* employing a tripodal *N,N,O* bis-3,5-dimethylpyrazolyl-derived phenolate ligand.[13]

The "butterfly" structure of **1** effectively gives rise to two distinct chemical environments for the benzimidazole groups of each **BenzImNNO** molecule (i.e. they are magnetically inequivalent), where one of the benzimidazoles from the first ligand molecule is located between a phenolate and a benzimidazole from the second ligand molecule, while the other benzimidazole group from the first ligand molecule is located between the two benzimidazoles of the second ligand molecule. This is in line with the solution-state structure of **1** observed by ^{1}H NMR spectroscopy (Figure 6), where three distinct singlets are observed at 4.34, 3.79 and 3.49 ppm with a 1:1:1 relative integral ratio, which correspond to the two N-methyl groups and the O-methyl group of the **BenzImNNO** scaffold. Similarly, the aromatic region of the spectrum contains 12 different multiplets with a relative integration of 1H, which correspond to the aromatic hydrogens of the benzimidazole and phenolate rings, per ligand molecule.

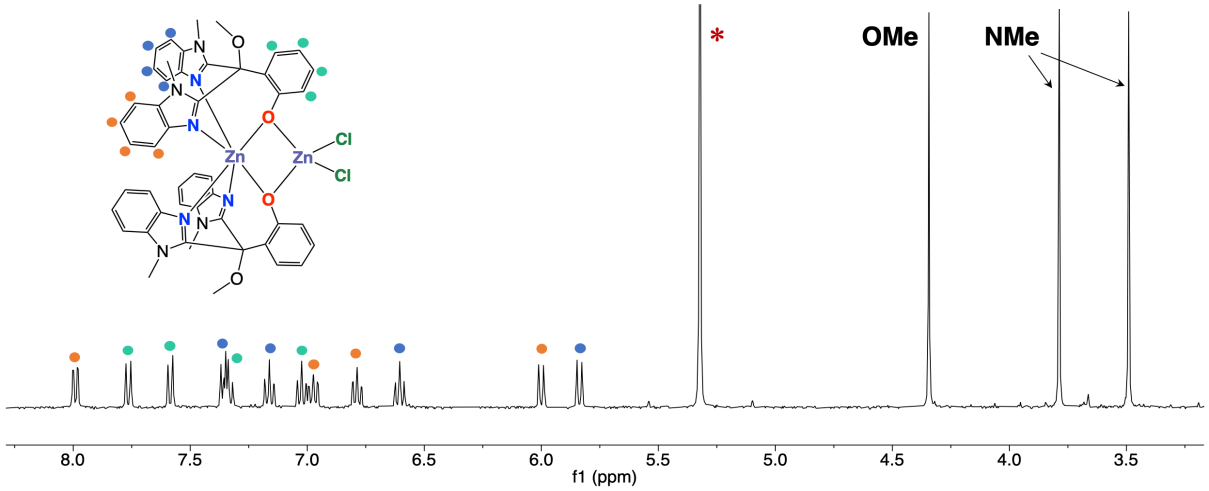

Figure 6. ^{1}H NMR spectrum (400 MHz) of **1**, recorded in CD_2Cl_2 at 25 °C.

2.2.2.2 *Reaction with Zn(OTf)$_2$*

Next, we investigated the coordination chemistry of **BenzImNNO** with $Zn(OTf)_2$ in order to examine the effect of potentially non-coordinating triflate anions. Analogously to the preparation of **1**, **H-BenzImNNO** was dissolved in THF and deprotonated using a slight excess of KH. The resulting bright yellow phenolate solution was filtered and one equivalent of $Zn(OTf)_2$ dissolved in THF was added dropwise to the filtrate. The mixture was stirred for a further 3 h, after which the solvent was removed under vacuum. The residual solid was extracted into CH_2Cl_2 solution, filtered and dried, affording $[Zn(BenzImNNO)_2Zn(OTf)_2]$ (**2**) as a pale yellow solid in 72% yield (Scheme 3).

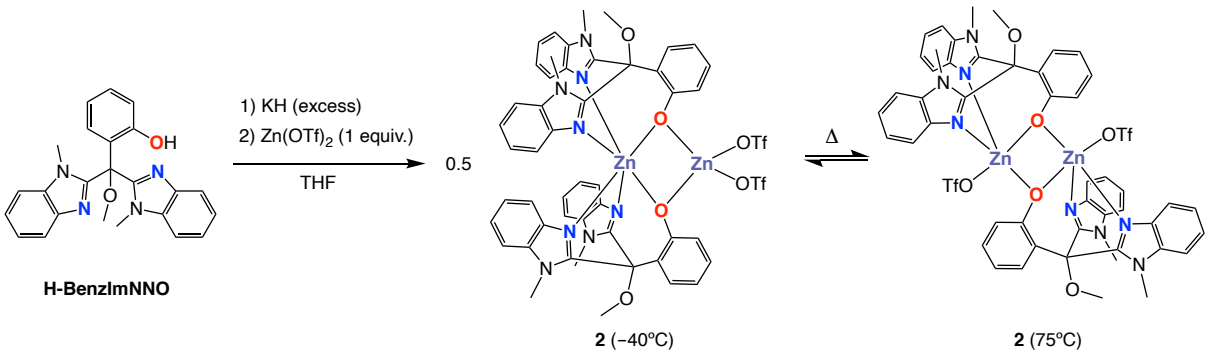

Scheme 3. The synthesis of $[Zn(BenzImNNO)_2Zn(OTf)_2]$ (**2**) and its temperature-dependent fluxional behaviour in solution, as observed by VT NMR analysis.

The ^{1}H NMR spectrum of the **2** recorded in acetonitrile-d_3 at 25 °C is shown in Figure 8 (middle). In the aliphatic region of the spectrum, we observe a sharp singlet at 3.47 ppm and a broad signal at 4.04 ppm, which, on the basis of their 1:2 relative integral ratio, are assigned to the O- and N-methyl groups of the **BenzImNNO** ligand scaffold, respectively. In the aromatic region of the spectrum, four well-resolved multiplets are detected at 7.98, 6.88, 6.44 and 5.70 ppm, all of which integrate to 1H relative to the O-methyl signal. These signals belong to the same spin system, as shown by means of 1D total correlation

spectroscopy (TOCSY) (see Appendix A, Figure A3). We assign these signals to the aromatic hydrogen atoms on the **BenzImNNO** phenolate ring. Other much broader aromatic signals are also observed, whose combined integration totals approximately 8H. Therefore, we tentatively assign these to the aromatic hydrogens of the benzimidazole rings. The severe broadening of the signals associated to the benzimidazole groups indicates that these are highly fluxional in acetonitrile solution. Similar broadening of the NMR signals is also observed in dichloromethane-d_2, so we exclude solvent coordination as being the cause of this fluxional behaviour. We investigated the fluxional behaviour of the complex by means of variable temperature (VT) NMR analysis (Figure 7).

Cooling the sample to –40 °C causes the broad N-methyl resonance to split into two sharp singlets at 4.12 and 3.94 ppm with a relative integral ratio of 1:1. Similarly, the broad signals of the aromatic region sharpen and produce eight new well-resolved multiplets, each of which integrates to 1H (the doublet at 7.57 ppm comprises two separate doublets that are perfectly overlapped). By means of 1D TOCSY, 1D NOE, EXSY and NOESY NMR experiments (see Appendix A, Figures A4-A8), we were able to assign all signals and, on this basis, we propose that **2** is analogous in structure to **1** at low temperature, involving μ_2-bridged phenolate coordination to $Zn(OTf)_2$ instead of $ZnCl_2$ (Scheme 3). Warming the sample to 75 °C causes the broad N-methyl benzimidazole resonance to sharpen significantly while retaining its 2:1 relative integral ratio with the O-methyl signal, consistent with C_S-symmetry of the **BenzImNNO** ligand scaffold. Similarly, the broad signals in the aromatic region of the spectrum assigned to the 5-, 6- and 7-positions of the benzimidazole rings coalesce to produce three well-resolved multiplets at 7.45, 7.13 and

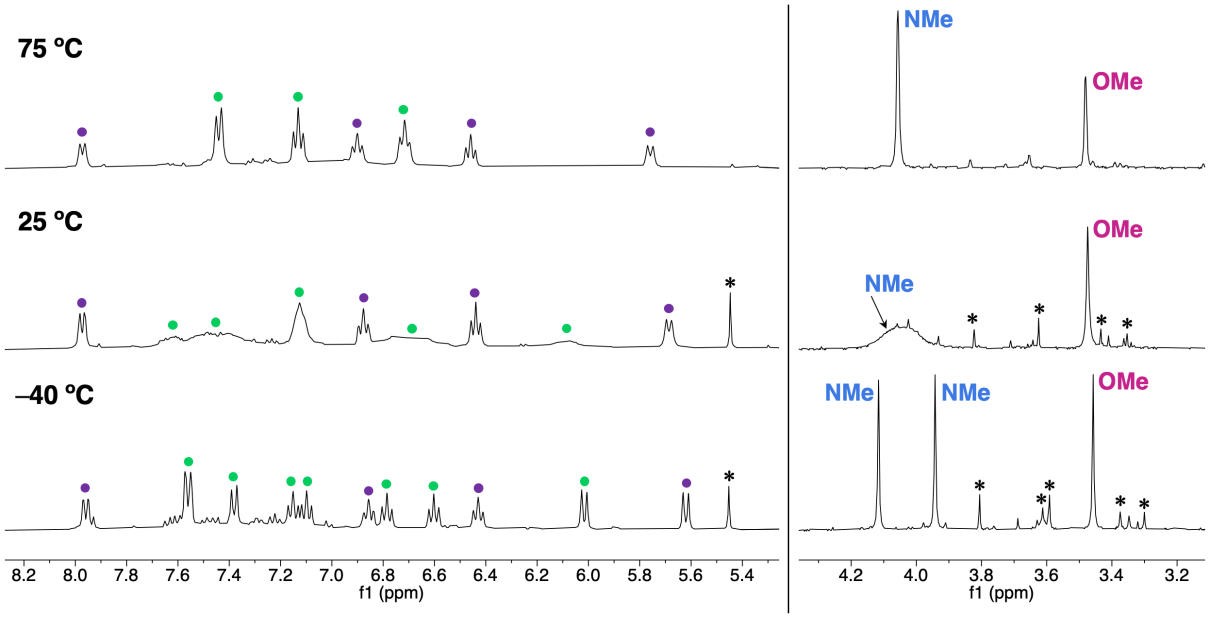

Figure 7. The stacked ^{1}H NMR spectra (400 MHz) of **2**, recorded in CD_3CN at 75 °C (top), 25 °C (middle) and –40 °C (bottom). Spectra are clipped for clarity. Aromatic phenolate and benzimidazole resonances are labelled with purple and green circles, respectively. Unknown impurities and residual solvent signals are denoted by black asterisks. Full VT NMR stack is given in Appendix A, Figure A2.

6.72 ppm, each of which integrates to 2H. However, the two aromatic resonances associated to the 4-position of benzimidazole scaffold broaden so significantly that they are no longer observed at high temperature. On this basis, we propose that higher temperatures provoke significant structural rearrangements of **2**, where both zinc atoms become pentacoordinate, bound to the κ_3-*N,N,O* donor set of a **BenzImNNO** ligand, a terminal OTf anion and the bridging phenolate of the second ligand molecule (Scheme 3).

We attribute the high fluxionality of **2** to the weakly coordinating nature of the triflate anions, which, in contrast to **1**, causes the benzimidazole groups of the supporting ligand scaffold to easily exchange between the two zinc ions. This would also explain why the protons at the 4-position of the rings (closest to the zinc centres) undergo such severe broadening at high temperature, while the resonances associated to the other aromatic positions sharpen and likely represent their average chemical environment. We believe that **2** retains a phenolate-bridged dinuclear diamond core structure across the entire temperature range of our NMR investigations, as the resonances associated to the phenolate rings remain sharp and well-resolved throughout all measurements.

For comparison, we reacted **BenzImNNO** with 0.5 equiv. $Zn(OTf)_2$. Interestingly, the resulting ^{1}H NMR spectrum contains two different sets of signals, indicating that two complexes are present in the mixture (Figure 8). The first set of signals, denoted by purple labels, is identical to those observed for **2** at 25 °C. The second set of signals, denoted by green labels, includes two sharp resonances at 3.68 and 3.35 ppm with a relative integral ratio of 2:1, that we assign to the N- and O-methyl groups of the **BenzImNNO** ligand, respectively. This is indicative of C_S ligand symmetry, where both benzimidazoles are chemically equivalent. In the aromatic region of the spectrum, four multiplets are observed at 7.62, 7.42, 7.27 and 7.21 ppm, that each integrate to 2H. Four other aromatic signals are detected at 6.90, 6.44, 6.07 and 5.96 ppm, that each integrate to 1H. Using COSY and

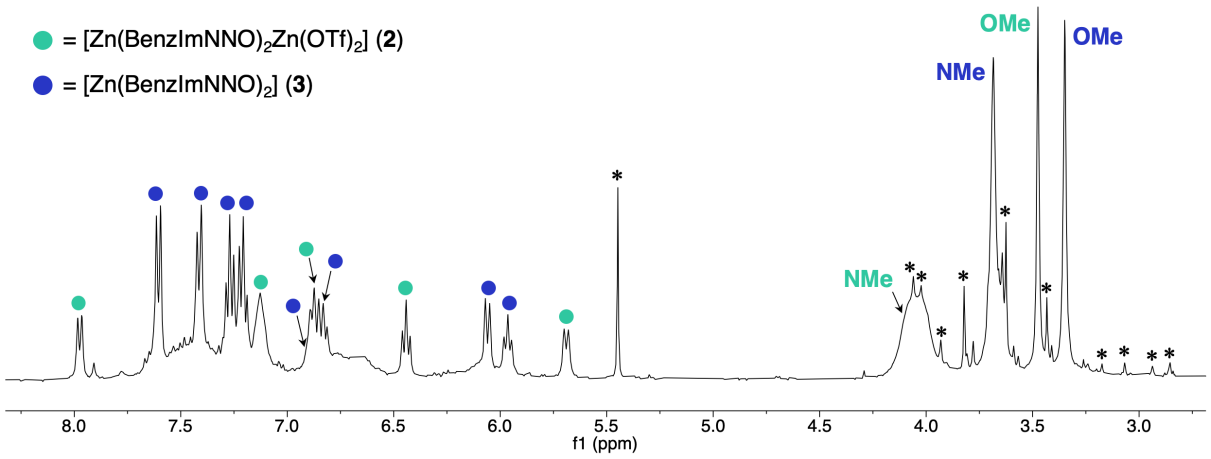

Figure 8. The ^{1}H NMR spectra (400 MHz) of the product obtained from the reaction of **BenzImNNO** with 0.5 equiv. $Zn(OTf)_2$, recorded in CD_3CN at 25 °C. Residual solvent signals and unknown impurities are labelled by black asterisks.

TOCSY NMR experiments, we assign these two sets of aromatic signals to the aromatic protons of the benzimidazole and phenolate groups, respectively. Given the sharp and well-resolved nature of all resonances, we hypothesise that this species has a much lower degree of fluxional behaviour in solution and likely corresponds to a homoleptic, bisligated zinc complex, [Zn(BenzImNNO)$_2$] (**3**). Based on the two OMe resonance integral values, we calculate that **2** and **3** were formed in approximately equimolar amounts. Importantly, the ^{1}H NMR signals we observe for **3** are different to those of **2** at 75 °C. On this basis, we exclude the formation of **3** when reacting **BenzImNNO** with 1 equiv. Zn(OTf)$_2$.

Single crystals suitable for X-ray diffraction were obtained from the slow diffusion of *n*-pentane into a CH_2Cl_2 solution of the reaction product mixture. The resulting X-ray crystal structure corroborates the structural hypothesis for **3**, where two **BenzImNNO** molecules coordinate facially by means of their *N,N,O* donor set to a single, octahedral zinc(II) ion (Figure 9). The phenolic O-donors are coordinated mutually *trans* at the axial sites of the complex and the imidazolyl nitrogen atoms are coordinated within the equatorial plane. The zinc ion is located on an inversion centre. Due to the mononucleating coordination mode of its phenolic O-donors, the Zn–O distances in **3** are significantly shorter than the octahedral Zn–O bond distances in **1**.

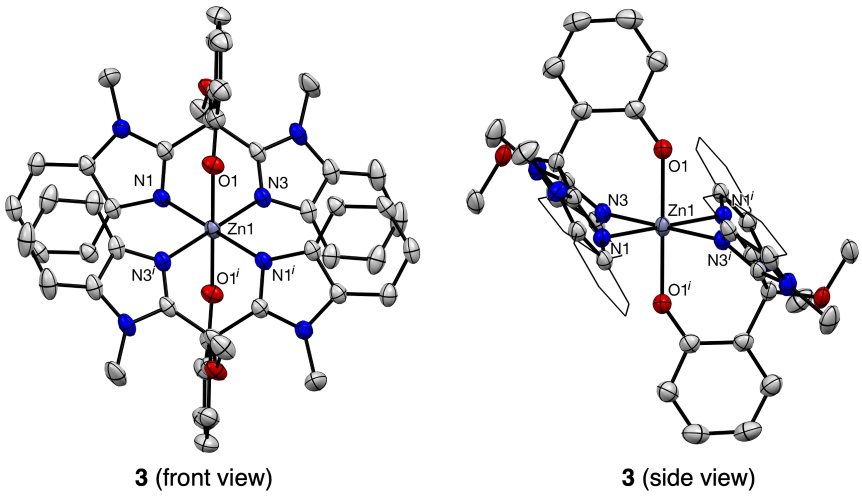

Figure 9. Displacement ellipsoid plot (50% probability level) for **3**. For the side view, the benzimidazole phenyl rings have been depicted in the wireframe format for clarity. All H-atoms and disordered solvent molecules have been omitted for clarity. Symmetry code *i*: 5/3-*x*, 4/3-*y*, 1/3-*z*.

Table 2. Selected bond lengths (Å) and bond angles (°) for [Zn(BenzImNNO)$_2$] (**3**).

[Zn(BenzImNNO)$_2$] (**3**)			
Bond	Length (Å)	Bond Angle	Degrees
Zn1–N1	2.1627(11)	N1–Zn1–O1	90.25(4)
Zn1–N3	2.0914(11)	N3–Zn1–O1	88.02(4)
Zn1–O1	2.1004(10)	N1–Zn1–N3	82.22(4)

Overall, these results demonstrate that ligand **BenzImNNO** is capable of facially capping a metal centre by means of its anionic *N,N,O* donor set. However, the ligand is small enough to allow two ligand molecules to coordinate the same metal centre and the thermodynamic formation of mononuclear, monoligated complexes is not observed. Interestingly, the increased steric bulk of the benzimidazole groups in **BenzImNNO** compared to the imidazoles in **ImNNO** does have an impact on the coordination of the phenolic oxygen atom, promoting its coordination through the distal oxygen lone pair (*e.g.* in **1** and in the proposed structure of **2**) as well as the proximal lone pair (*e.g.* in **3**). Based on these results, we decided not to proceed with the corresponding iron(II) chemistry of **BenzImNNO** as we believe homoleptic bisligated iron complexes are likely to form. Instead, we proceeded to investigate the coordination chemistry of the bulkier **Im^{Ph2}NNO** ligand variant in the quest for monoligated *N,N,O*-bound metal complexes.

2.2.3 The Coordination Chemistry of Im^{Ph2}NNO

2.2.3.1 Complex Synthesis

The coordination chemistry of anionic **Im^{Ph2}NNO** was explored with both iron and zinc (Scheme 4). The ligand precursor was dissolved in THF and deprotonated using a slight excess of KH. After stirring for 1 h, the yellow ligand salt solution was filtered and an equimolar amount of iron(II) or zinc(II) triflate in THF was added dropwise to the solution. This caused a rapid colour change to orange (in the case of iron) or to pale yellow (in the case of zinc). The reaction mixtures were stirred for 1 h and were subsequently filtered and concentrated under vacuum. The residual solids were then extracted with dichloromethane and the solutions were filtered to remove the insoluble KOTf. [Fe$_2$(Im^{Ph2}NNO)$_2$(OTf)$_2$] (**4**) and [Zn$_2$(Im^{Ph2}NNO)$_2$(OTf)$_2$] (**5**) were obtained as white solids in yields of 70% and 59%, respectively. Analogous reactions involving FeCl$_2$ and ZnCl$_2$ afforded highly insoluble products, which hampered any further purification or characterisation.

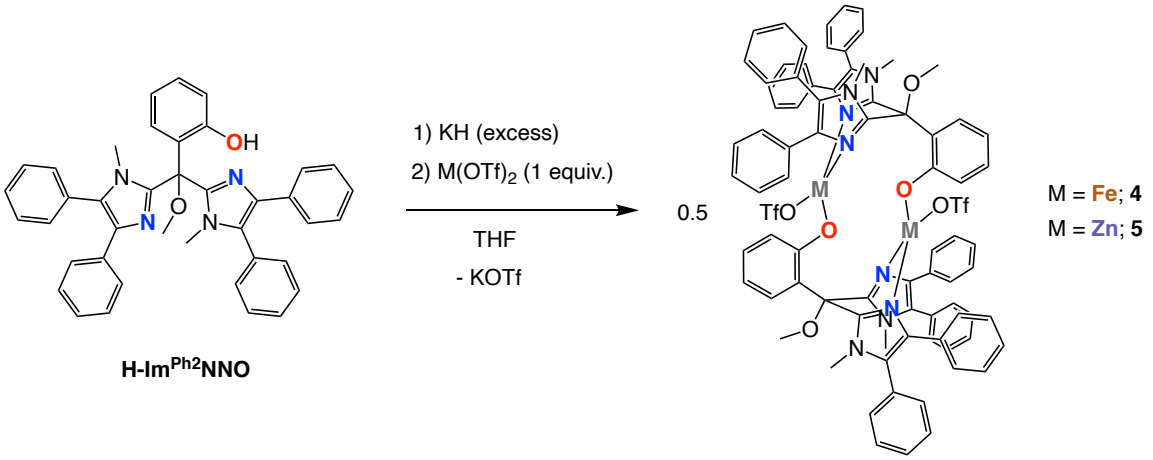

Scheme 4. The synthesis of complexes [Fe$_2$(Im^{Ph2}NNO)$_2$(OTf)$_2$] (**4**) and [Zn$_2$(Im^{Ph2}NNO)$_2$(OTf)$_2$] (**5**).

2.2.3.2 X-ray Crystal Structure Analysis

Single crystals of **4** and **5** suitable for X-ray diffraction were obtained by slow vapour diffusion of *n*-hexane into THF solutions of the complexes under ambient conditions. The X-ray crystal structures show that **4** and **5** are analogous in structure, comprising two metal ions and two ligand molecules bound together in a cyclic 14-membered ring configuration. Each metal centre is tetracoordinate and has a distorted tetrahedral geometry (Figure 10). The **Im^{Ph2}NNO** ligands assume a bridging μ_2:κ_2-*N,N*:κ_1-*O* coordination mode, where the two imidazole N-donors bind to one metal centre and the anionic phenolate O-donor binds to the second metal centre. Although this is not a κ_3 coordination mode, each metal ion is effectively coordinated by a tripodal *N,N,O* binding motif. The fourth "apical" coordination site of each metal ion is occupied by a triflate anion. The cyclic, dinuclear configuration of **4** and **5** means their metal centres can be regarded as occupying facially opposing sites,[32,33] with large intermetallic distances of 4.2589(6) Å and 3.9940(4) Å respectively. Selected bond lengths and bond angles are provided in Table 3.

The X-ray crystal structures obtained for **4** and **5** are centrosymmetric. Selected bond lengths and bond angles are given in Table 3. The Fe1–O_{phen} bond length of 1.9061(12) Å and the Zn1–O_{phen} bond length of 1.8767(13) Å are similar to those previously reported for other four-coordinate iron and zinc centres bound to monodentate, anionic phenolic oxygen atoms. The Fe–N bond lengths in **4** (>2 Å) are consistent with high-spin iron(II).[26,27]

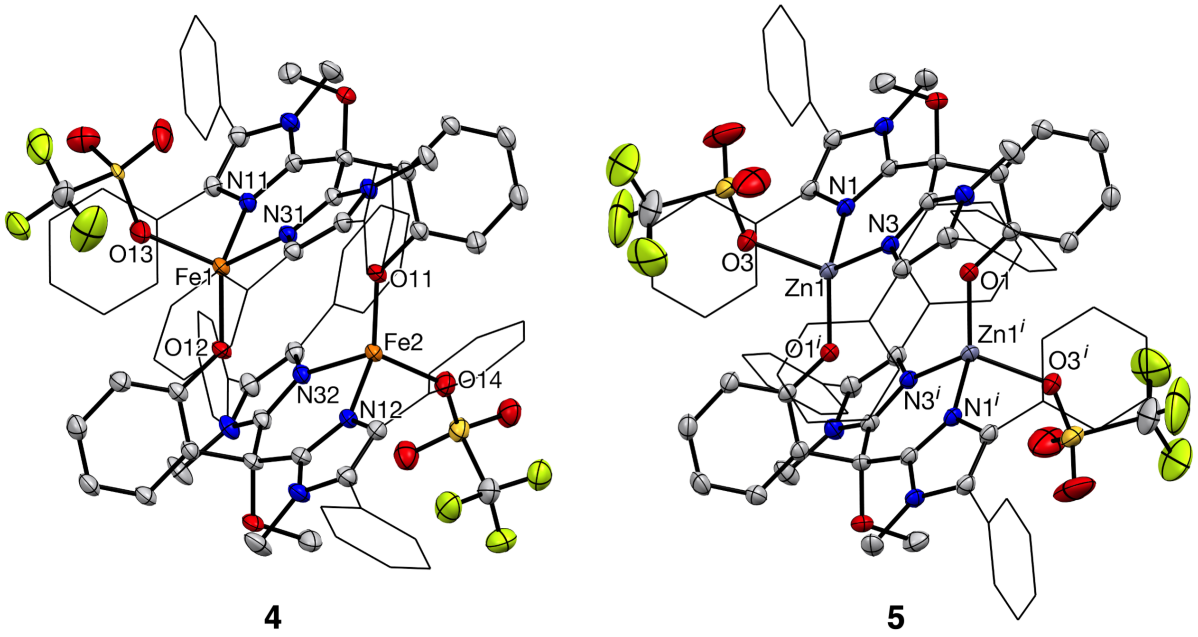

Figure 10. Displacement ellipsoid plots (50% probability level) for **4** (left) and **5** (right). All H-atoms, disorder at the OTf groups and any co-crystallised solvent molecules have been omitted for clarity. Imidazole phenyl substituents are depicted in the wireframe format. Symmetry code *i*: 1-*x*, 1-*y*, 1-*z*.

Table 3. Selected bond lengths (Å) and bond angles (°) for **4** and **5**. Symmetry code *i*: 1-*x*, 1-*y*, 1-*z*. Only the crystallographic parameters associated to Fe1 in **4** are given.

$[Fe_2(Im^{Ph2}NNO)_2(OTf)_2]$ (**4**)			
Bond	Length	Bond Angle	Degrees
Fe1–N11	2.0628(14)	N11–Fe1–O12	117.37(5)
Fe1–N31	2.0554(14)	N31–Fe1–O12	119.87(6)
Fe1–O12	1.9061(12)	N11–Fe1–N31	88.62(5)
Fe1–O13	2.1074(14)	O12–Fe1–O13	116.92(5)
		C32–O12–Fe1	130.86(11)
$[Zn_2(Im^{Ph2}NNO)_2(OTf)_2]$ (**5**)			
Bond	Length	Bond Angle	Degrees
Zn1–N1	1.9827(15)	N1–Zn1–O1^i	123.83(6)
Zn1–N3	1.9867(16)	N3–Zn1–O1^i	115.03(6)
Zn1–O1^i	1.8767(13)	N1–Zn1–N3	95.23(6)
Zn1–O3	2.0428(14)	O3–Zn1–O1^i	113.39(6)
		C3–O1–Zn1^i	131.10(12)

Due to the ligand's bridging coordination mode, the triadic *N,N,O* donor set bound to each metal atom in **4** and **5** is not linked by a central quaternary carbon atom, as would be the case for a κ$_3$-*N,N,O* ligand. This has an influence on the tetrahedral distortion at each metal centre, exemplified by the large N–M–O$_{phen}$ and O$_{phen}$–M–O$_{OTf}$ angles that are all greater than 109.5°. For comparison, corresponding angles within mononuclear iron and zinc complexes supported by κ$_3$-*N,N,O* ligands are generally smaller than 100°.[9,26,27] The absence of the κ$_3$-type "cage" effect enables the metal ions in **4** and **5** to bind in an almost planar fashion with respect to the aromatic planes of the imidazole rings. Indeed, the Fe–N and Zn–N bond lengths in **4** and **5** are slightly shorter compared to those previously reported in our group for iron and zinc complexes bound to κ$_3$-*N,N,O* bis-imidazole-derived ligands.[26,27,30,34] We attribute this to better overlap of the imidazole lone pair with the in-plane metal *d*-orbitals, enabled by the bridging coordination of the **Im^{Ph2}NNO** ligand.

Finally, we observe C^{Ar}–C^{Ar}–O–M torsion angles (ϕ) of 176.59(12)° and –174.53(15)° in **4** and **5**, respectively, which indicates that the phenolate O-atoms coordinate exclusively through their distal lone pair to the second metal centre. Indeed, the C^{Ar}–C^{Ar}–O–M torsion angle is a useful parameter to determine which phenolate lone pair engages in metal coordination (Figure 11). Coordination of the proximal lone pair results in a |ϕ(C^{Ar}–C^{Ar}–O–M)| that is smaller than 90° (i.e. a *cis*-type orientation), and coordination of the distal lone pair results in a |ϕ(C^{Ar}–C^{Ar}–O–M)| that is greater than 90° (i.e. a *trans*-type orientation). The involvement of the phenolate's proximal or distal lone pair in metal coordination therefore appears to be dependent on the bulkiness of the ligand's constituent imidazole groups: **ImNNO** coordinates exclusively through its proximal lone pair,[30]

whereas **BenzImNNO** can coordinate through both its proximal and distal lone pairs, and **Im^{Ph2}NNO** coordinates exclusively through its distal lone pair. The increased steric bulk of the imidazole also has the effect of reducing the coordination number of the metal centre, as evidenced by the 4-coordinate nature of the metal centres in **4** and **5** compared to the 6-coordinate metal centres in complexes supported by **ImNNO** or **BenzImNNO**.[30]

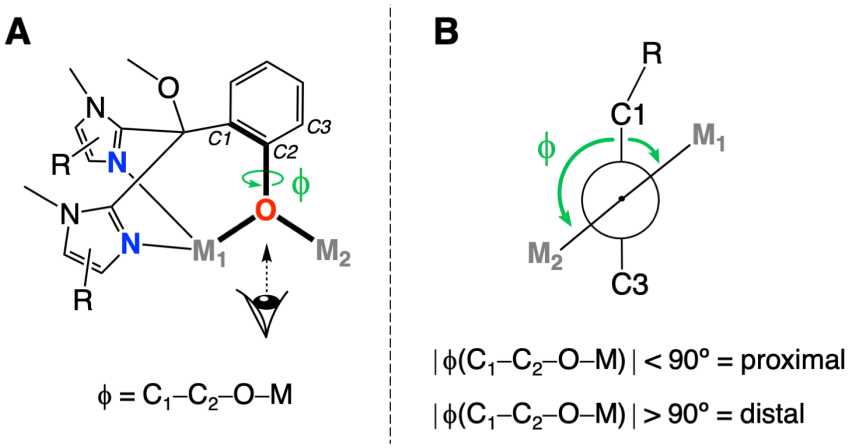

Figure 11. A: The C–C–O–M torsion angle (ϕ). B: Newman-type projection along the phenolate C-O bond, highlighting the C–C–O–M torsion angles associated to proximal or distal phenolate lone pair coordination.

2.2.3.3 Electronic Structure and Magnetism

The dinuclear nature of **4** offers further intrigue with respect to its electronic structure and magnetism. The zero-field ^{57}Fe Mössbauer spectrum of **4** (Figure 12) exhibits a single quadrupole doublet, with an isomer shift (δ) of 1.02 mm s^{-1} and a quadrupole splitting ($|\Delta E_Q|$) of 3.26 mm s^{-1}. These parameters are consistent with high-spin (S = 2) iron(II) and establish the equivalence of the two iron centres. SQUID magnetometry reveals an χT value of approximately 7 cm^3 K mol^{-1} at room temperature, consistent with the presence of two uncoupled high-spin (S = 2) iron(II) centres. Upon cooling, the χT value gradually increases and reaches a maximum of approximately 10.5 cm^3 K mol^{-1} at 10 K. The experimental findings thus indicate that the ground state of **4** features weak ferromagnetic coupling of the two iron(II) centres and that their local spin states do not change even at low temperature. The simulations give an exchange coupling constant (J) of approximately 2 cm^{-1}. On this basis, we argue that the coupling energy is too weak to play a significant role during the reactivity of **4** at room temperature, as its effects would be negligible compared to the thermal excitations on the order of kT at 300 K. Therefore, complex **4** may be regarded as containing two electronically independent high-spin Fe(II) sites within its biomimetic framework.

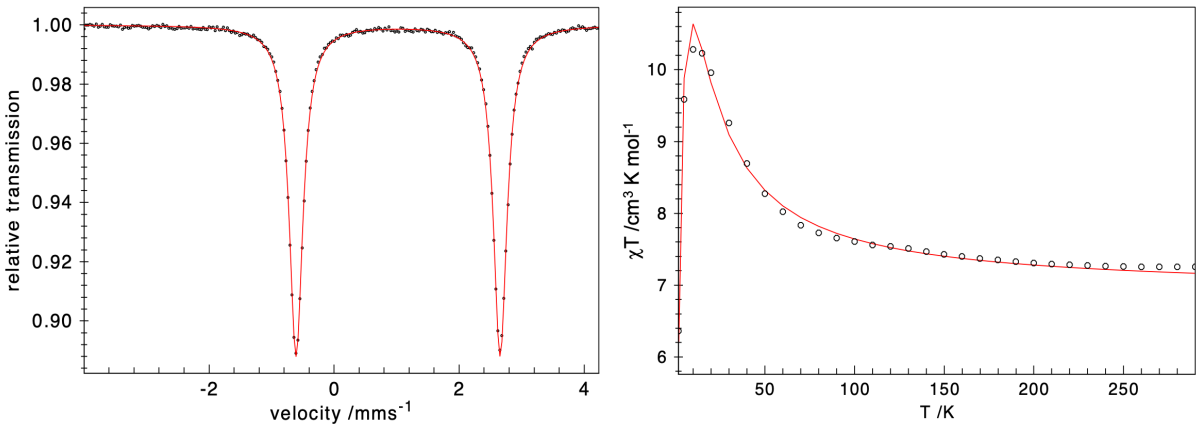

Figure 12. Left: The zero field ^{57}Fe Mössbauer spectrum of **4**, recorded at 80 K. The black points correspond to the experimental data and the red trace represents the best fit. Data fit parameters: δ = 1.02 mm s^{-1}, $|\Delta E_Q|$ = 3.26 mm s^{-1}. Right: temperature dependence of the magnetic moment of a powdered sample of **4**, measured by SQUID magnetometry. Black circles correspond to the experimental data and the red trace represents the best spin Hamiltonian fit with J = 1.9 cm^{-1}, D_{Fe} = 1.8 cm^{-1}, E_{Fe}/D_{Fe} = 0, g_{iso} = 2.145.

2.2.3.4 Solution State Behaviour

Next, we investigated the solution state behaviour of **4** and **5** by NMR spectroscopy in order to establish whether the ligand's dinucleating μ_2:κ_2-*N,N*,:κ_1-*O* coordination mode is retained in solution. The ^{1}H NMR spectrum of **5** in THF-d_8 (Figure 13) shows a well-resolved set of ligand signals, the assignment of which was achieved with 1D TOCSY NMR experiments (see Appendix A, Figures A9-A11). The spectrum contains two sharp singlets at 3.68 and 3.49 ppm, assigned to the N-methyl and O-methyl groups, respectively, on the basis of their 2:1 integral ratio. A single set of imidazole-derived aromatic signals is observed (resonances **E**–**J**), implying C_S ligand symmetry that is either consistent with the solid-state structure of **5** or, alternatively, could correspond to a mononuclear complex with κ_3-*N,N,O* ligand coordination.[28,30] The ^{19}F NMR spectra of **5** in THF-d_8 and MeCN-d_3 show a single, sharp resonance at –79 ppm, indicative of rapid exchange of the triflate anions in coordinating solvents.

We performed 1D NOE experiments in order to detect any long-range interactions that would only arise from a dinuclear structure in solution (Figure 13). Selective excitation of the resonances associated to the N-methyl group (**NMe**) and the H-atom *ortho* to the phenolate (**D**) produced NOE cross-peaks corresponding to **H** (the H-atoms on the *ortho* position of the imidazole 4-position phenyl ring). In the X-ray crystal structure of **5**, the **H**···**D** and **H**···**NMe** separations within the same ligand molecule (i.e. the"*intra*-ligand" distances) are measured as 6.81 Å and 5.46 Å, respectively, which surpass the generally accepted limit of 5 Å for NOE coherence transfer. In contrast, the **H**···**D** and **H**···**NMe** separations between the two different ligand molecules (i.e. the "*inter*- ligand" distances)

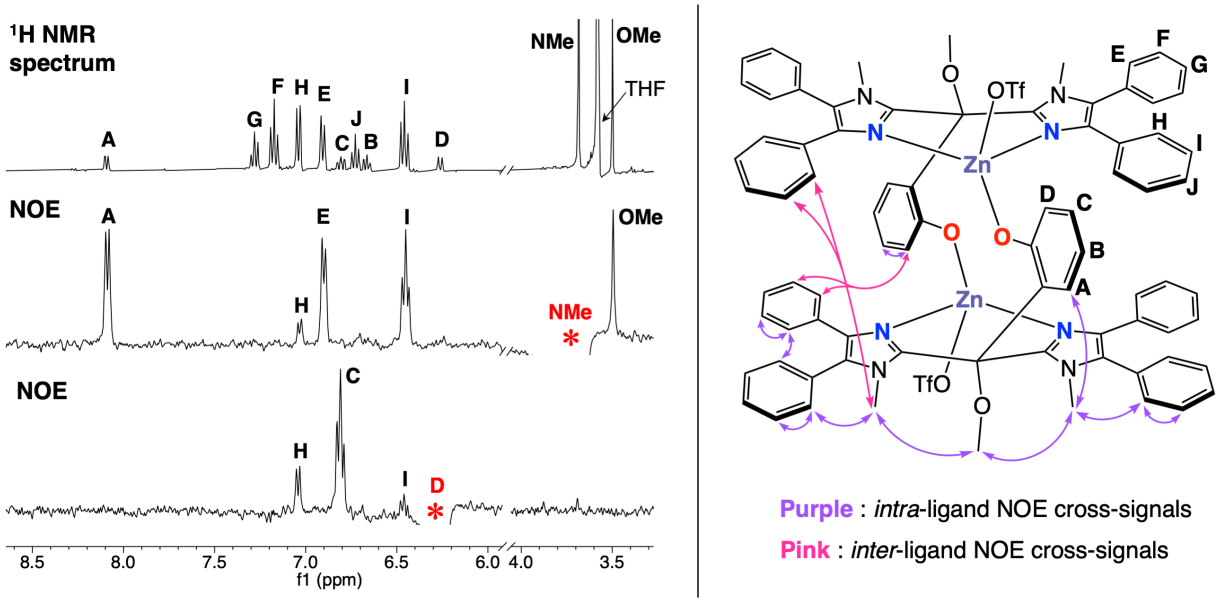

Figure 13. Left: Stacked ^{1}H NMR (400 MHz) spectrum of **5** and the NOESY NMR spectra recorded for the selective excitation of resonances **D** and **NMe**, recorded in THF-d_8 at 25 °C. Spectra are clipped vertically for clarity. Right: Schematic depiction of the through-space NOE interactions detected by NOESY NMR analysis of **5** in THF-d_8.

are 3.58 Å and 3.72 Å, respectively. Thus, the fact that NOE cross-signals for H are detected upon selective excitation of **NMe** and **D** provide evidence that **5** retains its dinuclear structure in THF solution. Additionally, no temperature-dependent fluxional processes were observed upon conducting VT NMR analysis of **5** in THF-d_8 (see Appendix A, Figure A12) On this basis, we conclude that the dinuclear structure of **5** is stable across a large temperature range.

The ^{1}H NMR spectrum of **4** in acetonitrile-d_3 (Figure 14) contains highly paramagnetically shifted signals between 90 and –90 ppm, consistent with the presence of high-spin iron(II). Due to the large number of peaks as well as the severely broadened and overlapped nature of certain signals, assignment of the spectrum could not be made. The ^{19}F NMR spectrum of **4** recorded in MeCN-d_3 contains a sharp resonance at –79 ppm. The effective magnetic moment (μ_{eff}) of the complex was determined by Evans NMR method as being 6.49 μ_B at 25 °C, consistent with the presence of two high-spin (S = 2) ferrous ions.[35] VT ^{1}H NMR of **4** in MeCN-d_3 shows an increase in magnetization at low temperature that is consistent with normal Curie behaviour (see Appendix A, Figure A13). The plot of signal shift (ppm) against 1/T (K^{-1}) produces linear fits for all peaks with convergence to the diamagnetic region upon extrapolation to infinite temperature (y-intercept). This demonstrates that no spin-cross-over phenomena occur and supports the absence of any solvent-related coordination equilibria or structural changes. Based on this data, we propose that, analogously to its zinc counterpart, **4** has a dinuclear structure in solution that remains intact across a wide temperature range.

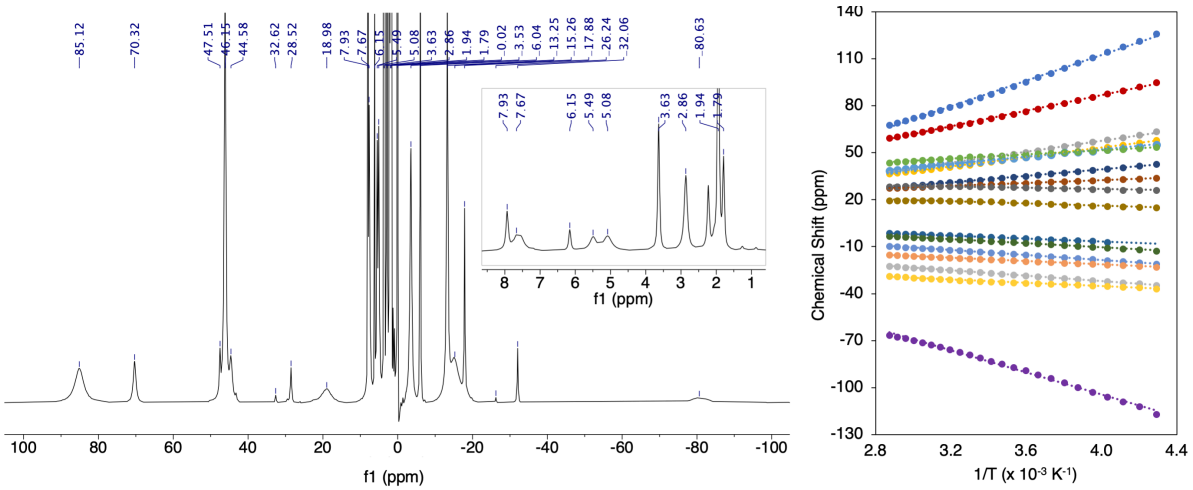

Figure 14. Left: The ^{1}H NMR (400 MHz) spectrum of **4**, recorded in CD_3CN at 25 °C. Right: Curie plot showing the inverse temperature dependence of the ^{1}H NMR signals of **4**, recorded in CD_3CN.

2.2.3.5 *Reactivity of $[Fe_2(Im^{Ph2}NNO)_2(OTf)_2$ (**4**)*

The presence of two magnetically and electronically independent iron(II) centres, each supported by a facial *N,N,O* ligand triad and bound to a labile triflate anion, means that **4** may be regarded as harbouring two independent catalytic sites. Therefore, we were keen to investigate its potential as an oxidation catalyst. We employed H_2O_2 as an oxidant and selected cyclohexane, *cis*-cyclooctene and *n*-propylbenzene as model substrates for possible epoxidation or hydroxylation reactivity (aliphatic, benzylic or aromatic) that may be exhibited by **4** (Scheme 5). The substrate (1 eq.) and **4** (1 mol%) were dissolved in 2 mL MeCN in a vial under inert N_2 atmosphere. The contents of the vial were then stirred at 0 °C and aqueous H_2O_2 solution (2 eq.) was added over the course of 30 min. This caused an almost instantaneous colour change of the solution from colourless to a dark inky blue-purple, indicative of iron oxidation. The reactions were stirred for 1 h after the complete addition of the oxidant. However, in all cases, no products of oxidation were observed and all of the substrate was recovered, indicating a lack of catalytic activity for **4**.

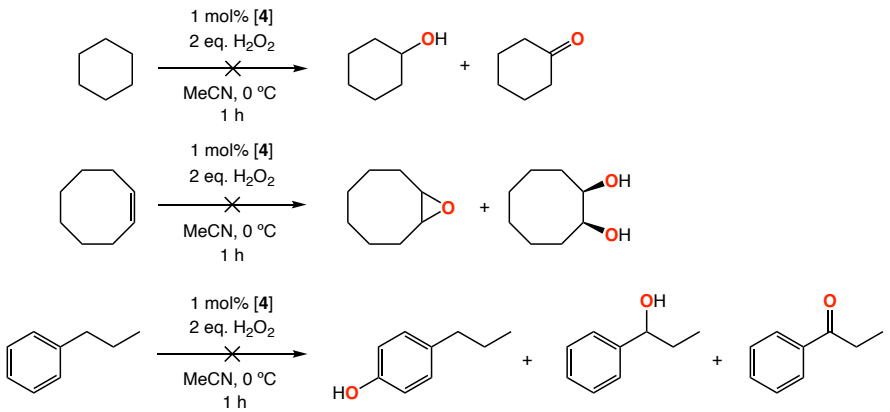

Scheme 5. Oxidation catalysis reaction attempts using $[Fe_2(Im^{Ph2}NNO)_2(OTf)_2]$ (**4**) as a catalyst. H_2O_2 was added over the course of 30 min at 0 °C. Reactions were stirred for 1 h after complete H_2O_2 addition.

Next, the oxidation of **4** itself was monitored by UV-vis spectroscopy (Figure 15). Exposure of a THF solution of **4** to air at room temperature resulted in a rapid colour change to blue-purple and the development of a strong absorption band at 580 nm (ε = ~630 dm^3 mol^{-1} cm^{-1}), very similar to that reported by Bruijnincx *et al.* for the homoleptic, bisligated iron(III) complex [Fe(ImNNO)$_2$](NO$_3$) (λ_{max} = 570 nm). On this basis, we assign the band at 580 nm to a phenolate-to-Fe^{3+} charge transfer and propose that O_2 exposure leads to an outer-sphere oxidation of **4** to the corresponding diiron(III) complex.[30] Similarly, addition of an excess of an aqueous H_2O_2 solution to a MeCN solution of **4** at room temperature causes an immediate colour change to blue-purple, coupled to the development of an absorption band at 515 nm (ε = 500 dm^3 mol^{-1} cm^{-1}). We tentatively assign this band to a hydroperoxo-to-Fe^{3+} charge transfer, which exhibits significant broadening due to the additional phenolate-to-iron(III) contribution in the spectrum. We hypothesise that a diiron(III) complex is formed and that the triflate ligands are substituted for aqua or hydroxo ligands that may cause the blue shift in the absorption band. For both the O_2 and H_2O_2 reactions, the colour of the sample eventually changes from blue-purple to red over the course of 1 h.

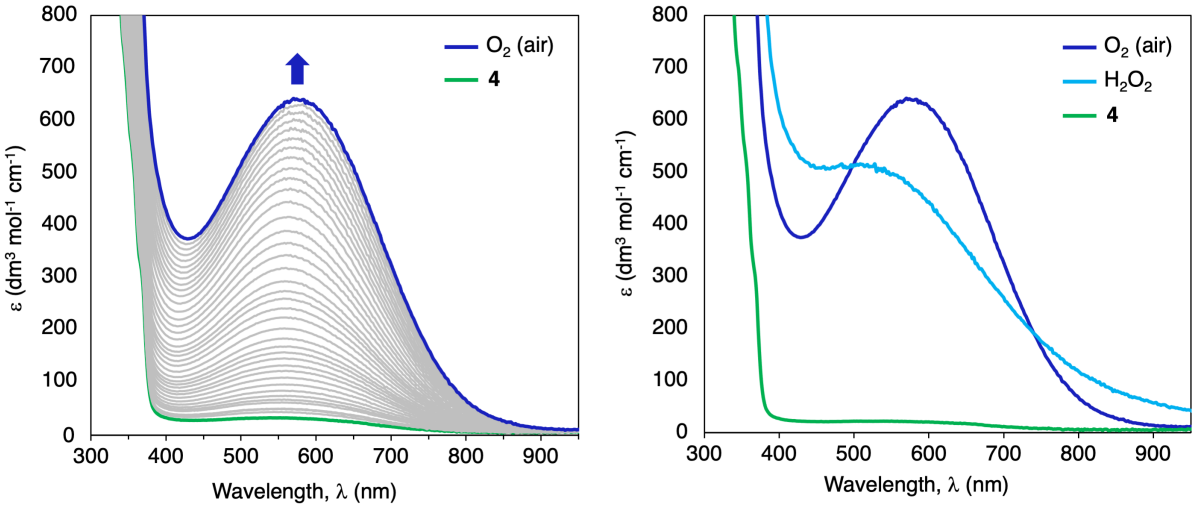

Figure 15. Left: Optical spectrum changes upon exposing a solution of **4** in THF to air under ambient conditions (diffusion-limited). Spectra were recorded every 48 seconds for a period of 30 minutes. Right: Overlay of the optical spectra obtained after reacting **4** with excess H_2O_2 or O_2 (air). Spectra recorded in MeCN and THF, respectively.

2.2.4 Dinuclear Metal Thiolate Complexes

2.2.4.1 Complex Synthesis

Despite the lack of catalytic activity of **4** in oxidation reactions, we were keen to investigate the substitutional lability of the triflate ligand in both **4** and **5** for biorelevant co-ligands and test the robustness of the ligand's dinucleating μ_2:κ_2-*N,N*,:κ_1-*O* coordination mode during substitution reactions. We employed thiophenolate for these investigations as a

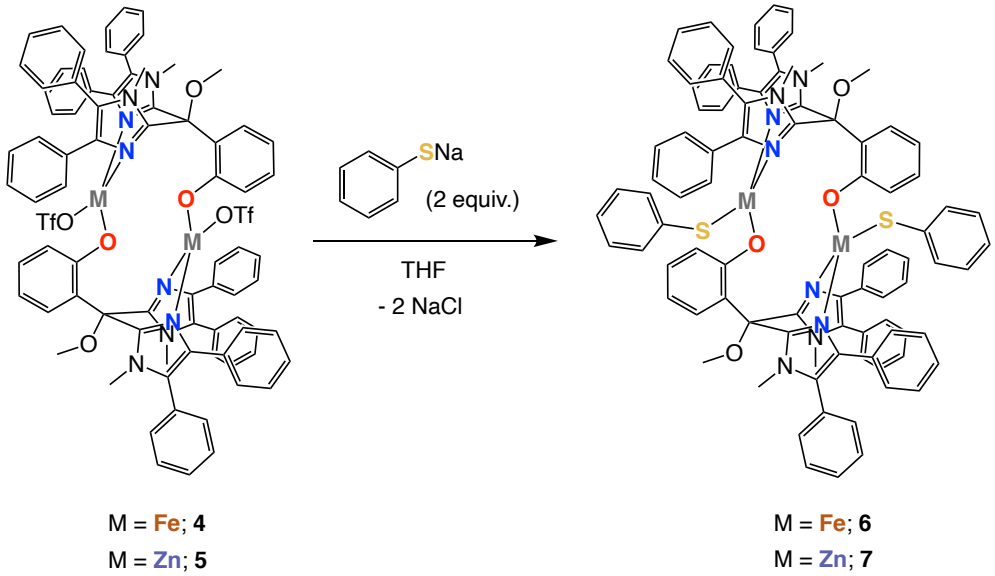

Scheme 6. Synthesis of complexes $[Fe_2(Im^{Ph2}NNO)_2(SPh)_2]$ (**6**) and $[Zn_2(Im^{Ph2}NNO)_2(SPh)_2]$ (**7**).

simple monodentate thiolate that is of structural relevance to the substrate-bound active site of isopenicillin N synthase (IPNS). Analogous procedures were employed for the substitution reactions involving **4** and **5** (Scheme 6). The dinuclear triflate complex was dissolved in THF under inert conditions, after which two equivalents of NaSPh suspended in THF were added dropwise to the solution. After a period of approximately 5 min, a white, amorphous solid precipitated from the mixture. The suspension was stirred for a further 1.5 h before removal of all solvents under vacuum. The crude solid was subsequently extracted into dichloromethane solution, filtered, and dried under vacuum. The resulting dinuclear thiolate complexes $[Fe_2(Im^{Ph2}NNO)_2(SPh)_2]$ (**6**) and $[Zn_2(Im^{Ph2}NNO)_2(SPh)_2]$ (**7**) were obtained as white solids in yields of 78% and 71%, respectively.

2.2.4.2 X-ray Crystal Structure Analysis

Crystals of **6** and **7** suitable for X-ray diffraction were obtained by slow vapour diffusion of *n*-hexane into THF solutions of each complex under ambient conditions. The resulting X-ray crystal structures are displayed in Figure 16 and selected bond lengths and bond angles are provided in Table 4. The results show that **6** and **7** have retained a dinuclear, cyclic structure analogous to that of their triflate counterparts. In other words, substitution of the OTf ligands in **4** and **5** for one equivalent of SPh per metal ion was successful and did not cause any disruption of the supporting ligand's unique dinucleating μ_2:κ_2-*N,N*:κ_1-*O* coordination mode. Each metal centre has a distorted tetrahedral geometry, bound by the *N,N,O* donor set of the supporting ligand scaffold and the anionic sulfur atom of a thiophenolate co-ligand. Notwithstanding the dinuclear nature of **6** and **7**, the independent metal sites in these complexes can be regarded as structural models of the substrate-bound active site of IPNS.[36]

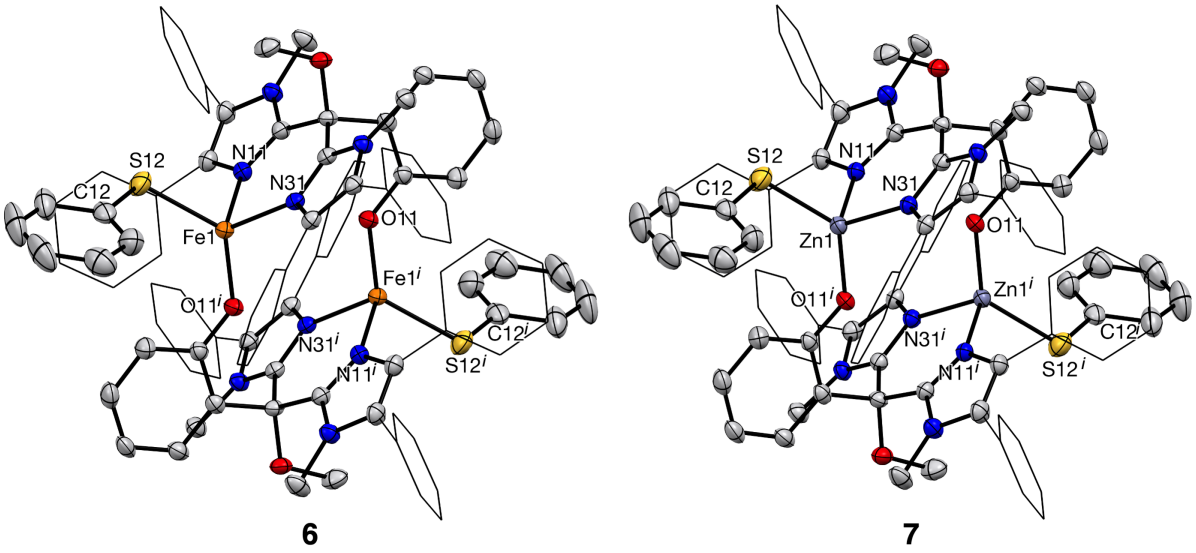

Figure 16. Displacement ellipsoid plots (50% probability level) for **6** (left) and **7** (right). All hydrogen atoms and disorder at the phenyl substituents have been omitted for clarity. Imidazole phenyl substituents have been depicted in the wireframe format for clarity. Symmetry code *i*: 1-*x*, 1-*y*, 1-*z*.

Table 4. Selected bond lengths (Å) and bond angles (°) for **6** and **7**. Symmetry code *i*: 1-*x*, 1-*y*, 1-*z*.

$[Fe_2(Im^{Ph2}NNO)_2(SPh)_2]$ (**6**)			
Bond	Length	Bond Angle	Degrees
Fe1–N11	2.093(2)	N11–Fe1–O11^i	110.44(8)
Fe1–N31	2.087(2)	N31–Fe1–O11^i	112.65(8)
Fe1–O11^i	1.9256(17)	N11–Fe1–N31	90.72(8)
Fe1–S12	2.3243(8)	S12–Fe1–O11^i	127.73(6)
		Fe1–S12–C12	115.19(11)
$[Zn_2(Im^{Ph2}NNO)_2(SPh)_2]$ (**7**)			
Bond	Length	Bond Angle	Degrees
Zn1–N11	2.0485(19)	N11–Zn1–O11^i	109.88(8)
Zn1–N31	2.0478(19)	N31–Zn1–O11^i	108.51(7)
Zn1–O11^i	1.9180(16)	N11–Zn1–N31	93.61(8)
Zn1–S12	2.2870(7)	S12–Zn1–O11^i	128.81(5)
		Zn1–S12–C12	114.40(10)

The X-ray crystal structures of **6** and **7** are centrosymmetric. As was the case for their triflate counterparts, large C–C–O–M torsion angles of –179.07° and 176.60° are observed for **6** and **7**, respectively, consistent with the coordination of the phenolic oxygen atom through its distal lone pair. Similarly, the metal centres are bound in an almost co-planar fashion with respect to the bis-imidazole methane moiety of the ligand scaffold. The tetrahedral distortion at each metal centre is manifested by the N–M–O and S–M–O angles that are all larger than that of an ideal tetrahedron. The M–S–C bond angles of 115.20(11)° and 114.41(9)° for **6** and **7**, respectively, are consistent with the sp^3 hybridisation and

tetrahedral geometry of the thiolate sulfur atoms. The angles, however, are somewhat larger compared to those reported for other metal thiophenolate complexes supported by a tripodal *N,N,O* ligand.[15,37] We attribute this to the relatively close proximity of the thiophenolate and phenolate rings. The M–S bond distances of 2.3245(9) Å and 2.2870(9) Å for **6** and **7**, respectively, are in line with those of other previously reported iron(II) and zinc(II) complexes with monodentate thiolate ligands.[15,34,38,39]

Interestingly, the intermetallic distances of 4.4996(6) Å and 4.5072(6) Å in **6** and **7**, respectively, are almost identical and represent an increase of 0.2407(8) Å and 0.5132(7) Å relative to their respective parent triflate complexes. We attribute this phenomenon to a change in the hybridisation of the metal-ligand bonds in the thiolate dimers compared to those in the triflate dimers (Figure 17). Assuming that classical valence bond theory applies, the metal's 4s and 4p orbitals are those that dictate the bonding interactions between the metal centre and the ligand donor set, since all d-orbitals are either singly or fully occupied in Fe^{2+} ([Ar]3d^6) and Zn^{2+} ([Ar]3d^{10}). According to Bent's rule, the s- and p-character of the bonding interactions is described as a function of the electronegativity (χ) of the substituents.[40–42] Throughout the dinuclear complexes **4**–**7**, an identical *N,N,O* donor set is bound to each metal centre as well as an exogenous ligand, which varies between OTf and SPh. This exogenous ligand therefore modulates the hybridization of the metal-ligand bonding interactions to the greatest extent. Thus, the more electronegative oxygen atoms of the OTf ligands induce greater p-character in the M–O_{OTf} bonds. This has the effect of increasing the s-character in the M–[*N,N,O*] bonds, which causes a shortening of the corresponding bonds. Conversely, the lesser electronegativity and softer nature of the thiolate ligands demands more s-character from the M–S bonds, which increases the p-character of the metal-[*N,N,O*] bonds and causes an increase of their corresponding bond lengths. This is consistent with the X-ray crystal structures obtained for the complexes, where longer metal–[*N,N,O*] bond lengths are measured in **6** and **7** than for their triflate

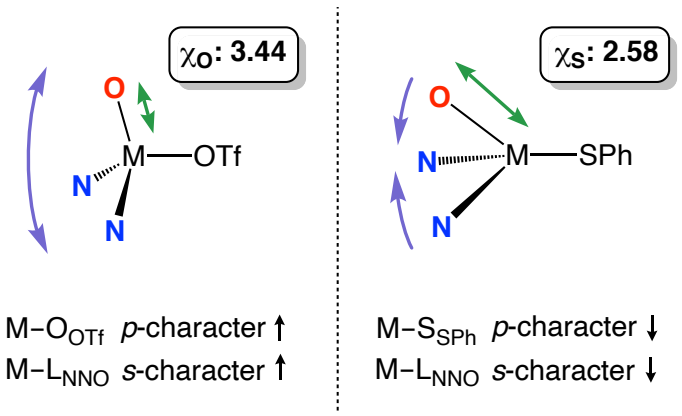

Figure 17. Schematic representation of how changes in hybridisation affect the geometry in $[M_2(Im^{Ph2}NNO)_2(OTf)_2]$ (**4** and **5**), and $[M_2(Im^{Ph2}NNO)_2(SPh)_2]$ (**6** and **7**). Purple arrows depict the increase or decrease in the N–M–N and N–M–O angles about the metal centre. Green arrows depict the shorter or longer M–[*N,N,O*] bonds. χ_E = element electronegativity.

analogues. Moreover, the N–M–N and N–M–O bond angles lie closer to 90° and are more acute in **6** and **7** than they are in **4** and **5**, which is consistent with an increase in the p-character of the metal-[*N,N,O*] bonds. Correspondingly, a smaller sum of angles associated to the *N,N,O* coordination of the ligand is found for **6** and **7** (Σ_{NNO} = 313.31(8)° and 312.00(8)°, respectively) compared to **4** and **5** (Σ_{NNO} = 325.85(6)° and 334.10(7)°, respectively). We also considered steric effects as a possible cause to the increase in intermetallic distance. In principle, any additional strain from the proximity of the thiophenolate ring to the phenolate could cause a distortion of the supporting ligand framework. However, the angles about the ligand's central methoxy-bound carbon lie closer to those of an ideal tetrahedron in the thiolate dimers compared to the triflate dimers and, on this basis, we exclude sterics from having any significant influence on the increase in intermetallic distances.

2.2.4.3 *Electronic Structure*

The zero-field ^{57}Fe Mössbauer spectrum of **6** (Figure 18) shows a single quadrupole doublet, best described by an isomer shift of 0.96 mm s^{-1} and a quadrupole splitting of 3.07 mm s^{-1}. The Mössbauer lines are unusually broad and a slight asymmetry in the quadrupole doublet is observed, which we attribute to a distribution of quadrupole splittings that may arise from some slight (micro)heterogeneity in the powder sample of **6**.[43] This likely causes some inequivalence of the dimers within the powder macrostructure rather than the inequivalence of the two iron sites within the dinuclear complex. Low crystallinity and high surface effects of an amorphous powder sample have typically been invoked as origin effects for this phenomenon.

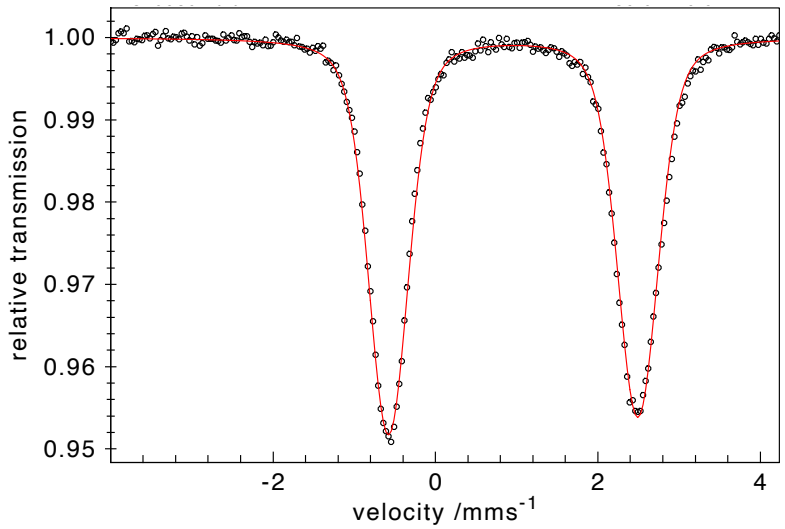

Figure 18. The zero-field ^{57}Fe Mössbauer spectrum of **6**, recorded at 80 K. The black points correspond to the data and the red trace corresponds to the best fit. Data fit parameters: isomer shift (δ) = 0.96 mm s^{-1}, quadrupole splitting ($|\Delta E_Q|$) = 3.07 mm s^{-1}.

Overall, the Mössbauer spectrum obtained for **6** is consistent with the presence of two electronically equivalent high-spin iron(II) centres. Finally, we observe that the isomer shift for **6** is slightly lower compared to that of **4**. This is due to the substitution of the hard oxygen-rich triflates for soft sulfur atoms of the thiophenolate ligands, whose stronger covalent interactions cause more s-electron density to be donated to the iron centre, giving rise to a more negative isomer shift.

2.2.4.4 Solution State Behaviour

The ^{1}H NMR spectrum of **7** recorded in THF-d_8 (Figure 19) contains two sharp singlets at 3.51 and 2.57 ppm that we assign to the N-methyl and O-methyl groups, respectively, on the basis of their 2:1 integral ratio. This is indicative of C_S ligand symmetry, which is consistent with the solid state structure of **7**. Strikingly, the OMe signal has shifted significantly upfield compared to that of **5**. We ascribe this to the close proximity of the thiophenolate, whose magnetic anisotropy has a shielding effect shield on the methoxy group. In the aromatic region of the spectrum, a single set of imidazole-derived signals is observed, all of which could be assigned using a combination of 1D TOCSY and NOESY NMR experiments (see Appendix A, Figures A14-A17).

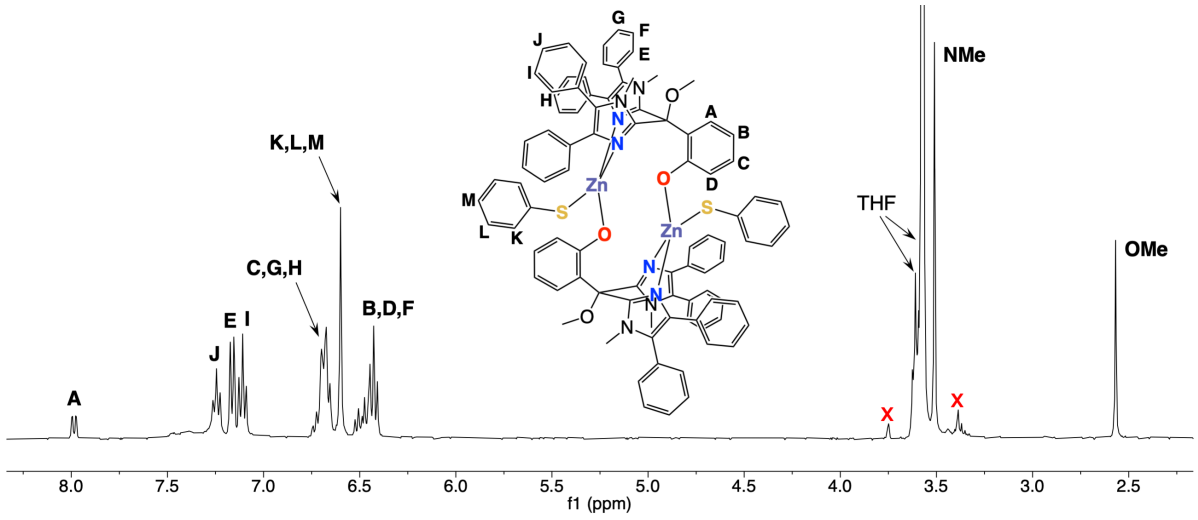

Figure 19. ^{1}H NMR (400 MHz) spectrum of **7**, recorded in THF-d_8. Small unknown impurities are indicated by red crosses.

Interestingly, the signals assigned to the thiophenolate (resonances **K**, **L** and **M**) coincide at the same chemical shift (6.60 ppm) and manifest themselves as a slightly broadened singlet. We hypothesise that free rotation of the thiophenolate ring within its binding pocket, and strong coupling of its aromatic protons may be the cause of such severe signal overlap and indistinguishable multiplicity. The ^{1}H–^{13}C ASAP-HMQC spectrum of **7** (see Appendix A, Figure A18) shows a correlation between the signal at 6.60 ppm and three different ^{13}C signals, supporting its assignment to the thiophenolate ring.

The ^{1}H NMR spectrum of **6** recorded in dichloromethane-d_2 contains paramagnetically shifted signals ranging between 50 and −50 ppm (Figure 20). The effective magnetic moment of **6** was determined by Evans NMR method to be 7.30 μ_B, consistent with two magnetically independent high-spin (S = 2) iron(II) nuclei. Cooling the sample to −80 °C causes a significant increase in magnetization (see Appendix A, Figure A19), consistent with normal Curie behaviour of the complex in solution. The Curie plot of signal shift (ppm) against 1/T (K^{-1}) produces linear fits for all peaks with excellent convergence to the diamagnetic region upon extrapolation to infinite temperature. This demonstrates that no spin-crossover phenomena occur and that no structural changes take place in solution.

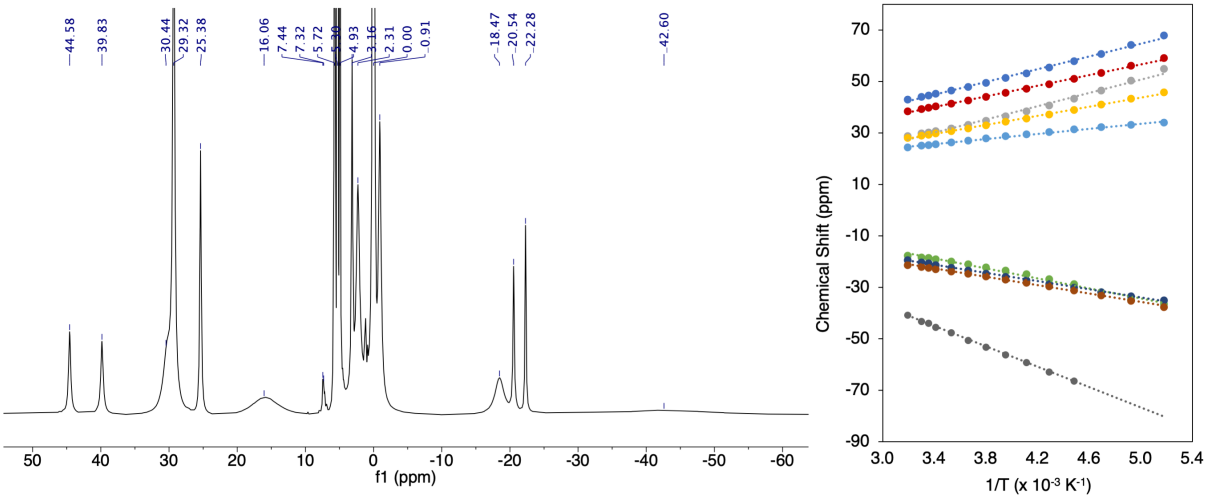

Figure 20. Left: The ^{1}H NMR spectrum (400 MHz) of **6**, recorded in CD_2Cl_2 at 25 °C. Right: Curie plot showing the inverse temperature dependence of the ^{1}H NMR signals of **6**, recorded in CD_2Cl_2.

2.2.4.5 Computational Analysis

Next, we performed density functional theory (DFT) calculations in order to investigate the influence of the thiophenolate ligands on the electronic properties of the dinuclear complexes. The gas-phase geometries of complexes **4**–**7** were optimised at the B3LYP/6-311g(d,p) level of theory. The Kohn-Sham molecular orbitals (MOs) were extracted from these geometries for zinc complexes **5** and **7**. For iron complexes **4** and **6**, the α and β MOs were biorthogonalized using the *Multiwfn* program (see Appendix G),[44] and their energies evaluated using the Fock matrix generated by natural bonding orbital (NBO) analysis.

The highest occupied molecular orbitals (HOMO) calculated for each complex is depicted in Figure 21. The HOMO in **5** is delocalised across both phenolic moieties of the supporting ligand molecules, which demonstrates their redox non-innocent character. However, substitution of the OTf groups for SPh ligands in **7** shifts the HOMO to the lone pairs of the sulfur atoms. We attribute the greater oxidation susceptibility of the thiophenolate ligands to the lower ionisation potential of sulfur in general. In contrast, the eight highest occupied molecular orbitals in **4** and **6** are all singly occupied iron-based orbitals, in line with the spin density being localised entirely on the iron centre. Thus,

theory predicts that the iron centres in both **4** and **6** are the sites most prone to oxidation despite the presence of redox active phenolate or thiophenolate moieties within the same complex architecture. Interestingly, computations show that the HOMO in **4** takes its greatest contribution from a d-orbital localised on one of the iron centres, whereas the HOMO in complex **6** takes an equal contribution from two d-orbitals, one per iron centre. This could be due to the very slight ferromagnetic magnetic coupling observed between the iron centres in **4** compared to **6**, where it is likely that no magnetic coupling occurs at all. The Fe···Fe distances observed in the X-ray crystal structures of **4** and **6** are 4.2589(6) Å and 4.4996(6) Å, respectively.

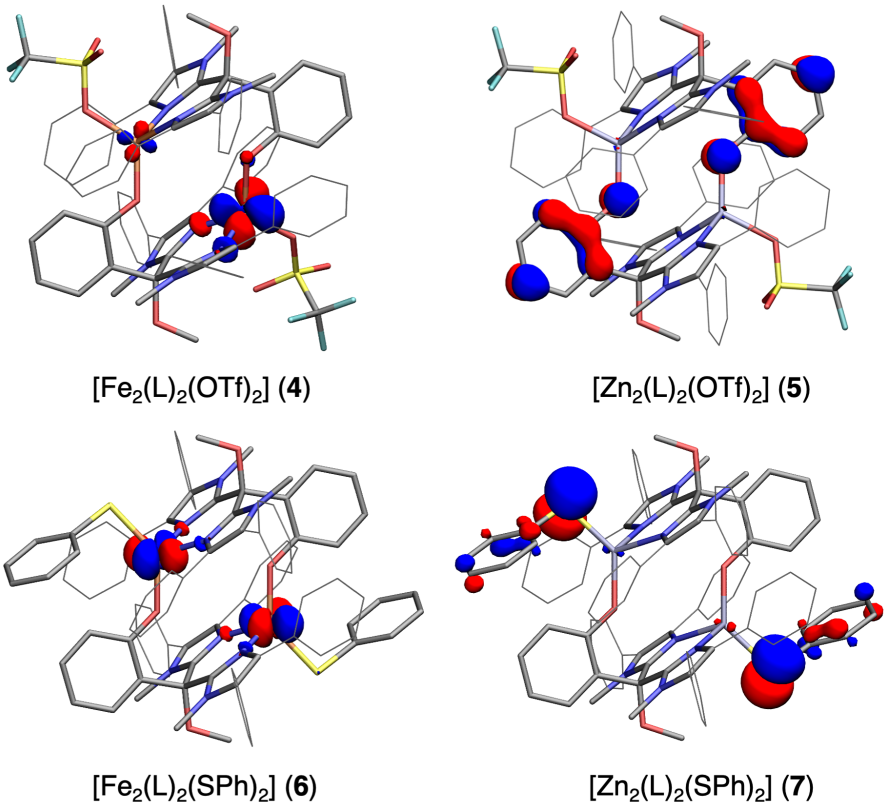

Figure 21. The HOMOs of the OTf dimers (**4** and **5**) and the SPh dimers (**6** and **7**) as calculated by DFT at the B3LYP/6-31g(d,p) level of theory. Isosurfaces are drawn at the ±0.05 level, with opposite phases drawn in red and blue. Imidazole phenyl substituents have been depicted in the wireframe format for clarity.

*2.2.4.6 Reactivity of [Fe$_2$(Im^{Ph2}NNO)$_2$(SPh)$_2$] (**6**)*

Complex [Fe$_2$(Im^{Ph2}NNO)$_2$(SPh)$_2$] (**6**) is of structural relevance to the substrate-bound active site of isopenicillin N synthase as it contains independent iron(II) centres, each capped by a supporting *N,N,O* ligand and bound to an exogenous thiolate. It is therefore of interest to investigate the site at which oxidation occurs when exposing the complex to different oxidants. DFT calculations predict that the iron centres are the sites most prone to oxidation. However, the thiolate sulfur atoms, situated at the apical sites of the complex, are relatively "exposed" and could easily be targeted by oxidants in solution.

Reacting **6** with PhIO (10 equiv.) in MeCN at room temperature induces a slow colour change from orange to deep red, coupled to the development of a UV-vis absorption band at 475 nm that shoulders the intense π–π* transition region of the spectrum (Figure 22). Analysis of the resulting solution by means of ESI-MS in negative mode shows a signal at m/z = 156.90, which corresponds to the phenylsulfonate anion (calculated m/z = 157.00 for $PhSO_3^-$). In positive mode ESI-MS, a strong signal is detected at m/z = 601.1, which corresponds to the free ligand. An additional much weaker signal is observed at m/z = 571.1, which corresponds to the methoxy-cleaved ligand (calculated m/z = 571.25 for $[L–OCH_3]^-$), and is likely the result of oxidative ligand degradation to its quinone form. No iron-containing ions could be detected, most probably due to hydrolysis of the complexes under the ESI-MS measurement conditions. For comparison, we monitored the oxidation of **6** in air by UV-vis spectroscopy and observed the development of the same absorption band at 475 nm (Figure 22). We do not observe any absorption band at 580 nm, as had been the case for the oxidation of $[Fe_2(Im^{Ph2}NNO)_2(OTf)_2]$ (**4**) in air. On this basis, we tentatively assign the band at 475 nm to an iron(III) sulfonate complex, which may derive from a short-lived iron-oxo intermediate that is not observed by UV-vis.

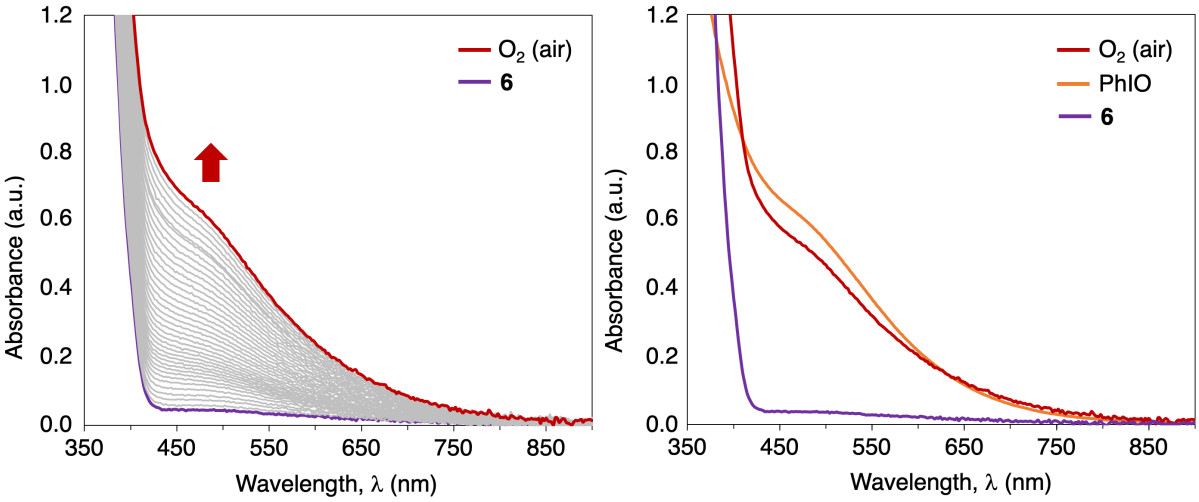

Figure 22. Left: UV-vis spectrum changes upon exposing a solution of **6** in CH_2Cl_2 to air at ambient temperature (under diffusion-limiting conditions). Spectra were recorded every 24 seconds for a period of 20 min. Right: overlay of the UV-vis spectra obtained after reacting **6** with PhIO (10 eq.) or O_2 (air).

2.2.5 Unexpected Ligand C–O Bond Cleavage in the Presence of $FeCl_3$

Reacting **K-Im^{Ph2}NNO** with one equivalent of $FeCl_3$ in MeCN resulted in the immediate formation of a deep blue solution. The solution was stirred for a further 1.5 h before being filtered and dried under vacuum, affording a dark blue solid. The UV-vis spectrum of this species in CH_2Cl_2 exhibits a broad absorption band at 612 nm (Figure 23). Interestingly, we observed that the sample solution progressively changed colour from blue to red, coupled to a shift in the absorption band to 470 nm. A similar phenomenon was observed when dissolving the blue solid in THF: the solution was initially blue but swiftly changed

colour to red. In UV-vis spectroscopy, we observe a shift in the absorption band from 590 to 470 nm. The spectrum recorded when the THF solution was visibly still blue is severely broadened due to a contribution from the band rapidly forming at 470 nm.

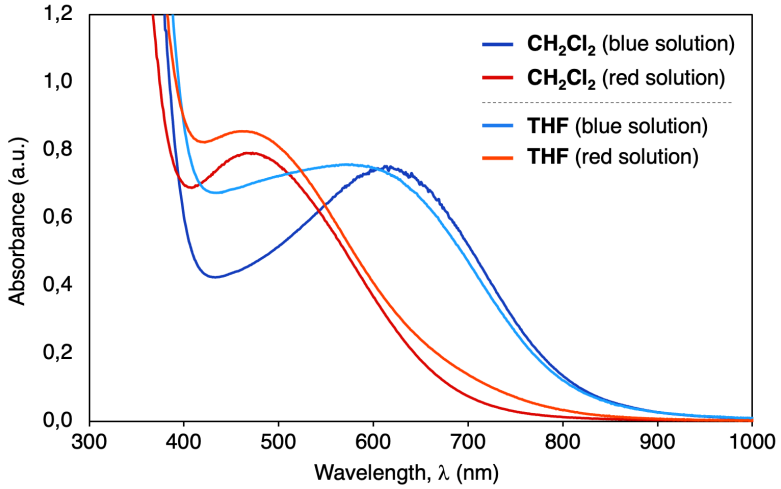

Figure 23. UV-vis spectra of the blue and red solutions of the product obtained from the reaction of **K-Im^{Ph2}NNO** and $FeCl_3$. Spectra were recorded at ambient temperature for CH_2Cl_2 and THF solutions of the product.

Red crystals suitable for X-ray diffraction were obtained by slow diffusion of *n*-hexane into a THF solution of the reaction product over the course of several days. The resulting X-ray crystal structure reveals the formation of a diiron(III) complex, [Fe_2(Im^{Ph2}NNO*)$_2$(Cl)$_2$] (**8**), featuring two ligand molecules (Im^{Ph2}NNO*) that have undergone methyl cleavage (C–O bond cleavage) at the methoxy group (Figure 24). The iron nuclei are bound within a diamond core structure, with an intermetallic distance of 3.0830(8) Å. Each iron centre is pentacoordinate and square pyramidal in geometry, bound to the imidazole group of one ligand molecule, the phenolate group of a second ligand molecule, a chloride ion and two anionic μ_2-bridging alkoxide oxygen atoms from the degraded ligand molecules. One imidazole group in both ligand molecules remains non-coordinated. Selected bond lengths and bond angles are given in Table 5.

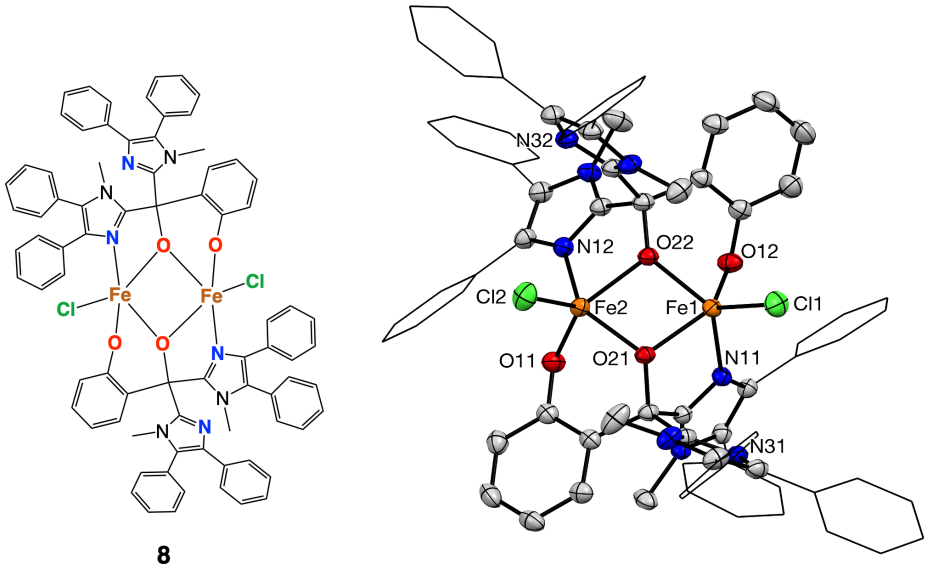

8

Figure 24. Displacement ellipsoid plot of $[Fe_2(Im^{Ph2}NNO^*)_2(Cl)_2]$ (**8**), drawn at the 50% probability level. All hydrogen atoms are omitted for clarity. Imidazole phenyl substituents are drawn in the wireframe format for clarity.

Table 5. Selected bond lengths and bond angles for $[Fe_2(Im^{Ph2}NNO^*)_2(Cl)_2]$ (**8**).

$[Fe_2(Im^{Ph2}NNO^*)_2(Cl)_2]$ (**8**)			
Bond	Length (Å)	Bond Angle	Degrees
Fe1–N11	2.0608(13)	O12–Fe1–O22	87.72(5)
Fe1–O12	1.8739(11)	O21–Fe1–O22	73.74(4)
Fe1–O21	2.0480(11)	N11–Fe1–O21	78.81(5)
Fe1–O22	2.0035(10)	O12–Fe1–Cl1	112.27(4)
Fe1–Cl1	2.1957(5)	N11–Fe1–Cl1	111.66(4)
Fe2–N12	2.0446(13)	O11–Fe2–O21	88.78(5)
Fe2–O11	1.8746(11)	O21–Fe2–O22	74.38(4)
Fe2–O21	1.9797(10)	N12–Fe2–O22	78.37(5)
Fe2–O22	2.0413(10)	O11–Fe2–Cl2	112.51(4)
Fe2–C12	2.1991(5)	N12–Fe2–C12	109.40(4)

The degradation of the ligand in this manner is somewhat unexpected given the poor leaving group ability generally associated to methyl groups. However, demethylation of protected hydroxyl groups through C–O bond cleavage has been reported in the presence of strong Lewis acids such as BBr_3,[45,46] $AlCl_3$,[47] and $FeCl_3$.[48,49] We hypothesise that reaction of **K-Im^{Ph2}NNO** with $FeCl_3$ initially produces a blue-coloured intermediate diiron(III) complex, $[Fe_2(Im^{Ph2}NNO)_2(Cl)_4]$ (**A**), which contains two ferric ions within the dinuclear, cyclic complex architecture associated to the ligand's μ_2-coordination mode (Scheme 7). However, the strong metal-halide interaction combined with the steric congestion associated to the presence of two chloride ions in the iron's coordination sphere likely causes one of the imidazole groups to dissociate, which has the effect of bringing the

methoxy groups into closer proximity to the metal centres,[34] and enables the red-coloured complex **8** to form through C–O bond cleavage. We also propose that the leaving group ability of the alkylate is enhanced by the coordination of the resulting anionic alkoxide oxygen atoms to the Fe^{3+} ions.

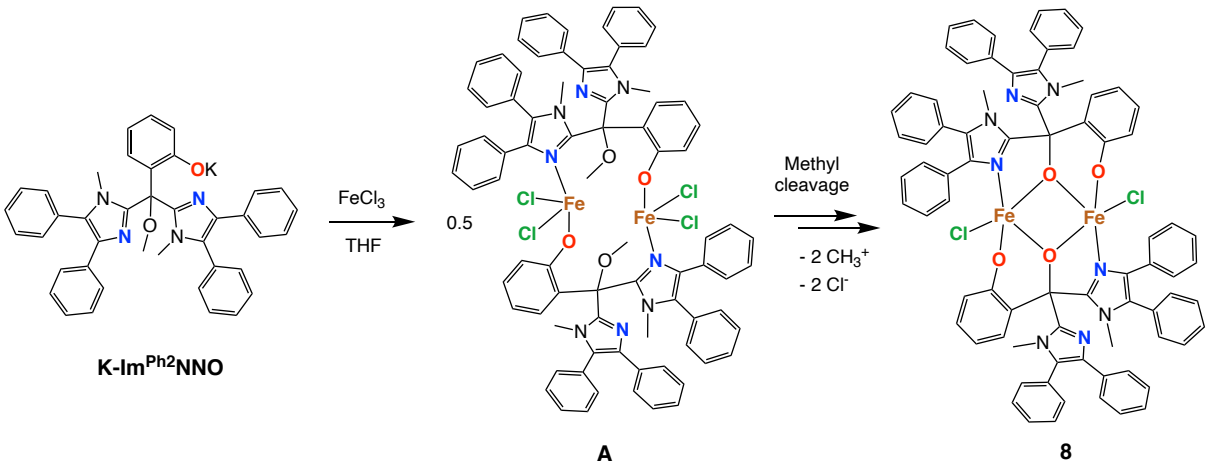

Scheme 7. The reaction between **K-Im^{Ph2}NNO** and $FeCl_3$ leading to the formation of complex **8** *via* the proposed intermediate **A**.

2.3 Conclusions

We have synthesised two new bis-imidazole-derived phenolate ligands, **BenzImNNO** and **Im^{Ph2}NNO**, which feature 1-methlbenzimidazole and 1-methyl-4,5-diphenylimidazole groups, respectively. These new ligands expand the library of bioinspired *N,N,O* ligands designed to structurally model the 2-His-1-Carboxylate facial triad (2H1C).

We have shown that **BenzImNNO** readily coordinates by means of a facial κ_3-*N,N,O* binding motif. However, the 1-methylbenzimidazole groups are small enough for homoleptic, bisligated complexes to form in reactions involving either one or two equivalents of ZnX_2 salt (X = Cl or OTf). In these complexes, the phenolic oxygen atoms have the propensity to adopt a μ_2-bridging coordination mode to a second metal centre, giving rise to dinuclear complexes of the type $[Zn(BenzImNNO)_2Zn(X)_2]$. The Zn_2O_2 diamond core structure in these complexes involves the coordination of both the proximal and distal lone pairs of the phenolic oxygen atoms.

In contrast, the 1-methyl-4,5-diphenylimidazole groups in **Im^{Ph2}NNO** are too sterically cumbersome to enable homoleptic, bisligated complexes to form. Instead, reacting the ligand with one equivalent of $M(OTf)_2$ (M = Fe or Zn) produces dinuclear complexes of the type $[M_2(Im^{Ph2}NNO)_2(OTf)_2]$, where the ligand adopts a unique μ_2:κ_2-*N,N*:κ_1-*O* coordination mode that locks the two metals within a large 14-membered ring structure. The phenolic oxygen atoms in these complexes coordinate exclusively through their distal

lone pairs. The two metal ions are separated by a large intermetallic distance and can be regarded as electronically and magnetically independent entities. In the case of iron, this is confirmed by Mössbauer spectroscopy and SQUID magnetometry. We have furthermore shown that the apical triflate ligands can be substituted for thiophenolate ligands, generating dinuclear thiolate complexes of the type $[M_2(Im^{Ph2}NNO)_2(SPh)_2]$. These complexes are of structural relevance to the substrate-bound active site of IPNS. Reacting $[Fe_2(Im^{Ph2}NNO)_2(SPh)_2]$ (**6**) with either O_2 or PhIO produces a new red-coloured species in solution that we assign as an iron(III) sulfonate species on the basis of UV-vis and ESI-MS studies. However, reacting $\mathbf{Im^{Ph2}NNO}$ with Lewis acidic $FeCl_3$ leads to the unexpected methyl cleavage of the ligand's methoxy group. These observations point out that more complex structural and chemical transformations take place upon oxidation of the iron centres in **6**, which are currently under further investigation in our laboratories.

Overall, these results demonstrate that subtle steric differences between ligands of the same family can have a drastic impact on the structure of their related metal complexes. However, it is also evident that additional ligand design considerations beyond imidazole steric bulk are necessary in order to achieve the desired monoligated *N,N,O*-bound complex architecture that truly models the 2H1C. Indeed, it is likely that inclusion of a sterically bulky group *ortho* to the phenolate group is necessary to block its coordination through the distal lone pair and prevent any bridging coordination modes from occurring.

2.4 Author Contributions

E.C.M. and B.K.G. devised the project, designed experiments and wrote the manuscript. E.C.M. and H.A.N. performed experiments and analysed the data. E.M.-R. performed catalysis experiments. M.L. performed X-ray crystal structure determinations. S.Y. and E.B. provided Mössbauer and SQUID data analysis. All authors provided comments on the experiments and manuscript during its preparation.

2.5 Experimental

2.5.1 Chemicals and Reagents

Unless stated otherwise, all reactions were performed under inert N_2 (g) atmosphere using standard Schlenk line and glovebox techniques and were stirred magnetically. The solvents acetonitrile, diethyl ether, and hexane were purified using an MBraun MB SPS-80 purification system. Dichloromethane and pyridine were dried over CaH_2 and distilled under inert N_2 (g) atmosphere before use. THF was dried over sodium benzophenone ketyl and distilled under inert N_2 (g) atmosphere before use. Pentane was dried using activated molecular sieves and was degassed using the freeze-pump-thaw technique. All other common solvents were degassed by bubbling N_2 (g) through them for a period of 30 min prior to use and were stored over activated molecular sieves. Acetonitrile was filtered over activated neutral alumina before use to remove molecular sieve debris. All solvents were tested for water content by the

Karl-Fischer titration or by ^{1}H NMR. Non-halogenated solvents were additionally tested with a standard purple solution of sodium benzophenone ketyl in THF to confirm effective oxygen and moisture removal. Deuterated solvents were purchased from the Cambridge Isotope Laboratory Incorporation (Cambridge, USA) and were degassed using the freeze-pump-thaw method and stored over activated molecular sieves. Deuterated acetonitrile was filtered over activated neutral alumina prior to use to remove molecular sieve debris. All reagents and starting materials were purchased from commercial sources and used without further purification, except when specified. Benzenethiol was converted to its respective sodium salt by treating it with an equimolar amount of NaH.

2.5.2 Physical Methods

NMR spectroscopy (^{1}H, ^{13}C{^{1}H}, ^{19}F, ^{1}H-^{13}C HSQC, 1D and 2D NOESY) was conducted using a 400 MHz Varian spectrometer or an Oxford NMR AS400 spectrometer. ^{1}H and^{13}C NMR chemical shift are reported in the standard δ notation of part per million (ppm) and are referenced to a residual peak of the solvent, as determined relative to $SiMe_4$.[50] ^{19}F NMR chemical shifts are reported in ppm and are externally referenced to an 85% aqueous solution of $CFCl_3$. Paramagnetic ^{1}H NMR spectra were recorded after having adjusted both the relaxation delay and acquisition time to 100 ms. IR spectroscopy was conducted using a PerkinElmer Spectrum Two FT-IR spectrometer. For air-sensitive compounds, a N_2 (g) flow was used. Peaks are annotated by (w), (m) and (s) to indicate weak, medium and strong signals, respectively. Absorption spectra were recorded using a Varian Cary 50 Scan spectrometer, using quartz cuvettes with a path length of 1 cm, sealed with a Teflon cap. Unless otherwise stated, UV-vis solutions were prepared in the glovebox using dried and degassed solvents. The acquisition of the absorption spectra was performed with the PerkinElmer UV Winlab software. High resolution ESI-MS measurements were performed with a Waters LCT Premier XE KE317. All other ESI-MS measurements were performed with an Advion Expression CMS instrument. X-ray crystal structure determinations were performed on a Bruker Kappa ApexII diffractometer with sealed tube and Triumph monochromator (λ = 0.71073 Å) at a temperature of 150(2) K (see Appendix A for further details). Elemental analyses were performed at the Medac Ltd laboratories in the UK. Mössbauer spectra (see Appendix F) were recorded on a conventional spectrometer with alternating constant acceleration of the g-source (^{57}Co/Rh, 1.8 GBq), which was kept at room temperature. The minimum experimental line width was 0.24 mm s^{-1} (full width at half-height). The sample temperature was maintained constant in an Oxford Instruments Variox cryostat. Isomer shifts are quoted relative to iron metal at 300 K. The zero-field spectra were simulated with Lorentzian doublets with the program *mf.SL* developed by Dr. Eckhard Bill. Magnetic susceptibility data were measured from powder samples of solid material in the temperature range 2–300 K by using a SQUID susceptometer with a field of 1 T (MPMS-7, Quantum Design, calibrated with a standard palladium reference sample, error < 2%). The experimental data were corrected for underlying diamagnetism by use of tabulated Pascal's constants.[51,52] The susceptibility data were simulated with software package julX[53] on the basis of the usual spin Hamiltonian:

$$H = -2J\,\vec{S}_1 \cdot \vec{S}_2 + \mu_B \vec{B} \cdot \tilde{g} \cdot (\vec{S}_1 + \vec{S}_2) + \sum_i D_i [S_z^2 - 1/3\,S(S+1) + E/D(\vec{S}_x^2 - \vec{S}_y^2)]$$

2.5.3 Computational Methods

DFT (density functional theory) calculations were performed using the Gaussian 16 software package.[54] Geometry optimisations used the B3LYP (Becke, three-parameter, Lee-Young-Parr) functional with the LANL2DZ basis set defined on Fe and Zn atoms and the 6-31g(d,p) basis set defined on all other

atoms. Initial *x,y,z* coordinates were extracted from the X-ray crystal structures of the respective complexes. Geometries were optimized without any symmetry restraints and empirical dispersion corrections were applied. Due to the large size of the dinuclear complexes, all attempts at frequency calculations were unsuccessful (convergence failure was reported in all cases despite increasing the available memory or the number of cores used for the calculations). Single point energy calculations were subsequently performed on the optimized geometries at the B3LYP/6-311g(d,p) level of theory. NBO (natural bond orbital) calculations were performed on the iron complexes using the *NBO06* program[55] up to the NLMO (natural localized molecular orbital) basis set. Cube files for molecular orbitals (MOs) were generated using the *Multiwfn* program.[44] Biorthogonalization of the α and β spin MOs for iron complexes **4** and **6** was performed using *Multiwfn* and the energies were evaluated using the Fock matrix from the .47 NBO file generated from NBO analysis (see Appendix G). MOs were visualized with the *Visual Molecular Dynamics* program[56] using the respective molecular orbital cube files and defining the isosurface at ±0.05.

2.5.4 Ligand Synthesis

Methyl 2-(methoxymethoxy)benzoate (LS1):[30] Methyl 2-hydroxybenzoate (7.00 mL, 54.1 mmol) was added dropwise to a stirred suspension of NaH (8.6 g, 215 mmol, 60 weight% dispersion in mineral oil) in THF (250 mL). After stirring for 1 h at room temperature, chloromethyl methyl ether (9.7 mL, 108 mmol) was added in one portion. The reaction mixture was stirred overnight, during which time the reaction gained a milky texture. Ice was added cautiously (gas and exotherm!) to quench the excess NaH, and CH_2Cl_2 was used to extract the organics (250 mL and 2 x 50 mL). The organic washings were combined, dried over $MgSO_4$, and the solvent removed under reduced pressure, affording a pale yellow crude oil. The oil was purified by vacuum distillation to yield the title compound as a colourless, clear oil (7.0 mL, 41.8 mmol, 77 %). **^{1}H NMR** (400 MHz, $CDCl_3$, 25 °C): δ = 7.78 (dd, 1H, *J* = 8 Hz, H_{arom}), 7.44 (td, 1H, *J* = 8 Hz, H_{arom}), 7.19 (dd, 1H, *J* = 8 Hz, H_{arom}), 7.04 (td, 1H, *J* = 8 Hz, H_{arom}), 5.25 (s, 2H, -CH_2OCH_3), 3.89 (s, 3H, CH_3), 3.52 (s, 3H, -CH_2OCH_3) ppm. **^{13}C NMR** (101 MHz, $CDCl_3$, 25 °C): δ = 166.77, 156.78, 133.41, 131.51, 121.71, 121.58, 116.55, 95.26, 56.47, 52.16 ppm. **ESI-MS** (acetonitrile): *m/z* = 197.09 {$[M+H]^+$, calc. 197.08}. **IR** (ATR): υ = 2952 (w), 2907 (w), 2829 (w), 1727 (s), 1600 (m), 1583 (w), 1489 (m), 1455 (m), 1434 (m), 1405 (w), 1297 (s), 1251 (s), 1237 (s), 1199 (m), 1153 (s), 1130 (s), 1074 (s), 1046 (m), 982 (s), 922 (s), 830 (w), 757 (s), 708 (m), 659 (w), 553 (w), 499 (w) cm^{-1}.

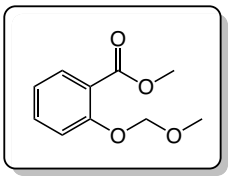

1-Methyl-4,5-diphenyl-*1H*-imidazole: NaH (6.0 g, 148 mmol, 60 weight% dispersion in mineral oil) was suspended in THF (150 mL) and cooled to 0 °C. Next, 4,5-diphenylimidazole (27.1g, 123 mmol,) was added in portions, keeping the temperature below 15 °C. After completing the addition of the imidazole, the reaction was allowed to stir overnight at room temperature, before the dropwise addition of iodomethane (9.2 mL, 148 mmol) at room temperature. During this time, the colour of the mixture changed from milky white to grey-orange. The reaction was allowed to stir overnight and finally quenched with a saturated aqueous NH_4Cl solution (30 mL). The organics were extracted into CH_2Cl_2 (3 x 200 mL) and the washings combined, dried over $MgSO_4$, and filtered. The organic solvent was removed under reduced pressure to afford a pale yellow powder, which was subsequently washed with cold toluene to yield the title compound as a microcrystalline white powder in 81% yield (23.2 g, 99 mmol). **^{1}H NMR** (400 MHz, $CDCl_3$, 25 °C): δ = 7.57 (s, 1H, C_{imid}–H), 7.47 (m, 5H, H_{arom}), 7.34 (m, 2H, H_{arom}), 7.20 (m, 2H, H_{arom}), 7.14 (m, 1H, H_{arom}), 3.49 (s, 3H,

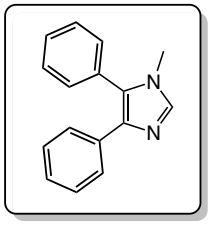

NC*H*$_3$) ppm. **^{13}C NMR** (101 MHz, $CDCl_3$, 25 °C): δ = 138.40, 137.56, 134.78, 130.81, 130.76, 129.12, 129.04, 128.72, 128.24, 126.74, 126.43, 32.32 ppm. **ESI-MS** (acetonitrile): *m/z* = 235.1226 {$[M+H]^+$, calc. 235.1235}. **IR** (ATR): υ = 3114 (w), 3044 (w), 2985 (w), 2954 (w), 1954 (w), 1887 (w), 1832 (w), 1763 (w), 1696 (w), 1638 (w), 1600 (m), 1578 (w), 1507 (m), 1479 (m), 1423 (w), 1388 (w), 1367 (m), 1317 (w), 1249 (m), 1194 (m), 1181 (w), 1159 (w), 1121 (w), 1068 (m), 1021 (m), 1000 (w), 985 (w), 952 (m), 917 (m), 851 (w), 771 (s), 734 (s), 719 (m), 699 (s), 647 (s), 617 (m), 565 (m), 507 (w) cm^{-1}.

(2-(Methoxymethoxy)phenyl)bis(1-methyl-1*H*-benzimidazol-2-yl)methanol (LS2): 1-Methyl-1*H*-benzimidazole (2.96 g, 22.4 mmol) was suspended in Et_2O (30 mL) and cooled to −78 °C. *n*-BuLi (14.5 mL, 23.2 mmol, 1.6 M in hexanes) was added dropwise, causing the solution to turn dark orange. The mixture was allowed to stir at low temperature for 3 h before the dropwise addition of **LS1** (2.16 g, 11.0 mmol). The mixture was stirred overnight and quenched by addition of a saturated aqueous NH_4Cl solution (30 mL). The organics were extracted into CH_2Cl_2 (3 x 100 mL), washed with distilled water, and dried over $MgSO_4$. The solvent was removed under vacuum to afford a yellow solid. The solid was washed with cold ethanol and collected by Büchner filtration. The title compound was isolated as an off-white powder (3.46 g, 8.1 mmol, 71 %). **^{1}H NMR** (400 MHz, $CDCl_3$, 25 °C): δ = 7.71 (d, 2H, *J* = 8 Hz, *H*$_{arom}$), 7.38 (m, 3H, *H*$_{arom}$), 7.31 (m, 3H, *H*$_{arom}$), 7.22 (m, 2H, *H*$_{arom}$), 6.92 (t, 1H, *J* = 8 Hz, *H*$_{arom}$), 6.59 (d, 1H, *J* = 8 Hz, *H*$_{arom}$), 6.28 (s, 1H, -O*H*), 4.93 (s, 2H, MOM-C*H*$_2$), 3.73 (s, 6H, NC*H*$_3$), 3.05 (s, 3H, MOM-C*H*$_3$) ppm. **^{13}C NMR** (101 MHz, $CDCl_3$, 25 °C): δ = 155.67, 154.27, 141.11, 137.78, 130.63, 129.74, 128.69, 122.96, 122.02, 120.37, 115.93, 109.59, 94.87, 56.15, 32.18 ppm. **ESI-MS** (acetonitrile): *m/z* = 429.1867 {$[M+H]^+$, calc. 429.1927}, 451.1668 {$[M+Na]^+$, calc. 451.1746}, 857.3643 {$[2M+H]^+$, calc. 857.3775}. **IR** (ATR): υ = 3433 (m), 3047 (w), 3004 (w), 2949 (w), 2927 (w), 2834 (w), 2815 (w), 1661 (w), 1613 (w), 1599 (w), 1587 (w), 1488 (m), 1467 (m), 1435 (m), 1383 (m), 1316 (m), 1282 (m), 1193 (m), 1157 (m), 1122 (w), 1112 (m), 1083 (m), 1048 (m), 992 (s), 940 (m), 928 (m), 891 (w), 840 (w), 811 (w), 754 (m), 738 (s), 650 (w), 608 (w), 592 (w), 581 (w), 557 (w), 536 (w), 522 (w), 450 (w) cm^{-1}.

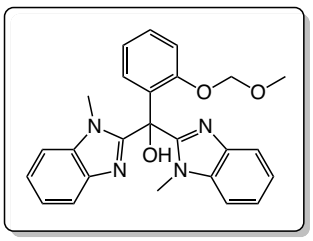

(2-(Methoxymethoxy)phenyl)bis(1-methyl-4,5-diphenyl-1*H*-imidazol-2-yl)methanol (LS3): 1-Methyl-4,5-diphenylimidazole (12.0 g, 51.2 mmol) was dissolved in THF (350 mL) and cooled to −78 °C. *n*-BuLi (38.4 mL, 61.5 mmol, 1.6 M in hexanes) was added dropwise, causing the solution to turn dark orange. The mixture was allowed to stir at low temperature for 3 h before the dropwise addition of **LS1** (5.02 g, 25.6 mmol). The mixture was stirred overnight and quenched by addition of a saturated aqueous NH_4Cl (100 mL) solution. The organics were extracted into EtOAc, washed with distilled water, and dried over $MgSO_4$. The solvent was removed under vacuum to afford a yellow gel-like crude material. The crude material stirred vigorously in petroleum ether, resulting in a fine suspension. The solid material was collected by Büchner filtration and air-dried before being washed with several portions of cold methanol. The title compound was isolated as an off-white fine powder (10.3 g, 16.3 mmol, 64 %). **^{1}H NMR** (400 MHz, $CDCl_3$, 25 °C): δ = 7.44 (m, 10H, *H*$_{arom}$), 7.36 (m, 4H, *H*$_{arom}$), 7.32 (m, 1H, *H*$_{arom}$), 7.16 (m, 5H, *H*$_{arom}$), 7.09 (m, 2H, *H*$_{arom}$), 6.98 (t, 1H, *J* = 8 Hz, *H*$_{arom}$), 6.80 (d, 1H, *J* = 8 Hz, *H*$_{arom}$), 6.48 (s (br), -O*H*), 5.01 (s, 2H, MOM-C*H*$_2$), 3.38 (s, 6H, NC*H*$_3$), 3.24 (s, 3H, MOM-C*H*$_3$) ppm. **^{13}C NMR** (101 MHz, $CDCl_3$, 25 °C): δ = 155.91, 135.23, 135.07, 131.45, 131.27, 130.99, 130.84, 130.31, 129.11, 129.00, 128.69, 128.10, 126.66, 126.08, 121.82, 115.88, 94.70, 75.71, 56.05, 33.31 ppm. **ESI-MS** (acetonitrile): *m/z* = 633.3074 {$[M+H]^+$, calc. 633.2866}. **IR** (ATR): υ = 3417 (w), 3061 (w), 2994 (w),

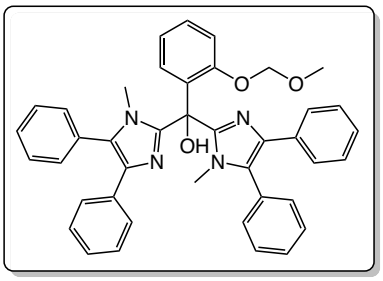

2952 (w), 2927 (w), 2823 (w), 1602 (m), 1582 (w), 1505 (m), 1481 (m), 1441 (m), 1395 (w), 1381 (w), 1354 (m), 1322 (m), 1285 (m), 1236 (m), 1199 (m), 1152 (m), 1113 (m), 1078 (s), 1059 (m(, 1038 (m), 1027 (m), 990 (s), 970 (s), 926 (s), 911 (s), 858 (w), 780 (s) 771 (s), 755 (s), 723 (s), 698 (s), 643 (s), 566 (w), 499 (w), 463 (w), 446 (w) cm^{-1}.

2,2'-(Methoxy(-2-(methoxymethoxy)phenyl)methylene)bis(1-methyl-1*H*-benzimidazole) (LS4):

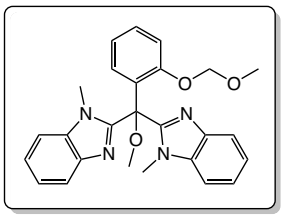

Compound **LS2** (2.05 g, 4.8 mmol) was added in portions to a stirring suspension of NaH (0.37 g, 9.3 mmol, 60 weight% dispersion in mineral oil) in THF (150 mL). The mixture was allowed to stir 6 h, during which time a slow release of gas was observed. Iodomethane (0.55 mL, 8.8 mmol) was then added dropwise, and the reaction allowed to stir overnight. The reaction was quenched with a saturated NH_4Cl aqueous solution (30 mL), and the organics extracted with EtOAc (3 x 100 mL). The organic washings were combined, dried over $MgSO_4$, and concentrated to yield a yellow gel-like crude material. Vigorous stirring of the crude material in petroleum ether afforded a pale yellow powder, which was collected by Büchner filtration and air-dried to afford the title compound as an off-white solid (2.10 g, 4.7 mmol, 98%). **^{1}H NMR** (400 MHz, $CDCl_3$, 25 ºC): δ = 7.79 (d, 2H, *J* = 8 Hz, H_{arom}), 7.60 (d, 1H, *J* = 8 Hz, H_{arom}), 7.39 (t, 1H, *J* = 8 Hz, H_{arom}), 7.37 (m, 8H, H_{arom}), 7.08 (t, 1H, *J* = 8Hz, H_{arom}), 4.79 (s, 2H, MOM-CH_2), 3.73 (s, 6H, NCH_3), 3.45 (s, 3H, -OCH_3), 3.04 (s, 3H, MOM-CH_3) ppm. **^{13}C NMR** (101 MHz, $CDCl_3$, 25 ºC): δ = 156.49, 151.97, 141.70, 137.01, 130.93, 130.20, 125.87, 122.94, 121.97, 121.44, 120.32, 115.86, 109.47, 94.95, 81.85, 55.97, 54.13, 32.03 ppm. **ESI-MS** (acetonitrile): *m/z* = 443.2006 {$[M+H]^+$, calc. 443.2083}, 907.3646 {$[2M+H]^+$, calc. 907.3907}. **IR** (ATR): υ = 3054 (w), 2.935 (m), 2828 (w), 1704 (w), 1614 (w), 1598 (w), 1584 (w), 1487 (m), 1465 (s), 1436 (m), 1375 (w), 1329 (m), 1239 (m), 1199 (w), 1152 (m), 1063 (s), 963 (m), 927 (m), 894 (w), 793 (w), 742 (s), 645 (w), 590 (w), 549 (w), 441 (w) cm^{-1}.

2,2'-(Methoxy(-2-(methoxymethoxy)phenyl)methylene)bis(1-methyl-4,5-diphenyl-1*H*-imidazole) (LS5): Compound **LS3** (10.3 g, 16.3 mmol) was added in portions to a stirring suspension of NaH (1.31

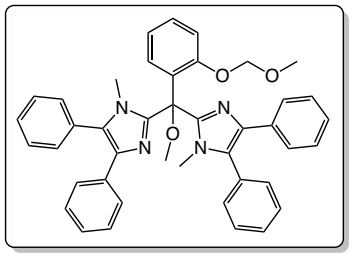

g, 32.6 mmol, 60 weight% dispersion in mineral oil) in THF (300 mL). The mixture was allowed to stir overnight, during which time a slow release of gas was observed. Iodomethane (2.0 mL, 32.6 mmol) was then added dropwise, and the reaction allowed to stir overnight. The reaction was quenched with a saturated NH_4Cl aqueous solution (100 mL), and the organics extracted with EtOAc (3 x 200 mL). The organic washings were combined and dried over $MgSO_4$, and concentrated to yield a yellow gel-like crude material. Vigorous stirring of the crude material in petroleum ether afforded a pale yellow powder, which was collected by Büchner filtrations and air-dried to afford the title compound as a pale yellow solid (9.1 g, 13.9 mmol, 85%). **^{1}H NMR** (400 MHz, $CDCl_3$, 25 ºC): δ = 7.52 (d, 1H, *J* = 4 Hz, H_{arom}), 7.44 (m, 9H, H_{arom}), 7.34 (m, 5H, H_{arom}), 7.26 (m, 2H, H_{arom}), 7.14 (t, 4H, *J* = 4 Hz, H_{arom}), 7.06 (m, 3H, H_{arom}), 4.98 (s, 2H, MOM-CH_2), 3.63 (s, 3H, -OCH_3), 3.33 (s, 6H, -NCH_3), 3.24 (s, 3H, MOM-CH_3) ppm. **^{13}C NMR** (101 MHz, $CDCl_3$, 25 ºC): δ = 156.77, 146.16, 135.56, 135.28, 131.57, 131.22, 130.68, 130.36, 130.26, 129.05, 128.60, 128.09, 127.72, 126.71, 126.00, 121.43, 115.98, 95.51, 81.37, 56.00, 54.41, 32.92 ppm. **ESI-MS** (acetonitrile): *m/z* = 647.3034 {$[M+H]^+$, calc. 647.3022}. **IR** (ATR): υ = 3059 (w), 2995 (w), 2952 (w), 2926 (w), 2824 (w), 1601 (w), 1581 (w), 1504 (m), 1487 (m), 1441 (m), 1406 (w), 1381 (w), 1322 (w), 1306 (w), 1286 (w), 1244 (m), 1203 (w), 1176 (w), 1151 (m), 1126 (w), 1115 (w), 1078 (s), 1068 (s), 1052 (s), 1025 (m), 990 (s), 979 (s), 968 (s), 929 (m), 922 (m), 913 (s), 854 (w), 843 (w), 781 (s), 770 (s), 754 (s), 724 (s), 708 (s), 696 (s), 649 (m), 634 (m), 563 (w), 545 (w), 522 (w), 502 (w), 486 (w), 461 (w), 418 (w), 411 (w) cm^{-1}.

H-BenzImNNO: Compound **LS4** (2.03 g, 4.6 mmol) was dissolved in 250 mL of acidified MeOH solution (1:4 HCl (30 %)/MeOH) and allowed to stir 3 h under reflux. The resulting mixture was rendered alkaline (pH 9) with 1M NaOH solution. The organics were extracted into CH_2Cl_2 (150 mL) and washed with distilled water (2 x 80 mL). Finally, the solvent was removed under reduced pressure, affording a pale yellow solid. The solid was then stirred vigorously in petroleum ether, forming a fine suspension. The ligand was collected by Büchner filtration and isolated as an off-white powder (1.52 g, 3.8 mmol, 83%). **^{1}H NMR** (400 MHz, $CDCl_3$, 25 °C): δ = 10.36 (s (br.), 1H, -O*H*), 7.83 (d, 2H, *J* = 8Hz, H_{arom}), 7.33 (m, 7H, H_{arom}), 7.23 (m, 1H, H_{arom}), 6.99 (d, 1H, *J* = 8 Hz, H_{arom}), 6.85 (t, 1H, *J* = 8 Hz, H_{arom}), 3.66 (s, 6H, NCH_3), 3.41 (s, 3H, OCH_3) ppm. **^{13}C NMR** (101 MHz, $CDCl_3$, 25 °C): δ = 156.42, 151.02, 140.94, 136.96, 130.94, 127.95, 123.75, 122.90, 122.72, 120.54, 120.19, 119.60, 109.76, 83.23, 54.09, 31.88 ppm. **ESI-MS** (acetonitrile): *m/z* = 399.1837 {[M+H]$^+$, calc. 399.1821}, 421.1640 {[M+Na]$^+$, calc. 421.1640}, 797.3488 {[2M+H]$^+$, calc. 797.3564}. **IR** (ATR): υ = 3393 (w), 3051 (w), 2937 (w), 1608 (w), 1579 (w), 1482 (m), 1464 (s), 1384 (w), 1331 (w), 1285 (w), 1242 (m), 1193 (w), 1152 (m), 1104 (w), 1067 (s), 1043 (m), 1008 (w), 988 (w), 961 (m), 944 (m), 934 (m), 894 (m), 843 (w), 827 (s), 763 (s), 743 (s), 709 (w), 642 (w), 576 (w), 561 (w), 475 (w), 456 (w) cm^{-1}.

H-Im^{Ph2}NNO: Compound **LS5** (9.0 g, 13.9 mmol) was dissolved in 250 mL of acidified MeOH solution (1:4 HCl (30 %)/MeOH) and allowed to stir 2 h under reflux. The resulting mixture was rendered alkaline (pH 9) with 1M NaOH solution, resulting in the precipitation of an off-white solid. The organics were extracted into EtOAc and washed with twice with distilled water. Finally, the solvent removed under reduced pressure, affording a clear gel-like material. The crude material was then vigorously stirred in pet. ether, which formed a fine suspension. The ligand was collected by Büchner filtration and isolated as a pale pink powder (7.02 g, 11.7 mmol, 84%). **^{1}H NMR** (400 MHz, $CDCl_3$, 25 °C): δ = 10.34 (s (br.), 1H, -O*H*), 7.46 (*m*, 10H, H_{arom}), 7.36 (*m*, 4H, H_{arom}), 7.29 (m, 1H, H_{arom}), 7.24 (m, 1H, H_{arom}), 7.19 (*m*, 4H, H_{arom}), 7.12 (*m*, 2H, H_{arom}), 7.03 (*d*, 1H, H_{arom}), 6.86 (*t*, 1H, H_{arom}), 3.52 (*s*, 3H, -OCH_3), 3.32 (*s*, 6H, -NCH_3) ppm. **^{13}C NMR** (101 MHz, $CDCl_3$, 25 °C): δ = 156.69, 144.84, 135.67, 134.44, 131.54, 131.28, 130.85, 130.45, 129.17, 128.23, 128.19, 128.01, 126.78, 126.45, 124.07, 119.78, 119.14, 54.00, 33.04 ppm. **ESI-MS** (acetonitrile): *m/z* = 603.2866 {[M+H]$^+$, calc. 603.2760}. **IR** (ATR): υ = 3389 (m), 3049 (w), 2954 (w), 1600 (m), 1583 (m), 1505 (m), 1486 (s), 14768 9m), 1443 (m), 1366 (m),1302 (m), 1244 (m), 1229 (m), 1206 (w), 1153 (m), 1128 (w), 1106 (w), 1073 (s), 1055 (m), 1043 (m), 1026 (m), 1000 (w), 979 (m), 970 (m), 932 (w), 915 (m), 828 (w), 774 (s), 756 (s), 726 (s), 696 (s), 645 (m), 535 (w), 503 (w), 482 (w), 450 (w) cm^{-1}.

2.5.5 Complex Synthesis

[Zn(BenzImNNO)$_2$ZnCl$_2$] (1): Ligand **H-BenzImNNO** (31.0 mg, 77.8 μmol) was dissolved in THF (7 mL) and deprotonated using an excess of KH. The reaction mixture was stirred for 1 h, during which time the solution turned bright yellow and gas formation was observed. The phenolate solution was subsequently filtered into a new vial and a THF suspension of $ZnCl_2$ (10.3 mg, 75.6 μmol) was added dropwise to the mixture. The reaction was stirred for a further 3 h, after which time the solution was filtered and the solvent removed under vacuum. The crude solid was extracted into MeCN solution (8 mL), then filtered and dried under vacuum. The title complex was obtained as an off-white powder in 52% yield (20.2 mg, 20.3 μmol). Single crystals were obtained from the slow vapour diffusion of Et_2O into a MeCN solution of the complex. **^{1}H NMR** (400 MHz, CD_2Cl_2, 25 °C): δ = 8.00 (d, 1H, J = 8 Hz, H_{phen}), 7.77 (d, 1H, J = 8 Hz, H_{im1}), 7.60 (dd, 1H, J = 8 Hz, H_{im1}), 7.37 (d, 1H, J = 8 Hz, H_{im2}), 7.34 (t, 1H, J = 8 Hz, H_{im1}), 7.16 (t, 1H, J = 8 Hz, H_{im2}), 7.02 (t, 1H, J = 8 Hz, H_{im1}), 6.98 (dt, 1H, J = 8 Hz, H_{phen}), 6.79 (dt, 1H, J = 8 Hz, H_{phen}), 6.60 (t, 1H, J = 8 Hz, H_{im2}), 6.01 (dd, 1H, J = 8 Hz, H_{phen}), 5.85 (d, 1H, J = 8 Hz, H_{im2}), 4.34 (s, 3H, -OCH_3), 3.79 (s, 3H, -NCH_3), 3.49 (s, 3H, -NCH_3) ppm. **IR** (ATR): υ = 3058 (w), 2928 (w), 2852 (w), 1654 (w), 1616 (w), 1590 (m), 1492 (m), 1471 (s), 1447 (s), 1386 (m), 1330 (w), 1301 (m), 1256 (m), 1200 (w), 1176 (w), 1153 (w), 1071 (m), 1044 (w), 1009 (w), 998 (w), 960 (m), 936 (w), 911 (m), 836 (m), 812 (w), 744 (s), 719 (w), 708 (w), 575 (w), 558 (w), 550 (w), 529 (w), 473 (w), 436 (w) cm^{-1}. **E.A.** for $C_{48}H_{42}Cl_2N_8O_4Zn_2$ (996.58 g mol^{-1}): calc. C 57.85, H 4.25, N 11.24; found C 57.84, H 4.20, N 11.30.

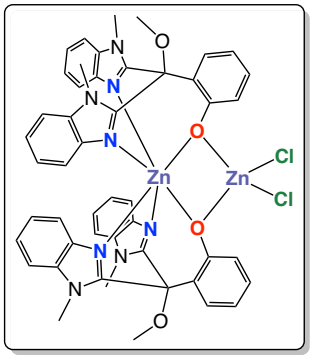

[Zn(BenzImNNO)$_2$Zn(OTf)$_2$] (2): Ligand **H-BenzImNNO** (31.2 mg, 78.3 μmol) was dissolved in THF (7 mL) and deprotonated using an excess of KH. The reaction mixture was stirred for 1 h, during which time the solution turned bright yellow and gas formation was observed. The phenolate solution was subsequently filtered into a new vial and a THF suspension of $Zn(OTf)_2$ (28.5 mg, 78.4 μmol) was added dropwise to the mixture. The solution turned ochre yellow. The reaction was stirred for a further 3 h, after which time the solution was filtered and the solvent removed under vacuum. The crude solid was extracted into CH_2Cl_2 solution, then filtered and dried under vacuum. The title complex was obtained as a yellow solid in 72% yield (34.6 mg, 28.3 μmol). **^{1}H NMR** (400 MHz, CD_3CN, –40 °C): δ = 7.97 (d, 1H, J = 8 Hz, H^A), 7.57 (d, 2H, J = 8 Hz, H^{I+J}), 7.39 (d, 1H, J = 8 Hz, H_{im2}), 7.15 (t, 1H, J = 8 Hz, H_{im1}), 7.12 (t, 1H, J = 8 Hz, H_{im2}), 6.86 (t, 1H, J = 8 Hz, H_{phen}), 6.79 (t, 1H, J = 8 Hz, H_{im1}), 6.60 (t, 1H, J = 8 Hz, H_{im2}), 6.43 (t, 1H, J = 8 Hz, H_{phen}), 6.03 (d, 1H, J = 8 Hz, H_{phen}), 5.63 (d, 1H, J = 8 Hz, H_{phen}) ppm. **^{19}F NMR** (376 MHz, CD_3CN, –40 °C): δ = –79.64 ppm. **IR** (ATR): υ = 3051 (w), 2951 (w), 2925 (w), 2853 (w), 1668 (w), 1615 (w), 1587 (m), 1496 (m), 1463 (s), 1450 (s), 1379 (m), 1327 (m), 1285 (m), 1263 (m), 1247 (m), 1225 (w), 1200 (w), 1171 (m), 1146 (m), 1112 (m), 1067 (s), 1031 (s), 1008 (m), 999 (m), 957 (m), 934 (m), 906 (m), 839 (w), 812 (w), 739 (s), 707 (m), 661 (w), 638 (s), 570 (w), 559 (w), 541 (w), 531 (w), 517 (w), 478 (w), 409 (w) cm^{-1}. **E.A.** no satisfactory elemental analysis could be obtained, possibly due to the presence of triflate anions with high fluorine content.

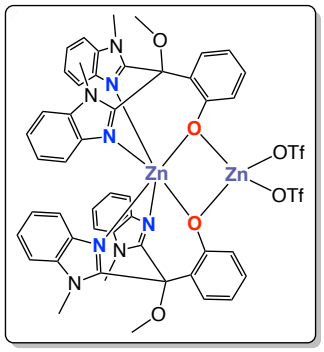

[$Fe_2(Im^{Ph2}NNO)_2(OTf)_2$] (4): Ligand **H-$Im^{Ph2}$NNO** (102.4 mg, 170 µmol) was dissolved in THF (15 mL) and deprotonated with an excess of KH. The reaction mixture was stirred for 1 h, during which time the solution turned bright yellow. The solution was subsequently filtered into a new vial and a THF solution of $Fe(OTf)_2 \cdot 2MeCN$ (74.1 mg, 169 µmol) was added dropwise to the mixture, causing a rapid colour change to copper-orange. The solution was stirred for 2 h and then filtered. The solution was concentrated under vacuum until approximately 5 mL of solution remained, at which point *n*-hexane was added dropwise to the mixture until the solution became just cloudy. The mixture was left to stand for 3 h for the complex to crystallise out of solution, after which the THF/hexane supernatant was removed. The solid was washed with hexane and then dried under vacuum, affording the crude complex as a pale brown crystalline powder. Next, the crystalline solid was redissolved in CH_2Cl_2, filtered and dried under vacuum affording the title complex as a white powder in 70% yield (95.6 mg, 59.2 µmol). Single crystals suitable for X-ray diffraction were obtained by slow diffusion of *n*-hexane into a THF solution of the complex. **^{1}H NMR** (400 MHz, CD_3CN, 25 °C): δ = 85.12, 70.32, 47.51, 46.15, 44.58, 32.62, 28.52, 18.98, 7.93. 7.67, 6.15, 5.49, 5.08, 3.63, 2.86, 1.79, –3.53, –6.04, –8.53, –15.26, –17.88, –26.24, –32.06, –80.63 ppm. **^{19}F NMR** (376 MHz, CD_3CN, 25 °C): δ = –79.08 ppm. Solution state magnetic susceptibility (Evans method, 1%TMS in CD_3CN): μ_{eff} = 6.49 μ_B. **UV-vis** (THF): λ_{max} = 365 (ε = 315 $dm^3\ mol^{-1}\ cm^{-1}$), 520 (ε = 16 $dm^3\ mol^{-1}\ cm^{-1}$) nm. **^{57}Fe Mössbauer** (80 K): δ = 1.02 mm s^{-1}, $|\Delta E_Q|$ = 3.26 mm s^{-1}. **IR** (ATR): υ = 3057 (w), 2960 (w), 2924 (w), 2853 (w), 1657 (w), 1588 (w), 1566 (w), 1477 (m), 1443 (w), 1321 (m), 1310 (m), 1260 (m), 1234 (m), 1211 (s), 1178 (m), 1164 (m), 1063 (m), 1042 (m), 1021 (s), 1002 (m), 924 (w), 914 (m), 849 (m), 790 (m), 768 (w), 759 (m), 742 (m), 699 (s), 661 (w), 633 (s), 608 (m), 585 (w), 511 (m), 425 (w) cm^{-1}. **E.A.** for $C_{82}H_{66}F_6Fe_2N_8O_{10}S_2$ (1613.28 g mol^{-1}): calc. C 61.05, H 4.12, N 6.95; found C 60.91, H 4.19, N 6.88.

[$Zn_2(Im^{Ph2}NNO)_2(OTf)_2$] (5): Ligand **H-$Im^{Ph2}$NNO** (78.9 mg, 131 µmol) was dissolved in approximately 10 mL of THF and deprotonated with an excess of KH. The reaction mixture was stirred for 1 h, during which time the solution turned bright yellow. The solution was subsequently filtered into a new vial and a THF solution of $Zn(OTf)_2$ (47.6 mg, 131 µmol) was added dropwise to the mixture, causing the solution to turned pale yellow in colour. The solution was stirred for 2 h and was then filtered. The solution was concentrated under vacuum until approximately 5 mL of solution remained, at which point 8 mL *n*-hexane was added dropwise to the mixture in order to precipitate the complex. The mixture was left to stand for a period of 3 h, after which the THF/hexane supernatant was removed. The residual solid was then washed twice with hexane and dried under vacuum, affording a white powder. The solid was extracted into CH_2Cl_2 and the solution filtered. The solvent was removed under vacuum, affording the title complex as a white powder (63.1 mg, 38.6 µmol, 59%). **^{1}H NMR** (400 MHz, THF-d_8, 25 °C): δ = 8.08 (d, 1H, J = 8 Hz, H^A), 7.27 (t, 2H, H^G), 7.16 (t, 4H, J = 8 Hz, H^F), 7.03 (d, 4H, J = 8 Hz, H^H), 6.90 (d, 4H, J = 8 Hz, H^H), 6.80 (t, 1H, J = 8 Hz, H^C), 6.72 (t, 2H, J = 8 Hz, H^J), 6.66 (t, 1H, J = 8 Hz, H^B), 6.45 (t, 4H, J = 8 Hz, H^I), 6.25 (d, 1H, J = 8 Hz, H^D), 3.68 (s, 6H, NCH_3), 3.49 (s, 3H, OCH_3) ppm. **^{13}C NMR** (101 MHz, THF-d_8, 25 °C): δ = 163.29, 146.21, 136.38, 133.10, 132.40, 130.90, 130.05, 129.73, 129.28, 128.73, 127.86, 124.19, 123.53, 123.41, 113.91, 80.47, 34.64 ppm. **^{19}F NMR** (376 MHz, CD_3CN): δ = –79.38 ppm. **IR** (ATR): υ = 3057 (w),

2959 (w), 2924 (w), 2853 (w), 1728 (w), 1654 (w), 1589 (w), 1506 (w), 14478 (w), 1445 (w), 1396 (w), 1314 (w), 1258 (s), 1229 (s), 1161 (s), 1096 (w), 1038 (s), 1008 (m), 994 (m), 916 (w), 890 (w), 849 (w), 793 (m), 760 (m), 744 (w), 723 (w), 700 (m), 640 (s), 602 (w), 577 (w), 538 (w), 518 (w), 421 (w) cm^{-1}. **E.A.** for $C_{82}H_{66}F_6N_8O_{10}S_2Zn_2$ (1632.35 g mol^{-1}): calc. C 60.34, H 4.08, N 6.86; found C 60.91, H 4.19, N 6.84.

[Fe_2(Im^{Ph2}NNO)$_2$($SPh)_2$] (6): Complex **4** (70.7 mg, 43.8 µmol) was dissolved in THF (5 mL) and stirred while 2 equiv. of NaSPh (11.9 mg, 89 µmol), suspended in (3-5 mL) THF, were added dropwise to the mixture. The colour of the solution changed from pale yellow to dark orange and became gradually more cloudy until an opaque white suspension formed over the course of 2 h. The solvent was subsequently removed under vacuum, affording a pinkish powder. The crude solid was redissolved in CH_2Cl_2 and filtered, after which the solution was dried under vacuum. The title complex was obtained as an off-white powder (52.4 mg, 3.42 µmol, 78%). **^{1}H NMR** (400 MHz, CD_2Cl_2, 25 °C): δ = 44.58, 39.83, 30.44, 20.32, 25.38, 16.06, 7.44, 7.32, 5.72, 5.93, 3.16, 2.31, –18.47, –20.54, –22.28, –42.60 ppm. Solution state magnetic susceptibility (Evans method, 1%TMS in CD_2Cl_2): μ_{eff} = 7.30 μ_B. **^{57}Fe Mössbauer** (80 K): δ = 0.96 mm s^{-1}, $|\Delta E_Q|$ = 3.07 mm s^{-1}. **IR** (ATR): υ = 3056 (w), 2958 (w), 2925 (w), 1589 (w), 1562 (w), 1505 (w), 1484 (m), 1444 (m), 1474 (m), 1382 (w), 1237 (w), 1312 (m), 1258 (s), 1230 (s), 1165 (s), 1091 (w), 1041 (s), 988 (w), 918 (w), 848 (w), 817 (m), 790 (m), 766 (w), 745 (w), 701 (s), 648 (s), 625 (m), 579 (w), 156 (m), 462 (w), 432 (w) cm^{-1}. **E.A.** for $C_{92}H_{76}Fe_2N_8O_4S_2$ (1533.48 g mol^{-1}): calc. C 72.06, H 5.00, N 7.31; no satisfactory elemental analysis could be obtained, likely due to the presence of inorganic salts in the sample.

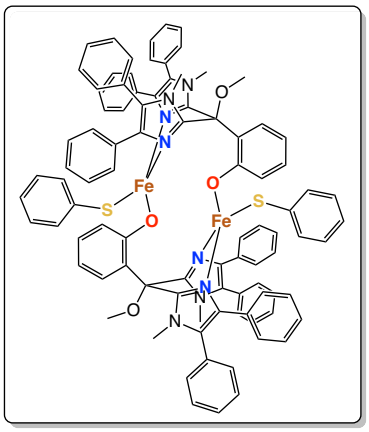

[Zn_2(Im^{Ph2}NNO)$_2$($SPh)_2$] (7): Complex **5** (52.3 mg, 32.0 µmol) was dissolved in THF and stirred while 2.2 equivalents of NaSPh (9.3 mg, 70.5 µmol) suspended in THF was added dropwise to the mixture. The colour of the solution changed stayed pale yellow in colour but became gradually more cloudy until an opaque white suspension formed over the course of 2 h. The solvent was subsequently removed under vacuum, affording a white powder. The crude solid was redissolved in CH_2Cl_2 and filtered, after which the solution was dried under vacuum. The title complex was obtained as a white powder (35.3 mg, 22.7 µmol, 71%). **^{1}H NMR** (400 MHz, THF-d_8, 25 °C): δ = 8.00 (dd, 1H, J = 8 Hz, H^A), 7.26 (t, 2H, J = 8 Hz H^J), 7.17 (d, 4H, J = 8 Hz, H^E), 7.11 (t, 4H, J = 8 Hz, H^I), 6.72 (m, 1H, H^C), 6.67 (m, 6H, $H^{G,H}$), 6.60 (s, 5H, $H^{K,L,M}$), 6.52 (t, 1H, J = 8 Hz, H^B), 6.47 (d, 1H, J = 8 Hz, H^D), 6.43 (t, 4H, J = 8 Hz, H^F), 3.51 (s, 6H, NCH_3), 2.57 (s, 3H, OCH_3) ppm. **^{13}C NMR** (101 MHz, THF-d_8, 25 °C): δ = 165.32, 146.13, 137.29, 135.51, 134.29, 133.25, 132.52, 132.34, 130.37, 129.33, 129.16, 128.66, 128.45, 125.19, 124.36, 123.50, 122.22, 120.31, 111.68, 80.18, 52.04, 34.66 ppm. **IR** (ATR): υ = 3057 (w), 2962 (w), 2923 (w), 1657 (w), 1577 (w), 1474 (w), 1444 (w), 1383 (w), 1256 (s), 1230 (m), 1164 (s), 1087 (w), 1043 (s), 990 (w), 918 (w), 887 (w), 800 (m), 765 (w), 718 (w), 699 (w), 650 (s), 578 (w), 517 (w), 432 (w) cm^{-1}. **E.A.** for $C_{92}H_{76}N_8O_4S_2Zn_2$ (1552.55 g mol^{-1}): calc. C 71.17, H 4.93, N 7.22; no satisfactory elemental analysis could be obtained, likely due to the presence of inorganic salts in the sample.

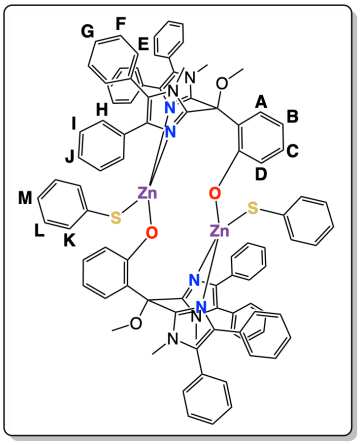

***In-situ* synthesis of $[Fe_2(Im^{Ph2}NNO^*)_2(Cl)_2]$ (8): K-Im^{Ph2}NNO** (54.4 mg, 84.9 µmol) was stirred in 8 mL MeCN and $FeCl_3$ (13.7 mg, 84.4 µmol) was added dropwise to the mixture, causing an instant change from yellow to deep blue. The reaction was stirred for 1.5 h and was subsequently filtered. A sparkly blue-purple precipitate was recovered on the filter, which was further washed with additional THF until the filtrate washed through colourless. The blue-purple filtrate solution was concentrated under vacuum, affording 54.1 mg of a blue-black solid (37.1 µmol, 88% yield, assuming no ligand degradation). Unfortunately, all attempts at elemental analysis were unsuccessful, presumably due to the partial degradation of the ligand over time. Slow diffusion of *n*-hexane into a blue THF solution of the product solid resulted in the growth of red crystals suitable for X-ray diffraction over the course of several says. The complex solution also turned reddish brown in this time. The crystals were characterised as complex $[Fe_2(Im^{Ph2}NNO^*)(Cl)_2]$ (**8**), where Im^{Ph2}NNO* is the ligand that has undergone methyl cleavage at the methoxy group. Conducting the same synthesis using THF as a solvent resulted in the formation of a brown solution after stirring for 2 h. After filtering and concentrating under vacuum, a brown powder was obtained.

2.6 References and Notes

(1) Koehntop, K. D.; Emerson, J. P.; Que, L. *J. Biol. Inorg. Chem.* **2005**, *10*, 87–93.
(2) Que, L. J. *Nat. Struct. Biol.* **2000**, *7*, 182–184.
(3) Que, L.; Tolman, W. B. *Nature* **2008**, *455*, 333–340.
(4) Park, H.; Lee, D. *Chem. - A Eur. J.* **2020**, *26*, 1–12.
(5) Bruijnincx, P. C. A.; van Koten, G.; Klein Gebbink, R. J. M. *Chem. Soc. Rev.* **2008**, *37*, 2716–2744.
(6) Vicens, L.; Olivo, G.; Costas, M. *ACS Catal.* **2020**, *10*, 8611–8631.
(7) Costas, M.; Mehn, M. P.; Jensen, M. P.; Que Jr., L. *Chem. Rev.* **2004**, *104*, 939–986.
(8) Valegård, K.; van Scheltinga, A. C. T.; Lloyd, M. D.; Hara, T.; Ramaswamy, S.; Perrakis, A.; Thompson, A.; Lee, H.-J.; Baldwin, J. E.; Schofield, C. J.; Hajdu, J.; Andersson, I. *Nature* **1998**, *394*, 805–809.
(9) Beck, A.; Weibert, B.; Burzlaff, N. *Eur. J. Inorg. Chem.* **2001**, 521–527.
(10) Beck, A.; Barth, A.; Hübner, E.; Burzlaff, N. *Inorg. Chem.* **2003**, *42*, 7182–7188.
(11) Hegelmann, I.; Beck, A.; Eichhorn, C.; Weibert, B.; Burzlaff, N. *Eur. J. Inorg. Chem.* **2003**, *2003*, 339–347.
(12) Burzlaff, N. *Tripodal N,N,O-Ligands for Metalloenzyme Models and Organometallics*; van Eldik, R., Ed.; Elsevier, 2008; Vol. 60.
(13) Higgs, T. C.; Carrano, C. J. *Inorg. Chem.* **1997**, *36*, 298–306.
(14) Hammes, B. S.; Carrano, C. J. *Inorg. Chem.* **1999**, *38*, 3562–3568.
(15) Smith, J. N.; Shirin, Z.; Carrano, C. J. *J. Am. Chem. Soc.* **2003**, *125*, 868–869.
(16) Cappillino, P. J.; Miecznikowski, J. R.; Tyler, L. A.; Tarves, P. C.; McNally, J. S.; Lo, W.; Kasibhatla, B. S. T.; Krzyaniak, M. D.; McCracken, J.; Wang, F.; Armstrong, W. H.; Caradonna, J. P. *Dalt. Trans.* **2012**, *41*, 5662.
(17) McCracken, J.; Cappillino, P. J.; McNally, J. S.; Krzyaniak, M. D.; Howart, M.; Tarves, P. C.; Caradonna, J. P. *Inorg. Chem.* **2015**, *54*, 6486–6497.
(18) Oldenburg, P. D.; Shteinman, A. A.; Que, L. J. *J. Am. Chem. Soc.* **2005**, *127*, 15672–15673.
(19) Oldenburg, P. D.; Ke, C.-Y.; Tipton, A. A.; Shteinman, A. A.; Que, L. *Angew. Chemie Int. Ed.* **2006**, *45*, 7975–7978.
(20) Paria, S.; Halder, P.; Paine, T. K. *Inorg. Chem.* **2010**, *49*, 4518–4523.
(21) Dungan, V. J.; Wong, S. M.; Barry, S. M.; Rutledge, P. J. *Tetrahedron* **2012**, *68*, 3231–3236.
(22) Bruijnincx, P. C. A.; Lutz, M.; Spek, A. L.; van Faassen, E. E.; Weckhuysen, B. M.; van Koten, G.; Klein Gebbink, R. J. M. *Eur. J. Inorg. Chem.* **2005**, *2005*, 779–787.
(23) Bruijnincx, P. C. A.; Lutz, M.; den Breejen, J. P.; Spek, A. L.; van Koten, G.; Klein Gebbink, R. J. M. *JBIC J. Biol. Inorg. Chem.* **2007**, *12*, 1181–1196.
(24) Bruijnincx, P. C. A.; Buurmans, I. L. C.; Gosiewska, S.; Moelands, M. A. H.; Lutz, M.; Spek, A. L.; van Koten, G.; Klein Gebbink, R. J. M. *Chem. - A Eur. J.* **2008**, *14*, 1228–1237.

(25) Bruijnincx, P. C. A.; Lutz, M.; Spek, A. L.; Hagen, W. R.; Weckhuysen, B. M.; van Koten, G.; Klein Gebbink, R. J. M. *J. Am. Chem. Soc.* **2007**, *129*, 2275–2286.
(26) Moelands, M. A. H.; Nijsse, S.; Folkertsma, E.; de Bruin, B.; Lutz, M.; Spek, A. L.; Klein Gebbink, R. J. M. *Inorg. Chem.* **2013**, *52*, 7394–7410.
(27) Folkertsma, E.; de Waard, E. F.; Korpershoek, G.; van Schaik, A. J.; Solozabal Mirón, N.; Borrmann, M.; Nijsse, S.; Moelands, M. A. H.; Lutz, M.; Otte, M.; Moret, M.-E.; Klein Gebbink, R. J. M. *Eur. J. Inorg. Chem.* **2016**, *2016*, 1319–1332.
(28) Monkcom, E. C.; Ghosh, P.; Folkertsma, E.; Negenman, H. A.; Lutz, M.; Klein Gebbink, R. J. M. *Chim. Int. J. Chem.* **2020**, *74*, 450–466. (Chapter 6 of this thesis).
(29) Fernández-Baeza, J.; Antiñolo, A.; Tejeda, J.; Lara-Sánchez, A.; Otero, A. *Dalt. Trans.* **2004**, *0*, 1499–1510.
(30) Bruijnincx, P. C. A.; Lutz, M.; Spek, A. L.; Hagen, W. R.; van Koten, G.; Klein Gebbink, R. J. M. *Inorg. Chem.* **2007**, *46*, 8391–8402.
(31) Jameson, D. L.; Hilgen, S. E.; Hummel, C. E.; Pichla, S. L. *Tetrahedron Lett.* **1989**, *30*, 1609–1612.
(32) Lindsay, S.; Lo, S. K.; Maguire, O. R.; Bill, E.; Probert, M. R.; Sproules, S.; Hess, C. R. *Inorg. Chem.* **2013**, *52*, 898–909.
(33) Lindsay, S.; Mader, S. L.; Kaila, V. R. I.; Hess, C. R. *ChemistrySelect* **2018**, *3*, 1602–1608.
(34) Monkcom, E. C.; de Bruin, D.; de Vries, A. J.; Lutz, M.; Ye, S.; Klein Gebbink, R. J. M. *Chem. – A Eur. J.* **2021**, *27*, 5191–5204. (Chapter 3 of this thesis).
(35) Weber, B.; Kaps, E. *Heteroat. Chem.* **2005**, *16*, 391–397.
(36) Roach, P. L.; Clifton, I. J.; Hensgens, C. M. H.; Shibata, N.; Schofield, C. J.; Hajdu, J.; Baldwin, J. E. *Nature* **1997**, *387*, 827–830.
(37) Hammes, B. S.; Carrano, C. J. *Inorg. Chem.* **1999**, *38*, 4593–4600.
(38) Zang, Y.; Que, L. *Inorg. Chem.* **1995**, *34*, 1030–1035.
(39) Chiang, K. P.; Barrett, P. M.; Smith, J. M.; Kingsley, S.; Brennessel, W. W.; Clark, M. M.; Lachicotte, R. J.; Holland, P. L. *Inorg. Chem.* **2009**, *48*, 5106–5116.
(40) Bent, H. A. *J. Chem. Educ.* **1960**, *37*, 616.
(41) Foster, J. P.; Weinhold, F. *J. Am. Chem. Soc.* **1980**, *102*, 7211–7218.
(42) Alabugin, I. V.; Bresch, S.; Manoharan, M. *J. Phys. Chem. A* **2014**, *118*, 3663–3677.
(43) Hans, M.; Buckel, W.; Bill, E. *JBIC J. Biol. Inorg. Chem.* **2008**, *13*, 563–574.
(44) Lu, T.; Chen, F. *J. Comput. Chem.* **2012**, *33*, 580–592.
(45) Grieco, P. A.; Nishizawa, M.; Oguri, T.; Burke, S. D.; Marinovic, N. *J. Am. Chem. Soc.* **1977**, *99*, 5773–5780.
(46) Demuynck, M.; De Clercq, P.; Vandewalle, M. *J. Org. Chem.* **1979**, *44*, 4863–4866.
(47) Baars, S. M.; Hoberg, J. O. *Carbohydr. Res.* **2006**, *341*, 1680–1684.
(48) Ganem, B.; Small, V. R. *J. Org. Chem.* **1974**, *39*, 3728–3730.
(49) Sawama, Y.; Masuda, M.; Asai, S.; Goto, R.; Nagata, S.; Nishimura, S.; Monguchi, Y.; Sajiki, H. *Org. Lett.* **2015**, *17*, 434–437.
(50) Fulmer, G. R.; Miller, A. J. M.; Sherden, N. H.; Gottlieb, H. E.; Nudelman, A.; Stoltz, B. M.; Bercaw, J. E.; Goldberg, K. I. *Organometallics* **2010**, *29*, 2176–2179.
(51) Weast, R. C.; Astle, M. J. *CRC Handbook of Chemistry and Physics*; CRC Press Inc.: Boca Raton, Florida, 1979.
(52) O'Connor, C. J. *Prog. Inorg. Chem.* **1982**, *29*, 203–283.
(53) Bill, E. julX http://ewww.mpi-muelheim.mpg.de/bac/logins/bill/julX_en.php.
(54) Gaussian 16, Revision C.01; Frisch, M. J.; Trucks, G. W.; Schlegel, H. B.; Scuseria, G. E.; Robb, M. A.; Cheeseman, J. R.; Scalmani, G.; Barone, V.; Petersson, G. A.; Nakatsuji, H.; Li, X.; Caricato, M.; Marenich, A. V.; Bloino, J.; Janesko, B. G.; Gomperts, R.; Mennucci, B.; Hratchian, H. P.; Ortiz, J. V.; Izmaylov, A. F.; Sonnenberg, J. L.; Williams-Young, D.; Ding, F.; Lipparini, F.; Egidi, F.; Goings, J.; Peng, B.; Petrone, A.; Henderson, T.; Ranasinghe, D.; Zakrzewski, V. G.; Gao, J.; Rega, N.; Zheng, G.; Liang, W.; Hada, M.; Ehara, M.; Toyota, K.; Fukuda, R.; Hasegawa, J.; Ishida, M.; Nakajima, T.; Honda, Y.; Kitao, O.; Nakai, H.; Vreven, T.; Throssell, K.; Montgomery, J. A. J.; Peralta, J. E.; Ogliaro, F.; Bearpark, M. J.; Heyd, J. J.; Brothers, E. N.; Kudin, K. N.; Staroverov, V. N.; Keith, T. A.; Kobayashi, R.; Normand, J.; Raghavachari, K.; Rendell, A. P.; Burant, J. C.; Iyengar, S. S.; Tomasi, J.; Cossi, M.; Millam, J. M.; Klene, M.; Adamo, C.; Cammi, R.; Ochterski, J. W.; Martin, R. L.; Morokuma, K.; Farkas, O.; Foresman, J. B.; Fox, D. J. Gaussian 16, Revision C.01, 2016.
(55) Glendening, E. D.; Landis, C. R.; Weinhold, F. *J. Comput. Chem.* **2013**, *34*, 1429–1437.
(56) Humphrey, W.; Dalke, A.; Schulten, K. *J. Mol. Graph.* **1996**, *14*, 33–38.

Chapter 3

Structurally Modelling the 2-His-1-Carboxylate Facial Triad with a Bulky *N,N,O* Phenolate Ligand

Abstract

We present the synthesis and coordination chemistry of a bulky, tripodal *N,N,O* ligand, $\mathbf{Im^{Ph2}NNO^{tBu}}$ (**L**), designed to model the 2-His-1-Carboxylate facial triad (2H1C) by means of two imidazole groups and an anionic 2,4-di-*tert*-butyl-substituted phenolate. Reacting **K-L** with MCl_2 (M = Fe, Zn) affords the isostructural, tetrahedral complexes [Fe(L)(Cl)] (**1**) and [Zn(L)(Cl)] (**2**) in high yield. The tridentate *N,N,O* ligand coordination observed in their X-ray crystal structures remains intact and well-defined in MeCN and CH_2Cl_2 solution. Reacting **2** with NaSPh affords a tetrahedral zinc thiolate complex, [Zn(L)(SPh)] (**4**), that is relevant to isopenicillin N synthase (IPNS) biomimicry. Cyclic voltammetry studies demonstrate the ligand's redox non-innocence, where the phenolate oxidation is the first electrochemical response observed in **K-L**, **2** and **4**. However, the first oxidation in **1** is iron-centred, the assignment of which is supported by DFT calculations. Overall, $\mathbf{Im^{Ph2}NNO^{tBu}}$ provides access to well-defined mononuclear, monoligated, *N,N,O*-bound metal complexes, enabling more accurate structural modelling of the 2H1C to be achieved.

This chapter is based on:
E. C. Monkcom, D. de Bruin, A. J. de Vries, M. Lutz, S. Ye, R. J. M. Klein Gebbink,
Chemistry – A European Journal, **2021**, 27, 16, 5191–5204.

3.1 Introduction

The 2-His-1-Carboxylate facial triad (2H1C) is a bioinorganic motif characterised by the facial, tripodal *N,N,O* coordination of two neutral histidine (His) residues and an anionic carboxylate group, typically aspartate (Asp) or glutamate (Glu), to a single metal ion.[1–3] It occurs at the active site of many oxygen-activating mononuclear non-heme iron enzymes, and is considered one of the most versatile platforms with which nature catalyses oxidative transformations.[4,5] It has attracted particular interest from the bioinorganic and catalysis communities due to its ability to activate molecular oxygen and mediate an astoundingly diverse scope of oxidative transformations in a highly stereo- and regioselective manner. Many of these reactions are synthetically challenging, and developing small molecular iron-based catalysts that can achieve similar reactivity and selectivity remains a long-standing goal in homogeneous catalysis.

More recently, the 3-His facial triad (3His) has emerged as a recurring bioinorganic motif at the active site of, amongst others, a small group of mononuclear non-heme enzymes collectively known as thiol dioxygenases (TDO), which activate O_2 and catalyse the dioxygenation of thiols to their corresponding sulfinic acids.[6] Similarly to the 2H1C, the 3His involves the facial arrangement of three amino acid residues to a single iron centre. However, unlike the 2H1C, the 3His comprises three neutral histidine residues, and no carboxylate ligand is required for catalytic activity. In this regard, the different reactivities of isopenicillin N synthase (IPNS), a 2H1C-containing enzyme, and cysteine dioxygenase (CDO), a TDO enzyme, make for a particularly interesting comparison. In both cases, the native substrate's anionic thiolate binds directly to the iron centre *trans* to a His residue (Figure 1). Yet, in IPNS, O_2 subsequently binds *trans* to an Asp residue and the δ-(L-α-aminoadipoyl)-L-cysteine-D-valine (ACV) substrate undergoes a 4-electron oxidative

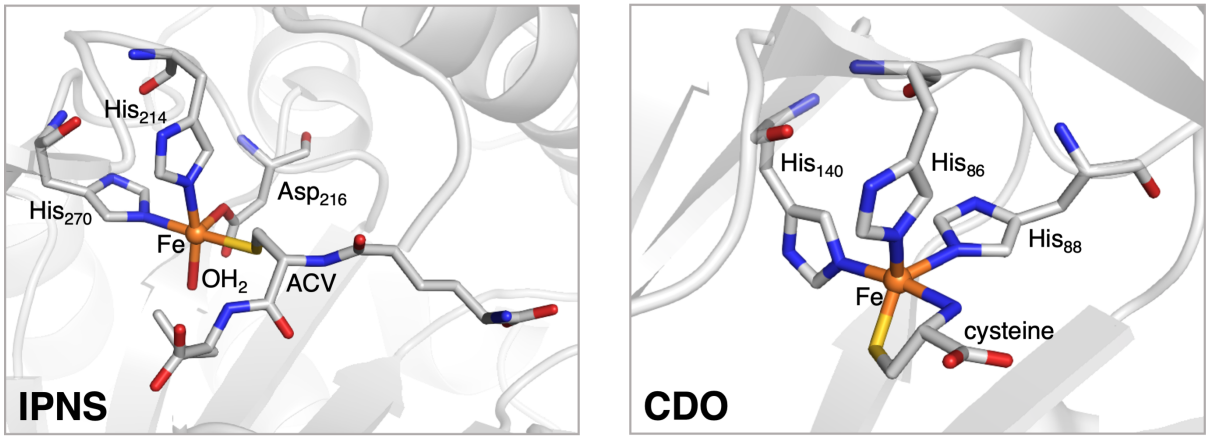

Figure 1. Protein crystal structures of the substrate-bound active sites of IPNS and CDO, which contain the 2H1C and 3His, respectively. Left: the [Fe·IPNS·ACV·OH_2] complex from *Aspergillus nidulans* (PDB 1BK0).[7] Right: the [Fe·CDO·Cys] complex from *Homo sapiens* (PDB 2IC1).[6] Carbon, iron, nitrogen, oxygen and sulfur are depicted in grey, orange, blue, red and yellow, respectively.

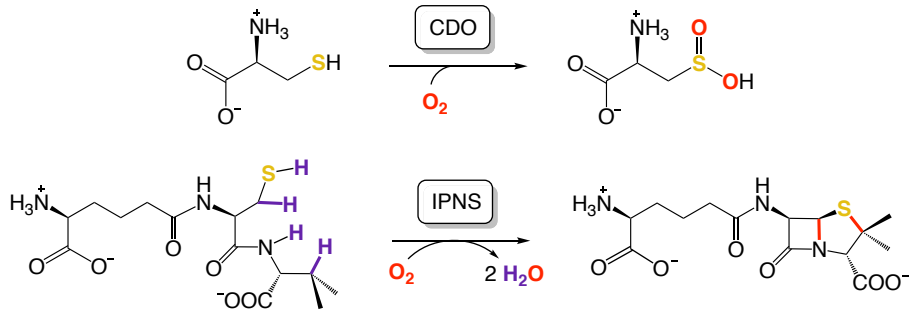

Figure 2. The native reactions catalysed by IPNS and CDO.

bicyclisation,[7–9] whereas in CDO, O_2 binds *trans* to a His residue and the cysteine substrate undergoes sulfur oxygenation (Figure 2).[6,10,11] This has stimulated a deeper examination of the carboxylate's mechanistic role in 2H1C-containing enzymes. An important strategy to this end is the study of synthetic complexes that model metalloenzyme active sites.

The 2H1C has been an inspiration for the design of many biomimetic ligands,[12] some of the most well-known being the **Tp**,[13] **TPA**,[14] **14-TMC**,[15] **PyTACN**,[16] **PyNMe$_3$**,[17] **BPBP**,[18] and **N4Py**[19] ligands (Figure 3, top). These polydentate N-donor ligands support the formation of high-valent iron-oxo species and have greatly helped the scientific community understand the role of such entities in enzymatic reactions and oxidation catalysis.[20,21] However, these ligands can, arguably, be considered closer in structure to the 3His than the 2H1C due to the lack of anionic O-donor. Moreover, many of these ligands have a denticity greater than three, which deviates from the tricoordinate nature of the 2H1C. In order to structurally model the 2H1C with greater structural accuracy, it remains of interest

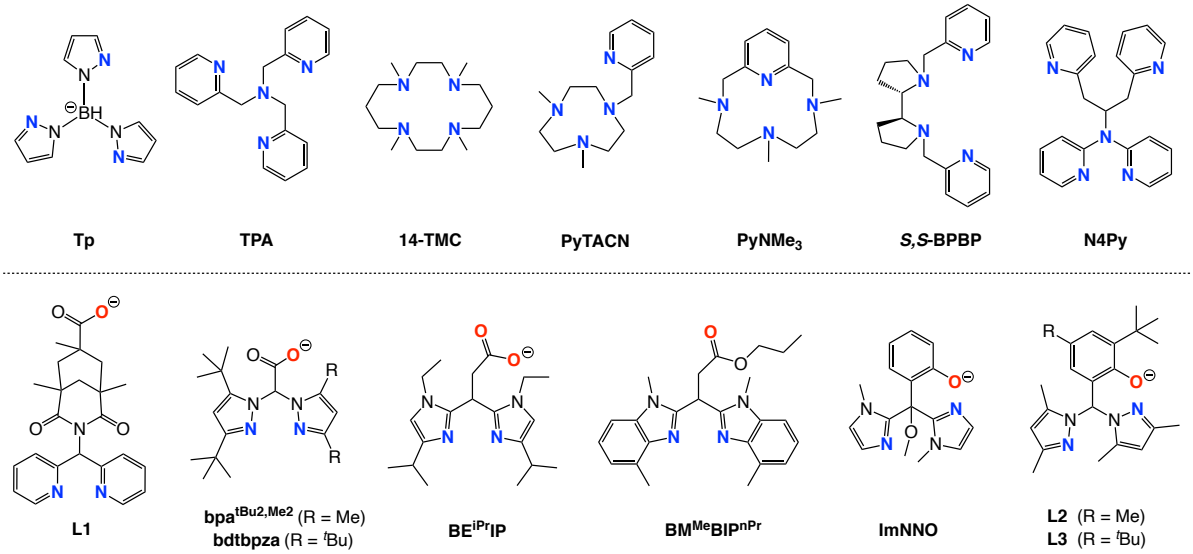

Figure 3. Selected N-donor ligands (top) and tripodal *N,N,O* ligands (bottom) that have been used to synthesise mononuclear, monoligated biomimetic metal complexes. Mononuclear, monoligated complexes of **BE^{iPr}IP** and **ImNNO** have only been reported in combination with an organic co-ligand, *e.g.* a catecholate. No iron complexes have been crystallographically characterised with ligands **bpa^{tBu2,Me2}**, **bdtbpza**, **L2** or **L3**.

to develop facial, tridentate *N,N,O* ligands. Numerous examples of such ligands can be found in the literature, where the nature of constituent donor groups has been systematically varied.[22] However, the number of *N,N,O* ligands that can coordinate in a tripodal manner and support the formation of mononuclear, monoligated metal complexes is small. Typically, difficulties in achieving the desired coordination mode are encountered due to the formation of bis-ligand homoleptic complexes,[23–25] the increase in nuclearity due to anionic O-donor bridging modes,[26–29] or rupture of the *N,N,O* motif due to lability of a neutral N- or O-donor.[30] The primary strategy to overcome these issues has been to increase the ligand's steric demand and bite angle,[25,30,31] or to use an organic co-ligand.[24,32] In the few cases where monoligation *and N,N,O* coordination were successfully achieved (Figure 3, bottom),[24,25,30–35] little or no further exploration of the solution state behaviour was conducted. The robustness of the ligands' facial *N,N,O* coordination to iron in solution therefore remains largely unknown, making their use disadvantageous from a practical point of view compared to the well-established coordination chemistry of polydentate N-donor ligands.

Previously, our group has explored the facial capping potential of bis-imidazole-derived *N,N,O* phenolate ligands, **ImNNO**, **BenzImNNO** and **Im^{Ph2}NNO**.[22,24,36] However, these were shown to readily form bisligated or dinuclear complexes. Here, we describe the synthesis of a new *N,N,O* ligand, **Im^{Ph2}NNO^{tBu}** (Figure 4), whose imidazole and phenolate groups have been functionalised with sterically demanding substituents to promote the thermodynamic formation of monoligated, mononuclear metal complexes.[37] While the ligand's imidazole groups are the most biologically relevant heterocycle for modelling histidine residues, the incorporation of a phenol deviates somewhat from the carboxylate residue of the 2H1C due to its redox-active properties. However, the ease with which phenols can be functionalised opens up more possibilities for ligand design and helps avoid certain drawbacks associated to carboxylic acids, such as decarboxylation, poor solubility, or the formation of coordination oligomers. The coordination chemistry of **Im^{Ph2}NNO^{tBu}** is explored with iron and zinc, the latter serving as a convenient diamagnetic analogue with which to conduct detailed studies of the complexes in their solution state. Finally, the synthesis and solution state behaviour of a zinc thiolate complex relevant to IPNS biomimicry is described. In this way, the robustness of the ligand's *N,N,O* facial triad in the presence of biorelevant co-ligands is established, making **Im^{Ph2}NNO^{tBu}** an ideal platform with which to model and further investigate the 2H1C.

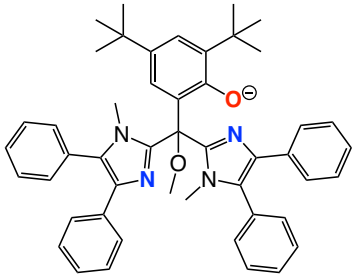

Figure 4. Ligand **Im^{Ph2}NNO^{tBu}**, with an *N,N,O* donor set.

3.2 Results and Discussion

3.2.1 Ligand Synthesis and Characterisation

Ligand **H-Im^{Ph2}NNO^{tBu}** can be readily synthesised in five steps, using a procedure adapted from Jameson *et al.* (Scheme 1).[24,38] An additional alkylation step has been incorporated to install *tert*-butyl substituents on the phenolate ring.[39] The synthesis also involves the use of 1-methyl-4,5-diphenylimidazole instead of the sterically less encumbered 1-methylimidazole, as our group has previously demonstrated that a higher degree of substitution on the imidazole favours the formation of monoligated complexes.[30] Overall, the synthesis involves the use of readily available starting materials, and the ligand can easily be prepared on a multigram scale.

The synthesis begins with the electrophilic aromatic substitution reaction of methyl salicylate with *tert*-butanol in methanol, using sulfuric acid as a catalyst. This results in the formation of **LS1**, which can be recrystallised from methanol and isolated as a white crystalline solid in 51% yield. Next, the salicylate's phenol group is protected using a methoxymethyl ether (MOM), producing **LS2** as a viscous yellow oil in 90% yield. Deprotonation of 1-methyl-4,5-diphenyl-*1H*-imidazole using *n*-BuLi, generates a lithium imidazolium salt, two equivalents of which can subsequently perform a nucleophilic attack on the carbonyl group of **LS2**. In doing so, the carbonyl group is reduced to a tertiary alcohol in **LS3**, which is formed in a yield of 89%. Due to its sterically encumbered nature, the subsequent methylation of the tertiary alcohol is kinetically slow and requires a two-fold excess of NaH and MeI as well as overnight stirring in order to form compound **LS4** in 82% yield. The final step involves the deprotection of the phenol in acidic conditions to yield the ligand **H-Im^{Ph2}NNO^{tBu}** as an off-white solid in 71% yield. The overall isolated yield of the ligand synthesis is 24%.

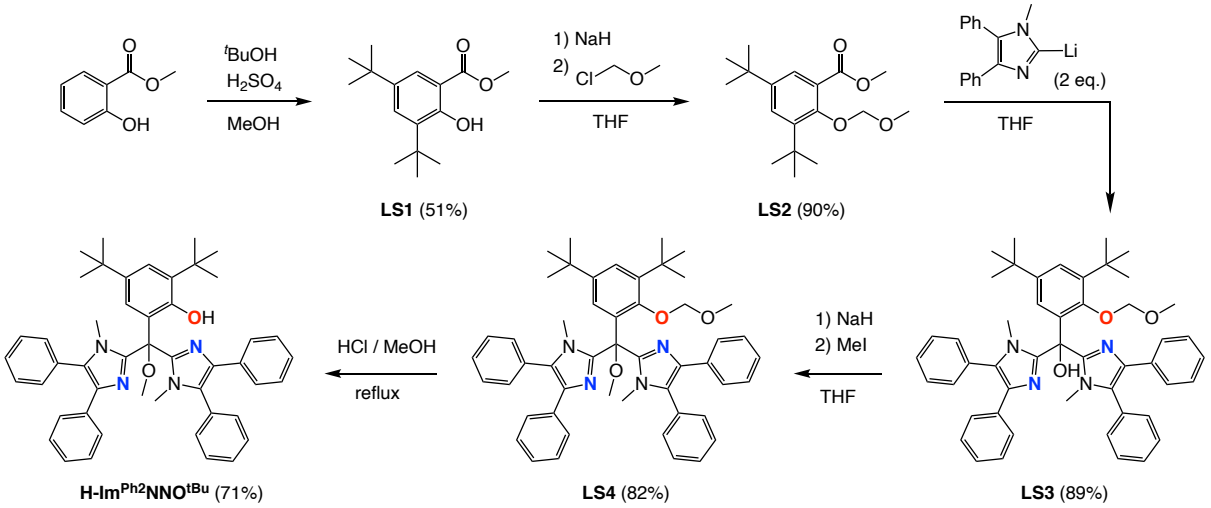

Scheme 1. Synthesis of ligand **H-Im^{Ph2}NNO^{tBu}**.

The phenol can easily be deprotonated using KH as a base. Stirring the ligand with an excess of KH in THF results in the fast release of hydrogen gas as well as a bright yellow solution, indicative of phenol deprotonation. The reaction was left to stir two hours, after which it was filtered to remove any unreacted KH. The solvent was removed under vacuum, affording an off-white crude solid. The solid was washed with hexane and dried, producing the desired potassium ligand salt (**K-Im^{Ph2}NNO^{tBu}**) in 92% yield. ^{1}H NMR analysis of the ligand salt in acetonitrile-d_3 clearly demonstrates the anionic nature of the phenolate through the absence of any OH signal (Figure 5). This is further corroborated by the absence of an O–H stretch in the IR analysis. However, the singlet assigned to the N-methyl groups at 3.29 ppm is severely broadened, indicating fluxional exchange of the two imidazole groups at 25 °C. Cooling the measurement to –30 °C produces a spectrum with two distinct singlets of equal integration at 3.49 and 2.92 ppm, assigned to the N-methyl groups. This demonstrates that the fluxional behaviour no longer occurs on the NMR time scale at low temperature and that the imidazole groups are magnetically inequivalent. From this data, it may be reasonably concluded that the two imidazole heterocycles of the ligand salt exist in two different coordination modes, and can exchange between them by means of a temperature-dependent fluxional process. It should also be noted that the spectrum recorded at –30 °C has a significant degree of line-broadening due to the poorer solubility of the ligand salt at this temperature and its tendency to precipitate out of solution over time. This also causes small impurities to become more noticeable in the spectrum.

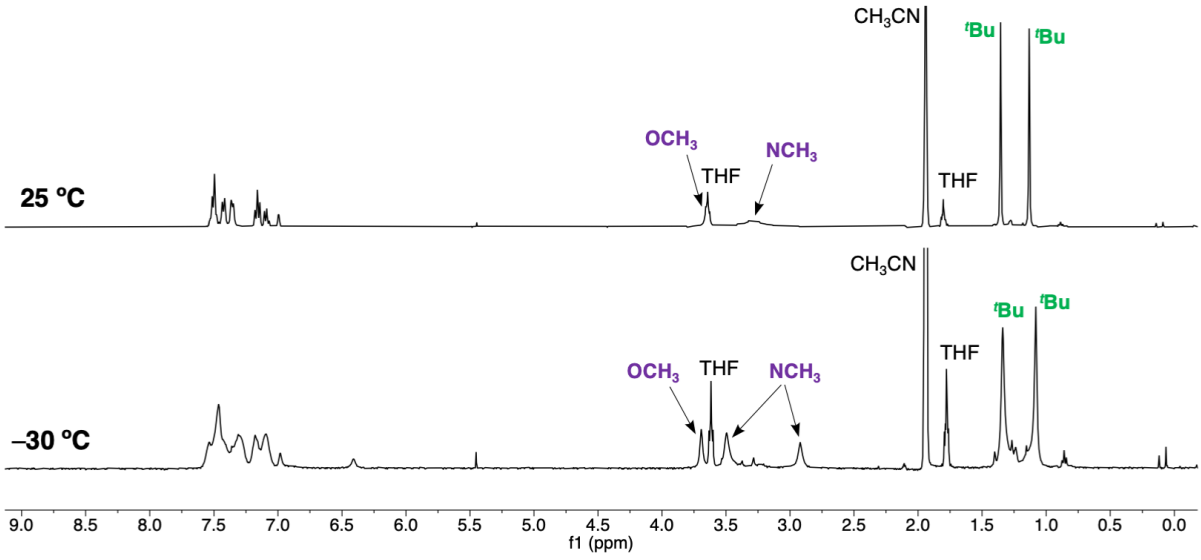

Figure 5. ^{1}H NMR (400 MHz) spectrum of **K-Im^{Ph2}NNO^{tBu}** in acetonitrile-d_3 at 25 °C and at –30 °C.

Crystals of **K-Im^{Ph2}NNO^{tBu}** suitable for X-ray diffraction were grown from slow vapour diffusion of diethyl ether into a dichloromethane solution of the ligand salt at –40 °C. The crystal structure of the ligand salt reveals the coordination of two potassium ions within a centrosymmetric dimeric diamond core structure, involving two ligand molecules whose phenolic O atoms adopt a μ_2-bridging coordination mode (Figure 6). Each potassium ion is further stabilised by the coordination of the methoxy group from one ligand molecule

and an imidazole group from the other ligand molecule. Each ligand molecule features one non-coordinated imidazole group. Coordination of a diethyl ether molecule completes the overall pentacoordinate geometry of the potassium ions. The C–O bond length of the phenolate is measured as 1.306(3) Å, which is somewhat shortened compared to the C–O bond length of a neutral phenol (1.36 Å).

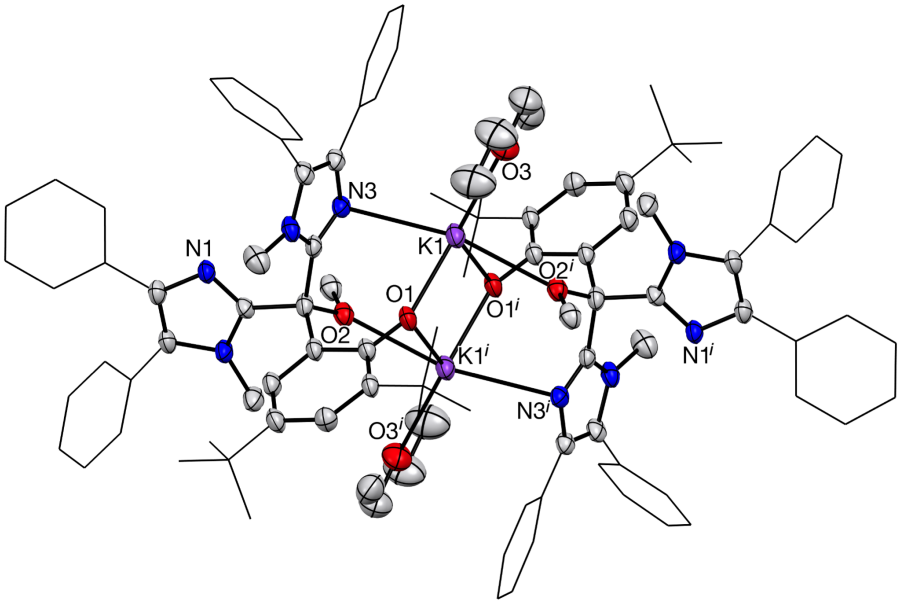

Figure 6. Displacement ellipsoid plot of $[K_2(\mathbf{Im^{Ph2}NNO^{tBu}})_2(OEt_2)_2]$ (50% probability level). Only the major form of the disordered ^{t}Bu group is drawn. Symmetry code *i*: 1-x, 1-y, 1-z. Hydrogen atoms and severely disordered solvent molecules are omitted for clarity. Ph and ^{t}Bu substituents have been depicted in the wireframe format for clarity.

3.2.2 Synthesis and Solid State Characterisation of 1 and 2

The facial capping potential of anionic $\mathbf{Im^{Ph2}NNO^{tBu}}$ was investigated by exploring its coordination chemistry with Fe^{2+} and Zn^{2+}. Both iron and zinc complexes were prepared using analogous methods, depicted in Scheme 2. $\mathbf{K\text{-}Im^{Ph2}NNO^{tBu}}$ was dissolved in acetonitrile, and one equivalent of the desired metal(II) chloride precursor was added to the solution. The mixture was stirred for two hours and was subsequently filtered and dried under vacuum. The crude solid was washed three times with hexane and was then dried under vacuum. The final reaction products were identified as mononuclear complexes $[Fe(Im^{Ph2}NNO^{tBu})(Cl)]$ (**1**) and $[Zn(Im^{Ph2}NNO^{tBu})(Cl)]$ (**2**), obtained in yields of 97% and 94%, respectively. Analogous triflate complexes $\mathbf{1^{OTf}}$ and $\mathbf{2^{OTf}}$ could be synthesised using the same procedure, substituting MCl_2 for the corresponding anhydrous $M(OTf)_2$ salt. However, their isolation was hampered by the presence of unknown impurities as well as their lower stability in solution over time. Therefore, we did not pursue any subsequent coordination chemistry using these complexes.

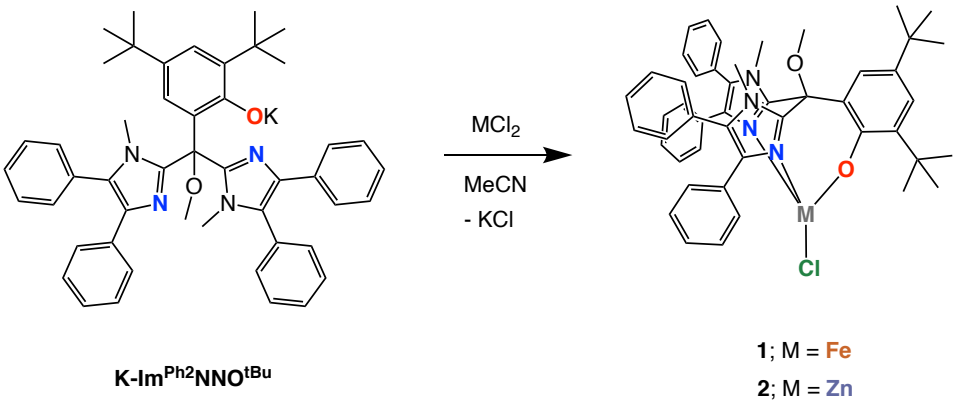

Scheme 2. Synthesis of complexes [Fe(Im^{Ph2}NNO^{tBu})(Cl)] (**1**) and [Zn(Im^{Ph2}NNO^{tBu})(Cl)] (**2**).

IR analysis of **1** and **2** supports the anionic coordination of the phenolate ligand in each complex through the absence of an O–H stretching vibration. Zero-field ^{57}Fe Mössbauer analysis (80 K) on a powder sample of **1** produced a single quadrupole doublet with an isomer shift (δ) of 0.94 mm s^{-1} and a quadrupole splitting ($|\Delta E_Q|$) of 2.58 mm s^{-1}, consistent with a high-spin iron(II) nucleus (Appendix B, Figure B14).

Crystals of **1** and **2** suitable for X-ray diffraction were grown from the slow vapour diffusion of *n*-hexane into a THF solution of each complex under ambient conditions. The crystal structures of complexes **1** and **2** are isostructural (Figure 7). In each complex, **Im^{Ph2}NNO^{tBu}** chelates to a single metal ion by means of a tridentate *N,N,O* motif comprising both neutral imidazole N-donors and the anionic phenolate O-donor. The fourth coordination site is occupied by a chloride ligand, which completes the distorted tetrahedral geometry of each metal centre. Selected bond lengths and bond angles are given in Table 1. Based on these results, **Im^{Ph2}NNO^{tBu}** can be regarded as a heteroscorpionate ligand that imparts a metallobicyclo[2.2.3]nonane topology to each complex.

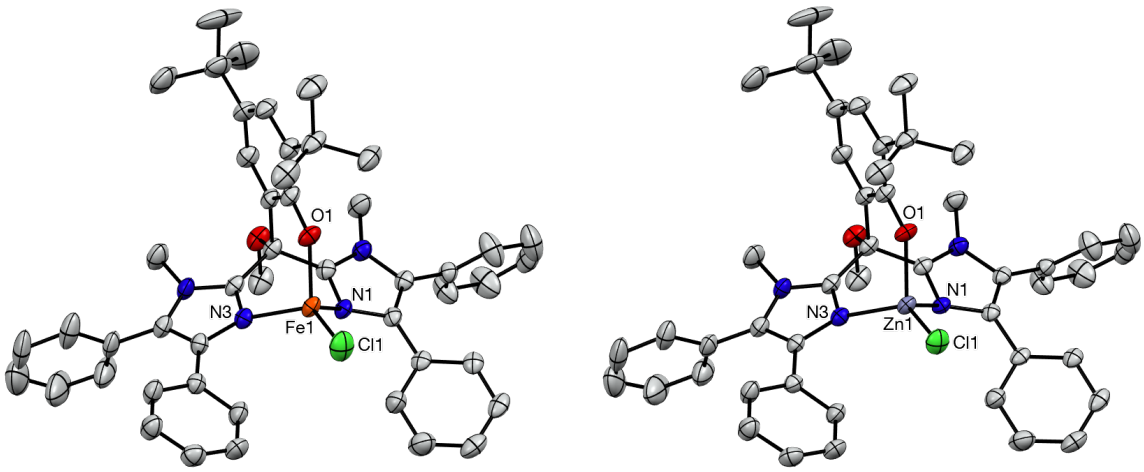

Figure 7. Displacement ellipsoid plots of **1** (left) and **2** (right), drawn at the 50% probability level. Only the major form of the disordered ^{t}Bu groups is drawn. Hydrogen atoms and severely disordered solvent molecules are omitted for clarity.

Table 1. Selected bond lengths (Å) and bond angles (°) observed in the X-ray crystal structures of **1** and **2**, as well as the protein X-ray crystal structures of DAOCS (PDB 1RXF)[40] and BphC (PDB 1EIL).[41]

Bond Length	**1**	**2**	**DAOCS**	**BphC**
M–N1	2.131(2)	2.0754(14)	2.19 (His_{183})	2.24 (His_{145})
M–N3	2.089(2)	2.0248(14)	2.15 (His_{243})	2.30 (His_{209})
M–O1	1.8915(19)	1.9265(12)	2.15 (Asp_{185})	2.09 (Glu_{260})
M–Cl1	2.2187(9)	2.1701(5)	-	-
Bond Angle	**1**	**2**	**DAOCS**	**BphC**
N1–M–O1	95.10(8)	95.91(5)	86.3	106.7
N3–M–O1	98.92(9)	100.97(5)	99.4	103.9
N1–M–N3	84.05(9)	88.23(5)	89.3	87.0
O1–Fe1–Cl1	115.82(6)	111.30(4)	-	-

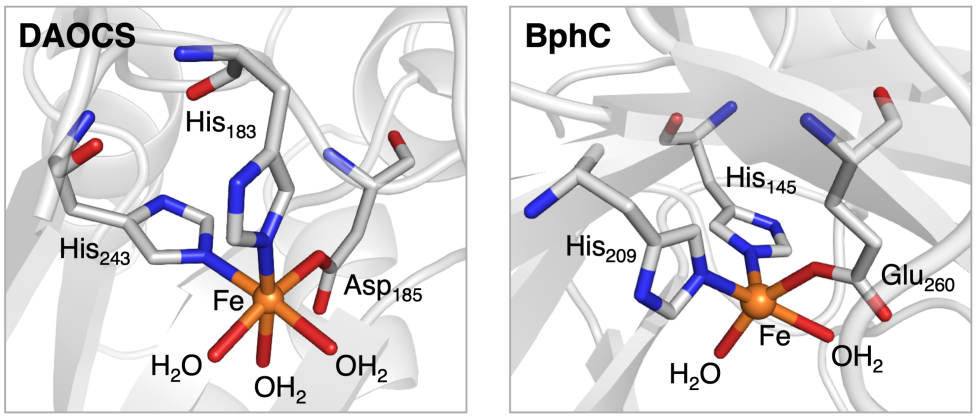

Figure 8. Active site structures of DAOCS from *Streptomyces clavuligerus* (PDB 1RXF)[40] and BphC from *Pseudomonas sp. KKS102* (PDB 1EIL).[41] Carbon, iron, nitrogen and oxygen are depicted in grey, orange, blue and red, respectively.

To the best of our knowledge, **1** is only one of three crystallographically characterised mononuclear non-heme iron(II) complexes that feature a tripodal *N,N,O* ligand and do not require additional stabilisation from an organic co-ligand. The distorted tetrahedral geometry of **1** and **2** differs somewhat form the typically penta- or hexacoordinate nature of 2H1C-containing enzyme resting states (Figure 8). A comparison of the crystallographic parameters of **1** and **2** with those of deacetoxy-cephalosporin C synthase (DAOCS, octahedral)[40] and 2,3-dihydroxybipheny dioxygenase (BphC, square pyramidal)[41] is given in Table 1. Overall, **1** shows the greatest similarity to DAOCS, both in terms of the Fe–N bond lengths and the bonds angles between the ligand donor atoms and the iron centre. However, the short Fe–O bond in **1** differs strongly from the enzyme Fe–O bond lengths, each of which is longer than 2 Å.

The tetrahedral distortion in **1** and **2** is characterised by N–M–O and N–M–N angles that are smaller than in the ideal tetrahedron, while the O–M–Cl and N–M–Cl angles are larger than ideal. This is due to the strain caused by the "cage" effect of the ligand scaffold, whose

donor groups are linked by a single quaternary carbon atom, thereby imposing a certain degree of rigidity to the tripod and contracting the bite angles between the three donor atoms. The Fe–O bond length of 1.8915(19) Å in **1** is relatively short and reflects the anionic nature of the phenolic oxygen atom. For comparison, an Fe–O bond length of 2.1979(14) Å was previously reported in our group for complex [Fe(BM^{Me}BIP^{nPr})(OTf)$_2$], whose supporting *N,N,O* ligand contains a neutral *n*-propyl ester group.[30] Similarly, the Zn–N bond lengths in **2** fall well within the expected range for a zinc(II) nucleus of tetrahedral geometry bound to neutral N-donors.[25] The Zn–O bond distance of 1.9266(12) Å in **2** is shorter than those reported for similar tetrahedral zinc(II) complexes [Zn(bdtbpza)(Cl)] and [Zn(bpa^{tBu2,Me2})(CH$_3$)] that feature an *N,N,O* ligand with a carboxylate group (Zn–O bond lengths of 1.9902(2) and 2.054(6) Å, respectively).[25,33] This indicates a greater degree of charge localisation on the phenolate oxygen atom of **2** compared to a carboxylic acid oxygen donor. The slightly elongated Fe–N bonds (>2.0 Å) in **1** are consistent with the high-spin nature of the iron(II) centre and lie within the range of Fe–N bond lengths previously obtained for other high-spin non-heme iron(II) complexes bearing imidazole-derived *N,N,O* ligands.[30,42]

In both complexes, the M–N bonds are found to have slightly different lengths, contributing to the distortion of the tetrahedron. This asymmetry correlates with the different angles between the plane of the imidazole heterocycles and their respective M–N bond vectors (θ, Figure 9). Angles of 146.13(13)° and 167.99(13)° are observed for C$_{im}$–N1–Fe1 and C$_{im}$–N3–Fe1 in **1**, which correspond to Fe–N bond lengths of 2.131(2) Å and 2.089(2) Å, respectively. A similar phenomenon is observed for **2**. In other words, the greater the distortion away from co-planarity, the longer the observed M–N bond length and the weaker the strength of the coordination bond. We attribute these effects to the inherent geometric restrictions imposed by the tripodal nature of the ligand, which force the metal out of plane relative to the imidazole rings and also cause a slight twisting of the phenolate ring out of the approximate mirror plane.

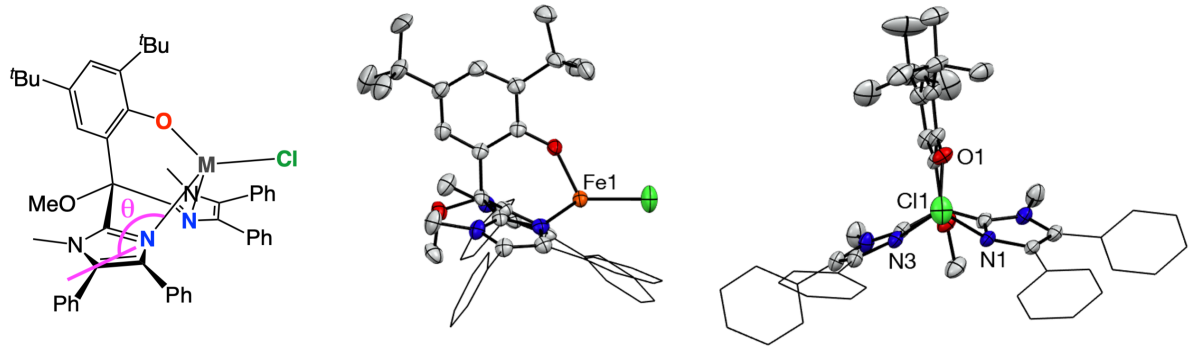

Figure 9. Schematic representation of the C$_{im}$–M–N angle, θ (left) and the views perpendicular (centre) and parallel (right) to the Fe–Cl bond in the solid-state structure of **1** (drawn at the 50% probability level). H-atoms and disorder at the ^{t}Bu groups have been omitted for clarity. Phenyl substituents on the imidazole rings have been depicted in the wireframe format for clarity.

The ability of the ligand to monoligated is proposed to derive principally from the steric demands of its constituent groups, where the diphenyl-substituted imidazole groups hinder the coordination of a second ligand equivalent, and the *ortho*-^{t}Bu substituent of the phenolate reduces the accessibility of the lone pair on the phenolic oxygen atom, preventing any bridging coordination modes from occurring.[22,27,34] Together, these bulky substituents contribute to the relatively large buried volume of the ligand, 58.9 and 59.6%V_{buried} for **1** and **2** respectively (Figure 10).

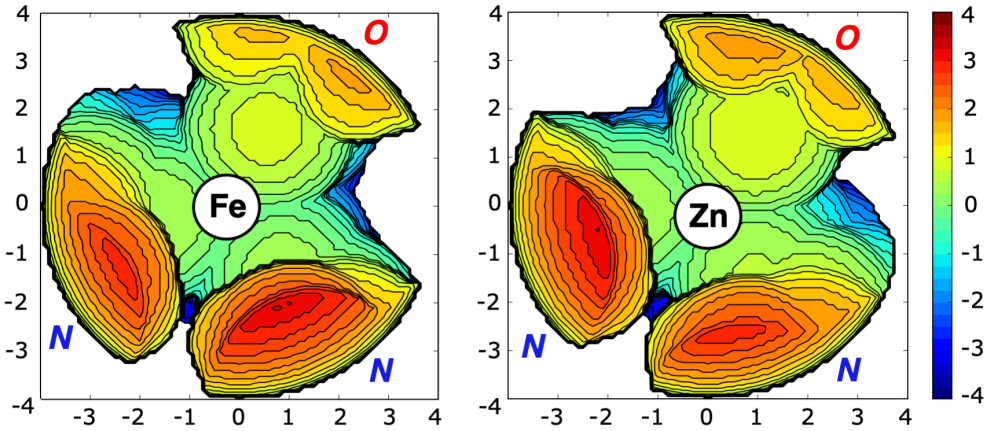

Figure 10. Steric maps of **Im^{Ph2}NNO^{tBu}** in **1** (left) and **2** (right) generated using the Samb*V*ca software.[43] Spheres are defined with a radius of 4 Å from the metal centre and H-atoms are included in the calculation.

3.2.3 Solution State Behaviour of Complexes 1 and 2

In order to establish the rigidity of the **Im^{Ph2}NNO^{tBu}** ligand's tripodal *N,N,O* binding motif, we investigated the solution state behaviour of **1** and **2** in solvents of different binding affinities and varying steric bulk (CD_3CN, CD_2Cl_2, THF-d_8, and pyridine-d_5). In this way, the sensitivities of our newly developed biomimetic complexes can be elucidated, and further coordination chemistry can be controlled with greater precision. The solution state behaviour of **2** will be discussed first.

3.2.3.1 Solution State Behaviour of ***2***

The ^{1}H NMR analysis of **2** in various deutero solvents is depicted in Figure 11. One of the most noticeable features of this data-set is the similarity between the spectra recorded in CD_3CN and CD_2Cl_2, despite their different coordination affinities. In comparison, the spectra recorded in THF-d_8 or pyridine-d_5 are more complex and contain a larger number of peaks, possibly stemming from solvent-specific interactions or complex speciation in solution that arise from the sterically more demanding nature of these solvents.

The ^{1}H NMR spectrum of **2** in CD_3CN features two sharp singlets at 3.51 and 3.45 ppm, assigned to the N- and O-methyl protons of the supporting ligand, respectively. The 2:1

integral ratio is consistent with the metallobicyclo[2.2.3]nonane topology observed in the solid state, indicating that the tripodal *N,N,O* coordination of **Im^{Ph2}NNO^{tBu}** is retained in solution. Analogous peaks at 3.52 and 3.45 ppm are observed in CD_2Cl_2, which show a high degree of structural similarity between the solute structure of **2** in both solvents. Indeed, only minor differences are observed in the aromatic region of the spectra as well as the *tert*-butyl signals, which are ascribed to non-specific solvent interactions.

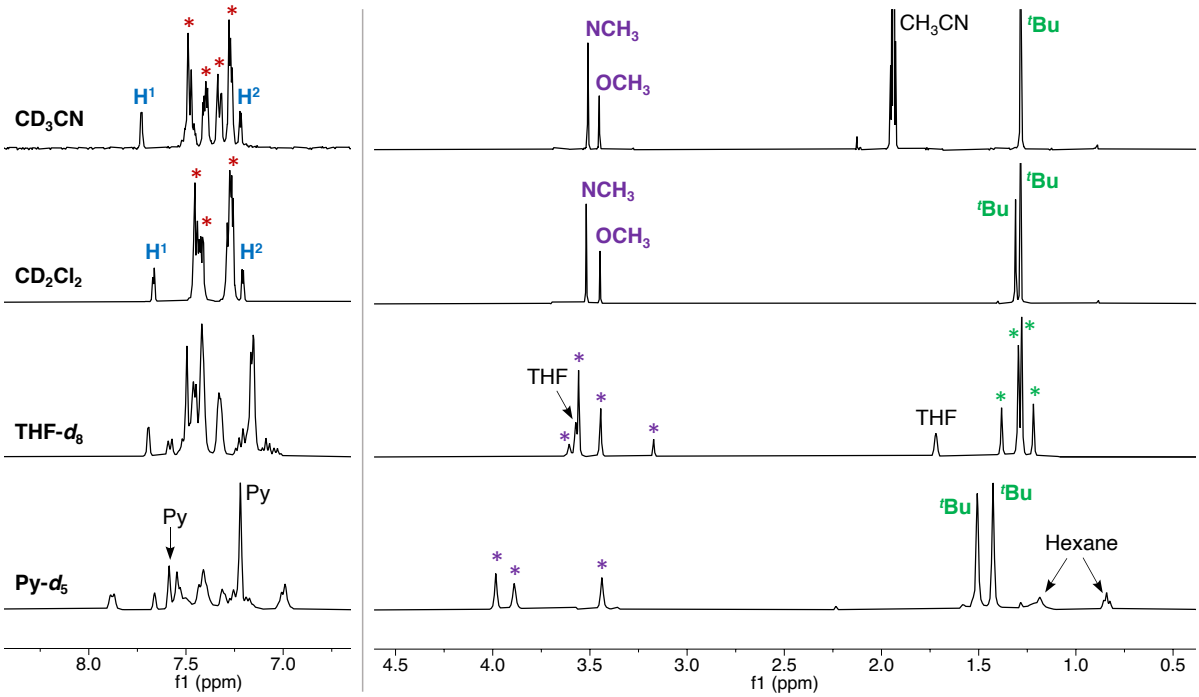

Figure 11. Stacked ^{1}H NMR (400 MHz) spectra of **2** recorded in different deutero-solvents at 25 °C. The region between 4.5 and 6.5 ppm has been omitted for clarity, and the intensity of the aromatic region has been amplified. Spectra are clipped vertically for clarity. Green asterisks indicate peaks associated to the *tert*-butyl groups. Purple asterisks indicate peaks associated to the N-methyl and O-methyl groups. Red asterisks indicate aromatic protons belonging to the imidazole phenyl groups.

To further investigate the three-dimensional structure of **2** in solution, we conducted 1D NOE NMR experiments in CD_3CN (Figure 12). Selective excitation of the N-methyl signal produced correlation signals to the O-methyl signal (3.45 ppm) as well as the ^{t}Bu signal (1.28 ppm), whereas the selective excitation of OCH_3 did not produce any correlation response to the ^{t}Bu signals. In three-dimensional space, this places the methoxy group further away from the *tert*-butyl groups of the phenol ring than the imidazole N-methyl groups, which is in line with the observed H…H distances within the crystal structure (approximately 5.8 Å and 4.8 Å for the O-methyl and N-methyl groups, respectively). We therefore conclude that the solution state structure of **2** (in MeCN and CH_2Cl_2) is equivalent to its structure in the solid state. VT ^{1}H NMR conducted in CD_3CN and CD_2Cl_2 demonstrates that no temperature-dependent fluxional processes occur in these solvents and that the structural integrity of **2** remains intact across a wide temperature range (see Appendix B, Figures B1 and B2).

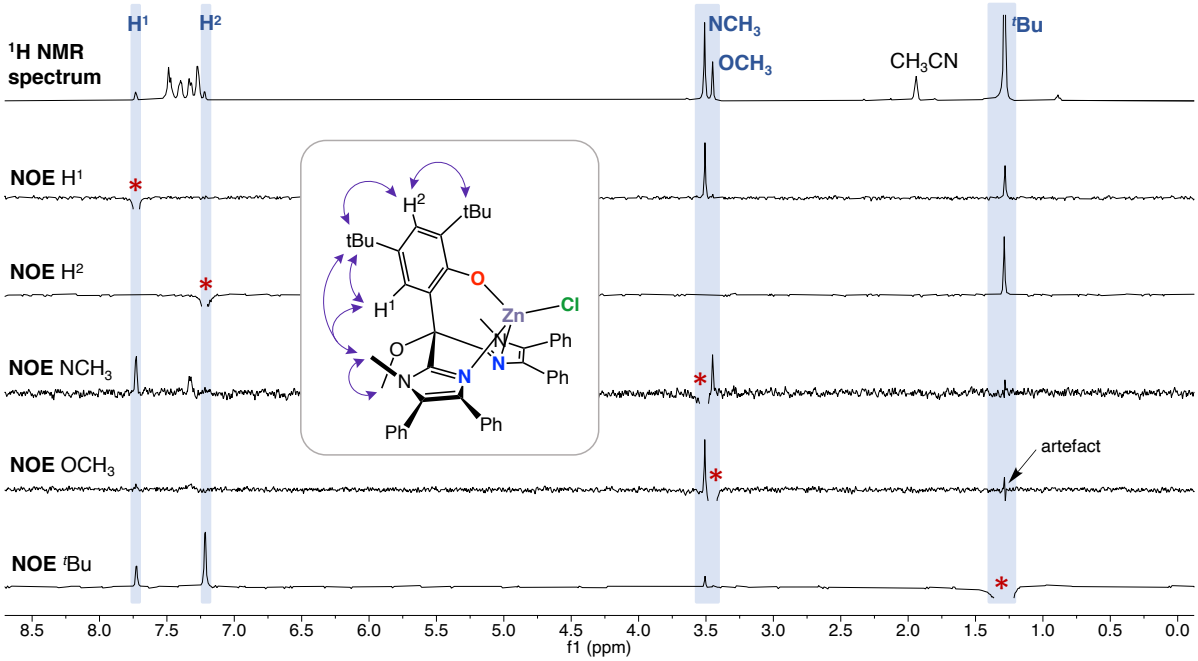

Figure 12. Stacked 1D NOE ^{1}H NMR spectra of **2** in CD_3CN at 25 °C. The selectively excited NMR resonances are highlighted with a red asterisk and are in the negative phase (not depicted). The through-space correlation signals are depicted in the positive phase and are schematically depicted with purple arrows within the insert diagram of **2**.

The ^{1}H NMR spectrum of **2** in THF-d_8 differs significantly from the previously discussed spectra. Most strikingly, four singlets are observed between 1.25 and 1.50 ppm in the region of the *tert*-butyl groups. The two central signals occur very close together at 1.30 and 1.28 ppm, which is similar in chemical shift to the *tert*-butyl resonances observed in CD_3CN and CD_2Cl_2. The two outer singlets at 1.38 and 1.22 ppm have equal integral values, and together have a 1:2 integral ratio relative to the two large singlets. Overall, this would suggest that two species are present in solution. Further evidence to support this can be found in the spectral region between 3.10 and 3.70 ppm associated to the N-methyl and O-methyl groups, where four signals are observed instead of the expected two. In addition, the aromatic region of the spectrum is very disordered, which also suggests that multiple species may be present in solution. Over the course of several days, the relative intensities and chemical shifts of these different NMR signals do not change. Similarly, the spectrum remains unchanged after cooling or heating the sample and repeating the measurement at room temperature, suggesting that the two species present in THF solution are in thermal equilibrium. VT NMR of **2** in THF-d_8 reveals a temperature-dependent fluxional process that occurs on the NMR time-scale (see Appendix B, Figure B3). This is most pronounced in the region around 3.5 ppm where two signals are seen to coalesce as the temperature increases. Another important observation is the appearance of a small shoulder at 1.75 ppm next to the residual THF-d_8 peak at low temperature. This suggests that the solvent participates in the coordination equilibrium, possibly through direct coordination to the metal centre. By coordinating to the metal, we hypothesise that THF may cause of one of the two imidazole N-donors to dissociate.

Dissolving **2** in pyridine-d_5 produces a yellow solution, whose ^{1}H NMR spectrum indicates that a disruption in the complex symmetry has taken place. This is most clearly identified by the presence of three singlets at 3.98, 3.89 and 3.44 ppm, each with an integral value of 3H. This suggests that the imidazole groups no longer coordinate in an equivalent manner. Slow diffusion of hexane into a pyridine solution of **2** under ambient conditions produced yellow needles that were identified as the $[Zn(Cl)_2(py)_2]$ adduct.[44] Based on this data, we hypothesise that the strongly coordinating and sterically demanding nature of pyridine disrupts the *N,N,O* coordination of $\mathbf{Im^{Ph2}NNO^{tBu}}$ and enables pyridine to scavenge a portion of the available zinc. This causes a mixture of decomposition products to form, possibly including a bisligated compound of the type $[Zn(Im^{Ph2}NNO^{tBu})]_2$ (*vide infra*).

*3.2.3.2 Solution State Behaviour of **1***

By analogy to **2**, complex **1** is expected to retain the same structure in acetonitrile and dichloromethane solution. Using Evans' NMR method, the effective magnetic moment (μ_{eff}) of **1** in CD_3CN was determined to be 4.50 μ_B, which corresponds to a high-spin (S = 2) electronic configuration and is consistent with the solid state Mössbauer parameters previously described. The ^{1}H NMR spectra of **1** in CD_3CN and CD_2Cl_2 contain paramagnetic signals between 0 and 58 ppm (Figure 13), and certain signals are observed to have almost identical chemical shifts in both solvents (*e.g.* the signals at 58, 50 and 10 ppm), which supports the assumption that the hyperfine interactions between protons of

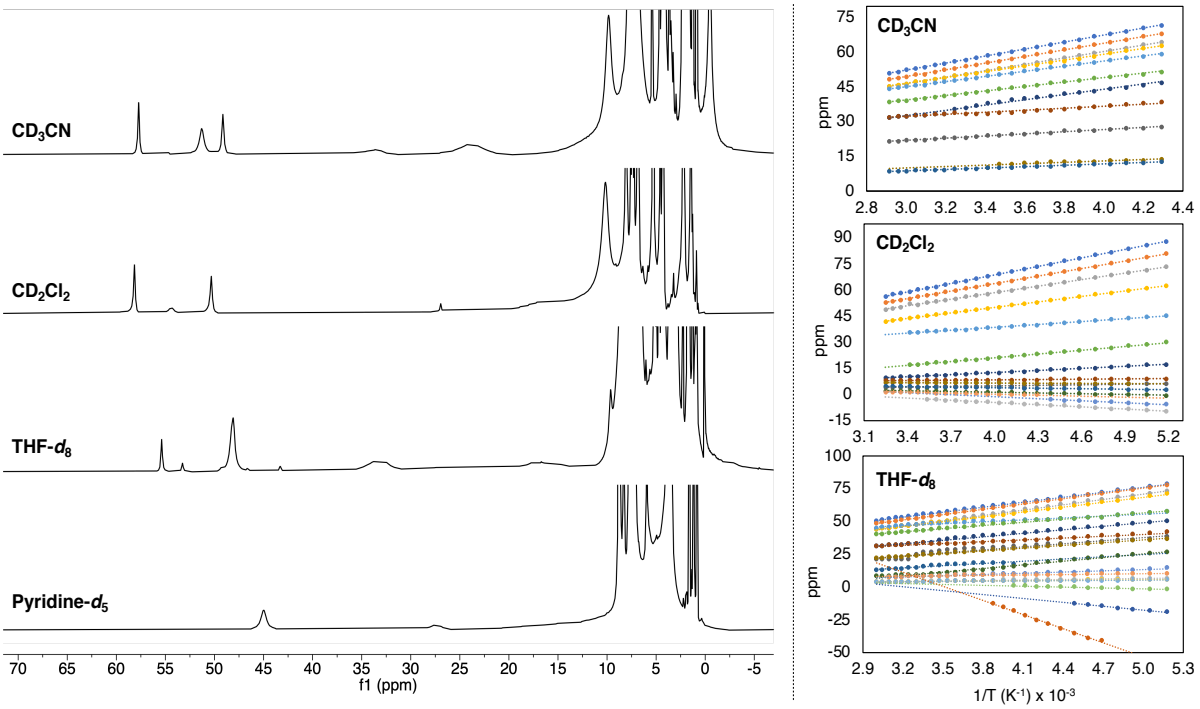

Figure 13. Left: Stacked paramagnetic ^{1}H NMR (400 MHz) spectra of **1** recorded in different deutero-solvents at 25 °C. Spectra are clipped vertically for clarity. Right: Curie plots showing the inverse temperature dependence of the paramagnetic ^{1}H NMR chemical shifts (ppm) for **1** in CD_3CN, CD_2Cl_2 and THF-d_8.

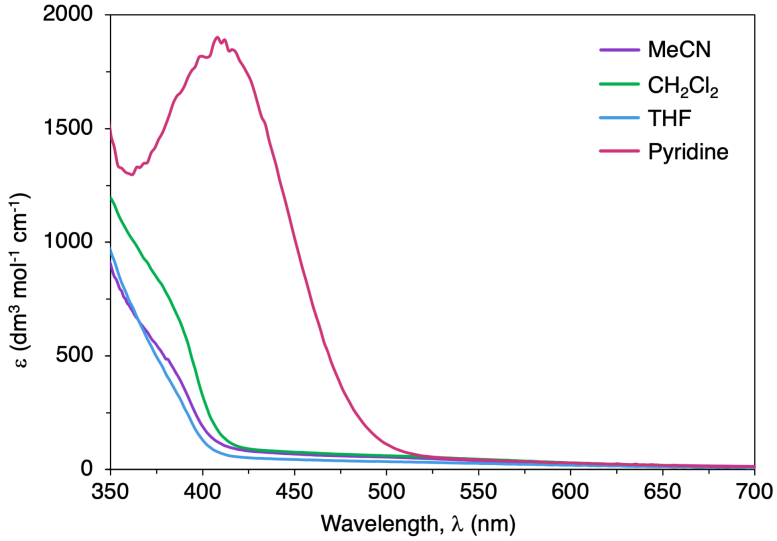

Figure 14. UV-vis spectra of **1** in different solvents at 25 °C.

the ligand scaffold and the paramagnetic iron centre are similar in both solvents. However, additional broad signals are observed in CD_3CN (*e.g.* the signals at 51, 36, 33, and 23 ppm) that are not present in CD_2Cl_2. VT ^{1}H NMR analysis of **1** in both solvents (see Appendix B, Figures B4 and B5) showed normal Curie behaviour with highly linear Curie plots that converge to the diamagnetic region upon extrapolation to infinite temperature, thereby excluding the presence of any spin crossover phenomena or reversible solvent coordination in solution. This suggests that differences between the ^{1}H NMR spectra may simply arise from the different solvent-specific effects. Moreover, the electronic absorption spectra of **1** in CH_3CN and CH_2Cl_2 are almost identical, featuring a very weak, broad band at approximately 500 nm as well as a broad band at 380 nm that shoulders the intense ligand-based π–π^* transitions (<350 nm) (Figure 14). The UV-vis spectrum of **1** in CH_3CN displays no temperature dependence within the range of –40 °C to 25 °C.

Unlike **2**, the ^{1}H NMR spectrum of **1** in THF-d_8 does not reveal the presence of multiple species in solution at 25 °C. Indeed, the UV-vis spectrum of **1** in THF is very similar to those recorded in CH_3CN and CH_2Cl_2, which suggests that an electronically similar species is present in solution. However, conducting VT ^{1}H NMR analysis in THF-d_8 reveals more deviation from ideal Curie behaviour, which is indicative of additional processes occurring in solution at low temperature (Figure 13 and Figure B6 in Appendix B). Recording a ^{1}H NMR spectrum at 25 °C after having either cooled or heated the sample produced the same spectrum as that recorded prior to any temperature change. This suggests that a reversible solvent-related coordination equilibrium in THF solution occurs. Similarly to **2**, dissolving **1** in pyridine produces a yellow solution, indicating the formation of a $FeCl_2$-pyridyl adduct in solution.[45,46] The electronic absorption spectrum of **1** in pyridine contains a strong band at 420 nm, which deviates significantly from the spectra recorded in other solvents (Figure 14). Moreover, the paramagnetic ^{1}H NMR spectrum of **1** in pyridine-d_5 contains fewer peaks and bears little resemblance to the spectra recorded the other deutero solvents, which suggests that a new species has formed in solution.

Slow vapour diffusion of *n*-hexane into a pyridine solution of **1** at room temperature resulted in the growth of needle-like pale yellow crystals that were suitable for X-ray diffraction. The resulting structure reveals the formation of a mononuclear bisligated complex, [Fe($\kappa_{N,O}$-Im^{Ph2}NNO^{tBu})$_2$] (**3**). The iron centre has a distorted tetrahedral geometry and is bound by two ligand molecules, both of which chelate by means of a new bidentate *N,O* coordination mode involving the anionic phenolic oxygen atom and a neutral imidazole N-donor. The second imidazole remains unbound, orientated away from the iron in such a way that the methoxy group is forced into relatively close proximity to the metal (Fe1…O21 and Fe1…O22 distances of 2.4598(18) and 2.513(2) Å, respectively). This result confirms the disrupting effect that pyridine has on the tripodal coordination of **Im^{Ph2}NNO^{tBu}**.

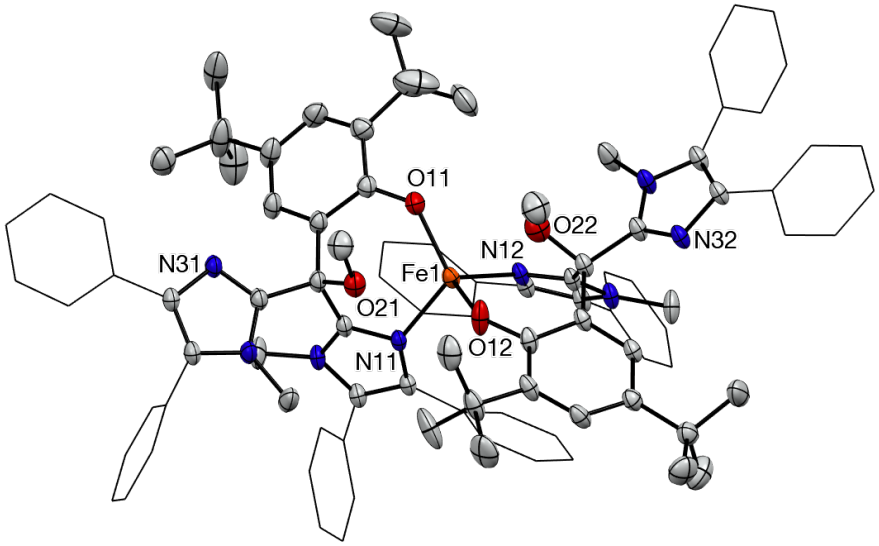

Figure 15. Displacement ellipsoid plot of **3** (50% probability level). Only the major form of the disordered ^{t}Bu group is drawn. Hydrogen atoms, pyridine molecules and severely disordered solvent molecules are omitted for clarity. Ph substituents are depicted in the wireframe format for clarity. Selected bond distances: Fe1–O11 = 1.9402(16) Å, Fe1–O12 = 1.9341(18) Å, Fe1–N11 = 2.1519(16) Å, Fe1–N12 = 2.1395(19) Å. Selected bond angles: N11–Fe1–O11 = 108.80(7)°, N12–Fe1–O12 = 105.50(8)°, O11–Fe1–O12 = 131.43(8)°, N11–Fe1–N12 = 99.33(7)°.

3.2.4 Synthesis of a Mononuclear Zinc Thiolate Complex

The substitutional lability of the chloride ligand in **2** was investigated using a monodentate thiophenolate ligand (Scheme 3). Complex **2** was dissolved in CH_2Cl_2 and a slight excess of NaSPh was added. The reaction mixture was left to stir for 3 h and was subsequently filtered and dried under vacuum. The crude product was washed with hexane and dried under vacuum, affording the zinc thiolate complex [Zn(Im^{Ph2}NNO^{tBu})(SPh)] (**4**) as a white powder in 97% yield.

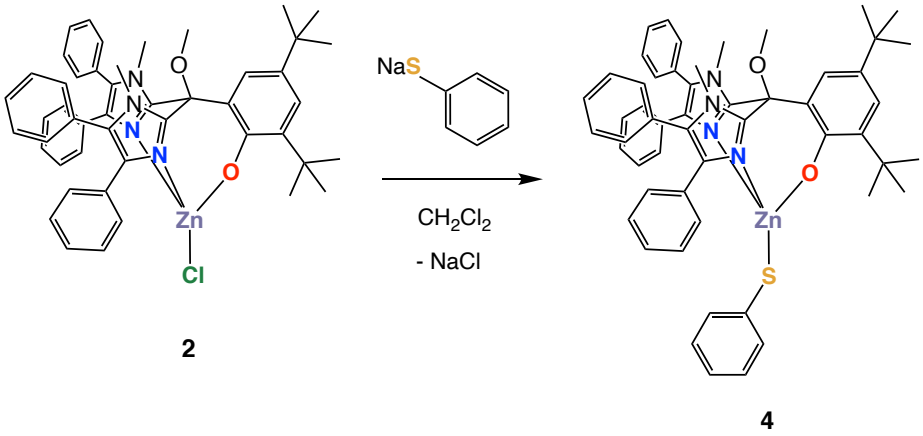

Scheme 3. Synthesis of the zinc thiolate complex [Zn(Im^{Ph2}NNO^{tBu})(SPh)] (**4**).

Colourless crystals suitable for X-ray diffraction were grown from slow diffusion of *n*-hexane into a THF solution of **4** at room temperature. The crystal structure of **4** reveals the formation of a mononuclear zinc(II) complex with a distorted tetrahedral geometry (Figure 16A). **Im^{Ph2}NNO^{tBu}** has retained its tripodal *N,N,O* binding mode, and its buried volume is calculated as being 59.4%V_{buried}. The thiophenolate ligand occupies the zinc's fourth coordination site and binds through its anionic sulfur atom. Selected bond lengths and bond angles given in Table 2.

The Zn1–S1–C49 angle of 101.67(11)° is typical for an arylthiolate coordinated to a transition metal and the Zn–S bond length of 2.2249(9) Å lies is comparable to those reported for other tetrahedral zinc(II) thiophenolate complexes (2.2201(13) Å – 2.418(1) Å).[47–53] Similarly to **2**, the tetrahedral distortion in **4** is characterised by N–Zn–O and N–Zn–N angles that are significantly smaller than the ideal tetrahedron angle, and N–Zn–S and O–Zn–S angles that are larger than 109.5°. Interestingly, the thiolate appears to be coordinated in such a way that its aryl substituent "bends" towards one of the two imidazole groups, effectively imparting chirality to the complex. However, the overall crystal structure of **4** must be considered racemic as can be seen by the centrosymmetric space group (Figure 16B). Overall, the low coordination number, the single metal-sulfur bond, and the facial *N,N,O* triad qualify **4** as an accurate (diamagnetic) structural model of the ACV-bound active site of IPNS.

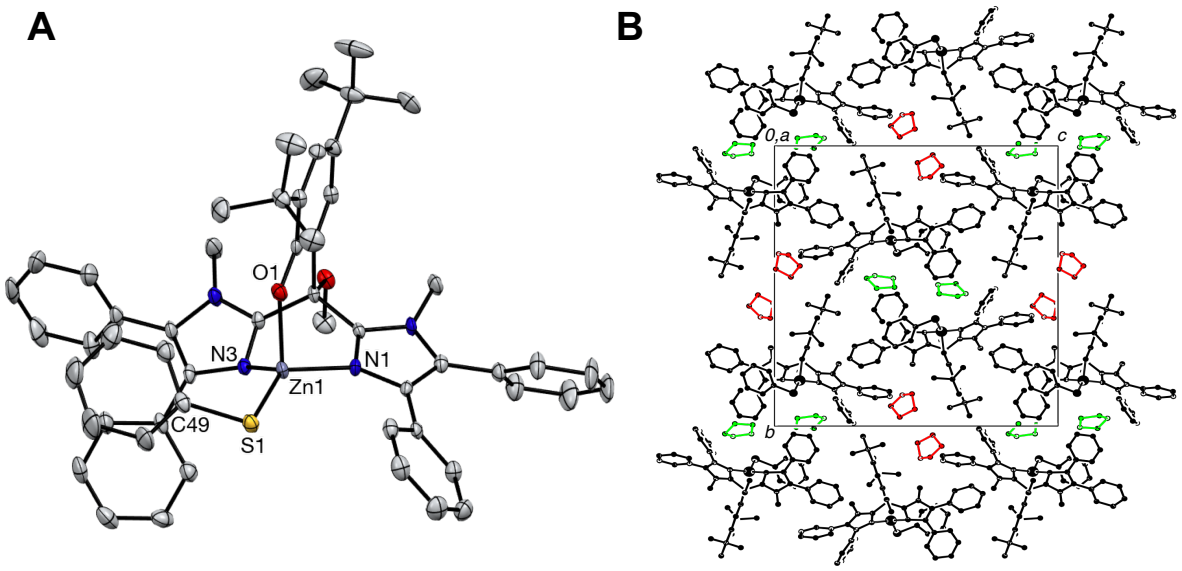

Figure 16. A: Displacement ellipsoid plot of **4** (50% probability level). Hydrogen atoms and disordered THF solvent molecules are omitted for clarity. **B:** Packing of **4** in the crystal, shown along the *a*-axis. Hydrogen atoms are omitted for clarity. There are two independent THF molecules in asymmetric unit (red, green). Only the major form of the disordered THF is shown.

Table 2. Selected bond lengths (Å) and bond angles (°) for complex **4**.

[Zn(Im^{Ph2}NNO^{tBu})(SPh)] (**4**)					
Bond	Length	Angle	Degrees	Angle	Degrees
Zn1–N1	2.028(2)	Zn1–S1–C49	101.67(11)	N1–Zn1–S1	131.21(7)
Zn1–N3	2.062(3)	N1–Zn1–O1	94.92(9)	N3–Zn1–S1	120.07(7)
Zn1–O1	1.967(2)	N3–Zn1–O1	96.27(9)	O1–Zn1–S1	116.13(7)
Zn1–S1	2.2249(9)	N1–Zn1–N3	90.33(10)		

3.2.5 Solution State Behaviour of 4

Next, we investigated the solution state behaviour of **4** in order to evaluate the rigidity of the supporting ligand's *N,N,O* coordination in the presence of a biorelevant thiophenolate ligand. The ^{1}H NMR spectrum of **4** in different deutero solvents is depicted in Figure 17.

The ^{1}H NMR spectra of **4** in CD_3CN and CD_2Cl_2 both feature sharp singlets at 3.51 ppm and 3.44 ppm, assigned to the N-methyl and O-methyl groups of the supporting ligand framework, respectively. Their relative integral ratio of 2:1 supports the metallobicyclo-[2.2.3]nonane topology associated to the facial binding motif of the **Im^{Ph2}NNO^{tBu}** ligand. In both spectra, the thiolate ligand can be identified by the presence of two multiplets in the aromatic region of the spectra, the most deshielded being assigned to the two protons *ortho* to the sulfur atom. Interestingly, the chemical shifts of the phenolic protons have not changed compared to those of **2**, which suggests that chloride substitution for the thiophenolate does not have a significant impact on the electronic properties of the phenolate ring. VT ^{1}H NMR analysis in CD_3CN and CD_2Cl_2 (see Appendix B, Figures B7 and B8) demonstrates that **4** retains its structural integrity across a wide temperature range, as no fluxional behaviour of the supporting ligand nor any thiophenolate dissociation was observed in either solvent. Finally, 1D NOE ^{1}H NMR experiments in CD_3CN (see Appendix B, Figures B9) confirmed the three-dimensional structure of **4** as being the same in solution as it is in the solid state.

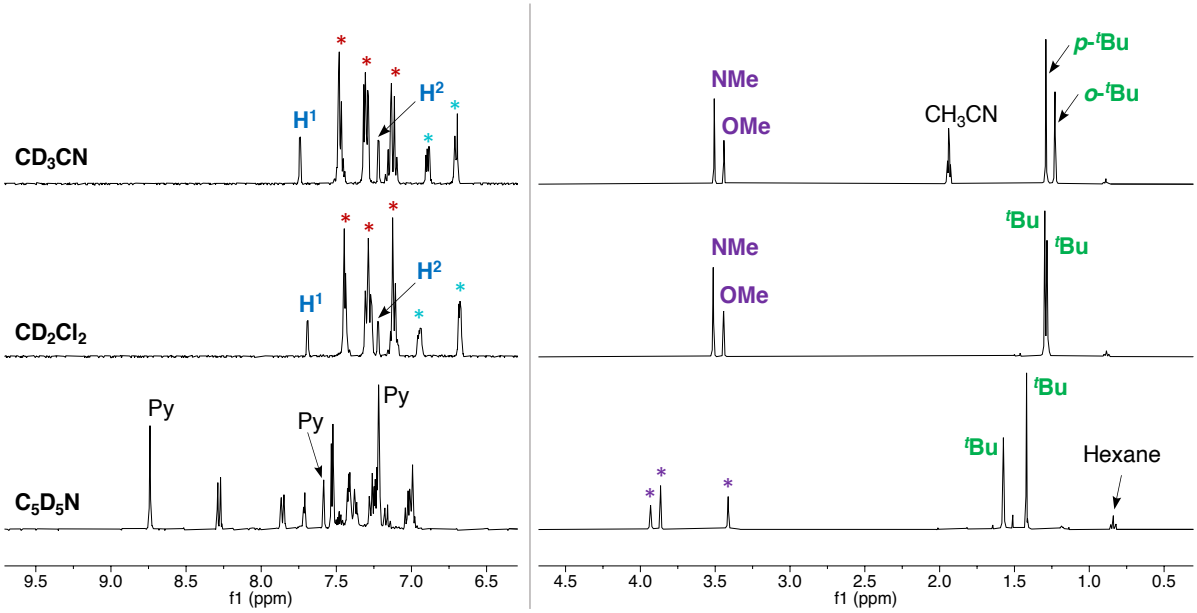

Figure 17. Stacked ^{1}H NMR (400 MHz) spectra of **4** recorded in different deutero-solvents at 25 °C. The region between 4.5 and 6.5 ppm has been omitted for clarity, and the intensity of the aromatic region has been amplified. Spectra are clipped vertically for clarity. Purple asterisks indicate peaks associated to the N-methyl and O-methyl groups. Red asterisks indicate aromatic protons associated to the imidazole phenyl substituents. Blue asterisks denote the multiplets assigned to the SPh ligand.

Dissolving **4** in pyridine-d_5 produced a pale pink solution whose ^{1}H NMR spectrum reveals a number of significant changes compared to the spectra recorded in CD_3CN and CD_2Cl_2. Most importantly, three singlets are observed at 3.93, 3.87, and 3.41 ppm, each with a relative integral of 3H. This strongly suggests that the supporting ligand's facial binding motif has been disrupted and that a break in symmetry has occurred.

Colourless crystals suitable for X-ray diffraction were grown from slow vapour diffusion of hexane into a pyridine solution of **4** at room temperature. The resulting crystal structure reveals the formation of a new complex, [Zn(Im^{Ph2}NNO^{tBu})(SPh)(py)] (**5**), that features direct coordination of a pyridine molecule to the zinc ion (Figure 18). As a result, the zinc's coordination sphere has expanded to five-coordinate, and a disruption of the supporting ligand's *N,N,O* coordination has occurred. The steric demands of the pyridine ligand have caused one of the imidazole groups to dissociate, resulting in a closer proximity of the methoxy group to the zinc ion. This results in the coordination of the supporting ligand by means of an alternative facial *N,O,O* coordination mode to the zinc metal centre, comprising an anionic phenolic O-donor, one of the neutral imidazole N-donors and the loosely bound neutral methoxy O-donor (Zn1–O2 distance of 2.455(3) Å).

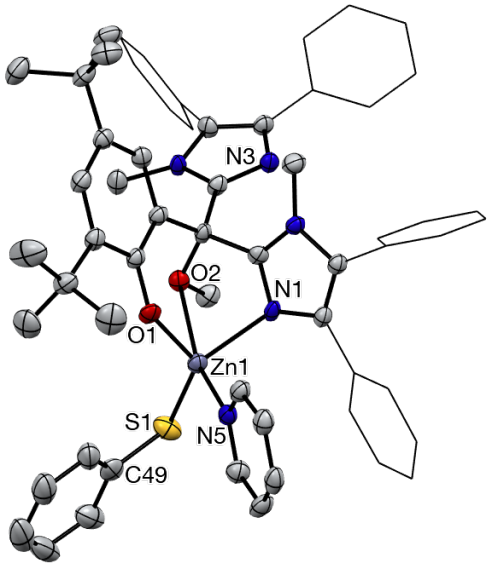

Figure 18. Displacement ellipsoid plot of **5** (50% probability level). Hydrogen atoms and partially occupied non-coordinated pyridine solvent molecule are omitted for clarity. Phenyl substituents on the imidazole rings have been depicted in the wireframe format for clarity.

Table 3. Selected bond lengths (Å) and bond angles (°) for complex **5**.

[Zn(Im^{Ph2}NNO^{tBu})(SPh)(py)] (**5**)			
Bond	Length	Bond Angle	Degrees
Zn1–N1	2.108(3)	Zn1–S1–C49	105.63(17)
Zn1–N5	2.120(3)	N1–Zn1–O1	98.95(12)
Zn1–O1	1.941(3)	N1–Zn1–O2	70.35(10)
Zn1–O2	2.455(3)	N5–Zn1–O1	94.43(12)
Zn1–S1	2.2835(12)	O1–Zn1–S1	127.91(9)

3.2.6 Electrochemistry

Phenolate ligands are known to be redox non-innocent in character, which prompted us to investigate the electrochemical properties of complexes **1**, **2** and **4**, and examine the effect of combining the redox non-innocent character of the supporting ligand with zinc (redox inert), iron (redox non-innocent), as well as a redox non-innocent thiophenolate ligand. The redox properties of the complexes were investigated by cyclic voltammetry (CV) under an inert N_2 (g) atmosphere in acetonitrile, using [*n*-Bu_4N]PF_6 as a supporting electrolyte. All quoted potentials are referenced versus the ferrocene/ferrocenium couple (Fc/Fc^+). The redox behaviour of the ligand salt was investigated for comparison. The voltammograms are displayed in Figure 19.

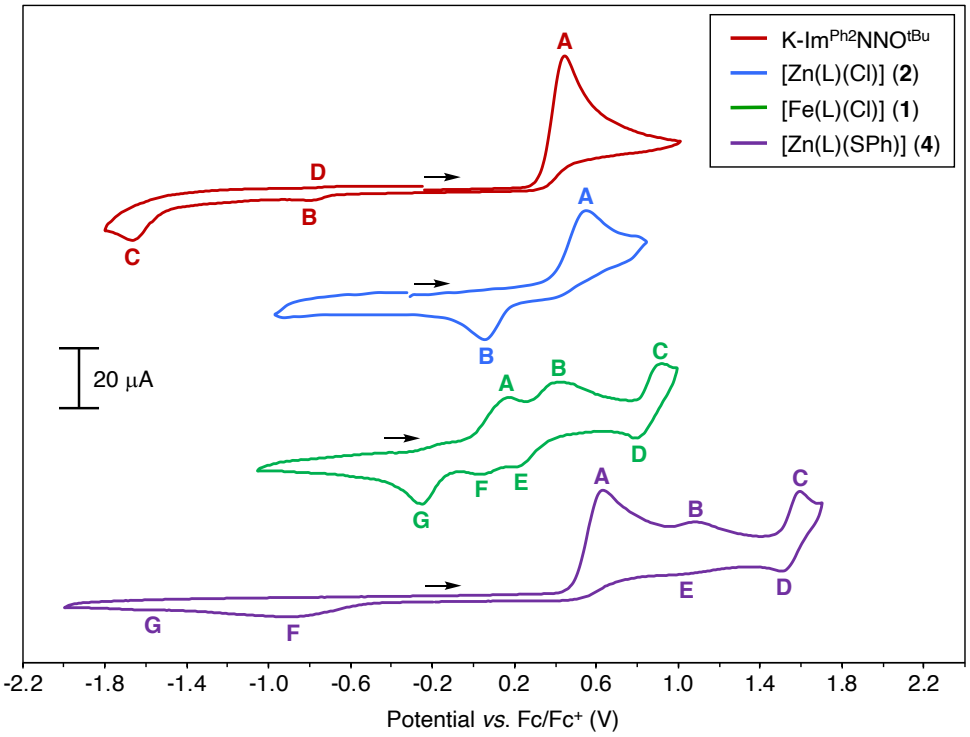

Figure 19. Cyclic voltammograms of **K-Im^{Ph2}NNO^{tBu}**, **2**, **1** and **4**, recorded in a 0.1 M solution of [*n*-Bu_4N]PF_6 in acetonitrile at ambient temperature and with a scan rate of 100 mV/s.

Scanning across the potential range of –2.1 V to +1.1 V, the voltammogram of **K-Im^{Ph2}NNO^{tBu}** features a strong oxidation wave, **A** ($E_{p,a}$ = +0.46 V), that we ascribe to the phenolate oxidation to its phenoxyl form.[54–56] This is approximately 0.5 V lower compared to the oxidation potential of tri-substituted phenols such as 2,4,6-tri-*tert*-butylphenol or 2,4,6-trimethylphenol that oxidize at *ca.* 1.0 V (vs. Fc/Fc^+).[57,58] This reflects the anionic state of the phenolic oxygen atom in **K-Im^{Ph2}NNO^{tBu}**. A reduction event, **C** ($E_{p,c}$ = –1.66 V), is observed that only occurs after **A** has taken place (see Appendix B, Figure B11), prompting us to assign it to the electrochemical reduction of the phenoxyl radical. The large peak separation between **A** and **C** (ca. 2 V) and the relatively diffuse nature of both signals reflects the highly irreversible nature of this redox couple and is consistent with previous observations made for the electrochemical behaviour of substituted phenols in

coordinating solvents.[57,58] Moreover, the structure of the ligand salt in solution is likely very dynamic, involving imidazole lability, solvent coordination to the potassium ion and possible coordination equilibria between monomeric and dimeric states, all of which contribute to the diffuse and irreversible nature of the electrochemical events. The electrochemical responses **B** and **D** (that occur at approximately –0.75 V) are very minor and become less well defined at higher scan rates. We therefore tentatively ascribe them either to the presence of small amounts of structural isomers or to the presence of a minor impurity.

The voltammogram of complex **2** features a single irreversible redox couple within the potential range of –1.0 V to +0.8 V with the oxidation (**A**) and reduction (**B**) occurring at $E_{p,a}$ = +0.56 V and $E_{p,c}$ = +0.07 V, respectively. Given the redox-inert nature of divalent zinc, these electrochemical responses are assigned as phenolate-based electron transfers. The phenolate oxidation potential is comparable to that of other zinc(II) phenolate complexes bearing mixed N,O-donor ligands.[59,60] Compared to the ligand salt, the phenolate oxidation in **2** has undergone a 100 mV anodic shift. This is likely due to a depletion in the electron density on the phenolate's oxygen atom as a result of its coordination to the Lewis acidic zinc ion.[61] Additionally, we ascribe the smaller peak-to-peak separation of **A** and **B** in **2** (compared to **A** and **C** in **K-Im^{Ph2}NNO^{tBu}**) to the rigid, tripodal coordination of the ligand to zinc in acetonitrile solution, which may help to increase the (electro)chemical reversibility of the phenolate-centred electron transfers. Scanning beyond +0.85V, additional irreversible oxidations were observed with no reduction events taking place on the return scan, indicating decomposition of the complex on the surface of the working electrode.

The presence of a redox-active metal in **1** produces a voltammogram of greater complexity than that of **2**, with three oxidative waves (**A**–**C**) and four reductive responses (**D**–**G**) observed within the potential range of –1.0 V and +1.0 V. The voltammogram is reproducible over at least 20 cycles, which implies that the electrochemical cycle it represents is overall chemically reversible. The first oxidation event, **A** ($E_{p,a}$ = +0.18 V) is assigned to iron oxidation on the basis of its low oxidation potential. It forms an irreversible redox couple to **G** ($E_{p,c}$ = –0.25), which suggests that the formation of a ferric ion is accompanied by additional chemical or structural changes in solution (Figure 20). One possibility is that the preference for an octahedral geometry may drive the ferric ions into coordination equilibria with acetonitrile, deviating from the original tetrahedral geometry of the complex. Indeed, this is reflected by the diffuse nature of the subsequent oxidation, **B** ($E_{p,a}$ = +0.42 V), ascribed to phenolate oxidation.[62] By means of segmentation experiments, **B** was shown to be redox-coupled to both **E** (+0.23 V) and **F** (+0.04 V), supporting the hypothesis that a mixture of species is present in solution after the initial oxidation event **A**. Finally, a quasi-reversible redox couple comprising **C** and **D** ($E_{1/2}$ = +0.88 V) is observed that we tentatively assign to a Fe^{IV}/Fe^{III} couple, based on similar potentials reported for other non-heme iron complexes supported by tripodal ligands.[63,64]

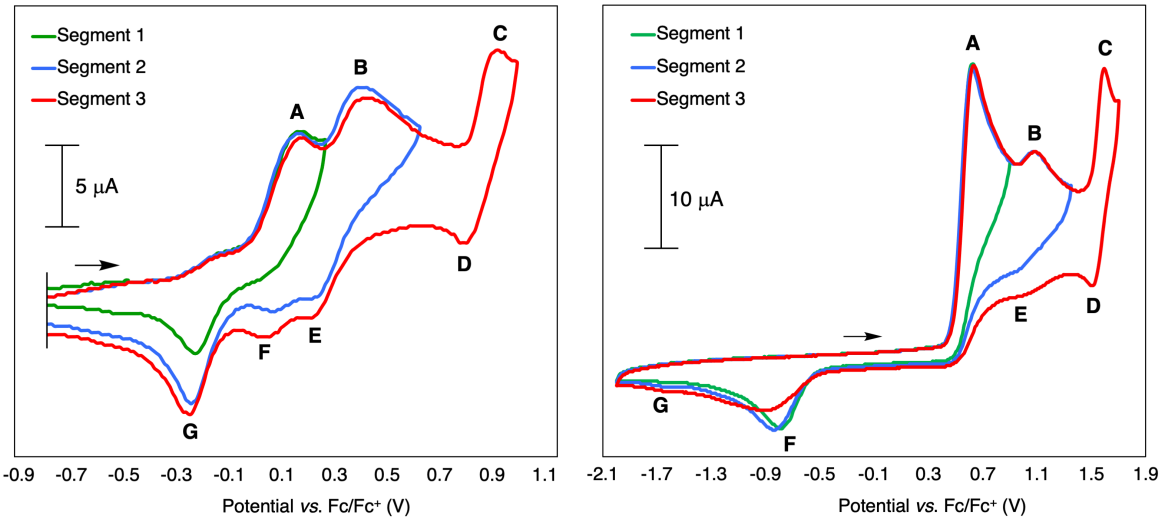

Figure 20. Segmented CVs for **1** (left) and **4** (right), recorded in 0.1 M [^{n}Bu$_4$N]PF$_6$ in acetonitrile.

Substitution of the chloride ligand in **2** for the thiophenolate ligand in **4** can be regarded as the addition of a redox centre within the zinc complex framework. Scanning oxidatively from the OCP, a strong irreversible oxidation, **A** ($E_{p,a}$ = +0.65 V), is observed that is followed by a second more diffuse oxidation, **B** ($E_{p,a}$ = +1.07 V). We ascribe these to the sequential oxidation of the phenolate and thiophenolate moieties, on the basis of literature precedent.[55,61,65] The presence of the thiolate ligand has therefore caused the phenolate oxidation to shift anodically by approximately 0.1 V compared to **2**. Scanning beyond +1.4 V, a quasi-reversible redox couple is observed, **C** and **D** ($E_{1/2}$ = +1.57 V), which we assign to a ligand-centred electron transfer, although we are unable to assign it definitively to the thiolate or to the phenolate. Reduction **F** ($E_{p,c}$ = –0.89 V) was observed not to occur without **A** having previously taken place (see Appendix B, Figure B13), which prompted our assignment of **F** to the phenoxyl reduction. Interestingly, segmentation experiments revealed that **F** is less broad when **C** has not taken place (Figure 20), demonstrating that sequential electrochemical oxidations of **4** provoke structural changes in solution that increase the activation energy required for **F**. Presumably, these structural changes account for the overall irreversibility the electrochemical responses observed for **4**.

Overall, these results demonstrate the redox non-innocence of **Im^{Ph2}NNO^{tBu}** and show that phenolate oxidation is the first electrochemical response observed upon subjecting **K-Im^{Ph2}NNO^{tBu}**, **2** and **4** to oxidative conditions. The thiolate ligand in **4** is slightly more difficult to oxidise than phenolate, which suggests that its soft nature may help create more covalent bonds with transition metals than the phenolic oxygen, thereby reducing its charge localisation and rendering it less prone to oxidation. Moreover, the 2,4-disubtitution of the phenolate group helps stabilise the phenoxyl radical and make its oxidation more thermodynamically favourable. The cyclic voltammogram of **1**, however, is more difficult to interpret due to the redox non-innocent nature of both the iron and the phenolate. A more definitive assignment of these electrochemical processes has been made by means of computational studies (*vide infra*).

3.2.7 Computational Studies

In order to better understand the electronic structure of complexes **1**, **2** and **4**, we resorted to density functional theory (DFT) calculations. For ease of comparison, we also performed DFT calculations on the theoretical monomeric structure of the ligand's potassium salt (**K-L^{opt}**), where a tripodal *N,N,O* ligand binding mode to the potassium cation has been imposed. Overall, the geometries (**1^{opt}**, **2^{opt}** and **4^{opt}**) obtained from the gas-phase geometry optimisations are consistent with the solid-state X-ray crystal structures. The electron density was therefore recalculated at the B3LYP and 6-311g(d,p) level of theory. For **K-L^{opt}**, **2^{opt}** and **4^{opt}**, the energies of the Kohn-Sham molecular orbitals (MOs) were extracted from these geometries. For **1^{opt}**, the *Multiwfn* program[66] was used to biorthogonalize the α and β molecular orbitals, using the Fock matrix from natural bond orbital (NBO) analysis in order to evaluate their energies (see Appendix G). The MO energies calculated for **K-L^{opt}**, **1^{opt}**, **2^{opt}** and **4^{opt}** are depicted schematically in Figure 21. The MO energies for **1^{opt}** have been ordered according to the average energy of the α and β orbitals generated upon biorthogonalization.

Our calculations show that the HOMO in **K-L^{opt}**, **2^{opt}** and **4^{opt}** is consistently localised on the phenolate group. This demonstrates clearly that **Im^{Ph2}NNO^{tBu}** has redox non-innocent character and supports our assignment of the first electrochemical oxidation of these compounds as being ligand-centred. The calculations also show that the HOMO in **K-L^{opt}** (–4.26 eV) is more energetically accessible than that in **2^{opt}** and **4^{opt}**, which reflects the electronic effect imparted by the more Lewis acidic zinc centre. In contrast, the HOMO in **1^{opt}** is localised on the iron centre and lies much higher in energy than for the other complexes. Indeed, the occupied MOs of highest energy in **1^{opt}** are calculated as being the five iron *d*-orbitals, four of which are singly occupied and one of which is filled. NBO calculations also show the natural spin density to be almost entirely localised on the iron centre (Figure 21). Together, these calculations indicate that the ferrous centre in **1** remains most prone to oxidation despite the redox-active nature of the phenolate group, and support our assignment of the first electrochemical oxidation in **1** to the Fe^{II}/Fe^{III} couple.

Computations also reveal that the HOMOs in **2^{opt}** and **4^{opt}** are similar in energy (–4.97 eV and –4.84 eV, respectively), thereby supporting the hypothesis that the oxidation potential of the supporting phenolate is not significantly affected by the exogenous ligand substitution on the zinc centre. Similarly, the presence of a thiolate ligand in **4^{opt}** has no effect on the energy of the LUMO compared to **2^{opt}**. We attribute this to the highly aromatic character of the LUMO, which is delocalised across the bis-imidazole ligand backbone in both cases and is, presumably, highly energetically inaccessible. Finally, the HOMO–1 in **4^{opt}** is calculated as being localised on the sulfur atom, which demonstrates that the thiolate is slightly less prone to oxidation than the phenolate group and supports our assignment of the sequential phenolate and thiophenolate oxidations during the electrochemical oxidation of **4**.

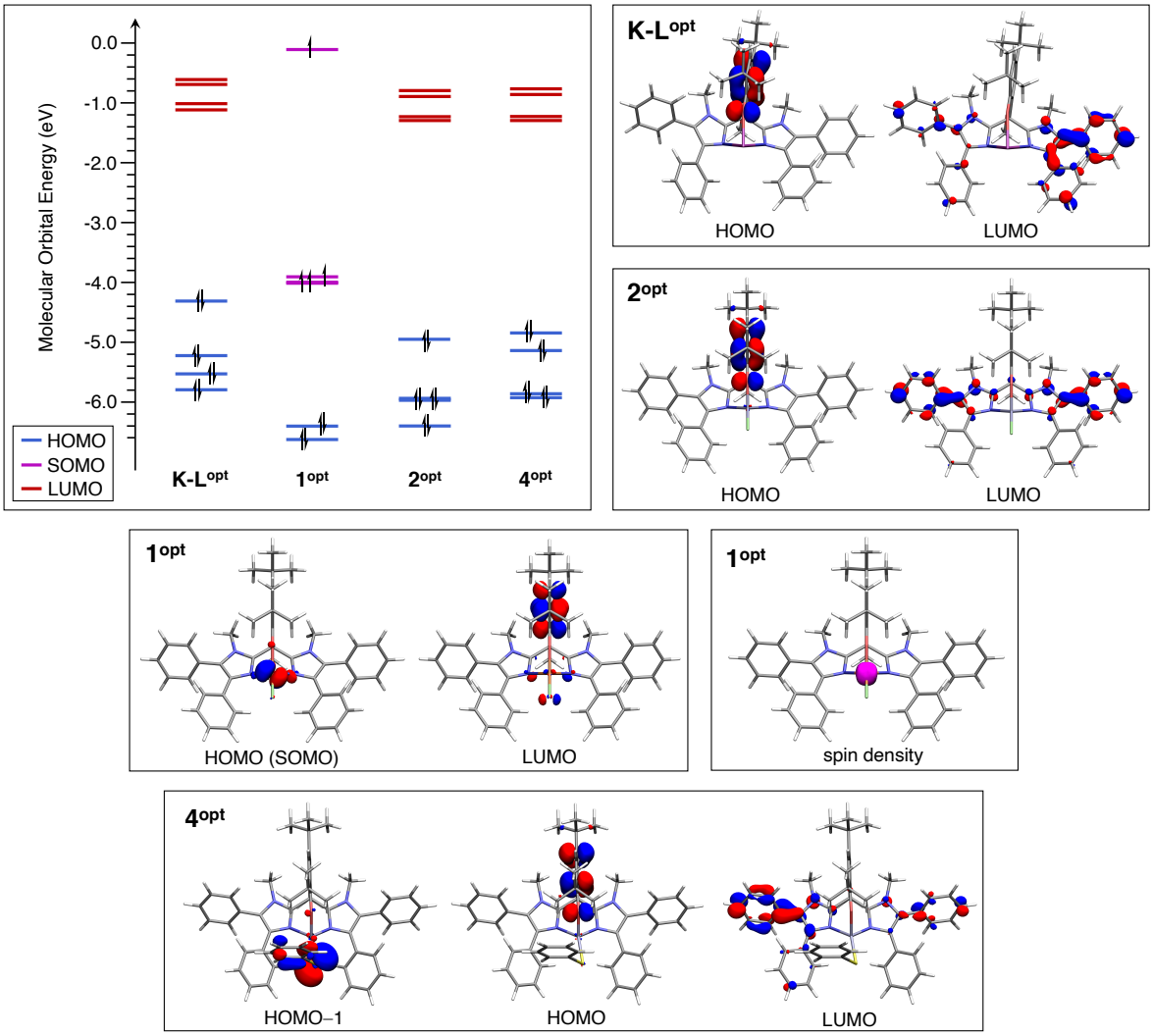

Figure 21. Calculated MO energies for **L-K**^{opt}, **1**^{opt}, **2**^{opt} and **4**^{opt}. LUMOs for **1**^{opt} are not depicted as they occur higher in energy than the given scale. Relevant MO diagrams for each complex are also provided (isosurface: ±0.05). HOMO: highest occupied molecular orbital; LUMO: lowest unoccupied MO; SOMO: singly occupied MO.

3.3 Conclusion

This work has shown that **Im^{Ph2}NNO^{tBu}** is a synthetically accessible, bioinspired ligand that can structurally model the 2H1C by means of a facial *N,N,O* binding motif. Reacting K-Im^{Ph2}NNO^{tBu} with iron(II) or zinc(II) chloride afforded the isostructural, tetrahedral complexes [Fe(Im^{Ph2}NNO^{tBu})(Cl)] (**1**) and [Zn(Im^{Ph2}NNO^{tBu})(Cl)] (**2**) in high yield. These complexes can be regarded as highly convenient synthons from which a range of biomimetic complexes bearing biorelevant co-ligands could be created. In this work, the substitutional lability of the chloride ligand in **2** was investigated using a simple thiophenolate ligand, producing complex [Zn(Im^{Ph2}NNO^{tBu})(SPh)] (**4**) in high yield. The low coordination number, single metal-sulfur bond and *N,N,O* supporting triad qualify **4** as an accurate (diamagnetic) structural model of the substrate-bound IPNS active site.

Detailed investigation of the solution state behaviour of complexes **1**, **2** and **4** showed that these retain their structural integrity in acetonitrile and dichloromethane solutions, while coordinating solvents of greater bulk such as THF and pyridine provoke structural rearrangements and lead to alternative bidentate (κ_2-*N,O*) and tridentate (κ_3-*N,O,O*) coordination modes of the supporting ligand. Having elucidated its sensitivities and solution-state dependencies, ligand **Im^{Ph2}NNO^{tBu}** has now been established as a robust platform from which to structurally model the 2H1C. Cyclic voltammetry studies, supported by DFT calculations, demonstrated the redox non-innocence of **Im^{Ph2}NNO^{tBu}** as phenolate oxidation was the first electrochemical response observed in **K-Im^{Ph2}NNO^{tBu}**, **2** and **4**. However, the initial electrochemical of **1** was shown to occur at the iron centre and not at the phenolate. Therefore, **1** is an interesting complex with which to investigate the spectroscopy and oxidative transformations of derivative iron complexes that model 2H1C-containing iron enzymes. Our group currently focuses on the development of mononuclear non-heme iron thiolate complexes that model the IPNS active site.

3.4 Author Contributions

E.C.M. and B.K.G. devised the project, designed experiments and wrote the manuscript. E.C.M., D.B., and A.J.V. performed experiments and analysed the data. M.L. performed X-ray crystal structure determinations. S.Y. provided Mössbauer data analysis. All authors provided comments on the experiments and manuscript during its preparation.

3.5 Experimental

3.5.1 Chemicals and Reagents

Unless stated otherwise, all reactions were performed under inert N_2 (g) atmosphere using standard Schlenk line and glovebox techniques and were stirred magnetically. The solvents acetonitrile, diethyl ether, and hexane were purified using an MBraun MB SPS-80 purification system. Dichloromethane and pyridine were dried over CaH_2 and distilled under inert N_2 (g) atmosphere before use. THF was dried over sodium benzophenone ketyl and distilled under inert N_2 (g) atmosphere before use. Pentane was dried using activated molecular sieves and was degassed using the freeze-pump-thaw technique. All other common solvents were degassed by bubbling N_2 (g) through them for a period of 30 mins prior to use and were stored over activated molecular sieves. Acetonitrile was filtered over activated neutral alumina before use to remove molecular sieve debris. All solvents were tested for water content by the Karl-Fischer titration or by ^{1}H NMR. Non-halogenated solvents were additionally tested with a standard purple solution of sodium benzophenone ketyl in THF to confirm effective oxygen and moisture removal. Deuterated solvents were purchased from the Cambridge Isotope Laboratory Incorporation (Cambridge, USA) and were degassed using the freeze-pump-thaw method and stored over activated molecular sieves. Deuterated acetonitrile was filtered over activated neutral alumina prior to use to remove molecular sieve debris. All reagents and starting materials were purchased from commercial sources and used without further purification, except when specified. Benzenethiol was converted to its respective sodium salt by treating it with an equimolar amount of NaH.

3.5.2 Physical Methods

NMR spectroscopy (^{1}H, ^{13}C{^{1}H}, ^{19}F, ^{1}H-^{13}C HSQC, 1D and 2D NOESY) was conducted using a 400 MHz Varian spectrometer or an Oxford NMR AS400 spectrometer. ^{1}H and ^{13}C{^{1}H} NMR chemical shifts are reported in the standard δ notation of part per million (ppm) and are referenced to residual solvent signals, as determined relative to $SiMe_4$.[67] ^{19}F NMR chemical shifts are reported in ppm and are externally referenced to an 85% aqueous solution of $CFCl_3$. Paramagnetic ^{1}H NMR spectra were recorded after having adjusted both the relaxation delay and acquisition time to 100 ms. IR spectroscopy was conducted using a PerkinElmer Spectrum Two FT-IR spectrometer. For air-sensitive compounds, a N_2 (g) flow was used. Peaks are annotated by (w), (m) and (s) to indicate weak, medium and strong signals, respectively. Absorption spectra were recorded using a Varian Cary 50 Scan spectrometer, using Quartz cuvettes with a path length of 1 cm, sealed with a Teflon cap. Unless otherwise stated, UV-vis solutions were prepared in the glovebox using dried and degassed solvents. The acquisition of the absorption spectra was performed with the PerkinElmer UV Winlab software. High resolution ESI-MS measurements were performed with a Waters LCT Premier XE KE317. All other ESI-MS measurements were performed with an Advion Expression CMS instrument. X-ray crystal structure determinations were performed on a Bruker Kappa ApexII diffractometer with sealed tube and Triumph monochromator (λ = 0.71073 Å) at a temperature of 150(2) K (see Appendix B for further details). CCDC 2035728-2035733 contain the supplementary crystallographic data for this work. These data can be obtained free of charge from The Cambridge Crystallographic Data Centre via *www.ccdc.cam.ac.uk/dats_request/cif.* Elemental analyses were performed at the Medac Ltd. laboratories in the UK.Mössbauer spectra (see Appendix F) were recorded on a conventional spectrometer with alternating constant acceleration of the g-source (^{57}Co/Rh, 1.8 GBq), which was kept at room temperature. The minimum experimental line width was 0.24 mm s^{-1} (full width at half-height). The sample temperature was maintained constant in an Oxford Instruments Variox cryostat. Isomer shifts are quoted relative to iron metal at 300 K. The zero-field spectra were simulated with Lorentzian doublets with the program *mf.SL* developed by Eckhard Bill. Electrochemical analysis was done by means of potentiodynamic measurements in which the working electrode potential is ramped linearly versus time (cyclic voltammetry (CV)). All measurements were performed in a nitrogen-filled glovebox on an IVIUM potentiostat/galvanostat using a 3-electrode setup. The setup included a glassy carbon (GC) working electrode, a platinum counter electrode, and a silver wire pseudo reference electrode. All electrodes were purchased from either BASi or Redox.me. The potentiostat was kept external to the glovebox, and the electrode leads were connected with a custom shielded electrode cable feedthrough. All scans were absolutely referenced to ferrocene, measured at the start and end of each measurement set. GC electrodes were 2 and 3 mm in diameter, with surfaces of 50.3 mm^2 and 113.1 mm^2, respectively. GC electrodes were polished with 0.3μm alumina powder deionized water slurries, rinsed with MeOH, water and dilute HCl solution (1 M), and ultrasonicated in pure deionized water for 30 sec, to remove residual polishing powder. The pseudo reference silver wire electrode and platinum wire counter electrode were rinsed with MeOH and water. All electrodes were dried in the ante chamber of the glovebox for at least 12 h. All electrodes were used directly in solution. Each working electrode was pre-treated with at least two cyclical scans from approximately +1.5 to −2.8 V at 200 mV/s in the corresponding solvent containing 0.1 M [*n*-Bu_4N][PF_6]. For all experiments, background voltammograms of the electrolyte were recorded at the respective scan rate. Solutions were gently shaken between experiments to renew the diffusion layer. No indication of solution resistance was observed during experiments, as described by McCarthy *et al,* which state that the solution resistance in the presence of >0.05 M electrolyte is estimated to be <30 mV in reduction potentials.[68]

3.5.3 Computational Methods

Density functional theory (DFT) calculations were conducted using the *Gaussian 16* software package.[69] Geometry optimisations use the B3LYP (Becke, three-parameter, Lee-Young-Parr) functional with the LanL2DZ basis set defined on Fe and Zn atoms and the 6-31g(d,p) basis set defined on all other atoms. The geometries were optimized without any symmetry restraints and empirical dispersion corrections were applied. The structures were confirmed as energy minima by the absence of any imaginary frequencies. Frequency analyses were performed on all geometries as the B3LYP/6-31g(d,p) level of theory. Single point energy calculations were re-run on all geometries as the B3LYP/6-311g(d,p) level of theory. For NBO (natural bond orbital) calculations, the *NBO06* program[70] up to the NLMO (natural localized molecular orbital) basis set at the B3LYP/6-311g(d,p) level of theory. Cube files for molecular orbitals were generated using the *Multiwfn* program.[66] Biorthogonalization of the α and β spin molecular orbitals for **2** were performed with the *Multiwfn* program, using the Fock matrix from the .47 NBO file generated for **2** (see Appendix G). Molecular orbitals were visualised with the *Visual Molecular Dynamics* program[71] using the respective molecular orbital cube file and defining the isosurface level as ±0.05.

3.5.4 Ligand Synthesis

Methyl 3,5-di-*tert*-butyl-2-hydroxybenzoate (LS1):[39] Methyl salicylate (25.6 mL g, 197 mmol), *tert*-butanol (47.7 mL, 500 mmol) and methanol (20.0 mL, 494 mmol) were combined in a 3-neck round-bottomed flask, equipped with a stirring bar (or a mechanical stirrer for larger-scale), a thermometer and a dropping funnel. The mixture was cooled using a salt-ice bath and stirred vigorously during the dropwise addition of 100 mL concentrated sulfuric acid, keeping the temperature between 0 °C and 5 °C. The mixture was subsequently left to stir 4 h at low temperature. The pale yellow acidic supernatant was removed (decanted), and the remaining white precipitate washed thoroughly with water to render the pH neutral. The solid was subsequently filtered and recrystallized from methanol. The title compound was isolated as a white crystalline solid by Büchner filtration in 51% yield (26.61 g, 100 mmol). **^{1}H NMR** (400 MHz, $CDCl_3$, 25 °C): δ = 11.35 (s, 1H, O*H*), 7.71 (d, 1H, *J* = 4 Hz, CH_{arom}) ppm, 7.53 (d, 1H, *J* = 4 Hz, CH_{arom}), 3.94 (*s*, 3H, OCH_3), 1.43 (s, 9H, C(CH_3)$_3$), 1.31 (s, 9H, C(CH_3)$_3$) ppm. **^{13}C{^{1}H} NMR** (101 MHz, $CDCl_3$, 25 °C): δ = 171.89, 159.13, 140.58, 137.34, 130.56, 123.75, 111.48, 52.32, 35.28, 34.41, 31.56, 29.54 ppm. **ESI-MS** (acetonitrile): m/z = 265.20 {[M+H]$^+$, calc. 265.18}. **IR** (ATR): υ = 3088 (w), 3011 (w), 2957 (m), 2907 (m), 2869 (m), 1807 (w), 1727 (w), 1669 (s), 1601 (m), 1472 (m), 1454 (m), 1438 (s), 1411 (m), 1389 (m), 1360 (s), 1332 (s), 1273 (s), 1244 (s), 1216 (s), 1196 (s), 1180 (s), 1116 (s), 1025 (w), 983 (m), 930 (w), 916 (w), 895 (m), 823 (m), 800 (s), 758 (s), 740 (m), 723 (s), 641 (m), 588 (w), 536 (w), 513 (w), 452 (m) cm^{-1}.

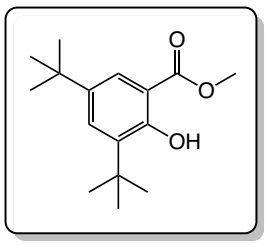

Methyl 3,5-di-*tert*-butyl-2-(methoxymethoxy)benzoate (LS2): NaH (2.44 g, 61 mmol, 60 weight% dispersion in mineral oil) was washed thoroughly with hexane and THF before being suspended in THF (300 mL). Next, **LS1** (10.6 g, 38 mmol) was added in portions at room temperature. The reaction was allowed to stir 1 h, during which time the reaction mixture became yellow-green in colour. Methoxy methyl chloride (5.18 g, 64 mmol) was added in one portion, and the mixture left to stir overnight at ambient temperature. Ice was added cautiously (gas and exotherm!) to quench the excess NaH, and EtOAc was used to extract the organics (3 x 200 mL). The organic washings were combined, washed

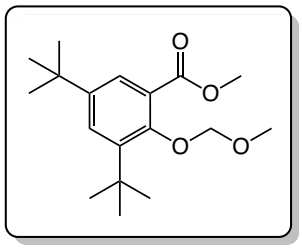

once with saturated NaCl solution (200 mL), then dried over $MgSO_4$, filtered and concentrated under vacuum, affording the product as a viscous yellow oil in 90% yield (10.8 mL, 11.2 g, 36 mmol). *Note:* this oil is too viscous to be distilled under vacuum (up to 200 °C); it is therefore advised to wash the NaH prior to use and purify by column chromatography using EtOAc as an eluent. The density is calculated as being 0.96 g/mol. **^{1}H NMR** (400 MHz, $CDCl_3$, 25 °C): δ = 7.50 (s, 2H, CH_{arom}), 4.97 (s, 2H, OCH_2), 3.87 (s, 3H, OCH_3), 3.55 (s, 3H, MOM-CH_3), 1.42 (s, 9H, C(CH_3)$_3$), 1.29 (s, 9H, C(CH_3)$_3$) ppm. **^{13}C{^{1}H} NMR** (101 MHz, $CDCl_3$, 25 °C): δ = 168.59, 153.68, 145.29, 142.45, 127.88, 125.50, 125.09, 100.88, 57.61, 52.15, 35.42, 34.55, 31.38, 30.75 ppm. **ESI-MS** (acetonitrile): m/z = 331.20 {[M+Na]$^+$, calc. 331.19}. **IR** (ATR): υ = 2954 (s), 2907 (m), 2871 (m), 1723 (s), 1599 (w), 1476 (m), 1435 (s), 1393 (m), 1363 (m), 1315 (m), 1267 (m), 1244 (s), 1221 (s), 1196 (s), 1159 9s), 1110 (m), 1073 (s), 1024 (w), 959 (s), 937 (s), 912 (m), 892 (m), 875 (m), 806 (m), 792 (m), 757 (w), 649 (w), 545 (w) 497 (w) cm^{-1}.

(3,5-di-*tert*-butyl-2-(methoxymethoxy)phenyl)bis(1-methyl-4,5-diphenyl-1*H*-imidazol-2-yl)-methanol (LS3): 1-methyl-4,5-diphenylimidazole (3.05 g, 13 mmol) was dissolved in THF (150 mL) at room temperature. *n*-BuLi (8.75 mL, 14 mmol, 1.6 M in hexanes) was added dropwise at –78 °C, causing the solution to turn dark orange. The mixture was allowed to stir for 1 h at room temperature before the dropwise addition of **LS2** (2.00 mL, 6.2 mmol). The mixture was stirred overnight and finally quenched by addition of saturated aqueous NH_4Cl solution (50 mL). EtOAc was used to extract the organics (50 mL) and the organic layer washed once with distilled water (100 mL), before being dried over $MgSO_4$, and concentrated to afford a crude yellow solid. The solid was washed by stirring vigorously in petroleum ether (80 mL), filtered and air-dried before being washed with several portions of petroleum ether. The title compound was isolated as a pale yellow fine powder (4.13 g, 5.5 mmol, 89 %). **^{1}H NMR** (400 MHz, $CDCl_3$, 25 °C): δ = 7.43 (m, 16H, CH_{arom}), 7.14 (m, 4H, CH_{arom}), 7.08 (m, 2H, CH_{arom}), 6.74 (s, 1H, O*H*), 6.61 (d, 1H, CH_{arom}), 5.08 (br. s, 2H, OCH_2O), 3.33 (br. s, 6H, NCH_3), 3.29 (s, 3H, OCH_3), 1.45 (s, 9H, C(CH_3)$_3$), 1.20 (s, 9H, C(CH_3)$_3$) ppm. **^{13}C{^{1}H} NMR** (101 MHz, $CDCl_3$, 25 °C): δ = 152.94, 146.01, 144.30, 135.89, 135.18, 131.75, 131.31, 129.17, 128.71, 128.05, 126.47, 125.94, 101.36, 57.19, 35.80, 34.56, 33.16, 31.46, 31.23 ppm. **ESI-MS** (acetonitrile): m/z = 745.4198 {[M+H]$^+$, calc. 745.4117}. **IR** (ATR): υ = 3338 (br. w), 3063 (w), 2950 (w), 2868 (w), 1602 (w), 1505 (w), 1476 (w), 1443 (w), 1434 (w), 1409 (w), 1389 (w), 1363 (w), 1323 (w), 1287 (w), 1264 (w), 1233 (w), 1193 (w), 1154 (m), 1135 (w), 1074 (m), 1065 (m), 1050 (w), 1026 (w), 984 (w), 953 (m), 931 (m), 913 (w), 903 (w), 883 (w), 835 (w), 820 (w), 783 (w), 773 (s), 697 (s), 649 (w), 626 (w), 617 (w), 607 (w), 526 (w), 491 (w), 471 (w), 430 (w) cm^{-1}.

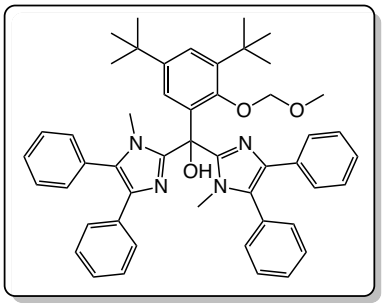

2,2'-((3,5-di-*tert*-butyl-2-(methoxymethoxy)phenyl)(metho-xy)methylene)bis(1-methyl-4,5-diphenyl-1*H*-imidazole) LS4: Sodium hydride (0.32 g, 8.0 mmol, 60 weight% dispersion in mineral oil) was suspended in THF (100 mL) and compound **LS3** (3.00 g, 4.0 mmol) was added in portions at room temperature, causing a colour change to yellow. The reaction was allowed to proceed for 2 h at room temperature, during which time a slow release of gas was observed and a white precipitate accumulated. After this time, iodomethane (0.50 mL, 9.80 mmol) was added dropwise, and the reaction allowed to stir overnight at room temperature. The reaction was quenched with saturated aqueous NH_4Cl solution (50 mL), and the organics extracted with EtOAc (2 x 100 mL) . The organic layer

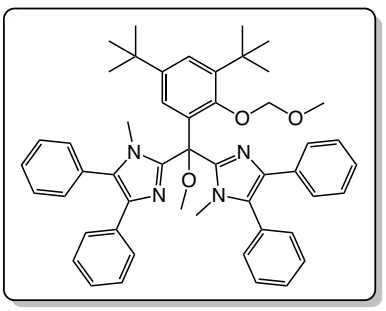

was washed once with distilled water (50 mL) before being dried over $MgSO_4$, and concentrated to yield a crude yellow solid. Vigorous stirring of the crude material in petroleum ether afforded a pale yellow powder, which was filtered and air-dried to afford **LS4** as an off-white powder in 82% yield (2.49 g, 3.3 mmol). **^{1}H NMR** (400 MHz, $CDCl_3$, 25 °C): δ = 7.45 (m, 11H, C*H*$_{arom}$), 7.34 (m, 4H, C*H*$_{arom}$), 7.13 (m, 4H, C*H*$_{arom}$), 7.06 (m, 2H, C*H*$_{arom}$), 5.16 (br. s, 2H, OC*H*$_2$), 3.69 (br. s, 3H, OC*H*$_3$), 3.34 (br. s, 6H, NC*H*$_3$), 3.18 (s, 3H, MOM-C*H*$_3$), 1.47 (s, 9H, C(C*H*$_3$)$_3$), 1.28 (s, 9H, C(C*H*$_3$)$_3$) ppm. **^{13}C{^{1}H} NMR** (101 MHz, $CDCl_3$, 25 °C): δ = 153.74, 144.35, 143.87, 135.37, 135.16, 131.83, 131.22, 130.81, 129.09, 128.62, 128.03, 126.42, 125.85, 125.44, 101.36, 56.98, 35.77, 34.75, 33.01, 31.61, 30.87 ppm. **ESI-MS** (acetonitrile): m/z = 759.4092 {$[M+H]^+$, calc. 759.4274}. **IR** (ATR): υ = 3061 (w), 2947 (w), 2824 (w), 1601 (w), 1505 (w), 1462 (w), 1444 (m), 1435 (w), 1392 (w), 1380 (w), 1362 (w), 1320 (w), 1303 (w), 1270 (w), 1231 (w), 1202 (w), 1158 (s), 1140 (m), 1079 (s), 1072 (s), 1057 (m), 1026 (m), 1002 (w), 959 (m), 951 (s), 931 (s), 901 (s) 85 (m), 383 (w), 820 (w), 773 (s), 745 (w), 727 (m), 695 (s), 686 (m), 649 (w), 625 (w), 617 (w), 593 (w), 528 (w), 502 (w), 474 (w), 461 (w), 427 (w) cm^{-1}.

H-Im^{Ph2}NNO^{tBu}: Compound **LS4** (6.45 g, 8.5 mmol) was dissolved in an acidified MeOH solution (1:8 HCl (15 %)/MeOH, 125 mL) and allowed to stir for 1 h under reflux, monitoring the reaction closely by NMR. The resulting mixture was rendered alkaline (pH ~8) with 1 M NaOH solution, resulting in the precipitation of a dark red solid. The organics were extracted into EtOAc (2 x 250 mL) and the solvent removed under reduced pressure, affording a dark red foamy solid. The solid was dissolved in petroleum ether (400 mL) and the dark red solution was vigorously stirred overnight, which lead to the precipitation of an off-white powder. The solid was collected by Büchner filtration and was washed with portions of cold petroleum ether. The title compound was obtained as an off-white solid (4.30 g, 6.0 mmol, 71 %). **^{1}H NMR** (400 MHz, $CDCl_3$, 25 °C): δ = 9.31 (*br. s*, 1H, -O*H*), 7.49 (m, 10H, *H*$_{arom}$), 7.37 (m, 4H, *H*$_{arom}$), 7.32 (d, 1H, *H*$_{arom}$), 7.19 (m, 4H, *H*$_{arom}$), 7.12 (m, 2H, *H*$_{arom}$), 3.65 (s, 3H, OC*H*$_3$), 3.27 (s, 6H, NC*H*$_3$), 1.44 (s, 9H, C(C*H*$_3$)$_3$), 1.24 (s, 9H, C(C*H*$_3$)$_3$) ppm. **^{13}C{^{1}H} NMR** (101 MHz, $CDCl_3$, 25 °C): δ = 153.22, 145.28, 139.82, 138.36, 135.60, 134.79, 131.30, 131.26, 129.17, 128.87, 126.67, 126.25, 124.29, 124.23, 122.32, 83.43, 54.64, 35.51, 34.29, 32.97, 31.70, 29.68 ppm. **ESI-MS** (acetonitrile): m/z = 715.3909 {$[M+H]^+$, calc. 715.4012}. **IR** (ATR): υ = 3388 (w), 3058 (w), 2953 (w), 2868 (w), 1738 (w), 1603 (w), 1505 (w), 1476 (m), 1443 (m), 1389 (m), 1361 (m), 1319 (w), 1296 (w), 1228 (m), 1156 (w), 1132 (w), 1056 (m), 1026 (m), 1000 (w), 971 (m), 932 (m), 916 (w), 886 (m), 834 (w), 818 (w), 781 (m), 773 (s), 742 (m), 718 (m), 694 (s), 649 (m), 609 (w), 589 (w), 524 (w), 460 (w) cm^{-1}.

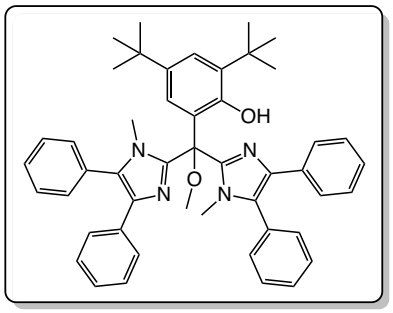

K-Im^{Ph2}NNO^{tBu}: Ligand **H-Im^{Ph2}NNO^{tBu}** (1.77 g, 2.48 mmol) was dissolved in THF (40 mL) and stirred vigorously during the addition of KH (0.12 g, 2.99 mmol). Instant bubble formation was observed that indicated H_2 (g) formation. Over the course of 3 h the solution became dark yellow in colour. The mixture was subsequently filtered to remove excess KH and THF was removed under reduced pressure, affording a crude yellow solid. The solid was then washed twice by vigorously stirring in hexane (150 mL). The hexane washings were discarded, and the resulting white solid dried under vacuum, affording the ligand salt as a free-flowing white powder in 92% yield (1.79 g, 2.38 mmol). *Note:* purity of the sample determined by NMR and residual solvent THF and hexane content was quantified by ^{1}H NMR. The molecular weight of the ligand salt adjusted appropriately for use in

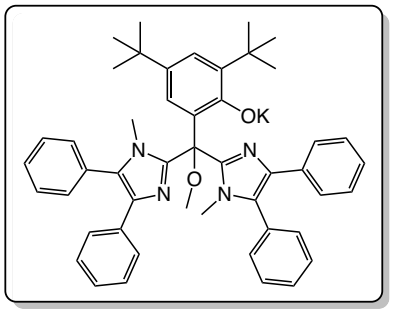

subsequent complexation reactions. **^{1}H NMR** (400 MHz, CD_3CN, 25 °C): δ = 7.50 (m, 6H, H_{arom}), 7.43 (d, 4H, J = 8 Hz, H_{arom}), 7.36 (d, 4H, J = 8 Hz, H_{arom}), 7.16 (t, 4H, J = 8 Hz, H_{arom}), 7.09 (t, 2H, J = 8 Hz, H_{arom}), 7.00 (br. s, 1H, H_{arom}), 6.63 (br. s, 1H, H_{arom}), 3.64 (br. s, 3H, OCH_3), 3.29 (br. s, 6H, NCH_3), 1.35 (s, 9H, $C(CH_3)_3$), 1.13 (s, 9H, $C(CH_3)_3$) ppm. **IR** (ATR): υ = 3059 (w), 3029 (w), 2947 (m), 2904 (w), 2865 (w), 1952 (w), 1887 (w), 1809 (w), 1602 (m), 1504 (m), 1462 (m), 1431 (s), 1379 (m), 1359 (m), 1279 (w), 1257 (w), 1235 (w), 1201 (w), 1138 (w), 1071 (m), 1048 (m), 1026 (m), 1000 (w), 968 (m), 928 (m), 914 (m), 884 (w), 831 (w), 795 (w), 773 (s), 1743 (w), 748 (m), 728 (m), 697 (s), 649 (w), 629 (w), 613 (w), 582 (w), 525 (w), 471 (w) cm^{-1}.

3.5.5 Complex Synthesis

[Fe(Im^{Ph2}NNO^{tBu})(Cl)] (1): A solution of $FeCl_2$•1.5THF (0.046 g, 0.196 mmol) in CH_3CN (4 mL) was added dropwise to a suspension of **K-Im^{Ph2}NNO^{tBu}** (0.152 g, 0.193 mmol) in CH_3CN (12 mL). The mixture was allowed to stir for 2 h, during which time the ligand salt visibly dissolved and the mixture developed a slight brown colour. A fine white precipitate also formed over the course of the reaction. The mixture was filtered and the filtrate concentrated under vacuum. The residual pale brown solid was washed with hexane (3 x 8 mL) and dried under vacuum. The title complex was obtained as cream-coloured powder in 97% yield (0.151 g, 0.187 mmol). Pale brown needles suitable for X-ray analysis were obtained by slow vapour diffusion of hexane into a THF solution of the complex at room temperature. **^{1}H NMR** (400 MHz, CD_3CN, 25 °C): δ = 57.73, 54.68, 51.30, 49.14, 42.94, 36.53, 33.68, 23.64, 9.84, 7.59, 7.17, 6.85, 5.41, 4.65, 4.22, 4.12, 3.65, 2.29 ppm. Solution state magnetic susceptibility (Evans method, 1% TMS in CD_3CN): μ_{eff} = 4.50 μ_B. **UV-vis** (CH_3CN, ε [$dm^3\ mol^{-1}\ cm^{-1}$]): λ_{max} = 375 (547), 500 (54) nm. **^{57}Fe Mössbauer** (80 K): δ = 0.94 mm s^{-1}, $|\Delta E_Q|$ = 2.58 mm s^{-1}. **IR** (ATR): υ = 3057 (w), 2956 (w), 2905 (w), 2867 (w), 1656 (w), 1603 (w), 1505 (w), 1475 (m), 1467 (m), 1438 (m), 1412 (w), 1391 (w), 1360 (w), 1303 (m), 1261 (m), 1235 (w), 1201 (w), 1179 (w), 1157 (w), 1132 (w), 1074 (m), 1055 (m), 1024 (m), 1004 (m), 978 (w), 928 (w), 915 (w), 899 (w), 887 (w), 788 (s), 772 (m), 748 (m), 732 (m), 695 (s), 6498 (w), 610 (w), 587 (w), 542 (m), 513 (w), 475 (w) cm^{-1}. **E.A.** (Formula: $C_{48}H_{49}ClN_4O_2Fe$, M_w: 805.24 g mol^{-1}): calc. C 71.60, H 6.13, N 6.96; found C 71.68, H 6.17, N 6.55.

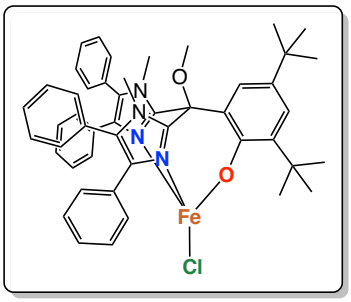

[Zn(Im^{Ph2}NNO^{tBu})(Cl)] (2): A solution of $ZnCl_2$ (0.028 mg, 0.208 mmol) in CH_3CN (3 mL) was added dropwise to a suspension of **K-Im^{Ph2}NNO^{tBu}** (0.172 g, 0.218 mmol) in CH_3CN (12 mL). The mixture was stirred 2 h, during which time the ligand salt visibly dissolved and pale brown solution formed. A fine white precipitate also developed over the course of the reaction. The mixture was filtered and the solution concentrated under vacuum. As the solution cooled, small colourless crystals were seen to develop. The residual solid was washed with hexane (3 x 8 mL) and dried under vacuum. The title complex was obtained as a white solid in 94% yield (0.160 g, 0.196 mmol). Colourless needles suitable for X-ray diffraction were obtained by slow diffusion of hexane into a THF solution of the complex at room temperature. **^{1}H NMR** (400 MHz, CD_3CN, 25 °C): δ = 7.73 (d, 1H, J = 4 Hz, H_{phen}^1), 7.50 (m, 6H, CH_{arom}), 7.40 (m, 4H, CH_{arom}), 7.33 (m, 4H, CH_{arom}), 7.27 (m, 6H, CH_{arom}), 7.22 (d, 1H, J = 4 Hz, H_{phen}^2), 3.51 (s, 6H, NCH_3), 3.45 (s, 3H, OCH_3), 1.28 (s, 18H, $C(CH_3)_3$) ppm. **^{13}C{^{1}H} NMR** (101 MHz, CD_3CN, 25 °C): δ = 162.08, 148.05, 140.60, 136.12, 134.07, 133.09, 132.39, 132.08, 131.99, 130.54, 130.14, 130.01,

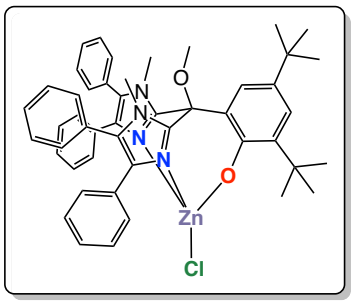

129.77, 129.48, 129.15, 129.10, 128.83, 127.38, 127.28, 125.35, 121.44, 119.69, 81.49, 53.86, 36.06, 34.72, 34.45, 33.55, 32.07, 31.77, 30.07, 29.80 ppm. **IR** (ATR): υ = 3057 (w), 2952 (m), 2866 (w), 1662 (w), 1603 (w), 1586 (w), 1506 (w), 1476 (m), 1468 (m), 1440 (s), 1411 (w), 1393 (w), 1360 (w), 1312 (m), 1262 (m), 1234 (w), 1201 (w), 1157 (w), 1133 (w), 1075 (m), 1056 (m), 1025 (m), 1005 (m), 979 (w), 928 (w), 915 (w), 899 (w), 887 (w), 838 (m), 790 (s), 773 (m), 746 (w), 734 (w), 700 (s), 648 (w), 612 (w), 539 (w), 525 (w) cm^{-1}. **E.A.** (Formula: $C_{48}H_{49}ClN_4O_2Zn$, M_w: 814.78 g mol^{-1}): calc. C 70.76, H 6.06, N 6.88; found C 70.67, H 6.38, N 6.76.

[Zn(Im^{Ph2}NNO^{tBu})(SPh)] (4): A suspension of NaSPh (10.4 mg, 57.0 µmol) in CH_2Cl_2 (4 mL) was added dropwise to a stirring solution of **2** (44.5 mg, 54.6 µmol) in CH_2Cl_2 (12 mL). The mixture was allowed to stir for 2.5 h, during which time the mixture turned pale yellow in colour and became slightly cloudy. The mixture was filtered and the filtrate concentrated under vacuum. The residual solid was washed by stirring vigorously in hexane (2 x 8 mL) and dried under vacuum, affording the title complex as a free-flowing white powder in 91% yield (46 mg, 52.1 µmol). **^{1}H NMR** (400 MHz, CD_3CN, 25 °C): δ = 7.75 (d, 1H, J = 4 Hz, H_{phen}^1), 7.48 (m, 6H, CH_{arom}), 7.31 (m, 8H, CH_{arom}), 7.22 (d, 1H, J = 4 Hz, H_{phen}^2), 7.13 (m, 6H, CH_{arom}), 6.90 (m, 2H, H_{SPh}^3), 6.71 (m, 3H, $H_{SPh}^{4,5}$), 3.51 (s, 6H, NCH_3), 3.44 (s, 3H, OCH_3), 1.29 (s, 9H, *ortho*-C(CH_3)$_3$), 1.23 (s, 9H, *para*-C(CH_3)$_3$) ppm. **^{13}C{^{1}H} NMR** (101 MHz, CD_3CN, 25 °C): δ = 148.16, 142.61, 140.51, 136.43, 134.03, 133.18, 132.88, 132.39, 132.20, 130.46, 129.98, 129.68, 129.35, 128.98, 128.47, 128.30, 125.22, 122.58, 122.17, 119.66, 53.82, 35.97, 34.71, 34.30, 32.09, 29.90 ppm. **IR** (ATR): υ = 3054 (w), 2950 (w), 2904 (w), 2866 (w), 1603 (w), 1579 (w), 1505 (w), 1475 (m), 1466 (m), 1436 (s), 1410 (w), 1392 (w), 1360 (w), 1304 (m), 1262 (m), 1234 (w), 1201 (w), 1183 (w), 1157 (w), 1133 (w), 1074 (s), 1055 (m), 1025 (m), 1004 (m), 978 (w), 928 (m), 915 (m), 896 (w), 886 (m), 836 (m), 789 (s), 772 (m), 735 (s), 694 (s), 646 (w), 612 (w), 585 (w), 538 (m), 524 (w), 514 (w), 476 (w) cm^{-1}. **E.A.** (Formula: $C_{54}H_{54}N_4O_2SZn$, M_w: 888.49 g mol^{-1}): calc. C 73.00, H 6.13, N 6.31; found C 73.14, H 6.42, N 5.93.

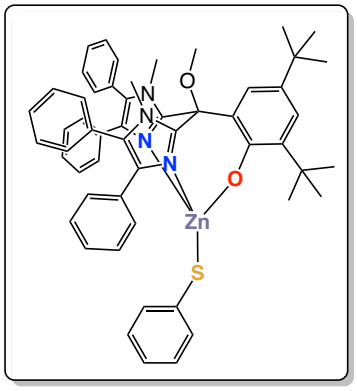

3.6 References and Notes

(1) Lange, S. J.; Que, L. *Curr. Opin. Chem. Biol.* **1998**, *2*, 159–172.
(2) Hegg, E. L.; Que, L. *Eur. J. Biochem.* **1997**, *250*, 625–629.
(3) Que, L. J. *Nat. Struct. Biol.* **2000**, *7*, 182–184.
(4) Costas, M.; Mehn, M. P.; Jensen, M. P.; Que Jr., L. *Chem. Rev.* **2004**, *104*, 939–986.
(5) Bruijnincx, P. C. A.; van Koten, G.; Klein Gebbink, R. J. M. *Chem. Soc. Rev.* **2008**, *37*, 2716–2744.
(6) Ye, S.; Wu, X.; Wei, L.; Tang, D.; Sun, P.; Bartlam, M.; Rao, Z. *J. Biol. Chem.* **2007**, *282*, 3391–3402.
(7) Tamanaha, E.; Zhang, B.; Guo, Y.; Chang, W.; Barr, E. W.; Xing, G.; St. Clair, J.; Ye, S.; Neese, F.; Bollinger, J. M.; Krebs, C. *J. Am. Chem. Soc.* **2016**, *138*, 8862–8874.
(8) Roach, P. L.; Clifton, I. J.; Hensgens, C. M. H.; Shibata, N.; Schofield, C. J.; Hajdu, J.; Baldwin, J. E. *Nature* **1997**, *387*, 827–830.
(9) Peck, S. C.; van der Donk, W. A. *J. Biol. Inorg. Chem.* **2016**, 1–14.
(10) Blaesi, E. J.; Gardner, J. D.; Fox, B. G.; Brunold, T. C. *Biochemistry* **2013**, *52*, 6040–6051.
(11) Blaesi, E. J.; Fox, B. G.; Brunold, T. C. *Biochemistry* **2015**, *54*, 2874–2884.
(12) Park, H.; Lee, D. *Chem. - A Eur. J.* **2020**, *26*, 1–12.
(13) Sheet, D.; Paine, T. K. *Chem. Sci.* **2016**, *7*, 5322–5331.
(14) Rohde, J.-U.; Stubna, A.; Bominaar, E. L.; Münck, E.; Nam, W.; Que, L. J. *Inorg. Chem.* **2006**, *45*, 6435–6445.
(15) Rohde, J.-U.; In, J.-H.; Lim, M. H.; Brennessel, W. W.; Bukowski, M. R.; Stubna, A.; Münck, E.;

Nam, W.; Que, L. *Science (80-.).* **2003**, *299*, 1037–1039.
(16) Andris, E.; Jašík, J.; Gómez, L.; Costas, M.; Roithová, J. *Angew. Chemie* **2016**, *128*, 3701–3705.
(17) Dantignana, V.; Serrano-Plana, J.; Draksharapu, A.; Magallón, C.; Banerjee, S.; Fan, R.; Gamba, I.; Guo, Y.; Que, L.; Costas, M.; Company, A. *J. Am. Chem. Soc.* **2019**, *141*, 15078–15091.
(18) Chen, J.; Lutz, M.; Milan, M.; Costas, M.; Otte, M.; Klein Gebbink, R. J. M. *Adv. Synth. Catal.* **2017**, *359*, 2590–2595.
(19) Singh, R.; Ganguly, G.; Malinkin, S. O.; Demeshko, S.; Meyer, F.; Nordlander, E.; Paine, T. K. *Inorg. Chem.* **2019**, *58*, 1862–1876.
(20) McDonald, A. R.; Que, L. *Coord. Chem. Rev.* **2013**, *257*, 414–428.
(21) Krebs, C.; Galonić Fujimori, D.; Walsh, C. T.; Bollinger, J. M. *Acc. Chem. Res.* **2007**, *40*, 484–492.
(22) Monkcom, E. C.; Ghosh, P.; Folkertsma, E.; Negenman, H. A.; Lutz, M.; Klein Gebbink, R. J. M. *Chim. Int. J. Chem.* **2020**, *74*, 450–466. (Chapter 6 of this thesis).
(23) Bruijnincx, P. C. A.; Lutz, M.; Spek, A. L.; van Faassen, E. E.; Weckhuysen, B. M.; van Koten, G.; Klein Gebbink, R. J. M. *Eur. J. Inorg. Chem.* **2005**, *2005*, 779–787.
(24) Bruijnincx, P. C. A.; Lutz, M.; Spek, A. L.; Hagen, W. R.; van Koten, G.; Klein Gebbink, R. J. M. *Inorg. Chem.* **2007**, *46*, 8391–8402.
(25) Beck, A.; Weibert, B.; Burzlaff, N. *Eur. J. Inorg. Chem.* **2001**, 521–527.
(26) Bruijnincx, P. C. A.; Lutz, M.; den Breejen, J. P.; Spek, A. L.; van Koten, G.; Klein Gebbink, R. J. M. *JBIC J. Biol. Inorg. Chem.* **2007**, *12*, 1181–1196.
(27) Higgs, T. C.; Carrano, C. J. *Inorg. Chem.* **1997**, *36*, 298–306.
(28) Strianese, M.; Milione, S.; Bertolasi, V.; Pellecchia, C.; Grassi, A. *Inorg. Chem.* **2011**, *50*, 900–910.
(29) Beck, A.; Barth, A.; Hübner, E.; Burzlaff, N. *Inorg. Chem.* **2003**, *42*, 7182–7188.
(30) Folkertsma, E.; de Waard, E. F.; Korpershoek, G.; van Schaik, A. J.; Solozabal Mirón, N.; Borrmann, M.; Nijsse, S.; Moelands, M. A. H.; Lutz, M.; Otte, M.; Moret, M.-E.; Klein Gebbink, R. J. M. *Eur. J. Inorg. Chem.* **2016**, *2016*, 1319–1332.
(31) Oldenburg, P. D.; Ke, C.-Y.; Tipton, A. A.; Shteinman, A. A.; Que, L. *Angew. Chemie Int. Ed.* **2006**, *45*, 7975–7978.
(32) Bruijnincx, P. C. A.; Lutz, M.; Spek, A. L.; Hagen, W. R.; Weckhuysen, B. M.; van Koten, G.; Klein Gebbink, R. J. M. *J. Am. Chem. Soc.* **2007**, *129*, 2275–2286.
(33) Hegelmann, I.; Beck, A.; Eichhorn, C.; Weibert, B.; Burzlaff, N. *Eur. J. Inorg. Chem.* **2003**, *2003*, 339–347.
(34) Hammes, B. S.; Carrano, C. J. *Inorg. Chem.* **1999**, *38*, 3562–3568.
(35) Schofield, A. D.; Barros, M. L.; Cushion, M. G.; Schwarz, A. D.; Mountford, P. *Dalt. Trans.* **2009**, *0*, 85–96.
(36) Monkcom, E. C.; Negenman, H. A.; Masferrer-Rius, E.; Lutz, M.; Ye, S.; Bill, E.; Klein Gebbink, R. J. M. *Eur. J. Inorg. Chem.* **2022**. (Chapter 2 of this thesis).
(37) Groysman, S.; Sergeeva, E.; Goldberg, I.; Kol, M. *Eur. J. Inorg. Chem.* **2006**, *2006*, 2739–2745.
(38) Jameson, D. L.; Hilgen, S. E.; Hummel, C. E.; Pichla, S. L. *Tetrahedron Lett.* **1989**, *30*, 1609–1612.
(39) Jiménez, C. A.; Belmar, J. B. *Synth. Commun.* **2007**, *37*, 2391–2397.
(40) Valegård, K.; van Scheltinga, A. C. T.; Lloyd, M. D.; Hara, T.; Ramaswamy, S.; Perrakis, A.; Thompson, A.; Lee, H.-J.; Baldwin, J. E.; Schofield, C. J.; Hajdu, J.; Andersson, I. *Nature* **1998**, *394*, 805–809.
(41) Uragami, Y.; Senda, T.; Sugimoto, K.; Sato, N.; Nagarajan, V.; Masai, E.; Fukuda, M.; Mitsui, Y. *J. Inorg. Biochem.* **2001**, *83*, 269–279.
(42) Moelands, M. A. H.; Nijsse, S.; Folkertsma, E.; de Bruin, B.; Lutz, M.; Spek, A. L.; Klein Gebbink, R. J. M. *Inorg. Chem.* **2013**, *52*, 7394–7410.
(43) Falivene, L.; Cao, Z.; Petta, A.; Serra, L.; Poater, A.; Oliva, R.; Scarano, V.; Cavallo, L. *Nat. Chem.* **2019**, *11*, 872–879.
(44) Steffen, W. L.; Palenik, G. J. *Acta Crystallogr. Sect. B* **1976**, *32*, 298–300.
(45) Long, G. J.; Clarke, P. J. *Inorg. Chem.* **1978**, *17*, 1394–1401.
(46) Ton, T. M. U.; Tejo, C.; Tania, S.; Chang, J. W. W.; Chan, P. W. H. *J. Org. Chem.* **2011**, *76*, 4894–4904.
(47) Smith, J. N.; Shirin, Z.; Carrano, C. J. *J. Am. Chem. Soc.* **2003**, *125*, 868–869.
(48) Chiou, S.-J.; Riordan, C. G.; Rheingold, A. L. *Proc. Natl. Acad. Sci. U. S. A.* **2003**, *100*, 3695–3700.
(49) Notni, J.; Görls, H.; Anders, E. *Eur. J. Inorg. Chem.* **2006**, *2006*, 1444–1455.
(50) Chiou, S.-J.; Innocent, J.; Riordan, C. G.; Lam, K.-C.; Liable-Sands, L.; Rheingold, A. L. *Inorg. Chem.* **2000**, *39*, 4347–4353.

(51) Brand, U.; Rombach, M.; Seebacher, J.; Heinrich, V. *Inorg. Chem.* **2001**, *40*, 6151–6157.
(52) Ibrahim, M. M.; Seebacher, J.; Steinfeld, G.; Vahrenkamp, H. *Inorg. Chem.* **2005**, *44*, 8531–8538.
(53) Wilker, J. J.; Lippard, S. J. *J. Am. Chem. Soc.* **1995**, *117*, 8682–8683.
(54) Song, X.-W.; Guo, C.; Chen, C.-N. *Zeitschrift für Anorg. und Allg. Chemie* **2017**, *643*, 2110–2115.
(55) Dean, R. K.; Fowler, C. I.; Hasan, K.; Kerman, K.; Kwong, P.; Trudel, S.; Leznoff, D. B.; Kraatz, H.-B.; Dawe, L. N.; Kozak, C. M. *Dalt. Trans.* **2012**, *41*, 4806.
(56) Enache, T. A.; Oliveira-Brett, A. M. *J. Electroanal. Chem.* **2011**, *655*, 9–16.
(57) Tan, Y. S.; Chen, S.; Hong, W. M.; Kan, J. M.; Kwek, E. S. H.; Lim, S. Y.; Lim, Z. H.; Tessensohn, M. E.; Zhang, Y.; Webster, R. D. *Phys. Chem. Chem. Phys.* **2011**, *13*, 12745.
(58) Zabik, N. L.; Virca, C. N.; McCormick, T. M.; Martic-Milne, S. *J. Phys. Chem. B* **2016**, *120*, 8914–8924.
(59) Itoh, S.; Taki, M.; Kumei, H.; Takayama, S.; Nagatomo, S.; Kitagawa, T.; Sakurada, N.; Arakawa, R.; Fukuzumi, S. *Inorg. Chem.* **2000**, *39*, 3708–3711.
(60) Halfen, J. A.; Jazdzewski, B. A.; Mahapatra, S.; Berreau, L. M.; Wilkinson, E. C.; Que, L. J.; Tolman, W. B. *J. Am. Chem. Soc.* **1997**, *119*, 8217–8227.
(61) Wing-Wah Yam, V.; Pui, Y.-L.; Cheung, K.-K.; Zhu, N. *New J. Chem.* **2002**, *26*, 536–542.
(62) Adam, B.; Bill, E.; Bothe, E.; Goerdt, B.; Haselhorst, G.; Hildenbrand, K.; Sokolowski, A.; Steenken, S.; Weyhermüller, T.; Wieghardt, K. *Chem. - A Eur. J.* **1997**, *3*, 308–319.
(63) Gordon, J. B.; Vilbert, A. C.; DiMucci, I. M.; MacMillan, S. N.; Lancaster, K. M.; Moënne-Loccoz, P.; Goldberg, D. P. *J. Am. Chem. Soc.* **2019**, *141*, 17533–17547.
(64) Wang, D.; Ray, K.; Collins, M. J.; Farquhar, E. R.; Frisch, J. R.; Gómez, L.; Jackson, T. A.; Kerscher, M.; Waleska, A.; Comba, P.; Costas, M.; Que, L. *Chem. Sci.* **2013**, *4*, 282–291.
(65) Yu, T.; Au, V. K.-M.; Tsang, D. P.-K.; Chan, M.-Y.; Yam, V. W.-W. *Dalt. Trans.* **2015**, *44*, 18983–18992.
(66) Lu, T.; Chen, F. *J. Comput. Chem.* **2012**, *33*, 580–592.
(67) Fulmer, G. R.; Miller, A. J. M.; Sherden, N. H.; Gottlieb, H. E.; Nudelman, A.; Stoltz, B. M.; Bercaw, J. E.; Goldberg, K. I. *Organometallics* **2010**, *29*, 2176–2179.
(68) McCarthy, B. D.; Martin, D. J.; Rountree, E. S.; Ullman, A. C.; Dempsey, J. L. *Inorg. Chem.* **2014**, *53*, 8350–8361.
(69) Gaussian 16, Revision C.01; Frisch, M. J.; Trucks, G. W.; Schlegel, H. B.; Scuseria, G. E.; Robb, M. A.; Cheeseman, J. R.; Scalmani, G.; Barone, V.; Petersson, G. A.; Nakatsuji, H.; Li, X.; Caricato, M.; Marenich, A. V.; Bloino, J.; Janesko, B. G.; Gomperts, R.; Mennucci, B.; Hratchian, H. P.; Ortiz, J. V.; Izmaylov, A. F.; Sonnenberg, J. L.; Williams-Young, D.; Ding, F.; Lipparini, F.; Egidi, F.; Goings, J.; Peng, B.; Petrone, A.; Henderson, T.; Ranasinghe, D.; Zakrzewski, V. G.; Gao, J.; Rega, N.; Zheng, G.; Liang, W.; Hada, M.; Ehara, M.; Toyota, K.; Fukuda, R.; Hasegawa, J.; Ishida, M.; Nakajima, T.; Honda, Y.; Kitao, O.; Nakai, H.; Vreven, T.; Throssell, K.; Montgomery, J. A. J.; Peralta, J. E.; Ogliaro, F.; Bearpark, M. J.; Heyd, J. J.; Brothers, E. N.; Kudin, K. N.; Staroverov, V. N.; Keith, T. A.; Kobayashi, R.; Normand, J.; Raghavachari, K.; Rendell, A. P.; Burant, J. C.; Iyengar, S. S.; Tomasi, J.; Cossi, M.; Millam, J. M.; Klene, M.; Adamo, C.; Cammi, R.; Ochterski, J. W.; Martin, R. L.; Morokuma, K.; Farkas, O.; Foresman, J. B.; Fox, D. J. Gaussian 16, Revision C.01, 2016.
(70) Glendening, E. D.; Landis, C. R.; Weinhold, F. *J. Comput. Chem.* **2013**, *34*, 1429–1437.
(71) Humphrey, W.; Dalke, A.; Schulten, K. *J. Mol. Graph.* **1996**, *14*, 33–38.

Chapter 4

A Family of *N,N,O*-Bound Iron and Zinc Thiolate Complexes that Structurally Model IPNS

Abstract

We present the synthesis, structure and reactivity of a family of mononuclear, tetracoordinate iron and zinc thiolate complexes, [M(Im^{Ph2}NNO^{tBu})(SR)] (M = Fe, Zn; R = ^{t}Bu, Bn, Ph, Mes, *p*-OMe-Ph, *p*-CF_3-Ph). These complexes model the substrate-bound isopenicillin N synthase (IPNS) active site to an unprecedented degree of structural fidelity, thanks to their tridentate, anionic *N,N,O* supporting ligand (**Im^{Ph2}NNO^{tBu}**) that mimics the 2-His-1-Carboxylate facial triad (2H1C). X-ray crystal structures and solid-state Mössbauer parameters show that the M–S bond lengths and the sulfur-to-metal charge transfer vary according to the approximate donicity and steric bulk of the thiolate co-ligands. Using NMR spectroscopy, we show that the complexes have a well-defined, mononuclear structure in solution. Electrochemical studies by cyclic voltammetry (CV) show that the first oxidation occurs on the iron centre for all iron thiolate complexes, and that the Fe^{III}/Fe^{II} redox potential is tuned by the donicity of the thiolate ligand. We investigate the reactivity of the iron thiolate complexes to different oxidants, including O_2, NO, PhIO and $[Ph_3C]PF_6$. In all cases, we observe that the iron is oxidised to its ferric form, with sulfonate formation during the reactions with O_2 and PhIO. We also observe that the **Im^{Ph2}NNO^{tBu}** ligand is susceptible to oxidative degradation, through either methyl- or methoxy-cleavage at the ligand backbone.

E. C. Monkcom, A. J. de Vries, D. de Bruin, M. Lutz, G. Tripodi, J. Roithová, S. Ye, E. Bill, R. J. M. Klein Gebbink, *manuscript in preparation*

4.1 Introduction

Penicillins were first discovered in 1929 by Sir Alexander Fleming, and they have since become one of the most important types of antibiotic in the world.[1] Penicillin antimicrobial activity derives from the β-lactam moiety of their bicyclic molecular structure, which forms a covalent adduct with the bacteria's transpeptidase enzymes and disrupts the biosynthesis of their cell walls.[2] However, due to over-prescription of antibiotics, certain strains of bacteria have developed antimicrobial resistance, posing a major threat to global health.[3] Gaining a better understanding of how penicillins are synthesised naturally, and applying this knowledge to the development of new and more diverse β-lactam antibiotics remain important goals in today's medicinal and pharmaceutical industry.[4]

Isopenicillin N Synthase (IPNS) is a mononuclear non-heme iron oxidase enzyme that catalyses the oxidative double ring-closure of δ-(L-α-aminoadipoyl)-L-cysteine-D-valine (ACV) to isopenicillin N (IPN).[5,6] In the course of this reaction, two aliphatic C–H bonds are activated to form a new C–N and C–S bond, sequentially closing the fused β-lactam and thiazolidine rings of IPN, respectively (Scheme 1). Concomitantly, O_2 is reduced to two equivalents of water and is not incorporated into the final product. In this respect, IPNS is one of the few mononuclear non-heme iron enzymes capable of activating O_2 and achieving its four-electron reduction by extracting all necessary electrons from its substrate.[7] The remarkable selectivity of IPNS for hydrogen atom abstraction (HAA) instead of sulfur oxygenation has faced much scrutiny, and has lead to extensive investigation of its catalytic mechanism by means of crystallographic,[8–10] spectroscopic,[11–14] substrate analogue,[15–19] and, more recently, computational studies.[13,20–22] The generally accepted catalytic mechanism for IPNS is depicted in Figure 1 and some of its main considerations will be described here.

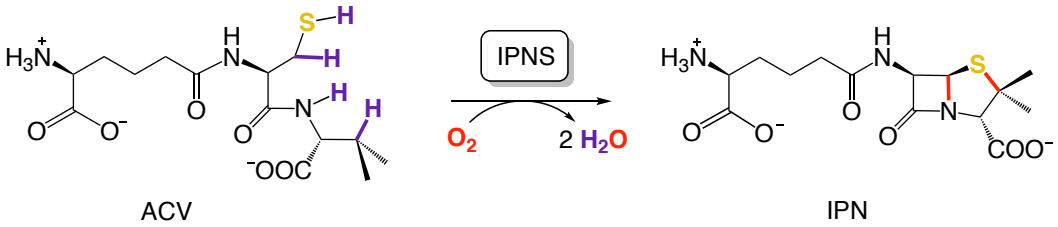

Scheme 1. The double oxidative ring closure of ACV to IPN, catalysed by IPNS.

At its active site, IPNS contains a single high-spin iron(II) centre bound by the 2-His-1-Carboxylate facial triad (2H1C), a bioinorganic motif comprising two histidines (His) and an aspartate (Asp) residue.[23] During the resting state (**A**), a loosely bound glutamine (Gln) and two water molecules occupy the coordination sites *trans* to the 2H1C.[8] Catalysis is initiated by ACV coordination to the iron centre through its anionic cysteinyl sulfur atom (**B**), at the position *trans* to the His-270 residue.[9] This displaces the glutamine residue and one of the water molecules and, in doing so, triggers a conformational change in the protein's tertiary structure that encloses ACV rigidly within the active site cavity.[9,24]

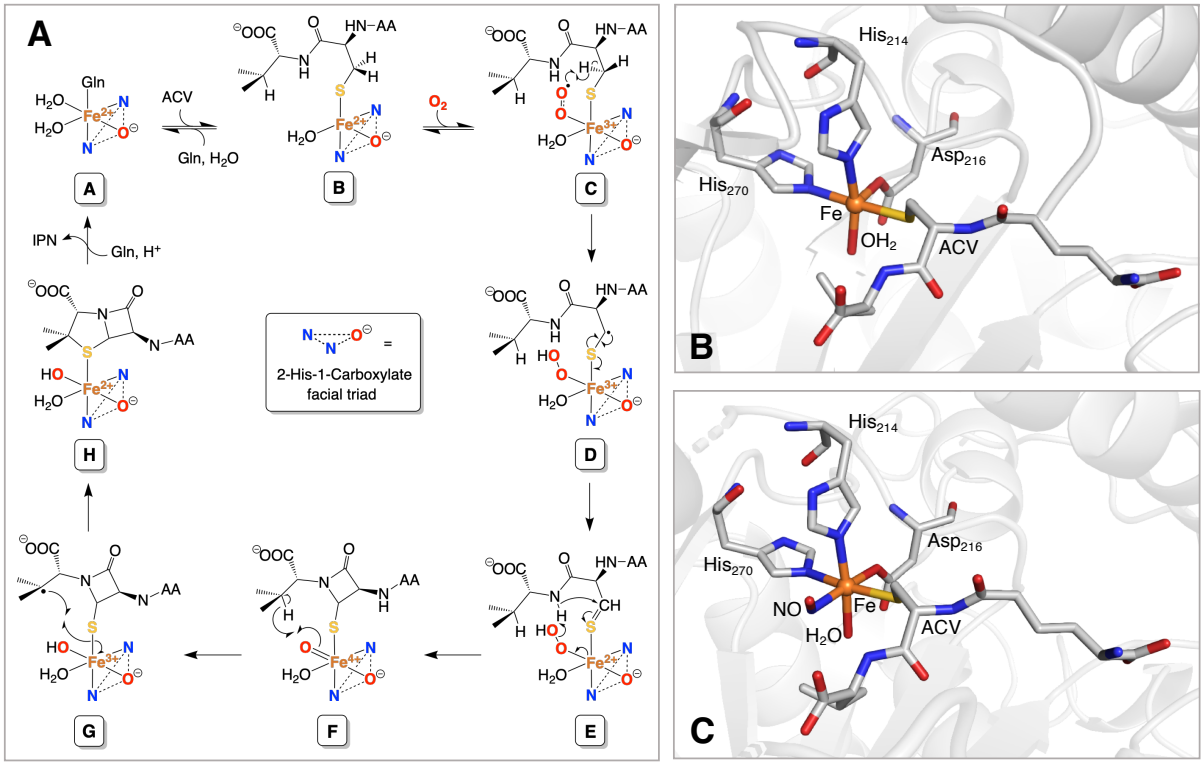

Figure 1. A: The proposed mechanism for the conversion of ACV to IPN, catalysed by IPNS using O_2 as the oxidant (AA = δ-(L-α-amino)adipoyl). **B:** The X-ray crystal structure of the [Fe·IPNS·ACV·OH_2] complex from *Aspergillus nidulans* (PDB 1BK0).[9] **C:** The X-ray crystal structure of the [Fe·IPNS·ACV·NO·OH_2] complex from *Aspergillus nidulans* (PDB 1BLZ).[9] Carbon, iron, nitrogen, oxygen and sulfur are depicted in grey, orange, blue, red and yellow, respectively.

The X-ray crystal structure of the ACV-bound active site (Figure 1B) shows the remaining water ligand to be bound *trans* to His-214, giving the iron a pentacoordinate, square pyramidal geometry, with an Fe–S bond length of 2.41 Å. However, EXAFS studies determine the Fe–S bond length to be approximately 2.32 ± 0.03 Å, which suggests that the aqua ligand is labile, and that the substrate-bound IPNS active site also exists in a tetracoordinate form.[25,26]

Importantly, sulfur-to-iron charge donation lowers the iron's redox potential and promotes end-on O_2 binding.[13,22] The resulting Fe^{3+}–OO^{-} intermediate (**C**), which was recently detected spectroscopically,[14] is responsible for the first aliphatic C–H bond activation, whereby the cysteinyl *pro-3-S* hydrogen is abstracted and an Fe^{3+}–OOH intermediate is formed (**D**).[5,17,27] Subsequent electron transfer from the thioalkyl radical generates a thioaldehyde-bound Fe^{2+}–OOH intermediate (**E**). Deprotonation of the amide by the hydroperoxide's distal oxygen atom leads to O–O heterolysis and loss of water, in concert with the nucleophilic attack of the amide on the thiocarbonyl. This generates a high-valent Fe^{4+}=O complex *cis*-coordinated to the thiolate of the monocyclic β-lactam moiety (**F**).[14] This highly oxidising intermediate, which was recently detected spectroscopically,[14] is responsible for the second aliphatic C–H bond activation at the tertiary valinyl *β*-carbon.

The resulting Fe^{3+}–OH intermediate (**G**) is bound to a valinyl radical, which attacks the thiolate and closes the thiazolidine ring, thereby completing the formation of the bicyclic IPN (**H**).[10]

Despite the detailed structural and mechanistic understanding of IPNS, only a handful of bioinspired IPNS model complexes have been reported and, to the best of our knowledge, none have successfully been able to reproduce its unique bicyclisation reactivity. The reasons for this are two-fold. Firstly, much of the chemistry taking place at the IPNS active site is aided by second coordination sphere effects of the encapsulating protein scaffold. Indeed, computational studies by Solomon and co-workers have shown that the iron(III)-superoxo intermediate (**C**) is primed for hydrogen atom abstraction (HAA) due to optimal alignment of the in-plane $O_2^{\bullet-}$ π^* frontier molecular orbital (FMO) for σ-overlap with the cysteinyl H-atom.[13] Similarly, the barrier for sulfur oxygenation reactivity in IPNS is calculated as being uphill by 3.7 kcal mol^{-1} relative to its native HAA reactivity, due to an unfavourable steric interaction between the Fe–O–O–S transition state structure required for sulfur oxygenation and the valine residue of the ACV substrate, which is locked in place by the protein scaffold.[20] These second coordination sphere effects are extremely challenging to reproduce synthetically in model compounds. Secondly, studies by Baldwin and co-workers have shown that the O_2 binds *trans* to the Asp residue (Figure 1C) and that, consequently, the reactivity of the superoxide intermediate (**C**) is likely to be significantly influenced by the *trans* effect of the 2H1C's carboxylate group.[289] This is substantiated by site specific mutagenesis studies of IPNS where substitution of the Asp residue for glutamic acid, histidine or cysteine resulted in significant or complete loss of the enzyme's catalytic activity.[29]

Strikingly, very few bioinspired ligands have been reported that are able to structurally model the 2H1C by providing a well-defined tripodal, mononucleating *N,N,O* coordination motif. Typically, problems in achieving the desired *N,N,O* coordination mode arise due to the formation of bisligated complexes, bridging coordination modes of anionic O-donors,[30,31] or coordination lability of neutral N- or O-donors.[32] The groups of Carrano,[33] Burzlaff,[34] and Klein Gebbink[35] have successfully synthesised mononuclear zinc(II) thiolate complexes supported by facial *N,N,O* ligands (Figure 2). However, no iron counterparts have been reported and, to the best of our knowledge, investigations on the spectroscopy and reactivity of *N,N,O*-bound iron thiolate complexes are still lacking.

One of the earliest iron-based IPNS modelling studies was published by the group of Que in the mid-1990s.[36] In this study, a family of $[Fe^{II}(TPA)(SAr)]^+$ complexes was synthesised, featuring different substituted thiophenolate ligands (Figure 2). The sulfur-to-iron charge transfer in these complexes was shown to increase the rhombicity in the EPR spectra of their corresponding nitrosyl adducts. At the time, this provided strong supporting evidence that O_2 binds directly to the ACV-bound IPNS active site. Reacting these complexes with O_2 resulted in the one-electron oxidation of the iron centres with concomitant disulfide formation. Later, the group of Goldberg demonstrated that the reaction of complex

[Fe^{II}(^{iPr}BIP)(SPh)(X)] (Figure 2) with O_2 leads either to Fe-oxidation (when X = Cl) or S-oxygenation (when X = OTf), as a result of the thiophenolate positioning in or out of the meridonal bis-iminopyridine plane, respectively.[37] This demonstrated that subtle structural differences can have a dramatic impact on the reactivity of iron thiolate complexes and that gaining synthetic control of their oxidation chemistry is not trivial. However, the neutral and nitrogen-rich donor sets provided by the **TPA** and ^{iPr}**BIP** ligand scaffolds may, arguably, be considered structurally more relevant to the 3-His facial triad than the 2H1C.[28,30,35,38,39] Very recently, Goldberg and co-workers reported an interesting iron thiolate complex, [Fe^{II}(BNPA^{Ph2}O)(SPh^{NO2})] (Figure 2), supported by a tripodal, tetradentate mixed N,O-donor ligand. Reacting this complex with O_2 produced an iron(III) hydroxide complex, [Fe^{III}(BNPA^{Ph2}O)(SPh^{NO2})(OH)], whose terminal OH ligand is bound *cis* to the thiophenolate. This octahedral complex showed temperature dependent reactivity to tertiary carbon radicals, where OH transfer was observed at room temperature and C–S bond formation was observed at –35 °C, in line with IPNS reactivity.

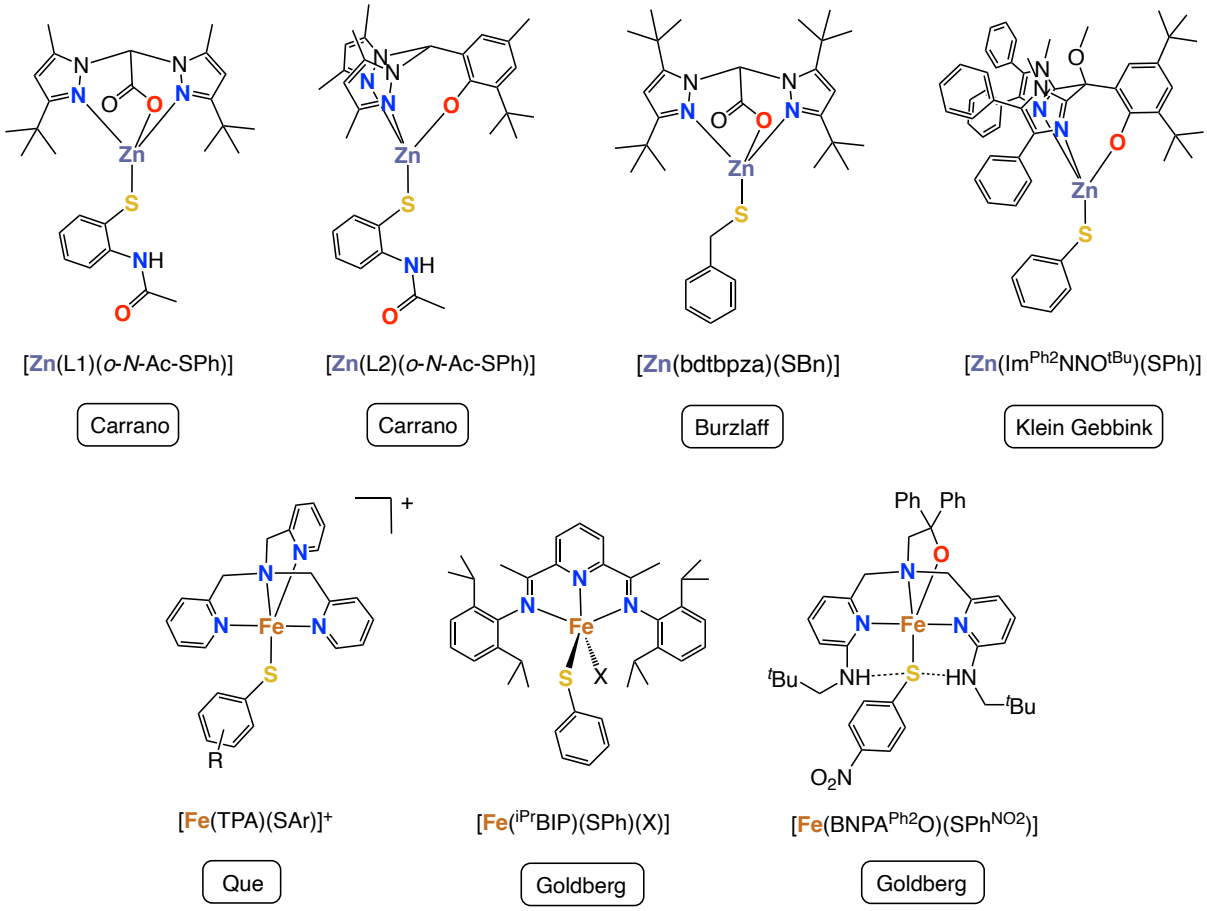

Figure 2. Examples of previously reported zinc(II) and iron(II) thiolate complexes that model the substrate-bound IPNS active site (Ar = Ph, Mes, 4-Me-Ph, 4-Cl-Ph; X = Cl, OTf) .[33,36,37]

In this study, we present the synthesis, structure and reactivity of a family of mononuclear, tetracoordinate iron(II) and zinc(II) thiolate complexes, [M(Im^{Ph2}NNO^{tBu})(SR)] (M = Fe, Zn; R = ^{t}Bu, Bn, Ph, Mes, 4-OMe-Ph, 4-CF_3-Ph) (Figure 3). These complexes qualify as some of the most structurally faithful models of the substrate-bound active site of IPNS

reported to date. Their metal centre is facially capped by a bulky, tridentate phenolate ligand (**Im^{Ph2}NNO^{tBu}**)[35] that models the 2H1C by providing a well-defined, anionic *N,N,O* coordination motif, while simultaneously accommodating a range of electronically and sterically diverse thiolate co-ligands. Moreover, the tetracoordinate nature of the [M(Im^{Ph2}NNO^{tBu})(SR)] complexes models the coordinatively unsaturated substrate-bound IPNS active site prior to its reaction with O_2. Using NMR spectroscopy, we demonstrated that the complexes have a well-defined structure in the solution state that is akin to that observed in their X-ray crystal structures.

We examined the electronic structure of the complexes by Mössbauer spectroscopy and DFT calculations, and showed that the sulfur-to-metal charge transfer is dependent on the approximate donicity of the thiolate ligands. Electrochemical investigations by cyclic voltammetry (CV) showed that the first oxidation takes place on the iron centre and that the Fe^{II}/Fe^{III} redox potential is influenced by the relative donicity of the thiolate co-ligand. Finally, we explored the reactivity of the iron thiolate complexes with different oxidants, including O_2, NO (using Ph_3CSNO), PhIO and $[Ph_3C]PF_6$. During the reactions with O_2 and PhIO the iron is oxidised to its ferric form with concomitant sulfonate formation. We also observed that the **Im^{Ph2}NNO^{tBu}** ligand is susceptible to oxidative degradation, through either methyl- or methoxy-cleavage at the ligand backbone.

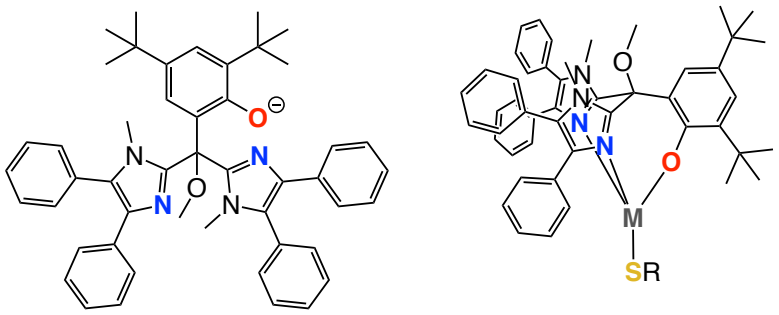

Im^{Ph2}NNO^{tBu}

[M(Im^{Ph2}NNO^{tBu})(SR)]
M = Fe, Zn

Figure 3. Left: Ligand **Im^{Ph2}NNO^{tBu}**, with a tridentate, anionic *N,N,O* donor set. Right: general structure of the mononuclear, *N,N,O*-bound metal(II) thiolate complex series, [M(Im^{Ph2}NNO^{tBu})(SR)] (M = Zn, Fe; R = ^{t}Bu, Bn, Ph, Mes, 4-OMe-Ph, 4-CF_3-Ph).

4.2 Results and Discussion

4.2.1 Complex Synthesis

The mononuclear [M(Im^{Ph2}NNO^{tBu})(Cl)] complexes **1** (M = Fe) and **2** (M = Zn) have previously been reported in our group, and can be regarded as convenient synthons from which to make a range of different mononuclear, *N,N,O*-bound metal thiolate complexes.[35] The chloride ligand in **1** or **2** is readily exchanged for a thiolate ligand by treating the complex with a slight excess of desired sodium thiolate salt, in CH_2Cl_2 (Scheme 2). After stirring for approximately 2.5 h, the reaction mixtures are filtered and dried under vacuum. The crude solids are subsequently washed with hexane and dried, affording the desired metal thiolate complexes, [M(Im^{Ph2}NNO^{tBu})(SR)] (**3-14**), as free-flowing powders. This reproducible synthetic method enables all complexes to be obtained cleanly in good to excellent yields. The IR spectra obtained for all complexes show the absence of O–H or S–H stretching vibrations, consistent with the anionic coordination of both phenolate and thiolate moieties.

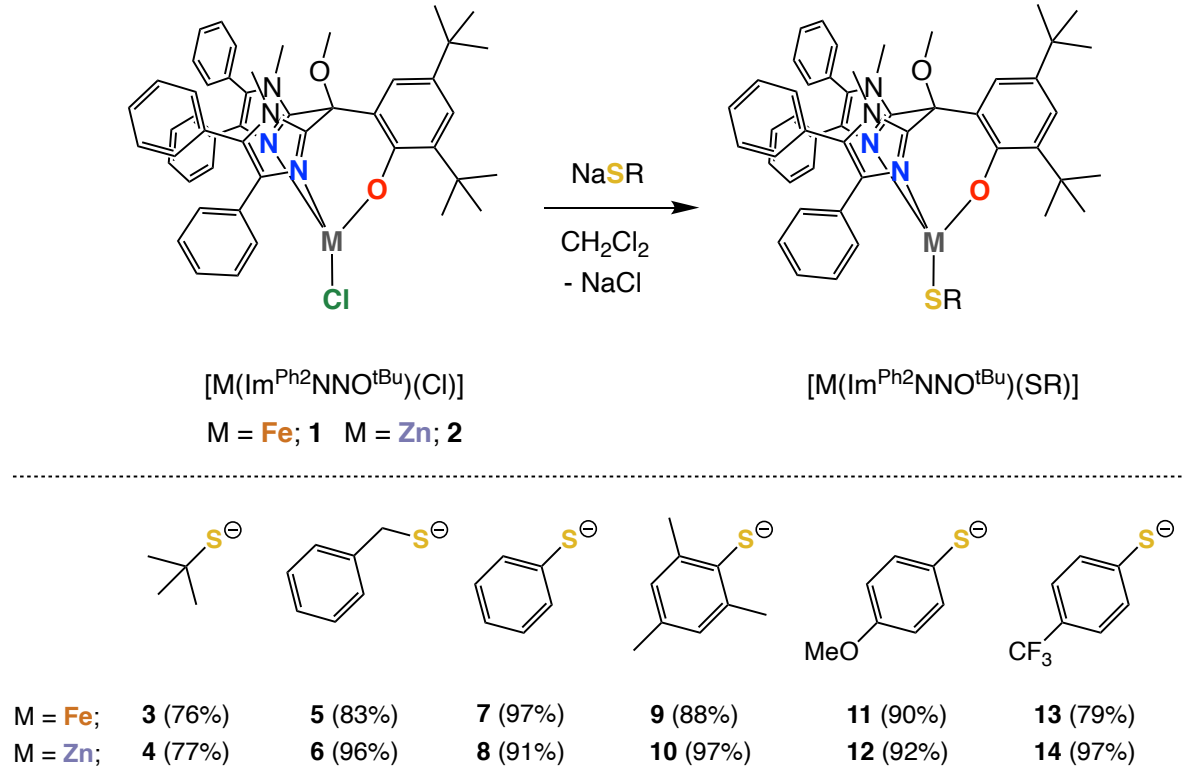

Scheme 2. The synthesis of mononuclear metal thiolate complexes [M(Im^{Ph2}NNO^{tBu})(SR)] (**3-14**).

4.2.2 X-ray Crystal Structure Analysis

Crystals suitable for X-ray diffraction were obtained for all [M(L)(SR)] complexes (M = Fe, Zn; L = $\mathbf{Im^{Ph2}NNO^{tBu}}$), with the exception of [Fe(L)(SPh^{CF3})] (**13**). The X-ray crystal structures for the zinc and iron thiolate complexes are displayed in Figure 5 and Figure 6, respectively, with selected bond lengths and bond angles given in Table 1 and Table 2. The X-ray crystal structure of [Zn($Im^{Ph2}NNO^{tBu}$)(SPh)] (**8**) was previously described in Chapter 3 and has been included here for completeness of the discussion.[35] The structures show that each complex contains a single metal(II) centre of distorted tetrahedral geometry, where three coordination sites are occupied by the *N,N,O* donor set of the $\mathbf{Im^{Ph2}NNO^{tBu}}$ ligand and the fourth coordination site is occupied by the monodentate thiolate co-ligand. Importantly, these results confirm the successful substitution of the chloride in [M(L)(Cl)] complexes **1** (M = Fe) or **2** (M = Zn) for the desired thiolate ligand, with retention of the supporting ligand's tridentate *N,N,O* coordination mode even in the presence of very bulky thiolates such as S^{t}Bu or SMes. This demonstrates the high tunability of our synthetic IPNS model complexes.

Metal–Sulfur Bond Length. The X-ray crystal structures show that the M–S bond lengths are generally dependent on the donicity of the thiolate co-ligands. The shortest M–S bond lengths occur in [M(L)(S^{t}Bu)] complexes **3** (2.2711(8) Å) and **4** (2.2179(4) and 2.2185(4) Å for two independent molecules found within the same asymmetric unit), which feature the strongly electron-donating *tert*-butylthiolate. Similarly, the longest Zn–S bond length (2.2359(5) Å) is found in complex [Zn(L)(SPh^{CF3})] (**14**), whose electron-withdrawing CF_3 group has a weakening effect on the Zn–S bond. By analogy to complex **14**, the longest Fe–S bond is expected for **13**. However, despite numerous attempts, no crystals suitable for X-ray diffraction were obtained. In contrast, relatively long M–S bonds are observed for [M(L)(SMes)] complexes **9** (2.2891(6) Å) and **10** (2.2301(4) Å), despite the electron-donating nature of the mesityl groups. We therefore attribute the M–S bond elongation to the steric clash between the mesityl substituent and the supporting ligand framework. Overall, the metal–sulfur bond lengths in all complexes fall within the expected range for mononuclear high-spin (S = 2) iron(II) complexes (2.254 – 2.375 Å)[40] and zinc(II) complexes (2.220 – 2.418 Å).[33,41–46]

***N,N,O* Ligand Symmetry.** The tridentate, *N,N,O* coordination of the $\mathbf{Im^{Ph2}NNO^{tBu}}$ ligand imparts a metallobicyclo[2.2.3]nonane topology to each complex. The tetrahedral distortion in all complexes is characterised by N–M–O and N–M–N angles that are smaller than in the ideal tetrahedron, and O–M–S and N–M–S angles that are all larger than ideal. We attribute this to the tripodal chelation of the $\mathbf{Im^{Ph2}NNO^{tBu}}$ ligand, whose donor groups are linked by a single quaternary carbon atom. This "cage effect" reduces the bite angle between the *N,N,O* donors and increases the overall strain in the system.[35] The Zn–N bond lengths range between 2.0202(16) and 2.121(2) Å and are typical for a zinc(II) ion of tetrahedral geometry bound to neutral N-donors.[33,34] The Fe–N bond lengths range

between 2.088(3) Å and 2.139(3) Å, and are consistent with those of a high-spin iron(II) centre bound to neutral imidazole groups.[30,32] As was previously reported for **1** and **2**,[35] the tetrahedral distortion is also noticeable in complexes whose M–N bonds are non-identical. Longer M–N bonds are observed where the angle between the plane of the imidazole heterocycle and its respective M–N bond vector deviates most strongly from 180°, resulting in poorer overlap between the imidazole lone pair and the metal *d*-orbitals. This tetrahedral distortion is further reflected by the high quadratic elongation ($<\lambda_{tet}>$) and angle variance (σ_{tet}^2) values obtained for all complexes (where an ideal tetrahedron has $<\lambda_{tet}> = 0$ and $\sigma_{tet}^2 = 0$).[47] We attribute the higher σ_{tet}^2 values observed for the iron compounds to the paramagnetic nature and more diffuse coordination sphere of the metal centres. The Fe–O bonds range between 1.8958(13) Å and 1.9157(18) Å, and the Zn–O bonds range between 1.9385(11) and 1.967(2) Å. These relatively short M–O bonds reflect the strongly donating, anionic nature of the phenolate O-donor compared to related complexes featuring *N,N,O* ligands with ester or carboxylate groups.[32–34,48]

Thiolate Orientation. The sterically demanding bis-imidazole backbone of the ligand scaffold prevents a staggered (*anti*) O–M–S–C conformation from occurring, where the organic substituent of the thiolate would point downwards between the imidazole phenyl groups (Figure 4). Instead, the thiolate ligands bend (or "tilt") themselves towards one of the two imidazole groups in a *gauche*-type conformation, with O–M–S–C torsion angles ranging from 46.40(8)° to –77.79(10)°. While this renders each individual molecule chiral, all crystal structures have a centrosymmetric space group and are therefore racemic. This phenomenon was previously observed for **8** (Chapter 3).[35] In contrast, the bulky mesitylthiolate ligand in complexes **9** and **10** is unable to adopt a bent orientation, due to the steric clash between its *ortho*-CH_3 substituents and the phenyl groups on the 4-positions of the imidazole heterocycles. This results in an almost *eclipsed* O–M–S–C conformation, with torsion angles of –12.93(9) for **9** and –10.93(8)° for **10** (Figure 4).

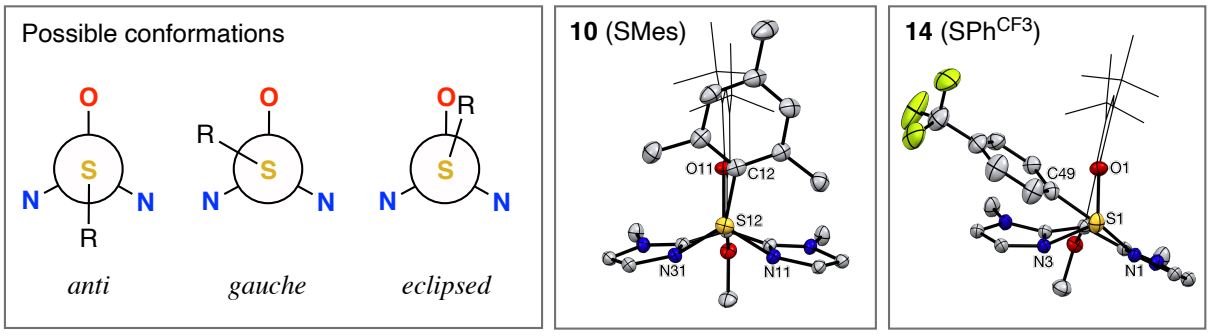

Figure 4. Left: Newman-type projections along the M–S bond. Middle and right: Projection along the Zn–S bond for the crystal structures of complexes **10** and **14**, showing their *eclipsed*- and *gauche*-type conformations, respectively. The imidazole phenyl substituents are omitted and the phenolate rings are depicted in the wireframe format for clarity.

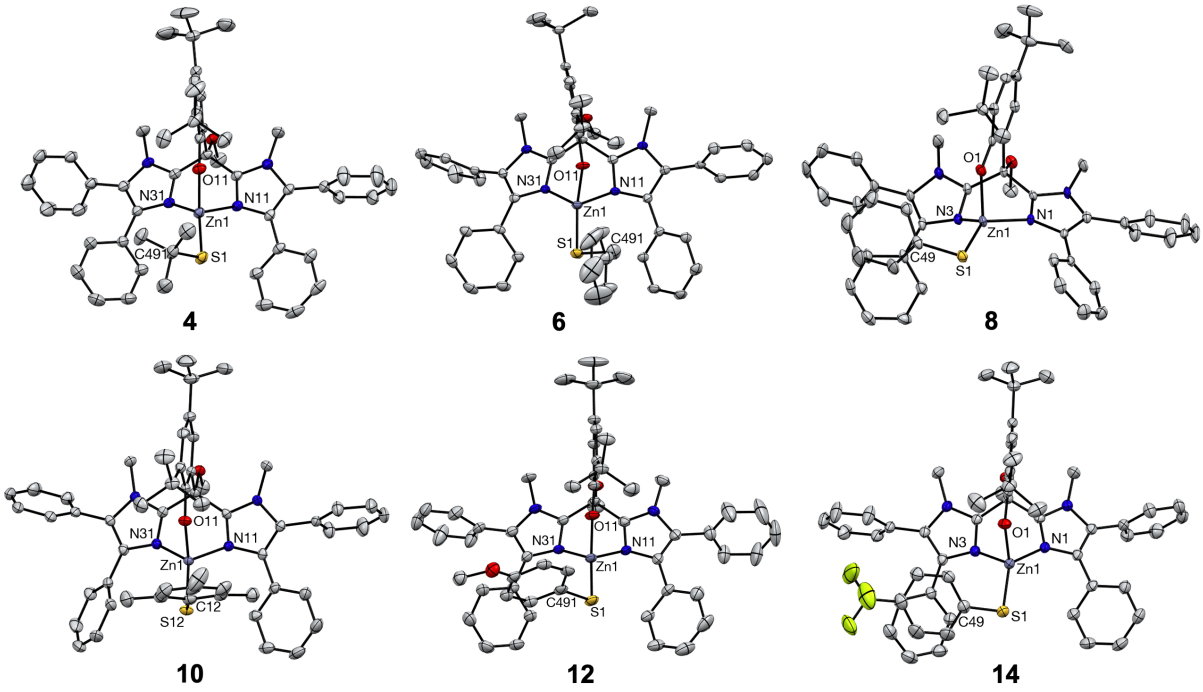

Figure 5. Displacement ellipsoid plots of zinc thiolate complexes **4**, **6**, **8**, **10**, **12** and **14** (50% probability level). All H-atoms and any co-crystallised solvent molecules have been omitted for clarity. Only the major form of any disordered ^{t}Bu and CF_3 substituents has been depicted. The second residue in the asymmetric unit of **4** is not depicted.

Table 1. Selected bond lengths (Å), bond angles and torsion angles (°) for zinc thiolate complexes **4**, **6**, **8**, **10**, **12** and **14**.[47] [*] Only one of two independent molecules is given.

Bond	**4**[*] (S^{t}Bu)	**6** (SBn)	**8** (SPh)	**10** (SMes)	**12** (SPh^{OMe})	**14** (SPh^{CF3})
Zn1–S1	2.2179(4)	2.2242(8)	2.2249(9)	2.2301(4)	2.2229(8)	2.2359(5)
Zn1–O1	1.9636(11)	1.9527(19)	1.967(2)	1.9385(11)	1.9527(18)	1.9477(13)
Zn1–N1	2.0704(12)	2.121(2)	2.028(2)	2.0601(13)	2.038(2)	2.0202(16)
Zn1–N3	2.0722(12)	2.026(2)	2.062(3)	2.0810(13)	2.065(2)	2.0909(16)
Angle	**4**[*] (S^{t}Bu)	**6** (SBn)	**8** (SPh)	**10** (SMes)	**12** (SPh^{OMe})	**14** (SPh^{CF3})
Zn1–S1–C49	105.46(6)	101.97(12)	101.67(11)	102.50(6)	99.89(8)	101.14(7)
N1–Zn1–O1	96.98(5)	90.90(9)	94.92(9)	97.60(5)	95.58(8)	96.76(6)
N3–Zn1–O1	97.07(5)	99.96(9)	96.27(9)	95.15(5)	97.89(8)	95.15(6)
N1–Zn1–S1	115.16(4)	121.00(7)	131.21(7)	122.33(4)	121.68(6)	131.21(5)
N3–Zn1–S1	128.25(4)	126.16(7)	120.07(7)	126.18(4)	125.83(6)	116.95(4)
N1–Zn1–N3	86.03(5)	88.27(9)	90.33(10)	89.56(5)	87.23(9)	89.18(6)
O1–Zn1–S1	123.79(3)	121.26(6)	116.13(7)	118.55(4)	120.40(6)	118.96(4)
Torsion	**4**[*] (S^{t}Bu)	**6** (SBn)	**8** (SPh)	**10** (SMes)	**12** (SPh^{OMe})	**14** (SPh^{CF3})
O–Zn–S–C	46.40(8)	–49.33(13)	61.12(13)	–10.93(8)	49.52(12)	55.00(9)
Parameter	**4**[*] (S^{t}Bu)	**6** (SBn)	**8** (SPh)	**10** (SMes)	**12** (SPh^{OMe})	**14** (SPh^{CF3})
Volume$_{tet}$ (Å^3)	4.144	4.155	4.111	4.181	4.107	4.121
$\langle\lambda_{tet}\rangle$	1.078	1.077	1.073	1.069	1.073	1.075
σ_{tet}^2 (deg^2)	289.91	286.92	276.15	253.75	271.47	279.23

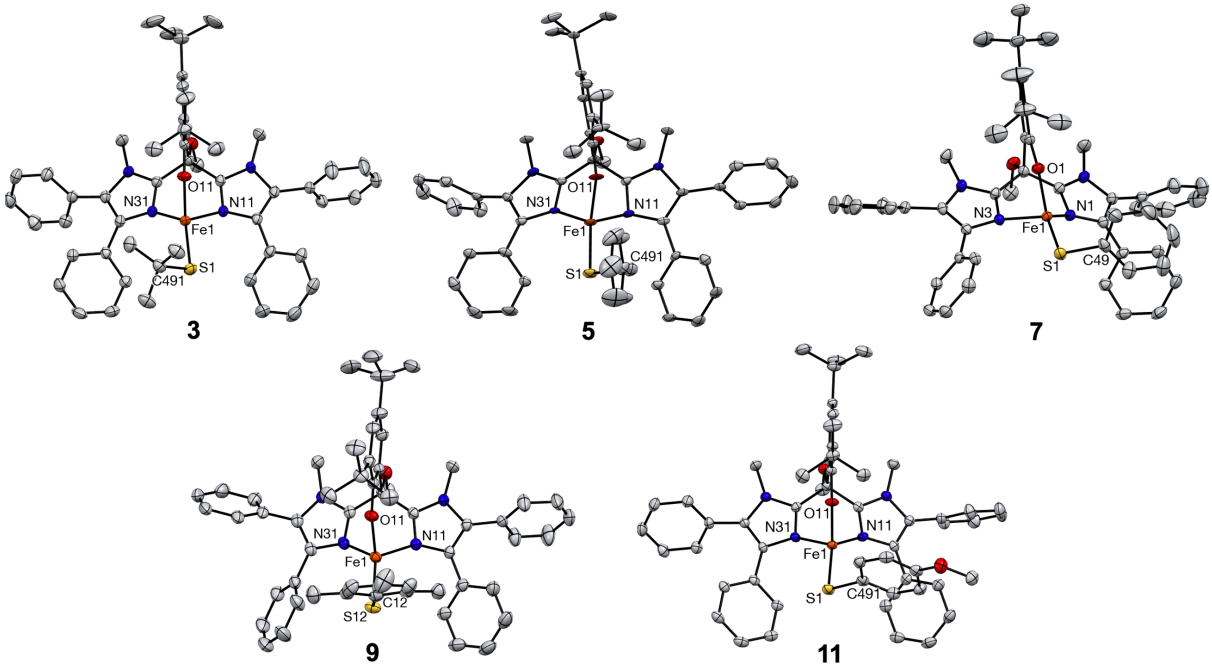

Figure 6. Displacement ellipsoid plots of iron thiolate complexes **3**, **5**, **7**, **9** and **11** (drawn at the 50% probability level). All H-atoms and any co-crystallised solvent molecules have been omitted for clarity. Only the major form of any disordered *t*Bu substituents has been depicted.

Table 2. Selected bond lengths (Å), bond angles and torsion angles (°) for iron thiolate complexes **3**, **5**, **7**, **9** and **11**. [47]

Bond	**3** (S^{t}Bu)	**5** (SBn)	**7** (SPh)	**9** (SMes)	**11** (SPh^{OMe})
Fe1–S1	2.2711(8)	2.2869(11)	2.2830(7)	2.2891(6)	2.2760(8)
Fe1–O1	1.9157(18)	1.913(3)	1.9108(15)	1.8958(13)	1.9116(19)
Fe1–N1	2.105(2)	2.139(3)	2.0962(17)	2.1020(15)	2.095(2)
Fe1–N3	2.105(2)	2.088(3)	2.1164(19)	2.1303(16)	2.100(2)
Angle	**3** (S^{t}Bu)	**5** (SBn)	**7** (SPh)	**9** (SMes)	**11** (SPh^{OMe})
Fe1–S1–C49	104.25(10)	100.53(14)	104.70(8)	102.09(6)	97.24(10)
N1–Fe1–O1	95.36(9)	92.49(12)	101.47(7)	97.18(6)	98.89(9)
N3–Fe1–O1	95.93(9)	98.32(11)	88.68(7)	94.03(6)	96.59(9)
N1–Fe1–S1	115.01(7)	119.66(9)	125.65(5)	121.83(5)	129.60(7)
N3–Fe1–S1	126.08(7)	122.77(9)	121.38(5)	123.38(5)	118.31(7)
N1–Fe1–N3	85.71(9)	85.46(12)	86.48(7)	87.98(6)	82.94(9)
O1–Fe1–S1	127.84(6)	127.41(9)	122.63(5)	123.70(4)	120.74(6)
C35–O1–Fe1	143.23(19)	141.7(3)	143.14(14)	143.63(12)	142.98(18)
Torsion	**3** (S^{t}Bu)	**5** (SBn)	**7** (SPh)	**9** (SMes)	**11** (SPh^{OMe})
O–Fe–S–C	48.46(13)	–51.5(2)	–77.79(10)	–12.93(9)	–56.74(13)
Parameter	**3** (S^{t}Bu)	**5** (SBn)	**7** (SPh)	**9** (SMes)	**11** (SPh^{OMe})
Volume$_{tet}$ (Å^3)	4.208	4.255	4.202	4.298	4.167
$\langle\lambda_{tet}\rangle$	1.087	1.088	1.092	1.078	1.091
σ_{tet}^2 (deg^2)	317.94	318.44	320.25	279.95	318.42

Structural Comparison to IPNS. The X-ray crystal structure of the substrate-bound IPNS active site shows a single iron(II) centre, facially capped by the 2H1C and bound to both the monodentate thiolate substrate (*trans* to His-270) and a well-ordered water ligand (*trans* to His-214) (Figure 1B).[9] The iron(II) centre is therefore pentacoordinate and has a square pyramidal geometry, with a Fe–S bond length of 2.41 Å. However, independent EXAFS studies on IPNS from *Cephalosporum acremonium* and *Aspergillus nidulans* determine the Fe–S(ACV) bond lengths to be 2.32±0.02 Å and 2.34±0.03 Å, respectively.[25,26] This suggests that the water ligand is labile and that the substrate-bound IPNS active site may also exist in a tetracoordinate form.

Our synthetic iron(II) thiolate complexes, [Fe($Im^{Ph2}NNO^{tBu}$)(SR)], feature a tridentate, *N,N,O* supporting ligand and a monodentate thiolate co-ligand. They have a neutral electronic configuration and a distorted tetrahedral geometry, and Fe–S bond lengths ranging between 2.2711(8) Å and 2.2891(6) Å. In other words, the complexes model the tetracoordinate form of the substrate-bound IPNS active site. Given the fragmentary data for this species in the literature, our synthetic complexes could serve as convenient structural and spectroscopic models with which to identify it in biological systems. The capacity of the supporting **$Im^{Ph2}NNO^{tBu}$** ligand to structurally model the 2H1C is reflected by the N–Fe–O and N–Fe–N angles that compare well to the N_{His}–Fe–O_{Asp} and N_{His}–Fe–N_{His} angles reported in the [Fe·IPNS·ACV·OH_2] crystal structure. However, the Fe–$N_{imidazole}$ bonds lengths observed throughout the complex series are somewhat shorter than the enzymatic Fe–N_{His} bond distances (2.21 Å and 2.20 Å), presumably due to the iron's lower coordination number throughout the model complex series. Similarly, the Fe–O_{phen} bond lengths are shorter that the enzyme Fe–O_{Asp} bond length of 2.07 Å. We ascribe this to the more strongly donating nature of the anionic phenolate compared to the carboxylate of the 2H1C.

Table 3. A comparison between selected bond lengths and bond angles extracted from the X-ray crystal structure of the [Fe·IPNS·ACV·OH_2] complex from *Aspergillus nidulans* (Figure 1B, PDB 1BK0).[9]

[Fe·IPNS·ACV·OH_2] from *A. nidulans* (PDB 1BK0)			
Bond	Length (Å)	Bond Angle	Degrees (°)
Fe–S_{ACV}	2.41 Å	Fe–S_{ACV}–C_{ACV}	108.10
Fe–O_{Asp216}	2.07 Å	N_{His214}–Fe–O_{Asp}	99.38
Fe–N_{His214}	2.21 Å	N_{His270}–Fe–O_{Asp}	87.64
Fe–N_{His270}	2.20 Å	N_{His}–Fe–N_{His}	85.67

4.2.3 NMR Spectroscopy

4.2.3.1 Zinc Thiolate Complexes

The diamagnetic nature of zinc thiolate complexes **4**, **6**, **8**, **10**, **12** and **14** provides a convenient handle for examining their solution-state structure by means of NMR spectroscopy. The ^{1}H NMR spectra of all zinc thiolate complexes, recorded in acetonitrile-d_3, show the successful substitution of the chloride ligand in **2** for one equivalent of thiolate co-ligand per complex. Importantly, the spectra show that the solution-state structures of the complexes are well-defined and are analogous to those observed in the solid state.

In the aliphatic region of the spectra (Figure 7), the resonances assigned to the N-methyl and O-methyl groups have a relative integral ratio of 2:1, in line with the metallobicyclo[2.2.3]nonane topology associated to the tridentate *N,N,O* coordination of the supporting ligand. This provides strong evidence that the structural connectivity observed in the X-ray crystal structures of the complexes is retained in solution, at least on the measurement time-scale. Compared to [Zn(L)(Cl)] (**2**),[35] the NMR spectra of the zinc thiolate complexes differ in that two distinct singlets are obtained for the ^{t}Bu groups of the supporting ligand. Based on NOE NMR analysis (see Appendix C, Figures C1-C5), the *ortho*-^{t}Bu resonance is shifted upfield in all of the complexes bearing a thiophenolate ligand (i.e. **8**, **10**, **12** and **14**), presumably due the magnetic anisotropy shielding effect of the

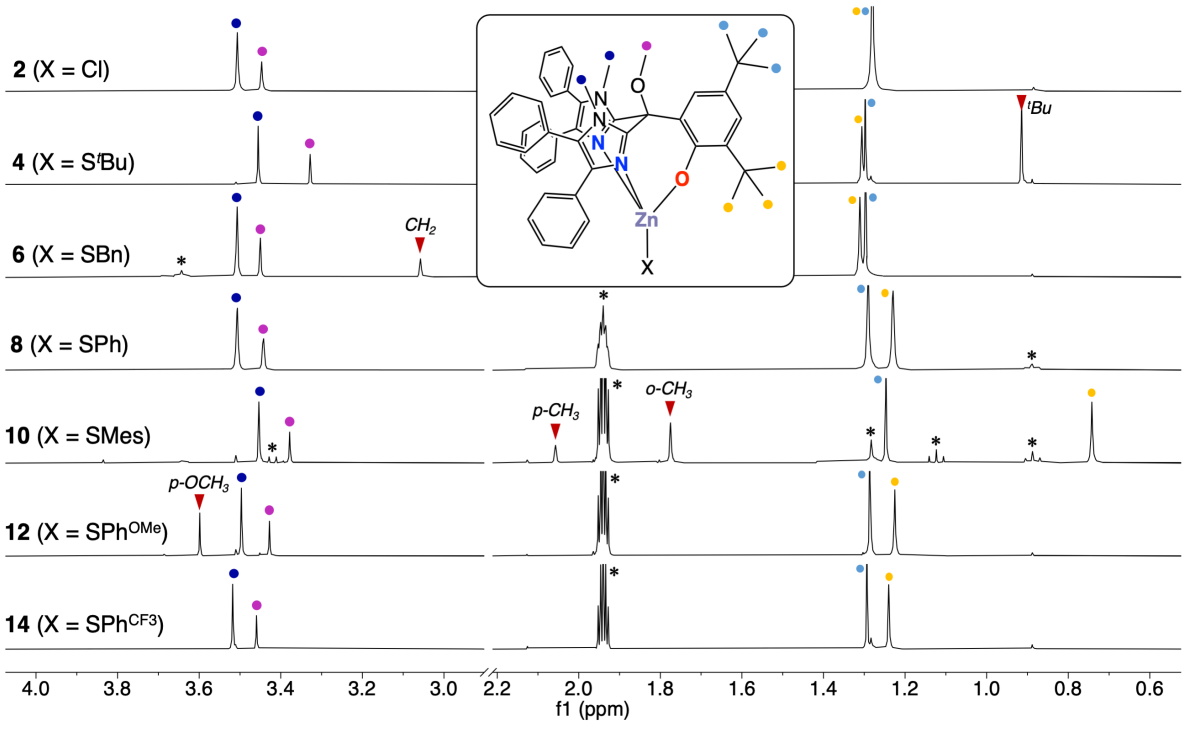

Figure 7. Comparison of the aliphatic region of the ^{1}H NMR spectra (400 MHz) of zinc complexes **2**, **4**, **6**, **8**, **10**, **12**, and **14**, recorded in CD_3CN at 25 °C. Spectra are clipped for clarity. Thiolate resonances are labelled with red triangles. The spectra of **2** and **8** were reported in Chapter 3 and are included for comparison.[35] Black asterisks denote residual solvent signals.

nearby arylthiolate ring. This is particularly noticeable for **10**, where the *ortho*-^{t}Bu signal is shifted significantly upfield to 0.74 ppm due to the close proximity of the mesityl ring, which is locked in place by its *ortho*-CH_3 substituents. Similarly, the resonance associated to the mesityl *ortho*-CH_3 substituents lies significantly upfield (1.78 ppm) due to the shielding effect of the nearby imidazole phenyl groups. Aliphatic thiolate resonances are also observed for complexes **4**, **6** and **12**. The *tert*-butylthiolate resonance in **4** occurs at 0.91 ppm. In **6**, the benzylic protons are observed at 3.06 ppm. In **12**, the signal associated to the *para*-OMe group occurs at 3.59 ppm.

In the aromatic region of the spectra (Figure 8), arylthiolate signals are observed for complexes **6**, **8**, **10**, **12** and **14**. For **6**, one doublet at 6.86 ppm and two triplets at 7.01 ppm and 7.08 ppm are observed that correspond to the protons at the *ortho*, *para* and *meta* positions of the benzyl aromatic ring, respectively. In **8**, two multiplets are observed at 6.70 ppm and 6.89 ppm, assigned to the *meta*/*para* and *ortho* protons of the phenyl ring, respectively. In **10**, a singlet is observed at 6.52 ppm, assigned to the *meta* protons of the mesityl group. In complexes **12** and **14**, two doublets are observed that correspond to the *ortho* and *meta* protons of the *para*-substituted thiophenolate rings. The electron-rich nature of the thiolate in **12** causes these resonances to occur more upfield, at 6.30 ppm (*meta*) and 6.73 ppm (*ortho*), whereas the electron-poor nature of the thiolate in **14** shifts these

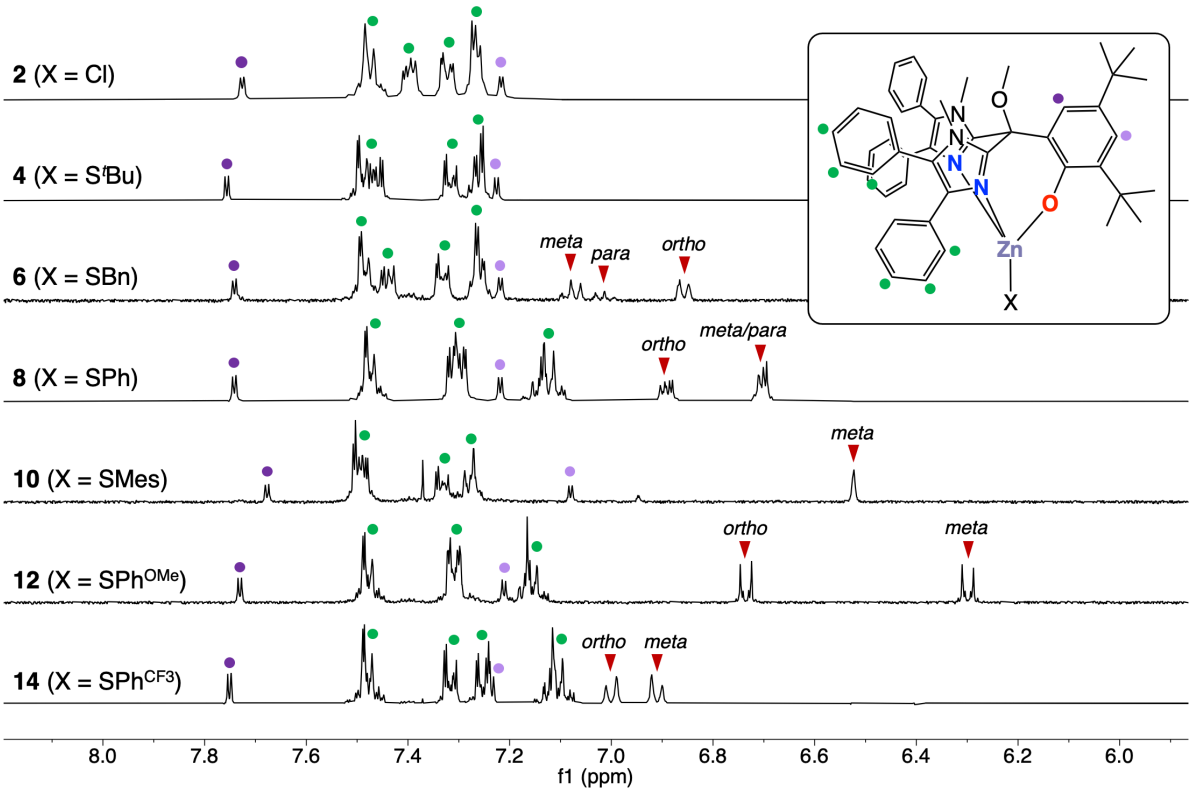

Figure 8. Comparison of the aromatic region of the ^{1}H NMR (400 MHz) spectra for zinc complexes **2**, **4**, **6**, **8**, **10**, **12**, and **14**, recorded in CD_3CN at 25 °C. Thiolate resonances are labelled with red triangles. The ^{1}H NMR spectra of **2** and **8** were reported in Chapter 3 and have been included for comparison.[35]

resonances downfield to 6.91 ppm (*meta*) and 7.00 (*ortho*) ppm. Other aromatic ^{1}H NMR signals that are observed in all complexes are the aromatic signals associated to the imidazole phenyl substituents. However, these signals are highly overlapped and cannot be fully assigned.

The doublets assigned to the phenolic protons are diagnostic of the electronic environment of the aromatic phenolate ring. In the parent complex **2**, these doublets occur at 7.22 and 7.73 ppm and are assigned to the 3- and 5-position of the phenolate, respectively. These resonances experience an almost negligible change in chemical shift in complexes **4**, **6**, **8**, **12** and **14**. It would seem, therefore, that substitution of the chloride for a thiolate ligand, whether aliphatic or aromatic, electron-rich or electron-poor does not significantly affect the electronic environment of the phenolic protons. In **10**, however, the phenolic resonances shift upfield to 7.08 and 7.68 ppm, likely due to the strong shielding effect of the nearby mesityl group.

4.2.3.2 Iron Thiolate Complexes

The ^{1}H NMR spectra of complexes **3**, **5**, **7**, **9**, **11** and **13** recorded in acetonitrile-d_3 are displayed in Figure 9. Using Evans NMR method,[49] the effective magnetic moment (μ_{eff}) of the complexes was found to lie within the range of 4.50 to 5.21 μ_B, consistent with

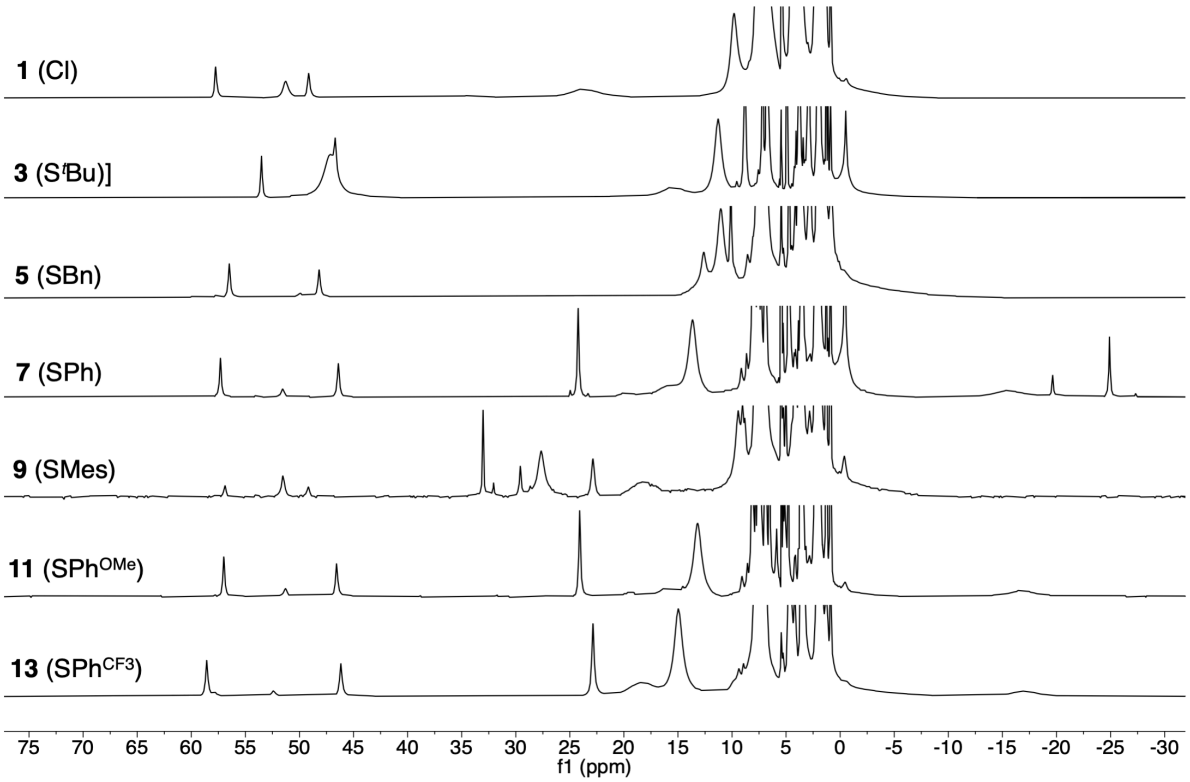

Figure 9. Stacked ^{1}H NMR (400 MHz) spectra of iron complexes **1**, **3**, **5**, **7**, **9**, **11** and **13**, recorded in CD_3CN at 25 °C. Spectra are clipped vertically for clarity. The ^{1}H NMR spectrum of **1** was reported in Chapter 3 and has been included for comparison.[35]

high-spin (S = 2) iron(II) in all cases (expectation value 4.90 μ_B).[50] This is corroborated by the presence of paramagnetically shifted resonances in all spectra. The number of signals in each spectrum is in line with the number of different H-atom environments per complex. However, due to the strong overlap and extreme linewidth of certain signals, assignment of the paramagnetic resonances was not possible. Nonetheless, the spectra do share some common features, including two sharp signals of equal integration at approximately 45 and 60 ppm and a broad signal at approximately 10 to 15 ppm, all of which are also present in the ^{1}H NMR spectrum of the parent complex [Fe(Im^{Ph2}NNO^{tBu})(Cl)] (**1**). This is a strong indication that the speciation of all iron thiolate complexes in solution is equivalent. Indeed, based on the general structural analogy between Zn^{2+} and Fe^{2+} complexes that is frequently drawn in the literature, corroborated by the isostructural nature of the iron and zinc thiolate complexes in their solid state (*vide supra*), we have strong reasons to assume that the solution state structures of the iron thiolate complexes are analogous to those of their zinc counterparts.

4.2.4 Absorption Spectroscopy

Dissolving iron thiolate complexes **3**, **5**, **7**, **9**, **11** and **13** in dichloromethane produces very pale yellow solutions in all instances. Their UV-vis spectra, although rather featureless, are all similar in that they are characterised by two bands (Figure 10). The first band is very broad, spanning between 430 and 800 nm with a λ_{max} at approximately 500 nm and a weak extinction coefficient (< 100 $M^{-1}\,cm^{-1}$). We assign this band to the spin-forbidden *d-d* transitions. The second absorption feature occurs between 360 and 410 nm, shouldering the intense π-π^* transitions (<350 nm). We tentatively assign this band to a ligand-to-metal charge transfer (LMCT).

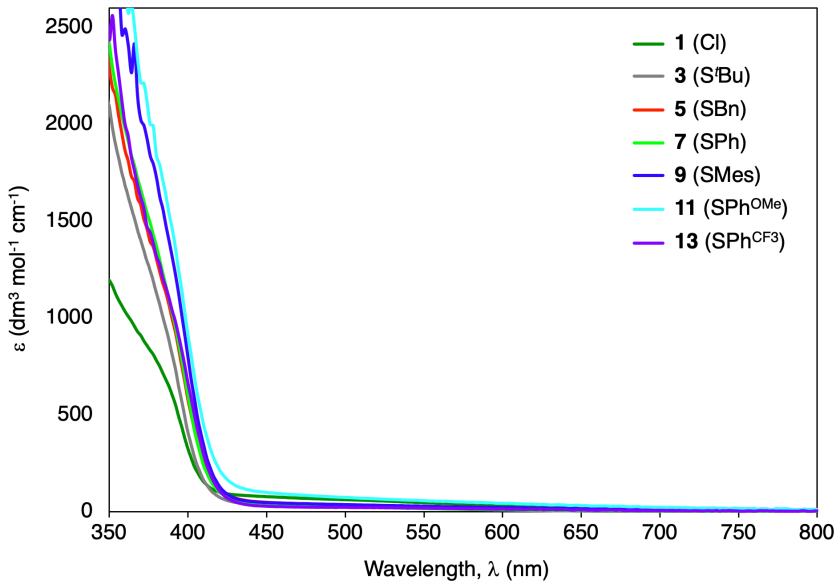

Figure 10. Overlay of the UV-vis spectra of iron complexes **1**, **3**, **5**, **7**, **9**, **11** and **13**, recorded in CH_2Cl_2.

Overall, the UV-vis spectra for the iron(II) thiolate complexes are similar to that obtained for the IPNS enzyme-substrate complex, which also features a weak, almost indistinguishable band at ~500 nm and an LMCT shoulder band at ~350 nm.[11] We ascribe the red shift of the LMCT band in our IPNS model complexes to the more localised negative charge of the phenolic oxygen atom compared to the carboxylate ligand present in IPNS. Compared to [Fe(L)(Cl)] (**1**), the intensity of the LMCT shoulder band for the iron thiolate complexes is greater, presumably due to the greater contribution of sulfur to the charge transfer. This difference is very similar to that reported for the optical spectra of IPNS with and without ACV bound to its active site.[11]

4.2.5 ^{57}Fe Mössbauer Spectroscopy

The zero-field ^{57}Fe Mössbauer spectra recorded at 80 K for powder samples of iron thiolate complexes **3**, **5**, **7**, **9**, **11** and **13** are depicted in Figure 11, with isomer shifts (δ) and quadrupole splittings (ΔE_Q) given in Table 4. This complex series displays isomer shifts within the range of 0.86 and 0.91 mm s^{-1}, consistent with the high-spin state ($S = 2$) of the iron centres. Compared to the parent complex [Fe(L)(Cl)] (**1**) (δ = 0.94 mm s^{-1}),[35] the presence of a soft thiolate ligand causes a decrease in isomer shift throughout the series, which reflects the greater donicity of the sulfur atom. This parallels the decrease in isomer shift reported upon ACV ligation to the IPNS active site: from 1.30 to 1.10 mm s^{-1}.[11,12,14] The relatively small isomer shift difference between **1** and its thiolate derivatives reflects the fact that both the oxidation state and the coordination number of the metal centre remain unchanged. The quadrupole splittings of the thiolate complexes range between 2.51 and 2.92 mm s^{-1}, which is consistent with the high-spin state of the iron(II) centres.

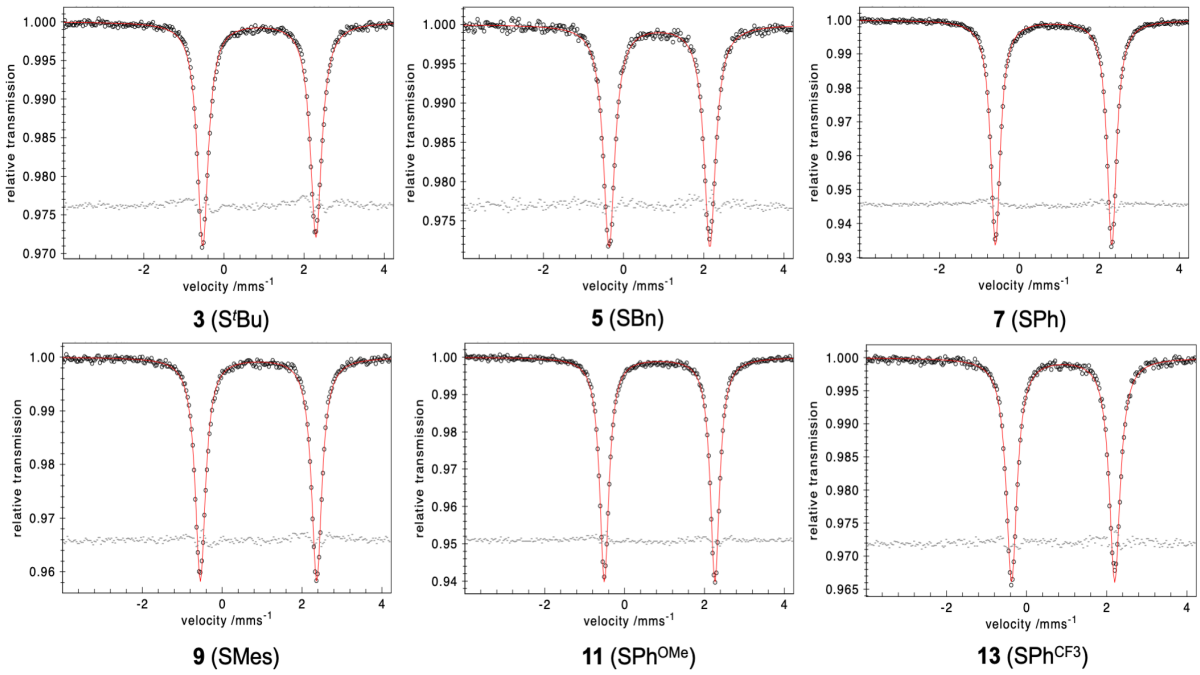

Figure 11. The zero-field ^{57}Fe Mössbauer spectra for complexes **3**, **5**, **7**, **9**, **11** and **13**, obtained at 80 K. Data points are depicted by black circles and the best fit is given by the red trace.

Due to the consistent coordination environment throughout the iron thiolate series, the Mössbauer parameters can be regarded as a measure of the thiolate donation to the iron centre. Complexes **9** (SMes) and **13** (SPh^{CF3}) both have an isomer shift of 0.91 mm s^{-1}, which is the largest value across the series and is in line with the expected weaker S→Fe charge transfer and, hence, the longer Fe–S bonds as obtained from X-ray crystallography. Complexes **3** (S^tBu) and **11** (SPh^{OMe}) both have an isomer shift of 0.88 mm s^{-1}, in line with stronger S→Fe charge donation and shorter Fe–S bonds. The smallest isomer shift in the series (δ = 0.86 mm s^{-1}) is observed for **7** (SPh). That being said, while the Mössbauer isomer shifts do correlate with the expected variation in electronics, any qualitative conclusions remain tentative since the shift variation across the series is 0.05 mm s^{-1} while the measurement error is ca. 0.03 mm s^{-1}.

Experimental Mössbauer parameters are reasonably well reproduced by density functional theory (DFT) calculations, for which both computationally optimised (B3LYP/6-311g(d,p)) and experimental solid-state X-ray crystal structure geometries were used. The initial isomer shift calculations were performed using the correlation curves published by Neese and co-workers.[51] However, we consistently obtained isomer shift values that deviated significantly from the experiment (by 0.10–0.24 mm s^{-1}). This prompted us to use the correlation curves developed by the group of Holland.[52] Although these were initially developed for iron diketiminate complexes, they have been validated using a "training set" of iron complexes bearing a variety of different supporting ligands. In our case, the correlation curve that operates at the B3LYP/def2-TZVP/CP(PPP) level of theory gave the best results, with calculated δ values within 0.01–0.11 mm s^{-1} of those obtained experimentally.

Table 4. Zero-field Mössbauer isomer shift (δ_{exp}, mm s^{-1}) and quadrupole splitting ($|\Delta E_Q|_{exp}$, mm s^{-1}) obtained for powder samples of complexes **1**, **3**, **5**, **7**, **9**, **11** and **13** at 80 K. Theoretical Mössbauer parameters obtained by DFT for the X-ray crystal structure (δ_{xrd}, $|\Delta E_Q|_{xrd}$) and DFT-optimised geometries (δ_{opt}, $|\Delta E_Q|_{opt}$), calculated using the correlation curve [$\delta = \alpha(\rho(0) - C) + \beta$], where α = –0.30, β = 1.49, and C = 14760, as defined for the B3LYP / def2-TZVP / CP(PPP) level of theory.[52]

Complex	δ_{exp}	$\lvert\Delta E_Q\rvert_{exp}$	δ_{xrd}	$\lvert\Delta E_Q\rvert_{xrd}$	δ_{opt}	$\lvert\Delta E_Q\rvert_{opt}$
1 (Cl)	0.94	2.58	0.99	2.68	1.05	2.49
3 (S^tBu)	0.88	2.83	0.89	2.68	0.93	2.57
5 (SBn)	0.90	2.51	0.91	2.40	0.92	2.74
7 (SPh)	0.86	2.91	0.92	2.59	0.96	2.60
9 (SMes)	0.91	2.92	0.93	2.72	0.95	2.57
11 (SPh^{OMe})	0.88	2.77	0.90	2.77	0.97	2.54
13 (SPh^{CF3})	0.91	2.57	*n/a*	*n/a*	0.97	2.63

The isomer shifts derived from both X-ray diffraction-based (δ_{xrd}) and computational (δ_{opt}) geometries are similar (Table 4), with the latter being somewhat higher than the former. Overall, certain experimental trends are reproduced by the δ_{xrd} and δ_{opt} values. For instance, the isomer shift values calculated for the parent complex **1** are consistently higher than for any of the thiolates. In addition, lower δ values tend to be computed for complexes bearing aliphatic or electron-rich thiolates. That being said, the values derived from computational and X-ray diffraction-based geometries follow different trends, which we interpret in terms of subtle differences between optimised gas-phase and experimental solid-state geometries. Furthermore, both the computed and experimental isomer shifts also follow different trends, which we attribute to the mean average error of the calibration curve, reported to be 0.04 mm s^{-1}. Based on the above, the significance of the isomer shift values must be treated with caution, and direct correlation between the Fe–S bond covalency (as probed by the isomer shift) and complex reactivity cannot be drawn. Finally, the calculated quadrupole splitting values $|\Delta E_Q|_{xrd}$, and $|\Delta E_Q|_{opt}$ are in a general agreement with the experiment, $|\Delta E_Q|_{exp}$, although no clear trends can be derived due to the inherent dependency of these values on small differences in ligand field symmetry around the iron centre.

4.2.6 Computational Analysis

In order to gain further insight into their electronic structures, we studied complexes **3**-**14** computationally by means of DFT calculations and natural bonding orbital (NBO) analysis, performed using the *Gaussian 16* software package at the B3LYP/6-311g(d,p) level of theory.[53] Full computational details can be found in the experimental section of this chapter.

4.2.6.1 Zinc Thiolate Complexes

The optimised gas-phase geometries obtained for zinc thiolate complexes **4**, **6**, **8**, **10**, **12** and **14** are consistent with those observed in their X-ray crystal structures. Our calculations show that the highest occupied molecular orbital (HOMO) is consistently localized on the phenolate moiety of the supporting ligand scaffold throughout the zinc thiolate complex series (Figure 12). This nicely reflects the redox non-innocence of the $\mathbf{Im^{Ph2}NNO^{tBu}}$ ligand, which was previously established in Chapter 3 of this thesis.[35] Interestingly, the computations show that an increasingly large contribution to the HOMO is made by the sulfur atom lone pair in complexes **10** (SMes), **12** (SPh^{OMe}), **6** (SBn) and **4** (S^tBu), in direct correlation with their approximate thiolate donicities. In contrast, the HOMO in **8** and **14** is exclusively localized on the phenolate moiety. For all the zinc thiolate complexes, the lowest unoccupied molecular orbital (LUMO) is consistently delocalised across the bis-imidazole ligand backbone and is relatively energetically inaccessible.

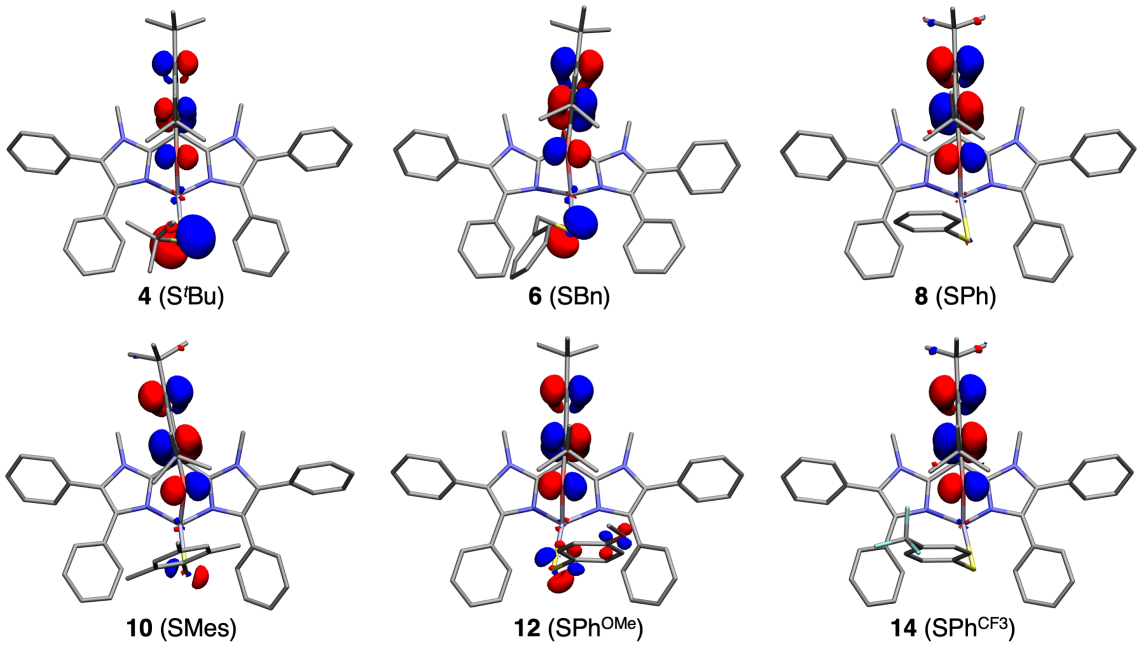

Figure 12. The DFT-calculated HOMOs obtained for complexes **4**, **6**, **8**, **10**, **12** and **14**.

4.2.6.2 Iron Thiolate Complexes

Since the experimental Mössbauer parameters for iron thiolates **3**, **5**, **7**, **9**, **11** and **13** are well-reproduced by the DFT-calculations based on computationally-optimized geometries, the derived electron density can be used for a more detailed analysis of their electronic structure. NBO analysis shows that the natural charge of the Fe atoms decreases from +1.49 in parent complex [Fe(L)(Cl)] (**1**)[35] to approximately +1.46 for the thiolate series (Table 5). This demonstrates an increased degree of charge transfer from the sulfur to the iron centres, consistent with the formation of more covalent Fe–S bonds. Depending on the electronic properties of the tethered organic substituent, the natural charge on the sulfur is seen to vary from –0.58 for **3** (S^{t}Bu) to –0.48 for **13** (SPh^{CF3}). DFT calculations show that the four occupied MOs of highest energy are singly occupied iron-based *d*-orbitals (Figure 13), in line with the natural spin density being largely localised on the iron centre in each complex. On this basis, we predict the iron to be most prone to electrochemical oxidation, even in the presence of redox non-innocent (thio)phenolate moieties.

Table 5. Natural charge and natural spin density obtained for the iron thiolate complex series.

Complex	Calculated Fe–S (Å)	Natural charge **Fe**	Natural charge **S**	Natural spin density **Fe**	Natural spin density **S**
3 (S^{t}Bu)	2.29046	+1.45934	–0.58180	3.69584	0.09221
5 (SBn)	2.30423	+1.46208	–0.55485	3.69380	0.08826
7 (SPh)	2.29654	+1.46756	–0.49995	3.68982	0.07554
9 (SMes)	2.28976	+1.46699	–0.51076	3.68061	0.08094
11 (SPh^{OMe})	2.29644	+1.46906	–0.50297	3.68812	0.07957
13 (SPh^{CF3})	2.30696	+1.47081	–0.48415	3.68873	0.06726

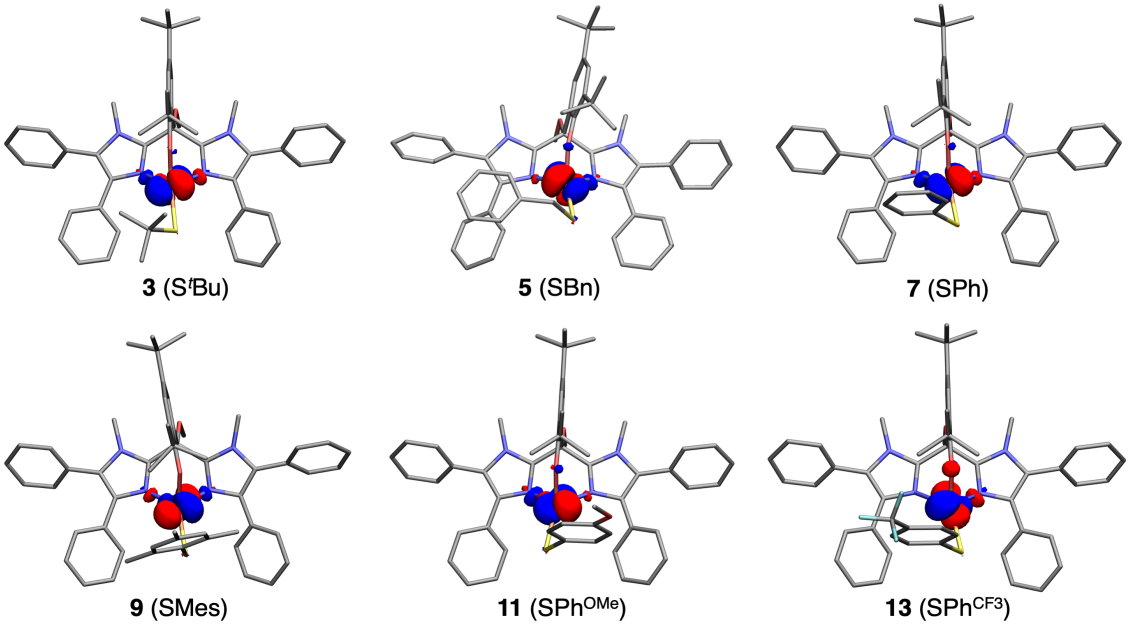

Figure 13. The DFT-calculated HOMOs of iron thiolate complexes **3**, **5**, **7**, **9**, **11** and **13**.

4.2.7 Electrochemistry

The influence of the different thiolate co-ligands on the electrochemical behaviour of [M(Im^{Ph2}NNO^{tBu})(SR)] complexes **3**-**14** was investigated by means of cyclic voltammetry (CV). All CVs were recorded under an inert atmosphere (N_2), in acetonitrile solution and using [*n*-Bu_4N]PF_6 as a supporting electrolyte. All quoted potentials are referenced to the ferrocene/ferrocenium redox couple (Fc/Fc^+).

4.2.7.1 Zinc Thiolate Complexes

The cyclic voltammograms of zinc thiolate complexes **4**, **6**, **8**, **10**, **12** and **14** are displayed in Figure 14. We previously reported the CV of **8** and assigned all electrochemical events (see Chapter 3).[35] Its CV has been included for completeness. All CVs feature a strong, irreversible oxidation event at approximately +0.50 V, denoted by a black asterisk in Figure 14. We assign this event to the electrochemical oxidation of the phenolate moiety in each complex, on the basis of the comparable redox potential and similar waveform we previously observed for **8**.[35] This assignment is further substantiated by our computational analysis (*vide supra*) that shows the HOMO to be localised principally on the phenolate moiety throughout the complex series. This nicely demonstrates the redox non-innocence of the supporting phenolate, in line with our previously reported electrochemical studies involving ligand **Im^{Ph2}NNO^{tBu}** in Chapter 3.[35] A clear trend in the phenolate oxidation potential can be observed, which appears to be dependent on the donicity of the thiolate co-ligand. For instance, the phenolate oxidations in complexes **4** (+0.43 V), **6** (+0.47 V), **10** (+0.35 V) and **12** (+0.50 V) occur at relatively low redox potentials, in line with the more electron-donating nature of their thiolate ligands. Similarly, the higher redox potentials of the phenolate oxidations in complexes **8** (+0.65 V) and **14** (+0.68 V), reflect

the less electron-donating character of the thiolates. Of note is the remarkably low potential of the phenolate oxidation in complex **10**, which deviates from the expected trend. We speculate that this may be related to more rigid mesitylthiolate coordination to the metal centre. The phenolate oxidation is electrochemically irreversible in all complexes, which we ascribe to structural rearrangements that may occur in solution upon oxidation of the phenolate group.

Scanning to higher potentials, a second irreversible oxidation event is observed at around +1.1 V in complexes **4**, **6**, **8** and **14**, denoted by a triangle in Figure 14. We assign this event to electrochemical thiolate oxidation. This feature is not easily distinguishable for all complexes, and in the case of complexes **10** and **12** it appears to be severely overlapped with the electrochemical phenolate oxidation. In these cases, we hypothesise that the electron-rich and aromatic nature of the thiolate co-ligands helps stabilise formation of the thiophenoxide radical. Finally, we note that all [Zn(Im^{Ph2}NNO^{tBu})(SR)] complexes exhibit a similar electro-chemical profile within the potential window +1.5 V and –2.0 V. This indicates that the complexes are of similar speciation and have a well-defined structure in solution, which is in agreement with our NMR data (*vide supra*).

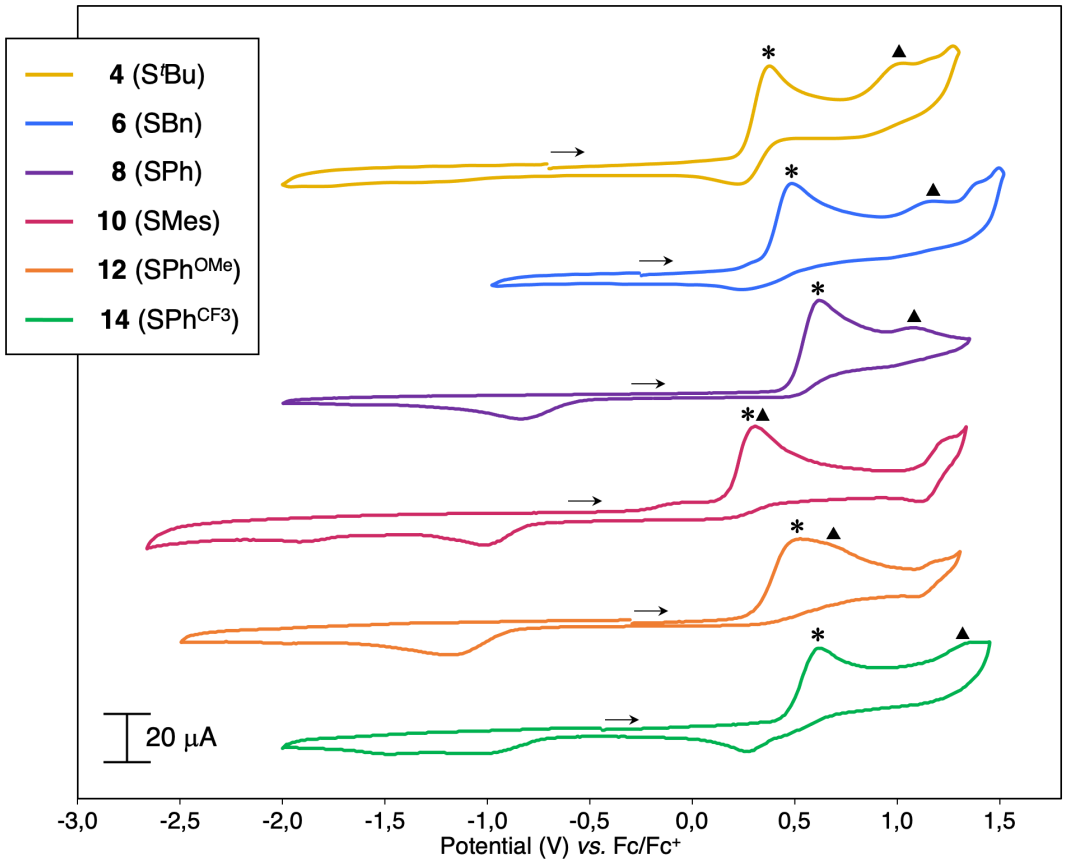

Figure 14. CVs of zinc thiolate complexes **4**, **6**, **8**, **10**, **12**, and **14**, recorded at ambient temperature, in MeCN solution, using 0.1 M [*n*-Bu$_4$N]PF$_6$ as a supporting electrolyte and with a scan rate of 100 mV/s. The electrochemical responses assigned to phenolate and thiolate oxidations are denoted by asterisks and triangles, respectively.

4.2.7.2 Iron Thiolate Complexes

The cyclic voltammograms of iron thiolate complexes **3**, **5**, **7**, **9**, **11** and **13** are displayed in Figure 15. The first electrochemical oxidation, denoted by a black asterisk, occurs close to 0 V for all complexes. We assign this event to the Fe^{2+}/Fe^{3+} redox couple, as the corresponding one-electron oxidation of the iron centre in parent complex [Fe($Im^{Ph2}NNO^{tBu}$)(Cl)] (**1**) was also seen to occur at the low potential of +0.18 V (Chapter 3).[35] Our assignment is further substantiated by DFT calculations (*vide supra*), which show that the singly-occupied HOMO in the iron thiolate complex series is consistently localised on the iron centre. The iron-based oxidations occur at –0.07 V (for **3**), +0.01 V (for **5**), +0.04 V (for **7**), +0.05 V (for **9**), +0.00 V (for **11**), and +0.10 V (for **13**).

While the overall variation between the redox potentials is relatively small, a clear trend is distinguished: iron centres bound to more electron-rich thiolates have lower oxidation potentials than those bound to electron-poor thiolates. In other words, iron complexes with the most sulfur-to-iron charge transfer have the most electron-rich iron centres and are most prone to oxidation. This trend is very much in line with the solid-state structural data

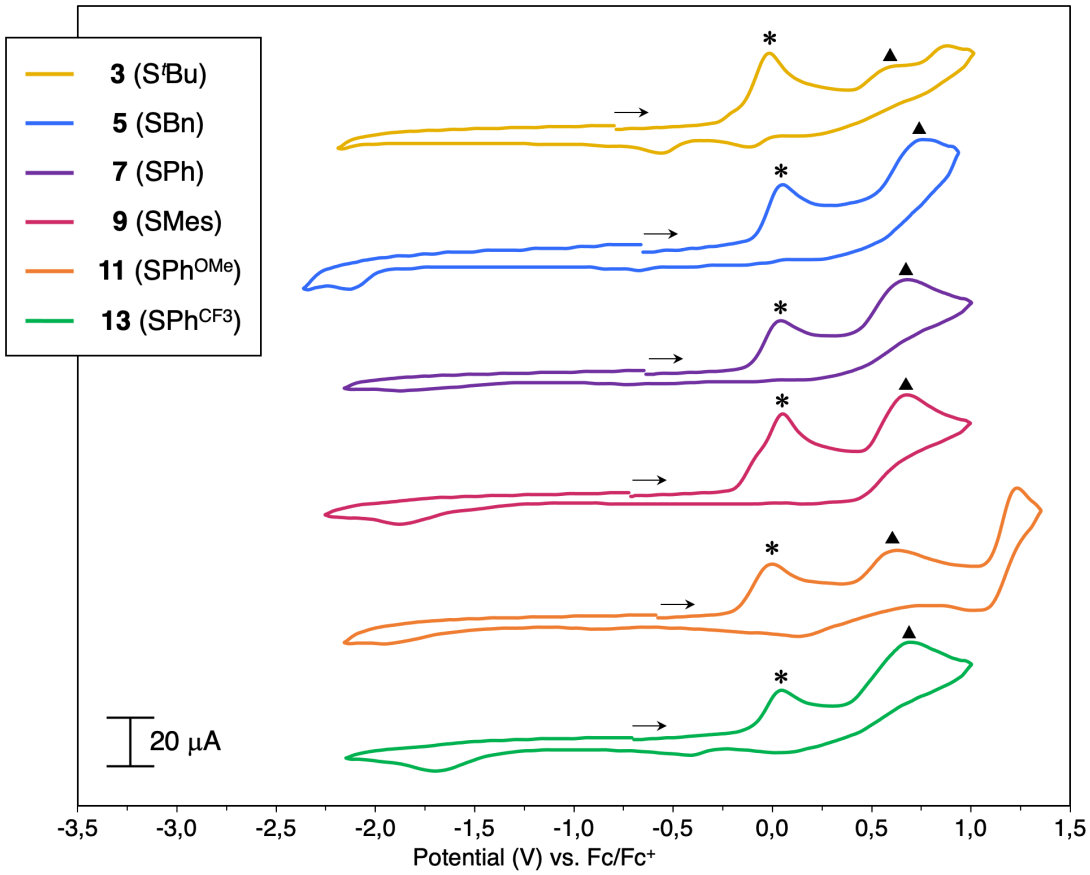

Figure 15. CVs of iron thiolate complexes **3**, **5**, **7**, **9**, **11**, and **13**, recorded at ambient temperature, in MeCN solution, using 0.1 M [*n*-Bu_4N]PF_6 as a supporting electrolyte and with a scan rate of 100 mV/s. The electrochemical responses assigned to iron and phenolate oxidations are denoted by asterisks and triangles, respectively.

and Mössbauer parameters (*vide supra*). Interestingly, the electron-donating effect of the mesitylthiolate co-ligand appears to be less pronounced in **9** than it was for the analogous zinc complex **10**, since complexes **7** and **9** have almost identical Fe^{2+}/Fe^{3+} redox potentials. Overall, the iron oxidation appears to be electrochemically irreversible for all iron thiolate complexes. We attribute this to structural changes that occur upon oxidation of the iron to its ferric state, which is known to favour higher coordination numbers.

In all complexes, a second redox event occurs at approximately +0.5 V (denoted by triangles in Figure 15). We assign this event to the electrochemical oxidation of the supporting phenolate moiety, based on the similar phenolate oxidation potential observed for **1**, as well as the comparable phenolate oxidation potentials recorded for the analogous zinc thiolate complex series. We also observe that phenolate oxidation is electrochemically irreversible, likely due to structural changes in solution that occur upon phenoxide formation in the presence of iron(III). Strikingly, much less variation in phenolate oxidation potentials is observed throughout the iron complexes series than for the zinc counterparts. We attribute this to the fact that electrochemical iron oxidation precedes that of the phenolate, and that phenolate oxidation therefore occurs in the presence of a strong Lewis acid (Fe^{3+}), leading to very different electrochemical trends. Finally, we note that, unlike the zinc thiolate complex series, electrochemical thiolate oxidation is not easily distinguished for any of iron thiolate complexes.

We conclude this section with the observation that all iron complexes exhibit a similar electrochemical profile, as was the case for the sister zinc thiolate complex series. This is a strong indication that the iron thiolate complexes have a well-defined structure in solution. Our results also show that, despite the redox non-innocence of the $\mathbf{Im^{Ph2}NNO^{tBu}}$ ligand, the iron(II) centres are the sites most prone to electrochemical oxidation in all complexes. It is therefore of great interest to explore the reactivity of these complexes to different oxidants.

4.2.8 Reactivity with O_2

Complexes **3**, **5**, **7**, **9**, **11** and **13** are highly sensitive to dioxygen. Exposing a CH_2Cl_2 solution of each complex to air at ambient temperature causes an instant colour change from almost colourless to deep red. This colour persists for approximately 2 h before slowly fading and eventually forming a yellow solution overnight. In UV-vis spectroscopy, exposure of the complexes to air is linked to the rapid development of an intense absorption band that varies between 472 nm for **3** (S^{t}Bu) and 550 nm for **13** (SPh^{CF3}), in accordance with the approximate donicity of the different thiolate ligands (Figure 16).

Previously, it has been shown that initial exposure of the substrate-bound IPNS active site to O_2 produces a short-lived band at 515 nm, assigned to the Fe^{3+}–OO^- intermediate.[14] The new absorption bands observed for our complexes are therefore indicative of an increase in oxidation state of the iron centres to their ferric state and we tentatively ascribe these bands to ligand-to-metal charge transfer (LMCT). Interestingly, the band at 550 nm for **13** develops more slowly under the diffusion-limited measurement conditions than for the other iron thiolate complexes. We ascribe this to the electron-withdrawing nature of the thiolate co-ligand, which increases the Fe^{III}/Fe^{II} redox potential and reduces the rate at which the iron centre is oxidised. However, on the basis of UV-vis spectroscopy alone we are unable to say whether outer-sphere iron oxidation occurs or whether any oxygenated intermediates or products form.

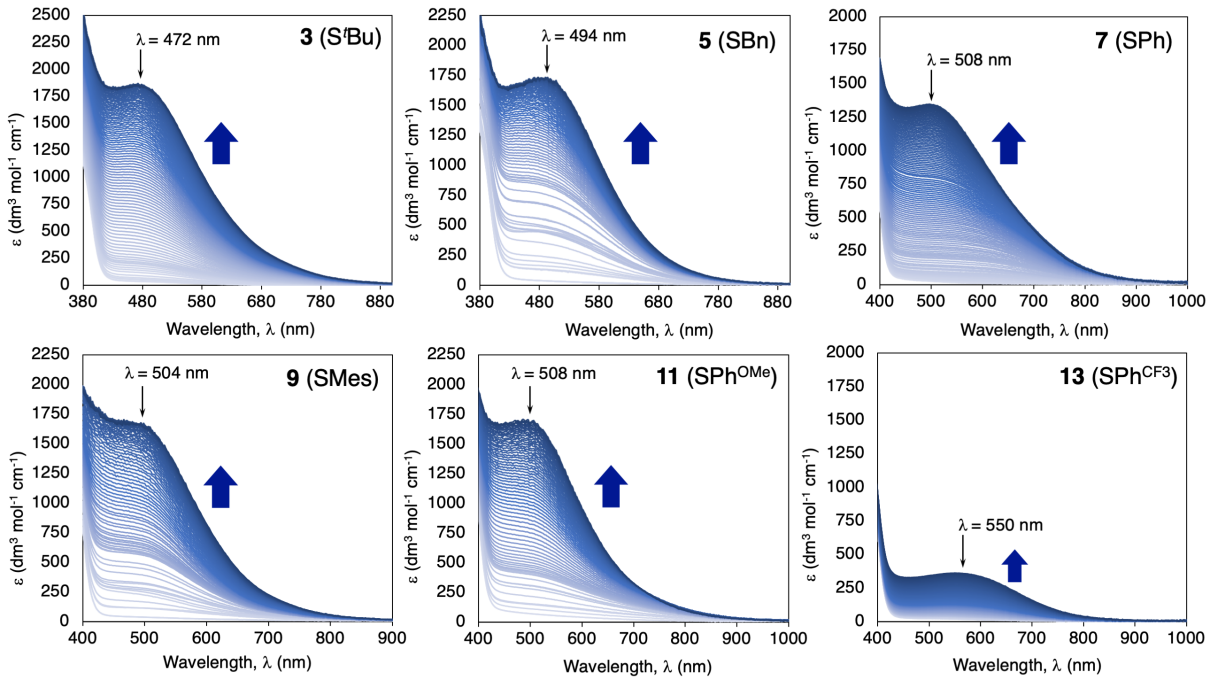

Figure 16. The UV-vis spectra of the air-exposure of complexes **3**, **5**, **7**, **9**, **11** and **13**, recorded in CH_2Cl_2 (ambient temperature, diffusion-controlled). Spectra were recorded every 12 seconds until a maximum was reached. Blue arrows indicate the increase in absorption over time.

We resorted to ESI-MS in order to examine the nature of the species present in solution upon exposing **7** to air. Positive mode ESI-MS analysis of an anaerobic solution of **7** in MeCN shows a single peak at m/z = 810.6, which corresponds to the $[Fe^{II}(L)+MeCN]^+$ ion (L = $Im^{Ph2}NNO^{tBu}$). This ion is most abundant in the ESI-MS spectrum due to the natural positive charge of the complex that arises upon dissociation of the thiolate co-ligand compared to the neutral charge of the $[Fe(Im^{Ph2}NNO^{tBu})(SR)]$ structure. Positive mode ESI-MS of a solution of **7** in MeCN that was exposed to air for a period of 5 minutes at ambient temperature shows the principal ion to be that at m/z = 810.5 (Figure 17), indicating that **7** is still the main species present in solution during this time. However, several new ions are also observed at m/z = 713.5, 868.6, 991.6 and 1061.9. We assign the peak at m/z = 713.5 to the $[L]^+$ ion (calculated m/z = 713.4), which may simply arise as a result of phenolate oxidation during the ionization process. We assign the very small peak at m/z = 868.6 to the $[Fe^{III}(L)+2MeCN+OH]^+$ ion (calculated m/z = 868.4). This indicates that the iron(II) centre is able to undergo outer-sphere oxidation in the presence of O_2.

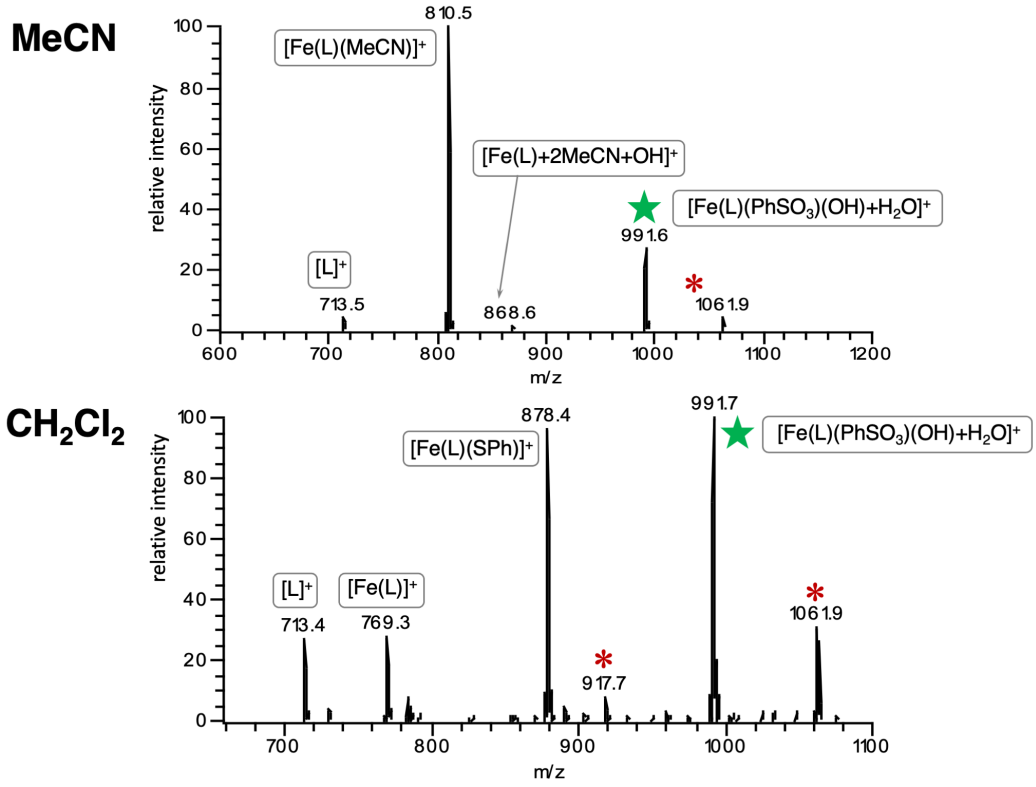

Figure 17. ESI(+)-MS spectra obtained after exposing a solution of **7** in MeCN (top) and CH_2Cl_2 (bottom) to air. L = **$Im^{Ph2}NNO^{tBu}$**. Red asterisks indicate ions that could not be assigned. The green star denotes the proposed $[Fe(L)(PhSO_3)(OH)+H_2O]+$ ion.

The ion at 991.6 is of particular interest, as we calculate that it could correspond to either $[Fe^{III}(L)(SPh)(OOH)+MeCN+K]^+$ or $[Fe^{III}(PhSO_3)(OH)+H_2O]^+$ (both ions calculated as m/z = 991.3). MS-MS measurements on this ion show the loss of a fragment with m/z of 32, although we are unable to determine whether this is indeed loss of O_2 or loss of a $[OCH_3+H]$ fragment (*e.g.* through methoxy cleavage of the ligand backbone). Collision induced dissociation (CID) experiments targeting the ion at m/z 991.3 show that it

fragments to produce the $[Fe(L)]^+$ ion (m/z = 769.7). However, we were unable to assign the nature of the species lost during this fragmentation process and we are therefore unable to assign the ion at m/z = 991.3 with any certainty. In negative mode ESI-MS, two peaks were observed at m/z = 157.0 and 337.2, which correspond to the $[PhSO_3]^-$ and $[2PhSO_3+Na]^-$ ions, respectively.

For comparison, we monitored the oxidation of **7** in CH_2Cl_2 by ESI-MS. After 5 minutes of air exposure, a strong signal at m/z = 878.4 was observed, which corresponds to the $[Fe^{III}(L)(SPh)]^+$ ion (calculated m/z = 878.3) (Figure 17). This shows that **7** can undergo outer-sphere oxidation with relative ease, producing the corresponding cationic iron(III) complex. Compared to the ESI-MS spectrum recorded in MeCN, we do not observe the presence of the $[Fe^{II}(L)(solvent)]^+$ ion, due to the non-coordinating nature of CH_2Cl_2. We do, however, observe a weak signal for the $[Fe^{II}(L)]^+$ ion at m/z = 769.3 (calculated m/z = 769.3), which once again shows the ease with which these ions are detected due to the natural positive charge that arises upon dissociation of the thiolate ligand. At m/z = 713.4, we observe another weak signal that corresponds to the $[L]^+$ ion. Interestingly, we also observe a relatively strong signal at m/z = 991.7, which increases in relative abundance over time. The presence of this ion in CH_2Cl_2 solution suggests that a common oxidised product is formed upon exposing **7** to air in both coordinating and non-coordinating solvents. It also forces us to deduce that MeCN is not incorporated within the structure of this ion and, therefore, that it is most likely to correspond to the iron(III) sulfonate ion, $[Fe^{III}(L)(PhSO_3)(OH)+H_2O]^+$. On this basis, we propose that sulfonate-to-iron(III) charge transfer is responsible for the strong LMCT bands observed in the UV-vis spectra shown in Figure 16. Finally, we note the presence of two other signals at m/z = 917.7 and 1061.9, which we were unable to assign.

Overall, these results demonstrate interesting oxidative transformations of **7** in solution. We observe that the iron(II) thiolate complex can undergo outer-sphere oxidation to its ferric form with relative ease, and also that the thiolate co-ligand undergoes oxygenation. However, the neutral charge of complex **7**, and indeed all of its sister complexes, render it somewhat challenging to draw definite conclusions as to the nature of the main species in solution. In order to further these mechanistic investigations and more easily monitor oxidative transformations by ESI-MS, it would be of interest to synthesise variants of the iron thiolate complexes that incorporate an electronically charged moiety at a site remote to the iron centre, for example an ammonium group tethered to the supporting ligand or to the thiophenolate ligand. It is also desirable to include ^{18}O isotopic labelling studies and investigate the manner in which oxygen atoms are incorporated into any transient iron-oxygen intermediates as well as the oxygenated sulfonate products.

4.2.9 Reactivity with Ph_3CSNO

Nitric oxide (NO) has been used as an O_2 surrogate in the study of many non-heme iron enzymes, including that of IPNS.[9,11,13] NO binds at the iron(II) centre to create a (generally) stable, chromophoric, EPR-active $\{FeNO\}^7$ species that can be studied using a multitude of spectroscopic methods. The [Fe·IPNS·ACV·NO] complex has been reported to have a distinct pink colour in solution, associated to two optical absorption features at 508 nm (λ_{max}) and 720 nm.[11] In EPR spectroscopy, two features at $g = 4$ and $g = 2$ are observed that are characteristic for a $S = {}^3/_2$ iron nitrosyl complex, denoted $\{FeNO\}^7$ according to the Enemark-Feltham notation,[54] which is generally rationalised as comprising a high-spin ($S = {}^5/_2$) Fe^{3+} ion antiferromagnetically coupled to NO^- ($S = 1$).[13,55,56]

Here, we employ trityl-*S*-nitrosothiol (Ph_3CSNO) as a convenient substitute for NO gas. Use of Ph_3CSNO as an NO donor has previously been reported to yield iron nitrosyl compounds analogous to those obtained from reaction with NO gas, notably by the groups of Lippard, Meyer, Lehnert and Majumdar.[57–59] The advantage hereof is that Ph_3CSNO is a solid that can easily be weighed out for use in stoichiometric reactions. We investigated the reaction of complexes **3** (S^tBu), **7** (SPh) and **9** (SMes) with Ph_3CSNO, as these complexes incorporate a good degree of structural and electronic variation.

Reactions were conducted by stirring the desired iron thiolate complex with one equivalent of Ph_3CSNO in CH_2Cl_2 solution at ambient temperature for a period of 3 h, in a darkened container (Scheme 3). In all cases, the colour of the mixture changed from bright green (the colour of the nitrosothiol reagent) to brown during the course of the reaction. After this time, small aliquots of the reaction mixtures were taken for UV-vis, IR and EPR analysis. Unfortunately, despite numerous attempts, no crystals suitable for X-ray diffraction could be obtained of the reaction products.

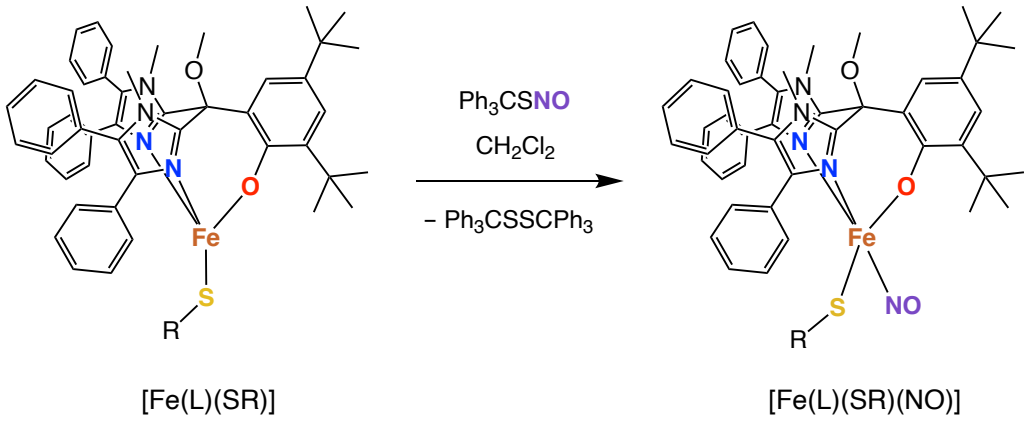

Scheme 3. The reaction of [Fe($Im^{Ph2}NNO^{tBu}$)(SR)] with Ph_3CSNO, including the proposed structure of the iron nitrosyl product complex.

The UV-vis spectra of the three reaction products (hereafter referred to as $\mathbf{3}^{NO}$, $\mathbf{7}^{NO}$ and $\mathbf{9}^{NO}$) contain three new absorption features, including a band at around 460 nm (λ_{max}) and two weaker shoulder bands at approximately 350 nm and 645 nm (Figure 18). Similar absorption features have previously been reported by the groups of Que and Fiedler for mononuclear thiolate-bound intermediate-spin ($S = {}^3/_2$) $\{FeNO\}^7$ adducts, supported by tripodal N3 or N4 ligands.[36,60,61] Interestingly, the λ_{max} is seen to vary slightly according to the nature of the thiolate co-ligand, where $\mathbf{3}^{NO}$, $\mathbf{7}^{NO}$ and $\mathbf{9}^{NO}$ exhibit an increasingly red-shifted λ_{max} at 458 nm, 465 nm and 469 nm, respectively. This correlates with the increasingly long Fe–S bond lengths of complexes **3**, **7**, and **9** in the solid state. We therefore assign this band to thiolate-to-metal charge transfer, and we hypothesise the thiolate remains bound to the iron upon formation of the NO adducts. Finally, we note that the λ_{max} in $\mathbf{3}^{NO}$, $\mathbf{7}^{NO}$ and $\mathbf{9}^{NO}$ is somewhat blue-shifted compared to that of the [Fe·IPNS·ACV·NO] complex (λ_{max} = 508 nm).[11] We attribute this to the more electron-donating nature of the phenolate O-donor in $\mathbf{Im^{Ph2}NNO^{tBu}}$ compared to the 2H1C carboxylate in IPNS.

Compared to their parent complexes, the IR spectra of $\mathbf{3}^{NO}$, $\mathbf{7}^{NO}$ and $\mathbf{9}^{NO}$ contain two new signals at approximately 1765 cm^{-1} and 1696 cm^{-1}, denoted by black asterisks in Figure 18. This demonstrates the formation of an NO-bound iron complex. These signals are significantly downshifted compared to NO gas (υ_{NO} = 1875 cm^{-1})[62] and distinct from the Ph_3CSNO precursor (υ_{NO} = 1513 cm^{-1}).[57] However, the presence of two signals is likely due to multiple NO-bound species present in solution.

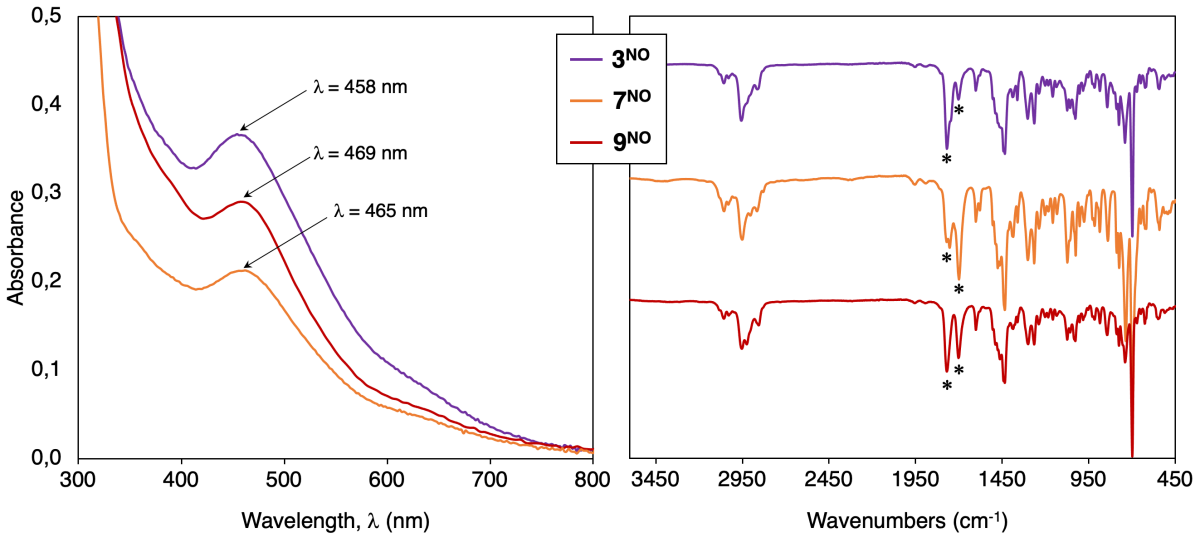

Figure 18. UV-vis spectra (left) and IR spectra (right) obtained for the reactions of [Fe(L)(S^{t}Bu)] (**3**), [Fe(L)(SPh)] (**7**) and [Fe(L)(SMes)] (**9**) with Ph_3CSNO, which are proposed to form $\mathbf{3}^{NO}$, $\mathbf{7}^{NO}$ and $\mathbf{9}^{NO}$, respectively. UV-vis spectra were recorded in CH_2Cl_2 at ambient temperature and are not corrected for concentration.

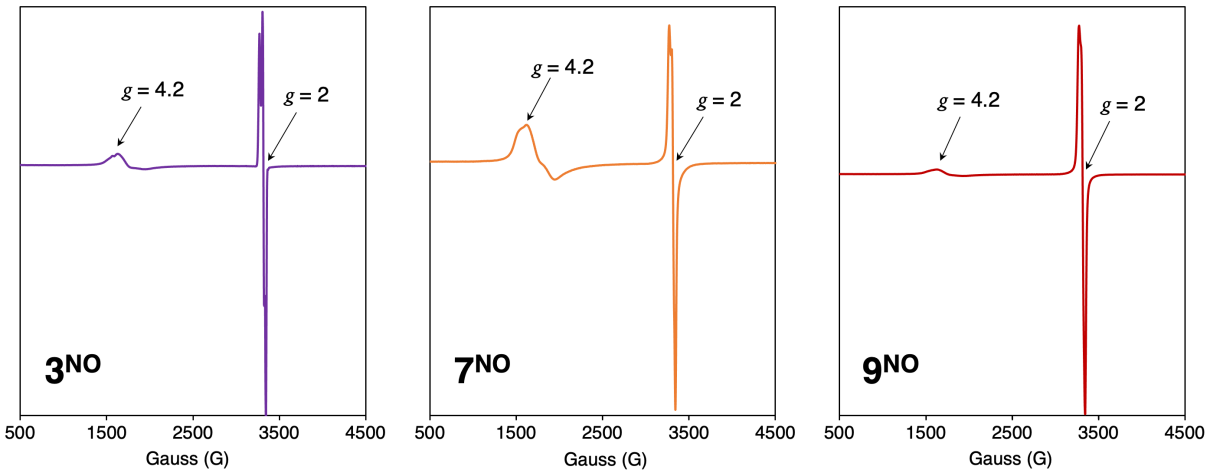

Figure 19. X-band EPR spectra obtained for the reaction product mixtures $\mathbf{3}^{NO}$, $\mathbf{7}^{NO}$ and $\mathbf{9}^{NO}$, recorded in a CH_2Cl_2/toluene glass (1:1 v/v) at 100 K. Instrument: frequency = 9.39871 GHz, power = 2.000 mW, modulation amplitude = 1.00 G.

The X-band EPR spectra of the product mixtures all contain a broad signal at $g_{eff} \sim 4$ and a sharper signal at $g = 2$ (Figure 19). This is an indication that the iron centres in **3**, **7** and **9** have undergone an oxidative process upon reaction with Ph_3CSNO. From these spectra, it may be deduced that two different paramagnetic species have formed in each reaction. The first corresponds to a $\{FeNO\}^7$ adduct and exhibits a derivative signal at $g_{eff} \sim 4$ and a negative peak at $g_{eff} \sim 2$, which can be ascribed to the lower Kramers doublet of the $S = {}^3/_2$ ground spin state. The highly broadened nature of this signal is attributed to E/D strain, which typically arises from a (micro)heterogeneity in molecular structure, as caused by *e.g.* solvation effects. The second paramagnetic species is presumably a $S = {}^1/_2$ dinitrosyl iron complex (DNIC), as its nearly isotropic signal at $g_{eff} \sim 2$ is similar to those found for a large majority of DNICs with an isotropic g-value of 2.03.[60] From the three EPR spectra, it can be seen that the relative abundance of these two paramagnetic species varies significantly, ranging from approximately 5% DNIC impurity for $\mathbf{7}^{NO}$ to 25% DNIC impurity for $\mathbf{9}^{NO}$ (see Appendix C, Figure C6).

Overall, these results show that the iron centres in complexes **3**, **7** and **9** undergo a redox change upon reaction with NO (using Ph_3CSNO). We tentatively propose that a pentacoordinate, $S = {}^3/_2$ $\{FeNO\}^7$ adduct forms in all cases, and that NO can bind directly to the iron centre in the presence of different alkyl- or arylthiolate co-ligands. However, these experiments clearly demonstrate that other species are also formed at the same time, including DNICs, thus deviating from the native reactivity of IPNS. Further research is required in order to fully elucidate the nature of the iron nitrosyl adducts forming in solution and establish the optimal conditions with which to control the accessibility of small molecule oxidants such as NO (and therefore O_2) to the iron centre.

4.2.10 Reactivity with $[Ph_3C]PF_6$

During IPNS' catalytic cycle, the first hydrogen atom abstraction leads to the formation of a unique iron(II) thioaldehyde intermediate. This intermediate directly precedes the closure of the β-lactam ring and, as such, is of great interest to the bioinorganic community. Studying this intermediate using small biomimetic models could provide a better understanding of the structural and electronic properties governing β-lactam ring closure and could lead to improved methods for the synthesis of other β-lactam-containing molecules and antibiotics using bioinspired iron catalysts.

In previous research, Schenk and co-workers reported the efficient synthesis of ruthenium thioaldehyde complexes from the corresponding thiolates, using a triphenylcarbenium (tritylium) salt.[63] To the best of our knowledge, no iron-based counterpart to this chemistry has been attempted and no iron(II) thioaldehyde complexes have been reported to date. Here, we attempt the synthesis of an iron(II) thioaldehyde starting from complex [Fe(Im^{Ph2}NNO^{tBu})(SBn)] (**5**) and using tritylium hexafluorophosphate, $[Ph_3C](PF_6)$. Tritylium salts are widely used as hydride abstracting agents,[64,65] although the highly aromatic nature of the carbocation means it can also readily act as a one-electron oxidant.[66] Consequently, there are two mechanisms with which **5** could plausibly be converted to iron thioaldehyde complex **5a** (Scheme 4). In *Path 1*, the tritylium salt could abstract a β-hydride from the benzylic CH_2, which would be followed by nucleophilic attack of the sulfur lone pair on the carbocation. In *Path 2*, the tritylium salt could mediate the one-

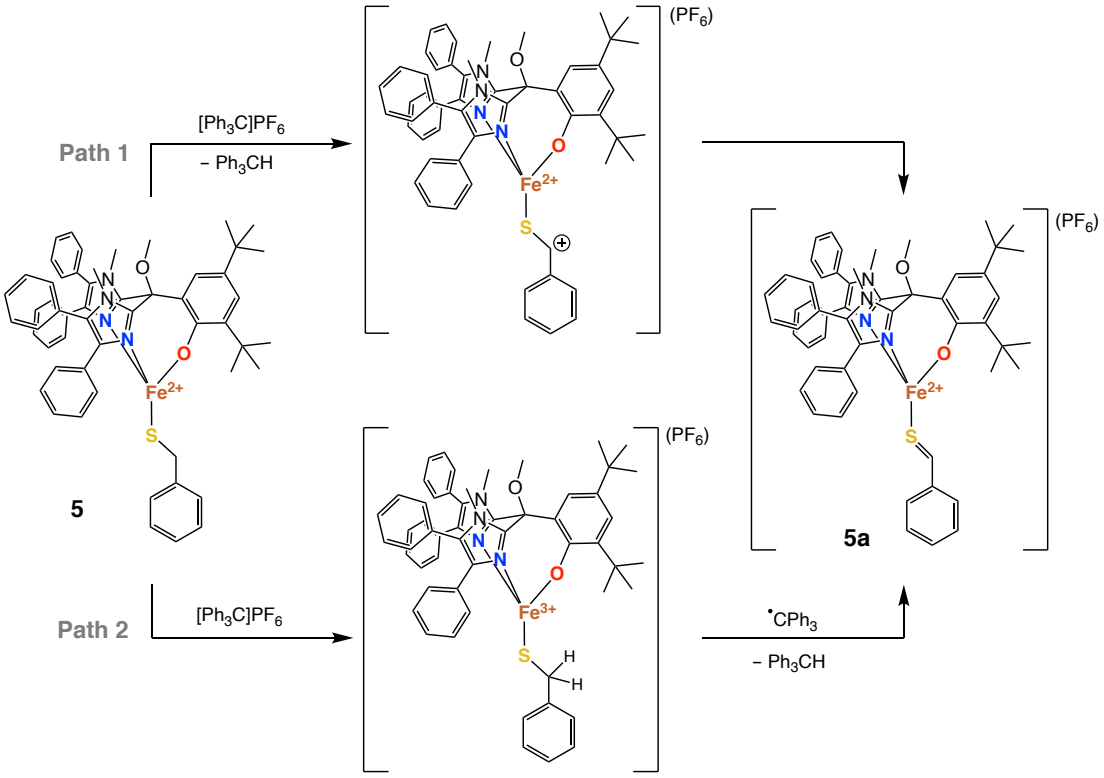

Scheme 4. Proposed reaction pathways towards iron thioaldehyde complex **5a**.

electron oxidation of the iron centre, after which the trityl radical would abstract a H-atom from the carbon adjacent to the sulfur atom. A radical rearrangement would result in the formation of the S=C bond and the reduction of the iron to its ferrous state.

Complex **5** was dissolved in CH_2Cl_2 and cooled to –80 °C. Next, a slight excess of $[Ph_3C](PF_6)$ dissolved in CH_2Cl_2 was added dropwise, causing the colour of the solution to change from almost colourless to bright yellow (the colour of the carbocation). The mixture was initially stirred at –80 °C for 45 min, although no colour change was observed in this time. The mixture was subsequently stirred for a further 90 min while warming to room temperature, which caused the reaction mixture to turn deep red in colour. The solvent was removed under vacuum and the reddish-brown residual solid was washed with hexane. In ^{1}H NMR spectroscopy, signals associated to **5** were no longer present and new paramagnetic signals were observed, indicative of the presence of a new iron complex. In UV-vis spectroscopy, a new absorption band was observed at 465 nm (Figure 21, *vide infra*). X-band EPR analysis of the red product showed a negligible presence of EPR-active material and, on this basis, we exclude the formation of an iron(III) complex.

Red crystals suitable for X-ray diffraction were obtained from the slow diffusion of hexane into a THF solution of the solid over a period of several days. The resulting X-ray crystal structure is that of a tetrahedral iron(II) complex, $[Fe(L^{quinone})_2](PF_6)_2$ (**15**), bound by two ligand molecules whose phenolate groups have been oxidised to their quinone form (Figure 20). Dearomatisation of the phenol ring has resulted in the formation of a C=C bond between the bridgehead carbon atom and the quinone ring, with concomitant loss of the methoxy group. Selected bond lengths and bond angles are given in Table 6.

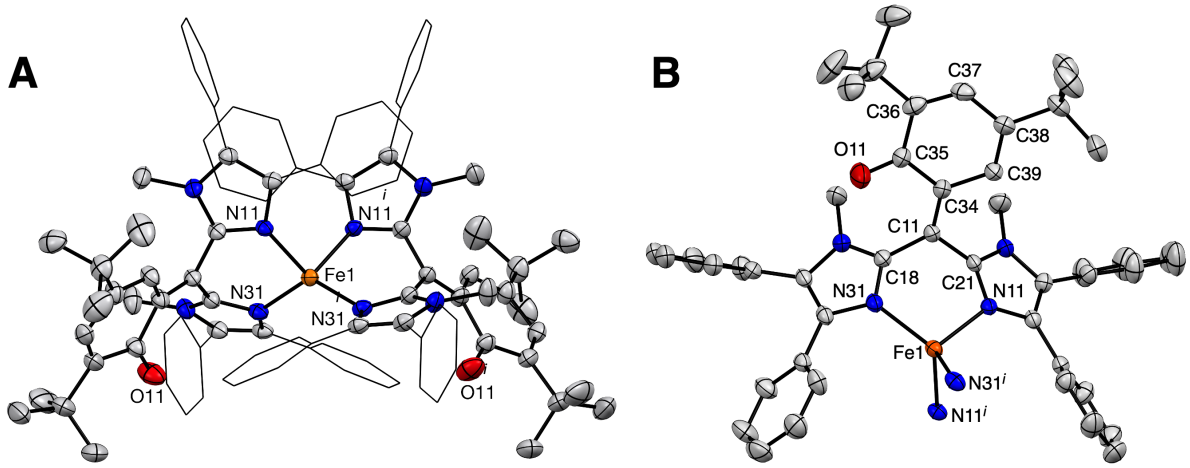

Figure 20. A: Displacement ellipsoid plot of the $[Fe(L^{quinone})_2]^{2+}$ cation in complex **15** (50% probability level). All hydrogen atoms and severely disordered solvent molecules have been omitted for clarity. Phenyl substituents have been depicted in the wireframe format for clarity. The disordered PF_6 anions are not depicted. **B**: The X-ray crystal structure of **15** with one quinone ligand omitted for clarity.

Table 6. Selected bond lengths (Å) and bond angles (°) for $[Fe(L^{quinone})_2](PF_6)_2$ (**15**). Symmetry code *i*: ½-*x*, *y*, 1-*z*.

$[Fe(L^{quinone})_2](PF_6)_2$ (**15**)					
Bond	Length	Bond	Length	Angle	Degrees
Fe1–N11	2.066(3)	C351–C361	1.474(5)	N11–Fe1–N31	98.41(10)
Fe1–N31	2.036(3)	C361–C371	1.344(5)	N11–Fe1–N11^i	98.82(14)
C11–C341	1.361(5)	C371–C381	1.457(5)	N11–Fe1–N31^i	114.77(10)
C351–O11	1.219(4)	C381–C391	1.341(5)	N31–Fe1–N31^i	128.52(16)
C341–C351	1.504(5)	C391–C341	1.456(5)	C181–C11–C21	114.5(3)

We speculate that **15** forms as a result of the initial one-electron oxidation of **5** to its ferric state by the tritylium salt followed by homolytic cleavage of the Fe^{3+}–O bond, whereby a ferrous ion and a phenoxide radical are generated. Radical rearrangement of the phenoxide would generate the conjugated quinone structure with concomitant release of a methoxy radical. The electrons needed to reduce the methoxy radical to the corresponding anion may then be obtained from the oxidation of two benzylthiolate anions to the disulfide (Scheme 5). As is clearly demonstrated by the X-ray crystal structure of **15**, the newly formed quinone ligand does not sustain tridentate *N,N,O* coordination to the metal centre and, instead, adopts a bidentate *N,N* coordination mode through its imidazole groups. This allows significant structural rearrangements to take place at the metal centre, including the formation of a thermodynamically favourable bisligated, homoleptic complex.

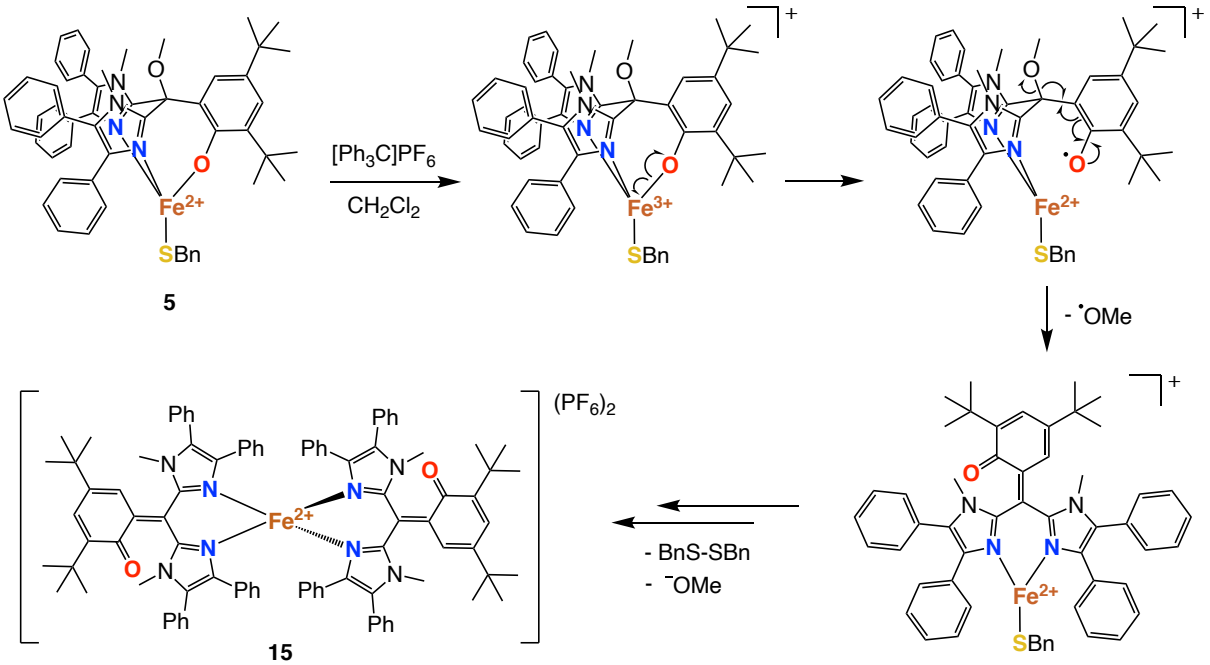

Scheme 5. Reaction of **5** with $[Ph_3C]PF_6$, resulting in the formation of **15**.

For comparison, we also performed the reaction between $[Fe(Im^{Ph2}NNO^{tBu})(SPh)$ (**7**) and $[Ph_3C]PF_6$. We observed a similar change in colour of the reaction mixture, from bright

yellow to red over the course of 3 h. The UV-vis of the resulting product is depicted in Figure 21. As can be seen, we observe the development of a similar band at 465 nm, indicative of the formation of **15**, whereas for **7** a broad feature at lower energy is also observed. These results show that ligand **Im^{Ph2}NNO^{tBu}** is susceptible to degradation through phenolate oxidation in the presence of higher iron oxidation states, presumably due to the higher Lewis acidity.

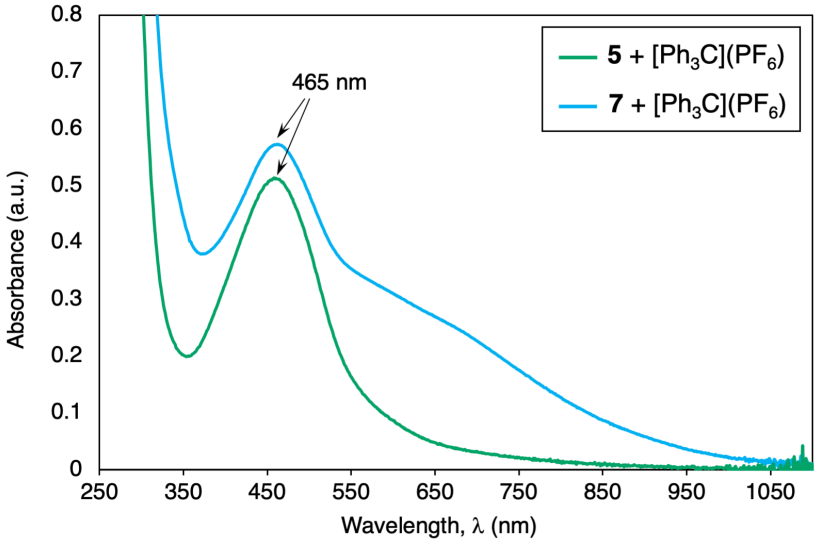

Figure 21. The UV-vis spectra of the products obtained from the reaction between $[Ph_3C](PF_6)$ and either [Fe(Im^{Ph2}NNO^{tBu})(SBn)] (**5**) or [Fe(Im^{Ph2}NNO^{tBu})(SPh)] (**7**) (green and blue traces, respectively).

4.2.11 Reactivity with PhIO

Next, we were keen to investigate the reactivity of [Fe(Im^{Ph2}NNO^{tBu})(SR)] complexes with iodosylbenzene (PhIO), a 2-electron oxidant that typically reacts as an oxo-atom transfer reagent. Although the use of PhIO deviates somewhat from the native O_2 reactivity of IPNS, it is a particularly useful reagent with which to examine the site of oxidation in non-heme iron(II) thiolate compounds, as these are typically able to undergo sulfur or iron oxidation, or in some cases both.[67]

We opted to investigate the reactivity of complexes [Fe(Im^{Ph2}NNO^{tBu})(SBn)] (**5**) and [Fe(Im^{Ph2}NNO^{tBu})(SPh)] (**7**) with PhIO, due to their differing alkyl- and arylthiolate co-ligands. Additionally, the benzylic position of the benzylthiolate ligand in **5** could be a site for H-atom abstraction by a short-lived oxidising iron-oxo intermediate. Each complex was dissolved in 6 mL MeCN and the solutions cooled to –80 °C. Excess PhIO (10 equivalents) was added in one portion to the solutions at low temperature and the mixtures stirred for 1 h. During this time, no change in the colour or in the composition of the reaction mixtures was observed. The reaction mixtures were subsequently stirred for a further hour while warming to room temperature. During this time, the reactions turned deep red and the amount of suspended PhIO visibly decreased. The mixtures were subsequently filtered and small aliquots were taken for UV-vis and ESI-MS analysis. UV-vis analysis of the

solids revealed the development of a new absorption band at 510 nm for the reaction with **5**, and at 520 nm for the reaction with **7** (Figure 22) These bands are red-shifted by approximately 10 nm compared to the UV-vis spectra recorded for the complexes upon exposure to O_2 (*vide supra*). We tentatively assign these bands to phenolate-to-iron(III) charge transfer bands.

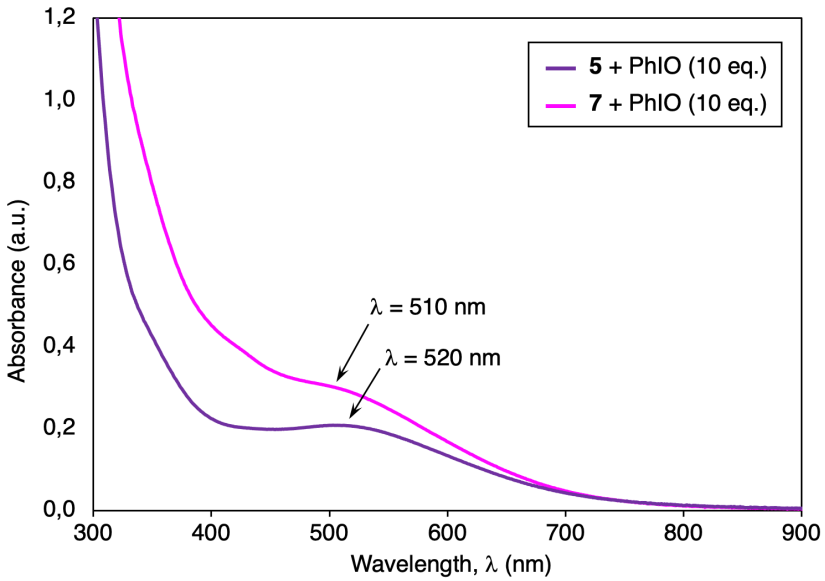

Figure 22. The UV-vis spectra obtained for the reaction of **5** and **7** with PhIO (10 eq.). Spectra were recorded in MeCN at ambient temperature.

Negative mode ESI-MS analysis of the reaction products showed signals at m/z = 170.9 and 156.9 for the reactions of **5** and **7**, respectively, which correspond to the benzyl- and phenyl-sulfonate ions (calculated m/z = 171.01 and 157.00 for $PhCH_2SO_3^-$ and $PhSO_3^-$, respectively). In both cases, a strong signal at m/z = 863.0 was observed that we were unable to assign. Positive mode ESI-MS analysis showed two signals at m/z = 713.3 and 729.3 for both reaction mixtures. We assign the signal at 713.3 to the $[L]^+$ ion (calculated m/z = 713.4). Interestingly, the peak at m/z = 729.3 corresponds to that of the mono-hydroxylated ligand scaffold (calculated m/z = 729.4 for $[L+OH]^+$). This suggests that a transient high-valent iron(IV)-oxo intermediate is formed that is capable not only of oxygenating the sulfur atom of the thiolate ligands but also of activating and hydroxylating ligand C–H bonds, likely those of nearby imidazole phenyl groups. Additional weak signals were detected at m/z = 698.1 and 683.2, which correspond to the demethylated $[L–CH_3]^+$ and methoxy-cleaved $[L–OCH_3]^+$ ions, respectively. This indicates that the ligand is somewhat susceptible to degradation in highly oxidising conditions. Unfortunately, no iron-containing ions could be identified by ESI-MS in either positive or negative mode, likely due to hydrolysis of the ions during the measurement conditions. Further mechanistic studies are required to investigate the nature of any oxygenated iron intermediates.

4.2.12 Unexpected C–O Bond Cleavage in the Presence of $FeCl_3$

Reacting **K-Im^{Ph2}NNO^{tBu}** with one equivalent of $FeCl_3$ in THF resulted in the immediate formation of a reddish-purple solution. The solution was stirred for a further 1.5 h before being filtering and dried under vacuum, affording a brownish solid. The UV-vis spectrum of the product recorded in THF and MeCN is displayed in Figure 23. In both spectra, a broad absorption feature centred at around 520 nm is observed, as well as a band at 360 nm that shoulders the intense π–π* transitions in the spectrum (<350 nm). We assign the band at 520 nm to phenolate-to-iron(III) charge transfer.

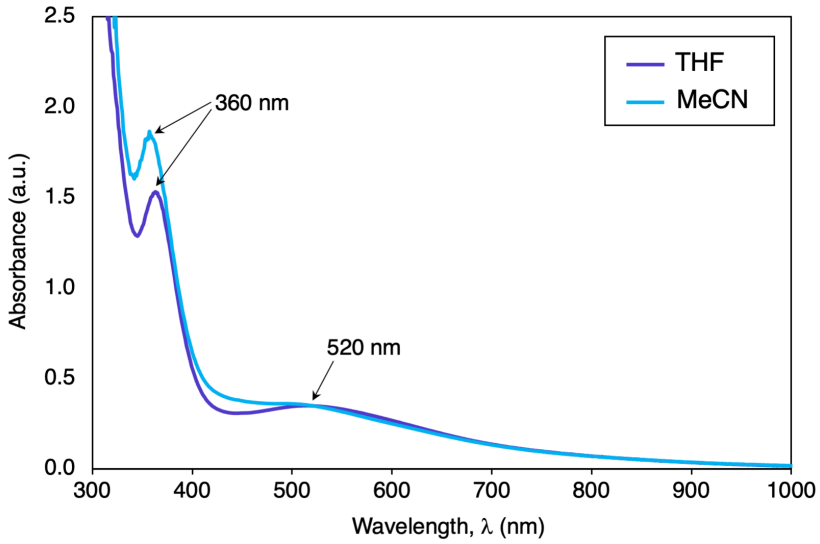

Figure 23. The UV-vis spectra for the product obtained from the reaction between $FeCl_3$ and **K-Im^{Ph2}NNO^{tBu}**, recorded in THF and MeCN at ambient temperature.

Red crystals suitable for X-ray diffraction were obtained by slow diffusion of *n*-hexane into a THF solution of the reaction product over the course of several days. The resulting X-ray crystal structure reveals the formation of a dinuclear iron(III) complex (**16**) involving two ligand molecules and two pentacoordinate iron centres, with an intermetallic distance of 3.2368(7) Å. Each iron atom is bound to the imidazole group of one ligand molecule, the phenolate group of a second ligand molecule, a chloride ion and two anionic μ_2-bridging alkoxide oxygen atoms from the ligand backbones (Figure 24). Interestingly, these alkoxide groups are the result of methyl cleavage from the ligand methoxy groups (C–O bond cleavage). One imidazole group in both ligand molecules remains non-coordinated. Selected bond lengths and bonds angles are given in Table 7.

The degradation of the ligand in this manner is somewhat unexpected given the poor leaving group ability generally associated to methyl groups. However, demethylation of ether-protected hydroxyl groups through C–O bond cleavage has been reported in the presence of strong Lewis acids such as BBr_3,[68,69] $AlCl_3$,[70] and $FeCl_3$.[71,72] We previously observed the same phenomenon when reacting related ligand **Im^{Ph2}NNO** with $FeCl_3$, as described in Chapter 2 of this thesis.[73] We propose that reaction of **K-Im^{Ph2}NNO^{tBu}** with

$FeCl_3$ initially produces a mononuclear iron(III) complex, supported by the **Im^{Ph2}NNO^{tBu}** ligand and bound to two chloride anions (Scheme 6). However, the steric congestion and the strong metal-halide interaction between the iron and the chloride ions likely causes one of the supporting imidazole groups to dissociate, which has the effect of bringing the methoxy groups into closer proximity to the metal centres.[35] This would enable the Lewis-acid catalysed C–O bond cleavage to occur, affording complex **16**. We also propose that the leaving group ability of the methyl groups is enhanced by coordination of the resulting alkoxide oxygen atoms to the Fe^{3+} ions. Finally, we believe that the dinuclear structure of **16** arises from the fact that iron(III) centres readily adopt higher coordination numbers, and that strain at the ligand's bridgehead carbon atom is reduced through bridging coordination modes.

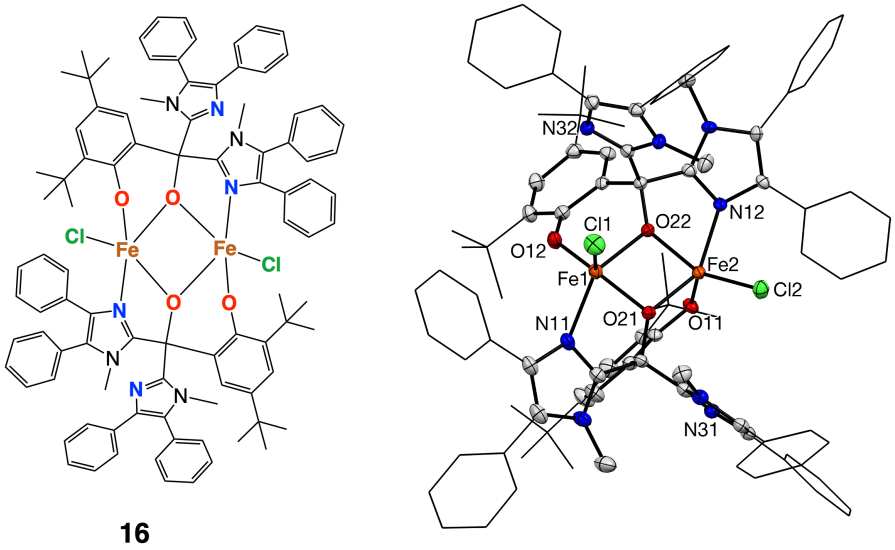

16

Figure 24. Schematic depiction and displacement ellipsoid plot of $[Fe_2(L^*)_2(Cl)_2]$ (**16**), drawn at the 50% probability level. Hydrogen atoms and co-crystallised benzene and water molecules are omitted for clarity. Only the major form of the disordered phenyl ring is shown.

Table 7. Selected bond lengths (Å) and bond angles (°) for $[Fe_2(L^*)_2(Cl)_2]$ (**16**).

$[Fe_2(L^*)_2(Cl)_2]$ (**16**)			
Bond	Length	Bond Angle	Degrees
Fe1–N11	2.137(2)	O12–Fe1–O22	87.62(7)
Fe2–N12	2.105(2)	O21–Fe1–O22	71.10(6)
Fe1–O12	1.8415(17)	N11–Fe1–O21	76.39(7)
Fe2–O11	1.8398(15)	O12–Fe1–Cl1	114.58(6)
Fe1–O21	1.9877(16)	N11–Fe1–Cl1	101.73(6)
Fe2–O21	1.9878(16)	O11–Fe2–O21	88.88(7)
Fe1–O22	2.0026(16)	O21–Fe2–O22	71.37(6)
Fe2–O22	1.9895(15)	N12–Fe2–O22	76.50(7)
Fe1–Cl1	2.2133(7)	O11–Fe2–Cl2	118.95(6)
Fe2–C12	2.2330(7)	N12–Fe2–C12	98.13(6)

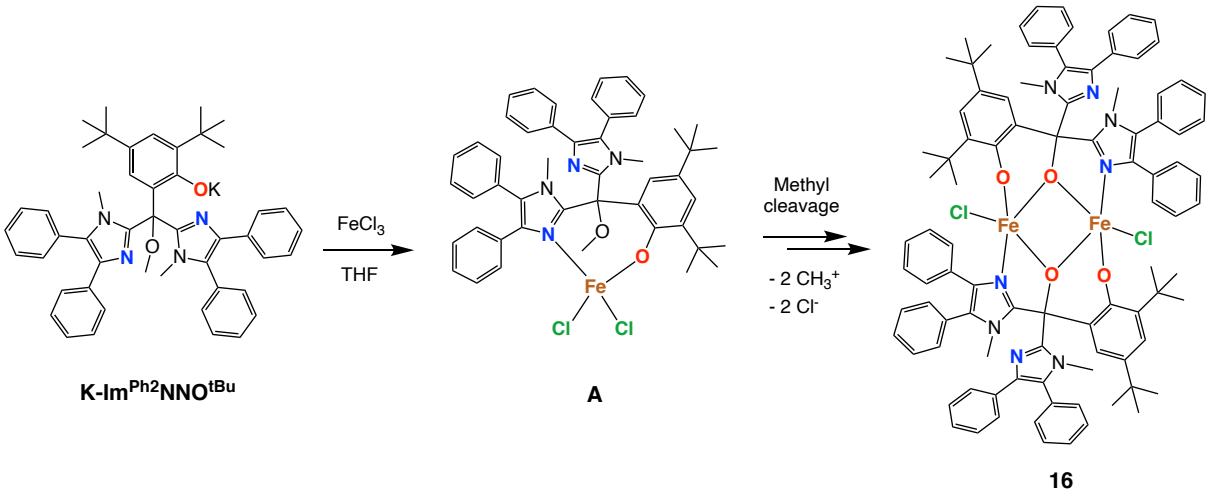

K-Im^{Ph2}NNO^{tBu} **A** **16**

Scheme 6. Formation of complex **16** *via* the proposed intermediate **A**.

This data shows that disruption of the supporting ligand's κ$_3$-*N,N,O* can become a source of irreversible complex decomposition if the OMe group comes into close proximity with a Lewis acidic metal centre such as Fe(III). Together with our observations that the ligand can oxidise to its quinone form and undergo methoxy cleavage, this data highlights the fact that the primary weakness in the ligand design is the methoxy group on the bridgehead carbon atom. Thus, it would seem that the ligand is somewhat susceptible to decomposition in oxidising conditions, which may challenge its use as a scaffold for supporting and studying high-valent and oxygenated reaction intermediates.

Nevertheless, while **16** appears to be the main product formed by reacting **K-Im^{Ph2}NNO^{tBu}** directly with $FeCl_3$, it remains unclear whether decomposition of the ligand in this manner is a major phenomenon occurring in solution during oxidative transformations of the [Fe(Im^{Ph2}NNO^{tBu})(SR)] complex series. Indeed, ESI-MS data shown in the previous reactivity sections of this chapter often shows that the methyl-cleaved (or indeed methoxy-cleaved) ligand is only a very minor species formed in solution. Given the very small number of tridentate *N,N,O* ligands available for the synthesis of well-defined mononuclear non-heme iron complexes, we believe that ligand **Im^{Ph2}NNO^{tBu}** still qualifies as a valuable bioinspired platform with which to model non-heme iron enzyme active sites. Of course, further research is necessary in order to find conditions that could prevent the oxidative decomposition of the ligand, including modification of the ligand design such that the methoxy group is removed or replaced by a more robust group (*e.g.* a fluorine). Another possible structural modification to the ligand is the instalment of more electron-withdrawing groups *ortho* and *para* to the phenolate in order to reduce its oxidation susceptibility while still enabling the ligand to coordinate in a κ$_3$-*N,N,O* fashion to a single metal centre.

4.3 Conclusion

We reported a reproducible and high-yielding method to prepare a family of mononuclear iron(II) and zinc(II) thiolate complexes, [M($Im^{Ph2}NNO^{tBu}$)(SR)] (M = Fe, Zn; R = ^{t}Bu, Bn, Ph, Mes, 4-OMe-C_6H_4, 4-CF_3-C_6H_4). These complexes feature a bulky, tridentate *N,N,O* ligand (**$Im^{Ph2}NNO^{tBu}$**) and an exogenous thiolate co-ligand, qualifying them as some of the most structurally faithful synthetic models of the substrate-bound IPNS active site reported to date. The X-ray crystal structures of the complexes show that the tripodal *N,N,O* coordination of the supporting ligand is retained in all cases, despite the variation in steric and electronic properties of the different thiolates. Depending on the steric bulk of their organic substituents, the thiolate co-ligands are able to adopt different orientations within the coordination sphere of the iron centre. NMR analysis shows that the complexes have a well-defined structure in solution, consistent with those observed in the solid state. Overall, this demonstrates high synthetic and structural tunability of our IPNS model complexes.

Using Mössbauer spectroscopy and DFT analysis, we showed that the sulfur-to-iron metal charge transfer in the [Fe($Im^{Ph2}NNO^{tBu}$)(SR)] complexes is modulated by the relative donicity of the thiolate co-ligand. This trend is reflected in the metal–sulfur bond lengths observed in the X-ray crystal structures of the [M($Im^{Ph2}NNO^{tBu}$)(SR)] complex series. We employed cyclic voltammetry to further demonstrate that, despite the redox non-innocence of the supporting *N,N,O* phenolate ligand, the iron centres remain most prone to electrochemical oxidation. This is substantiated by DFT calculations that show the HOMO to be consistently localised on the iron centres throughout the complex series. Overall, these results establish the electronic tunability and biomimetic potential of our IPNS model system.

Having established that our complexes act as structural and electronic models for the active site of IPNS, we next explored the oxidation reactivity of the iron thiolate complexes with different oxidants, including O_2, NO, PhIO and [Ph_3C](PF_6). Exposing the complexes to O_2 resulted in the swift development of a phenolate-to-iron(III) charge transfer band, associated to the outer-sphere oxidation of the iron to its ferric state. Using ESI-MS, we also observed the formation of sulfonate ions and a sulfonate-bound iron(III) complex. Reactions with NO (using Ph_3CSNO) indicate that NO is capable of binding directly to the iron centre, in line with native IPNS reactivity. However, the formation of dinitrosyl complexes is also observed, which shows that oxidant accessibility of the iron centre is difficult to control. Reactions with PhIO suggest that the iron(II) is oxidised to iron(III), along with the formation of sulfonate anions. Interestingly, we also detect small amounts of hydroxylated ligand by ESI-MS, which suggests that a transient high-valent iron-oxo intermediate is formed that is capable of C–H bond activation as well as S-oxygenation. While these studies have demonstrated some interesting and IPNS-related oxidative reactivity of our complexes, further research in order to better understand these oxidative transformations is ongoing in our laboratories.

Finally, these reactivity studies have also highlighted important vulnerabilities in our ligand design, particularly with respect to the methoxy group of the ligand backbone. Indeed, we exposed two ways in which the ligand can undergo oxidative degradation involving the methoxy group. Firstly, we found that irreversible oxidation of the phenolate moiety to its quinone form is rendered thermodynamically favourable by the triply benzylic position in the bridgehead, which increases the leaving group ability of the methoxy group. Secondly, we found that the methyl group is susceptible to Lewis acid catalysed C–O bond cleavage, which affords an anionic alkoxide group that can bind to the metal centre and disrupt the *N,N,O* coordination motif of the ligand scaffold. Nonetheless, given the very small number of tridentate *N,N,O* ligands available for the synthesis of well-defined mononuclear non-heme iron complexes, we believe that ligand **Im^{Ph2}NNO^{tBu}** qualifies as a valuable bioinspired platform with which to model non-heme iron enzyme active sites.

4.4 Author Contributions

E.C.M. and B.K.G. devised the project, designed experiments and wrote the manuscript. E.C.M., A.J.V., and D.B. performed experiments and analysed the data. M.L. performed X-ray crystal structure determinations. G.T. and J.R. provided ESI-MS data analysis. S.Y. and E.B. provided Mössbauer data analysis. All authors provided comments on the experiments and manuscript during its preparation.

4.5 Experimental

4.5.1 Chemicals and Reagents

Unless stated otherwise, all reactions were performed under inert N_2 (g) atmosphere using standard Schlenk line and glovebox techniques and were stirred magnetically. The solvents acetonitrile, diethyl ether, and hexane were taken from an MBraun MB SPS-80 purification system. Dichloromethane was dried over CaH_2 and distilled under inert N_2 (g) atmosphere before use. THF was dried over sodium benzophenone ketyl and distilled under inert N_2 (g) atmosphere before use. All solvents were degassed by bubbling N_2 (g) through them for a period of 30 mins prior to use and were stored over activated molecular sieves. Acetonitrile was filtered over activated neutral alumina before use to remove molecular sieve debris. All solvents were tested for water content by the Karl-Fischer titration or by ^{1}H NMR. Non-halogenated solvents were additionally tested with a standard purple solution of sodium benzophenone ketyl in THF to confirm effective oxygen and moisture removal. Deuterated solvents were purchased from the Cambridge Isotope Laboratory Incorporation (Cambridge, USA) and were degassed using the freeze-pump-thaw method and stored over activated molecular sieves. Deuterated acetonitrile was filtered over activated neutral alumina prior to use to remove molecular sieve debris. All reagents and starting materials were purchased from commercial sources and used without further purification, except when specified. Ligand **H-Im^{Ph2}NNO^{tBu}** and complexes [Fe(Im^{Ph2}NNO^{tBu})(Cl)] (**1**), [Zn(Im^{Ph2}NNO^{tBu})(Cl)] (**2**) and [Zn(Im^{Ph2}NNO^{tBu})(SPh) (**8**) were synthesised according to procedures previously reported by our group (Chapter 3 of this thesis).[35] Trityl-*S*-nitrosomethanethiol (Ph_3CSNO) was synthesised according to a reported procedure,[57] and was stored as a green crystalline solid at –40

°C under inert atmosphere in the dark. All thiols were converted to their respective sodium thiolate salt by reaction with an equimolar amount of NaH in THF. The corresponding sodium thiolate salts (NaSR) were obtained as free-flowing powders and any residual solvent was quantified by ^{1}H NMR prior to use.

4.5.2 Physical Methods

NMR spectroscopy (^{1}H, ^{13}C{^{1}H}, ^{19}F, ^{1}H-^{13}C HSQC, 1D and 2D NOESY) was conducted using a 400 MHz Varian spectrometer or an Oxford NMR AS400 spectrometer. ^{1}H and ^{13}C{^{1}H} NMR chemical shifts are reported in the standard δ notation of part per million (ppm) and are referenced to residual solvent signals, as determined relative to $SiMe_4$.[74] ^{19}F NMR chemical shifts are reported in ppm and are externally referenced to an 85% aqueous solution of $CFCl_3$. Paramagnetic ^{1}H NMR were recorded after having adjusted both the relaxation delay and acquisition time to 100 ms. IR spectroscopy was conducted using a PerkinElmer Spectrum Two FT-IR spectrometer. For air-sensitive compounds, a N_2 (g) flow was used. Peaks are annotated by (w), (m) and (s) to indicate weak, medium and strong signals, respectively. Absorption spectra were recorded using a Varian Cary 50 Scan spectrometer, using Quartz cuvettes with a path length of 1 cm, sealed with a Teflon cap. Unless otherwise stated, UV-vis solutions were prepared in the glovebox using dried and degassed solvents. The acquisition of the absorption spectra was performed with the PerkinElmer UV Winlab software. High resolution ESI-MS measurements were performed with a Waters LCT Premier XE KE317. Other ESI-MS measurements were performed with an Advion Express CMS instrument. X-ray crystal structure determinations were performed on a Bruker Kappa ApexII diffractometer with sealed tube and Triumph monochromator (λ = 0.71073 Å) at a temperature of 150(2) K (further details are given in Appendix C). ^{57}Fe Mössbauer spectra (see Appendix F) were recorded on a conventional spectrometer with alternating constant acceleration of the g-source (^{57}Co/Rh, 1.8 GBq), which was kept at room temperature. The minimum experimental line width was 0.24 mm s^{-1} (full width at half-height). The sample temperature was maintained constant in an Oxford Instruments Variox cryostat. Isomer shifts are quoted relative to iron metal at 300 K. The zero-field spectra were simulated with Lorentzian doublets with the program *mf.SL* developed by Eckhard Bill. EPR measurements were performed on a Bruker EMX Plus 6000 Gauss machine equipped with an ER 041 XG X-Band Microwave Bridge. Electrochemical analysis was done by means of cyclic voltammetry (CV)). All measurements were performed in a nitrogen-filled glovebox on an IVIUM potentiostat/galvanostat using a 3-electrode setup. The setup included a glassy carbon (GC) working electrode, a platinum counter electrode, and a silver wire pseudo reference electrode. All electrodes were purchased from either BASi or Redox.me. The potentiostat was kept external to the glovebox, and the electrode leads were connected with a custom shielded electrode cable feedthrough. All scans were absolutely referenced to ferrocene, measured at the start and end of each measurement set. GC electrodes were 2 and 3 mm in diameter, with surfaces of 50.3 mm^2 and 113.1 mm^2, respectively. GC electrodes were polished with 0.3μm alumina powder deionized water slurries, rinsed with MeOH, water and dilute HCl solution (1 M), and ultrasonicated in pure deionized water for 30 sec, to remove residual polishing powder. The pseudo reference silver wire electrode and platinum wire counter electrode were rinsed with MeOH and water. All electrodes were dried in the ante chamber of the glovebox for at least 12 h. All electrodes were used directly in solution. Each working electrode was pre-treated with at least two cyclical scans from approximately +1.5 to −2.8 V at 200 mV/s in the corresponding solvent containing 0.1 M [*n*-Bu_4N][PF_6]. For all experiments, background voltammograms of the electrolyte were recorded at the respective scan rate. Solutions were gently shaken between experiments to renew the diffusion layer. No indication of solution resistance was observed during experiments, as described by McCarthy *et al,* which state that the solution resistance in the presence of >0.05 M electrolyte is estimated to be <30 mV in reduction potentials.[75] Elemental analyses were carried out in the laboratories of Medac Ltd. in the UK.

4.5.3 Computational Methods

All calculations were performed using the *Gaussian 16* software package.[53] Geometry optimisations and frequency calculations were conducted using the B3LYP (Becke 3-parameter Lee-Young-Parr) functional with the LANL2DZ basis functional defined for Fe and Zn and the 6-31g(d,p) basis defined for all other atoms. Where possible, *x,y,z* coordinates from the complex X-ray crystal structure were used as initial coordinates for the calculations. For [Fe(L)(SPh^{CF3})] (**13**), initial coordinates were taken from the X-ray crystal structure of its zinc counterpart. All optimised geometries were confirmed as energy minima through the absence of imaginary frequencies. A single point energy calculation was run on all optimised geometries at the B3LYP/6-311g(d,p) level of theory. NBO analysis was performed using the *NBO6.0* programme,[76] at the B3LYP/6-311g(d,p) level of theory. Cube files for molecular orbitals and spin density were generated using the *Multiwfn* program.[77] The α and β molecular orbital subsets for the iron complexes were biorthogonalized using the *Multiwfn* program (see Appendix G). The energies of the biorthogonalised molecular orbitals were evaluated using the Fock matrix from NBO analysis (provided in the .47 file). Molecular orbitals were visualised with the *Visual Molecular Dynamics* program,[78] using the respective molecular orbital cube file and defining the isosurface level at ±0.05. Mössbauer parameter calculations were performed using the *ORCA 4.2.1* software package. Calculations were performed at the B3LYP/def2-TZVP level of theory, defining the CP(PPP) basis set on iron. The ρ(0) value from the output file was used to calculate the isomer shift, according to the calibration curve reported by Holland and co-workers: $\delta = [\alpha(\rho(0) - C] + \beta$ (where $\alpha = -0.30$; $\beta = 1.49$; $C = 14760$).[52]

4.5.4 Complex Synthesis

[Fe(Im^{Ph2}NNO^{tBu})(S^{t}Bu)] (3): A suspension of NaS^{t}Bu (7.0 mg, 62.8 μmol) in CH_2Cl_2 was added dropwise to a stirring solution of **1** (50.6 mg, 62.8 μmol) in CH_2Cl_2. The mixture was stirred for 2.5 h, during which time the mixture turned brown-orange in colour and became slightly cloudy. The mixture was filtered and the pale brown filtrate dried under vacuum. The crude solid was washed twice by stirring vigorously in hexane until a fine powder suspension was obtained. The hexane washings were separated by centrifugation and discarded, and the product was dried under vacuum, affording the title complex as a pale brown powder (41.1 mg, 47.8 μmol, 76%). Crystals suitable for X-ray diffraction were grown in 2 days from slow vapour diffusion of hexane into a THF solution of the complex at room temperature. **^{1}H NMR** (400 MHz, 298 K, CD_3CN): δ = 53.51, 50.77, 47.12, 46.69, 40.11, 20.72, 15.39, 11.29, 8.82, 7.15, 6.78, 5.45, 4.93, 3.76, 2.91 ppm. χ (Evans method, 1%TMS in CD_2Cl_2): μ_{eff} = 5.50 μ_B. **UV-vis** (CH_2Cl_2, ε [mol^{-1} dm^3 cm^{-1}]): λ_{max} = 380 (1096), 500 (26) nm. **^{57}Fe Mössbauer** (80 K): δ = 0.88 mm s^{-1}, $|\Delta E_Q|$ = 2.83 mm s^{-1}. **IR** (ATR): υ = 3057 (w), 2951 (m), 2867 (w), 1681 (w), 1603 (w), 1505 (w), 1476 (m), 1466 (s), 1438 (s), 1412 (w), 1391 (w), 1358 (w), 1302 (s), 1262 (m), 1235 (w), 1202 (w), 1157 (m), 1133 (w), 1074 (s), 1056 (m), 1025 (m), 1004 (w), 977 (w), 929 (w), 915 (w), 899 (w), 887 (m), 788 (s), 772 (s), 748 (m), 728 (w), 700 (s), 649 (w), 610 (w), 587 (w), 540 (m) cm^{-1}. **E.A.** (Formula: $C_{52}H_{58}N_4O_2SFe$, M_w = 858.97 g mol^{-1}): calc. C 72.71, H 6.81, N 6.52; found C 72.52, 7.15, N 6.24.

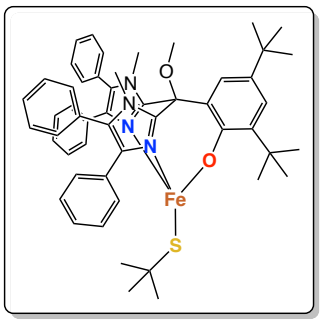

[Zn(Im^{Ph2}NNO^{tBu})(S^{t}Bu)] (4): A suspension of NaS^{t}Bu (3.5 mg, 31.2 μmol) in CH_2Cl_2 was added dropwise to a stirring solution of **2** (25.4 mg, 31.3 μmol) in CH_2Cl_2. The mixture was stirred for 2.5 h, during which time the mixture turned pale brown in colour and became slightly cloudy. The mixture was filtered and the filtrate was dried under vacuum. The crude solid was washed twice by stirring vigorously in hexane until a fine powder suspension was obtained. The hexane washings were separated by centrifugation and discarded, and the product was dried under vacuum, affording the title complex as a white powder (20.9 mg, 24.1 μmol, 77%). Crystals suitable for X-ray diffraction were grown overnight from slow vapour diffusion of hexane into a THF solution of the complex at room temperature. **^{1}H NMR** (400 MHz, 298 K, CD_3CN): δ = 7.76 (d, 1H, *J* = 4 Hz, H_{phen}^1), 7.47 (m, 10H, H_{arom}), 7.32 (m, 4H, H_{arom}), 7.26 (m, 6H, H_{arom}), 7.23 (d, 1H, *J* = 4 Hz, H_{phen}^2), 3.46 (s, 6H, NCH_3), 3.33 (s, 3H, OCH_3), 1.31 (s, 9H, *ortho*-C(CH_3)$_3$), 1.30 (s, 9H, *para*-C(CH_3)$_3$), 0.91 (s, 9H, SC(CH_3)$_3$) ppm. **^{13}C{^{1}H} NMR** (101 MHz, 298 K, CD_3CN): δ = 162.01, 148.14, 140.11, 136.30, 133.72, 132.79, 132.51, 132.45, 132.39, 130.49, 130.07, 130.03, 129.77, 129.72, 129.10, 129.08, 128.39, 125.13, 122.02, 119.86, 81.00, 68.29, 53.49, 40.13, 37.85, 36.12, 34.70, 34.45, 34.11, 32.11, 30.79, 30.09, 29.80, 26.25. **IR** (ATR): υ = 3056 (w), 2960 (m), 2855 (w), 1682 (w), 1632 (w), 1603 (w), 1466 (m), 1437 (m), 1411 (w), 1393 (w), 1359 (w), 1303 (m), 1260 (s), 1235 (w), 1202 (w), 1157 (w), 1074 (s), 1055 (s), 1023 (s), 979)w), 929 (w), 915 (w), 900 (w), 887 (w), 835 (m), 789 (s), 773 (m), 745 (m), 727 (w), 697 (s), 650 (w), 611 (w), 587 (w), 539 (w), 523 (w), 432 (w) cm^{-1}. **E.A.** (Formula: $C_{52}H_{58}N_4O_2SZn$, M_w = 868.50 g mol^{-1}): calc. C 71.91, H 6.73, N 6.45; found C 71.47, H 6.62, N 6.23.

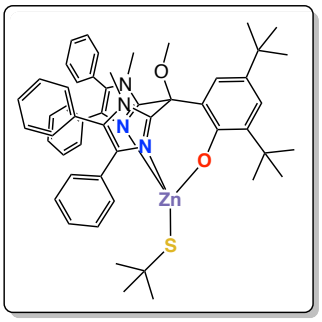

[Fe(Im^{Ph2}NNO^{tBu})(SBn)] (5): A suspension of $NaSCH_2C_6H_5$ (5.7 mg, 39.1 μmol) in CH_2Cl_2 was added dropwise to a stirring solution of **1** (31.5 mg, 39.1 μmol) in CH_2Cl_2. The mixture was stirred for 2.5 h, during which time the mixture turned light brown in colour and became slightly cloudy. The mixture was filtered and the filtrate dried under vacuum. The crude solid was washed twice by stirring vigorously in hexane until a fine powder suspension was obtained. The hexane washings were separated by centrifugation and discarded, and the product was dried under vacuum, affording the title complex as an pale yellow powder (29.1 mg, 32.6 μmol, 83%). Thin needle-like crystals suitable for X-ray diffraction analysis were obtained in 2 days from slow vapour diffusion of hexane into a THF solution of the complex at room temperature. **^{1}H NMR** (400 MHz, 298 K, CD_3CN): δ = 56.49, 49.94, 48.19, 12.62, 11.04, 10.12, 8.56, 8.10, 7.85, 7.52, 7.34, 6.77, 5.44, 4.73, 4.13, 3.82, 3.64, 3.48, 2.82, 2.13 ppm. χ (Evans method, 1%TMS in CD_2Cl_2): μ_{eff} = 5.14 μ_B. **UV-vis** (CH_2Cl_2, ε [mol^{-1} dm^3 cm^{-1}]): λ_{max} = 380 (1305), 500 (34) nm. **^{57}Fe Mössbauer** (80 K): δ = 0.90 mm s^{-1}, $|\Delta E_Q|$ = 2.51 mm s^{-1}. **IR** (ATR): υ = 3057 (w), 3027 (w), 2951 (m), 2904 (w), 2887 (w), 1601 (w), 1504 (w), 1476 (m), 1466 (m), 1438 (s), 1412 (w), 1391 (w), 1360 (w), 1303 (m), 1270 (w), 1233 (w), 1201 (w), 1158 (w), 1132 (w), 1074 (m), 1056 (w), 1025 (w), 1004 (m), 977 (w), 899 (w), 887 (w), 843 (m), 772 (m), 747 (w), 730 (w), 696 (s), 647 (w), 611 (w), 560 (w), 540 (m), 454 (w) cm^{-1}. **E.A.** (Formula: $C_{55}H_{56}N_4O_2SFe$, M_w = 892.98 g mol^{-1}): calc. C 73.98, H 6.32. N 6.27; found C 73.80, H 6.55, N 5.80.

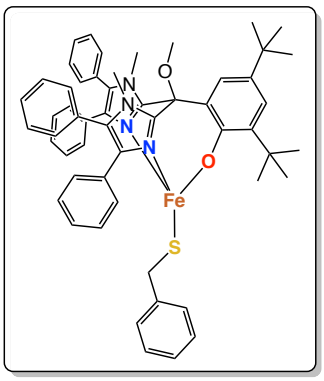

[Zn(Im^{Ph2}NNO^{tBu})(SBn)] (6): A suspension of $NaSCH_2C_6H_5$ (6.0 mg, 41.1 µmol) in CH_2Cl_2 was added dropwise to a stirring solution of **2** (33.5 mg, 41.1 µmol) in CH_2Cl_2. The mixture was stirred for 2.5 h, during which time the mixture turned pale yellow in colour and became slightly cloudy. The mixture was filtered and the filtrate dried under vacuum. The crude solid was washed twice by stirring vigorously in hexane until a fine powder suspension was obtained. The hexane washings were separated by centrifugation and discarded, and the product was dried under vacuum, affording the title complex as an off-white powder (35.6 mg, 39.4 µmol, 96%). Thin needle-like crystals suitable for X-ray diffraction analysis were obtained from slow vapour diffusion of hexane into a THF solution of the complex at room temperature. **^{1}H NMR** (400 MHz, 298 K, CD_3CN): δ = 7.75 (d, 1H, *J* = 4 Hz, H_{phen}^1), 7.48 (m, 10H, H_{arom}), 7.33 (m, 4H, H_{arom}), 7.26 (m, 6H, H_{arom}), 7.22 (d, 1H, *J* = 4 Hz, H_{phen}^2), 7.08 (t, 2H, *J* = 8 Hz, H_{benzyl}^5), 7.01 (t, 1H, *J* = 8 Hz, H_{benzyl}^6), 6.87 (d, 2H, *J* = 8 Hz, H_{benzyl}^4), 3.51 (s, 6H, NC*H*$_3$), 3.45 (3H, OC*H*$_3$), 1.31 (s, 9H, C(C*H*$_3$)$_3$), 1.30 (s, 9H, C(C*H*$_3$)$_3$) ppm. **^{13}C{^{1}H} NMR** (101 MHz, 298 K, CD_3CN): δ = 147.96, 132.41, 130.48, 130.01, 129.79, 129.46, 129.21, 129.14, 128.73, 128.65, 126.23, 68.29, 36.14, 35.37, 34.72, 32.12, 29.83, 29.72, 26.25 ppm. **IR** (ATR): υ = 3054 (w), 2951 (w), 2864 (w), 1601 (w), 1505 (w), 1466 (m), 1438 (m), 1412 (w), 1392 (w), 1359 (w), 1306 (m), 1262 (m), 1232 (w), 1201 (w), 1158 (w), 1133 (w), 1083 (m), 1055 (m), 1024 (m), 1005 (m), 978 (w), 929 (w), 915 (w), 897 (w), 886 (w), 836 (m), 790 (m), 772 (m), 746 (m), 735 (m), 653 (w), 648 (w), 619 (w), 583 (w), 563 (w), 539 (m), 524 (w), 515 (w) cm^{-1}. **E.A.** (Formula: $C_{55}H_{56}N_4O_2SZn$, M_w = 902.52 g mol^{-1}): calc. C 73.20, H 6.25, N 6.21; found C 73.22, H 6.56, N 5.96.

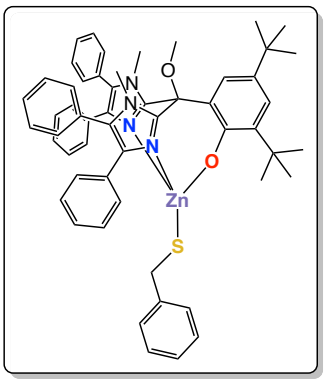

[Fe(Im^{Ph2}NNO^{tBu})(SPh)] (7): A suspension of NaSPh (12.6 mg, 68.9 µmol) in CH_2Cl_2 was added dropwise to a solution of **1** (55.6 mg, 69.1 µmol) in CH_2Cl_2. The mixture was stirred for 2.5 h, during which time the mixture turned pale yellow in colour and became slightly cloudy. The mixture was filtered and the filtrate dried under vacuum. The crude solid was washed twice by stirring vigorously in hexane until a fine powder suspension was obtained. The hexane washings were separated by centrifugation and discarded, and the product was dried under vacuum, affording the title complex as a cream-coloured powder (59.2 mg, 67.4 µmol, 97%). Needle-like crystals suitable for X-ray diffraction were grown in 3 days from slow vapour diffusion of hexane into a THF solution of the complex at room temperature. **^{1}H NMR** (400 MHz, 298 K, CD_3CN): δ = 57.34, 51.56, 46.43, 24.23, 19.76, 19.76, 15.75, 13.51, 9.13, 8.64, 8.07, 7.84, 7.55, 7.35, 6.92, 5.45, 4.64, 3.60, –0.49, –15.39, –19.67, –24.93 ppm. χ (Evans method, 1%TMS in CD_2Cl_2): μ_{eff} = 5.07 μ_B. **UV-vis** (CH_2Cl_2, ε [mol^{-1} dm^3 cm^{-1}]): λ_{max} = 380 (1303), 500 (26) nm. **^{57}Fe Mössbauer** (80 K): δ = 0.86 mm s^{-1}, $|\Delta E_Q|$ = 2.91 mm s^{-1}. **IR** (ATR): υ = 3054 (w), 2958 (w), 2902 (w), 2866 (w), 1603 (w), 1577 (w), 1505 (w), 1472 (m), 1436 (s), 1412 (w), 1392 (w), 1386 (w), 1360 (w), 1301 (m), 1261 (m), 1235 (w), 1202 (w), 1180 (w), 1157 (w), 1074 (s), 1054 (m), 1024 (s), 1004 (m), 977 (w), 929 (w), 914 (w), 899 (m), 887 (m), 841 (m), 801 (s), 789 (s), 771 (m), 736 (m), 693 (s), 647 (w), 617 (w), 611 (w), 587 (w), 541 (m), 514 (w) cm^{-1}. **E.A.** (Formula: $C_{54}H_{54}N_4O_2SFe$, M_w = 878.96 g mol^{-1}): calc. 73.79, H 6.19, N 6.37; found C 74.42, H 6.42, N 6.32.

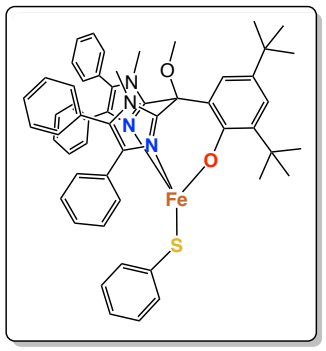

[Fe(Im^{Ph2}NNO^{tBu})(SMes)] (9): A suspension of $NaSC_6H_2$-2,4,6-Me_3 (19.3 mg, 73.0 µmol) in CH_2Cl_2 was added dropwise to a solution of **1** (56.9 mg, 70.7 µmol) in CH_2Cl_2. The mixture was stirred for 2.5 h, during which time the mixture turned brown in colour and became slightly cloudy. The mixture was filtered and the filtrate dried under vacuum. The crude solid was washed twice by stirring vigorously in hexane until a fine powder suspension was obtained. The hexane washings were separated by centrifugation and discarded, and the product was dried under vacuum, affording the title complex as an off-white powder (57.5 mg, 62.4 µmol, 88%). Crystals suitable for X-ray diffraction were obtained from slow evaporation of a concentrated solution of the complex in CH_2Cl_2 at –40 °C. **^{1}H NMR** (400 MHz, 298 K, CD_3CN): δ = 56.87, 51.52, 49.19, 33.03, 32.06, 29.59, 27.65, 22.86, 18.27, 9.44, 9.05, 8.82, 8.33, 8.02, 7.85, 7.69, 7.51, 7.30, 7.01, 6.75, 5.45, 5.28, 5.01, 4.09, 3.80, 3.64, 3.43, 2.83, 2.32, 2.09, 1.12, –0.54 ppm. χ (Evans method, 1%TMS in CD_2Cl_2): μ_{eff} = 5.05 μ_B. **UV-vis** (CH_2Cl_2, ε [mol^{-1} dm^3 cm^{-1}]): λ_{max} = 380 (1720), 500 (37) nm. **^{57}Fe Mössbauer** (80 K): δ = 0.91 mm s^{-1}, $|\Delta E_Q|$ = 2.92 mm s^{-1}. **IR** (ATR): υ = 3056 (w), 3030 (w), 2951 (m), 2907 (w), 2866 (w), 1603 (w), 1585 (w), 1576 (w), 1506 (w), 1476 (m), 1460 (s), 1438 (s), 1438 (s), 1412 (w), 1386 (m), 1360 (w), 1302 (m), 1270 (w), 1235 (w), 1202 (w), 1175 (w), 1158 (w), 1074 (m), 1056 (m), 1024 (m), 1004 (w), 977 (w), 953 (w), 929 (w), 914 (w), 900 (w), 887 (m), 844 (m), 788 (s), 771 (m), 749 (w), 732 (w), 718 (w), 701 (s), 694 (s), 650 (w), 623 (w), 610 (w), 587 (w), 572 (w), 513 (w) cm^{-1}. **E.A.** (Formula: $C_{57}H_{60}N_4O_2SFe$, M_w = 921.04 g mol^{-1}): no suitable elemental analysis could be obtained, likely due to residual solvent.

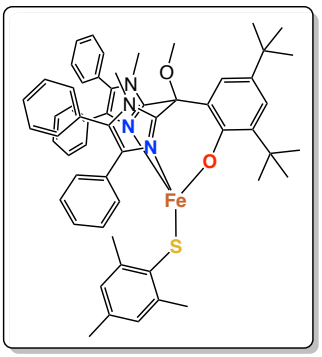

[Zn(Im^{Ph2}NNO^{tBu})(SMes)] (10): A suspension of $NaSC_6H_2$-2,4,6-Me_3 (14.0 mg, 52.9 µmol) in CH_2Cl_2 was added dropwise to a solution of **2** (41.1 mg, 50.4 µmol) in CH_2Cl_2. The mixture was stirred for 2.5 h, during which time the mixture turned brown in colour and became slightly cloudy. The mixture was filtered and the filtrate dried under vacuum. The crude solid was washed twice by stirring vigorously in hexane until a fine powder suspension was obtained. The hexane washings were separated by centrifugation and discarded, and the product was dried under vacuum, affording the title complex as an off-white powder (45.6 mg, 49.0 µmol, 97%). Crystals suitable for X-ray diffractions were obtained from the slow vapour diffusion of pentane into a CH_2Cl_2 solution of the complex at –40 °C. **^{1}H NMR** (400 MHz, 298 K, CD_3CN): δ = 7.68 (d, 1H, J = 4 Hz, H_{phen}^1), 7.50 (m, 10H, H_{arom}), 7.33 (m, 4H, H_{arom}), 7.27 (m, 6H, H_{arom}), 7.08 (d, 1H, J = 4 Hz, H_{phen}^2), 6.52 (s, 2H, *meta*-CH_{Mes}), 3.45 (s, 6H, NCH_3), 3.38 (s, 3H, OCH_3), 2.06 (s, 3H, *para*-CH_3), 1.78 (s, 6H, *ortho*-CH_3), 1.25 (s, 9H, *para*-C(CH_3)$_3$), 0.74 (s, 6H, *ortho*-C(CH_3)$_3$) ppm. **^{13}C{^{1}H} NMR** (101 MHz, CD_3CN, 25 °C): δ = 148.18, 141.68, 140.58, 136.63, 133.78, 132.78, 132.70, 132.45, 130.48, 130.03, 129.95, 129.73, 129.04, 128.48, 128.46, 124.89, 119.50, 53.62, 35.47, 34.11, 32.07, 29.47, 24.16, 20.77 ppm. **IR** (ATR): υ = 3057 (w), 3031 (w), 2949 (m), 2866 (w), 1683 (w), 1603 (w), 1506 (m), 1463 (s), 1438 (s), 1391 (w), 1360 (w), 1311 (m), 1272 (w), 1234 (w), 1202 (w), 1176 (w), 1157 (w), 1133 (w), 1075 (m), 1057 (m), 1025 (m), 1005 (w), 978 (w), 928 (w), 915 (w), 898 (w), 838 (m), 789 (s), 772 (m), 715 (m), 719 (m), 701 (s), 645 (w), 584 (w), 538 (w), 526 (w) cm^{-1}. **E.A.** (Formula: $C_{57}H_{60}N_4O_2SZn$, M_w = 930.57 g mol^{-1}): no suitable elemental analysis could be obtained, likely due to residual solvent.

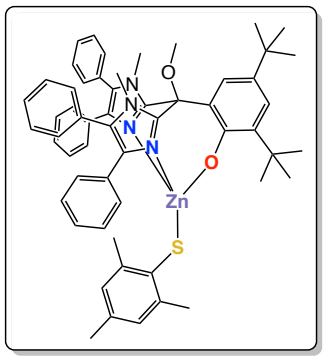

[Fe(Im^{Ph2}NNO^{tBu})(SPh^{OMe})] (11): A suspension of $NaSC_6H_4$-4-OMe (10.9 mg, 58.6 µmol) in CH_2Cl_2 was added dropwise to a solution of **1** (44.5 mg, 55.2 µmol) in CH_2Cl_2. The mixture was stirred for 2.5 h, during which time the mixture turned brown in colour and became slightly cloudy. The mixture was filtered and the filtrate dried under vacuum. The crude solid was washed twice by stirring vigorously in hexane until a fine powder suspension was obtained. The hexane washings were separated by centrifugation and discarded, and the product was dried under vacuum, affording the title complex as an off-white powder (45.1 mg, 49.6 µmol, 90%). Crystals suitable for X-ray diffraction were obtained from the slow vapour diffusion of pentane into a concentrated CH_2Cl_2 solution of the complex at –40 °C. **^{1}H NMR** (400 MHz, 298 K, CD_3CN): δ = 57.00, 51.30, 46.57, 24.09, 19.61, 15.79, 13.18, 9.08, 8.57, 8.13, 7.83, 7.68, 7.51, 6.90, 6.54, 5.87, 5.44, 5.26, 4.81, 4.22, 4.12, 3.89, 3.63, 3.43, 2.27, –0.43, –16.85 ppm. χ (Evans method, 1%TMS in CD_2Cl_2): μ_{eff} = 5.13 μ_B. **UV-vis** (CH_2Cl_2, ε [mol^{-1} dm^3 cm^{-1}]): λ_{max} = 380 (1792), 500 (73) nm. **^{57}Fe Mössbauer** (80 K): δ = 0.88 mm s^{-1}, $|\Delta E_Q|$ = 2.77 mm s^{-1}. **IR** (ATR): υ = 3056 (w), 2951 (m), 2903 (w), 2866 (w), 2830 (w), 1603 (w), 1590 (w), 1566 (w), 1505 (w), 1486 (s), 1465 (s), 1438 (s), 1412 (w), 1392 (m), 1360 (w), 1302 (m), 1271 (m),1233 (s), 1202 (w), 1177 (w0, 1158 (w), 1074 (m), 1025 (m), 1004 (w), 977 (w), 928 (w), 915 (w), 899 (w), 887 (m), 820 (m), 789 (s), 772 (m), 749 (w), 726 (w), 700 (s), 638 (w), 623 (w), 541 (m), 514 (w) cm^{-1}. **E.A.** (Formula: $C_{55}H_{56}N_4O_3SFe$, M_w = 908.98 g mol^{-1}): calc. C 72.68, H 6.21, N 6.16; found C 72.24, H 6.20, N 5.88.

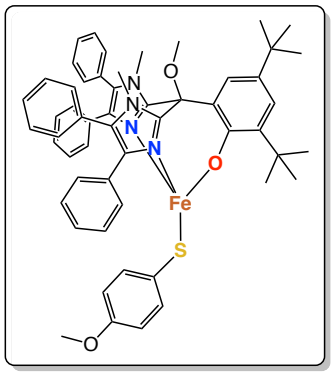

[Zn(Im^{Ph2}NNO^{tBu})(SPh^{OMe})] (12): A suspension of $NaSC_6H_4$-4-OMe (9.7 mg, 52.2 µmol) in CH_2Cl_2 was added dropwise to a solution of **2** (38.8 mg, 47.6 µmol) in CH_2Cl_2. The mixture was stirred for 2.5 h, during which time the mixture turned brown in colour and became slightly cloudy. The mixture was filtered and the filtrate dried under vacuum. The crude solid was washed twice by stirring vigorously in hexane until a fine powder suspension was obtained. The hexane washings were separated by centrifugation and discarded, and the product was dried under vacuum, affording the title complex as a white powder (40.3 mg, 43.9 µmol, 92%). Crystals suitable for X-ray diffraction were obtained from the slow vapour diffusion of hexane into a THF/hexane (2:1) solution of the complex at –40 °C. **^{1}H NMR** (400 MHz, 298 K, CD_3CN): δ = 7.73 (d, 1H, J = 4 Hz, H_{phen}^1), 7.48 (m, 6H, H_{arom}), 7.32 (m, 8H, H_{arom}), 7.21 (d, 1H, H_{phen}^2), 7.16 (m, 6H, H_{arom}), 6.73 (d, 2H, J = 8 Hz, H_{SAr}^3), 6.30 (d, 2H, J = 8 Hz, H_{SAr}^4), 3.60 (s, 3H, OMe_{SAr}), 3.50 (s, 6H, NCH_3), 3.43 (s, 3H, OCH_3), 1.29 (s, 9H, *para*-$C(CH_3)_3$), 1.23 (s, 9H, *ortho*-$C(CH_3)_3$) ppm. **^{13}C{^{1}H} NMR** (101 MHz, CD_3CN, 25 °C): δ = 147.15, 139.46, 135.36, 133.08, 131.82, 131.38, 131.20, 129.46, 128.98, 128.71, 128.29, 128.01, 127.47, 124.17, 121.16, 113.19, 54.73, 52.79, 34.96, 33.64, 33.26, 31.08, 28.90 ppm. **IR** (ATR): υ = 3058 (w), 2959 (m), 1603 (w), 1505 (w), 1488 (m), 1478 (m), 1465 (m), 1438 (m), 1412 (w), 1392 (w), 1360 (w), 1306 (m), 1261 (s), 1235 (m), 1201 (w), 1157 (w), 1133 (w), 1075 (s), 1055 (m), 1024 (s), 1006 (m), 979 (w), 928 (w), 913 (w), 989 (w), 886 (m), 836 (m), 789 (s), 772 (m), 743 (w), 733 (m), 678 (m), 640 (w), 623 (w), 537 (w), 513 (w) cm^{-1}. **E.A.** (Formula: $C_{55}H_{56}N_4O_3SZn$, M_w = 918.52 g mol^{-1}): calc. C 71.92, H 6.15, N 6.10; found C 71.40, H 6.70, N 5.96.

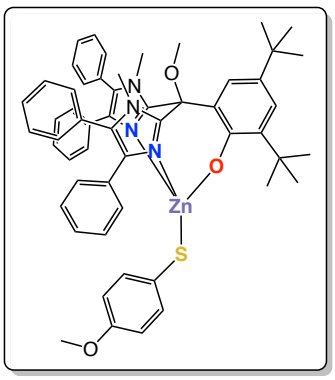

[Fe(Im^{Ph2}NNO^{tBu})(SPh^{CF3})] (13): A suspension of $NaSC_6H_4$-4-CF_3 (16.0 mg, 74.6 µmol) in CH_2Cl_2 was added dropwise to a solution of **1** (56.3 mg, 69.9 µmol) in CH_2Cl_2. The mixture was stirred for 2.5 h, during which time the mixture turned brown in colour and became slightly cloudy. The mixture was filtered and the filtrate dried under vacuum. The crude solid was washed twice by stirring vigorously in hexane until a fine powder suspension was obtained. The hexane washings were separated by centrifugation and discarded, and the product was dried under vacuum, affording the title complex as a yellow powder (52.6 mg, 55.5 µmol, 79%). **^{1}H NMR** (400 MHz, 298 K, CD_3CN): δ = 58.53, 52.37, 46.15, 22.85, 18.26, 14.95, 9.36, 8.94, 7.82, 7.50, 7.22, 6.90, 5.45, 4.78, 4.52, 3.47, 3.36 –0.46, –17.00 ppm. **^{19}F NMR** (376 MHz, 298 K, CD_3CN): δ = –2.66 ppm. χ (Evans method, 1%TMS in CD_2Cl_2): μ_{eff} = 5.00 μ_B. **UV-vis** (CH_2Cl_2, ε [mol^{-1} dm^3 cm^{-1}]): λ_{max} = 380 (1317), 500 (23) nm. **^{57}Fe Mössbauer** (80 K): δ = 0.91 mm s^{-1}, $|\Delta E_Q|$ = 2.57 mm s^{-1}. **IR** (ATR): υ = 3057 (w), 2959 (w), 2905 (w), 2868 (w), 1600 (m), 1562 (w), 1505 (w), 1476 (m), 1465 (m), 1437 (m), 1411 (w), 1394 (w), 1361 (w), 1324 (s), 1301 (m), 1235 (w), 1202 (w0, 1156 (m), 1091 (s), 1075 (s), 1060 (s), 1023 (s), 1014 (s), 978 (w), 929 (w), 914 (w), 899 (w), 801 (s0, 789 (s), 772 (s), 749 (m), 731 (w), 699 (s), 649 (w), 589 (w0, 541 (m), 502 (m) cm^{-1}. **E.A.** (Formula: $C_{55}H_{53}F_3N_4O_2SFe$, M_w = 946.96 g mol^{-1}): calc. C 69.76, H 5.64, N 5.92; found C 70.11, H 5.84, N 5.67.

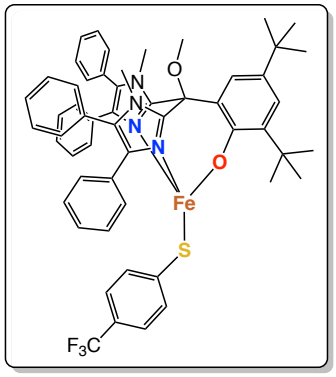

[Zn(Im^{Ph2}NNO^{tBu})(SPh^{CF3})] (14): A suspension of $NaSC_6H_4$-4-CF_3 (12.5 mg, 58.3 µmol) in CH_2Cl_2 was added dropwise to a solution of **2** (43.6 mg, 53.5 µmol) in CH_2Cl_2. The mixture was stirred for 2.5 h, during which time the mixture turned brown in colour and became slightly cloudy. The mixture was filtered and the filtrate dried under vacuum. The crude solid was washed twice by stirring vigorously in hexane until a fine powder suspension was obtained. The hexane washings were separated by centrifugation and discarded, and the product was dried under vacuum, affording the title complex as an off-white powder (49.7 mg, 52.0 µmol, 97%). Crystals suitable for X-ray diffraction were obtained from the slow vapour diffusion of hexane into a THF/hexane (2:1) solution of the complex at –40 °C, over the course of several days. **^{1}H NMR** (400 MHz, 298 K, CD_3CN): δ = 7.76 (d, 1H, *J* = 4 Hz, H_{phen}^1), 7.48 (m, 6H, H_{arom}), 7.32 (m, 4H, H_{arom}), 7.25 (m, 5H, H_{arom}), 7.11 (m, 6H, H_{arom}), 7.00 (d, 2H, *J* = 8 Hz, H_{SAr}^3), 6.91 (d, 2H, *J* = 8 Hz, H_{SAr}^4), 3.52 (s, 6H, NCH_3), 3.46 (s, 3H, OCH_3), 1.29 (s, 9H, *para*-C(CH_3)$_3$), 1.24 (s, 9H, *ortho*-C(CH_3)$_3$) ppm. **^{19}F NMR** (376 MHz, 298 K, CD_3CN): δ = –62.33 ppm. **^{13}C{^{1}H} NMR** (101 MHz, CD_3CN, 25 °C): δ = 161.95, 149.66, 148.16, 140.55, 136.38, 134.25, 132.97, 132.38, 132.05, 130.52, 129.99, 129.57, 129.16, 128.99, 128.53, 125.34, 124.84 (q), 124.01, 123.68, 122.26, 119.66, 81.39, 53.39, 35.94, 34.74, 34.30, 32.08, 29.91 ppm. **IR** (ATR): υ = 3059 (w), 2957 (w), 2906 (w), 2867 (w), 1602 (m), 1506 (w), 1477 (m), 1465 (m), 1438 (m), 1400 (w), 1360 (w), 1326 (s), 1311 (m), 1261 (m), 1234 (w), 1189 (w), 1156 (m), 1095 (s), 1075 (s0, 1061 (s), 1025 (m), 1014 (m), 1005 (m), 979 (w), 928 (w), 915 (w), 834 (m), 824 (m), 798 (s), 745 (w), 734 (w), 726 (w), 699 (s), 646 (w), 611 (w), 589 (w), 538 9w), 504 (m) cm^{-1}. **E.A.** (Formula: $C_{55}H_{53}F_3N_4O_2SZn$, M_w = 956.49 g mol^{-1}): calc. C 69.07, H 5.59, N 5.86; found C 69.47, H 5.82, N 5.48.

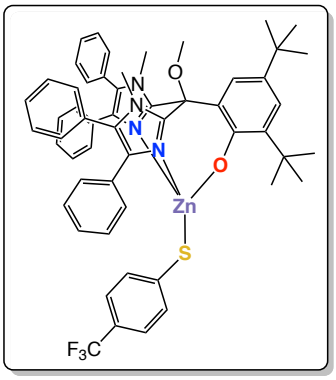

4.5.5 Reactivity Studies

***In-situ* nitrosylation of [Fe(Im^{Ph2}NNO^{tBu})(SR)] complexes with Ph_3CSNO:** In the glovebox, a CH_2Cl_2 solution of Ph_3CSNO (1 equiv.) was added dropwise to a CH_2Cl_2 solution of iron thiolate complex (1 equiv.), at –40 °C. The reaction mixture was stirred for 3 h while warming to room temperature. Reactions were conducted in brown glass containers in order to minimise any light-induced degradation of the nitrosothiol. Over the course of the reaction, the colour of the solutions changed from emerald green to brown. Small aliquots of the mixture were then taken for IR, UV-vis and EPR analysis. The rest of the reaction mixture was subsequently filtered and dried under reduced pressure to afford a brown solid. Recrystallisation attempts at room temperature or at –40 °C from various solvent mixtures, including THF/hexane, CH_2Cl_2/pentane, CH_2Cl_2/Et_2O, saturated hexane solution or saturated HDMSO solution did not yield any crystals suitable for X-ray diffraction.

General procedure for reactions between [Fe(Im^{Ph2}NNO^{tBu})(SR)] complexes and PhIO: In the glovebox, PhIO (10 equiv.) was added to a solution of iron thiolate complex (1 equiv.) in MeCN, cooled to –78 °C. Within 5 min, the colour of the reaction mixture changed from pale brown to deep copper-orange. The reaction was stirred for a further 1 h, after which the mixture was filtered and all solvent was removed under vacuum. A brown-red solid residue was obtained, which was analysed by UV-vis and ESI-MS spectroscopy. These reactions were performed on a scale of 25 μmol with complexes [Fe(Im^{Ph2}NNO^{tBu})(SBn)] (**3**) and [Fe(Im^{Ph2}NNO^{tBu})(SPh)] (**7**).

General procedure for reactions between [Fe(Im^{Ph2}NNO^{tBu})(SR)] complexes and [Ph_3C]PF_6: In the glovebox, a CH_2Cl_2 solution of [Ph_3C]PF_6 (1.1 eq.) was added dropwise to a CH_2Cl_2 solution of iron thiolate complex (1 eq.) at room temperature. The bright yellow solution slowly changed to red-brown while stirring for 2 h. The reaction mixture was subsequently filtered, and all solvent removed under vacuum. A brown-red solid residue was obtained, which was washed with hexane. The solid was analysed by NMR and UV-vis spectroscopy. Recrystallisation experiments were set up with slow diffusion of hexane into a THF solution of the compound at –40 °C. Crystals suitable for X-ray diffraction were only obtained for the reaction product obtained in the case of [Fe(Im^{Ph2}NNO^{tBu})(SBn)] (**3**). The product was characterised as complex [Fe(L^{quinone})$_2$](PF_6)$_2$ (**15**).

***In-situ* synthesis of [Fe_2(L*)$_2$(Cl)$_2$] (16): K-Im^{Ph2}NNO^{tBu}** (94.2 mg, 125 μmol) was stirred in 8 mL THF and $FeCl_3$ (20.2 mg, 125 μmol) was added dropwise to the mixture, causing an instant colour change from yellow to deep purple. The reaction was stirred for 1.5 h and was subsequently filtered. A grey precipitate was recovered on the filter, which was further washed with additional THF until the filtrate washed through colourless. The purple filtrate solution was concentrated under vacuum, affording 76.1 mg of a dark purple-black solid (90.5 μmol, 72% yield, assuming no ligand degradation). Unfortunately, all attempts at elemental analysis were unsuccessful, presumably due to the partial degradation of the ligand over time. Slow diffusion of *n*-hexane into a benzene solution of the product solid resulted in the growth of red crystals suitable for X-ray diffraction over the course of several says. The complex solution also turned reddish brown in this time. The crystals were characterised as complex [Fe_2(Im^{Ph2}NNO^{tBu}*)(Cl)$_2$] (**16**), where Im^{Ph2}NNO^{tBu}* is the ligand that has undergone methyl cleavage at the methoxy group.

4.6 References and Notes

(1) Fleming, A. *Br. J. Exp. Pathol.* **1929**, *10*, 226–236.
(2) Nicola, G.; Tomberg, J.; Pratt, R. F.; Nicholas, R. A.; Davies, C. *Biochemistry* **2010**, *49*, 8094–8104.
(3) Bagozzi, D.; Jasarevic, T.; Chaib, F. Lack of new antibiotics threatens global efforts to contain drug-resistant infections https://www.who.int/news-room/detail/17-01-2020-lack-of-new-antibiotics-threatens-global-efforts-to-contain-drug-resistant-infections (accessed May 14, 2020).
(4) Elander, R. P. *Appl. Microbiol. Biotechnol.* **2003**, *61*, 385–392.
(5) Baldwin, J. E.; Bradley, M. *Chem. Rev.* **1990**, *90*, 1079–1088.
(6) Schenk, W. *Angew. Chem. Int. Ed. Engl.* **2000**, *39*, 3409–3411.
(7) Peck, S. C.; van der Donk, W. A. *J. Biol. Inorg. Chem.* **2016**, 1–14.
(8) Roach, P. L.; Clifton, I. J.; Fülöp, V.; Harlos, K.; Barton, G. J.; Hajdu, J.; Andersson, I.; Schofield, C. J.; Baldwin, J. E. *Nature* **1995**, *375*, 700–704.
(9) Roach, P. L.; Clifton, I. J.; Hensgens, C. M. H.; Shibata, N.; Schofield, C. J.; Hajdu, J.; Baldwin, J. E. *Nature* **1997**, *387*, 827–830.
(10) Burzlaff, N. I.; Rutledge, P. J.; Clifton, I. J.; Hensgens, C. M.; Pickford, M.; Adlington, R. M.; Roach, P. L.; Baldwin, J. E. *Nature* **1999**, *401*, 721–724.
(11) Chen, V. J.; Orville, A. M.; Harpel, M. R.; Frolik, C. A.; Surerus, K. K.; Münck, E.; Lipscomb, J. D. *J. Biol. Chem.* **1989**, *264*, 21677–21681.
(12) Orville, A. M.; Chen, V. J.; Kriauciunas, A.; Harpel, M. R.; Fox, B. G.; Munck, E.; Lipscomb, J. D. *Biochemistry* **1992**, *31*, 4602–4612.
(13) Brown, C. D.; Neidig, M. L.; Neibergall, M. B.; Lipscomb, J. D.; Solomon, E. I. *J. Am. Chem. Soc.* **2007**, *129*, 7427–7438.
(14) Tamanaha, E.; Zhang, B.; Guo, Y.; Chang, W.; Barr, E. W.; Xing, G.; St. Clair, J.; Ye, S.; Neese, F.; Bollinger, J. M.; Krebs, C. *J. Am. Chem. Soc.* **2016**, *138*, 8862–8874.
(15) Rabe, P.; Kamps, J. J. A. G.; Schofield, C. J.; Lohans, C. T. *Nat. Prod. Rep.* **2018**, *35*, 735–756.
(16) Clifton, I. J.; Ge, W.; Adlington, R. M.; Baldwin, J. E.; Rutledge, P. J. *FEBS Lett.* **2013**, *587*, 2705–2709.
(17) Ogle, J. M.; Clifton, I. J.; Rutledge, P. J.; Elkins, J. M.; Burzlaff, N. I.; Adlington, R. M.; Roach, P. L.; Baldwin, J. E. *Chem. Biol.* **2001**, *8*, 1231–1237.
(18) Ge, W.; Clifton, I. J.; Stok, J. E.; Adlington, R. M.; Baldwin, J. E.; Rutledge, P. J. *J. Am. Chem. Soc.* **2008**, *130*, 10096–10102.
(19) Long, A. J.; Clifton, I. J.; Roach, P. L.; Baldwin, J. E.; Rutedge, P. J.; Schofield, C. J. *Biochemistry* **2005**, *44*, 6619–6628.
(20) Goudarzi, S.; Babicz, J. T.; Kabil, O.; Banerjee, R.; Solomon, E. I. *J. Am. Chem. Soc.* **2018**, *140*, 14887–14902.
(21) Lundberg, M.; Siegbahn, P. E. M.; Morokuma, K. *Biochemistry* **2008**, *47*, 1031–1042.
(22) Lundberg, M.; Morokuma, K. *J. Phys. Chem. B* **2007**, *111*, 9380–9389.
(23) Hegg, E. L.; Que, L. *Eur. J. Biochem.* **1997**, *250*, 625–629.
(24) McNeill, L. A.; Brown, T. J. N.; Sami, M.; Clifton, I. J.; Burzlaff, N. I.; Claridge, T. D. W.; Adlington, R. M.; Baldwin, J. E.; Rutledge, P. J.; Schofield, C. J. *Chem. - A Eur. J.* **2017**, *23*, 12815–12824.
(25) Randall, C. R.; Zang, Y.; True, A. E.; Que, L.; Charnock, J. M.; Garner, C. D.; Fujishima, Y.; Schofield, C. J.; Baldwin, J. E. *Biochemistry* **1993**, *32*, 6664–6673.
(26) Roach, P. L.; Clifton, I. J.; Hensgens, C. M. H.; Shibata, N.; Long, A. J.; Strange, R. W.; Hasnain, S. S.; Schofield, C. J.; Baldwin, J. E.; Hajdu, J. *Eur. J. Biochem.* **1996**, *242*, 736–740.
(27) Baldwin, J. E.; Adlington, R. M.; Robinson, N. G.; Ting, H.-H. *J. Chem. Soc., Chem. Commun.* **1986**, 409–411.
(28) Que, L. J. *Nat. Struct. Biol.* **2000**, *7*, 182–184.
(29) Kreisberg-Zakarin, R.; Borovok, I.; Yanko, M.; Frolow, F.; Aharonowitz, Y.; Cohen, G. *Biophys. Chem.* **2000**, *86*, 109–118.
(30) Monkcom, E. C.; Ghosh, P.; Folkertsma, E.; Negenman, H. A.; Lutz, M.; Klein Gebbink, R. J. M. *Chim. Int. J. Chem.* **2020**, *74*, 450–466. (Chapter 6 of this thesis).
(31) Beck, A.; Barth, A.; Hübner, E.; Burzlaff, N. *Inorg. Chem.* **2003**, *42*, 7182–7188.
(32) Folkertsma, E.; de Waard, E. F.; Korpershoek, G.; van Schaik, A. J.; Solozabal Mirón, N.; Borrmann, M.; Nijsse, S.; Moelands, M. A. H.; Lutz, M.; Otte, M.; Moret, M.-E.; Klein Gebbink, R. J. M. *Eur. J. Inorg. Chem.* **2016**, *2016*, 1319–1332.

(33) Smith, J. N.; Shirin, Z.; Carrano, C. J. *J. Am. Chem. Soc.* **2003**, *125*, 868–869.
(34) Beck, A.; Weibert, B.; Burzlaff, N. *Eur. J. Inorg. Chem.* **2001**, 521–527.
(35) Monkcom, E. C.; de Bruin, D.; de Vries, A. J.; Lutz, M.; Ye, S.; Klein Gebbink, R. J. M. *Chem. – A Eur. J.* **2021**, *27*, 5191–5204. (Chapter 3 of this thesis).
(36) Zang, Y.; Que, L. *Inorg. Chem.* **1995**, *34*, 1030–1035.
(37) Badiei, Y. M.; Siegler, M. A.; Goldberg, D. P. *J. Am. Chem. Soc.* **2011**, *133*, 1274–1277.
(38) de Visser, S. P.; Straganz, G. D. *J. Phys. Chem. A* **2009**, *113*, 1835–1846.
(39) Koehntop, K. D.; Emerson, J. P.; Que, L. *J. Biol. Inorg. Chem.* **2005**, *10*, 87–93.
(40) Gordon, J. B.; Goldberg, D. P. In *Reference Module in Chemistry, Molecular Sciences and Chemical Engineering*; Elsevier, 2020.
(41) Notni, J.; Görls, H.; Anders, E. *Eur. J. Inorg. Chem.* **2006**, *2006*, 1444–1455.
(42) Chiou, S.-J.; Riordan, C. G.; Rheingold, A. L. *Proc. Natl. Acad. Sci. U. S. A.* **2003**, *100*, 3695–3700.
(43) Chiou, S.-J.; Innocent, J.; Riordan, C. G.; Lam, K.-C.; Liable-Sands, L.; Rheingold, A. L. *Inorg. Chem.* **2000**, *39*, 4347–4353.
(44) Brand, U.; Rombach, M.; Seebacher, J.; Heinrich, V. *Inorg. Chem.* **2001**, *40*, 6151–6157.
(45) Ibrahim, M. M.; Seebacher, J.; Steinfeld, G.; Vahrenkamp, H. *Inorg. Chem.* **2005**, *44*, 8531–8538.
(46) Wilker, J. J.; Lippard, S. J. *J. Am. Chem. Soc.* **1995**, *117*, 8682–8683.
(47) Robinson, K.; Gibbs, G. V; Ribbe, P. H. *Science (80-.).* **1971**, *172*, 567–570.
(48) Moelands, M. A. H.; Nijsse, S.; Folkertsma, E.; de Bruin, B.; Lutz, M.; Spek, A. L.; Klein Gebbink, R. J. M. *Inorg. Chem.* **2013**, *52*, 7394–7410.
(49) Evans, D. F. *J. Chem. Soc.* **1959**, *81*, 2003–2005.
(50) Ribas Gispert, J. *Coordination Chemistry*; Ribas Gispert, J., Ed.; Wiley-VCH Verlag GmbH & Co. KGaA: Weinheim, Germany, 2008.
(51) Rӧmelt, M.; Ye, S.; Neese, F. *Inorg. Chem.* **2009**, *48*, 784–785.
(52) McWilliams, S. F.; Brennan-Wydra, E.; MacLeod, K. C.; Holland, P. L. *ACS Omega* **2017**, *2*, 2594–2606.
(53) Gaussian 16, Revision C.01; Frisch, M. J.; Trucks, G. W.; Schlegel, H. B.; Scuseria, G. E.; Robb, M. A.; Cheeseman, J. R.; Scalmani, G.; Barone, V.; Petersson, G. A.; Nakatsuji, H.; Li, X.; Caricato, M.; Marenich, A. V.; Bloino, J.; Janesko, B. G.; Gomperts, R.; Mennucci, B.; Hratchian, H. P.; Ortiz, J. V.; Izmaylov, A. F.; Sonnenberg, J. L.; Williams-Young, D.; Ding, F.; Lipparini, F.; Egidi, F.; Goings, J.; Peng, B.; Petrone, A.; Henderson, T.; Ranasinghe, D.; Zakrzewski, V. G.; Gao, J.; Rega, N.; Zheng, G.; Liang, W.; Hada, M.; Ehara, M.; Toyota, K.; Fukuda, R.; Hasegawa, J.; Ishida, M.; Nakajima, T.; Honda, Y.; Kitao, O.; Nakai, H.; Vreven, T.; Throssell, K.; Montgomery, J. A. J.; Peralta, J. E.; Ogliaro, F.; Bearpark, M. J.; Heyd, J. J.; Brothers, E. N.; Kudin, K. N.; Staroverov, V. N.; Keith, T. A.; Kobayashi, R.; Normand, J.; Raghavachari, K.; Rendell, A. P.; Burant, J. C.; Iyengar, S. S.; Tomasi, J.; Cossi, M.; Millam, J. M.; Klene, M.; Adamo, C.; Cammi, R.; Ochterski, J. W.; Martin, R. L.; Morokuma, K.; Farkas, O.; Foresman, J. B.; Fox, D. J. Gaussian 16, Revision C.01, 2016.
(54) Enemark, J. H.; Feltham, R. D. *Coord. Chem. Rev.* **1974**, *13*, 339–406.
(55) Zhang, Y.; Pavlosky, M. A.; Brown, C. A.; Westre, T. E.; Hedman, B.; Hodgson, K. O.; Solomon, E. I. *J. Am. Chem. Soc.* **1992**, *114*, 9189–9191.
(56) Brown, C. A.; Pavlosky, M. A.; Westre, T. E.; Zhang, Y.; Hedman, B.; Hodgson, K. O.; Solomon, E. I. *J. Am. Chem. Soc.* **1995**, *117*, 715–732.
(57) Harrop, T. C.; Tonzetich, Z. J.; Reisner, E.; Lippard, S. J. *J. Am. Chem. Soc.* **2008**, *130*, 15602–15610.
(58) Jana, M.; White, C. J.; Pal, N.; Demeshko, S.; Cordes (née Kupper), C.; Meyer, F.; Lehnert, N.; Majumdar, A. *J. Am. Chem. Soc.* **2020**, *142*, 6600–6616.
(59) Pal, N.; White, C. J.; Demeshko, S.; Meyer, F.; Lehnert, N.; Majumdar, A. *Inorg. Chem.* **2021**, *60*, 15890–15900.
(60) Ekanayake, D. M.; Fischer, A. A.; Elwood, M. E.; Guzek, A. M.; Lindeman, S. V.; Popescu, C. V.; Fiedler, A. T. *Dalt. Trans.* **2020**, *49*, 17745–17757.
(61) Fischer, A. A.; Stracey, N.; Lindeman, S. V.; Brunold, T. C.; Fiedler, A. T. *Inorg. Chem.* **2016**, *55*, 11839–11853.
(62) *Metal Nitrosyls*; Richter-Addo, G. B.; Legzdins, P., Eds.; Oxford University Press: New York, 1992.
(63) Burzlaff, N.; Schenk, W. A. *Eur. J. Inorg. Chem.* **1999**, *1999*, 1435–1443.
(64) Jerkunica, J. M.; Traylor, T. G. *J. Am. Chem. Soc.* **1971**, *93*, 6278–6279.
(65) Straus, D. A.; Zhang, C.; Tilley, T. D. *J. Organomet. Chem.* **1989**, *369*, C13–C17.
(66) Connelly, N. G.; Geiger, W. E. *Chem. Rev.* **1996**, *96*, 877–910.
(67) Villar-Acevedo, G.; Lugo-Mas, P.; Blakely, M. N.; Rees, J. A.; Ganas, A. S.; Hanada, E. M.;

Kaminsky, W.; Kovacs, J. A. *J. Am. Chem. Soc.* **2017**, *139*, 119–129.
(68) Grieco, P. A.; Nishizawa, M.; Oguri, T.; Burke, S. D.; Marinovic, N. *J. Am. Chem. Soc.* **1977**, *99*, 5773–5780.
(69) Demuynck, M.; De Clercq, P.; Vandewalle, M. *J. Org. Chem.* **1979**, *44*, 4863–4866.
(70) Baars, S. M.; Hoberg, J. O. *Carbohydr. Res.* **2006**, *341*, 1680–1684.
(71) Ganem, B.; Small, V. R. *J. Org. Chem.* **1974**, *39*, 3728–3730.
(72) Sawama, Y.; Masuda, M.; Asai, S.; Goto, R.; Nagata, S.; Nishimura, S.; Monguchi, Y.; Sajiki, H. *Org. Lett.* **2015**, *17*, 434–437.
(73) Monkcom, E. C.; Negenman, H. A.; Masferrer-Rius, E.; Lutz, M.; Ye, S.; Bill, E.; Klein Gebbink, R. J. M. *Eur. J. Inorg. Chem.* **2022**. (Chapter 2 of this thesis).
(74) Fulmer, G. R.; Miller, A. J. M.; Sherden, N. H.; Gottlieb, H. E.; Nudelman, A.; Stoltz, B. M.; Bercaw, J. E.; Goldberg, K. I. *Organometallics* **2010**, *29*, 2176–2179.
(75) McCarthy, B. D.; Martin, D. J.; Rountree, E. S.; Ullman, A. C.; Dempsey, J. L. *Inorg. Chem.* **2014**, *53*, 8350–8361.
(76) Glendening, E. D.; Landis, C. R.; Weinhold, F. *J. Comput. Chem.* **2013**, *34*, 1429–1437.
(77) Lu, T.; Chen, F. *J. Comput. Chem.* **2012**, *33*, 580–592.
(78) Humphrey, W.; Dalke, A.; Schulten, K. *J. Mol. Graph.* **1996**, *14*, 33–38.

Chapter 5

Synthesis, Structure and Reactivity of a Mononuclear *N,N,O*-Bound Fe(II) α-Keto-Acid Complex

Abstract

A bulky, tridentate phenolate ligand (**Im^{Ph2}NNO^{tBu}**) was used to synthesise the first example of a mononuclear, facial, *N,N,O*-bound iron(II) benzoylformate complex, [Fe(Im^{Ph2}NNO^{tBu})(BF)] (**2**). The X-ray crystal structure of **2** reveals that the iron centre is pentacoordinate ($\tau = 0.5$), with a vacant site located *cis* to the bidentate BF ligand. The Mössbauer parameters of **2** are consistent with high-spin ($S = 2$) iron(II), and are very close to those reported for α-ketoglutarate-bound, non-heme iron enzyme active sites. According to NMR and UV-vis spectroscopies, the structural integrity of **2** is retained in both coordinating and non-coordinating solvents. Cyclic voltammetry studies show that the iron centre has a very low oxidation potential and is more prone to electrochemical oxidation than the redox-active phenolate ligand. **2** reacts with NO (using Ph_3CSNO) to form a $S = {}^3/_2$ $\{FeNO\}^7$ adduct in which NO binds directly to the iron centre, according to EPR, UV-vis, IR spectroscopies and DFT analysis. Upon O_2 exposure, **2** undergoes oxidative decarboxylation to form a diiron(III) benzoate complex, $[Fe(Im^{Ph2}NNO^{tBu})_2(\mu_2\text{-OBz})(\mu_2\text{-OH})_2]^+$ (**3**). A small amount of hydroxylated ligand is also observed by ESI-MS, hinting at the formation of a high-valent iron(IV)-oxo intermediate. Initial reactivity studies show that **2** is capable of oxygen atom transfer reactivity with O_2, converting methyl(*p*-tolyl)sulfide to the respective sulfoxide.

E. C. Monkcom, L. Gómez Martín, M. Lutz, S. Ye, E. Bill, M. Costas, R. J. M. Klein Gebbink, *manuscript in preparation*

5.1 Introduction

α-Ketoglutarate (αKG, also known as 2-oxoglutarate) dependent oxidases and oxygenases are widely distributed across prokaryote, eukaryote and archaea organisms and constitute one of the largest sub-classes of mononuclear non-heme iron enzymes.[1–3] Their protein fold comprises a β-strand "jellyroll" motif, which chelates to a single iron(II) centre by means of two histidine residues (His) and a carboxylate group (Asp/Glu), collectively known as the 2-His-1-Carboxylate facial triad (2H1C).[4,5] More recently, αKG-dependent halogenase enzymes have also been identified, although these enzymes possess a 2-His-1-halogen motif at their active site instead of the typical 2H1C.[6–8] In general, αKG-dependent enzymes combine the oxidative decarboxylation of their αKG co-substrate with the 2-electron oxidation of their substrate, using O_2 as the oxidant.[1–3,5,9,10] Succinate and CO_2 are formed simultaneously as by-products (Scheme 1). Since their initial discovery in the 1960s, these enzymes are now known to catalyse an astoundingly diverse set of reactions, including (di)hydroxylation,[11–14] demethylation (*via* methyl group hydroxylation),[15–17] epoxidation,[18,19] chlorination,[6,8,20] desaturation,[14,21–25] ring-expansion,[24] cyclization,[13,25] $C(sp^2)$–$C(sp^3)$ coupling,[13,26] epimerization[25,27] and endoperoxidation.[28,29] Selected examples of these transformations are shown in Figure 1.

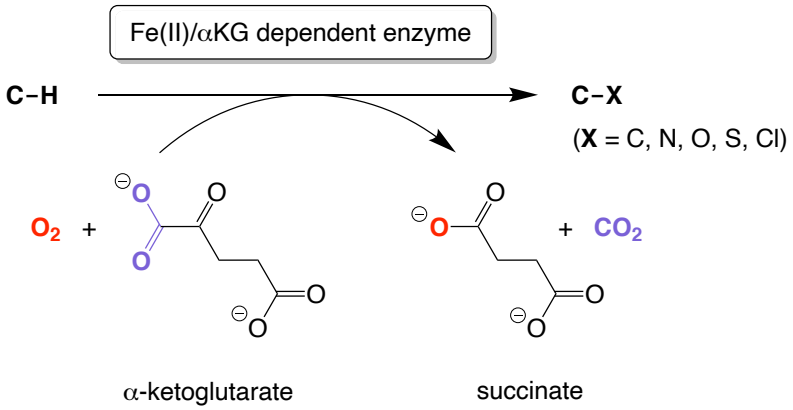

Scheme 1. The oxidative functionalisation of C–H bonds by αKG-dependent mononuclear non-heme iron enzymes. During this process, αKG is converted to succinate and CO_2.

Over the decades, different aspects of the superfamily of αKG-dependent non-heme iron enzymes have been extensively reviewed, including their reaction scope and diversity,[1–3,9,30,31] the biosynthetic pathways towards natural products,[12,15,32,33] enzyme mechanism and spectroscopy,[2,5,10,34–40] as well as mechanistic investigations by means of biomimetic model systems.[3,10,41] The malfunction of αKG-dependent non-heme iron enzymes is closely associated to several human diseases including anaemia,[42] cancer,[43] Hawkinsinuria,[44,45] Refsum disease,[46] and Ehlers-Danlos syndrome (type IV).[47–49] Gaining a better understanding of the structure and function of these enzymes therefore remains a long-standing biomedical goal for the appropriate treatment of these diseases using, for instance,

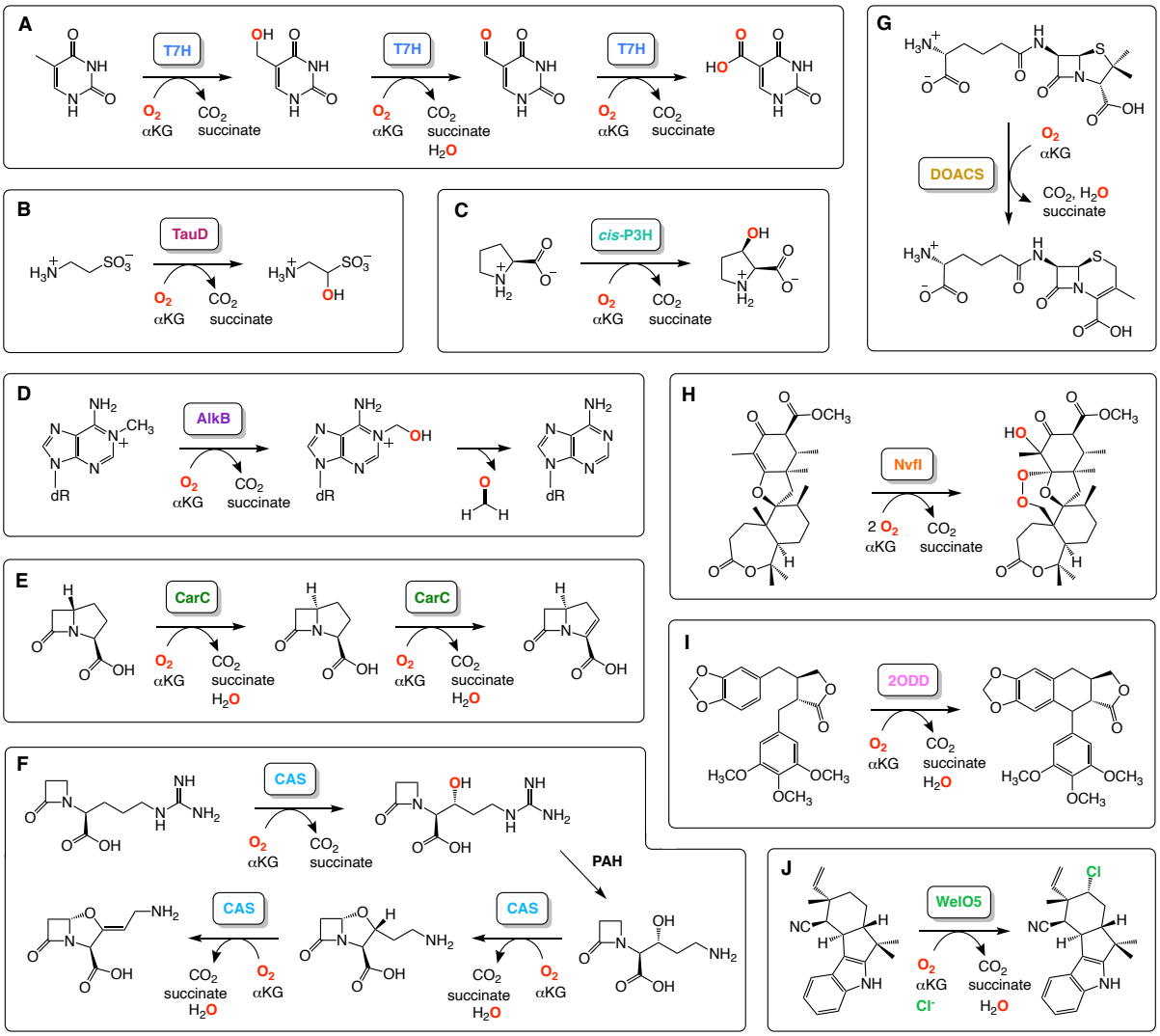

Figure 1. Examples of reactions catalysed by αKG-dependent mononuclear non-heme iron enzymes. **A:** The sequential oxidation of thymine to 5-carboxyuracil by T7H.[9,50,51] **B:** The hydroxylation of taurine by TauD.[36,37] **C:** The stereospecific *cis*-3-hydroxylation of proline by *cis*-P3H.[12,52] **D:** Demethylation of 1-methyladenine to the unmodified nucleobase by AlkB.[15] **E:** The sequential epimerisation and desaturation of (3*S*,5*S*)-carbapenam by CarC.[23] **F:** The sequential hydroxylation, cyclisation and desaturation reactions catalysed by CAS, forming clavaminic acid.[25] **G:** The oxidative ring expansion and desaturation of penicillin N, catalysed by DAOCS. **H:** The hydroxylation and endoperoxidation of asnovolin A, catalysed by NvfI.[29] **I:** A unique C(sp^3)–C(sp^2) coupling reaction, catalysed by 2ODD.[26] **J:** The chlorination of 12-*epi*-fischerindole U by WelO5.[53]

small molecular therapeutic agents that inhibit or modulate enzyme activity.[49,54–59] Many of the reactions catalysed by αKG-dependent iron enzymes are highly synthetically challenging and involve complex late-stage functionalisation. Those relating to penicillin and cephalosporin biosynthesis have faced particular scrutiny by the medicinal and pharmaceutical communities and have even prompted the commercial application of enzymes such as cephalosporin C synthase (CAS) from *Acremonium chrysogenum* as a biocatalyst in antibiotic production.[60,61] More recently, the application of αKG-dependent enzymes in chemoenzymatic synthesis has also been explored.[62]

Intense kinetic, spectroscopic and computational investigations have enabled a consensus mechanism to be put forward, depicted in Figure 2A.[3,11,39] Catalysis begins with the bidentate coordination of the αKG co-substrate to the iron centre through its C1 carboxylate and C2 keto groups, displacing two of the three water molecules from the resting state (**A**) and forming a new six-coordinate ferrous complex (**B**).[24,63] Next, the substrate enters the active site cavity and binds in the vicinity of the iron centre, displacing the third water molecule. This generates a five-coordinate ferrous complex (**C**) that is highly reactive to O_2 (Figure 2C).[63–66] Upon O_2 binding, a transient Fe^{III}–superoxo intermediate (**D**) forms, whose distal oxygen atom performs a nucleophilic attack on the αKG C2 carbon atom. This produces a cyclic Fe–O–O–C intermediate (**E**), best described as a Fe^{IV}–peroxy species on the basis of DFT calculations.[67] This intermediate undergoes rapid decarboxylation to afford a succinate-bound Fe^{IV}=O intermediate (**F**), which is responsible for substrate H-atom abstraction (HAA).[11,36,38,65,68,69] Following HAA, an Fe^{III}–OH intermediate is formed (**G**),[11] whose hydroxyl group recombines with the substrate radical,[34,70] affording the hydroxylated product and an Fe^{II}–succinate species (**H**).[37] Finally, succinate and the hydroxylated product are released from the active site, and water molecules re-populate the vacant sites.

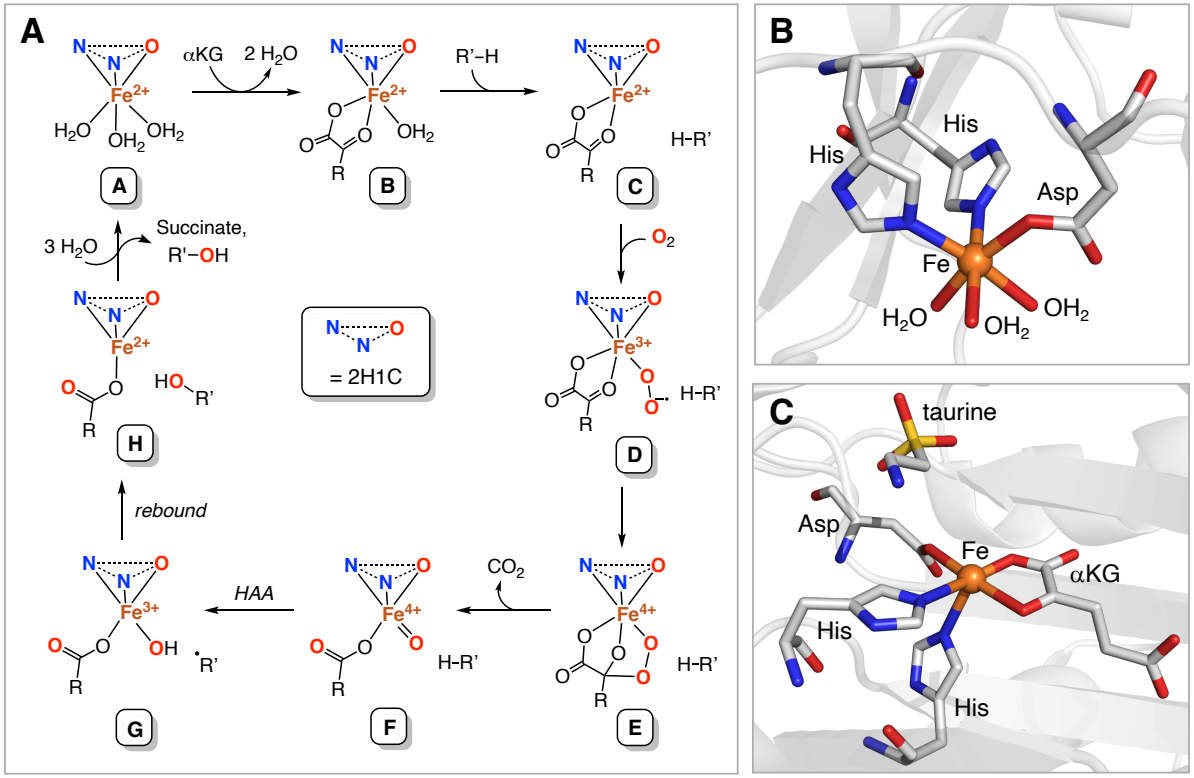

Figure 2. A: Generally accepted mechanism for αKG-dependent non-heme iron hydroxylase enzymes. **B:** Protein crystal structure of the resting state of DAOCS (PDB 1RXF), highlighting the facial coordination of the 2H1C.[24] **C:** Protein crystal structure of the [Fe·TauD·αKG·taurine] enzyme complex for TauD (PDB 1OS7).[71] Carbon, iron, nitrogen, oxygen and sulfur are depicted in grey, orange, blue, red and yellow, respectively.

Developing synthetic biomimetic iron complexes is a well-established strategy for studying the reactivity of non-heme iron enzymes and for developing novel iron-based oxidation catalysts. Numerous iron(II)-α-ketoacid complexes have been reported in the past, featuring a polydentate N-donor ligand in combination with an αKG surrogate such as benzoylformate (BF), pyruvate (PRV) or phenylpyruvate (HPP). These are generally termed *functional* model complexes, as they aim to reproduce important mechanistic aspects of enzyme function without necessarily incorporating all structural elements of the enzyme active site, such as the anionic O-donor of the 2H1C. Selected examples of iron(II) benzoylformato functional model complexes are depicted in Figure 3. These complexes demonstrate that a delicate balance exists between their structure and their reactivity, which is significantly affected by the steric bulk of the supporting ligand and the coordination mode of the α-ketoacid. For instance, Que and co-workers have employed the tripodal, tetradentate N4 ligands **TPA** and **6-Me$_3$-TPA** to synthesise cationic, high-spin iron(II)-BF complexes of octahedral geometry.[72–74] In the case of [Fe(TPA)(κ$_1$-BF)(solv)]$^+$, the binding pocket at the iron centre is large enough to accommodate solvent coordination, which causes the BF ligand to adopt a monodentate coordination mode. In contrast, the increased steric bulk of the supporting ligand in [Fe(6-Me$_3$-TPA)(κ$_2$-BF)]$^+$ prevents solvent binding to the iron centre and ensures bidentate α-ketoacid coordination. Both [Fe(TPA)(κ$_1$-BF)(solv)]$^+$ and [Fe(6-Me$_3$-TPA)(κ$_2$-BF)]$^+$ undergo oxidative decarboxylation in the presence of O_2 to afford the corresponding benzoate complexes in quantitative yield.[73] However, these reactions are rather sluggish, taking place over the course of several days. The slowness of these reactions is attributed to the coordinative saturation of the iron centre, which requires ligand dissociation in order for O_2 to bind.[74]

Similar studies have been conducted using the tris(pyrazolyl)borate ligand family (**Tp**), which provides a monoanionic, tripodal N3 coordination motif. Valentine and co-workers showed that complex [Fe(Tp^{Me2})(κ$_2$-BF)], which features one of the smallest Tp variants, is extremely reactive to air, even in its solid state, and undergoes oxidative decarboxylation to form the corresponding benzoate complex quantitatively within 2 minutes.[75] In contrast, Moro-oka and co-workers prepared complex [Fe(Tp$^{3t\text{Bu},5i\text{Pr}}$)(BF)], whose supporting ligand is so bulky that it is unreactive to O_2.[76] In later work, the groups of Que and Paine showed that complexes [Fe(Tp^{Ph2})(κ$_2$-BF)],[77,78] [Fe(Tp^{Ph,Me})(κ$_2$-BF)][79] and [Fe(Tp$^{i\text{Pr}2}$)(κ$_2$-BF)][80], which feature ligands of "medium" bulk, can undergo quantitative oxidative decarboyxlation in the presence of O_2 and can catalytically oxidise simple substrates such as sulfides and olefins to their corresponding sulfoxides and epoxides, respectively. Recently, Costas and co-workers employed the neutral, tridentate N3 **^{i}Pr$_3$tacn** ligand to prepare mononuclear iron(II) complex [Fe(^{i}Pr$_3$tacn)(κ$_2$-BF)(OTf)], which oxidatively decarboxylates in the presence of O_2 and catalytically oxidises sulfides to their corresponding sulfoxides.[81] In contrast, the reduced steric bulk of the related **^{t}Bu$_3$tacn** ligand was shown to promote the formation of a BF-bridged diiron(II) complex, [Fe$_2$(^{t}Bu$_3$tacn)$_2$(μ$_2$-BF)$_2$(μ$_2$-Cl)], that does not show any oxygen atom transfer (OAT) reactivity.

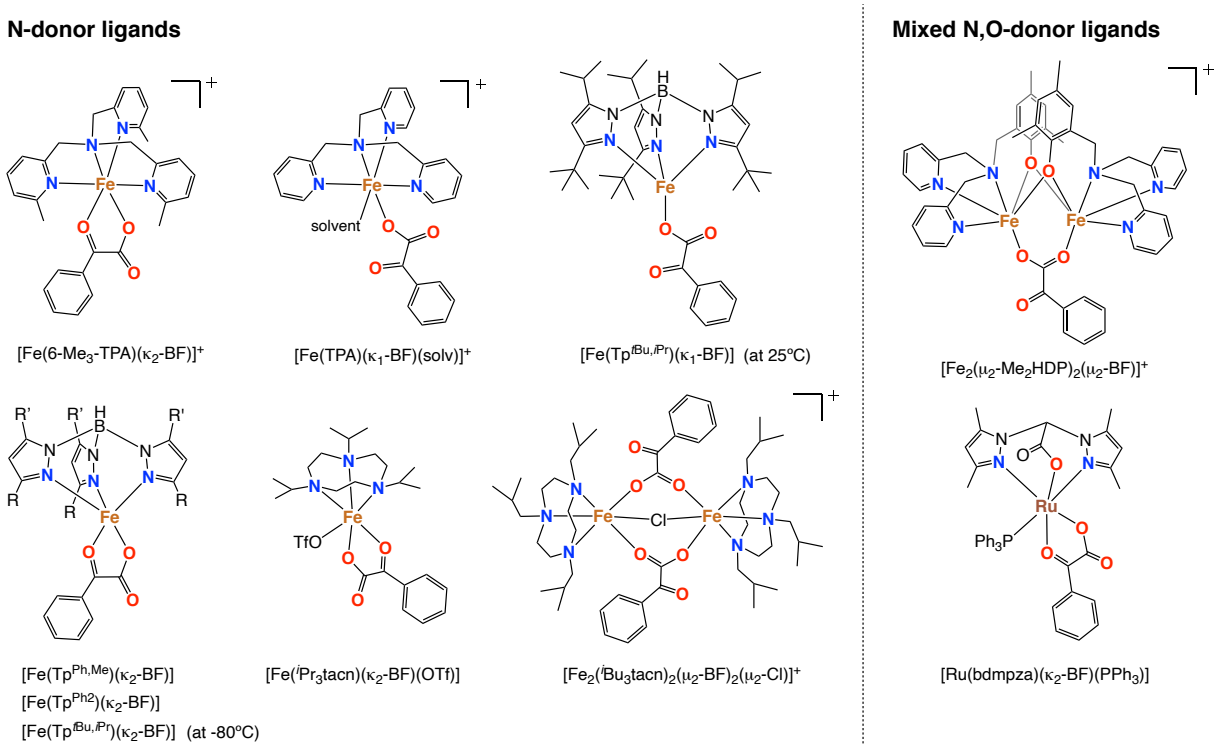

Figure 3. Selected examples of structurally characterised iron(II) or ruthenium(II) benzoylformate model complexes. Left: complexes supported by tripodal N3 and N4 ligands. Right: complexes supported by mixed N,O-donor ligands. **TPA** = tri(2-pyridylmethyl)amine; **6TLA** = tris[(6-methyl-2-pyridyl)methyl]amine; **Tp^{3R,5R}** = tris(3,5-disubstituted-pyrazolyl)borate, including **Tp^{Me2}**, **Tp^{Ph2}**, **Tp^{iPr2}** and **Tp^{tBu,iPr}**; **R$_3$tacn** = 1,4,7-tris(alkyl)-1,4,7-triazacyclononane, including **^{i}Pr$_3$tacn** and **^{i}Bu$_3$tacn**; **bdmpza** = 2,2-bis(3,5-dimethyl-1*H*-pyrazol-1-yl)acetate; **Me$_2$HDP** = 2-((bis(pyridin-2-yl-methyl)-amino)methyl)-4,6-dimethylphenol.

In past studies, it has been emphasised that the facial *N,N,O* coordination of the 2H1C plays an important role in enzyme reactivity by anchoring the iron centre in the protein scaffold and providing three mutually-*cis* coordination sites at which catalysis takes place.[63,82] It has also been suggested that the non-coordinated oxygen atom of the 2H1C carboxylate group partakes in H-bonding with the iron-bound water molecule in intermediate **B**, which could help prevent premature O_2 reactivity of the active site by ensuring coordinative saturation.[64,83] Thirdly, the anionic charge of the 2H1C has been proposed to stabilise the coordination of αKG in its monoanionic α-keto acid form instead of its tautomeric dianionic enolate form.[83,84] This ensures decarboxylation of the acid through C1–C2 cleavage and allows the co-substrate to provide the two electrons necessary for generation of the high-valent ferryl intermediate. Finally, the anionic O-donor also helps lower the Fe^{II}/Fe^{III} redox potential, which is important for enabling O_2 reactivity of the enzyme active site.

Strikingly, studies employing mixed *N,O*-donor ligands for *structurally* modelling the 2H1C at αKG-dependent enzyme active sites are scarce. This is largely due to the fact that very few tridentate *N,N,O* ligands have been reported that support the formation of

mononuclear, monoligated iron complexes.[85–88] Typically, problems are encountered through the formation of homoleptic bis-ligand iron complexes, the formation of polynuclear complexes due to bridging coordination modes of anionic O-donors, or disruption of the *N,N,O* triad due to labile N- or O-donors.[89,90] To the best of our knowledge, the dinuclear complex [$Fe_2(\mu_2\text{-}Me_2HDP)_2(\mu_2\text{-}BF)$], reported by the group of Que (Figure 3), is the only structurally characterised iron(II) benzoylformato complex to date that features a mixed *N,O*-donor ligand.[91] Burzlaff and co-workers have since reported a mononuclear ruthenium(II) complex, [$Ru(bdmpza)(\kappa_2\text{-}BF)(PPh_3)$], which features a bis(pyrazolyl)-acetate ligand (Figure 3).[92] However, the synthesis of mononuclear Fe-BF complexes supported by a facial, tridentate *N,N,O* ligand remains elusive, which reflects how under-developed and challenging the coordination chemistry of these ligands is compared to that of polydentate N-donor ligands.

In this study, we employed a bulky *N,N,O* phenolate ligand (**$Im^{Ph2}NNO^{tBu}$**) to synthesise a mononuclear non-heme iron(II) benzoylformato complex, [$Fe(Im^{Ph2}NNO^{tBu})(BF)$] (Figure 4). We report the solid- and solution-state structure of the complex using X-ray crystal structure determination, UV-vis and NMR spectroscopies, and its electronic structure by means of Mössbauer spectroscopy and SQUID magnetometry. Using cyclic voltammetry, we have also investigated the electrochemical behaviour of the complex in acetonitrile solution and show that the iron centre has a very low oxidation potential. Accordingly, we examined the reactivity of the complex with respect to O_2 and NO, the latter using trityl-S-nitrosothiol (Ph_3CSNO) as a convenient NO donor.

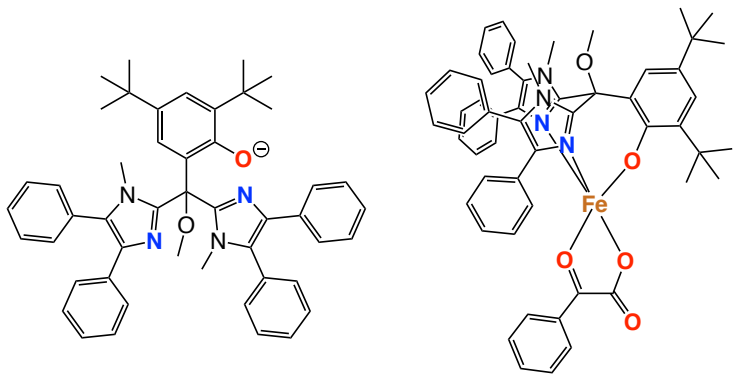

Figure 4. Ligand **$Im^{Ph2}NNO^{tBu}$** and mononuclear, non-heme iron complex [$Fe(Im^{Ph2}NNO^{tBu})(BF)$].

5.2 Results and Discussion

5.2.1 Complex Synthesis

Complex [Fe(Im^{Ph2}NNO^{tBu})(BF)] (**2**) was synthesised according to the reaction depicted in Scheme 2. [Fe(Im^{Ph2}NNO^{tBu})(Cl)] (**1**), whose preparation has previously been reported by our group,[85] was dissolved in CH_2Cl_2 and one equivalent of potassium benzoylformate (K-BF), suspended in CH_2Cl_2, was added dropwise to the solution. The reaction was left to stir overnight, during which time the colour of the mixture changed from pale brown to deep blue. The reaction was filtered and all solvent was removed under vacuum. The crude blue solid was washed with hexane and dried, affording **2** as a bright blue powder in 92% yield. IR analysis of **2** reveals a strong absorption band at 1673 cm^{-1}, assigned to the BF carboxylate stretching vibration. The absence of an O–H absorption band also confirms the anionic nature of both the supporting ligand and the BF co-ligand in **2**. Positive mode ESI-HRMS analysis of **2** in acetonitrile shows a signal at m/z = 941.3326, assigned to the [**2**+Na]$^+$ ion (calc m/z = 941.3337). However, the relative intensity of this signal is rather weak compared to the signals observed at m/z = 810.3462 and m/z = 828.3557, which correspond to the [Fe(L)(MeCN)]$^+$ and [Fe(L)(MeCN)(H$_2$O)]$^+$ ions, respectively. We attribute the greater relative abundancy of these ions to their natural positive charge, in contrast to the neutral charge of **2**.

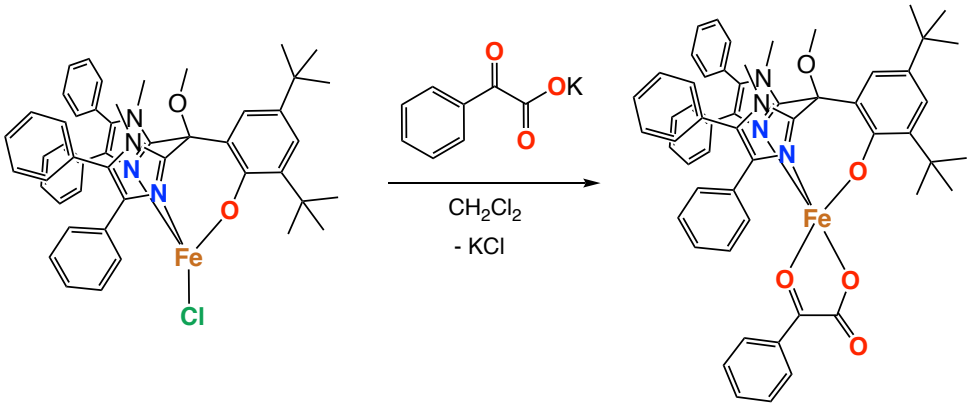

1 **2**

Scheme 2. The synthesis of [Fe(Im^{Ph2}NNO^{tBu})(BF)] (**2**).

Rather surprisingly, the analogous reaction between the zinc counterpart of **1**, [Zn(Im^{Ph2}NNO^{tBu})(Cl)], and K-BF did not produce the expected zinc benzoylformato complex, even upon heating the reaction mixture to 50 °C. Instead, the [Zn(Im^{Ph2}NNO^{tBu})(Cl)] complex was consistently recovered from the reaction mixture and no substitution of the chloride ligand was observed to have taken place. Therefore, no further efforts towards the development of biomimetic zinc complexes were undertaken.

5.2.2 X-ray Crystal Structure Analysis

Dark blue crystals suitable for X-ray diffraction were obtained from slow vapour diffusion of hexane into a THF solution of **2**. The X-ray crystal structure of **2** is depicted in Figure 5, with selected bond lengths and bond angles provided in Table 1. Importantly, this structure demonstrates the clean substitution of the chloride ligand in **1** for the benzoylformate ligand, with retention of the supporting ligand's tripodal *N,N,O* coordination motif. The BF ligand binds to the iron centre in a bidentate fashion, through asymmetric coordination of its carboxylate (O12) and keto (O32) groups. The pentacoordinate structure of **2** has a geometry that lies exactly between square pyramidal and trigonal bipyramidal, as defined by its geometric index ($\tau = 0.5$).[93] Assuming a square pyramidal geometry, the equatorial plane comprises the BF acid (O12) and keto (O32) groups as well as the supporting phenolate (O11) and imidazole (N31) donors. The apical position is occupied by the imidazole nitrogen N11. The steric clash between the BF phenyl group and the phenolate's *ortho*-^{t}Bu substituent causes the BF ligand to "tilt" towards one of the imidazole groups, which results in a relatively good degree of accessibility at the iron centre, as seen in the space-filling model (Figure 5). A putative binding site for small molecules like O_2 in **2** is hypothesised as being *trans* to N11, which would create an octahedron when occupied.

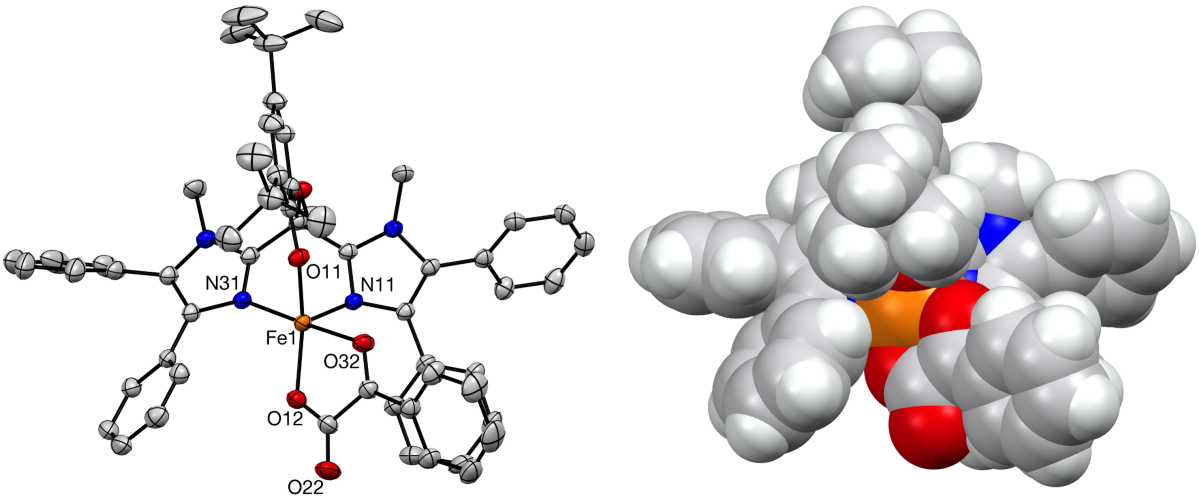

Figure 5. Displacement ellipsoid plot (50% probability level) and space-filling model of **2**. All H atoms and co-crystallised solvent molecules have been omitted for clarity.

Table 1. Selected bond lengths (Å) and bond angles (°) for **2**.

[Fe(Im^{Ph2}NNO^{tBu})(BF)] (**2**)					
Bond	Length	Angle	Degrees	Angle	Degrees
Fe1–N11	2.1255(16)	N11–Fe1–N31	86.96(6)	N11–Fe1–O32	94.39(6)
Fe1–N31	2.1301(16)	N11–Fe1–O11	97.61(6)	N31–Fe1–O32	176.89(6)
Fe1–O11	1.9235(13)	N31–Fe1–O11	89.13(6)	O11–Fe1–O12	146.78(6)
Fe1–O12	2.0105(14)	N11–Fe1–O12	112.31(6)	O11–Fe1–O32	87.91(5)
Fe1–O32	2.1775(13)	N31–Fe1–O12	105.96(6)	O12–Fe1–O32	76.12(5)

The Fe–O_{phen} bond length of 1.9235(14) Å is slightly elongated compared to that reported for **1**, which reflects the increase in coordination number for **2**. The Fe–O_{acid} and Fe–O_{keto} bond lengths of 2.0105(14) Å and 2.1774(13) Å, respectively, reflect the different charges of the oxygen atoms. The α-ketoacid moiety is nearly planar, with a O–C–C–O dihedral angle of 3.4(3)°. The Fe–O_{acid} bond length in **2** is slightly longer compared to those reported for pentacoordinate Fe-BF complexes supported by Tp ligands.[76,77,79] We attribute this to the more localised negative charge of the $\mathbf{Im^{Ph2}NNO^{tBu}}$ ligand, whose phenolate-to-iron charge transfer may quench the Lewis acidity of the iron somewhat. The Fe–N bond lengths are characteristic of a high-spin iron(II) centre bound to an imidazole-containing *N,N,O* ligand.[86,89]

5.2.3 UV-Vis Spectroscopy

One of the most distinctive ways to examine the solution-state structure of αKG-dependent iron enzymes and their model complexes is through UV-vis absorption spectroscopy. Bidentate α-ketoacid coordination to iron is well reported to produce distinctive blue-violet-coloured complexes. Spectroscopically, this is manifested by a characteristic "trio" of metal-to-ligand charge transfer (MLCT) bands between 500 and 600 nm, that correspond to charge donation from the iron's filled *d*-orbitals to the low-lying π* orbitals of the planar, conjugated α-ketoacid moiety. The lesser extent of π-conjugation in ligands such as pyruvate means their MLCT absorption bands are weaker compared to ligands such as BF.[74] Monodentate α-ketoacid coordination modes generally give rise to yellow or orange-coloured solutions that do not exhibit these MLCT bands.[73,81]

Dissolving **2** in either MeCN or CH_2Cl_2 produces a deep blue solution in both solvents, whose absorption spectra are given in Figure 6. The absorption spectrum of **2** in MeCN features a maximum absorption band at 610 nm (ε = 526 M^{-1} cm^{-1}), shouldered by two other bands at 545 nm and 735 nm. A similar spectrum is obtained in CH_2Cl_2, with a maximum absorption band at 600 nm (ε = 830 M^{-1} cm^{-1}) and two shoulders at 540 nm and 750 nm. This demonstrates that the bidentate coordination of the BF ligand, which was observed in the X-ray crystal structure of **2**, is retained in both coordinating and non-coordinating solvents. Variable temperature (VT) UV-vis of **2** in MeCN and CH_2Cl_2 shows an increase in molar absorptivity at low temperature (Figure 6). This phenomenon is typically observed for complexes undergoing spin-crossover, although VT NMR data (*vide infra*) excludes this as being the case for **2**. Therefore, we ascribe this to the quenching of the MLCT bands at higher temperature. We also ascribe the complex's lower extinction coefficient in MeCN compared to CH_2Cl_2 to the quenching of the MLCT bands in solvents of higher polarity. Finally, we note that the optical spectrum of **2** in both MeCN and CH_2Cl_2 is somewhat red-shifted compared to previously reported Fe-BF complexes, whose maximum absorptions typically range between 531 and 610 nm (Appendix D, Table D1). We ascribe this to phenolate-to-iron charge transfer from the anionic $\mathbf{Im^{Ph2}NNO^{tBu}}$ ligand.

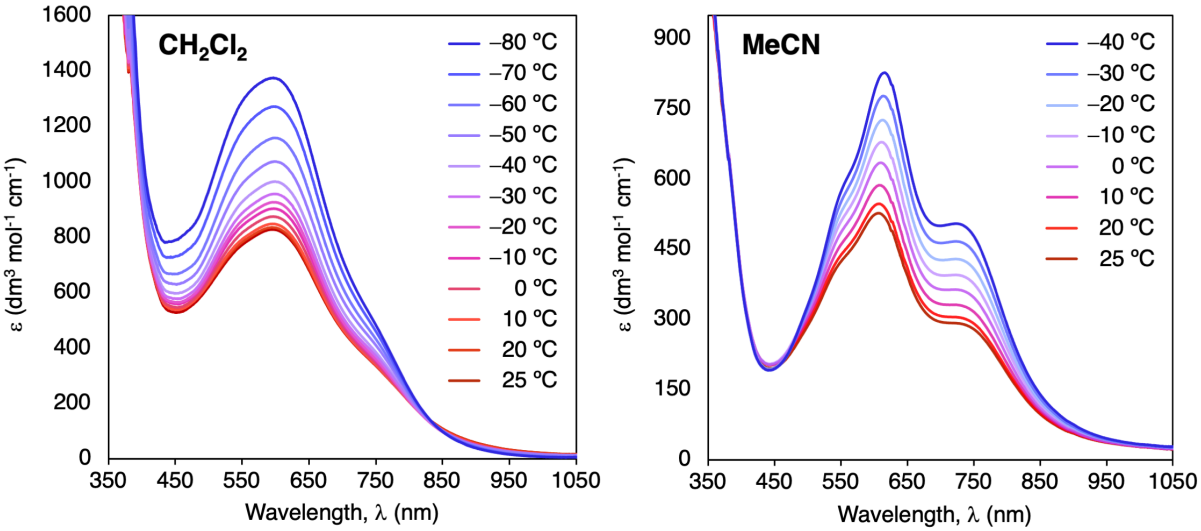

Figure 6. Variable temperature UV-vis spectra of **2** (1 mM solution) recorded in CH_2Cl_2 and MeCN.

5.2.4 ^{1}H NMR Spectroscopy

Having established the bidentate binding mode of the BF ligand in solution, we were also keen to investigate the temperature-dependent solution state behaviour of **2** by means for NMR spectroscopy. The ^{1}H NMR spectra of **2** recorded in acetonitrile-d_3 and dichloromethane-d_2 contain paramagnetically shifted signals in the range of –5 to 55 ppm (Figure 7). Using Evans' NMR method,[94] the effective magnetic moment (μ_{eff}) of **2** in acetonitrile solution was determined to be 4.45 μ_B, which corresponds to a high-spin (S = 2) electronic configuration and is consistent with solid-state Mössbauer and SQUID magnetometry data (*vide infra*). Due to their highly broad nature, assignment of the paramagnetic NMR resonances could not be made. However, the number of signals observed for **2** in both solvents is comparable to that previously reported for **1**,[85] whereby it may reasonably be assumed that **2** maintains a monomeric, pentacoordinate structure in solution, akin to that observed in the solid state.

Variable temperature (VT) ^{1}H NMR analysis in both CD_3CN and CD_2Cl_2 shows an increase in magnetisation of **2** as the temperature decreases, consistent with normal Curie behaviour (see Appendix D, Figures D1 and D2). Highly linear plots of chemical shift against reciprocal temperature were obtained in CD_2Cl_2, with intercepts extrapolating to the diamagnetic region at infinite temperature (Figure 7). In CD_3CN, slight deviation from linearity of the Curie plot is observed that we ascribe to the more strongly coordinating nature of the solvent, which may induce slight structural rearrangements in solution. Finally, no spin crossover phenomena were observed in either solvent, nor were any significant changes in speciation of the complex detected.

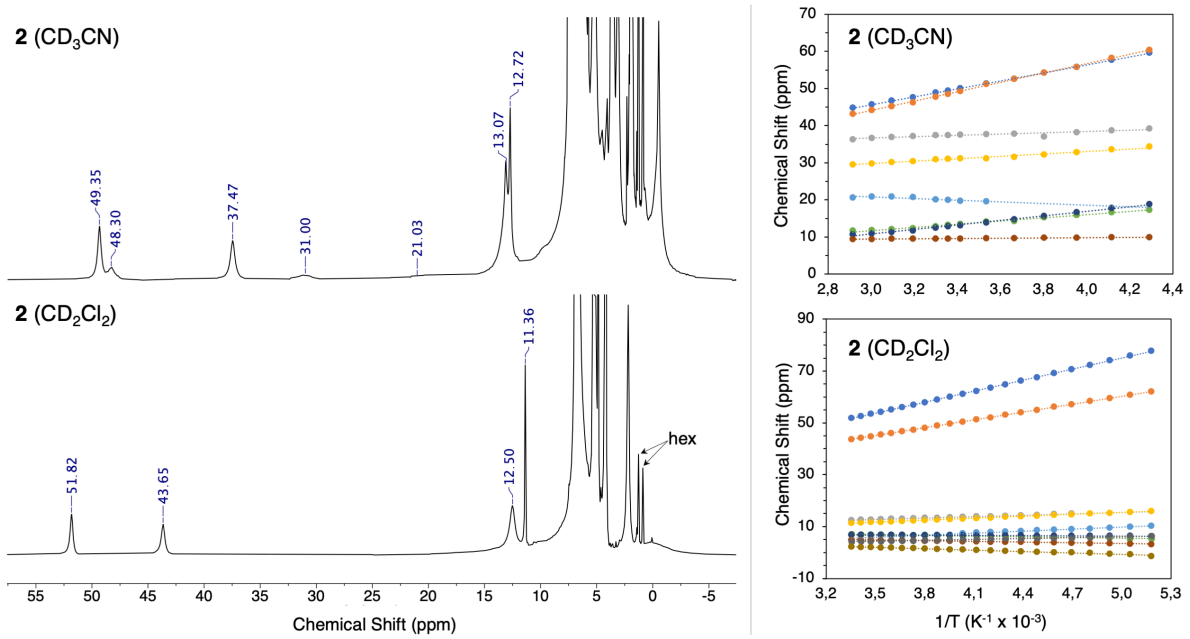

Figure 7. Left: Stacked ^{1}H NMR (400 MHz) spectra of **2** in CD_3CN (top) and CD_2Cl_2 (bottom), recorded at 25 °C. Spectra are clipped vertically for clarity. Right: Curie plots of chemical shift (ppm) versus reciprocal temperature (K^{-1}) for **2** in CD_3CN and CD_2Cl_2.

5.2.5 Electronic Structure Analysis

Zero-field ^{57}Fe Mössbauer analysis (80 K, 0 T) of **2** produced a single doublet with an isomer shift (δ) value of 1.17 mm s^{-1} and a quadrupole splitting ($|\Delta E_Q|$) of 2.64 mm s^{-1} (Figure 8). These values are typical for a high-spin (S = 2) iron(II) system and account for 96% of the total signal abundancy. A small high-spin ($S = {}^5/_2$) iron(III) impurity was also detected, accounting for 4% of the total signal abundancy. Compared to **1** (δ = 0.94 mm s^{-1})[85] the isomer shift of **2** has increased slightly due to the expansion of the coordination sphere from tetracoordinate to pentacoordinate, which causes a slight decrease in metal-ligand bond covalency and therefore a reduction in the *s*-electron density at the Fe nucleus.[95] The Mössbauer parameters found for **2** are very close to those reported for the pentacoordinate αKG-bound active sites of TauD (δ = 1.16 mm s^{-1})[11] and P4H (δ = 1.17 mm s^{-1}).[38]

Slight asymmetry of the quadrupole doublet for **2** is observed, due a slight broadening of the high-energy line. Since integer spin systems cannot be magnetic without an applied field (in contrast to half-integer spin systems), we exclude non-fast paramagnetic relaxation effects as being the cause of this asymmetry. Similarly, we exclude the asymmetry of the spectrum as deriving from any impurities, as the quadrupole doublet lines integrate equally. Therefore, we attribute the asymmetry to some unresolved (micro)heterogeneity of the iron site. Overall, the Mössbauer parameters obtained for **2** suggest that our structural model is electronically very similar to the pentacoordinate, O_2-reactive active sites of αKG-dependent iron enzymes.

Temperature-dependent magnetic susceptibility measurements were conducted by SQUID magnetometry on a powder sample of **2** (Figure 8). The complex has a χT value of 2.8 cm^3 K mol^{-1} at 300 K, consistent with a high-spin iron(II) complex (S = 2). Upon cooling, this value remains constant until approximately 50 K, in accordance with normal Curie behaviour. Below 50 K, the χT decreases sharply to approximately 1.1 cm^3 K mol^{-1}, indicative of a sizeable zero-field splitting. Thus, no temperature-dependent spin crossover phenomena are observed for **5** in the solid state. Finally, we note that the isotropic g-value of 1.94 is slightly lower than the expected value for a mononuclear high-spin ferrous centre, which is typically larger than 2. We attribute this to the small iron(III) impurity present in the sample (likely a Fe^{III}–O–Fe^{III} dimer species with an S = 0 ground state), which decreases the overall magnetization of the sample.

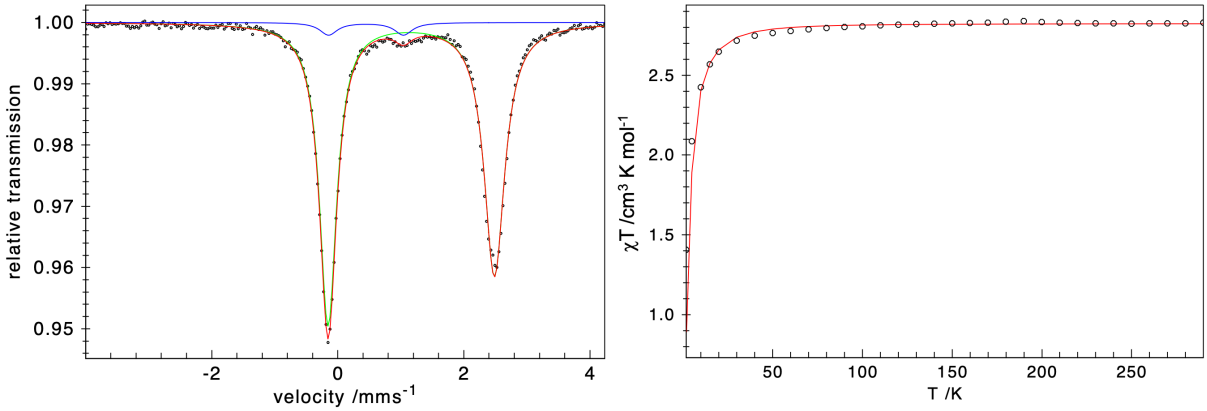

Figure 8. Left: Zero-field ^{57}Fe Mössbauer spectrum of **2**, recorded at 80 K. Black circles represent the experimental data points. The red trace represents the best combined fit. The green trace corresponds to the best fit for **2** (96% relative abundancy), where δ = 1.17 mm s^{-1} and $|\Delta E_Q|$ = 2.64 mm s^{-1}. The blue trace corresponds to a Fe^{3+} impurity (4% relative abundancy), where δ = 0.45 mm s^{-1} and $|\Delta E_Q|$ = 1.19 mm s^{-1}. Right: Solid-state temperature-dependent magnetic susceptibility of **2**, as measured by SQUID magnetometry. Black circles depict the data points and the red trace depicts the best fit ($g_{x,y,z}$ = 1.94, $D1$ = 8.20).

5.2.6 Electrochemistry

The redox behaviour of **2** was investigated by cyclic voltammetry (CV) under an inert N_2 atmosphere, in acetonitrile solution and using [n-Bu_4N]PF_6 as a supporting electrolyte. All quoted potentials are referenced versus the ferrocene/ferrocenium couple (Fc/Fc^+). The full voltammogram of **2** is displayed in Figure 9. A total of ten different electrochemical responses are observed within the potential range –2.7 to +1.5 V (**A**–**J**). Importantly, the section of the voltammogram comprising events **A**–**G** (i.e. between –0.75 V and +1.50 V) is very similar, both in terms of waveform and redox potentials, to the cyclic voltammogram previously reported for **1**.[85] We also observe that this region of the voltammogram is (electro)chemically reproducible for several consecutive cycles, as was previously observed for **1** (Figure 10 and Figure D4). We therefore hypothesise that these

events are related to the structural "unit" formed by the *N,N,O* ligand and the iron centre, which complexes **1** and **2** have in common. This also provides strong additional evidence that **2** exists as a single species in MeCN solution, as was previously demonstrated for **1**.

Segmentation experiments enabled the relationship between different electrochemical responses to be established (Figure 10 and Figure D4). The first oxidative response, **A**, occurs at –0.07 V and is coupled to a weak reductive response **G** ($E_{p,c}$ = –0.49 V). By analogy to **1**, we assign these events to the Fe^{III}/Fe^{II} couple and attribute its irreversible nature to additional structural changes in solution (*e.g.* solvent coordination) that accompany the formation of the more Lewis-acidic ferric iron, which is known to favour higher coordination numbers. The second oxidation event, **B**, occurs at +0.40 V and is ascribed to phenolate oxidation.

Oxidation **B** is partnered to two reduction events, **E** and **F**, which supports the hypothesis that multiple species are present in solution. Finally, the electrochemical events **C** and **D** form a quasi-reversible redox couple ($E_{1/2}$ = 1.12 V) that we tentatively assign to a Fe^{III}/Fe^{IV} couple. Scanning below –1.0 V, we observe three irreversible reductive responses (**H**–**J**). Interestingly, these electrochemical events cause significant disturbance to the region of the CV containing events **A**–**G**, including severe broadening of the waves, the appearance of new poorly defined features and depletion of the current output (see Appendix D, Figure D3). As responses **H**–**J** were not present in the CV previously reported for **1**,[85] we assign these to the BF ligand and propose that its electrochemical reduction prompts the irreversible structural disintegration of **2** in solution.

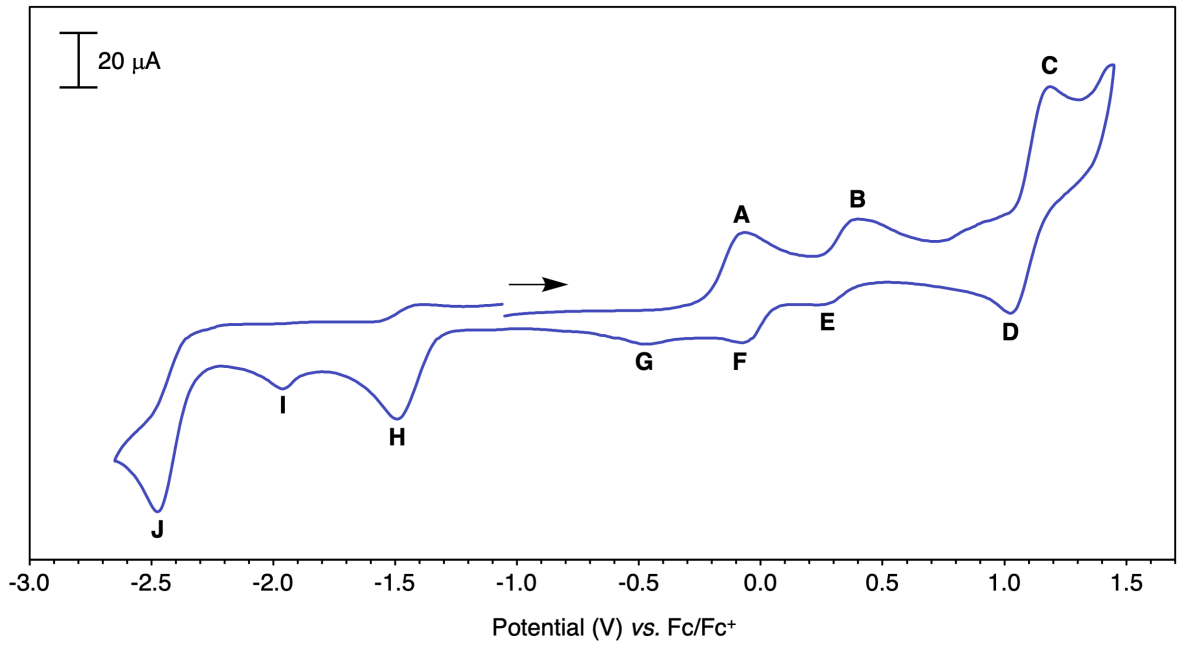

Figure 9. CV of **2** recorded in a 0.1 M [*n*-Bu_4N]PF_6 MeCN solution at room temperature, with a scan rate of 100 mV/s.

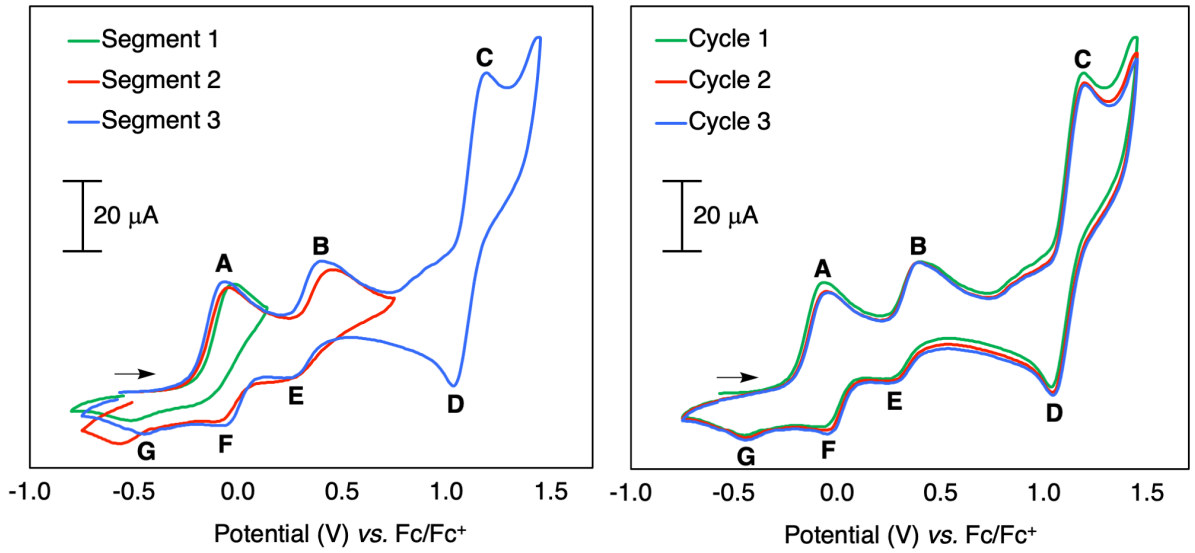

Figure 10. Left: Segmented CVs of **2**, recorded in 0.1 M [*n*-Bu_4N]PF_6 in acetonitrile. Right: Three consecutive CV scans of **2** between +1.5 V and –0.75 V, comprising electrochemical responses **A**-**G**.

Our CV assignments are further substantiated by the computational analysis of **2** (Figure 11). Density functional theory (DFT) calculations show the lowest unoccupied molecular orbital (LUMO) to be significantly delocalised across the BF ligand, the iron centre, and the ligand backbone. However, the principal contribution to the LUMO derives from the π* orbital of the keto group. The highest occupied molecular orbital (HOMO) is calculated as being a singly occupied iron-based d-orbital, supporting the assignment of **A** to the Fe^{II}/Fe^{III} redox couple. The low redox potential associated to the electrochemical oxidation of the iron centre is a strong indication that **2** reacts readily with O_2.

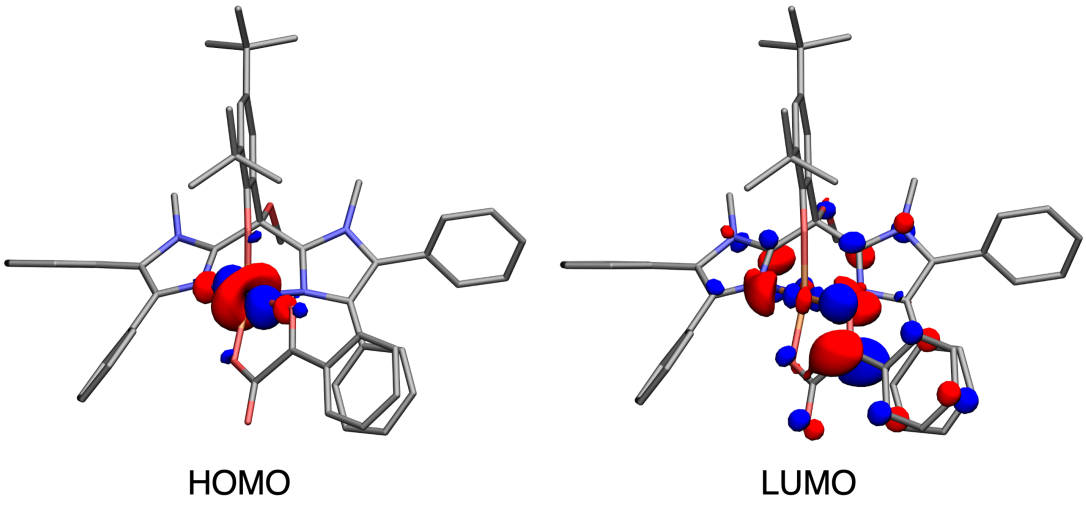

Figure 11. The DFT-calculated HOMO (left) and LUMO (right) obtained for **2**. Isosurfaces are drawn at the ±0.05 level, with opposite phases drawn in red and blue. H-atoms have been omitted for clarity.

5.2.7 Reactivity to O_2

Bubbling O_2 (or air) through a solution of **2** in acetonitrile at ambient temperature induces a rapid colour change from blue to violet. The oxidation of **2** by O_2 was monitored by absorption spectroscopy, with a spectrum recorded every six seconds from the moment at which the contents of the cuvette were exposed to O_2 (Figure 12). During the reaction, the MLCT bands of **2** at 745 nm, 606 nm and 540 nm disappear and a new intense band at 525 nm appears with a high extinction coefficient of 3750 M^{-1} cm^{-1}, which we assign to a phenolate-to-iron(III) charge transfer. The intensity of the band at 525 nm overrides the features associated to the coordination of BF and reaches a maximum after a period of approximately 400 seconds, persisting for approximately 1 hour before slowly decreasing in intensity. Overnight, the solution changed colour from violet to brown, and finally to yellow over the course of several days (Figure 13).

In ^{1}H NMR spectroscopy, exposing an acetonitrile-d_3 solution of **2** to air causes a rapid loss of all paramagnetic signals associated to **2**, presumably due to the formation of an NMR-silent iron species. Some signals in the diamagnetic region are observed, likely corresponding to the free ligand, which could indicate (partial) complex decomposition of the complex in solution upon oxidation. The X-band EPR spectrum obtained after exposing **2** to air for 5 minutes contains a highly isotropic signal at g = 4.15. This type of signal is typical for high-spin (S = $^5/_2$) iron(III) species.

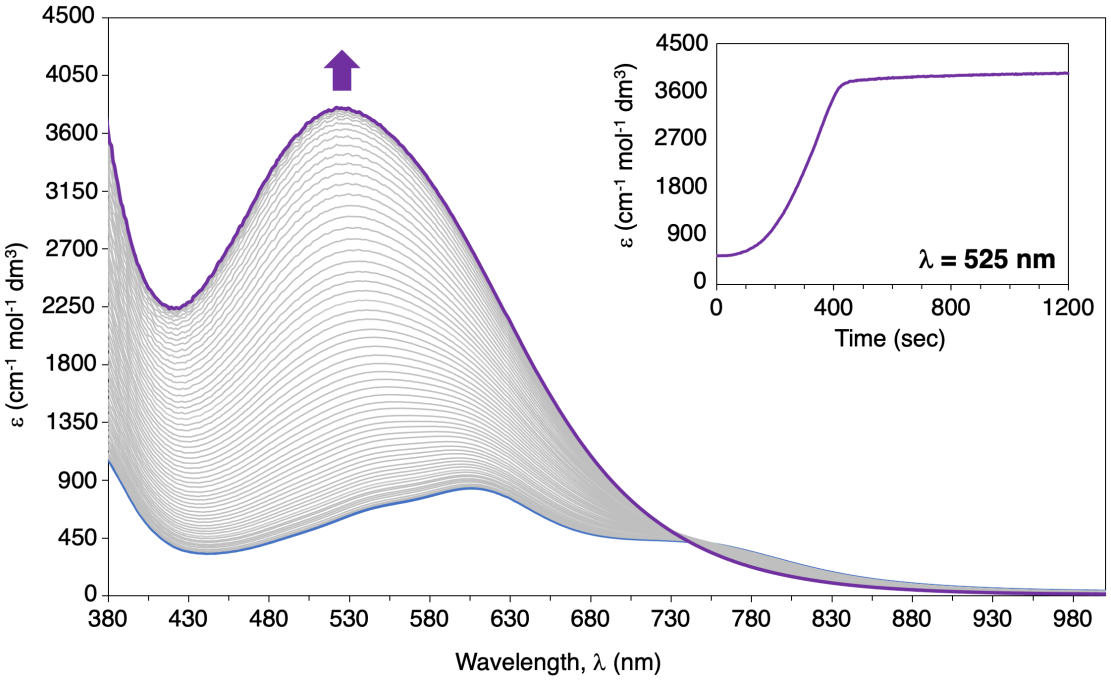

Figure 12. Spectral changes upon exposure of a 0.45 mM solution of **2** in acetonitrile to gaseous O_2 at 25 °C. Spectra have been plotted with time intervals of 6 seconds. Insert plot: evolution of the band at 525 nm for the first 20 minutes.

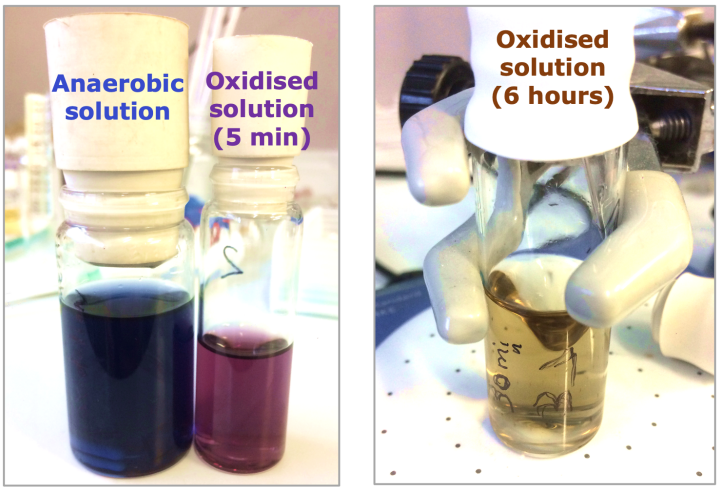

Figure 13. Photos of the anaerobic (blue), freshly O_2-exposed (purple, 5 min O_2 exposure), and long-term O_2-exposed solution (brown, 6 h O_2 exposure) of **2** in acetonitrile.

To gain further insight into the reaction of **2** with O_2 in acetonitrile, we resorted to ESI-MS analysis. After initial exposure of **2** to O_2 (i.e. within less than 5 minutes), a new positively charged ion was detected with m/z = 1693.6785 (Scheme 3 and Figure D5). This corresponds to a dinuclear ion of the composition $[Fe_2(L)_2(OBz)+2O+2H]^+$ (**3a**), comprising two Fe^{3+} ions, two ligand molecules and a benzoate molecule (Scheme 3). Two exogenous oxygen atoms and two protons are also incorporated within the structure of **3a**, presumably as two hydroxo ligands, accounting for the single positive charge of this ion. Exposing **2** to isotopically labelled dioxygen ($^{18}O_2$) produces a new ion, **3b**, with m/z = 1695.6796 (see Appendix D, Figure D6), corresponding to the incorporation of a single ^{18}O-atom within the ion structure.

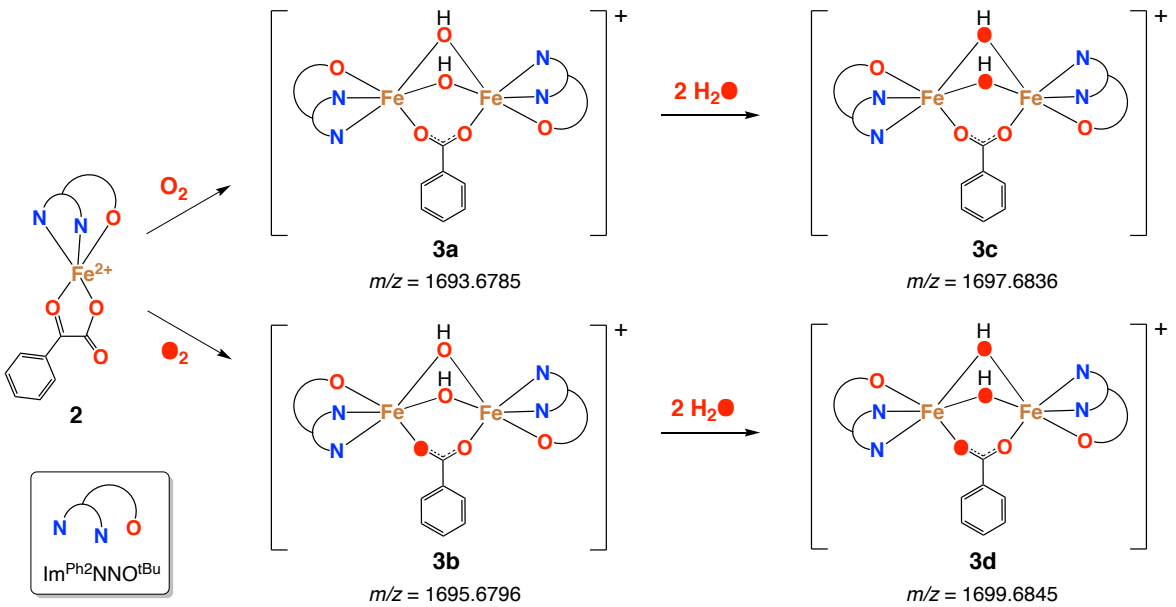

Scheme 3. The aerobic oxidation of **2** to form **3a-3d**, which feature bis(μ_2-hydroxo)-μ_2-beonzoate diiron(III) cores. Structures are proposed on the basis of ESI-MS experiments. ^{18}O-atoms are indicated by filled letters.

Treating a solution of **3a** with labelled water ($H_2{}^{18}O$) generates ion **3c**, with m/z = 1697.6836. This accounts for the incorporation of two ^{18}O-atoms within the structure. Similarly, treating a solution of **3b** with excess $H_2{}^{18}O$ produces a new ion, **3d**, with m/z = 1699.6845, containing three ^{18}O-atoms. On the basis of these observations, we propose that the reaction of **2** with O_2 leads to the oxidative decarboxylation of the BF ligand, whereby one oxygen atom from O_2 is incorporated into the benzoate moiety of **3a**. We exclude the incorporation of O_2 into the hydroxo ligands, as we would otherwise have detected an ion with three labelled oxygen atoms after exposing **2** to $^{18}O_2$. Therefore, we propose that the hydroxo ligands derive from traces of water present in the measurement conditions. Interestingly, the use of water was observed to enhance the detection of both **3a** and **3b** in ESI-MS, by increasing the relative intensity of the signals. This suggests that the exogenous hydroxo ligands coordinate in a μ_2-bridging fashion and that excess water promotes the formation (and therefore abundance in MS) of these dinuclear ions in solution.

The structural assignment of **3a** is supported by literature precedent, including dinuclear complex $[Fe_2(HDP)_2(\mu_2\text{-}O)(\mu_2\text{-}OBz)]^+$, reported by Que and co-workers, that exhibits a strong phenolate-to-iron(III) charge transfer band at 522 nm (ε = 3300 M^{-1} cm^{-1}) (Figure 14).[96] The same group also observed the development of a strong phenolate-to-iron(III) charge transfer band at 562 nm (ε = 4300 M^{-1} cm^{-1}) upon exposing dinuclear complex $[Fe_2(\mu_2\text{-}Me_2HDP)_2(\mu_2\text{-}BF)]^+$ to O_2, which was ascribed to the formation of a μ_2-oxo-μ_2-benzoate diiron(III) core (Figure 14).[91] From ESI-MS, we cannot determine the absolute structure of **3a**. However, considering the important steric bulk and structural rigidity of the **Im^{Ph2}NNO^{tBu}** ligand, as well as the highly comparable λ_{max} values of the MLCT bands, we tentatively propose that **3a** is similar in structure to $[Fe_2(HDP)_2(\mu_2\text{-}O)(\mu_2\text{-}OBz)]^+$ and features a bis(μ_2-hydroxo)-μ_2-benzoate diiron(III) core. This type of coordination has previously been reported in tri-bridged μ_2-hydroxo-bis(μ_2-acetate) diiron(III) complexes bearing tris(imidazolyl)phosphine (TIP) and tris(pyrazolyl)borate (Tp) ligands,[97,98] as well as di-bridged μ_2-oxo-μ_2-benzoate diiron(III) complexes bearing TPA ligands.[99,100]

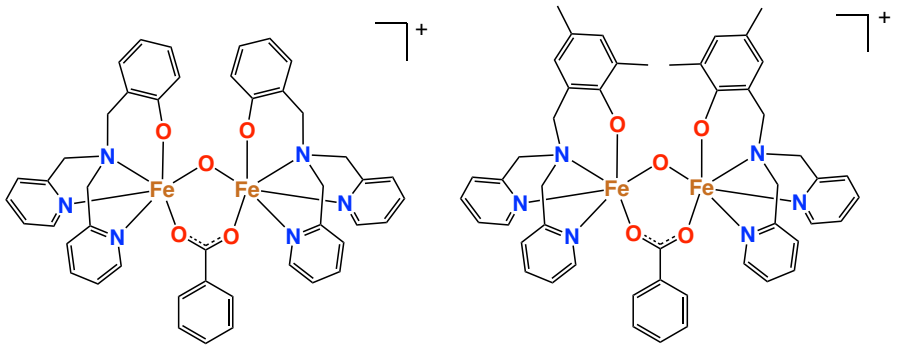

$[Fe_2(HDP)_2(\mu_2\text{-}OBz)(\mu_2\text{-}O]^+$ λ_{max} = 522 nm

$[Fe_2(Me_2HDP)_2(\mu_2\text{-}OBz)(\mu_2\text{-}O)]^+$ λ_{max} = 562 nm

Figure 14. The μ_2-benzoate-μ_2-oxo diiron(III) cores structurally characterised for $[Fe_2(HDP)_2(\mu_2\text{-}OBz)(\mu\text{-}O)]^+$ and proposed for $[Fe_2(Me_2HDP)_2(\mu_2\text{-}OBz)(\mu_2\text{-}O)]^+$, reported by Que and co-workers.[91,96]

Monitoring the reaction of **2** with O_2 over time with ESI-MS showed that the predominant species detected within the first 5 minutes is **3a**. However, after 20 minutes, another signal at m/z = 1483.7081 was detected, corresponding to a bisligated iron(III) species, $[Fe(L)_2]^+$ (**4**). It is probable that **4** is the source of the isotropic EPR signal described above, as the dinuclear nature of **3a** would likely render it EPR-silent as a result of strong spin coupling between the two ferric ions. Both **3a** and **4** were seen to persist for several hours, although the ESI-MS spectrum of the oxidised solution was observed to grow increasingly more complex over time, with new ions forming that we were unable to assign.

The presence of a single benzoate ligand in **3a** does not correspond to the 1:1:1 ligand-metal-benzoate stoichiometry expected for the quantitative oxidative decarboxylation of **2**. Formation of **3a** could therefore be due to the initial formation of an oxoiron(IV) species upon oxidative decarboxylation of **2**, which subsequently comproportionates with the remaining ferrous **2** in solution. Indeed, negative-mode ESI-MS analysis of the organic residue recovered after acidic work-up of the oxidised solution of **2** shows a weak signal at m/z = 148.7 assigned to the benzoylformate anion, which provides further evidence that **2** does not undergo quantitative decarboxylation. Positive mode ESI-MS of the organic residue shows the predominant species to be the ligand, with a strong signal for $[L+H]^+$ observed at m/z = 715.4 (calc. m/z = 715.40) (Figure 15).

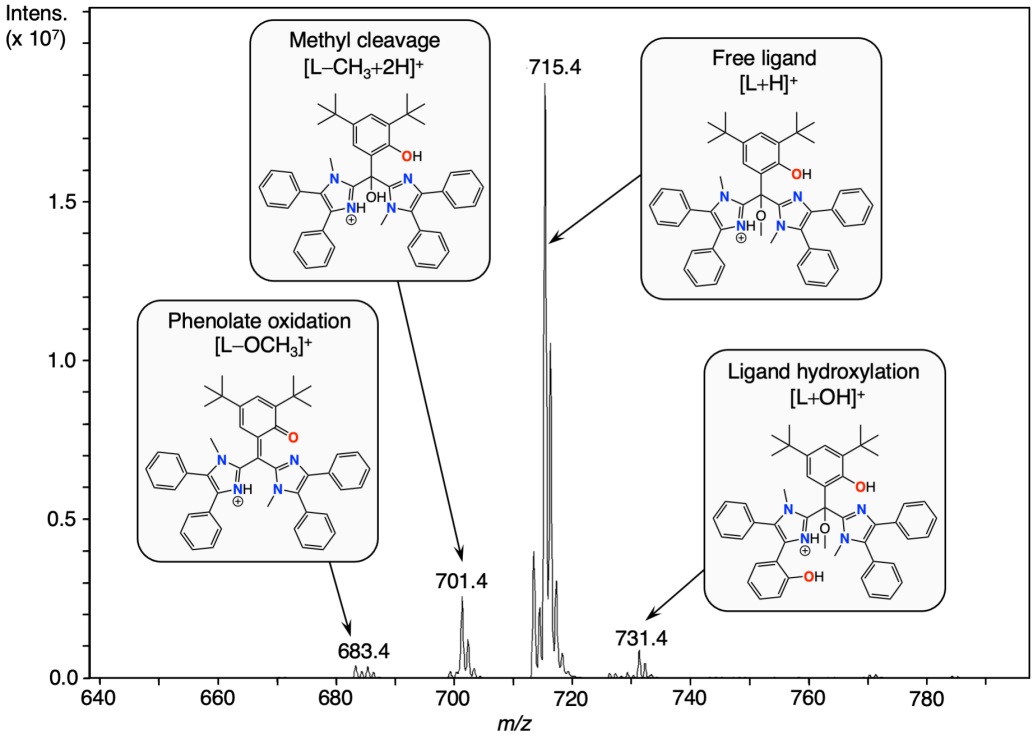

Figure 15. Positive mode ESI-MS spectrum obtained for the organic residue recovered after acidic work-up of an oxidised solution of **2** (shown between m/z 640 and 790). Structures are proposed on the basis of ESI-MS.

In addition, three other weak signals were observed at m/z = 731.4, 701.4 and 683.4, which we ascribe, respectively, to products of ligand degradation, namely those of: i) ligand hydroxylation, $[L+OH]^+$ (calc. m/z = 731.40), ii) methyl cleavage, $[L–CH_3+2H]^+$ (calc. m/z = 701.39), and iii) phenolate oxidation accompanied by methoxy cleavage, $[L–OCH_3]^+$ (calc. m/z = 683.39). These last two species indicate that the ligand is somewhat susceptible to oxidative degradation, as has previously been observed in our group during oxidative transformations of related iron thiolate complexes supported by $\mathbf{Im^{Ph2}NNO^{tBu}}$, as described in Chapter 4 of this thesis. The product of ligand hydroxylation is a very interesting observation as it provides (indirect) evidence for the formation of a short-lived high-valent iron(IV)-oxo intermediate. Previously, Que and co-workers also observed intramolecular ligand hydroxylation upon exposure of complexes [Fe(Tp^{Ph2})(κ_2-BF)] and [Fe(Tp^{iPr2})(κ_2-BF)] to O_2.[77,80] This was proposed to occur due to close proximity of the supporting ligand scaffold and the high-valent Fe^{IV}=O intermediate generated upon oxidative decarboxylation of the BF co-ligand.

5.2.8 Reactivity to "NO" using Ph_3CSNO

To further elucidate the changes occurring at the iron centre upon oxidation of **2**, we investigated the *in situ* reaction of **2** with nitric oxide (NO) using trityl-*S*-nitrosothiol (Ph_3CSNO) as a convenient NO donor. Use of Ph_3CSNO in this manner has been reported to yield iron nitrosyl compounds analogous to those obtained through reaction with NO gas, notably by the groups of Lippard, Meyer, Lehnert and Majumdar.[101–103] One of the advantages associated to the use of trityl-*S*-nitrosothiol is that it is a solid compound that can easily be weighed out for use in stoichiometric reactions.

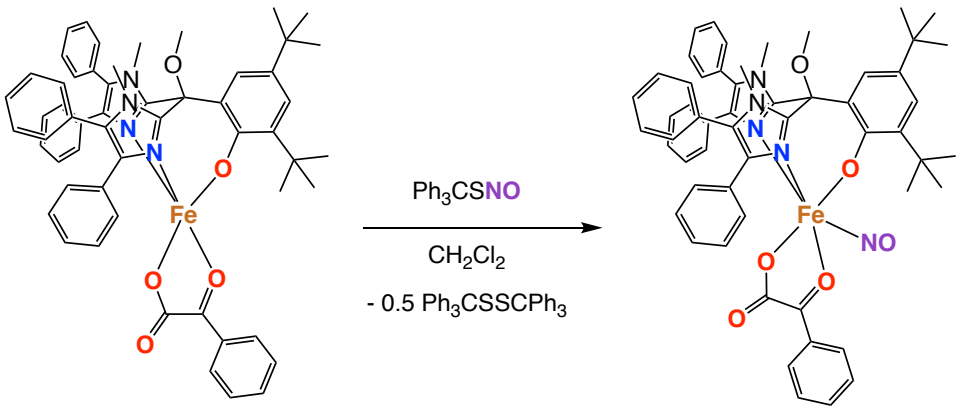

2 **5**

Scheme 4. The reaction of **2** with trityl-*S*-nitrosothiol. The structure of **5** is proposed.

Complex **2** was dissolved in CH_2Cl_2 at –70 °C and stirred vigorously while a bright green solution of Ph_3CSNO in CH_2Cl_2 was added dropwise to the mixture. Upon complete addition of the nitrosothiol, the mixture was sealed, placed in a dark container and stirred

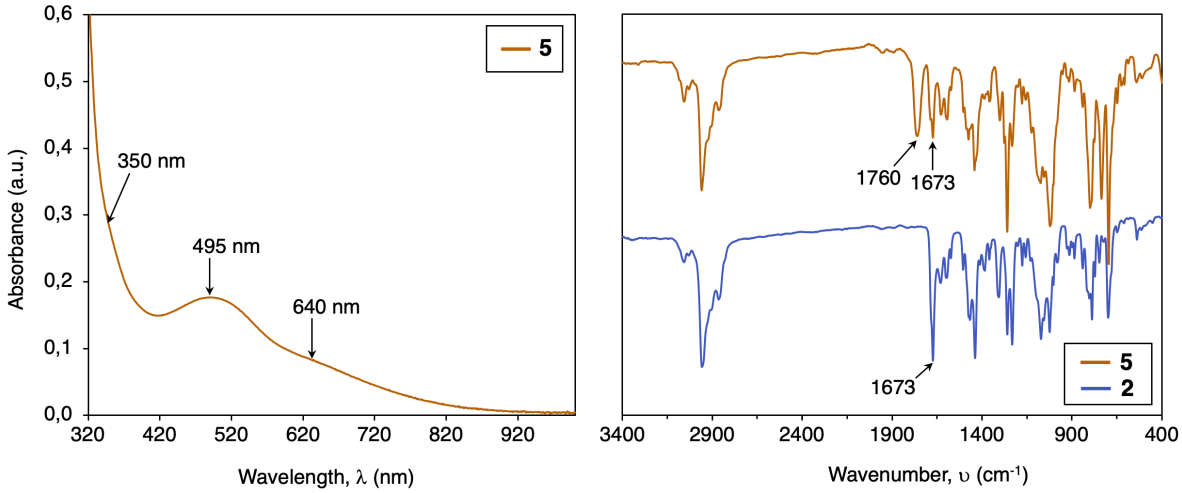

Figure 16. Left: The UV-vis absorption spectrum for **5**, recorded at 298 K in CH_2Cl_2. Right: The stacked IR (ATR) spectra of **2** (blue trace) and **5** (brown trace).

for a period of 90 min while warming to room temperature. During this time, the colour of the solution changed to brown, a colour typically observed for iron nitrosyl complexes. Small aliquots of the reaction mixture were subsequently taken for UV-vis, IR and EPR analysis. Unfortunately, despite numerous attempts, no crystals could be obtained of the proposed nitrosylated product, hereafter referred to as **5** (Scheme 4).

The UV-vis absorption spectrum of the reaction mixture exhibits a new band at 495 nm with a broad shoulder at 640 nm, as well as a feature at 350 nm that shoulders the intense π–π* transition region of the spectrum (Figure 16). Que and co-workers observed similar absorption bands (ascribed to NO-to-Fe charge transfer) for complexes [Fe(6TLA)(κ$_1$-BF)(NO)](ClO$_4$) and [Fe(TPA)(κ$_1$-BF)(NO)](ClO$_4$), although it should be noted that these complexes contain a monodentate BF ligand.[104] In IR spectroscopy, a new peak at 1760 cm^{-1} is observed, which is downshifted compared to free NO (υ_{NO} = 1875 cm^{-1})[105] and distinct from the trityl-*S*-nitrosothiol precursor (υ_{NO} = 1513 cm^{-1}) (Figure 16).[101] The IR stretch associated to the BF ligand (1673 cm^{-1}) in **5** is almost identical compared to that in **2**, which suggests that the coordination of the BF ligand remains unchanged after reaction with Ph_3CSNO.

The X-band EPR spectrum of the reaction mixture, recorded at 100 K, exhibits three features, centred at g = 4.26, 4.00 and 2.02 (Figure 17, *vide infra*). This data was simulated by considering three different spin contributions, plotted in sub-spectra **A** (green), **B** (blue) and **C** (grey). **A** corresponds to an $S = {}^3/_2$ iron nitrosyl complex, denoted {FeNO}^{7} according to Enemark-Feltham notation,[106] and accounts for 78% of the total paramagnetic species in the sample. This type of NO-adduct is best rationalised as comprising a high-spin ($S = {}^5/_2$) Fe^{3+} centre antiferromagnetically coupled to NO^-.[107,108] This species exhibits a derivative signal at g_{eff} ~ 4 and a negative peak at g_{eff} ~ 2, which can be ascribed to the lower Kramers doublet of the quartet ground spin state according to the $S = {}^3/_2$

rhombogram. Simulation **A** was performed using the spin Hamiltonian shown in Equation 1, where D and E are the axial and rhombic zero-field splitting (ZFS) parameters, respectively. The E/D ratio reflects the degree of rhombic distortion, with values ranging from 0 for a purely axial signal to $^1/_3$ for a purely rhombic signal.

$$H = \beta \cdot \mathrm{S} \cdot \mathrm{g} \cdot \mathrm{B} + D[S_z^2 - S(S+1)/3] + E(S_x^2 - S_y^2) \qquad \text{(eq.1)}$$

The best fit was obtained with the following parameters: D = 5 cm^{-1} (arbitrarily set), E/D = 0.046 (near-axial symmetry), $g_{x,y}$ = 2.01 and g_z = 2.02. In addition, E/D strain was applied ($\sigma(E/D)$ = 0.04) to account for the broadened shape of the spectrum. Such E/D strain usually arises from micro-heterogeneity of the ligand field, typically caused by a (micro)distribution of molecular structure as caused by solvation effects, etc. Overall, these parameters are in line with those previously reported for {FeNO}^{7} adducts of αKG-dependent enzymes[109] and relevant model complexes.[104,110,111] On this basis, we assign this species to nitrosylated complex **5** (Scheme 4).

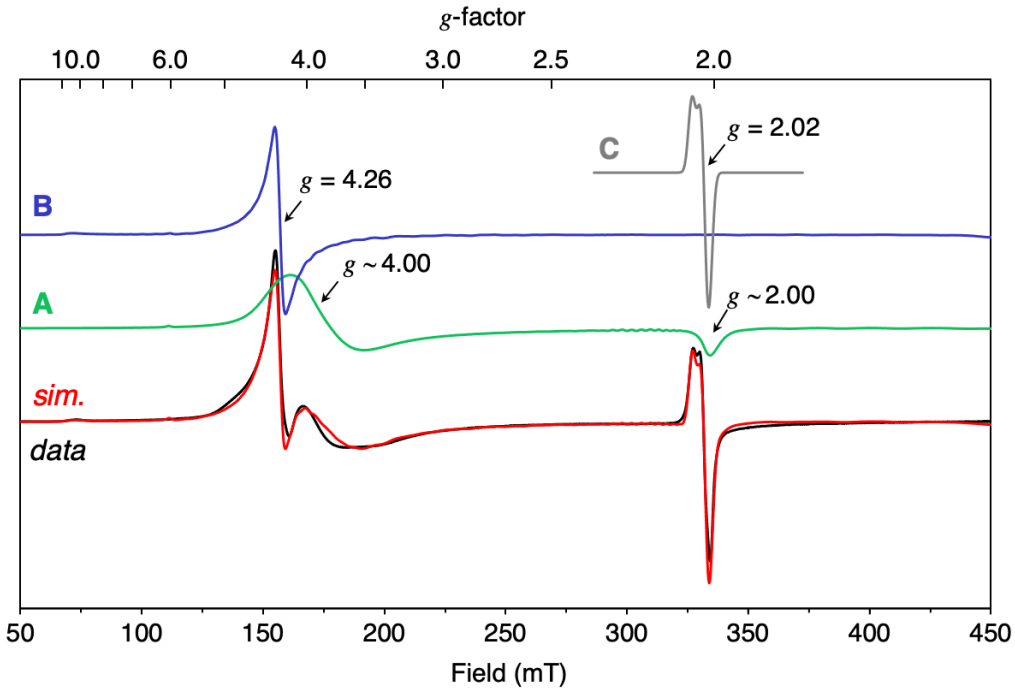

Figure 17. Experimental (black) and simulated (red) X-band EPR spectrum of **5**, recorded in a CH_2Cl_2/toluene glass (1:1 vol/vol) at 100 K. Sub-spectra **A** (green), **B** (blue) and **C** (grey) are depicted above. Instrument: freq. = 9.39862 GHz, power = 2.00 mW, mod. amp. = 1.00 G.

Species **B** is a high-spin (S = $^5/_2$) ferric species, which accounts for 20% of the total paramagnetic species in the sample. Due to its high rhombicity, (E/D = 0.28), the middle Kramers doublet has three nearly identical g-values that produce a highly isotropic signal at g_{eff} = 4.26, and its upper or lower Kramers doublet gives a positive peak at g_{eff} ~ 9.2. We speculate that this ferric impurity may form through the 1-electron oxidation of **2** by the $Ph_3CS^\bullet$ radical generated upon homolytic cleavage of Ph_3CSNO, likely facilitated by the

low oxidation potential of **2**. Species **C** is presumably a $S = {}^1/_2$ dinitrosyl iron complex (DNIC), as its nearly isotropic signal at g = 2.01, 2.02, 2.05 is similar to those found for a large majority of DNICs with an isotropic g-value of 2.03. This small DNIC impurity accounts for 2% of the total paramagnetic species in the sample.[110]

Using DFT calculations, we examined the electronic structure of two different possible structural isomers of **5**, since the geometric index for **2** ($\tau = 0.5$) suggests that NO could bind at two possible coordination sites (Figure 18). In the first structure (**A**), the NO ligand is coordinated *trans* to an imidazole donor, in the putative vacant site that is apparent in the solid-state structure of **2**. In the second structure (**B**), the NO ligand is coordinated *trans* to the phenolic oxygen atom. Geometry optimisations of both **A** and **B** produced structures where the nitrosyl ligand adopts a bent configuration and where the spin density is spatially polarised, with the α subset localised on iron and the β subset localised on the NO, consistent with diradical ($S = 1$) NO^- character. Both structures are similar in energy, although **A** was calculated as being approximately 5 kcal mol^{-1} lower in energy than **B**. On this basis, we propose that **A** is the most likely structure for complex **5**.

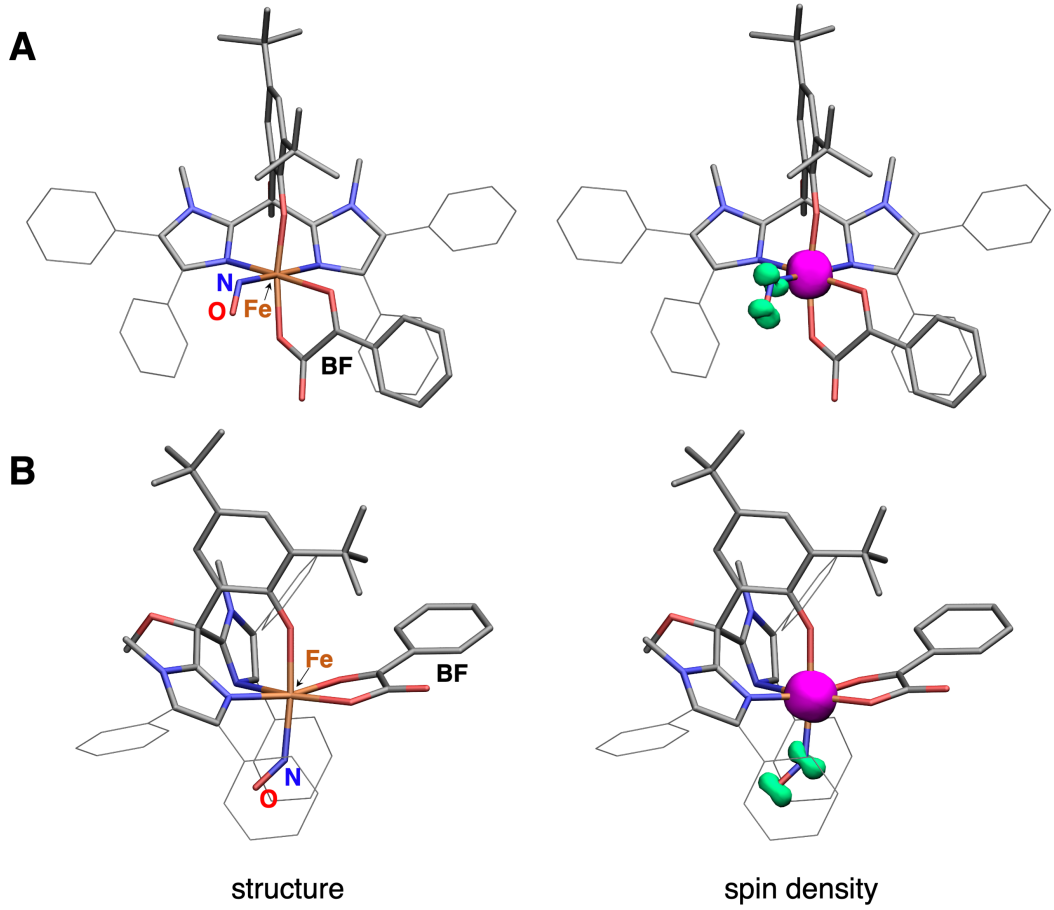

Figure 18. The DFT-optimised gas-phase geometries of **A** and **B** ($S = 3/2$). Imidazole phenyl substituents are drawn in the wireframe format for clarity. Spin density isosurfaces for the α (magenta) and β (green) subsets are drawn at the 0.05 level.

The DFT-obtained structural and EPR data for **A** and **B** is summarised in Table 2. In both cases, near axial symmetry is observed, with *g*-values similar to those observed experimentally. The *D*-values are calculated as 4.35 cm^{-1} (130,408 MHz) for **A** and 4.27 cm^{-1} (128,010 MHz) for **B**, respectively. These values deviate somewhat from the *D*-values typically reported in literature that are generally closer to 300,000 MHz. Nonetheless, we were able to produce a reasonable alternative EPR data simulation using the *D*-value obtained from DFT and keeping the *E*/*D* ratio constant at 0.047. The *E*/*D* ratios calculated by DFT did not produce a satisfactory simulation fit, nor are they consistent with the typically axial symmetry of $S = {}^3/_2$ $\{FeNO\}^7$ systems reported in literature. We attribute this to a relatively high degree of inaccuracy in the computational evaluation of the zero-field splitting parameters.

Table 2. Geometric and EPR parameters calculated for **A** and **B** ($S = {}^3/_2$).

Structure	Spin	Fe–N_{NO}	∠Fe–N–O	g_x	g_y	g_z	g_{iso}	***D*** (cm^{-1})	***E*/*D***
A	$S = {}^3/_2$	2.027 Å	129.47°	2.019	2.022	2.052	2.031	4.35	0.31
B	$S = {}^3/_2$	1.920 Å	139.31°	2.011	2.017	2.046	2.025	4.27	0.31

In summary, we propose that we have successfully performed the *in-situ* nitroxylation of **2** to form a new $\{FeNO\}^7$ complex, [Fe($Im^{Ph2}NNO^{tBu}$)(BF)(NO)] (**5**). However, EPR also suggests that some other (minor) products also form during the reaction. Given the five-coordinate nature of **2**, we envision that NO can bind to the iron's remaining vacant site, *trans* to an imidazole group, without any change in coordination mode needing to occur for either the supporting *N,N,O* ligand or the BF ligand. The fact that **2** can accommodate NO binding means O_2 is also likely to bind directly to the iron centre, forming a short-lived iron(III) superoxide intermediate whose distal oxygen atom could perform a nucleophilic attack on the BF ligand, leading to the oxidative decarboxylation of **2** in a manner that is mechanistically relevant to α-KG-dependent enzyme active sites.

5.2.9 Oxygen Atom Transfer Reactivity

Next, we were keen to investigate **2** as a potential oxidation catalyst. The reactivity of **2** was tested by means of interception experiments, using methyl(*p*-tolyl)sulfide and 1-octene as simple model substrates, and O_2 gas as the oxidant (Scheme 5). Overall, **2** was observed to oxidise methyl(*p*-tolyl)sulfide in 45% yield after a period of 10 minutes. No further increase in the yield was observed after allowing the reaction to progress for a longer period of time. We speculate that reactivity of **2** is hampered by a process of comproportionation similar to that described for the formation of **3**, whereby *ca*. 0.5 equiv. of initial complex successfully completes 1 reaction cycle to form a new Fe(II) species that is more easily oxidised than the substrate. For the reaction with 1-octene, no peaks were observed in GC that corresponded to either the epoxide or the diol product. We therefore conclude that **2**

is not active in the oxidation of 1-octene. Finally, we attempted the oxidation of methyl(*p*-tolyl)sulfide by **2** under catalytic conditions, in the presence of excess benzoylformic acid (H-BF) as a consumable co-substrate. However, no catalytic activity and no product formation was observed. Interestingly, the addition of excess H-BF to a solution of **2** was seen to provoke a swift colour change from blue to purple. This could indicate a change in the structure or speciation of **2** in solution, possibly with involvement of μ_2-bridging BF ligands. Indeed, examples of catalytically inactive BF-bridged diiron(II) complexes have been reported by the groups of Costas[81] and Que.[91] Alternatively, H-BF may disrupt the structure of **2** by protonating its imidazole or phenolate groups. Further investigations are required to elucidate the nature of these transformations and establish the optimal conditions with which with **2** could successfully occur. (*e.g.* slow addition of the co-substrate, and cold temperatures to ensure kinetic control).

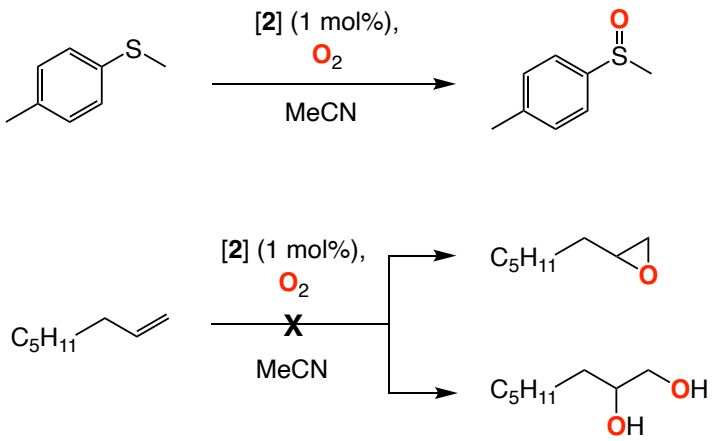

Scheme 5. Interception experiments using methyl(*p*-tolyl)sulfide and 1-octene as simple substrates. Oxidation of the sulfide to its corresponding sulfoxide was observed, while oxidation of 1-octene to either the epoxide or diol product was not observed.

5.3 Conclusion

We employed a bulky *N,N,O* phenolate ligand (**Im^{Ph2}NNO^{tBu}**) to synthesise a pentacoordinate, mononuclear non-heme iron(II) benzoylformato complex, [Fe(Im^{Ph2}NNO^{tBu})(BF)] (**2**). Using UV-vis and NMR spectroscopies, we demonstrate that the bidentate BF coordination and the facial *N,N,O* ligand coordination are retained in both coordinating and non-coordinating solvents, across a wide temperature range. The X-ray crystal structure of the complex suggests that a putative vacant site is available for O_2 binding, *cis* to the BF ligand and *trans* to one of the imidazole donors. This qualifies **2** as one of the most faithful structural and electronic models of αKG-dependent iron enzyme active sites to date, and the first model to include an anionic and facial *N,N,O* donor set. This is also reflected by its ^{57}Fe Mössbauer parameters, which are very close to those reported for taurine dioxygenase and proline 4-hydroxylase. Reacting **2** with NO (using

Ph_3CSNO) affords a $S = {}^3/_2$ $\{FeNO\}^7$ adduct, [Fe($Im^{Ph2}NNO^{tBu}$)(BF)(NO)] (**5**), whose spectroscopy suggests that NO can bind to the iron centre without disrupting the *N,N,O* coordination of the supporting ligand and the bidentate BF coordination.

Cyclic voltammetry studies show that the iron centre in **2** has a very low oxidation potential. Indeed, **2** reacts readily with O_2, generating a metastable purple intermediate. Using UV-vis and ESI-MS measurements, we assign this species as a diiron(III) μ_2-benzoate complex, [Fe_2($Im^{Ph2}NNO^{tBu}$)$_2$(μ_2-OBz)(μ_2-OH)$_2$] (**3**). Isotopic labelling experiments using $^{18}O_2$ demonstrate the inclusion of one ^{18}O atom in **3**, most likely within the benzoate moiety. This provides strong evidence that **2** undergoes oxidative decarboxylation in a manner that is mechanistically relevant to the αKG-dependent enzymes. We also observe a small amount of hydroxylated ligand by ESI-MS, which hints at the formation of a high-valent iron(IV)-oxo intermediate. Preliminary reactivity studies show that **2** is capable of oxygen atom transfer (OAT) reactivity and can oxidise methyl(*p*-tolyl)sulfide to its corresponding sulfoxide. Current investigations in our laboratory aim to further establish the biomimetic potential of the **$Im^{Ph2}NNO^{tBu}$** ligand and its iron keto-acid complexes, and to provide further insight in the reactivity of **2**.

5.4 Author Contributions

E.C.M and B.K.G. devised the project, designed experiments and wrote the manuscript. E.C.M. performed experiments and analysed the data. L.G.M. performed HR-ESIMS measurements. M.L. performed X-ray crystal structure determinations. S.Y. and E.B. provided the Mössbauer, SQUID and EPR data analysis. M.C. contributed to useful scientific discussions and hosted a secondment for E.C.M. All authors provided comments on the experiments and manuscript during its preparation.

5.5 Experimental

5.5.1 Chemicals and Reagents

Unless stated otherwise, all reactions were performed under an inert N_2 (g) atmosphere using standard Schlenk line and glovebox techniques and were stirred magnetically. The solvents acetonitrile and hexane were purified using an MBraun MB SPS-80 purification system, degassed by bubbling N_2 (g) through them for a period of 30 min prior to use, and were stored over activated molecular sieves. Acetonitrile was filtered over activated neutral alumina before use to remove molecular sieve debris. Dichloromethane was dried over CaH_2 and distilled under inert N_2 (g) atmosphere before use. All solvents were tested for water content by Karl-Fischer titration or by ^1H NMR. Non-halogenated solvents were additionally tested with a standard purple solution of sodium benzophenone ketyl in THF to confirm effective oxygen and moisture removal. Deuterated solvents were purchased from the Cambridge Isotope Laboratory Incorporation (Cambridge, USA) and were degassed using the freeze-pump-thaw method and stored over activated molecular sieves. Deuterated acetonitrile was filtered over

activated neutral alumina prior to use to remove molecular sieve debris. $^{18}O_2$ was purchased from Sigma-Aldrich. $H_2{}^{18}O$ (95% ^{18}O-enriched) was received from ICON isotopes. All reagents and starting materials were purchased from commercial sources and used without further purification, except when specified. Complex [Fe(Im^{Ph2}NNO^{tBu})(Cl)] (**1**) was prepared using a procedure previously reported in our group (Chapter 3 of this thesis).[85] Trityl-*S*-nitrosothiol (Ph_3CSNO) was synthesised according to a reported procedure,[101] and was stored as a green crystalline solid at –40 ºC under inert atmosphere and in the dark. Benzoylformic acid was converted to its respective potassium salt by treating it with an equimolar amount of KH.

5.5.2 Physical Methods

NMR spectroscopy (^1H, $^{13}C\{^1H\}$) was conducted using a 400 MHz Varian spectrometer or an Oxford NMR AS400 spectrometer. ^1H NMR chemical shifts are reported in the standard δ notation of part per million (ppm) and are referenced to residual solvent signals, as determined relative to $SiMe_4$.[112] Paramagnetic ^1H NMR spectra were recorded after having adjusted both the relaxation delay and acquisition time to 100 ms. IR spectroscopy was conducted using a PerkinElmer Spectrum Two FT-IR spectrometer. For air-sensitive compounds, a N_2 (g) flow was used. Peaks are annotated by (w), (m) and (s) to indicate weak, medium and strong signals, respectively. UV-vis measurements were performed in a 1 cm quartz cuvette using an Agilent Technology 8453 spectrophotometer equipped with a diode-array detector. For variable temperature UV-vis measurements, the spectrophotometer was coupled to a cryostat from Unisoku Scientific. High resolution ESI-MS measurements were performed with a Bruker MicrOTOF-Q IITM instrument using ESI ionization sources at Serveis Tècnics of the University of Girona. Samples were introduced into the mass spectrometer ion source by direct infusion using a syringe pump and were externally calibrated using sodium triflate. All other ESI-MS measurements were performed with an Advion Expression CMS instrument. X-ray crystal structure determinations were performed on a Bruker Kappa ApexII diffractometer with sealed tube and Triumph monochromator (λ = 0.71073 Å) at a temperature of 150(2) K (further details given in Appendix D). EPR analyses were performed using a Bruker EMX Plus 6000 Gauss machine equipped with an ER041 XG X-Band Microwave Bridge and an N_2 cryostat. EPR simulations were performed with the program *esimX* developed by Dr. Eckhard Bill. Mössbauer spectra (see Appendix F) were recorded on a conventional spectrometer with alternating constant acceleration of the g-source (^{57}Co/Rh, 1.8 GBq), which was kept at room temperature. The minimum experimental line width was 0.24 mm s^{-1} (full width at half-height). The sample temperature was maintained constant in an Oxford Instruments Variox cryostat. Isomer shifts are quoted relative to iron metal at 300 K. The zero-field spectra were simulated with Lorentzian doublets with the program *mf.SL* developed by Dr. Eckhard Bill. Magnetic susceptibility data were measured from powder samples of solid material in the temperature range 2 – 300 K by using a SQUID susceptometer with a field of 1 T (MPMS-7, Quantum Design, calibrated with standard palladium reference sample, error <2%). The experimental data were corrected for underlying diamagnetism by use of the tabulated pascal's constants. The susceptibility data were simulated with package *julX* on the basis of the usual spin Hamiltonian:

$$H = -2J\,\vec{S}_1 \cdot \vec{S}_2 + \mu_B \vec{B} \cdot \tilde{g} \cdot (\vec{S}_1 + \vec{S}_2) + \sum_i D_i [S_z^2 - 1/3\,S(S+1) + E/D(\vec{S}_x^2 - \vec{S}_y^2)]$$

Electrochemical analysis was done by means of potentiodynamic measurements in which the working electrode potential is ramped linearly versus time (cyclic voltammetry (CV)). All measurements were performed in a nitrogen-filled glovebox on an IVIUM potentiostat/galvanostat using a 3-electrode setup. The setup included a glassy carbon (GC) working electrode, a platinum counter electrode, and a silver wire pseudo reference electrode. All electrodes were purchased from either BASi or Redox.me. The potentiostat was kept external to the glovebox, and the electrode leads were connected with a

custom shielded electrode cable feedthrough. All scans were absolutely referenced to ferrocene, measured at the start and end of each measurement set. GC electrodes were 2 and 3 mm in diameter, with surfaces of 50.3 mm^2 and 113.1 mm^2, respectively. GC electrodes were polished with a 0.3 μm alumina powder slurry in deionized water, rinsed with MeOH, water and dilute HCl solution (1 M), and ultrasonicated in pure deionized water for 30 sec, to remove residual polishing powder. The pseudo reference silver wire electrode and platinum wire counter electrode were rinsed with MeOH and water. All electrodes were dried in the ante chamber of the glovebox for at least 12 h. All electrodes were used directly in solution. Each working electrode was pre-treated with at least two cyclical scans from approximately +1.5 to −2.8 V at 200 mV/s in the corresponding solvent containing 0.1 M [*n*-Bu_4N][PF_6]. For all experiments, background voltammograms of the electrolyte were recorded at the respective scan rate. Solutions were gently shaken between experiments to renew the diffusion layer. No indication of solution resistance was observed during experiments, as described by McCarthy *et al,* which state that the solution resistance in the presence of >0.05 M electrolyte is estimated to be <30 mV in reduction potentials.[113] GC product analyses were performed on an Agilent 7820A gas chromatograph equipped with a HP-5 capillary column 30mx0.32mmx0.25μm and a flame ionization detector. Elemental analyses were carried out in the laboratories of Medac Ltd. in the UK.

5.5.3 Computational Methods

Density functional theory (DFT) calculations were conducted using the *Gaussian 16* software package.[114] Geometry optimisations and frequency calculations were performed with the B3LYP (Becke, three-parameter, Lee-Young-Parr) functional, defining the LANL2DZ basis set for Fe atoms and the 6-31g(d,p) basis set for all other atoms. Geometry optimisations were performed without any symmetry restraints and empirical dispersion corrections were applied. DFT-optimised structures were confirmed as energy minima by the absence of any imaginary frequencies. Single point energy calculations were subsequently run on the optimised geometries at the B3LYP/6-311g(d,p) level of theory. Initial *x,y,z* coordinates for [Fe($Im^{Ph2}NNO^{tBu}$)(BF)] (**2**) were taken from the X-ray crystal structure. Initial *x,y,z* coordinates for [Fe($Im^{Ph2}NNO^{tBu}$)(BF)(NO)] (**5,** structures **A** and **B**) were built artificially starting from the DFT-optimised geometry of **2**. Natural bond orbital (NBO) analysis of **2** was performed using the *NBO06* program[115] at the B3LYP/6-311g(d,p) level of theory. Cube files for molecular orbitals were generated using the *Multiwfn* program.[116] Biorthogonalization of the α and β spin molecular orbitals for **2** was performed with the *Multiwfn* program, using the Fock matrix from the .47 NBO file (see Appendix G). Molecular orbitals were visualised with the *Visual Molecular Dynamics* program,[117] using the respective molecular orbital cube file and defining the isosurface level at ±0.05. EPR *g*-tensor values and zero-field spitting parameters (*D* and *E*) were calculated using the *ORCA 4.2.1* software package.

5.5.4 Synthesis

[Fe($Im^{Ph2}NNO^{tBu}$)(BF)] (2): Complex **1** (54.6 mg, 67.8 μmol) was dissolved in CH_2Cl_2 (5 mL) and

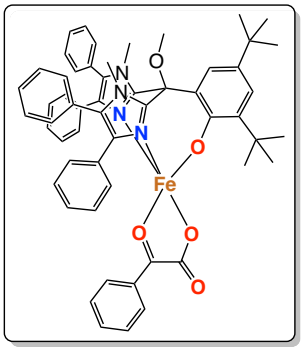

stirred at room temperature. A slight excess of K-BF (15.0 mg, 79.7 μmol) was suspended in CH_2Cl_2 (2 mL) and added dropwise to the solution. After complete addition of K-BF, the reaction mixture was stirred overnight. During the course of the reaction, the colour was observed to change from light brown to deep inky blue. The reaction mixture was subsequently filtered, and the blue solution was concentrated under vacuum, affording a blue solid. The solid was washed with hexane (3 x 4 mL) and dried under vacuum. The title complex was obtained as a bright blue solid in 92% yield (57.3 mg, 62.3 μmol). Blue crystals suitable for X-ray diffraction were grown by slow vapour diffusion of hexane into a THF solution of **2** under

ambient conditions. **^{1}H NMR** (400 MHz, CD_3CN, 298 K): δ = 49.35, 48.30, 37.47, 31.00, 20.16, 13.07, 12.72, 7.58, 7.50, 7.33, 7.20, 6.53, 6.36, 6.24, 5.77, 5.28, 4.07, 3.67, 3.57, 3.12 ppm. **^{1}H NMR** (400 MHz, CD_2Cl_2, 298 K): δ = 51.82, 43.65, 12.50, 11.36, 6.97, 6.78, 6.52, 5.14, 4.86, 4.21, 2.20, 0.15 ppm. χ (Evans method, 1%TMS in CD_3CN): μ_{eff} = 4.45 μ_B. **UV-vis (MeCN):** λ (ε, M^{-1} cm^{-1}) = 545 (430), 605 (530), 735 (300) nm. **UV-vis (CH_2Cl_2):** λ (ε, M^{-1} cm^{-1}) = 540 (760), 600 (830), 740 (360) nm. **^{57}Fe Mössbauer** (80 K): δ = 1.17 mm s^{-1}, $|\Delta E_Q|$ = 2.64 mm s^{-1}. **IR** (ATR): υ = 3053 (w), 2958 (s), 2908 (m), 2861 (m), 1675 (s), 1633 (w), 1599 (w), 1574 (w), 1506 (w), 1465 (m), 1440 (s), 1390 (w), 1359 (w), 1304 (m), 1261 (s0, 1233 (s), 1179 (w), 1160 (w), 1070 (s), 1057 (s), 1025 (s) 978 (w), 915 (w), 885 (w), 843 (w), 800 (m), 790 (m), 773 (m), 746 (w), 701 (m) cm^{-1}. **E.A.** (Formula: $C_{56}H_{54}FeN_4O_5$, M_w: 918.92 g mol^{-1}): calc. C 73.20, H 5.92, N 6.09; found C 73.20, H 6.15, N 5.62.

5.5.5 Reactivity Studies

Reaction of 2 with O_2: Complex **2** (45 mg, 49 μmol) was weighed into a vial and dissolved in anaerobic MeCN in the glovebox. The vial was sealed with a rubber septum and brought out of the glovebox. O_2 gas was bubbled through the solution for 5 seconds to saturate the solution before leaving the reaction mixture under O_2 pressure. After a period of 3 h, the reaction mixture was quenched by the addition of 0.1 M HCl aqueous solution. The organics were extracted with EtOAc and concentrated under vacuum. ^{1}H NMR and ESI-MS analyses were performed on the residual solid.

***In-situ* preparation of 5:** In the glovebox, a vial was charged with complex **2** (14.2 mg, 15.4 μmol) and CH_2Cl_2 (10 mL). The blue solution was stirred at –40 °C and a bright green solution of Ph_3CSNO (3.0 mg, 18.5 μmol) in CH_2Cl_2 (3 mL) was added dropwise to the mixture. The vial was sealed and placed in a darkened container at –40 °C. The reaction was stirred in the dark for a period of 90 min, while letting the temperature warm to room temperature. After this time, the solution had changed from blue to brown in colour. Small aliquots of the reaction mixture were taken for EPR, IR and UV-vis analysis.

Interception experiments: Complex **2** (1 equiv.) and the substrate (methyl(*p*-tolyl)sulfide or 1-octene, 100 equiv.) were combined in a vial and dissolved in anaerobic MeCN in the glovebox. The vial was sealed with a rubber septum and brought out of the glovebox. O_2 gas was bubbled through the blue solution for 5 sec before leaving the reaction mixture under O_2 pressure. Samples for GC were taken every 10 min for a period of 1 h, and subsequently every 30 min. The samples were passed over a short silica plug and each eluted with EtOAc (3 mL). Biphenyl (0.2 eq.) was used as an internal standard for each sample. Amounts used for methyl(*p*-tolyl)sulfide reaction: 13.4 mg of **2** (14.6 μmol), 0.20 g of sulfide (1.46 mmol). Amounts used for 1-octene reaction: 15.5 mg of **2** (16.9 μmol), 0.19 g of 1-octene (1.69 mmol).

Catalytic trial: Complex **2** (25.1 mg, 27.2 μmol, 1 equiv.) and the substrate (0.19 g, 1.37 mmol, 100 equiv.) were weighed into a vial and dissolved in anaerobic MeCN in the glovebox. Benzoylformic acid (0.12 g, 0.81 mmol, 30 eq.) was added to the mixture, which caused a colour change from blue to purple. The vial was sealed with a rubber septum and brought out of the glovebox. O_2 gas was bubbled through the solution for 5 sec before leaving the reaction mixture under O_2 pressure. Samples for GC were taken after 30 min, 1 h and 4 h. The samples were passed over a short silica plug and each eluted with EtOAc (3 mL). Biphenyl (0.5 eq.) was used as an internal standard for each sample.

5.6 References and Notes

(1) Gao, S.-S.; Naowarojna, N.; Cheng, R.; Liu, X.; Liu, P. *Nat. Prod. Rep.* **2018**, *35*, 792–837.
(2) Hausinger, R. P. *Crit. Rev. Biochem. Mol. Biol.* **2004**, *39*, 21–68.
(3) *2-Oxoglutarate-Dependent Oxygenases*; Schofield, C. J.; Hausinger, R. P., Eds.; RSC Publishing: Cambridge, 2015.
(4) Que, L. J. *Nat. Struct. Biol.* **2000**, *7*, 182–184.
(5) Bruijnincx, P. C. A.; van Koten, G.; Klein Gebbink, R. J. M. *Chem. Soc. Rev.* **2008**, *37*, 2716–2744.
(6) Blasiak, L. C.; Vaillancourt, F. H.; Walsh, C. T.; Drennan, C. L. *Nature* **2006**, *440*, 368–371.
(7) Timmins, A.; de Visser, S. P. *Catalysts* **2018**, *8*, 314.
(8) Mitchell, A. J.; Zhu, Q.; Maggiolo, A. O.; Ananth, N. R.; Hillwig, M. L.; Liu, X.; Boal, A. K. *Nat. Chem. Biol.* **2016**, *12*, 636–640.
(9) Simmons, J. M.; Müller, T. A.; Hausinger, R. P. *Dalt. Trans.* **2008**, 5132–5142.
(10) Costas, M.; Mehn, M. P.; Jensen, M. P.; Que Jr., L. *Chem. Rev.* **2004**, *104*, 939–986.
(11) Price, J. C.; Barr, E. W.; Tirupati, B.; Bollinger Jr., M. J.; Krebs, C. *Biochemistry* **2003**, *42*, 7497–7508.
(12) Gorres, K. L.; Raines, R. T. *Crit. Rev. Biochem. Mol. Biol.* **2010**, *45*, 106–124.
(13) Chen, W.; Huang, T.; He, X.; Meng, Q.; You, D.; Bai, L.; Li, J.; Wu, M.; Li, R.; Xie, Z.; Zhou, H.; Zhou, X.; Tan, H.; Deng, Z. *J. Biol. Chem.* **2009**, *284*, 10627–10638.
(14) Chang, W.; Liu, P.; Guo, Y. *Comments Inorg. Chem.* **2018**, *38*, 127–165.
(15) Fedeles, B. I.; Singh, V.; Delaney, J. C.; Li, D.; Essigmann, J. M. *J. Biol. Chem.* **2015**, *290*, 20734–20742.
(16) Klose, R. J.; Kallin, E. M.; Zhang, Y. *Nat. Rev. Genet.* **2006**, *7*, 715–727.
(17) Yi, C.; Yang, C.-G.; He, C. *Acc. Chem. Res.* **2009**, *42*, 519–529.
(18) Li, J.; Liao, H.-J.; Tang, Y.; Huang, J.-L.; Cha, L.; Lin, T.-S.; Lee, J. L.; Kurnikov, I. V.; Kurnikova, M. G.; Chang, W.; Chan, N.-L.; Guo, Y. *J. Am. Chem. Soc.* **2020**, *142*, 6268–6284.
(19) Bräuer, A.; Beck, P.; Hintermann, L.; Groll, M. *Angew. Chemie Int. Ed.* **2016**, *55*, 422–426.
(20) Wong, C.; Fujimori, D. G.; Walsh, C. T.; Drennan, C. L. *J. Am. Chem. Soc.* **2009**, *131*, 4872–4879.
(21) Kershaw, N. J.; Caines, M. E. C.; Sleeman, M. C.; Schofield, C. J. *Chem. Commun. (Camb).* **2005**, 4251–4263.
(22) Li, R.; Stapon, A.; Blanchfield, J. T.; Townsend, C. A. *J. Am. Chem. Soc.* **2000**, *122*, 9296–9297.
(23) Phelan, R. M.; Townsend, C. A. *J. Am. Chem. Soc.* **2013**, *135*, 7496–7502.
(24) Valegård, K.; van Scheltinga, A. C. T.; Lloyd, M. D.; Hara, T.; Ramaswamy, S.; Perrakis, A.; Thompson, A.; Lee, H.-J.; Baldwin, J. E.; Schofield, C. J.; Hajdu, J.; Andersson, I. *Nature* **1998**, *394*, 805–809.
(25) Zhou, J.; Kelly, W. L.; Bachman, B. O.; Gunsior, M.; Townsend, C. A.; Solomon, E. I. *J. Am. Chem. Soc.* **2001**, *123*, 7388–7398.
(26) Lau, W.; Sattely, E. S. *Science (80-.).* **2015**, *349*, 1224–1228.
(27) Li, H.; Zhu, W.; Liu, Y. *J. Chem. Inf. Model.* **2019**, *59*, 5086–5098.
(28) Yan, W.; Song, H.; Song, F.; Guo, Y.; Wu, C.-H.; Sae Her, A.; Pu, Y.; Wang, S.; Naowarojna, N.; Weitz, A.; Hendrich, M. P.; Costello, C. E.; Zhang, L.; Liu, P.; Jessie Zhang, Y. *Nature* **2015**, *527*, 539–543.
(29) Matsuda, Y.; Bai, T.; Phippen, C. B. W.; Nødvig, C. S.; Kjærbølling, I.; Vesth, T. C.; Andersen, M. R.; Mortensen, U. H.; Gotfredsen, C. H.; Abe, I.; Larsen, T. O. *Nat. Commun.* **2018**, *9*, 2587.
(30) Herr, C. Q.; Hausinger, R. P. *Trends Biochem. Sci.* **2018**, *43*, 517–532.
(31) Purpero, V.; Moran, G. R. *JBIC J. Biol. Inorg. Chem.* **2007**, *12*, 587–601.
(32) Wu, L.-F.; Meng, S.; Tang, G.-L. *Biochim. Biophys. Acta - Proteins Proteomics* **2016**, *1864*, 453–470.
(33) Townsend, C. A. *Curr. Opin. Chem. Biol.* **2002**, *6*, 583–589.
(34) Cho, K.-B.; Hirao, H.; Shaik, S.; Nam, W. *Chem. Soc. Rev.* **2016**, *45*, 1197–1210.
(35) Martinez, S.; Hausinger, R. P. *J. Biol. Chem.* **2015**, *290*, 20702–20711.
(36) Price, J. C.; Barr, E. W.; Glass, T. E.; Krebs, C.; Bollinger, J. M. *J. Am. Chem. Soc.* **2003**, *125*, 13008–13009.
(37) Price, J. C.; Barr, E. W.; Hoffart, L. M.; Krebs, C.; Bollinger, J. M. *Biochemistry* **2005**, *44*, 8138–8147.
(38) Hoffart, L. M.; Barr, E. W.; Guyer, R. B.; Bollinger, J. M. J.; Krebs, C. *Proc. Natl. Acad. Sci.* **2006**, *103*, 14738–14743.
(39) Chaturvedi, S. S.; Ramanan, R.; Lehnert, N.; Schofield, C. J.; Karabencheva-Christova, T. G.;

Christov, C. Z. *ACS Catal.* **2020**, *10*, 1195–1209.
(40) Hangasky, J. A.; Taabazuing, C. Y.; Valliere, M. A.; Knapp, M. J. *Metallomics* **2013**, *5*, 287.
(41) Paine, T. K.; Que, L. J. In *Structure and Bonding*; Springer-Verlag: Berlin, 2014; pp. 39–56.
(42) Yan, L.; Colandrea, V. J.; Hale, J. J. *Expert Opin. Ther. Pat.* **2010**, *20*, 1219–1245.
(43) Gilkes, D. M.; Chaturvedi, P.; Bajpai, S.; Wong, C. C.; Wei, H.; Pitcairn, S.; Hubbi, M. E.; Wirtz, D.; Semenza, G. L. *Cancer Res.* **2013**, *73*, 3285–3296.
(44) Hocart, C. H.; Halpern, B.; Hick, L. A.; Wong, C. O.; Hammond, J. W.; Wilcken, B. *J. Chromatogr. B Biomed. Sci. Appl.* **1983**, *275*, 237–243.
(45) Tomoeda, K.; Awata, H.; Matsuura, T.; Matsuda, I.; Ploechl, E.; Milovac, T.; Boneh, A.; Scott, C. R.; Danks, D. M.; Endo, F. *Mol. Genet. Metab.* **2000**, *71*, 506–510.
(46) Wierzbicki, A. S.; Lloyd, M. D.; Schofield, C. J.; Feher, M. D.; Gibberd, F. B. *J. Neurochem.* **2002**, *80*, 727–735.
(47) Cole, W. G.; Mäkitie, O. In *Textbook of Pediatric Rheumatology*; Pretty, R. E.; Laxer, R. M.; Lindsley, C. B.; Wedderburn, L., Eds.; W.B. Saunders, 2016; pp. 706-719.e3.
(48) Risteli, L.; Risteli, J.; Ihme, A.; Krieg, T.; Müller, P. K. *Biochem. Biophys. Res. Commun.* **1980**, *96*, 1778–1784.
(49) Kivirikko, K. I. *Ann. Med.* **1993**, *25*, 113–126.
(50) Liu, C.-K.; Hsu, C.-A.; Abbott, M. T. *Arch. Biochem. Biophys.* **1973**, *159*, 180–187.
(51) Abbott, M. T. *Methods Enzymol.* **1967**, *12*, 47–50.
(52) Pokidysheva, E.; Boudko, S.; Vranka, J.; Zientek, K.; Maddox, K.; Moser, M.; Fässler, R.; Ware, J.; Bächinger, H. P. *Proc. Natl. Acad. Sci.* **2014**, *111*, 161–166.
(53) Vaillancourt, F. H.; Yin, J.; Walsh, C. T. *Proc. Natl. Acad. Sci. U. S. A.* **2005**, *102*, 10111–10116.
(54) Rose, N. R.; McDonough, M. A.; King, O. N. F.; Kawamura, A.; Schofield, C. J. *Chem. Soc. Rev.* **2011**, *40*, 4364.
(55) Vasta, J. D.; Raines, R. T. *J. Med. Chem.* **2018**, *61*, 10403–10411.
(56) Bush, J. T.; Leśniak, R. K.; Yeh, T.-L.; Belle, R.; Kramer, H.; Tumber, A.; Chowdhury, R.; Flashman, E.; Mecinović, J.; Schofield, C. J. *Chem. Commun.* **2019**, *55*, 1020–1023.
(57) Rydzik, A. M.; Chowdhury, R.; Kochan, G. T.; Williams, S. T.; McDonough, M. A.; Kawamura, A.; Schofield, C. J. *Chem. Sci.* **2014**, *5*, 1765–1771.
(58) Hopkinson, R. J.; Tumber, A.; Yapp, C.; Chowdhury, R.; Aik, W.; Che, K. H.; Li, X. S.; Kristensen, J. B. L.; King, O. N. F.; Chan, M. C.; Yeoh, K. K.; Choi, H.; Walport, L. J.; Thinnes, C. C.; Bush, J. T.; Lejeune, C.; Rydzik, A. M.; Rose, N. R.; Bagg, E. A.; McDonough, M. A.; Krojer, T. J.; Yue, W. W.; Ng, S. S.; Olsen, L.; Brennan, P. E.; Oppermann, U.; Müller, S.; Klose, R. J.; Ratcliffe, P. J.; Schofield, C. J.; Kawamura, A. *Chem. Sci.* **2013**, *4*, 3110.
(59) Maxwell, P. H.; Eckardt, K.-U. *Nat. Rev. Nephrol.* **2016**, *12*, 157–168.
(60) Tollnick, C.; Seidel, G.; Beyer, M.; Schügerl, K. In *New Trends and Developments in Biochemical Engineering*; Scheper, T., Ed.; Springer, Berlin, Heidelberg, 2004; pp. 1–45.
(61) Conti, G.; Pollegioni, L.; Rosini, E. *Catal. Sci. Technol.* **2015**, *5*, 1854–1863.
(62) Renata, H. *Synlett* **2021**, *32*, 775–784.
(63) Pavel, E. G.; Zhou, J.; Busby, R. W.; Gunsior, M.; Townsend, C. A.; Solomon, E. I. *J. Am. Chem. Soc.* **1998**, *120*, 743–753.
(64) Neidig, M. L.; Brown, C. D.; Light, K. M.; Fujimori, D. G.; Nolan, E. M.; Price, J. C.; Barr, E. W.; Bollinger, J. M.; Krebs, C.; Walsh, C. T.; Solomon, E. I. *J. Am. Chem. Soc.* **2007**, *129*, 14224–14231.
(65) Neidig, M. L.; Brown, C. D.; Kavana, M.; Choroba, O. W.; Spencer, J. B.; Moran, G. R.; Solomon, E. I. *J. Inorg. Biochem.* **2006**, *100*, 2108–2116.
(66) Elkins, J. M.; Ryle, M. J.; Clifton, I. J.; Dunning Hotopp, J. C.; Lloyd, J. S.; Burzlaff, N. I.; Baldwin, J. E.; Hausinger, R. P.; Roach, P. L. *Biochemistry* **2002**, *41*, 5185–5192.
(67) Diebold, A. R.; Brown-Marshall, C. D.; Neidig, M. L.; Brownlee, J. M.; Moran, G. R.; Solomon, E. I. *J. Am. Chem. Soc.* **2011**, *133*, 18148–18160.
(68) Solomon, E. I.; Light, K. M.; Liu, L. V.; Srnec, M.; Wong, S. D. *Acc. Chem. Res.* **2013**, *46*, 2725–2739.
(69) Srnec, M.; Wong, S. D.; England, J.; Que, L.; Solomon, E. I. *Proc. Natl. Acad. Sci.* **2012**, *109*, 14326–14331.
(70) Drummond, M. J.; Ford, C. L.; Gray, D. L.; Popescu, C. V.; Fout, A. R. *J. Am. Chem. Soc.* **2019**, *141*, 6639–6650.
(71) O'Brien, J. R.; Schuller, D. J.; Yang, V. S.; Dillard, B. D.; Lanzilotta, W. N. *Biochemistry* **2003**, *42*, 5547–5554.
(72) Chiou, Y. M.; Que, L. *J. Am. Chem. Soc.* **1992**, *114*, 7567–7568.

(73) Chiou, Y.-M.; Que, L. *J. Am. Chem. Soc.* **1995**, *117*, 3999–4013.
(74) Paine, T. K.; England, J.; Que, L. *Chem. - A Eur. J.* **2007**, *13*, 6073–6081.
(75) Ha, E. H.; Ho, R. Y. N.; Kisiel, J. F.; Valentine, J. S. *Inorg. Chem.* **1995**, *34*, 2265–2266.
(76) Hikichi, S.; Ogihara, T.; Fujisawa, K.; Kitajima, N.; Akita, M.; Moro-oka, Y. *Inorg. Chem.* **1997**, *36*, 4539–4547.
(77) Hegg, E. L.; Ho, R. Y. N.; Que, L. *J. Am. Chem. Soc.* **1999**, *121*, 1972–1973.
(78) Mukherjee, A.; Martinho, M.; Bominaar, E. L.; Münck, E.; Que, L. *Angew. Chemie Int. Ed.* **2009**, *48*, 1780–1783.
(79) Sheet, D.; Paine, T. K. *Chem. Sci.* **2016**, *7*, 5322–5331.
(80) Mukherjee, A.; Cranswick, M. A.; Chakrabarti, M.; Paine, T. K.; Fujisawa, K.; Münck, E.; Que, L. *Inorg. Chem.* **2010**, *49*, 3618–3628.
(81) Sánchez-Eguía, B. N.; Serrano-Plana, J.; Company, A.; Costas, M. *Chem. Commun.* **2020**, *56*, 14369–14372.
(82) Hegg, E. L.; Que, L. *Eur. J. Biochem.* **1997**, *250*, 625–629.
(83) Diebold, A. R.; Neidig, M. L.; Moran, G. R.; Straganz, G. D.; Solomon, E. I. *Biochemistry* **2010**, *49*, 6945–6952.
(84) Diebold, A. R.; Straganz, G. D.; Solomon, E. I. *J. Am. Chem. Soc.* **2011**, *133*, 15979–15991.
(85) Monkcom, E. C.; de Bruin, D.; de Vries, A. J.; Lutz, M.; Ye, S.; Klein Gebbink, R. J. M. *Chem. – A Eur. J.* **2021**, *27*, 5191–5204. (Chapter 3 of this thesis).
(86) Folkertsma, E.; de Waard, E. F.; Korpershoek, G.; van Schaik, A. J.; Solozabal Mirón, N.; Borrmann, M.; Nijsse, S.; Moelands, M. A. H.; Lutz, M.; Otte, M.; Moret, M.-E.; Klein Gebbink, R. J. M. *Eur. J. Inorg. Chem.* **2016**, *2016*, 1319–1332.
(87) Oldenburg, P. D.; Ke, C.-Y.; Tipton, A. A.; Shteinman, A. A.; Que, L. *Angew. Chemie Int. Ed.* **2006**, *45*, 7975–7978.
(88) Bete, S. C.; Otte, M. *Angew. Chemie Int. Ed.* **2021**, *60*, 18582–18586.
(89) Monkcom, E. C.; Ghosh, P.; Folkertsma, E.; Negenman, H. A.; Lutz, M.; Klein Gebbink, R. J. M. *Chim. Int. J. Chem.* **2020**, *74*, 450–466. (Chapter 6 of this thesis).
(90) Monkcom, E. C.; Negenman, H. A.; Masferrer-Rius, E.; Lutz, M.; Ye, S.; Bill, E.; Klein Gebbink, R. J. M. *Eur. J. Inorg. Chem.* **2022**, *9*, e202101046. (Chapter 2 of this thesis).
(91) Chiou, Y.-M.; Que, L. *Angew. Chemie Int. Ed.* **1994**, *33*, 1886–1888.
(92) Müller, R.; Hübner, E.; Burzlaff, N. *Eur. J. Inorg. Chem.* **2004**, *2004*, 2151–2159.
(93) Addison, A. W.; Rao, T. N.; Reedijk, J.; van Rijn, J.; Verschoor, G. C. *J. Chem. Soc., Dalt. Trans.* **1984**, 1349–1356.
(94) Evans, D. F. *J. Chem. Soc.* **1959**, *81*, 2003–2005.
(95) Gütlich, P.; Bill, E.; Trautwein, A. *Mossbauer spectroscopy and transition metal chemistry : fundamentals and application*; Springer, 2011.
(96) Yan, S.; Que, L.; Taylor, L. F.; Anderson, O. P. *J. Am. Chem. Soc.* **1988**, *110*, 5222–5224.
(97) Armstrong, W. H.; Lippard, S. J. *J. Am. Chem. Soc.* **1984**, *106*, 4632–4633.
(98) Wu, F. J.; Kurtz, D. M.; Hagen, K. S.; Nyman, P. D.; Debrunner, P. G.; Vankai, V. A. *Inorg. Chem.* **1990**, *29*, 5174–5183.
(99) Yan, S.; Cox, D. D.; Pearce, L. L.; Juarez-Garcia, C.; Que, L.; Zhang, J. H.; O'Connor, C. J. *Inorg. Chem.* **1989**, *28*, 2507–2509.
(100) Yan, S.; Pan, X.; Taylor, L. F.; Zhang, J. H.; O'Connor, C. J.; Britton, D.; Anderson, O. P.; Que, L. *Inorganica Chim. Acta* **1996**, *243*, 1–8.
(101) Harrop, T. C.; Tonzetich, Z. J.; Reisner, E.; Lippard, S. J. *J. Am. Chem. Soc.* **2008**, *130*, 15602–15610.
(102) Jana, M.; White, C. J.; Pal, N.; Demeshko, S.; Cordes (née Kupper), C.; Meyer, F.; Lehnert, N.; Majumdar, A. *J. Am. Chem. Soc.* **2020**, *142*, 6600–6616.
(103) Pal, N.; White, C. J.; Demeshko, S.; Meyer, F.; Lehnert, N.; Majumdar, A. *Inorg. Chem.* **2021**, *60*, 15890–15900.
(104) Chiou, Y.-M.; Que, L. *Inorg. Chem.* **1995**, *34*, 3270–3278.
(105) *Metal Nitrosyls*; Richter-Addo, G. B.; Legzdins, P., Eds.; Oxford University Press: New York, 1992.
(106) Enemark, J. H.; Feltham, R. D. *Coord. Chem. Rev.* **1974**, *13*, 339–406.
(107) Zhang, Y.; Pavlosky, M. A.; Brown, C. A.; Westre, T. E.; Hedman, B.; Hodgson, K. O.; Solomon, E. I. *J. Am. Chem. Soc.* **1992**, *114*, 9189–9191.
(108) Brown, C. A.; Pavlosky, M. A.; Westre, T. E.; Zhang, Y.; Hedman, B.; Hodgson, K. O.; Solomon, E. I. *J. Am. Chem. Soc.* **1995**, *117*, 715–732.
(109) Ye, S.; Price, J. C.; Barr, E. W.; Green, M. T.; Bollinger, J. M.; Krebs, C.; Neese, F. *J. Am. Chem.*

Soc. **2010**, *132*, 4739–4751.
(110) Ekanayake, D. M.; Fischer, A. A.; Elwood, M. E.; Guzek, A. M.; Lindeman, S. V.; Popescu, C. V.; Fiedler, A. T. *Dalt. Trans.* **2020**, *49*, 17745–17757.
(111) McCracken, J.; Cappillino, P. J.; McNally, J. S.; Krzyaniak, M. D.; Howart, M.; Tarves, P. C.; Caradonna, J. P. *Inorg. Chem.* **2015**, *54*, 6486–6497.
(112) Fulmer, G. R.; Miller, A. J. M.; Sherden, N. H.; Gottlieb, H. E.; Nudelman, A.; Stoltz, B. M.; Bercaw, J. E.; Goldberg, K. I. *Organometallics* **2010**, *29*, 2176–2179.
(113) McCarthy, B. D.; Martin, D. J.; Rountree, E. S.; Ullman, A. C.; Dempsey, J. L. *Inorg. Chem.* **2014**, *53*, 8350–8361.
(114) Gaussian 16, Revision C.01; Frisch, M. J.; Trucks, G. W.; Schlegel, H. B.; Scuseria, G. E.; Robb, M. A.; Cheeseman, J. R.; Scalmani, G.; Barone, V.; Petersson, G. A.; Nakatsuji, H.; Li, X.; Caricato, M.; Marenich, A. V.; Bloino, J.; Janesko, B. G.; Gomperts, R.; Mennucci, B.; Hratchian, H. P.; Ortiz, J. V.; Izmaylov, A. F.; Sonnenberg, J. L.; Williams-Young, D.; Ding, F.; Lipparini, F.; Egidi, F.; Goings, J.; Peng, B.; Petrone, A.; Henderson, T.; Ranasinghe, D.; Zakrzewski, V. G.; Gao, J.; Rega, N.; Zheng, G.; Liang, W.; Hada, M.; Ehara, M.; Toyota, K.; Fukuda, R.; Hasegawa, J.; Ishida, M.; Nakajima, T.; Honda, Y.; Kitao, O.; Nakai, H.; Vreven, T.; Throssell, K.; Montgomery, J. A. J.; Peralta, J. E.; Ogliaro, F.; Bearpark, M. J.; Heyd, J. J.; Brothers, E. N.; Kudin, K. N.; Staroverov, V. N.; Keith, T. A.; Kobayashi, R.; Normand, J.; Raghavachari, K.; Rendell, A. P.; Burant, J. C.; Iyengar, S. S.; Tomasi, J.; Cossi, M.; Millam, J. M.; Klene, M.; Adamo, C.; Cammi, R.; Ochterski, J. W.; Martin, R. L.; Morokuma, K.; Farkas, O.; Foresman, J. B.; Fox, D. J. Gaussian 16, Revision C.01, 2016.
(115) Glendening, E. D.; Landis, C. R.; Weinhold, F. *J. Comput. Chem.* **2013**, *34*, 1429–1437.
(116) Lu, T.; Chen, F. *J. Comput. Chem.* **2012**, *33*, 580–592.
(117) Humphrey, W.; Dalke, A.; Schulten, K. *J. Mol. Graph.* **1996**, *14*, 33–38.

Chapter 6

Bioinspired Non-Heme Iron Complexes: The Evolution of Facial *N,N,O* Ligand Design

Abstract

Iron-containing metalloenzymes that contain the 2-His-1-Carboxylate facial triad at their active site are well known for their ability to activate molecular oxygen and catalyse a broad range of oxidative transformations. Many of these reactions are synthetically challenging, and developing small molecular iron-based catalysts that can achieve similar reactivity and selectivity remains a long-standing goal in homogeneous catalysis. This perspective focuses on the development of bioinspired facial *N,N,O* ligands that model the 2-His-1-Carboxylate facial triad to a greater degree of structural accuracy than many of the polydentate N-donor ligands commonly used in this field. By developing robust, well-defined *N,N,O* facial ligands, an increased understanding could be gained of the factors governing enzymatic reactivity and selectivity.

This chapter is partly based on:
E. C. Monkcom, P. Ghosh, E. Folkertsma, H. A. Negenman, M. Lutz, R. J. M. Klein Gebbink, *Chimia International Journal of Chemistry,* **2020***,* 74, 6, 450-466 (NoNoMeCat edition).

6.1 Introduction

The 2-His-1-Carboxylate facial triad (2H1C) is a bioinorganic motif that occurs at the active site of many oxygen-activating mononuclear non-heme iron enzymes, and is currently regarded as one of the most versatile platforms with which Nature catalyses oxidative transformations.[1–4] It has attracted particular interest from the bioinorganic and catalysis communities due to its ability to activate molecular oxygen and mediate an astoundingly diverse scope of oxidative transformations, including hydroxylation, *cis*-dihydroxylation, epoxidation, ring-opening, ring-closing and epimerization reactions, in a highly stereo- and regioselective manner.[2,5]

Modelling iron metalloenzyme active sites with synthetic iron complexes has become a key strategy towards better understanding enzyme mechanisms as well as developing more sustainable non-noble metal catalysts. Over the last 15 years, our group has focused on the development of so-called "*N,N,O* ligands", which model important structural aspects of the 2H1C, including its facially-capping, tridentate, anionic *N,N,O* coordination motif. This perspective presents an overview of the research efforts conducted in our group to date, specifically towards the development of bis-imidazole-derived *N,N,O* ligands that incorporate either a carboxylate, ester, amide or phenolate as O-donor. The principal considerations of bioinspired ligand design will be outlined, and the coordination chemistry of each ligand type will be discussed in detail, with general trends and the pro's and con's highlighted in all cases.

6.2 The 2-His-1-Carboxylate Facial Triad

The 2H1C is characterised by the facial, tripodal coordination of two neutral histidine (His) residues and an anionic carboxylate group, typically an aspartate (Asp) or glutamate residue (Glu), to an iron(II) centre (Figure 1). Together, these form a so-called "*N,N,O*" coordination motif. Using its remaining coordination sites, the iron can accommodate up to three different exogenous ligands on the opposite face of its coordination sphere. During the enzyme's resting state, these sites are typically occupied by labile water molecules.

So far, the 2H1C has been identified at the active site of five different sub-classes of mononuclear non-heme iron enzymes, categorised according to their specific mechanistic requirements. These are: 1) the α-ketoglutarate (αKG) dependent enzymes, 2) the extradiol ring-cleaving dioxygenases, 3) the pterin-dependent hydroxylases, 4) the Rieske dioxygenases, and 5) the cofactor-independent oxidase enzymes. These enzyme sub-classes have been extensively reviewed elsewhere,[1,3] and will therefore not be discussed exhaustively here. Despite exhibiting very different reactivities, the different sub-classes of enzymes share some common mechanistic features (Figure 1, right).

The first mechanistic step generally involves the binding of the substrate or co-substrate to the active site cavity, often directly to the iron centre. This displaces one or more of the loosely bound water molecules from the resting state (**A**) and generates a coordinatively unsaturated iron(II) centre (**B**), which is primed to react with dioxygen. The binding of dioxygen occurs directly to iron, *cis* to the (co)substrate (**C**) and *trans* to one of the three constituent residues of the 2H1C. The different *trans* effects exerted by a neutral histidine or an anionic carboxylate group have been proposed as playing an important role in modulating the reactivity of the bound dioxygen.[2,6,7] Dioxygen is then reduced to the peroxide level (**D**), after which the mechanisms for the various iron enzymes diverge significantly. In general, the O–O bonds is cleaved and a high valent iron-oxo complex (**E**) is generated, considered as being the true oxidizing species. Direct evidence for a high valent iron-oxo intermediate has been reported for several different types of mononuclear non-heme iron enzymes.[5,8–10]

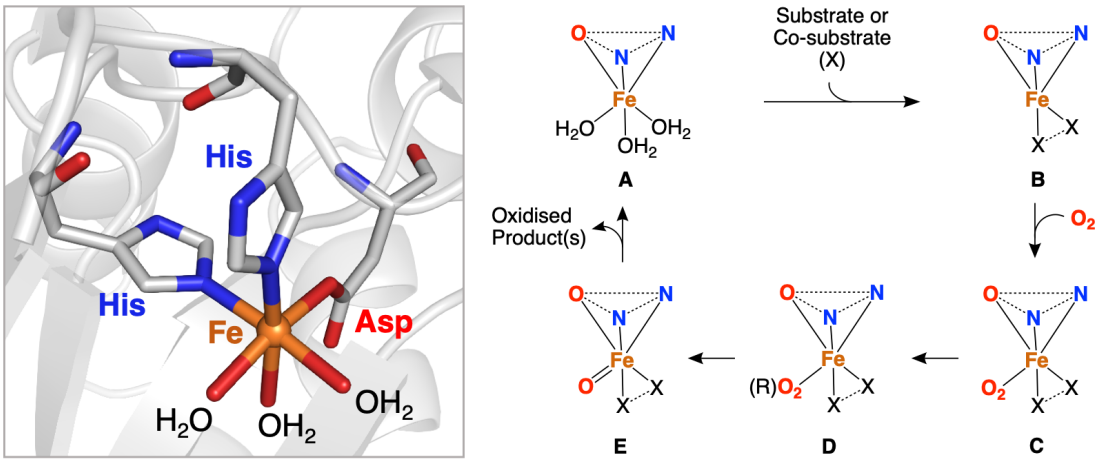

Figure 1. Left: the 2H1C at the active site of deacetoxycephalosporin C synthase (DAOCS) from *Streptomyces clavuligerus* (PDB 1RXF).[11] Right: generalised mechanism for the aerobic oxidation of substrates at non-heme iron enzyme active sites that contain the 2H1C. Figure adapted from Que *et al.*[5]

The flexibility in coordination chemistry enabled by the 2H1C is best exemplified by the different crystal structures of the enzyme-substrate complexes for enzymes such as 2,3-homoprotocatechuate dioxygenase (2,3-HPCD), taurine dioxygenase (TauD), and isopenicillin N synthase (IPNS), depicted in Figure 2. In 2,3-HPCD, an extradiol catechol cleaving dioxygenase enzymes, the catechol substrate binds as a bidentate ligand and one vacant site *trans* to the Glu residue is available for dioxygen binding.[12] In TauD, an αKG-dependent monohydroxylase enzyme, the αKG cofactor binds directly to the iron centre in a bidentate fashion and the substrate (taurine) docks within the active site cavity, in close proximity to the metal centre. One vacant site remains available for O_2 binding, *trans* to a His residue.[13] In IPNS, a cofactor-independent oxidase enzyme, the tripeptidic thiolate substrate L-δ-aminoadipoyl-L-cysteinyl-D-valine (ACV) binds as a monodentate ligand directly to the iron centre, and one of the loosely bound water molecules remains bound to the iron centre as a spectator ligand. One vacant site remains available for dioxygen binding, *trans* to the Asp residue.[14]

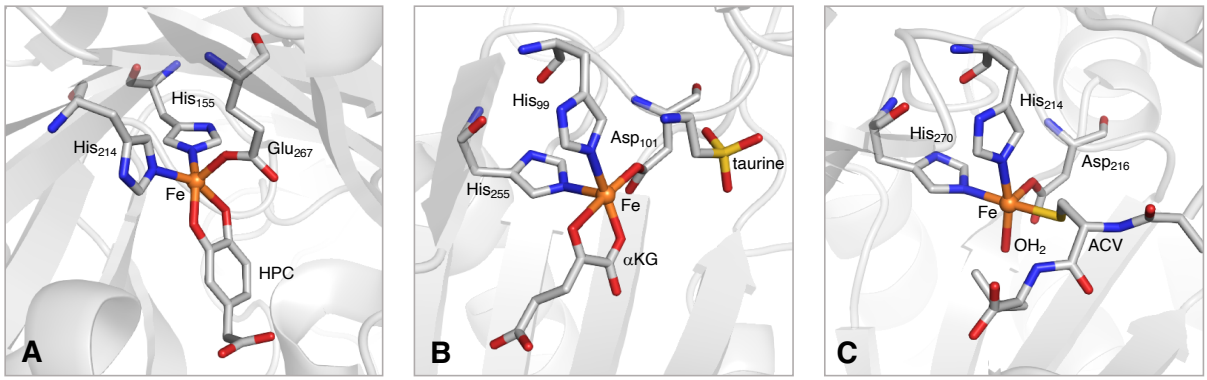

Figure 2. The substrate-bound active sites for A) 2,3-HPCD (PDB 1Q0C)[12], B) TauD (PDB 1OS7)[13] and C) IPNS (PDB 1BK0)[14]. Carbon, iron, nitrogen, oxygen and sulfur are depicted in grey, blue, red and yellow, respectively.

Central to the ability of mononuclear non-heme iron enzymes to activate and utilize molecular oxygen is the spin state of the iron centre during all stages of catalysis.[15,16] In its electronic ground state, dioxygen exists in an open-shell triplet state ($^3O_2$) triplet state with two unpaired electrons (S = 1). In contrast, organic molecules typically exist in a closed-shell singlet ground state with no unpaired electrons (S = 0), rendering their spontaneous reaction with O_2 sluggish and kinetically unfavourable due to the spin mismatch. Iron is capable of circumventing this spin mismatch by coordinating directly to $^3O_2$ and activating it (reductively) to form a reactive singlet (O_2^-) or doublet (O_2^{2-}) species. Typically, 2H1C-contiaining iron enzymes contain a ferrous ion (d^6) in their resting state, which exists in a high-spin electronic configuration (S = 2).

The 2H1C has fascinated the bioinorganic community for many years and much research has been undertaken to elucidate its role in determining the reactivity and selectivity of enzymes compared to other non-heme iron enzymes that contain the 3-His facial triad (3His) at their active site (*e.g.* thiol dioxygenases).[7,17,18] One of the strategies to gain further insight into the active sites of mononuclear non-heme iron enzymes is to study biomimetic non-heme iron complexes that replicate some of the structural features of the first coordination sphere of the enzyme active site.

6.3 Bioinspired Facial *N,N,O* Ligand Design

The 2H1C has served as the founding architectural model for many polydentate N-donor ligands,[19] some of the most well-known being the **Tp** (tris(pyrazolyl)borate),[20] **Me_3TACN** (1,4,7-trimethyl-1,4,7-triazacyclononane),[21] **TPA** (tris(2-pyridylmethyl)amine),[22–24] **TQA** (tris(2-quinolylmethyl)amine),[25] **$PyNMe_3$** (4,7,10-trimethyl-1,4,7,10-tetraaza-2,6-pyridinophane)[26] and **BPMEN** (bis(2-pyridylmethyl)-1,2-diaminoethane)[27] ligands. These ligands coordinate in a 1:1 stoichiometry with iron and support the formation of non-heme high-valent iron-oxo species. However, these ligands could arguably be considered closer in structure to the 3His than the 2H1C, due to the presence of only N-donors and the lack of

an anionic O-donor. For modelling the reactivity of IPNS, for example, this may present itself as a drawback. Furthermore, many of these ligands have a denticity greater than three, which deviates from the tricoordinate nature of the 2H1C.

In order to model the 2H1C with a greater degree of structural accuracy, it remains of great interest to develop tridentate *N,N,O* ligands that can coordinate to an iron centre in a facial manner while leaving *cis*-orientated coordination sites available for (co-)substrates to bind and reactions to take place. Two major challenges accompany this ligand design. Firstly, the connectivity of the ligand should promote facial (*fac*) coordination in a manner rather than meridional (*mer*) coordination (Figure 3). Typically, tripodal ligand designs that involve a central connecting atom are more likely to achieve facial coordination than linear ones. Secondly, the coordination of two ligand equivalents to an iron centre should be prevented, as this results in the formation of coordinatively saturated bisligated complexes that are generally unreactive.

Numerous examples of *N,N,O* ligands can be found in the literature, where the nature of constituent donor groups has been systematically varied.[28–31] By modifying the two N-donors and any of their tethered organic substituents, the steric or electronic properties of the ligands can easily be tuned. In some cases, two different N-donors have been installed, thereby imparting chirality to the ligand scaffold.[32,33] Other studies have also focused on

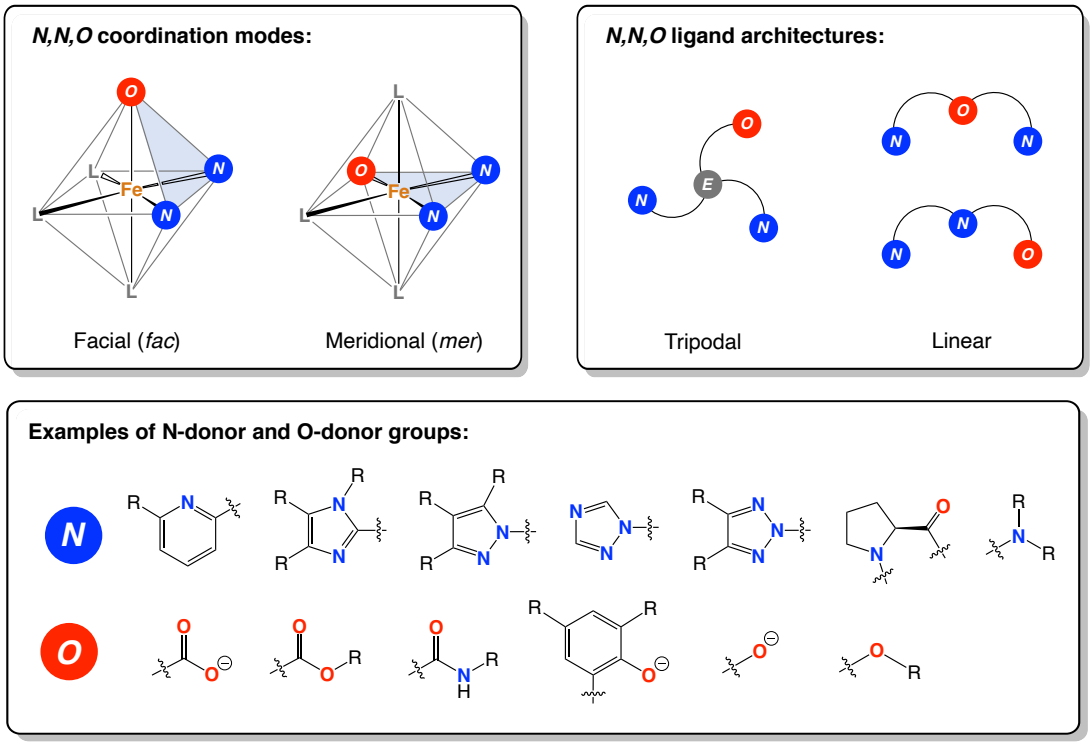

Figure 3. Left: schematic representation of the facial (*fac*) and meridional (*mer*) coordination modes of a tridentate *N,N,O* ligand (L = exogenous ligand). Right: simplified representation of tripodal and linear *N,N,O* ligand designs (*E* = B, C, N). Bottom: a list of different constituent N- and O-donor groups that have been used in *N,N,O* ligand design (R = organic substituent).

varying the nature of the central connecting atom. Incorporating a central borohydride group, for example, can lead to similar ligand properties and coordination chemistry to the well-known Tp ligand family.[34,35] Alternatively, incorporating a central nitrogen atom generally results in a tetradentate tripodal ligand framework, not unlike the TPA ligand scaffold.[36,37]

However, despite the diversity in *N,N,O* ligand designs, the number of ligands that can provide a facial *N,N,O* triad and support the formation of mononuclear, monoligated metal complexes is small. Typically, difficulties in achieving the desired coordination mode are encountered due to the formation of bisligated complexes, bridging coordination modes of an anionic O-donor, or lability of a neutral O-donor. The primary strategy to overcome these issues has been to increase the ligand's steric demand and bite angle by, for example, increasing the size of the N-/O-donor groups or by increasing the length of the organic linkers between donor group. In some cases, mono-ligation has been achieved with sterically less demanding ligands by using a co-ligand.

The typically weak-field nature of an *N,N,O* ligand's donor set generally results in the formation of high-spin non-heme iron complexes. Although this is in line with the high-spin electronic states of 2H1C-containing enzyme active sites, the paramagnetic nature of these complexes can pose challenges for the synthetic inorganic chemist. For instance, the occupancy of non-bonding or antibonding orbitals in high-spin (S = 2) non-heme iron(II) complexes is higher compared to intermediate-spin (S = 1) or low-spin (S = 0) iron(II) complexes.[16] This has the effect of increasing the Fe-N bond distances, for example, and may result in an increased lability of the *N,N,O* ligand donor set.[15] Spectroscopically, the paramagnetic nature of high-spin iron complexes requires the use of specialized spectroscopic methods (*e.g.* ^{57}Fe Mössbauer spectroscopy, X-ray absorption spectroscopy, MCD/CD, EPR, Evans NMR method and X-ray crystallography) in order to make an accurate description of their electronic structure, with computational studies often made to support these assignments. From a practical point of view, the (often) high reactivity of the iron complexes to O_2 necessitates careful handling (*e.g.* Schlenk line and glovebox techniques) under inert atmosphere conditions.

Some of the most notable *N,N,O* ligand contributions and corresponding non-heme iron complexes derive from the groups of Que,[38] Burzlaff,[39] Rutledge,[40] Paine,[41] Carrano,[42] Otte,[43] and Klein Gebbink.[29,44–46] The development and recent advances in *N,N,O* ligand design and coordination chemistry from our group will be described in this perspective chapter.

6.4 The Evolution of BAIP Facial *N,N,O* Ligands

In the quest for robust structural models of the 2H1C, our group has focused on the development of a series of *N,N,O* ligands derived from 3,3-bis(1-alkylimidazol-2-yl)propionic acid (BAIP). These ligands are tripodal in nature and comprise two imidazole N-donors and an O-donor, joined together in a heteroscorpionate fashion by means of a central carbon atom. The nature of the O-donor group can be systematically varied to be either a carboxylic acid, an ester, an amide, or a phenol group (Figure 4). Carboxylic acids can easily be converted to their anionic carboxylate form and are, therefore, the most relevant moiety with which to model the 2H1C, both structurally and electronically. Esters and secondary amide groups coordinate by means of their carbonyl group as neutral O-donors, but have the advantage of incorporating an additional organic substituent that can modulate the electronic properties of the carbonyl group and increase the steric bulk of the O-donor. Phenols are an attractive means with which to achieve anionic O-donor coordination while simultaneously having the option to tune the steric and electronic properties of the phenol ring by means of its *ortho*- and *para*-substituents (R^4). However, phenolates are known to be redox-active, which deviates somewhat from the carboxylate group of the 2H1C. Finally, the steric properties of the imidazoles themselves can be tuned by varying the nature of the organic substituent on the 1-, 4- and 5-positions of the heterocycle (R^1, R^2 and R^3). In general, the ligands used in our group require the imidazoles to always be functionalised on their 1-positions (R^1).

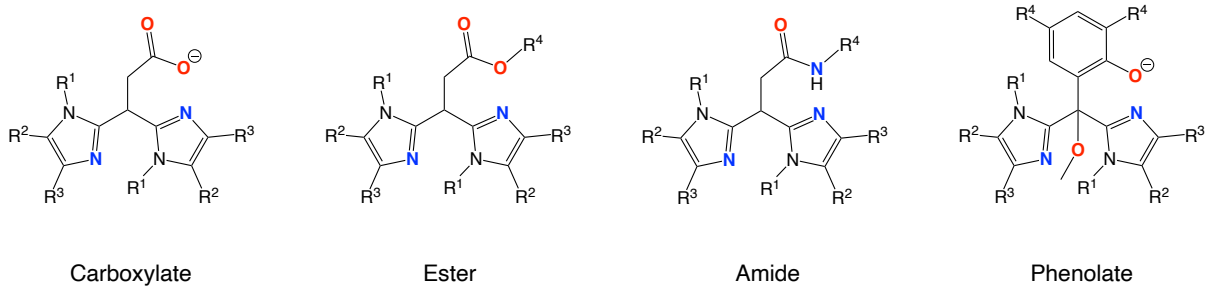

Figure 4. Facial *N,N,O* ligand designs employed in the Klein Gebbink group.

6.4.1 Synthesis

The synthesis of the different types of *N,N,O* ligands used in our group is schematically represented in Figure 5. Carboxylic acid, ester and amide ligands derive from the same synthetic pathway. Starting from the desired 1-alkyl(benz)imidazole precursor, the first step involves the formation of a bis-imidazole ketone moiety (**A**), which can be reduced with hydrazine to afford the bis-imidazole methane scaffold (**B**). Alternatively, N^1,3-dialkyllbenzene 1,2-diamine precursors (**C**) can undergo a double cyclization condensation reaction with diethyl malonate to form bis-(1,4-dialkyl)benzimidazole methane scaffolds. From here, the synthesis of esters or amides can easily be achieved by deprotonating the methylene bridge with *n*-BuLi, and reacting it with one equivalent of the desired alkyl 2-

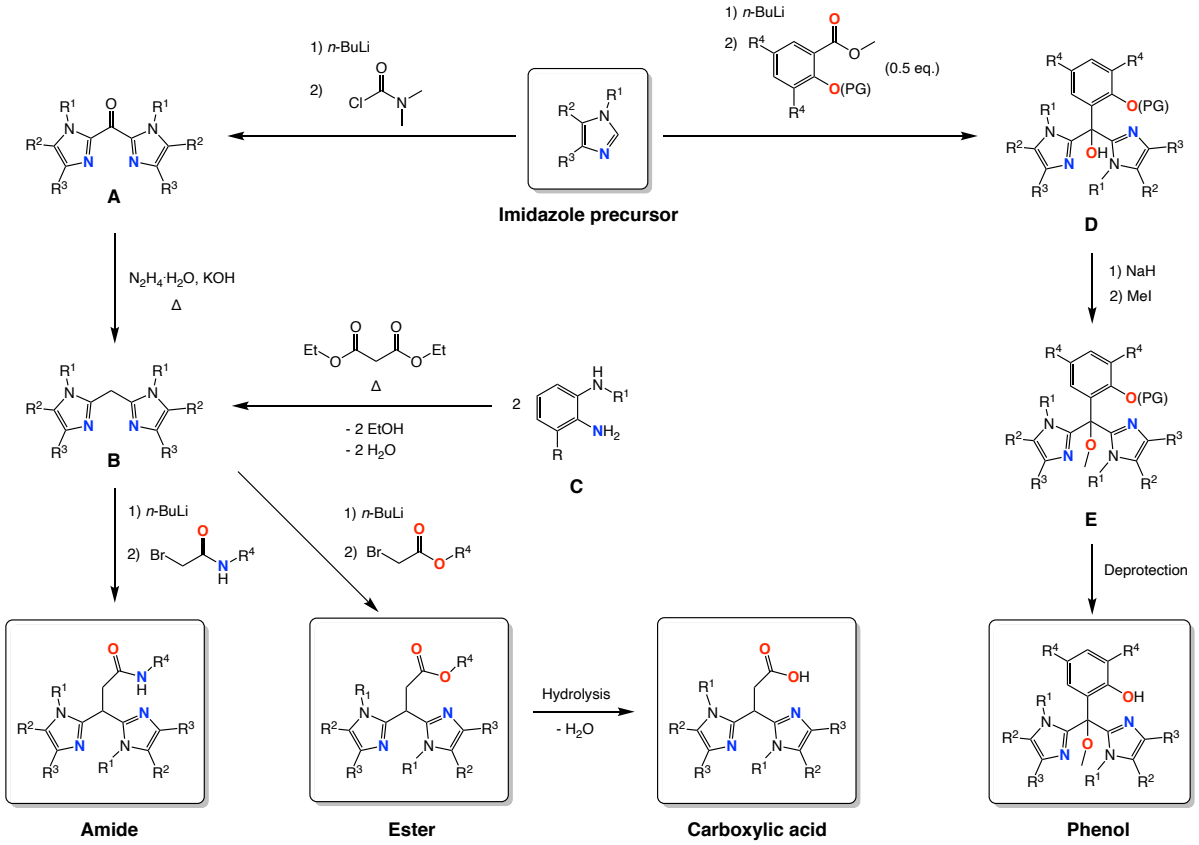

Figure 5. Synthesis map of different imidazole-derived *N,N,O* ligands in the Klein Gebbink group.

bromoacetate or 2-bromo-*N*-alkylacetamide precursor, respectively. The carboxylic acid ligands can conveniently be synthesised from the hydrolysis of the ester ligands. Phenol ligands are also conveniently synthesised from different 1-alkyl(benz)imidazole precursors, using a synthetic route previously described by Jameson *et al.*[47] The synthesis starts with the deprotonation of imidazole using *n*-BuLi, after which the lithium imidazolium salt is reacted with a hydroxy-protected methyl salicylate in a 2:1 stoichiometry. The resulting tertiary alcohol (**D**) is subsequently methylated (**E**), before deprotection of the phenol, thereby ensuring that the phenol is the only site that can be deprotonated for subsequent coordination chemistry.

6.4.2 Carboxylate Ligands

The family of BAIP-derived carboxylate ligands was designed with the incorporation of a simple carboxylic acid group, which can easily be deprotonated to generate the respective carboxylate. As previously mentioned, this can be regarded as the most electronically and structurally faithful group with which to model the anionic O-donor of the 2H1C. The BAIP ligands exist for a range of different substituted imidazoles, including the 1-methylimidazole (**L1**), 1-methylbenzimidazole (**L2**), 1-ethyl-4-*iso*propylimidazole (**L3**), 1,4-dimethylbenzimidazole (**L4**), 1-methyl-4,5-diphenylimidazole (**L5**).

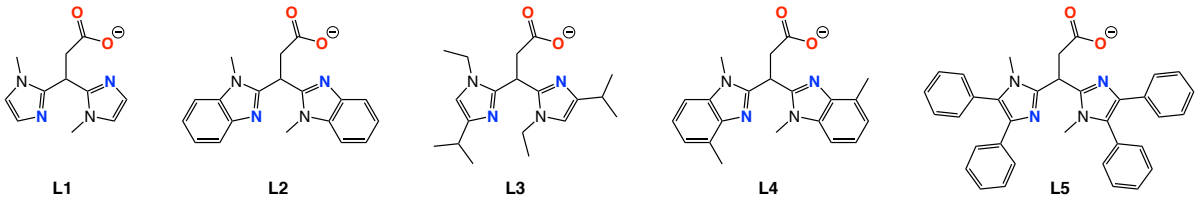

Figure 6. BAIP-derived *N,N,O* carboxylate ligands.

Depending on the choice of base, the counter-cation associated to the propionate salt (*e.g.* Na, K or Bu_4N) can be varied. Reaction of the propionate ligand salt with one equivalent of a transition metal salt (*e.g.* a divalent metal chloride), generally results in the formation of two new salts: the desired metal complex and an (inorganic) by-product (*e.g.* KCl). Choosing the appropriate counter-cation can therefore have an important role in determining the solubility properties of the metal complex and the by-product. In this respect, the choice of solvent also has an important role in determining how easily (inorganic) by-products are eliminated from the reaction mixture and the manner in which the metal complex is extracted or isolated. In our group, the coordination chemistry of the BAIP carboxylate ligand series has been explored with the biologically relevant metals Fe, Cu and Zn. The principal results of these studies will be summarised here.

The facial capping potential of **L1** and **L2** was first demonstrated in the work of Bruijnincx *et al.*,[46] where the coordination chemistry of these ligands was explored with copper. Reacting two equivalents of K[**L1**] or K[**L2**] with $CuCl_2 \cdot 2H_2O$ in hot ethanol afforded complexes **1** and **2**, of the type $[Cu^{II}(L)_2]$ (Figure 7). In these complexes, two ligand molecules coordinate by means of the desired anionic *N,N,O* facial triad, and are arranged in a centrosymmetric manner such that the carboxylate groups occupy mutually *trans* sites. The complexes both have a distorted octahedral geometry, where the four Cu–N bonds occupy the equatorial plane and the two Cu–O bonds in the axial positions are elongated slightly (2.4004(17) Å in **1** and 2.3475(14) Å in **2**) due to the Jahn-Teller distortion. Solid state and frozen solution EPR spectroscopy of **1** and **2** produced $g_{||}$ and $g_{\perp}$ values typical for an axially elongated geometry.

In another study,[48] similar zinc complexes of the type $[Zn^{II}(L)_2]$ (**4** and **5**) were obtained by reacting **L1** or **L3** in a 2:1 stoichiometry with $ZnCl_2$ in methanol (Figure 7, top). The binding modes of the ligands were established by means of ^{1}H NMR and IR spectroscopy. Whereas the ^{1}H NMR analysis for **4** was consistent with the structure of a centrosymmetric, bisligated complex, the ^{1}H NMR spectrum of **5** revealed two different sets of signals for the ligand's constituent imidazole groups. Supported by DFT, **5** was therefore proposed as being a bisligated zinc complex of tetrahedral geometry, where both ligand molecules adopt an alternative bidentate *N,O* coordination mode, involving a non-coordinated imidazole group. This is believed to derive from the larger steric component provided by the *iso*-propyl groups, which do not accommodate κ_3-*N,N,O* coordination of two **L3** molecules to a single metal ion.

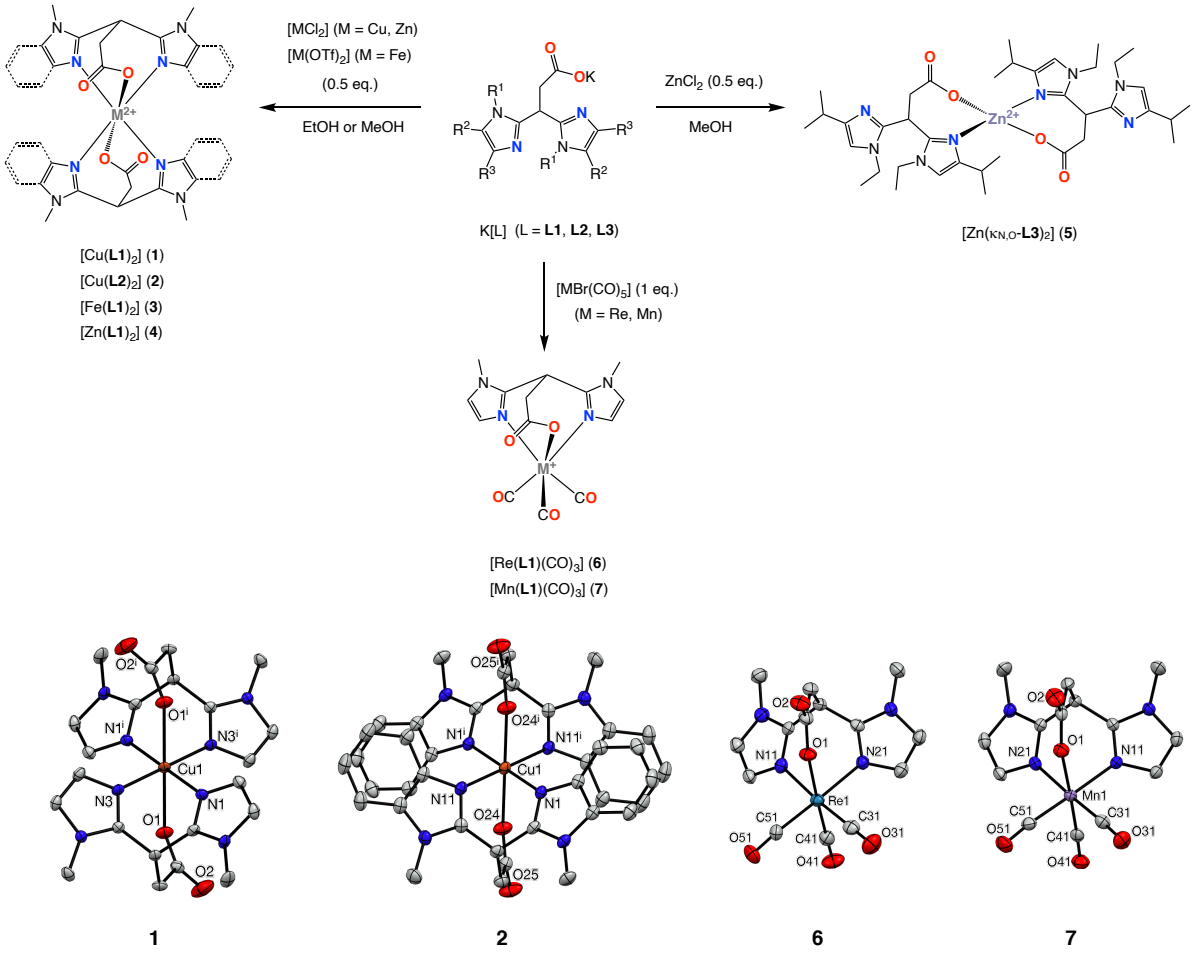

Figure 7. The synthesis of **1**-**4**,[46,48,49] as well as **6** and **7**.[50] The crystal structures of **1**, **2**, **6** and **7** are also provided. All H-atoms have been omitted for clarity and displacement ellipsoids are drawn at the 50% probability level.

The reaction of K[**L1**] with half an equivalent of $Fe(OTf)_2 \cdot 2MeCN$ in methanol afforded complex **3**, which was assigned as being analogous in structure to **1** and **4** by means of ESI-MS and IR spectroscopy as well as elemental analysis (Figure 7, top).[49] The structure was later confirmed by X-ray crystallography by Holland and co-workers.[51] Preliminary catalytic studies of **3** in alkane and alkene oxidations using H_2O_2 as an oxidant showed that **3** is ineffective as a catalyst for these kinds of transformations. This was attributed to the relatively strong interaction between the two monoanionic ligands and the metal ion, resulting in a low rate of ligand exchange and higher degree of coordinative saturation in solution, which reduces the interaction between the metal and the oxidant.

Independently, at approximately the same period, the Burlzaff group reported the synthesis of manganese and rhenium carbonyl complexes of the type $[M^{I}(L1)(CO)_3]$ (**6** and **7**), where facial *N,N,O* coordination of a single equivalent of **L1** was achieved due to the strongly-coordinating nature of the carbonyl ligands that blocked the coordination of a second equivalent of supporting ligand.[50] Using this knowledge, the strategy towards monoligated complexes in our group was adapted to include the addition of a biologically relevant co-

ligand (*e.g.* a catecholate), such that the coordination sites *trans* to the facial *N,N,O* supporting ligand would no longer be available for the formation of bisligated $[M(L)_2]$-type complexes.

In an important study by Bruijnincx *et al.*, novel non-heme iron catecholato complexes were developed that are able to successfully model, both structurally and functionally, the active site of extradiol cleaving catechol dioxygenases.[44] A series of high-spin (S = 2) ferrous complexes of the type $[Fe^{II}(L)(Htcc)]$ (**8-10**) were synthesised by combining equimolar amounts of K[L] (L = **L1**, **L2**, **L3**) and $Fe(OTf)_2 \cdot 2MeCN$ in methanol with a methanolic solution of equimolar amounts of tetrachlorocatechol (H_2tcc) and Et_3N (Figure 8). On the basis of ESI-MS and elemental analysis, the complexes were proposed as being neutral, pentacoordinate, complexes featuring the desired anionic *N,N,O* coordination of the supporting ligand and bidentate monoanionic coordination of the catechol. Analogous reactions using 3,5-di-*tert*-butylcatechol (H_2dtbc) afforded complexes $[Fe^{II}(L)(Hdtbc)]$ (**11-13**) that were so air-sensitive that they could not be isolated, and were generated *in situ*.

Corresponding high-spin (S = $^5/_2$) ferric complexes $[Fe^{III}(L)(tcc)]$ (**14-16**) and $[Fe^{III}(L)(dtbc)]$ (**17-19**) were synthesised by reacting equimolar amounts of K[L] (L = **L1**, **L2**, **L3**) and $Fe(NO_3)_3 \cdot 9H_2O$ in methanol with a methanolic solution of the desired catechol and two equivalents of Et_3N (Figure 8).[44] The crystal structure of **16** was obtained, revealing the desired *N,N,O* coordination of **L3**, as well as the bidentate dianionic coordination of tcc to the Fe^{3+} ion. An additional water molecule was observed to bind to

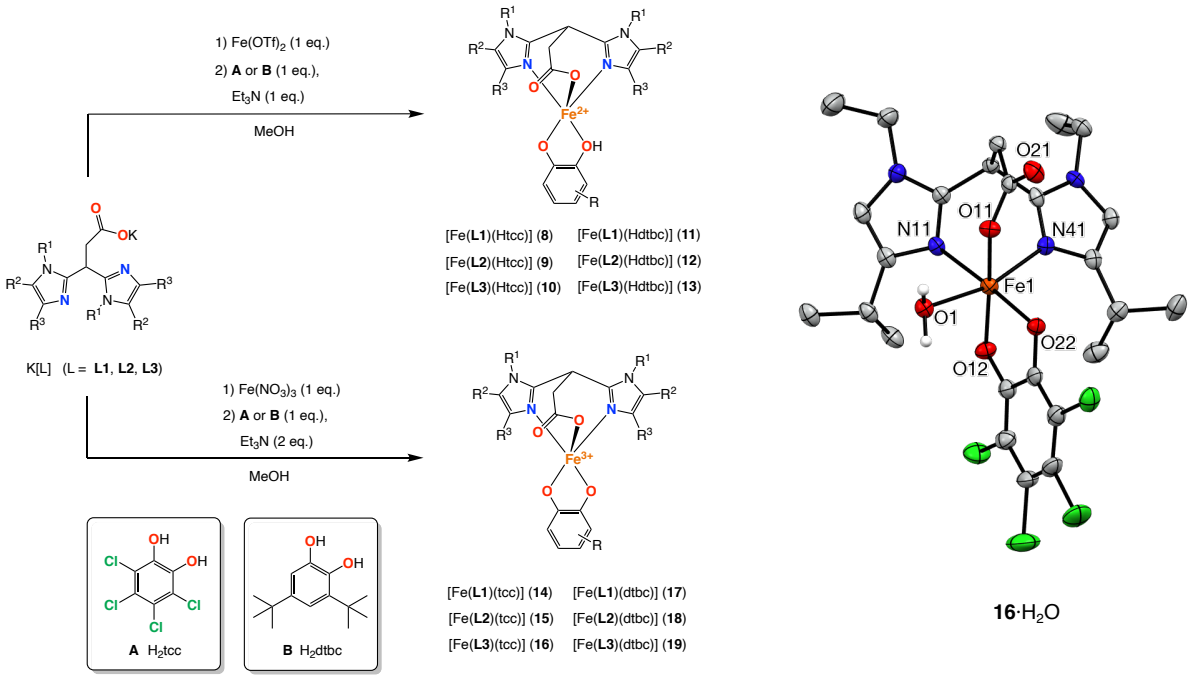

Figure 8. Synthesis of non-heme iron(II) and iron(III) catecholate complexes (**8-19**), supported by **L1**, **L2** and **L3**.[44] The crystal structure of **16**·H_2O is also provided, where all C–H hydrogen atoms have been omitted for clarity and displacement ellipsoids are drawn at the 50% probability level.

the sixth available coordination site, completing the distorted octahedral geometry of the complex. This coordination site can be regarded as a potential site for direct coordination of dioxygen to the metal centre, *cis* to the catecholate co-ligand and *trans* to one of the imidazole heterocycles. Overall, these complexes are some of the most accurate structural models of extradiol-cleaving catechol oxygenase enzymes to date.

Exposing methanolic solutions of complexes **11-13** to air resulted in a rapid colour change from pale yellow-brown to blue-purple. In the electronic absorption spectra, new bands were seen to develop at around 324, 490 and 800 nm, characteristic for catecholato-to-iron(III) LMCT bands and identical to those observed for the independently synthesised complexes **17-19**.[36] The first oxidative transformation was therefore ascribed to a one-electron redox oxidation of the ferrous complexes to their ferric counterparts. This was followed by a much slower colour change from blue-purple to green, ascribed to the oxidative degradation of the complexes as the catechol converted to products of ring-cleavage reactivity and auto-oxidation. The resulting product distribution isolated from the air-exposed reaction mixtures was seen to be strongly dependent on the solvent of choice. Strongly coordinating solvents such as acetonitrile or methanol can bind to the vacant site and are therefore hypothesised to inhibit the binding of dioxygen, thereby resulting predominantly in the formation of the auto-oxidation product, 3,5-di-*tert*-butyl-benzoquinone (Figure 9).

In non-coordinating solvents such as dichloromethane, the vacant site becomes available for dioxygen binding and, consequently, the product distribution was observed to change dramatically. Although a portion of the catechol was still observed to auto-oxidise to the quinone (approx. 45%), a considerable amount of intra- and extradiol cleavage products was also observed, accounting for about 30% of the organic products each. The selectivity for extradiol cleavage was seen to improve upon addition of a proton donor, such as $[Et_3NH]BF_4$. The ability of **11-13** to mediate both extradiol and intradiol cleavage reactivity is quite exceptional, and suggests that the two reaction pathways may share a common intermediate. This supports the hypothesis that extradiol cleaving catechol dioxygenases derive their selectivity from factors beyond the primary coordination sphere.

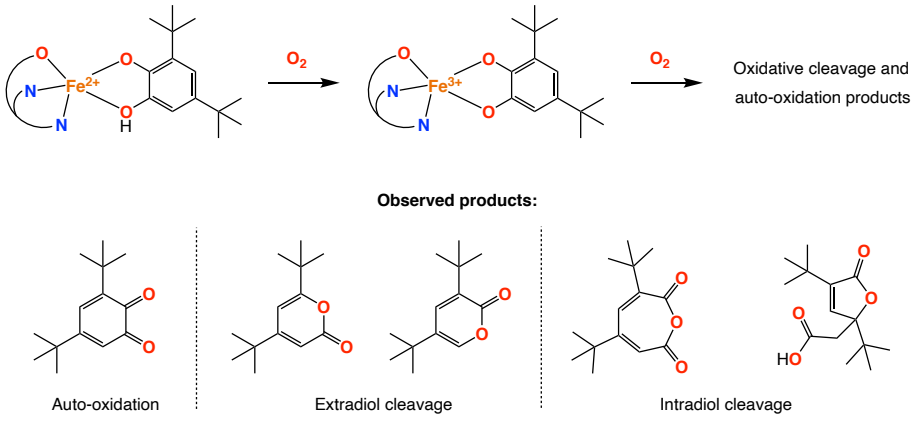

Figure 9. The dioxygen reactivity of complexes **11-13**. Figure adapted from Bruijnincx *et al.*[44]

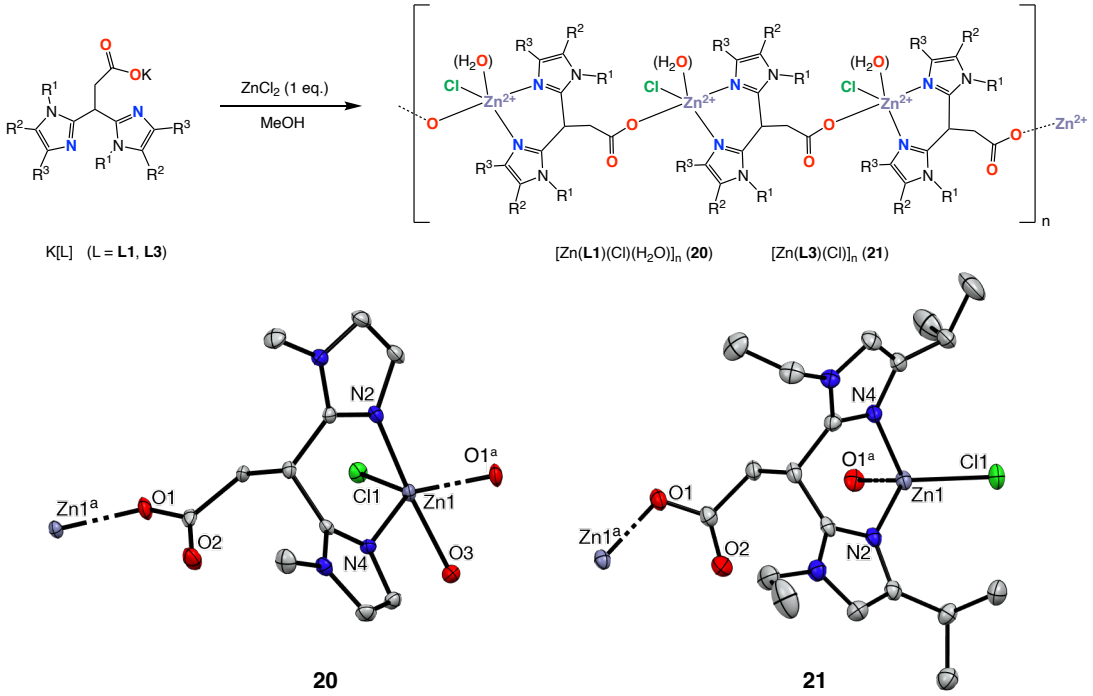

Figure 10. Synthesis of oligomeric zinc complexes **20** and **21**. Individual crystallographic monomers of **20** and **21** are also provided.[48]

One of the disadvantages associated to the BAIP carboxylate ligand series is the tendency for the carboxylate group to engage in alternative, bridging coordination modes. This was first observed by Bruijnincx *et al.* in an attempt to synthesise monoligated zinc complexes.[48] Reacting K[**L1**] or K[**L3**] with an equimolar amount of $ZnCl_2$ in methanol afforded complexes **20** and **21**, respectively, which were identified as having the desired composition, $[Zn^{II}(L)(Cl)]$, but which was identified by means of ESI-MS, NMR, IR and X-ray crystallography as being oligomeric in structure (Figure 10). In each complex, the zinc ion is coordinated by the bidentate bis-imidazole moiety of one ligand molecule and the monodentate carboxylate group of a neighbouring ligand molecule. Each zinc ion is bound to a chloride ligand, and an additional water ligand is observed in **20**.

Bridging coordination modes of the carboxylate group were also observed in the pentanuclear iron cluster complex, $[Fe_5(L5)_4(F)_4](BF_4)_2$ (**22**), obtained from the reaction of K[**L5**] with $Fe(BF_4)_2 \cdot 6H_2O$ in 1:1 stoichiometry (Figure 11).[52] The structure consists of a centrosymmetric cluster containing a total of five iron nuclei of distorted octahedral geometry. Each ligand molecule binds in a κ_3-*N,N,O* fashion to a single iron nucleus, although all ligands further engage in additional bridging carboxylate coordination modes to one or two neighbouring iron atoms. Two of the ligand molecules bridge to one other iron centre by means of one of their carboxylate oxygen atoms (μ_2:κ_1-carboxylate, **A**), whereas the two other ligand molecules bridge to two other iron centres using both of their carboxylate oxygen atoms (μ_3:κ_2-carboxylate, **B**). The fifth iron nucleus is located on the cluster's centre of inversion, bound by four fluoride ions on the equatorial positions and the two μ_3:κ_2-carboxylate groups on the axial positions. Although **22** is the product of BF_4

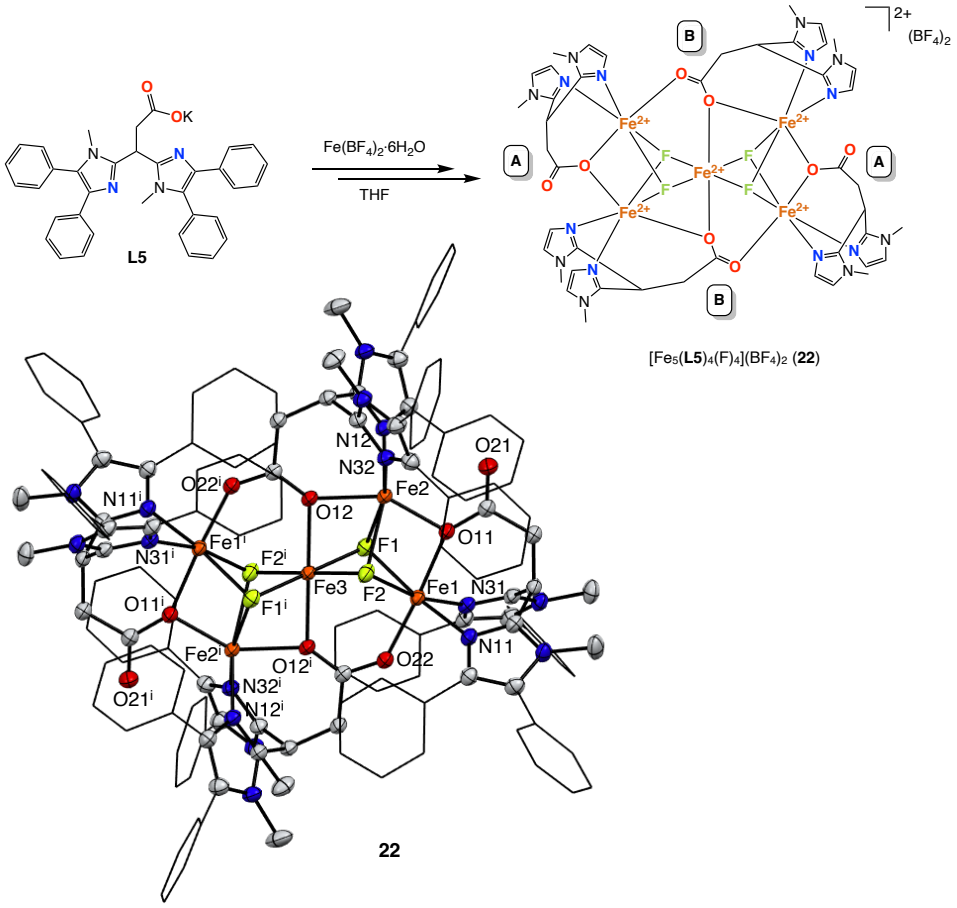

Figure 11. Synthesis of the pentanuclear iron complex **22**.[52] Phenyl groups on the imidazole groups are not drawn for clarity. The crystal structure of **22** is also provided, with BF_4 ions omitted for clarity. Phenyl substituents are depicted in the wireframe format for clarity.

anion degradation, this complex nonetheless demonstrates nicely the multiple different coordination modes with which BAIP carboxylate ligands can interact with metal ions.

In conclusion, it is evident that the coordination chemistry exhibited by BAIP carboxylate ligands is overall rich and diverse, but it can be difficult to control. It is governed by two important factors. The first is the steric bulk of the imidazole heterocycle. This determines the ease with which a second ligand equivalent can coordinate on the opposite face of the metal's coordination sphere. Small ligands such as **L1** and **L2** are capable of forming bisligated complexes, where both ligand molecules coordinate by means of a tridentate κ_3-*N,N,O* coordination mode. In contrast, the sterically more demanding **L3** can only bisligate by chelating in a bidentate κ_2-*N,O* fashion. The second factor is the propensity for carboxylate ligands to bridge when, for example, there is no co-ligand available to complete the coordination sphere of the metal ion. In these cases, the carboxylate ligands may compete to fill these vacant sites. For catalytic applications, it is desirable to avoid the formation of bisligated complexes and complexes featuring alternative ligand coordination modes. These complexes do not model the 2H1C to a high degree of accuracy, and may therefore be considered off-cycle species that could lead to loss of catalyst selectivity or even catalyst de-activation.

Overall, the most promising tactic toward a desired facial, tridentate *N,N,O* mode from a BAIP carboxylate ligand has been the use of co-ligands, such as mono- or dianionic catecholate ligands. The use of various co-ligands also provides opportunities to mimic a myriad of different members of the mononuclear non-heme enzyme superfamily, each of which has its own specific coordination chemistry. Other strategies have involved a modification of the nature of the ligand itself, to an ester, an amide or a phenolate.

6.4.3 Ester Ligands

As was the case for their carboxylate analogues, the BAIP ester ligands can be modulated by changing the nature of the imidazole heterocycle. However, the organic substituent on the ester itself can also be tuned easily (*e.g.* to an *n*-propyl or *tert*-butyl substituent). The BAIP-derived ester family of ligands is depicted in Figure 12. Changing a carboxylate group into an ester functionality also has significant consequences for the electronic properties of the ligand. Most importantly, the neutral configuration of the ester prohibits the ligand from coordinating in an anionic fashion. In many cases, counter-anions are present in the metal complexes formed, as they have the role of balancing the positive charge of the metal ion to which the ligand is bound. Depending on the nature of these counter-cations, the coordination chemistry of the ester ligands changes significantly.

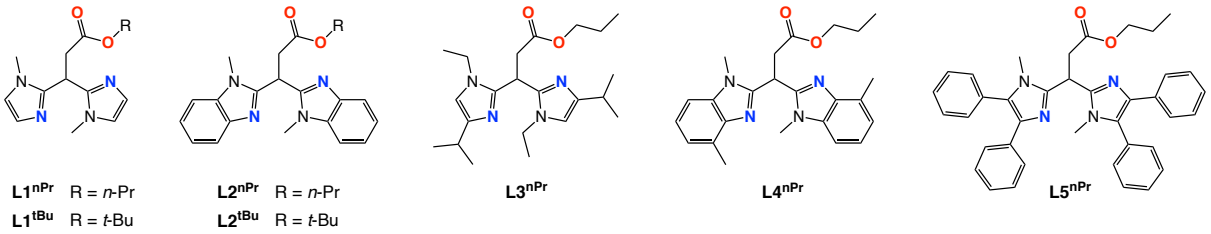

Figure 12. BAIP-derived *N,N,O* ester ligands.

The potential for the **L1^{R}** and **L2^{R}** (R = ^{n}Pr, ^{t}Bu) ester ligands to coordinate in a facial *N,N,O* manner was demonstrated in two separate studies, by Bruijnincx and Moelands.[49,53] Reacting the ligand with Fe(OTf)$_2$·2MeCN in a 2:1 stoichiometry afforded high-spin (S = 2) complexes of the type [Fe^{II}(L)$_2$](OTf)$_2$ (**23**-**24**). From the crystal structures, the ester ligands in all complexes were observed to coordinate by means of a tridentate *N,N,O* binding motif, comprising the two imidazole N-donors and the carbonyl oxygen atom of the ester functionality. All complexes were observed to have distorted octahedral geometries, although some differences could be seen in the manner with which the ligands wrapped themselves around the metal centre. In complexes **23**, **24** and **26**, the ligands coordinate *trans* with respect to each other, meaning that the four N-donors occupy the equatorial positions and the O-donors occupy the axial positions. However, the **L2^{nPr}** ligands in **25** are bound such that the O-donors coordinate *cis* with respect to each other. Although this was tentatively proposed as arising from the lesser steric clash of the *n*-propyl esters compared to that of *tert*-butyl group, it cannot be excluded that the *cis* isomer of **25**

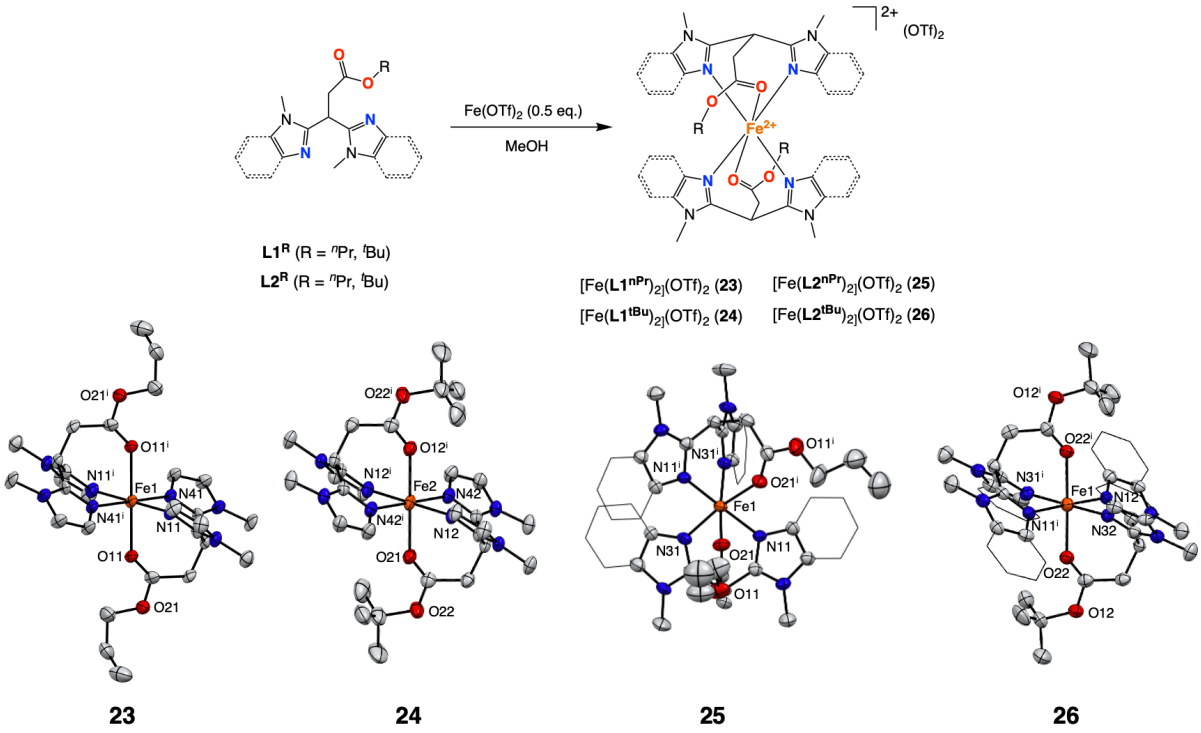

Figure 13. Synthesis and X-ray crystal structures of complexes **23**-**26**.[53] Displacement ellipsoids are drawn at the 50% probability level. H-atoms and non-coordinated OTf anions omitted for clarity. Aromatic benzimidazole rings have been depicted in the wireframe format.

may simply crystallise more easily from solution than the *trans* isomer. Overall, these complexes demonstrate once again the ease with which the **L1** and **L2** bis-benzimidazole backbones can accommodate the κ_3-*N,N,O* coordination of two ligand molecules simultaneously to the metal centre. Furthermore, it demonstrates the relatively small impact that the ester's organic substituents have on the coordination geometry about the metal centre. Due to the coordination of the ester's carbonyl oxygen atom to the metal centre, the organic substituents orientate away from the metal rather than towards it.

The analogous reaction between two equivalents of $\mathbf{L3^{nPr}}$ and $Fe(OTf)_2 \cdot 2MeCN$ (2:1) also afforded a product identified as a bisligated complex, $[Fe(L3^{nPr})_2](OTf)_2$ (**27**), although the presence of three different IR stretches, assigned to *cis*, *trans* and non-coordinating binding modes of the ester ligand, are an indication that the complex exists as several different isomers. This was confirmed by the X-ray crystal structure, where isomeric octahedral (**27a**) and tetrahedral (**27b**) complexes were observed within the same unit cell in a 1:2 ratio (Figure 13). In **27a**, the ligands coordinate with a facial, tridentate *N,N,O* binding motif and their two carbonyl groups are mutually *cis*. In **27b**, two ligand molecules bind the iron centre in bidentate *N,N* fashion, where the ester moiety remains unbound. These results demonstrate nicely the coordinative lability of the neutral ester functionality in $\mathbf{L3^{nPr}}$ that arises from the relatively weak interaction between the metal and the carbonyl group. However, this also indicates that off-cycle species may easily form during catalytic applications, which may lead to catalyst degradation or inactivation.

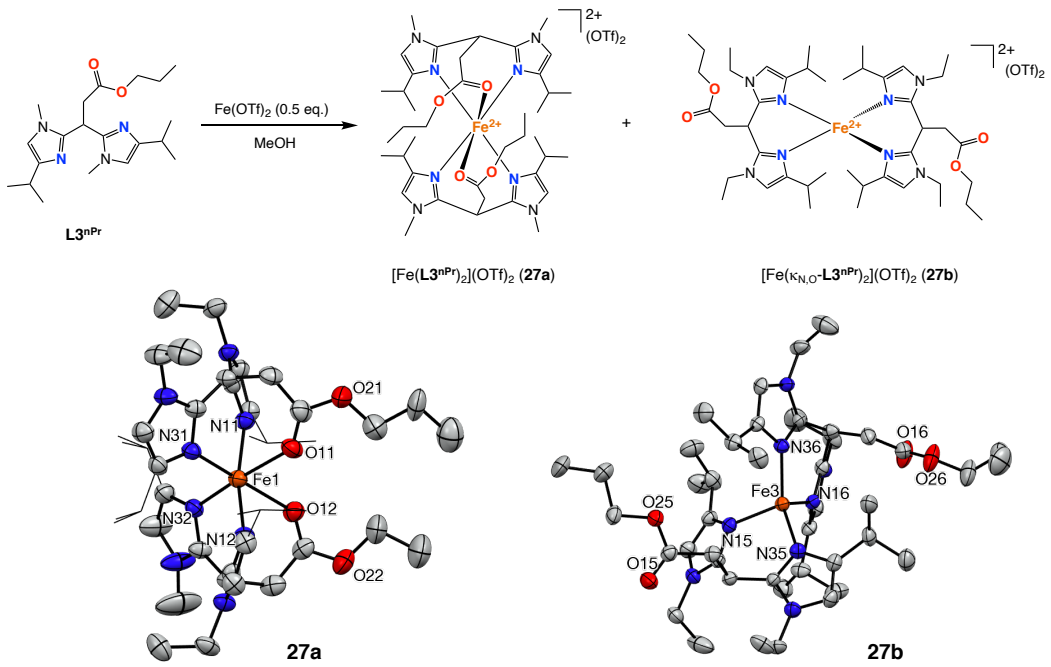

Figure 14. Synthesis and X-ray crystal structures of the of isomeric complexes **27a** and **27b**, where **L3^{nPr}** adopts two different coordination modes.[53] Displacement ellipsoids are drawn at the 50% probability level. H-atoms and OTf anions omitted for clarity.

Catalysis experiments showed that **23** is an active catalyst for the epoxidation and *cis*-dihydroxylation of various olefins, including cyclo-octene, styrene, 1-octene, cyclo-hexene, *trans*-2-heptene and *cis*-2-heptene, for a catalyst/oxidant/substrate ratio of 1:10:1000, with H_2O_2 conversion efficiencies ranging from 39-51%.[51] While the reaction with 1-octene produced the *cis*-diol product in almost 2:1 ratio with respect to the epoxide, reactions with the other substrates showed preferential selectivity for the epoxidation product. To date, only few non-heme iron catalysts featuring a tridentate *N,N,O* ligand are capable of catalysing both epoxidation and *cis*-dihydroxylation. Testing **24**-**27** as catalysis for the oxidation of cyclo-octene resulted in comparable product distributions as that obtained with **23**, although the complexes were observed to be less active than **23**.[57] The lability of the ester functionality is thought to play a vital role in catalysis by enabling *cis*-vacant sites to exist at the high-spin iron centre, enabling the oxidant and the substrates to bind directly to the iron in close proximity. It is likely that the larger size of the imidazole substituents in **25**-**27** reduces the accessibility of the iron centre, thereby reducing the efficacity of catalysis using these complexes.

An important breakthrough was published in a study by Folkertsma *et al.*, which demonstrated that the reaction between **L4^{nPr}** and $Fe(OTf)_2 \cdot 2MeCN$ in equimolar amount resulted in the formation of a mononuclear, high-spin (S = 2) iron complex, $[Fe^{II}(L4^{nPr})(OTf)]_2$ (**28**), in which the ligand coordinates with the desired facial, *N,N,O* binding motif, leaving two vacant sites available for the (loose) coordination of the triflate anionic.[45] This was the first example of a monoligated complex that could form in the absence of a co-ligand. On the basis of DFT calculations, it was proposed that the methyl

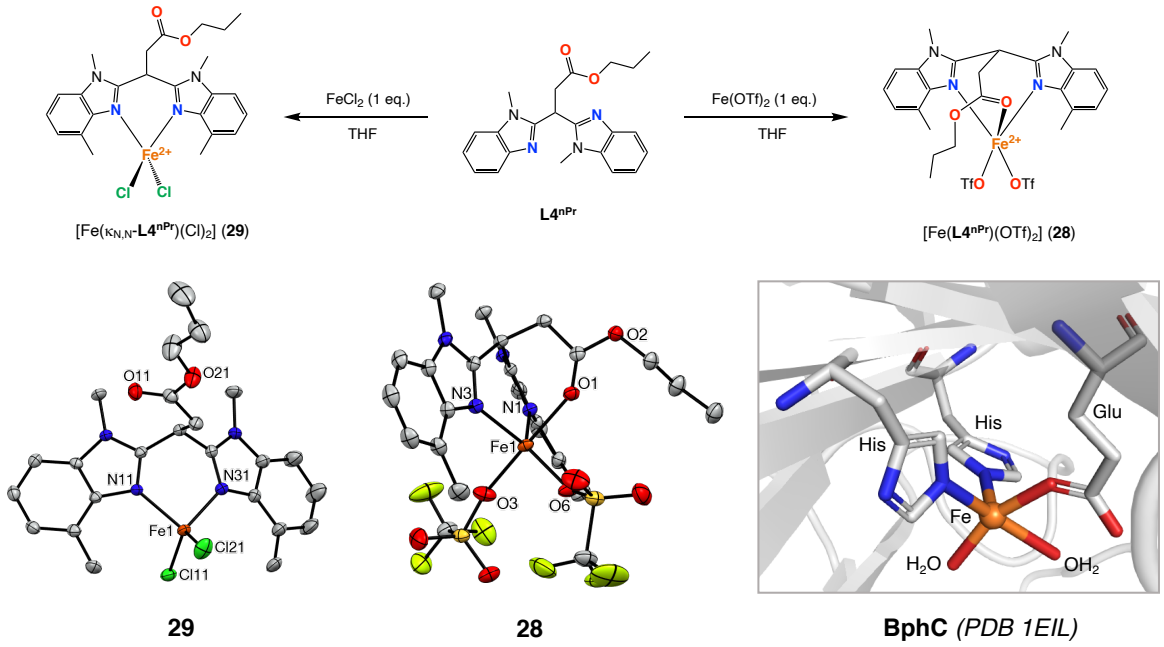

Figure 15. Synthesis of complexes **28** and **29** using **L4^{nPr}**. Crystal structures of both complexes are also provided, with H-atoms omitted for clarity and displacement ellipsoids drawn at the 50% probability level.[45] The crystal structure of the active site of BphC is provided for comparison.[54]

substituents on the 4-position of the benzimidazole rings are responsible for driving the coordination equilibrium towards the thermodynamically favourable formation of **28**. The pentacoordinate nature of **28**, as well as its geometrical parameters in the crystal structure, were observed to model closely the structure of the active site of2,3-dihydroxybiphenyl dioxygenase (BphC), an extradiol-type ring cleaving dioxygenase.[54] Nonetheless, ^{1}H NMR analysis in CD_3CN revealed that multiple paramagnetic species were present in solution, indicating that the complex undergoes coordination equilibria in strongly coordinating solvents. Whether this is simply solvent exchange with the triflate anions or lability of the ester functionality was not determined. Carrying out an analogous reaction using equimolar amounts of **L4^{nPr}** and $FeCl_2$ resulted in the formation of a mononuclear iron complex (**29**) in which **L4^{nPr}** binds in bidentate *N,N* fashion, with a non-coordinating ester functionality. This demonstrates the influence that the strongly coordinating chloride ligands have on promoting the dissociation of the ester moiety.

Given these results, **L5^{nPr}** was developed to incorporate a higher degree of steric bulk on the imidazole heterocycles.[52] Reacting **L5^{nPr}** with $Fe(OTf)_2 \cdot 2MeCN$ in 1:1 stoichiometry afforded a mononuclear, high-spin (S = 2) iron complex, [Fe^{II}(L5^{nPr})(OTf)(THF)](OTf) (**30**), similar in structure to **28** (Figure 16). The iron centre is pentacoordinate and trigonal bipyramidal in geometry (τ = 0.67),[55] bound by the tridentate, facial *N,N,O* arrangement of donor atoms from the supporting ligand, as well as a triflate molecule and a THF molecule, while the second triflate anion remains unbound. The substitutional lability of the triflate anions was subsequently explored using various biorelevant co-ligands, including aminophenol (deprotonated using Et_3N) and sodium pyruvate. Monitoring the reactions

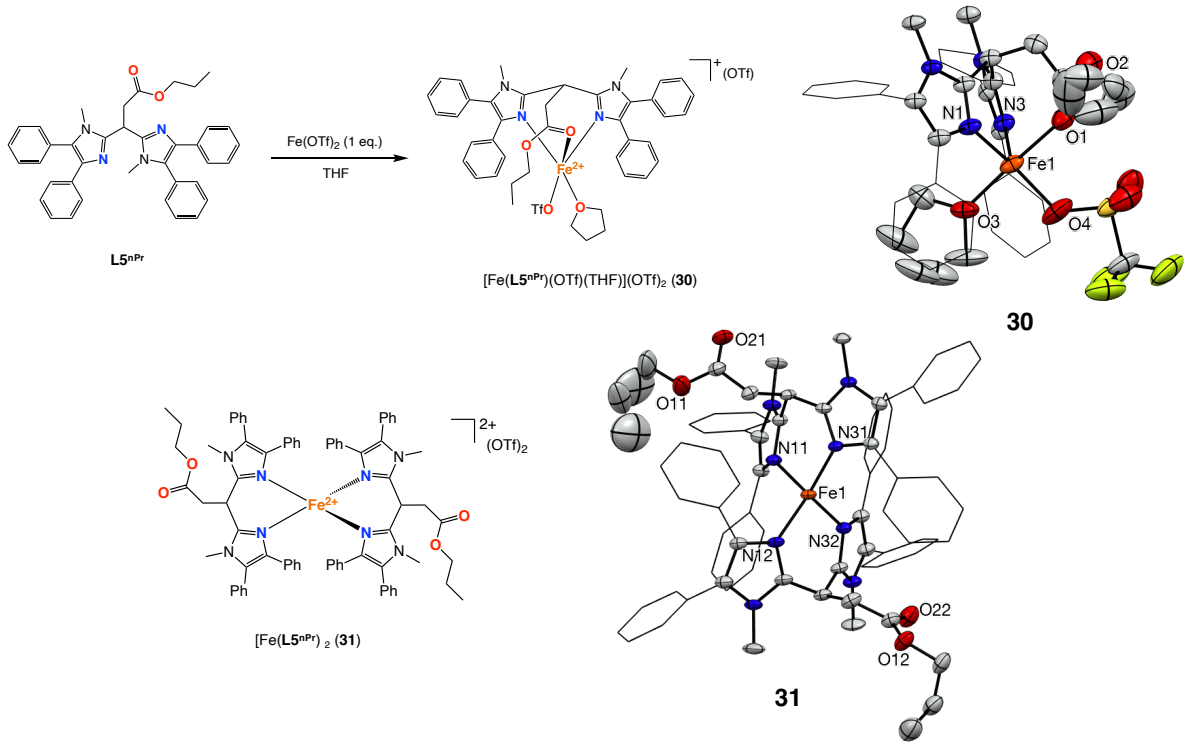

Figure 16. The synthesis of **30**, and the structure of **31**.[52] The crystal structures of the complexes are also provided,[52] with H-atoms omitted for clarity and displacement ellipsoids drawn at the 50% probability level. The imidazole phenyl substituents have been depicted in the wireframe format for clarity. Disorder is present at some of the *n*-propyl substituents, as well as the THF molecules in **30**. Non-coordinating OTf anions have been omitted for clarity.

with ESI-MS revealed the presence of ions corresponding to the desired [Fe(L5^{nPr})(co-ligand)]$^{+}$ complexes, however, the predominant species in both cases was observed to be a bisligated complex, [Fe(L5^{nPr})$_2$]. By means of X-ray crystallography, this complex (**31**) was identified as being tetrahedral in geometry, involving the coordination of two ligand equivalents in bidentate *N,N* fashion, and very similar in structure to **27b**. This result reinforces the trend that the BAIP ester ligands tend to show labile coordination of the ester moiety, thereby increasing the number of available coordination sites on the metal centre, which itself could be a driving force for the formation of these kinds of bisligated, homoleptic complexes.

Overall, tuning the design of the BAIP ester ligands has proven to be successful for achieving the formation of monoligated complexes featuring the desired facial, tridentate *N,N,O* coordination of the bioinspired ligand framework. The factors that influence the coordination of the BAIP ester ligands are the steric properties of the imidazole heterocycles, in particular, the bulk of the organic substituents that point towards the metal centre upon chelation. Coordination of the ester moiety seems to be particularly sensitive to the nature of the counter anions present. Generally, in the presence of triflate ligands, the ester is observed to bind by means of its carbonyl functionality. However, in the presence of chloride ligands, the ester is seen to dissociate from the iron centre. Based on the results obtained so far, coordination of the ester moiety seems not to be dependent on

the nature of its tethered organic substituent. Catalytic activity for the bisligated iron complexes containing BAIP ester ligands is dependent on the lability of the ester functionality, which enables the oxidant and substrate to bind directly to the metal centre. However, catalytic activity seems to decrease when the size of the imidazole heterocycle increases sufficiently enough to hinder the approach of oxidants or substrates into the coordination sphere of the iron metal.

6.4.4 Amide Ligands

The BAIP ligand family has also been modified to incorporate an amide functionality. This modification can be regarded as the BAIP-derived sister ligand design to the Ph-DPAH ligand (DPAH = di(2-pyridyl)methylbenzamide) previously reported by the group of Que, which also has an *N,N,O* donor set.[56] Amides are known to possess two different coordination modes, dependent on the protonation state of the amido nitrogen atom. In their neutral state, amides are most likely to coordinate through their carbonyl oxygen atom, as do the previously described BAIP ester ligands. Alternatively, deprotonation of the amide nitrogen atom could provide an anionic N-donor site, whose interaction with a metal atom is predicted to be stronger than that of an analogous carboxylic acid, due to the stronger Lewis acidity of its conjugate base.

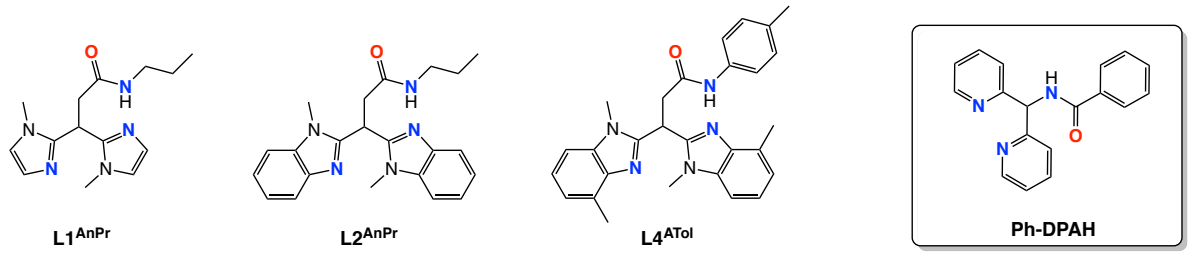

Figure 17. BAIP-derived *N,N,O* amide ligands, with the Ph-DPAH ligand displayed for comparison.

The coordination chemistry of **L1^{AnPr}** and **L2^{AnPr}** was explored in a study by Moelands *et al.*[53] Reacting **L1^{AnPr}** or **L2^{AnPr}** with $Fe(OTf)_2 \cdot 2MeCN$ in a 2:1 molar ratio in methanol afforded complexes **32** and **33**, respectively, of the type $[Fe^{II}(L)_2](OTf)_2$. Their crystal structures reveal centrosymmetric, octahedral geometries in both cases, where the imidazole N-donors occupy the equatorial plane and the amide oxygen atoms coordinate on the axial positions, *trans* with respect to each other. As was previously observed for complexes **23**, **24** and **26**, this particular orientation of the amide results in the tethered *n*-propyl groups pointing away from the metal centre, thereby exerting little effect on the geometry about the metal centre. The coordination of **L1^{AnPr}** and **L2^{AnPr}** is similar to that observed by Oldenburg *et al.* for complex $[Fe^{II}(Ph\text{-}DPAH)_2](OTf)_2$, where Ph-DPAH also coordinates facially, with the O-donors orientated *trans* with respect to each other.[56] The Fe–O bond lengths in **32** and **33** (2.157(5) Å and 2.0886(13) Å, respectively) are somewhat shorter than those in **23**-**26**, which range between 2.145(4) Å and 2.249(4) Å. This might reflect the more strongly coordinating nature of the amide carbonyl groups compared to

the ester ones. Cyclic voltammetry (CV) also revealed that **33** has a much lower Fe^{II}/Fe^{III} oxidation potential ($E_{p,a}$ = 0.63 V) than either **23** or **26** ($E_{p,a}$ = 0.82 V and 0.95 V, respectively).

In view of their greater affinity for (electrochemical) oxidation, complexes **32** and **33** were also tested as catalysts for oxidation of cyclooctene. However, both complexes were observed to exhibit low catalytic activity, which did not surpass the performance of the analogous ester complexes. A maximum of 5% and 8% in the conversion of H_2O_2 to oxidised products was obtained for **32** and **33**, respectively (catalyst/oxidant/substrate ratio of 1:20:1000). Furthermore, **33** exhibited no selectivity towards either the epoxide or diol product. Although it is not unprecedented for non-heme iron complexes with mixed N,O-donor ligand sets to exhibit low turnover numbers, the low (or lack of) product selectivity obtained with **32** and **33** compared to Que's Ph-DPAH system, for example, make them unfavourable for further catalysis applications.

More recently, attempts were made in our group to achieve anionic coordination modes of the amide ligand $\mathbf{L4^{ATol}}$. This ligand was designed to incorporate the bis-1,4-dimethylbenzimidazole ligand scaffold previously reported by Folkertsma *et al.*,[45] whose additional methyl groups were predicted to promote the formation of monoligated

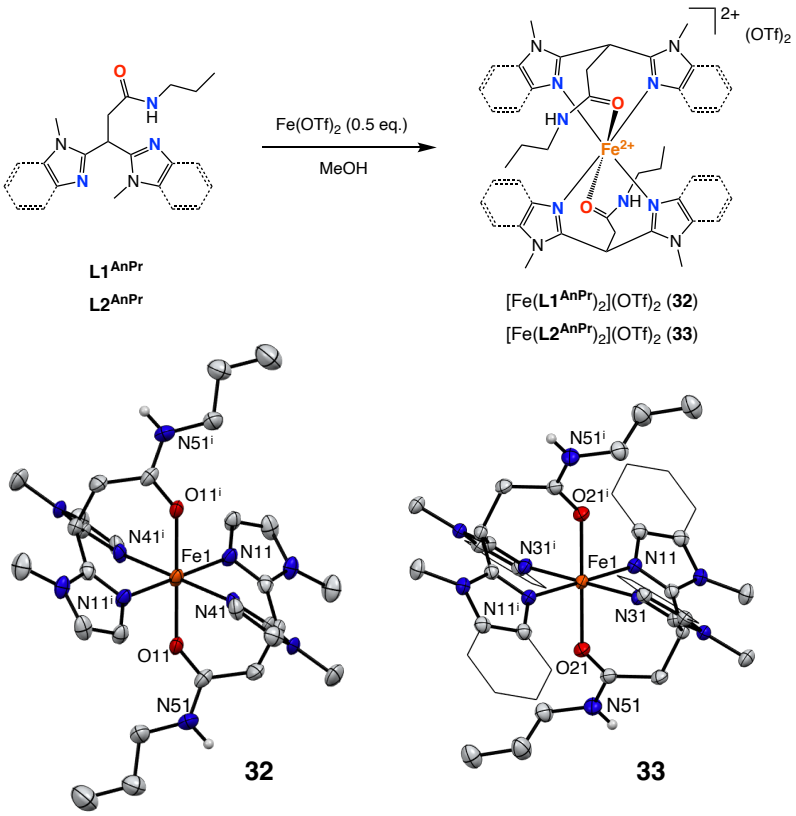

Figure 18. Synthesis of complexes **32** and **33**. Their respective crystal structures are also provided, with all C–H hydrogen atoms and the non-coordinated OTf anions omitted for clarity. Displacement ellipsoids have been drawn at the 50% probability level. Aromatic rings of the benzimidazole substituents in **33** have been depicted in the wireframe format for clarity.[53]

complexes. Mixing **L4^{ATol}** with one equivalent Fe(OTf)$_2$·2MeCN in THF resulted in the almost instantaneous precipitation of a white solid, to which one equivalent of NEt$_3$ was added, with the hypothesis that the amide N–H bonds would be weakened upon coordination to iron. The resulting product was analysed by ^{1}H NMR spectroscopy, which indicated that a single paramagnetic species was present in solution. Crystal structure determination revealed that a mononuclear, bisligated iron(II) complex had formed, [Fe^{II}(L4^{ATol})$_2$](OTf)$_2$ (**34**), (Figure 19). The amide proton can clearly be observed, and the amides bind in their neutral form to the iron centre by means of their carbonyl oxygen atoms, as was the case in **32** and **33**. Surprisingly, both ligand molecules are bound by a facial *N,N,O* coordination motif, each wrapped around the metal ion such that the amide carbonyl functionalities are *cis* to each other, which discredits the previous hypothesis that the bis(1,4-dimethylimidazole) scaffold only favours monoligation. A similar result was obtained upon reaction of **L4^{ATol}** with FeCl$_2$ in a 1:1 stoichiometry, followed by the addition of a base to attempt deprotonating the amide groups. Crystals suitable for X-ray diffraction were obtained by slow evaporation of an acetonitrile solution of the product, but the crystal structure revealed that a mononuclear, monoligated iron(II) complex, [Fe^{II}(L4^{ATol})(Cl)$_2$] (**35**), had formed, very similar in structure to **29** (Figure 19). The amide is protonated and therefore neutral, and is not bound to the iron centre.

In summary, the BAIP-derived amide ligands show coordination chemistry similar to that observed for the ester family of ligands. The amide moiety can bind in its neutral form as an O-donor by means of its carbonyl oxygen atom. Coordination of the amide in this

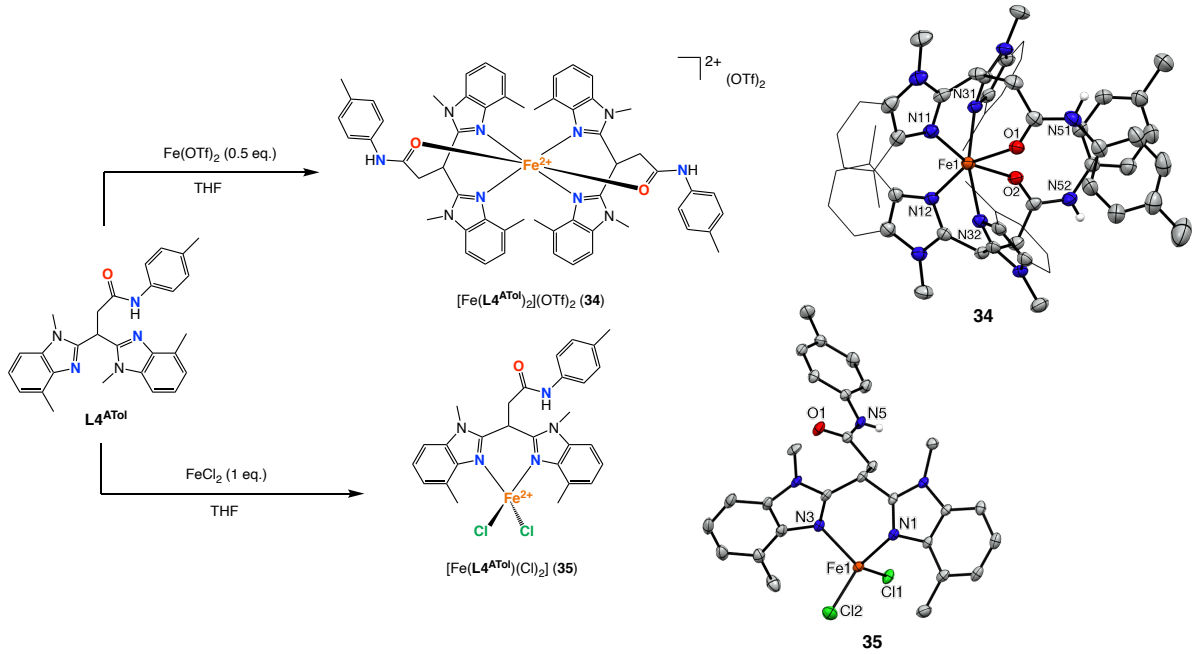

Figure 19. Synthesis and crystal structures of **34** and **35**. All C–H hydrogen atoms are omitted for clarity and displacement ellipsoids are drawn at the 50% probability level. The non-coordinated OTf anions in **34** are not depicted. Aromatic benzimidazole rings in **34** are depicted in the wireframe format for clarity. X-ray crystal structure determination details can be found in Appendix E.

manner was observed to be sensitive to the nature of the counter anions present, where strongly binding anionic (*e.g.* chloride) promote amide coordination lability. To date, no successful attempts at deprotonating the amide have been made. It is therefore unknown whether this family of ligands could adopt an alternative anionic *N,N,N* facial motif.

6.4.5 Phenolate Ligands

As previously mentioned, *N,N,O* phenolate ligands are an attractive means with which to achieve anionic O-donor coordination while simultaneously having the option to tune the steric and electronic properties of the phenol ring by means of its *ortho*- and *para*-substituents. In some ways, this may be regarded as a convenient way to combine the advantages associated to the BAIP carboxylate and ester ligands, previously described in this review. However, the phenolate ligand design diverges significantly in terms of the redox non-innocence character associated to aromatic phenolate rings compared to acid and ester groups. The use of 3,5-disubstituted phenolates in particular may stabilise the accumulation of spin density on the ligand scaffold and could be relevant for biomimetic studies of mononuclear non-heme enzymes such as intradiol cleaving dioxygenases (iron-based)[57] or galactose oxidase (copper-based)[58] that contain a tyrosinate at their active site.

Several pyrazole-derived *N,N,O* phenolate ligands have been described in the literature, some of the most notable contributions of which come from the Carrano group.[42,59–61] Our group has developed a series of similar imidazole-derived *N,N,O* phenolate ligands, depicted in Figure 20. As can be seen, the connectivity of the phenolic oxygen atom within the ligand scaffold is *iso*-structural to that of the anionic oxygen atom of the BAIP carboxylate ligands. In addition, the phenolate ligands include a methoxy group, installed on the quaternary carbon backbone, which ensures that the only site available for deprotonation is the phenolic O-H group.

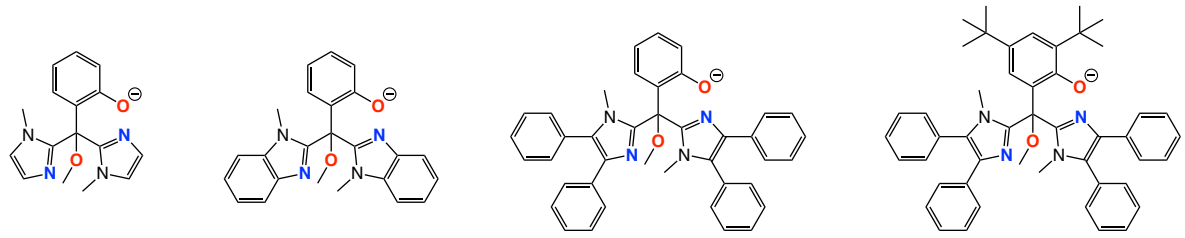

Figure 20. The *N,N,O* phenolate ligands used in the group of Klein Gebbink.

The facial *N,N,O* capping potential of **ImNNO** was first explored by Bruijnincx *et al.* in a study focused on the structural modelling of intradiol cleavage dioxygenase enzymes.[62] Deprotonation of the ligand using NEt_3, followed by reaction with half an equivalent of $Fe(NO_3)_3 \cdot 9H_2O$ afforded a high-spin ($S = {}^5/_2$) bisligated complex, $[Fe^{III}(ImNNO)_2](NO_3)$ (**36**). The crystal structure of the complex revealed that the iron has a distorted octahedral geometry and that the ligand molecules orientate themselves such that the phenolic oxygen

atoms are mutually *cis* (Figure 21). As well as demonstrating the ability of the ligand to bind in the desired coordination mode, this complex demonstrates once again the ease with which two ligand equivalents can coordinate simultaneously in a κ_3-*N,N,O* fashion to the metal ion.

The synthesis of iron(III) catecholato complexes supported by **ImNNO** was conducted according to the scheme depicted in Figure 21, which is similar to the method previously used for the synthesis of **8**-**19**. On the basis of elemental analysis and EPR, complexes **37** and **38** were identified as neutral, pentacoordinate, high-spin ($S = {}^5/_2$) iron(III) complexes, whose coordination spheres feature the facial monoanionic *N,N,O* coordination of **ImNNO** as well as the dianionic, bidentate coordination of the catecholate. The X-ray crystal structure of **37** confirmed the tridentate *N,N,O* coordination of the supporting ligand as well as the bidentate coordination of the catecholate ligand. The co-crystallised water molecule is proposed to occupy the vacant coordination site of the iron centre, *cis* to the catecholate O-donors, which would be available for the binding of dioxygen. Overall, the crystal structure obtained for **37**·H_2O is very similar to that obtained for **16**·H_2O, with the only significant difference being the nature of the O-donor (Figure 21). One of the most important differences is the longer Fe–O(phenolato) bond in **37**·H_2O (2.006(2) Å) compared to the Fe–O(carboxylate) bond in **16**·H_2O (1.9516(18) Å). Overall, complexes **37** and **38** were established as some of the closest biomimetic structural models of an intradiol cleavage dioxygenase enzyme-substrate complex obtained to date.

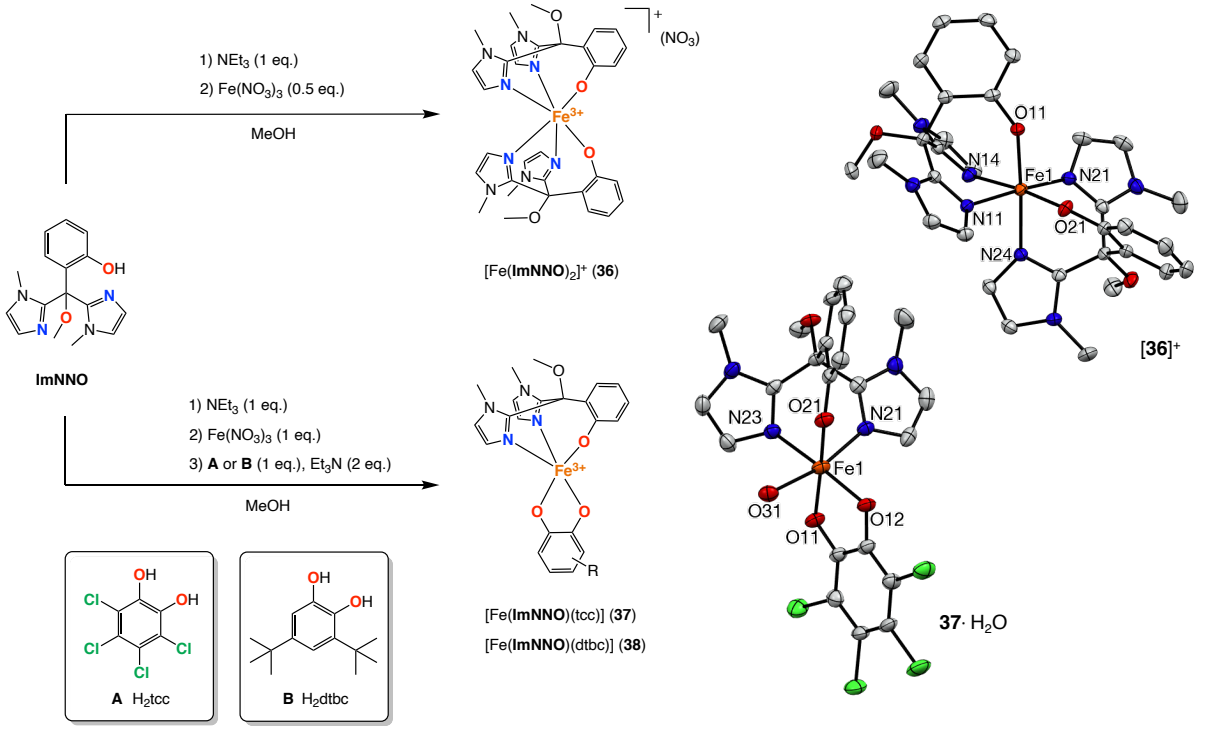

Figure 21. Synthesis of complexes **36**-**38**. The crystal structures of **36** and **37**·H_2O are also provided. H-atoms have been omitted for clarity and displacement ellipsoids are drawn at the 50% probability level. The NO_3 anion in **36** has been omitted for clarity.[62]

The oxidation of **38** in air was studied by means of UV-vis, ^{1}H NMR and GC-MS, in both coordinating and non-coordinating solvents. Overall, the conversion of the catechol to oxidised products was observed to take place much more slowly than **19**, only reaching full conversion after a period of approximately two weeks. This slow reactivity was ascribed to the quenching effect that the anionic mixed *N,O*-donor ligand scaffold has on the Lewis acidity of the ferric ion. Strikingly, the product distribution was seen to be much less dependent on the nature of the solvent used for the reaction compared to complexes **11-13**. Furthermore, only approximately 10% of quinone formation (auto-oxidation product) was observed when conducting the reaction in acetonitrile, with 90% of the products deriving from oxidative cleavage reactivity. Overall, no preferential selectivity for either extradiol or intradiol cleavage products was observed, which enabled the conclusion to be made that the factors determining intradiol or extradiol cleavage reactivity in catechol cleaving dioxygenases must in part be determined by factors beyond the primary coordination sphere of the metal ion.

As the most recent contribution to the development of *N,N,O* ligands in our group, this thesis has explored the coordination chemistry of the bulkier bis-imidazole-derived *N,N,O* phenolate ligands **BenzImNNO**, **Im^{Ph2}NNO** and **Im^{Ph2}NNO^{tBu}**. The results of these efforts are detailed throughout this thesis, and will be briefly discussed here.

Reacting **BenzImNNO** with 1 equiv. ZnX_2 (X = Cl, OTf) produces dinuclear complexes of the type $[Zn(BenzImNNO)_2ZnX_2]$ (Figure 22). In these complexes, one of the zinc ions is octahedral, facially capped by two κ_3-*N,N,O* ligand molecules, while the other zinc ion is tetrahedral, bound to both ligand phenolic O-donors.[63] Reacting **BenzImNNO** with 0.5 equiv. $ZnCl_2$ affords a mixture of products, including the mononuclear, bisligated complex $[Zn(BenzImNNO)_2]$ and some dinuclear complex $[Zn(BenzImNNO)_2ZnCl_2]$. It would seem, therefore, that formation of a bisligated complex is thermodynamically favourable, and that the excess ZnX_2 in solution is stabilised by coordination of the phenolate O-donors, resulting in the overall dinuclear complex structure.

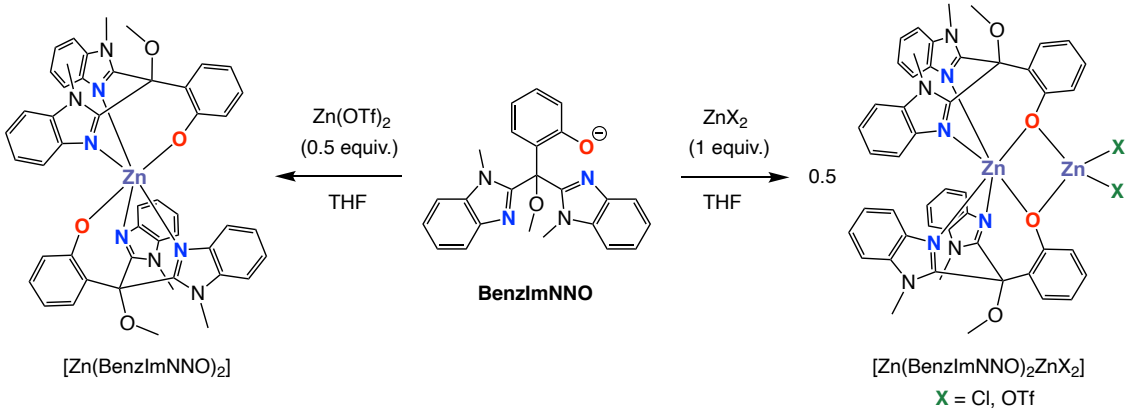

Figure 22. Synthesis of mono- and dinuclear zinc complexes supported by **BenzImNNO**.

In contrast, reacting the bulkier **Im^{Ph2}NNO** ligand with 1 equiv. $M(OTf)_2$ (M = Fe, Zn) affords dinuclear complexes of the type $[M_2(Im^{Ph2}NNO)_2(OTf)_2]$ (Figure 23). These complexes have a unique, cyclic structure that arises from the bridging μ_2:κ_2-*N,N*:κ_1-*O* coordination mode of the **Im^{Ph2}NNO** ligand.[63] The two metal centres are located on facially opposing sites,[64] and are both formally bound by an *N,N,O* coordination motif involving two imidazole N-donors from one ligand molecule and the anionic O-donor from a second ligand molecule. This dinuclear complex architecture is retained upon substitution of the OTf ligand for a thiophenolate (SPh) co-ligand. The formation of these complexes showcases the increased steric demands of the **Im^{Ph2}NNO** ligand and the consequences of the increase in steric bulk on the coordination chemistry of the ligand.

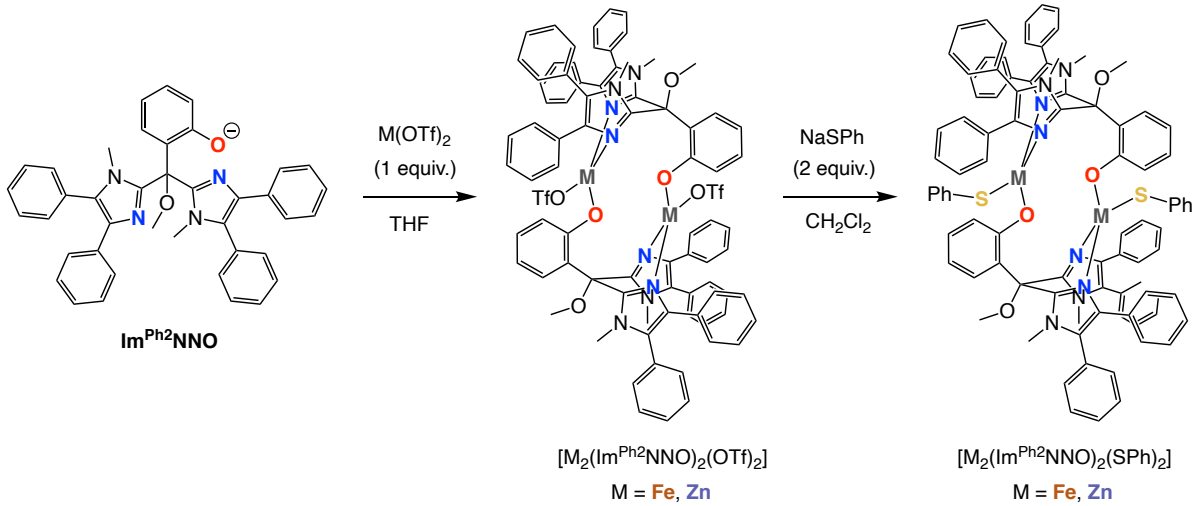

Figure 23. Synthesis of dinuclear iron and zinc complexes supported by **Im^{Ph2}NNO**.

The overall steric bulk of the bis-imidazole *N,N,O* phenolate ligands was further increased by incorporating *tert*-butyl substituents on the *ortho* and *para* positions of the phenolate ring, giving rise to ligand **Im^{Ph2}NNO^{tBu}**. Reacting this bulky ligand with 1 equiv. MCl_2 (M = Fe, Zn) affords mononuclear, tetracoordinate $[M(Im^{Ph2}NNO^{tBu})(Cl)]$ complexes cleanly and in very high yield (Figure 24).[65] The complexes are bound by the desired facial, anionic *N,N,O* donor set of the ligand scaffold, and the chloride ligand is subsequently shown to be readily substituted for bio-relevant co-ligands such as monodentate thiolates (SR, R = ^{t}Bu, Bn, Ph, Mes, 4-OMe-Ph, 4-CF_3-Ph) or bidentate α-ketoacids such as benzoylformate (BF). Importantly, the tridentate, anionic *N,N,O* coordination of the **Im^{Ph2}NNO^{tBu}** is retained in all cases, and is also very well-defined in the solution state. The $[M(Im^{Ph2}NNO^{tBu})(Cl)]$ complexes may therefore be regarded as convenient synthons from which to synthesise a range of different model complexes relevant to different sub-classes of mononuclear non-heme iron enzymes. Similarly, the **Im^{Ph2}NNO^{tBu}** ligand is a highly attractive bioinspired modelling platform with which to further investigate the role of the 2H1C in non-heme enzyme reactivity.

Overall, the coordination studies with *N,N,O* phenolate ligands **BenzImNNO**, **Im^{Ph2}NNO** and **Im^{Ph2}NNO^{tBu}** demonstrated that the steric bulk of the ligand's constituent imidazole groups and the degree of substitution on the phenolate ring have a significant impact on the coordination mode of the phenolic O-donor and, consequently, on the nuclearity of the complexes. This is related to the ease with which the phenolate oxygen atom can coordinate through either its proximal or distal lone pair (see further discussion in Chapter 2 of this thesis).

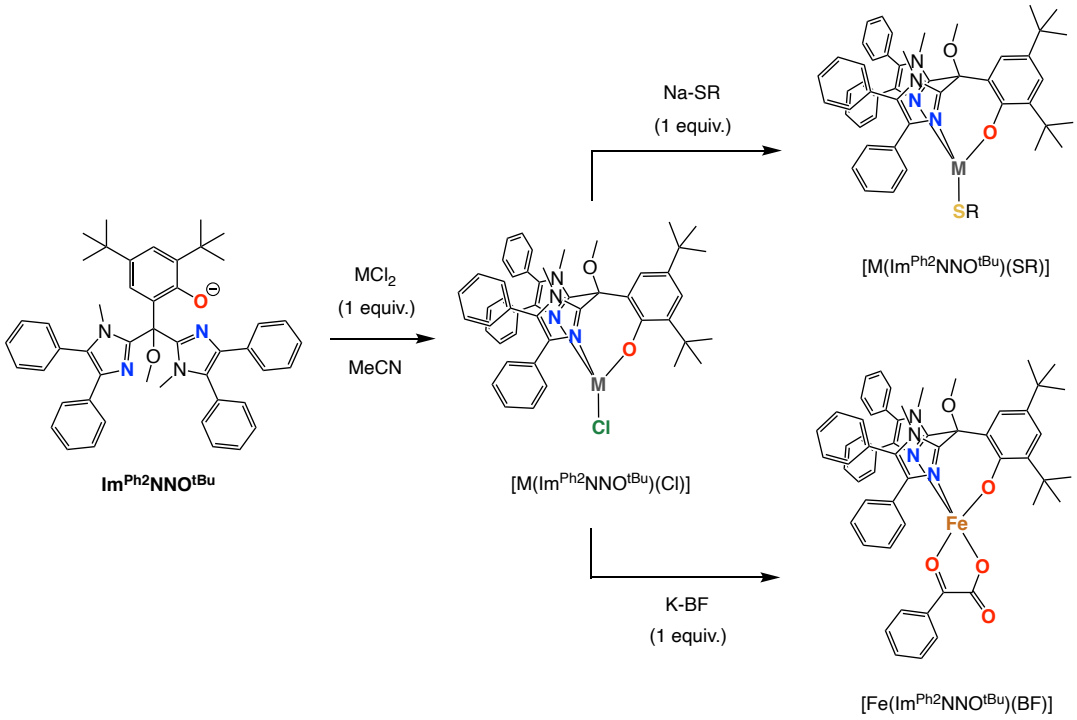

Figure 24. Synthesis of mononuclear *N,N,O*-bound metal(II) chloride complexes using ligand **Im^{Ph2}NNO^{tBu}** (M = Fe, Zn). Substitution of the chloride ligand by monodentate thiolate co-ligands (SR where R = ^{t}Bu, Bn, Ph, Mes, 4-OMe-Ph, 4-CF_3-Ph) or bidentate benzoylformate (BF) leads to the formation of tetra- and pentacoordinate *N,N,O*-bound complexes that are relevant for modelling a diverse range of non-heme iron enzymes.

Finally, it is worth noting that electrochemical investigations of the [Fe(Im^{Ph2}NNO^{tBu})(X)] (X = Cl, SR, BF) complexes by cyclic voltammetry consistently show the iron centre to be more prone to oxidation than the redox non-innocent phenolate moiety. Although this adheres mechanistically to the oxidation reactivity of non-heme iron enzymes, reactivity studies of these complexes using various oxidants (*e.g.* O_2 or $[Ph_3C]PF_6$) reveal that ligand degradation reaction may occur, which derives from the redox non-innocence of the ligand scaffold. One such example is that oxidation of the phenolate moiety to its quinone form can occur, with concomitant loss of the ligand backbone's methoxy group. Similarly, coordination studies using $FeCl_3$ demonstrate that methyl cleavage of the methoxy group occurs, likely enabled by the Lewis acidic nature of the ferric precursor.

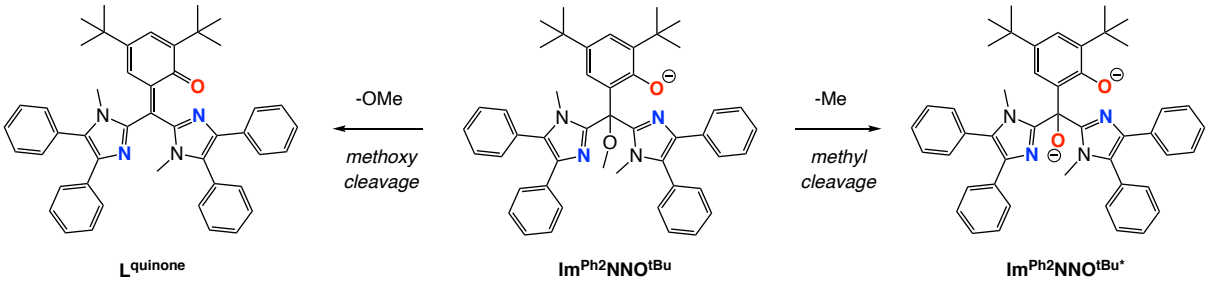

Figure 25. Examples of ligand degradation products observed for **Im^{Ph2}NNO^{tBu}**.

6.5 Conclusion

Our group has focused on the design of the facial *N,N,O* ligands derived from the so-called "BAIP" ligand scaffold, which incorporate the biologically relevant imidazole heterocycle, as well as a range of different O-donors, including carboxylates, esters, secondary amides and phenolates. These ligands have been designed to model the structural features of the 2H1C as closely as possible.

By varying the nature of the steric component of the imidazole heterocycle as well as the nature of the O-donor, the geometric and electronic properties of the resulting metal complexes can be tuned, and, therefore, their reactivity and performance in catalysis can also be modulated. Generally, it has been observed that increasing the steric bulk on the imidazole heterocycles is the most promising method towards the formation of thermodynamically stable mononuclear, monoligated complexes. In the case of the phenolate ligands, adding bulky substituents *ortho* to the phenolate O-donor promotes the desired *N,N,O* coordination mode. Other studies have also shown that use of a co-ligand can help circumvent the formation of bisligated complexes. Overall, mononuclear, monoligated complexes that feature the desired facial *N,N,O* coordination have been obtained using BAIP carboxylate, ester and phenolate ligands.

Although the *N,N,O* ligands discussed in this perspective were specifically designed to structurally model the 2H1C, this has not always guaranteed their ability to successfully model the functional aspects of non-heme iron enzyme active sites. Indeed, reactivity studies by Bruijnincx *et al.* involving structural model complexes of intra- and extradiol cleaving catechol dioxygenase enzymes did not reveal any particular trends in selectivity for either intra- or extradiol cleavage reactivity. While this may in part be due to unknown coordination equilibria taking place in solution (*e.g.* ligand lability or solvent coordination), it is also an indication that enzyme reactivity is governed by factors greater than simply the first coordination sphere of the enzyme active site. These effects are extremely difficult to model artificially, and present many new challenges in the development of bioinspired iron complexes and non-noble metal catalysts. Nonetheless, catalytic tests involving bisligated BAIP ester-bound iron complexes (*e.g.* complex **23**) show the ability to catalyse both *cis*-dihydroxylation as well as epoxidation of olefins. To date, these complexes constitute

members of a small, select family of non-heme iron(II) complexes bound to tridentate *N,N,O* ligands that exhibit such reactivity.

Overall, this perspective showcases the rich and diverse coordination chemistry of bioinspired *N,N,O* ligands. It also illustrates how much potential has yet to be unlocked in this field, and that much can still be learned about *N,N,O* ligand design as well as important mechanistic aspects of the 2H1C such as the role of the anionic O-donor in determining enzyme reactivity and selectivity. With the diverse family of BAIP-derived *N,N,O* ligands at hand, the current status in the development of the ligands enables us to carry out dedicated coordination chemistry and spectroscopic studies in order to mimic specific enzyme active site structural parameters and possibly address trends in the reactivity exhibited by the different classes of 2H1C-containing mononuclear non-heme iron enzymes.

6.6 Author Contributions

E.C.M. and B.K.G. wrote the manuscript. E.M. synthesised complexes **34** and **35**. E.F. and P.G. performed experiments related to complexes **22**, **30** and **31**. H.A.N. performed experiments towards the synthesis of ligand $\mathbf{L4^{ATol}}$. M.L. performed X-ray crystal structure determinations. All authors provided comments on manuscript during its preparation.

6.7 References and Notes

(1) Bruijnincx, P. C. A.; van Koten, G.; Klein Gebbink, R. J. M. *Chem. Soc. Rev.* **2008**, *37*, 2716–2744.
(2) Que, L. J. *Nat. Struct. Biol.* **2000**, *7*, 182–184.
(3) Costas, M.; Mehn, M. P.; Jensen, M. P.; Que Jr., L. *Chem. Rev.* **2004**, *104*, 939–986.
(4) Lange, S. J.; Que, L. J. *Curr. Opin. Chem. Biol.* **1998**, *2*, 159–172.
(5) Kal, S.; Que, L. *JBIC J. Biol. Inorg. Chem.* **2017**, *22*, 339–365.
(6) Koehntop, K. D.; Emerson, J. P.; Que, L. *J. Biol. Inorg. Chem.* **2005**, *10*, 87–93.
(7) de Visser, S. P.; Straganz, G. D. *J. Phys. Chem. A* **2009**, *113*, 1835–1846.
(8) Price, J. C.; Barr, E. W.; Tirupati, B.; Bollinger Jr., M. J.; Krebs, C. *Biochemistry* **2003**, *42*, 7497–7508.
(9) Tamanaha, E.; Zhang, B.; Guo, Y.; Chang, W.; Barr, E. W.; Xing, G.; St. Clair, J.; Ye, S.; Neese, F.; Bollinger, J. M.; Krebs, C. *J. Am. Chem. Soc.* **2016**, *138*, 8862–8874.
(10) Krebs, C.; Galonić Fujimori, D.; Walsh, C. T.; Bollinger, J. M. *Acc. Chem. Res.* **2007**, *40*, 484–492.
(11) Valegård, K.; van Scheltinga, A. C. T.; Lloyd, M. D.; Hara, T.; Ramaswamy, S.; Perrakis, A.; Thompson, A.; Lee, H.-J.; Baldwin, J. E.; Schofield, C. J.; Hajdu, J.; Andersson, I. *Nature* **1998**, *394*, 805–809.
(12) Vetting, M. W.; Wackett, L. P.; Que, L.; Lipscomb, J. D.; Ohlendorf, D. H. *J. Bacteriol.* **2004**, *186*, 1945–1958.
(13) O'Brien, J. R.; Schuller, D. J.; Yang, V. S.; Dillard, B. D.; Lanzilotta, W. N. *Biochemistry* **2003**, *42*, 5547–5554.
(14) Roach, P. L.; Clifton, I. J.; Hensgens, C. M. H.; Shibata, N.; Schofield, C. J.; Hajdu, J.; Baldwin, J. E. *Nature* **1997**, *387*, 827–830.
(15) *Spin States in Biochemistry and Inorganic Chemistry: Influence on Structure and Reactivity*; Swart, M.; Costas, M., Eds.; John Wiley & Sons: London, 2016.

(16) Costas, M.; Harvey, J. N. *Nat. Chem.* **2013**, *5*, 7–9.
(17) Blaesi, E. J.; Fox, B. G.; Brunold, T. C. *Biochemistry* **2015**, *54*, 2874–2884.
(18) Kreisberg-Zakarin, R.; Borovok, I.; Yanko, M.; Frolow, F.; Aharonowitz, Y.; Cohen, G. *Biophys. Chem.* **2000**, *86*, 109–118.
(19) Park, H.; Lee, D. *Chem. - A Eur. J.* **2020**, *26*, 1–12.
(20) Sheet, D.; Paine, T. K. *Chem. Sci.* **2016**, *7*, 5322–5331.
(21) Gordon, J. B.; Vilbert, A. C.; DiMucci, I. M.; MacMillan, S. N.; Lancaster, K. M.; Moënne-Loccoz, P.; Goldberg, D. P. *J. Am. Chem. Soc.* **2019**, *141*, 17533–17547.
(22) Puri, M.; Que, L. *Acc. Chem. Res.* **2015**, *48*, 2443–2452.
(23) Chiou, Y.-M.; Que, L. *J. Am. Chem. Soc.* **1995**, *117*, 3999–4013.
(24) Britovsek, G. J. P.; England, J.; White, A. J. P. *Inorg. Chem.* **2005**, *44*, 8125–8134.
(25) Biswas, A. N.; Puri, M.; Meier, K. K.; Oloo, W. N.; Rohde, G. T.; Bominaar, E. L.; Münck, E.; Que, L. *J. Am. Chem. Soc.* **2015**, *137*, 2428–2431.
(26) Dantignana, V.; Serrano-Plana, J.; Draksharapu, A.; Magallón, C.; Banerjee, S.; Fan, R.; Gamba, I.; Guo, Y.; Que, L.; Costas, M.; Company, A. *J. Am. Chem. Soc.* **2019**, *141*, 15078–15091.
(27) Chen, J.; Klein Gebbink, R. J. M. *ACS Catal.* **2019**, *9*, 3564–3575.
(28) Fernández-Baeza, J.; Antiñolo, A.; Tejeda, J.; Lara-Sánchez, A.; Otero, A. *Dalt. Trans.* **2004**, *0*, 1499–1510.
(29) Moelands, M. A. H.; Schamhart, D. J.; Folkertsma, E.; Lutz, M.; Spek, A. L.; Klein Gebbink, R. J. M. *Dalt. Trans.* **2014**, *43*, 6769.
(30) Cappillino, P. J.; Miecznikowski, J. R.; Tyler, L. A.; Tarves, P. C.; McNally, J. S.; Lo, W.; Kasibhatla, B. S. T.; Krzyaniak, M. D.; McCracken, J.; Wang, F.; Armstrong, W. H.; Caradonna, J. P. *Dalt. Trans.* **2012**, *41*, 5662.
(31) Hübner, E.; Fischer, N. V.; Heinemann, F. W.; Mitra, U.; Dremov, V.; Müller, P.; Burzlaff, N. *Eur. J. Inorg. Chem.* **2010**, *2010*, 4100–4109.
(32) Hegelmann, I.; Beck, A.; Eichhorn, C.; Weibert, B.; Burzlaff, N. *Eur. J. Inorg. Chem.* **2003**, *2003*, 339–347.
(33) Peters, L.; Burzlaff, N. *Polyhedron* **2004**, *23*, 245–251.
(34) Ghosh, P.; Parkin, G. *J. Chem. Soc. Dalt. Trans.* **1998**, 2281–2284.
(35) Young, C. G.; Malarek, M. S.; Evans, D. J.; Doonan, C. J.; Ng, V. W. L.; White, J. M. *Inorg. Chem.* **2009**, *48*, 1960–1966.
(36) Cox, D. D.; Benkovic, S. J.; Bloom, L. M.; Bradley, F. C.; Nelson, M. J.; Que, L.; Wallick, D. E. *J. Am. Chem. Soc.* **1988**, *110*, 2026–2032.
(37) Sundaravel, K.; Suresh, E.; Saminathan, K.; Palaniandavar, M. *Dalt. Trans.* **2011**, *40*, 8092.
(38) Oldenburg, P. D.; Ke, C.-Y.; Tipton, A. A.; Shteinman, A. A.; Que, L. *Angew. Chemie Int. Ed.* **2006**, *45*, 7975–7978.
(39) Beck, A.; Weibert, B.; Burzlaff, N. *Eur. J. Inorg. Chem.* **2001**, 521–527.
(40) Barry, S. M.; Mueller-Bunz, H.; Rutledge, P. J. *Org. Biomol. Chem.* **2012**, *10*, 7372.
(41) Paria, S.; Halder, P.; Paine, T. K. *Inorg. Chem.* **2010**, *49*, 4518–4523.
(42) Smith, J. N.; Shirin, Z.; Carrano, C. J. *J. Am. Chem. Soc.* **2003**, *125*, 868–869.
(43) Bete, S. C.; Otte, M. *Angew. Chemie Int. Ed.* **2021**, *60*, 18582–18586.
(44) Bruijnincx, P. C. A.; Lutz, M.; Spek, A. L.; Hagen, W. R.; Weckhuysen, B. M.; van Koten, G.; Klein Gebbink, R. J. M. *J. Am. Chem. Soc.* **2007**, *129*, 2275–2286.
(45) Folkertsma, E.; de Waard, E. F.; Korpershoek, G.; van Schaik, A. J.; Solozabal Mirón, N.; Borrmann, M.; Nijsse, S.; Moelands, M. A. H.; Lutz, M.; Otte, M.; Moret, M.-E.; Klein Gebbink, R. J. M. *Eur. J. Inorg. Chem.* **2016**, *2016*, 1319–1332.
(46) Bruijnincx, P. C. A.; Lutz, M.; Spek, A. L.; van Faassen, E. E.; Weckhuysen, B. M.; van Koten, G.; Klein Gebbink, R. J. M. *Eur. J. Inorg. Chem.* **2005**, *2005*, 779–787.
(47) Jameson, D. L.; Hilgen, S. E.; Hummel, C. E.; Pichla, S. L. *Tetrahedron Lett.* **1989**, *30*, 1609–1612.
(48) Bruijnincx, P. C. A.; Lutz, M.; den Breejen, J. P.; Spek, A. L.; van Koten, G.; Klein Gebbink, R. J. M. *JBIC J. Biol. Inorg. Chem.* **2007**, *12*, 1181–1196.
(49) Bruijnincx, P. C. A.; Buurmans, I. L. C.; Gosiewska, S.; Moelands, M. A. H.; Lutz, M.; Spek, A. L.; van Koten, G.; Klein Gebbink, R. J. M. *Chem. - A Eur. J.* **2008**, *14*, 1228–1237.
(50) Peters, L.; Hübner, E.; Burzlaff, N. *J. Organomet. Chem.* **2005**, *690*, 2009–2016.
(51) Rocks, S. S.; Brennessel, W. W.; Machonkin, T. E.; Holland, P. L. *Inorganica Chim. Acta* **2009**, *362*, 1387–1390.
(52) Folkertsma, E. Iron and Zinc Complexes of Bulky Bis-Imidazole Ligands Enzyme Mimicry and

Ligand-Centered Redox Activity, Utrecht University, 2016.
(53) Moelands, M. A. H.; Nijsse, S.; Folkertsma, E.; de Bruin, B.; Lutz, M.; Spek, A. L.; Klein Gebbink, R. J. M. *Inorg. Chem.* **2013**, *52*, 7394–7410.
(54) Uragami, Y.; Senda, T.; Sugimoto, K.; Sato, N.; Nagarajan, V.; Masai, E.; Fukuda, M.; Mitsui, Y. *J. Inorg. Biochem.* **2001**, *83*, 269–279.
(55) Addison, A. W.; Rao, T. N.; Reedijk, J.; van Rijn, J.; Verschoor, G. C. *J. Chem. Soc., Dalt. Trans.* **1984**, 1349–1356.
(56) Oldenburg, P. D.; Shteinman, A. A.; Que, L. J. *J. Am. Chem. Soc.* **2005**, *127*, 15672–15673.
(57) Vaillancourt, F. H.; Bolin, J. T.; Eltis, L. D. *Crit. Rev. Biochem. Mol. Biol.* **2006**, *41*, 241–267.
(58) Ito, N.; Phillips, S. E. V.; Yadav, K. D. S.; Knowles, P. F. *J. Mol. Biol.* **1994**, *238*, 794–814.
(59) Higgs, T. C.; Carrano, C. J. *Inorg. Chem.* **1997**, *36*, 298–306.
(60) Hammes, B. S.; Carrano, C. J. *Inorg. Chem.* **1999**, *38*, 4593–4600.
(61) Hammes, B. S.; Carrano, C. J. *Inorg. Chem.* **1999**, *38*, 3562–3568.
(62) Bruijnincx, P. C. A.; Lutz, M.; Spek, A. L.; Hagen, W. R.; van Koten, G.; Klein Gebbink, R. J. M. *Inorg. Chem.* **2007**, *46*, 8391–8402.
(63) Monkcom, E. C.; Negenman, H. A.; Masferrer-Rius, E.; Lutz, M.; Ye, S.; Bill, E.; Klein Gebbink, R. J. M. *Eur. J. Inorg. Chem.* **2022**. (Chapter 2 of this thesis).
(64) Lindsay, S.; Lo, S. K.; Maguire, O. R.; Bill, E.; Probert, M. R.; Sproules, S.; Hess, C. R. *Inorg. Chem.* **2013**, *52*, 898–909.
(65) Monkcom, E. C.; de Bruin, D.; de Vries, A. J.; Lutz, M.; Ye, S.; Klein Gebbink, R. J. M. *Chem. – A Eur. J.* **2021**, *27*, 5191–5204. (Chapter 3 of this thesis).

Appendix A

Supporting Information to Chapter 2

A.1 X-ray Crystal Structure Determinations

Crystallographic details for H-Im^{Ph2}NNO

$C_{40}H_{34}N_4O_2$, Fw = 602.71, colourless block, 0.15 × 0.10 × 0.08 mm^3, monoclinic, $P2_1/n$ (no. 14), a = 12.8028(4), b = 17.9476(5), c = 14.0372(4) Å, β = 106.133(2) °, V = 3098.43(16) Å^3, Z = 4, D_x = 1.292 g/cm^3, μ = 0.08 mm^{-1}. The diffraction experiment was performed on a Bruker Kappa ApexII diffractometer with sealed tube and Triumph monochromator (λ = 0.71073 Å) at a temperature of 150(2) K up to a resolution of $(\sin\theta/\lambda)_{max}$ = 0.65 Å^{-1}. The Eval15 software[1] was used for the intensity integration. A multi-scan absorption correction and scaling was performed with SADABS[2] (correction range 0.70-0.75). A total of 67658 reflections was measured, 7120 reflections were unique (R_{int} = 0.061), 5022 reflections were observed [I>2σ(I)]. The structure was solved with Patterson superposition methods using SHELXT.[3] Structure refinement was performed with SHELXL-2018[4] on F^2 of all reflections. Non-hydrogen atoms were refined freely with anisotropic displacement parameters. All hydrogen atoms were located in difference Fourier maps. The O–H hydrogen atom was refined freely with an isotropic displacement parameter. C–H hydrogen atoms were refined with a riding model. 422 Parameters were refined with no restraints. R1/wR2 [I > 2σ(I)]: 0.0428 / 0.1052. R1/wR2 [all refl.]: 0.0703 / 0.1170. S = 1.037. Residual electron density between –0.27 and 0.29 e/Å^3. Geometry calculations and checking for higher symmetry was performed with the PLATON program.[5]

Crystallographic details for [Zn(BenzImNNO)$_2$ZnCl$_2$] (1)

$C_{48}H_{42}Cl_2N_8O_4Zn_2$ + disordered solvent, Fw = 996.53[*], colourless block, 0.22 × 0.14 × 0.11 mm^3, orthorhombic, Pccn (no. 56), a = 22.5767(17), b = 23.0219(17), c = 19.5186(12) Å, V = 10145.0(12) Å^3, Z = 8, D_x = 1.305 g/cm^3[*], μ = 1.10 mm^{-1}[*]. Intensities were measured on a Bruker Kappa ApexII diffractometer with sealed tube and Triumph monochromator (l = 0.71073 A°) at a temperature of 100(2) K up to a resolution of $(\sin\theta/\lambda)_{max}$ = 0.61 Å^{-1}. The crystal appeared to be twinned with a twofold rotation about *hkl* = (–1,1,0) as twin operation (pseudo-tetragonal twinning). Consequently, two orientation matrices were used for the intensity integration with the Eval15 software.[1] 203616 Reflections were measured. Multiscan absorption correction and scaling was performed with TWINABS[2] (correction range 0.54-0.75). 9968 Reflections were unique (R_{int} = 0.130), of which 6385 were observed [I>2σ(I)]. The reflection data were characterized by pseudo-translational symmetry (pseudo I-centered lattice). The structure was solved with Patterson superposition methods using SHELXT.[3] Least-squares refinement was performed with SHELXL-2017[4] against F^2 of all reflections. The crystal structure contains voids (1960 Å^3/unit cell) filled with disordered *n*-hexane molecules. Their contribution to the structure factors was secured by back-Fourier transformation using the SQUEEZE algorithm[6] resulting in 311 electrons / unit cell. Non-hydrogen atoms were refined freely with anisotropic displacement parameters. Hydrogen atoms were introduced in calculated positions and refined with a riding model. 584 Parameters were refined with 1041 restraints (displacement parameters of all atoms). R1/wR2 [I > 2σ(I)]: 0.0626 / 0.1595. R1/wR2 [all refl.]: 0.1067 / 0.1881. S = 1.028. Twin fraction *BASF* = 0.354(2). Residual electron density between −0.74 and 1.41 e/Å^3. Geometry calculations and checking for higher symmetry were performed with the PLATON program.[5] [*] Derived values do not contain the contribution of the disordered solvent molecules.

Crystallographic details for [Zn(BenzImNNO)$_2$] (3)

$C_{48}H_{42}N_8O_4Zn$ + disordered solvent, Fw = 860.26[*], yellow needle, 0.44 × 0.13 × 0.08 mm^3, trigonal, R $\overline{3}$ (no. 148), *a* = *b* = 40.1520(11), *c* = 8.4262(3) Å, V = 11764.6(8) Å^3, Z = 9, D_x = 1.093 g/cm$^{3[*]}$, μ = 0.51 mm$^{-1[*]}$. The diffraction experiment was performed on a Bruker Kappa ApexII diffractometer with sealed tube and Triumph monochromator (λ = 0.71073 Å) at a temperature of 150(2) K up to a resolution of $(\sin\theta/\lambda)_{max}$ = 0.65 Å^{-1}. The Eval15 software[1] was used for the intensity integration. A multi-scan absorption correction and scaling was performed with SADABS[2] (correction range 0.64-0.75). A total of 54914 reflections was measured, 6005 reflections were unique (R_{int} = 0.040), 4927 reflections were observed [I>2σ(I)]. The structure was solved with Patterson superposition methods using SHELXT.[3] Structure refinement was performed with SHELXL-2018[4] on F^2 of all reflections. The crystal structure contains voids (3517 Å^3/unit cell) filled with disordered dichloromethane molecules. Their contribution to the structure factors was secured by back-Fourier transformation using the SQUEEZE algorithm[6] resulting in 1066 electrons / unit cell. Non-hydrogen atoms were refined freely with anisotropic displacement parameters. All hydrogen atoms were located in difference Fourier maps and refined with a riding model. 280 Parameters were refined with no restraints. R1/wR2 [I > 2σ(I)]: 0.0316 / 0.0832. R1/wR2 [all refl.]: 0.0412 / 0.0874. S = 1.050. Residual electron density between –0.29 and 0.35 e/Å^3. Geometry calculations and checking for higher symmetry was performed with the PLATON program.[5] [*] Derived values do not contain the contribution of the disordered solvent molecules.

Crystallographic details for [Fe$_2$(Im^{Ph2}NNO)$_2$(OTf)$_2$] (4)

$C_{82}H_{66}F_6Fe_2N_8O_{10}S_2 \cdot 1.5(C_4H_8O)$, Fw = 1721.40, colourless plate, 0.55 × 0.32 × 0.06 mm^3, monoclinic, $P2_1/n$ (no. 14), *a* = 17.5812(2), *b* = 22.5730(3), *c* = 20.3239(4) Å, β = 93.791(1) °, V = 8048.1(2) Å^3, Z = 4, D_x = 1.421 g/cm^3, μ = 0.49 mm^{-1}. The diffraction experiment was performed on a Bruker Kappa ApexII diffractometer with sealed tube and Triumph monochromator (λ = 0.71073 Å) at a temperature of 150(2) K up to a resolution of $(\sin\theta/\lambda)_{max}$ = 0.65 Å^{-1}. The Eval15 software[1] was used for the intensity integration. A numerical absorption correction and scaling was performed with SADABS[2] (correction range 0.82-0.99). A total of 142872 reflections was measured, 18482 reflections were unique (R_{int} = 0.036), 14836 reflections were observed [I>2σ(I)]. The structure was solved with Patterson superposition methods using SHELXT.[3] Structure refinement was performed with SHELXL-2018[4] on F^2 of all reflections. Non-hydrogen atoms were refined freely with anisotropic displacement parameters. One triflate anion was refined with a disorder model. One of the THF molecules was disordered on an inversion center (occupancy ½). Hydrogen atoms were introduced in calculated positions and refined with a riding model. 1151 Parameters were refined with 472 restraints (distances, angles and displacement parameters in triflate and THF). R1/wR2 [I > 2σ(I)]: 0.0367 / 0.0918. R1/wR2 [all refl.]: 0.0509 / 0.0995. S = 1.026. Residual electron density between -0.82 and 0.82 e/Å^3. Geometry calculations and checking for higher symmetry was performed with the PLATON program.[5]

Crystallographic details for [Zn$_2$(Im^{Ph2}NNO)$_2$(OTf)$_2$] (5)

$C_{82}H_{66}F_6N_8O_{10}S_2Zn_2 \cdot 2(C_4H_8O)$, Fw = 1776.49, colourless block, 0.28 × 0.14 × 0.06 mm^3, triclinic, P $\overline{1}$ (no. 2), *a* = 12.8843(3), *b* = 13.6862(4), *c* = 13.8744(3) Å, α = 61.130(2), β = 78.529(1), γ = 74.465(2) °, V = 2057.20(10) Å^3, Z = 1, D_x = 1.434 g/cm^3, μ = 0.72 mm^{-1}. The diffraction experiment was performed on a Bruker Kappa ApexII diffractometer with sealed tube and Triumph monochromator (λ = 0.71073 Å) at a temperature of 150(2) K up to a resolution of $(\sin\theta/\lambda)_{max}$ = 0.65 Å^{-1}. The Eval15 software[2] was used for the intensity integration. A multi-scan absorption correction and scaling was performed with SADABS[3] (correction range 0.65-0.75). A total of 45098 reflections was measured, 9437 reflections

were unique (R_{int} = 0.040), 7827 reflections were observed [I>2σ(I)]. The structure was solved with Patterson superposition methods using SHELXT.[4] Structure refinement was performed with SHELXL-2018[5] on F^2 of all reflections. Non-hydrogen atoms were refined freely with anisotropic displacement parameters. The THF solvent molecule was refined with a disorder model. Hydrogen atoms were introduced in calculated positions and refined with a riding model. 590 Parameters were refined with 153 restraints (distances, angles and displacement parameters in the THF). R1/wR2 [I > 2σ(I)]: 0.0374 / 0.0946. R1/wR2 [all refl.]: 0.0494 / 0.1009. S = 1.022. Residual electron density between -0.47 and 0.51 e/Å^3. Geometry calculations and checking for higher symmetry was performed with the PLATON program.[6]

Crystallographic details for [$Fe_2(Im^{Ph2}NNO)_2(SPh)_2$] (6)

$C_{92}H_{76}Fe_2N_8O_4S_2$, Fw = 1533.42, colourless needle, 0.36 × 0.07 × 0.06 mm^3, monoclinic, $P2_1/n$ (no. 14), *a* = 11.1227(3), *b* = 13.4286(5), *c* = 25.9443(9) Å, β = 101.076(1) °, V = 3802.9(2) Å^3, Z = 2, D_x = 1.339 g/cm^3, μ = 0.50 mm^{-1}. The diffraction experiment was performed on a Bruker Kappa ApexII diffractometer with sealed tube and Triumph monochromator (λ = 0.71073 Å) at a temperature of 150(2) K up to a resolution of $(\sin\theta/\lambda)_{max}$ = 0.65 Å^{-1}. The crystal appeared to be twinned with a twofold rotation about the *a*-axis as twin operation. Consequently, two orientation matrices were used for the integration with the Eval15 software.[2] A multi-scan absorption correction and scaling was performed with TWINABS[3] (correction range 0.64-0.75). A total of 84530 reflections was measured, 8919 reflections were unique (R_{int} = 0.064), 7206 reflections were observed [I>2σ(I)]. The structure was solved with Patterson superposition methods using SHELXT.[4] Structure refinement was performed with SHELXL-2018[5] on F^2 of all reflections. Non-hydrogen atoms were refined freely with anisotropic displacement parameters. One phenyl ring was orientationally disordered. Hydrogen atoms were introduced in calculated positions and refined with a riding model. 546 Parameters were refined with 283 restraints (distances, angles, flatness and displacement parameters in the disordered phenyl ring). R1/wR2 [I > 2σ(I)]: 0.0443 / 0.0975. R1/wR2 [all refl.]: 0.0629 / 0.1051. S = 1.032. Twin fraction BASF = 0.3997(8). Residual electron density between -0.57 and 0.60 e/Å^3. Geometry calculations and checking for higher symmetry was performed with the PLATON program.[6]

Crystallographic details for [$Zn_2(Im^{Ph2}NNO)_2(SPh)_2$] (7)

$C_{92}H_{76}N_8O_4S_2Zn_2$, Fw = 1552.46, colourless needle, 0.28 × 0.09 × 0.05 mm^3, monoclinic, $P2_1/n$ (no. 14), *a* = 11.0038(2), *b* = 13.4530(3), *c* = 25.9499(6) Å, β = 100.796(1) °, V = 3773.48(14) Å^3, Z = 2, D_x = 1.366 g/cm^3, μ = 0.75 mm^{-1}. The diffraction experiment was performed on a Bruker Kappa ApexII diffractometer with sealed tube and Triumph monochromator (λ = 0.71073 Å) at a temperature of 150(2) K up to a resolution of $(\sin\theta/\lambda)_{max}$ = 0.65 Å^{-1}. The Eval15 software[2] was used for the intensity integration. For the prediction of the reflection profiles a split-mosaic model was used. A numerical absorption correction and scaling was performed with SADABS[3] (correction range 0.85-1.00). A total of 53744 reflections was measured, 8686 reflections were unique (R_{int} = 0.068), 6129 reflections were observed [I>2σ(I)]. Coordinates of the isostructural Fe complex were used as the starting model. Structure refinement was performed with SHELXL-2018[5] on F^2 of all reflections. Non-hydrogen atoms were refined freely with anisotropic displacement parameters. One phenyl ring was orientationally disordered. Hydrogen atoms were introduced in calculated positions and refined with a riding model. 545 Parameters were refined with 283 restraints (distances, angles, flatness and displacement parameters in the disordered phenyl ring). R1/wR2 [I > 2σ(I)]: 0.0435 / 0.0933. R1/wR2 [all refl.]: 0.0769 / 0.1049. S = 1.023. Residual electron density between -0.29 and 0.44 e/Å^3. Geometry calculations and checking for higher symmetry was performed with the PLATON program.[6]

Crystallographic details for $[Fe_2(Im^{Ph2}NNO^*)_2(Cl)_2]$ (8)

$C_{78}H_{60}Cl_2Fe_2N_8O_4$ + disordered solvent, Fw = 1355.94[*], dark red plate, 0.50 × 0.39 × 0.08 mm^3, monoclinic, $P2_1/n$ (no. 14), a = 12.5344(3), b = 35.3166(6), c = 17.8513(4) Å, β = 95.701(1) °, V = 7863.2(3) $Å^3$, Z = 4, D_x = 1.145 g/cm^3[*], μ = 0.49 mm^{-1}[*]. The diffraction experiment was performed on a Bruker Kappa ApexII diffractometer with sealed tube and Triumph monochromator (λ = 0.71073 Å) at a temperature of 150(2) K up to a resolution of $(\sin\theta/\lambda)_{max}$ = 0.65 $Å^{-1}$. The Eval15 software[9] was used for the intensity integration. A multi-scan absorption correction and scaling was performed with SADABS[10] (correction range 0.68-0.75). A total of 154009 reflections was measured, 18073 reflections were unique (R_{int} = 0.043), 14273 reflections were observed [I>2σ(I)]. The structure was solved with Patterson superposition methods using SHELXT.[11] Structure refinement was performed with SHELXL-2018[12] on F^2 of all reflections. The crystal structure contains voids (1870 $Å^3$ / unit cell) filled with disordered THF and hexane molecules. Their contribution to the structure factors was secured by back-Fourier transformation using the SQUEEZE algorithm[15] resulting in 398 electrons / unit cell. Non-hydrogen atoms were refined freely with anisotropic displacement parameters. Minor disorder in the phenyl rings was not resolved. Hydrogen atoms were introduced in calculated positions and refined with a riding model. 851 Parameters were refined with 108 restraints (displacement parameters in phenyl rings). R1/wR2 [I > 2σ(I)]: 0.0351 / 0.0883. R1/wR2 [all refl.]: 0.0486 / 0.0937. S = 1.044. Residual electron density between -0.30 and 0.43 $e/Å^3$. Geometry calculations and checking for higher symmetry was performed with the PLATON program.[13] [*] Derived values do not contain the contribution of the disordered solvent molecules.

A.2 NMR Data

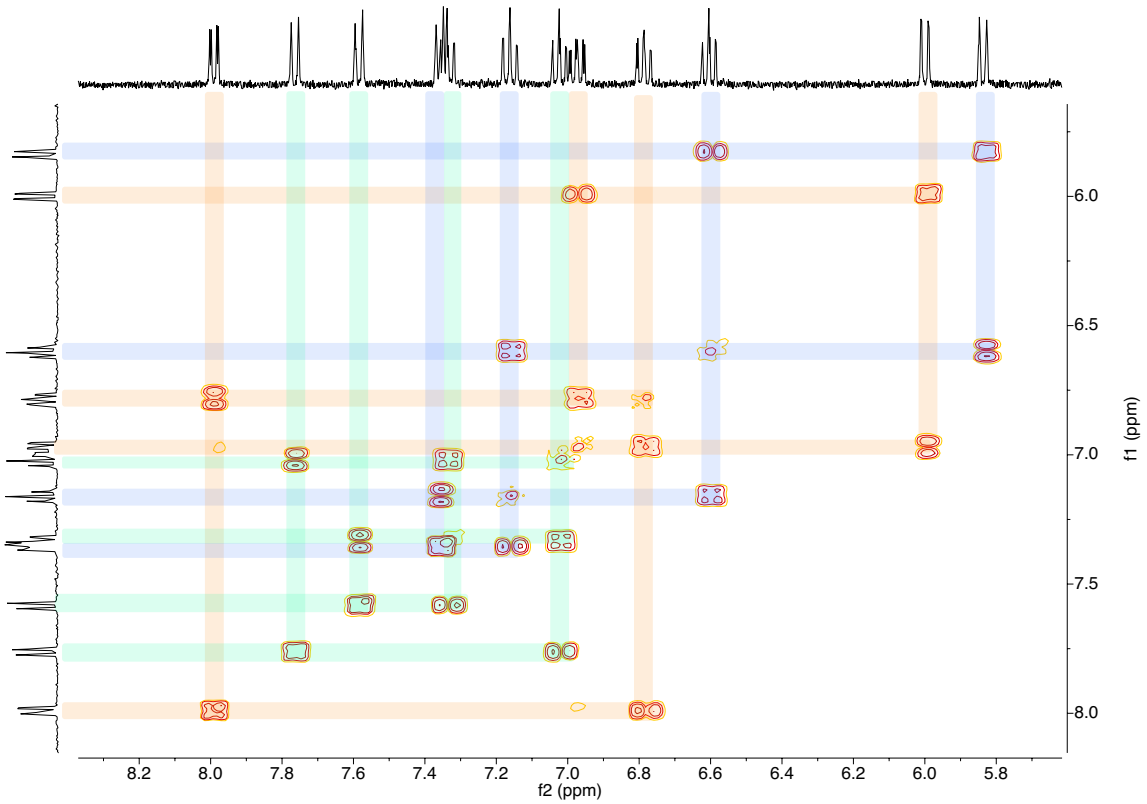

Figure A1. ^1H-^1H COSY NMR spectrum (400 MHz) of **1**, recorded in CD_2Cl_2 at 25 °C.

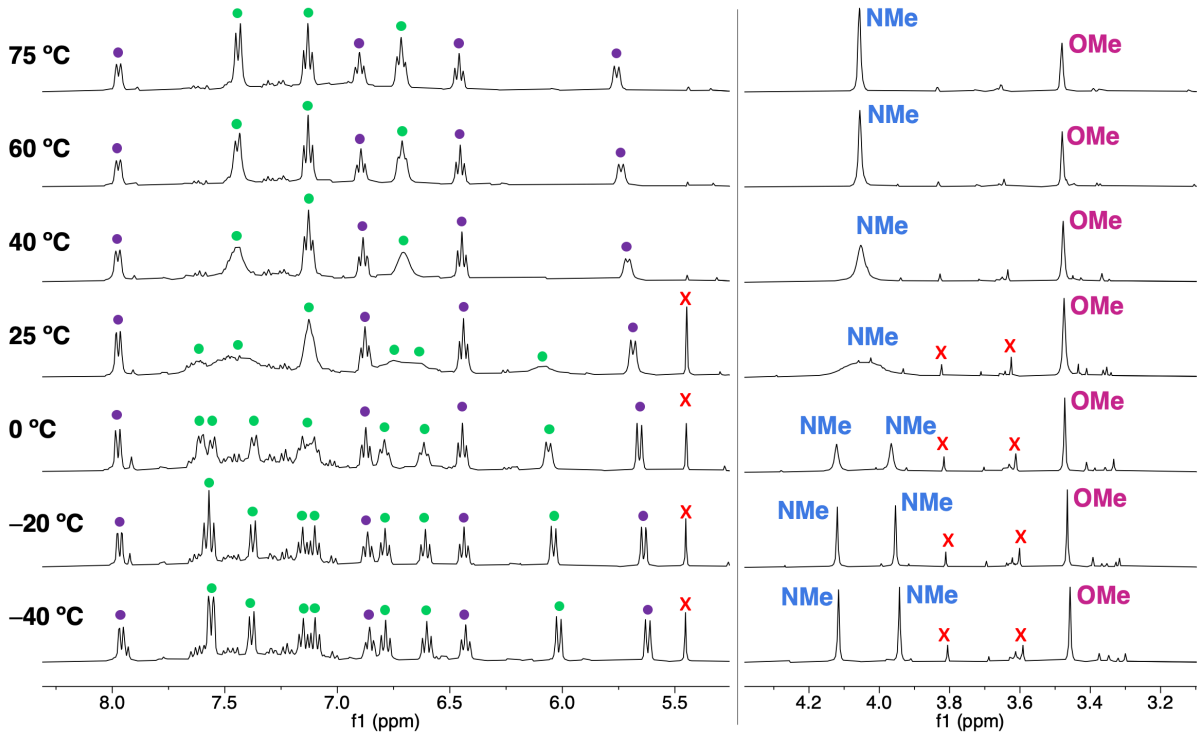

Figure A2. Variable temperature ^{1}H NMR spectra (400 MHz) of **2**, recorded in CD_3CN. Spectra have been cut between 4.3 and 5.3 ppm. The aromatic regions of the spectra have been scaled for clarity. Residual solvent signals and unknown impurities are highlighted with red crosses.

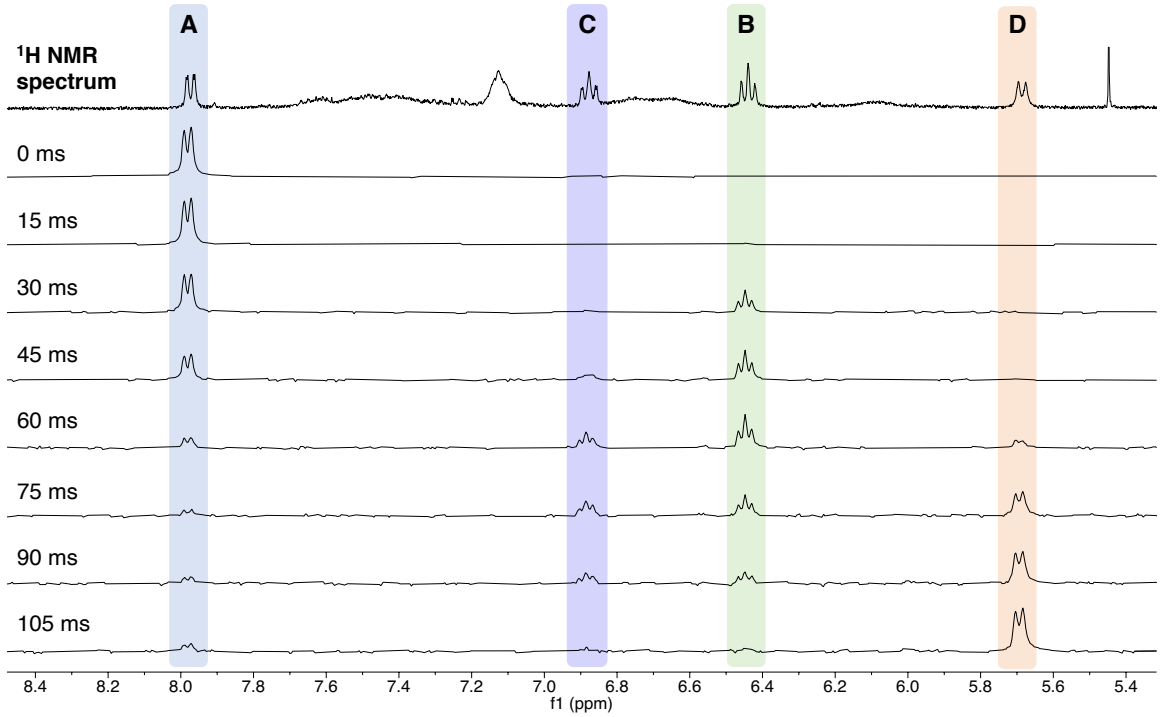

Figure A3. Stacked 1D TOCSY ^{1}H NMR (400 Hz) spectra of **2**, recorded in CD_3CN at 25 °C. Only the aromatic region of the spectra is shown.

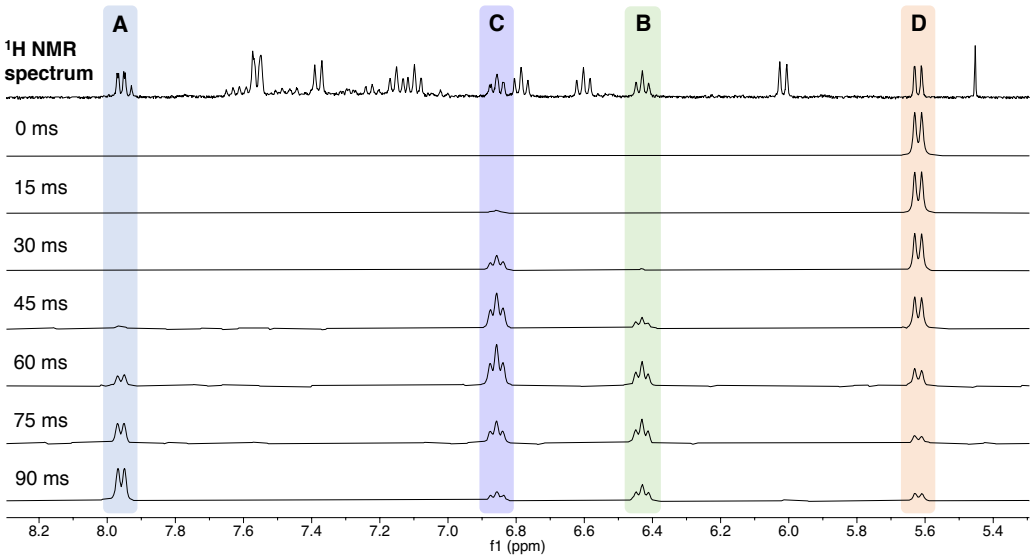

Figure A4. Stacked 1D TOCSY ^{1}H NMR (400 Hz) spectra of **2**, recorded in CD_3CN at –40 °C.

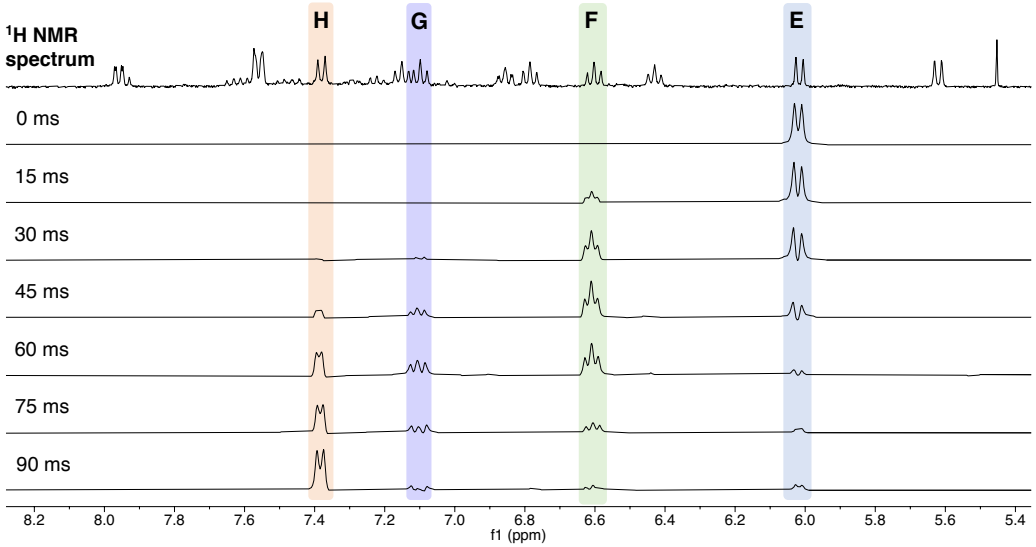

Figure A5. Stacked 1D TOCSY ^{1}H NMR (400 Hz) spectra of **2**, recorded in CD_3CN at –40 °C.

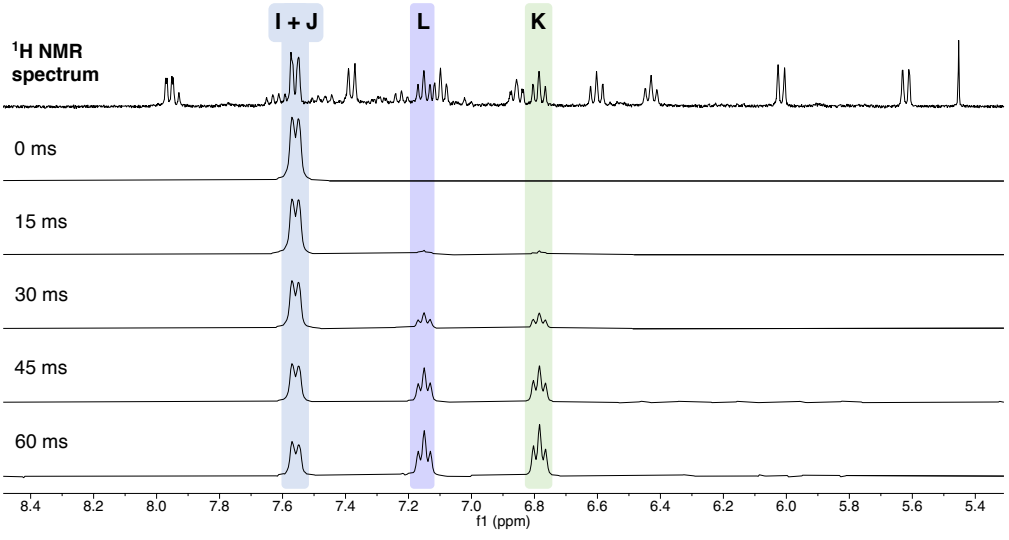

Figure A6. Stacked 1D TOCSY ^{1}H NMR (400 Hz) spectra of **2**, recorded in CD_3CN at –40 °C.

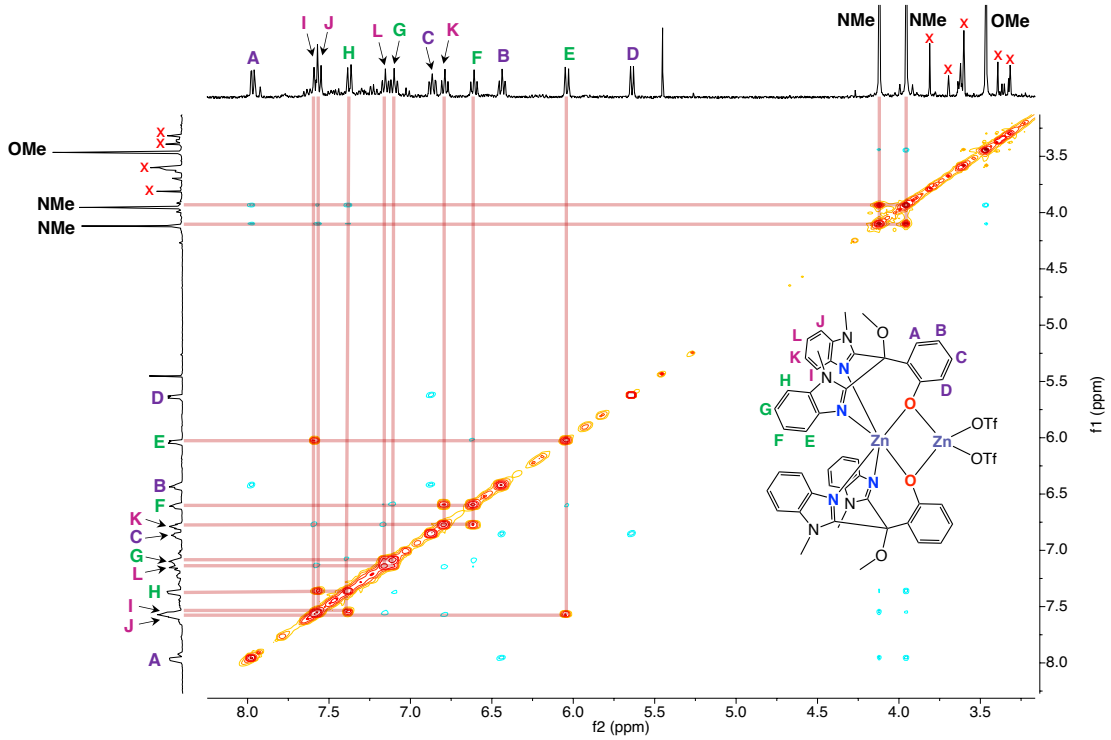

Figure A7. ^{1}H NOESY and EXSY NMR spectrum (400 MHz) of **2**, recorded in CD_3CN at –40 °C. Red phase indicates peaks that are in chemical exchange with each other. Blue phase indicates peaks that feel each other through space, i.e. an NOE interaction (<5Å). Red guides for identifying exchange peaks have been inserted for clarity.

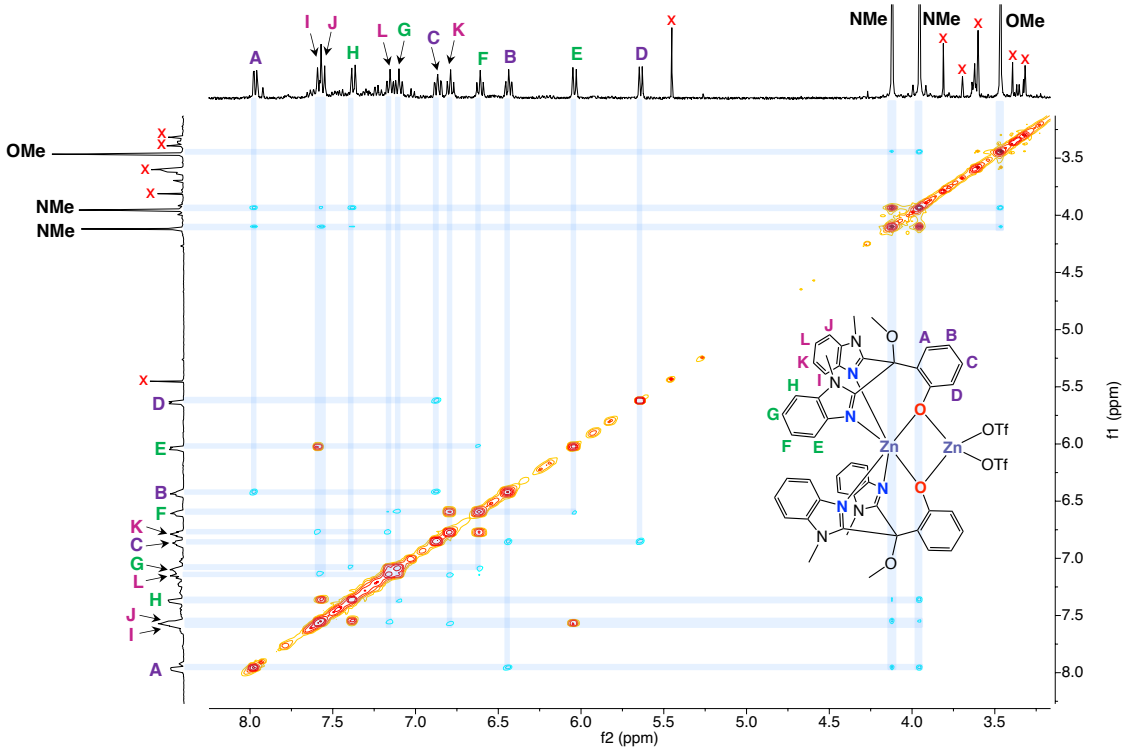

Figure A8. ^{1}H NOESY and EXSY NMR spectrum (400 MHz) of **2**, recorded in CD_3CN at –40 °C. Red phase indicates peaks that are in chemical exchange with each other. Blue phase indicates peaks that feel each other through space, i.e. an NOE interaction (<5Å). Blue guides for identifying NOE interactions have been inserted for clarity.

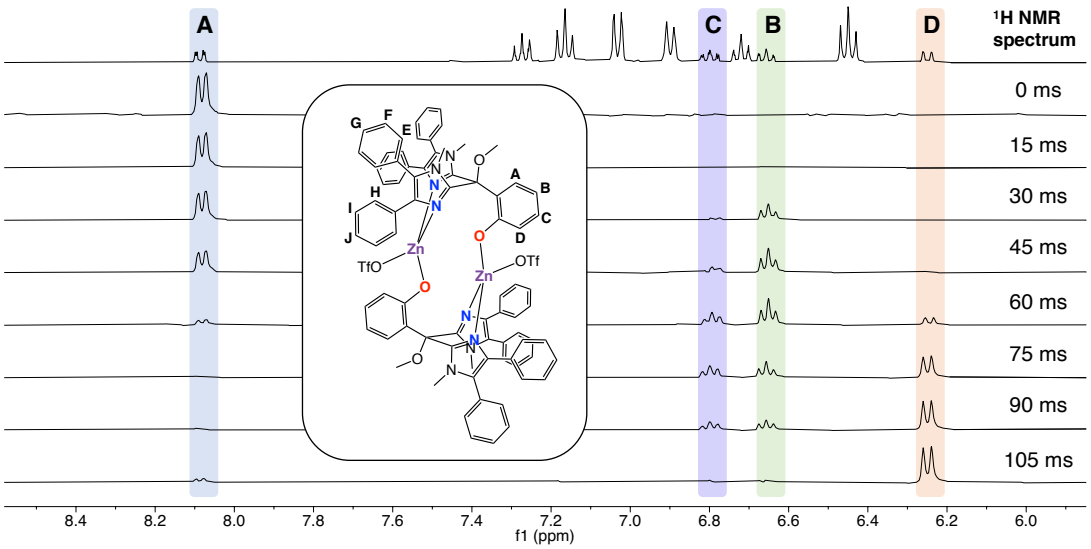

Figure A9. Stacked 1D TOCSY ^{1}H NMR (400 Hz) spectra of **5**, recorded in THF-d_8 at 25 °C.

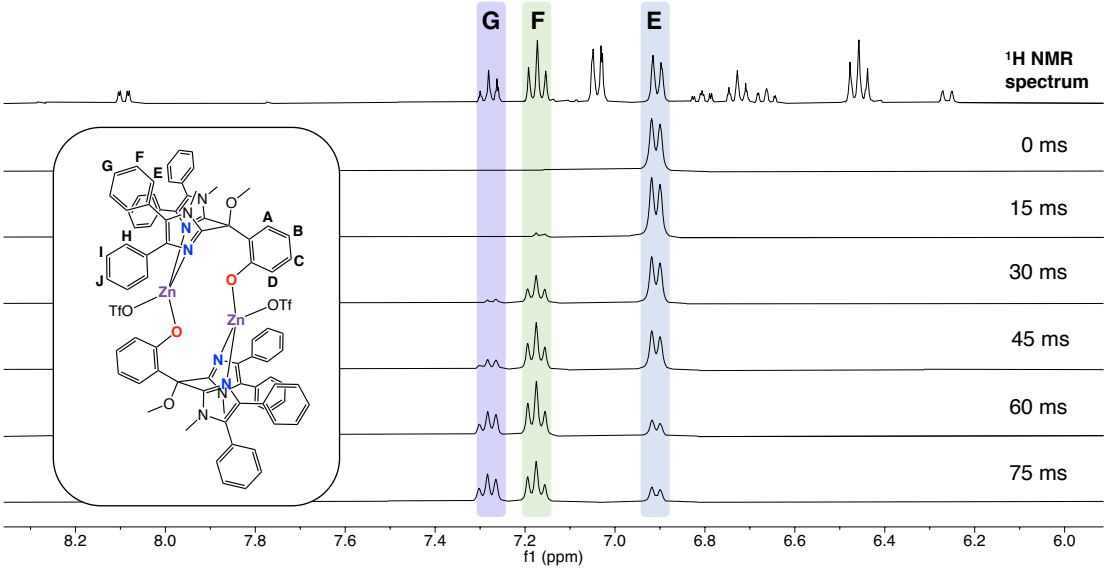

Figure A10. Stacked 1D TOCSY ^{1}H NMR (400 Hz) spectra of **5**, recorded in THF-d_8 at 25 °C.

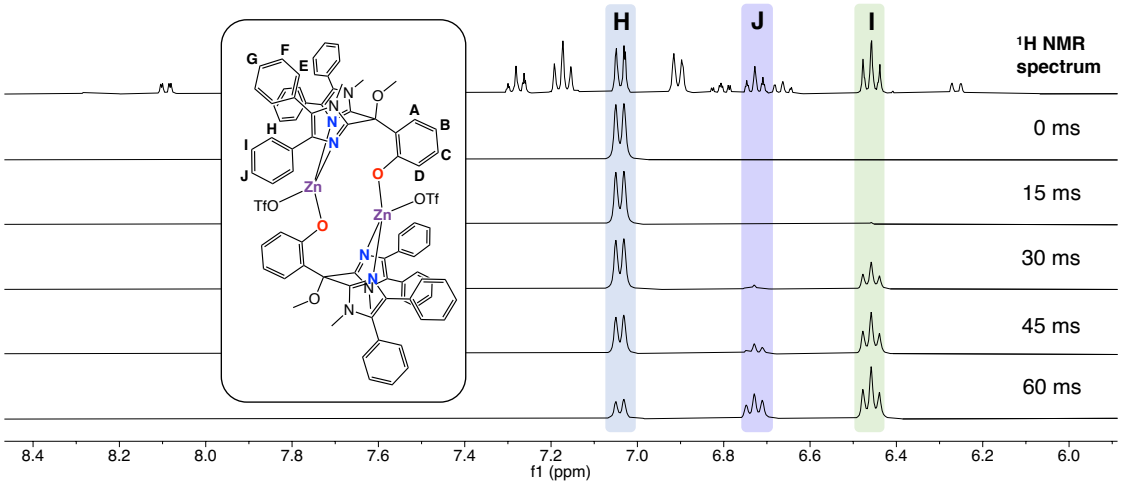

Figure A11. Stacked 1D TOCSY ^{1}H NMR (400 Hz) spectra of **5**, recorded in THF-d_8 at 25 °C.

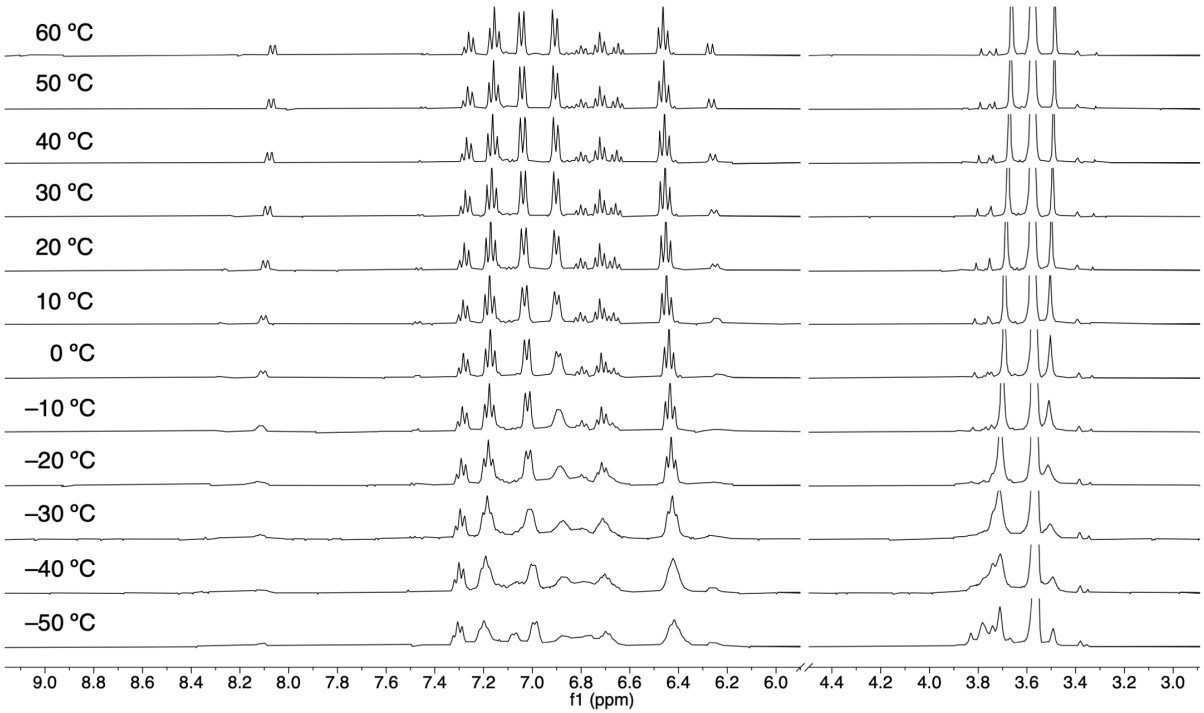

Figure A12. Stacked VT ^{1}H NMR (400 Hz) spectra of **5**, recorded in THF-d_8.

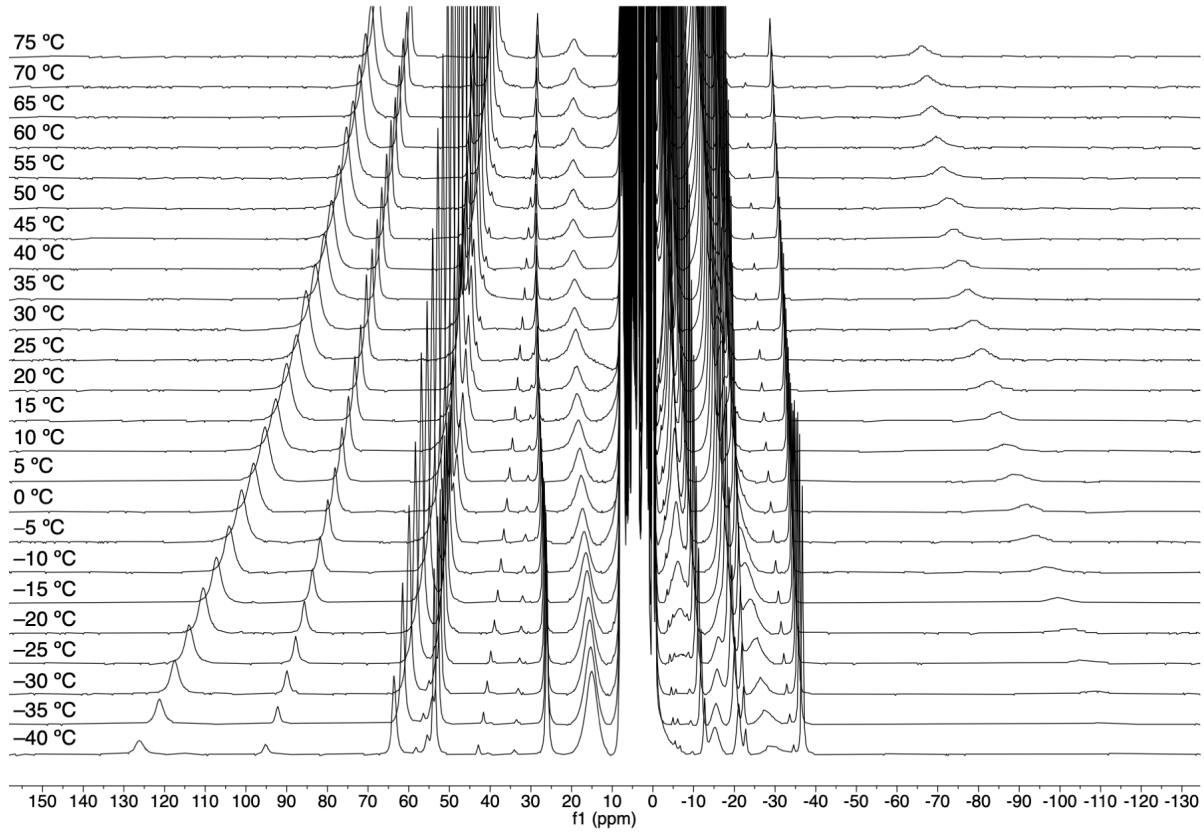

Figure A13. Stacked VT ^{1}H NMR (400 Hz) spectra of **4**, recorded in CD_3CN.

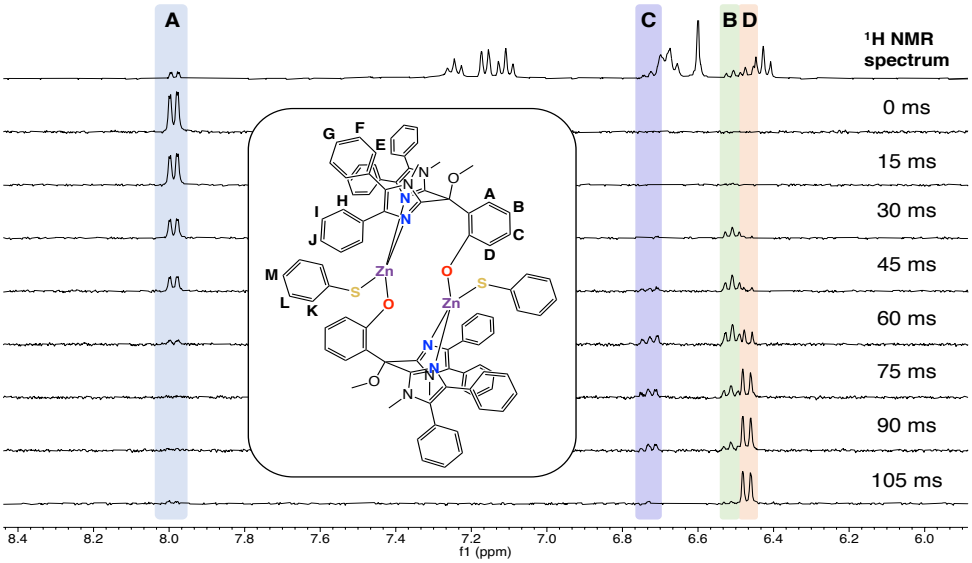

Figure A14. Stacked TOCSY ^{1}H NMR (400 Hz) spectra of **7**, recorded in THF-d_8 at 25 °C.

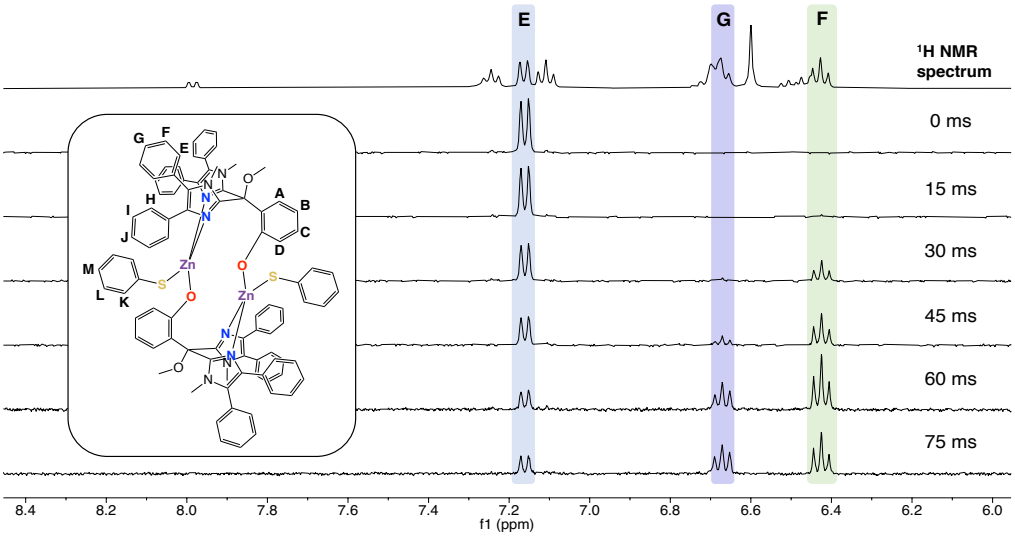

Figure A15. Stacked TOCSY ^{1}H NMR (400 Hz) spectra of **7**, recorded in THF-d_8 at 25 °C.

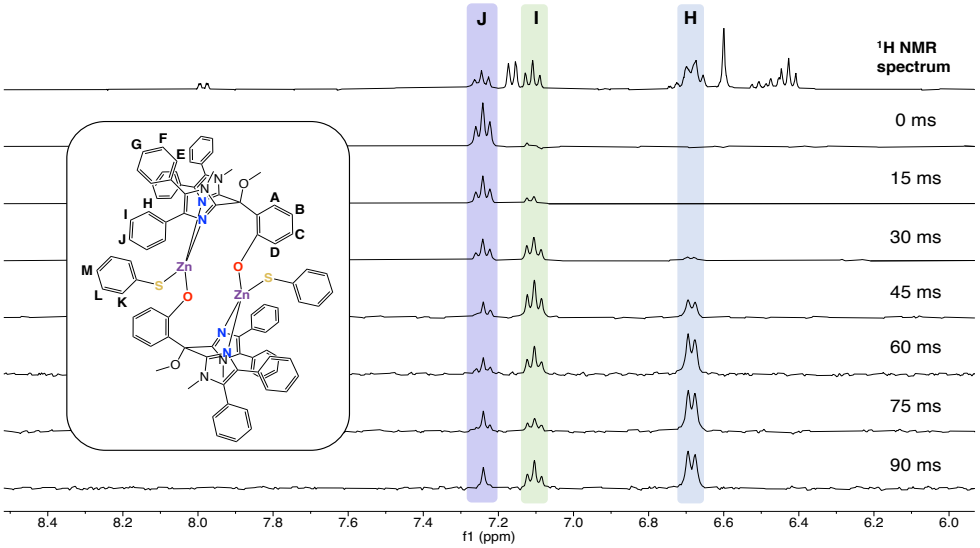

Figure A16. Stacked TOCSY ^{1}H NMR (400 Hz) spectra of **7**, recorded in THF-d_8 at 25 °C.

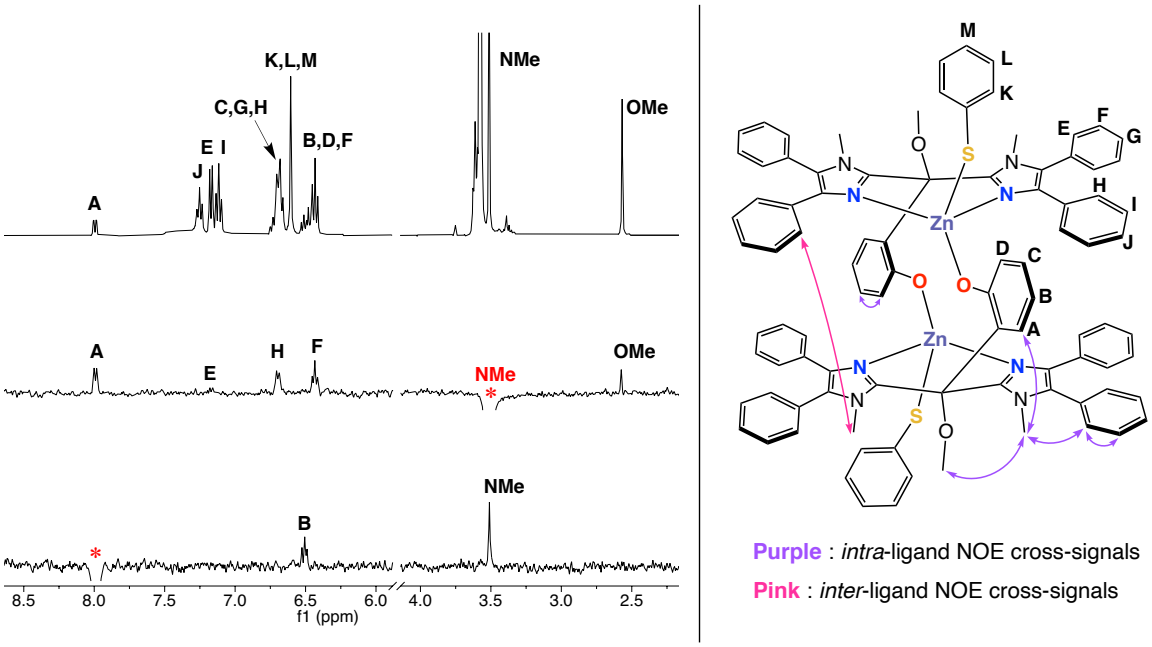

Figure A17. Stacked 1D NOE ^{1}H NMR spectra of **5**, recorded in THF-d_8 at 25 °C. The selectively excited NMR signals are highlighted with a red asterisk and are in the negative phase (not depicted).

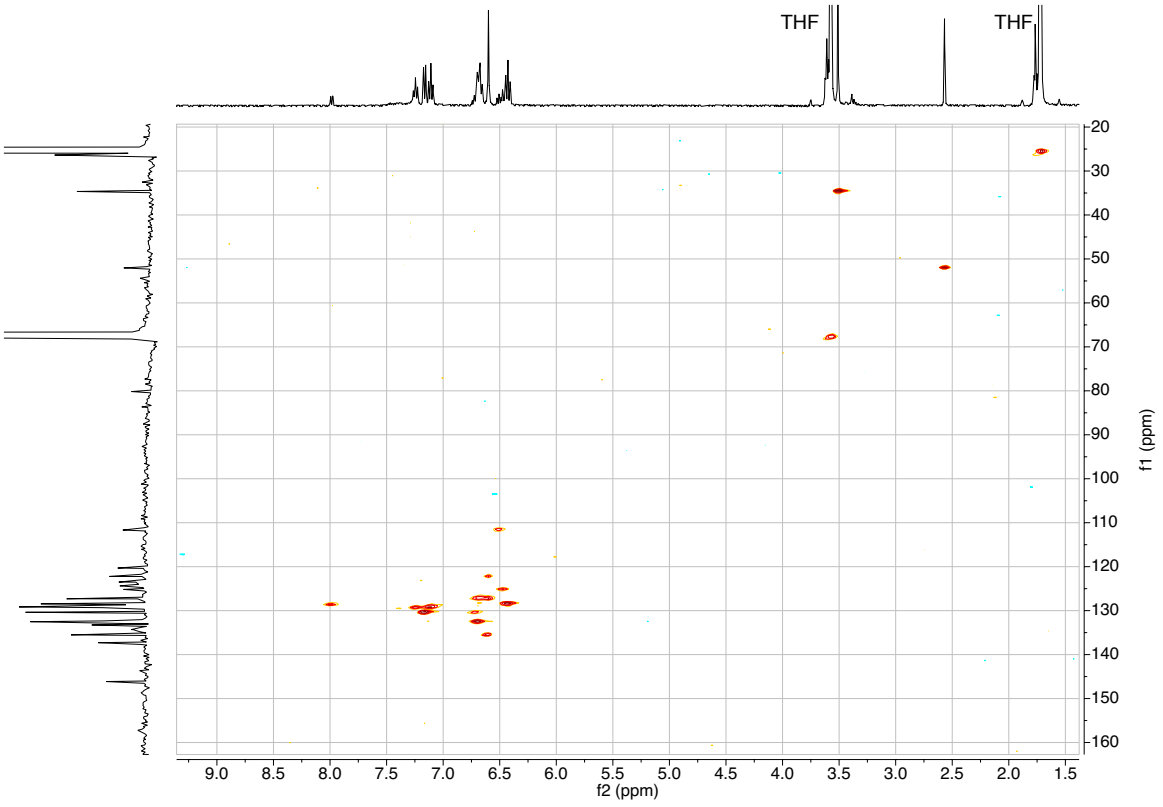

Figure A18. ^{1}H-^{13}C ASAP-HMQC NMR spectrum of **7**, recorded in THF-d_8 at 25 °C.

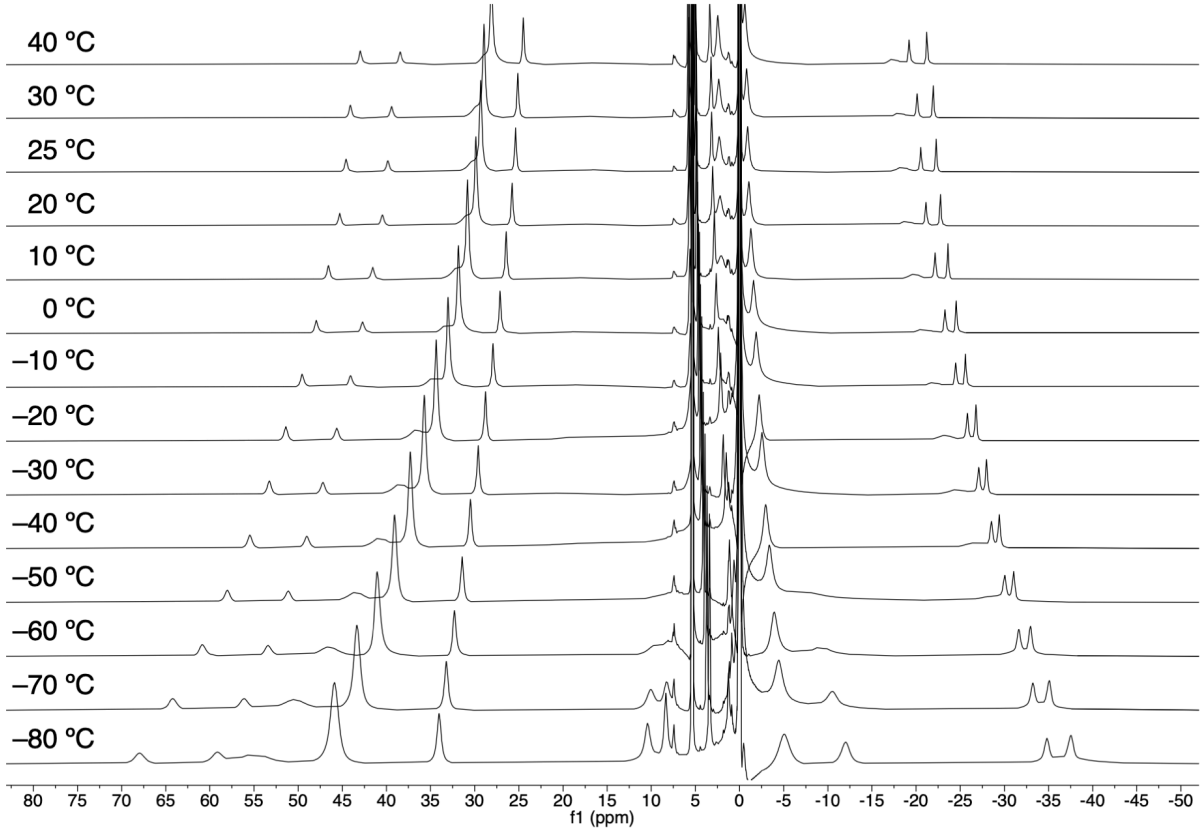

Figure A19. Stacked VT ^{1}H NMR (400 Hz) spectra of **6** in CD_2Cl_2.

A.3 References and Notes

(1) Schreurs, A. M. M.; Xian, X.; Kroon-Batenburg, L. M. J. *J. Appl. Crystallogr.* **2010**, *43*, 70–82.
(2) Sheldrick, G. M. SADABS and TWINABS, 2014.
(3) Sheldrick, G. M. *Acta Crystallogr. Sect. A Found. Crystallogr.* **2015**, *71*, 3–8.
(4) Sheldrick, G. M. *Acta Crystallogr. Sect. C Struct. Chem.* **2015**, *71*, 3–8.
(5) Spek, A. L. *Acta Crystallogr. Sect. D Biol. Crystallogr.* **2009**, *65*, 148–155.
(6) Spek, A. L. *Acta Crystallogr. Sect. C Struct. Chem.* **2015**, *71*, 9–18.

Appendix B

Supporting Information to Chapter 3

B.1 X-ray Crystal Structure Determinations

Crystallographic details for $[K_2(Im^{Ph2}NNO^{tBu})_2(Et_2O)_2]$

$C_{104}H_{118}K_2N_8O_6$ + disordered solvent, Fw = 1654.26[*], colourless needle, 0.35 × 0.11 × 0.10 mm^3, triclinic, $P\overline{1}$ (no. 2), a = 14.0405(8), b = 14.4688(12), c = 15.4666(11) Å, α = 67.071(2), β = 76.924(2), γ = 61.093(2)°, V = 2530.4(3) Å^3, Z = 1, D_x = 1.086 g/cm$^{3[*]}$, μ = 0.15 mm$^{-1[*]}$. The diffraction experiment was performed on a Bruker Kappa ApexII diffractometer with sealed tube and Triumph monochromator (λ = 0.71073 Å) at a temperature of 150(2) K up to a resolution of $(\sin\theta/\lambda)_{max}$ = 0.61 Å^{-1}. The Eval15 software[1] was used for the intensity integration. A large anisotropic mosaicity[2] about *hkl*=(0,0,1) was used for the prediction of the reflection profiles. A multi-scan absorption correction and scaling was performed with SADABS[3] (correction range 0.60-0.75). A total of 32107 reflections was measured, 9419 reflections were unique (R_{int} = 0.079), 4913 reflections were observed [I>2σ(I)]. The structure was solved with Patterson superposition methods using SHELXT.[4] Structure refinement was performed with SHELXL-2018[5] on F^2 of all reflections. The crystal structure contains large voids (339 Å^3/unit cell) filled with severely disordered solvent molecules. Their contribution to the structure factors was secured by the SQUEEZE algorithm[6] resulting in 74 electrons / unit cell. Non-hydrogen atoms were refined freely with anisotropic displacement parameters. Hydrogen atoms were introduced in calculated positions and refined with a riding model. One t-butyl group was refined with a disorder model. Slight disorder in the phenyl groups was not resolved. 577 Parameters were refined with 144 restraints (distances, angles and displacement parameters in the t-butyl groups). R1/wR2 [I > 2σ(I)]: 0.0635 / 0.1427. R1/wR2 [all refl.]: 0.1379 / 0.1719. S = 0.981. Residual electron density between -0.27 and 0.34 e/Å^3. Geometry calculations and checking for higher symmetry was performed with the PLATON program.[7] [*] Derived values do not contain the contribution of the disordered solvent.

Crystallographic details for $[Fe(Im^{Ph2}NNO^{tBu})(Cl)]$ (1)

$C_{48}H_{49}ClFeN_4O_2$ + disordered solvent, Fw = 805.21[*], brown needle, 0.42 × 0.12 × 0.04 mm^3, monoclinic, I2/a (no. 15), a = 26.8538(12), b = 10.0334(4), c = 35.8465(13) Å, β = 93.790(3) °, V = 9637.2(7) Å^3, Z = 8, D_x = 1.110 g/cm$^{3[*]}$, μ = 0.41 mm$^{-1[*]}$. The diffraction experiment was performed on a Bruker Kappa ApexII diffractometer with sealed tube and Triumph monochromator (λ = 0.71073 Å) at a temperature of 150(2) K up to a resolution of $(\sin\theta/\lambda)_{max}$ = 0.65 Å^{-1}. The Eval15 software[1] was used for the intensity integration. A numerical absorption correction and scaling was performed with SADABS[3] (correction range 0.81-1.00). A total of 61423 reflections was measured, 11054 reflections were unique (R_{int} = 0.086), 6676 reflections were observed [I>2σ(I)]. Initial coordinates were taken from the isostructural Zn complex (**2**). Structure refinement was performed with SHELXL-2018[5] on F^2 of all reflections. The crystal structure contains large voids (1661 Å^3/unit cell) filled with severely disordered solvent molecules. Their contribution to the structure factors was secured by the SQUEEZE algorithm[6] resulting in 383 electrons / unit cell. Non-hydrogen atoms were refined freely with anisotropic displacement parameters. Hydrogen atoms were introduced in calculated positions and refined with a riding model. One t-butyl group was refined with a disorder model. 527 Parameters were refined with 48 restraints (distances, angles and displacement parameters in the disordered t-butyl group). R1/wR2 [I > 2σ(I)]: 0.0596 / 0.1408. R1/wR2 [all refl.]: 0.1101 / 0.1598. S = 1.040. Residual electron density

between –0.42 and 0.74 e/Å^3. Geometry calculations and checking for higher symmetry was performed with the PLATON program.[7] [*] Derived values do not contain the contribution of the disordered solvent.

Crystallographic details for [Zn(Im^{Ph2}NNO^{tBu})(Cl)] (2)

$C_{48}H_{49}ClN_4O_2Zn$ + disordered solvent, Fw = 814.73[*], colourless needle, 0.68 × 0.14 × 0.06 mm^3, monoclinic, I2/a (no. 15), a = 26.8000(7), b = 10.00770(18), c = 35.6762(8) Å, β = 93.730(3) °, V = 9548.3(4) Å^3, Z = 8, D_x = 1.134 g/cm$^{3[*]}$, μ = 0.61 mm$^{-1[*]}$. The diffraction experiment was performed on a Bruker Kappa ApexII diffractometer with sealed tube and Triumph monochromator (λ = 0.71073 Å) at a temperature of 150(2) K up to a resolution of $(\sin\theta/\lambda)_{max}$ = 0.65 Å^{-1}. The Eval15 software[1] was used for the intensity integration. A multi-scan absorption correction and scaling was performed with SADABS[3] (correction range 0.60-0.75). A total of 88827 reflections was measured, 10955 reflections were unique (R_{int} = 0.057), 8529 reflections were observed [I>2σ(I)]. The structure was solved with Patterson superposition methods using SHELXT.[4] Structure refinement was performed with SHELXL-2018[5] on F^2 of all reflections. The crystal structure contains large voids (1643 Å^3/unit cell) filled with severely disordered solvent molecules. Their contribution to the structure factors was secured by the SQUEEZE algorithm[6] resulting in 397 electrons / unit cell. Non-hydrogen atoms were refined freely with anisotropic displacement parameters. Hydrogen atoms were introduced in calculated positions and refined with a riding model. One *t*-butyl group was refined with a disorder model. 527 Parameters were refined with 48 restraints (distances, angles and displacement parameters in the disordered t-butyl group). R1/wR2 [I > 2σ(I)]: 0.0365 / 0.0917. R1/wR2 [all refl.]: 0.0527 / 0.0976. S = 1.051. Residual electron density between –0.39 and 0.38 e/Å^3. Geometry calculations and checking for higher symmetry was performed with the PLATON program.[7] [*] Derived values do not contain the contribution of the disordered solvent.

Crystallographic details for [Fe(Im^{Ph2}NNO^{tBu})$_2$] (3)

$C_{96}H_{98}FeN_8O_4 \cdot 4C_5H_5N$ + disordered solvent, Fw = 1800.07[*], yellow block, 0.60 × 0.33 × 0.21 mm^3, triclinic, $P\overline{1}$ (no. 2), a = 14.8821(3), b = 17.9631(5), c = 22.1346(4) Å, α = 110.681(1), β = 91.354(1), γ = 107.963(1) °, V = 5207.33(19) Å^3, Z = 2, D_x = 1.148 g/cm$^{3[*]}$, μ = 0.20 mm$^{-1[*]}$. The diffraction experiment was performed on a Bruker Kappa ApexII diffractometer with sealed tube and Triumph monochromator (λ = 0.71073 Å) at a temperature of 150(2) K up to a resolution of $(\sin\theta/\lambda)_{max}$ = 0.65 Å^{-1}. The Eval15 software[1] was used for the intensity integration. A multi-scan absorption correction and scaling was performed with SADABS[3] (correction range 0.69-0.75). A total of 144002 reflections was measured, 23928 reflections were unique (R_{int} = 0.031), 19632 reflections were observed [I>2σ(I)]. The structure was solved with Patterson superposition methods using SHELXT.[4] Structure refinement was performed with SHELXL-2018[5] on F^2 of all reflections. In addition to the pyridine solvent molecules, the crystal structure contains large voids (608 Å^3/unit cell) filled with severely disordered solvent molecules. Their contribution to the structure factors was secured by the SQUEEZE algorithm[6] resulting in 145 electrons / unit cell. Non-hydrogen atoms were refined freely with anisotropic displacement parameters. Hydrogen atoms were introduced in calculated positions and refined with a riding model. One *t*-butyl group was refined with a disorder model. The methoxy groups were refined with full occupancy but a minor substitutional disorder cannot be ruled out. 1240 Parameters were refined with 404 restraints (distances, angles and displacement parameters in the t-butyl groups and pyridine molecules; molecular flatness in the pyridine molecules). R1/wR2 [I > 2σ(I)]: 0.0588 / 0.1803. R1/wR2 [all refl.]: 0.0701 / 0.1902. S = 1.043. Residual electron density between -0.69 and 0.97 e/Å^3. Geometry calculations and checking for higher symmetry was performed with the PLATON program.[7] [*] Derived values do not contain the contribution of the disordered solvent.

Crystallographic details for [Zn(Im^{Ph2}NNO^{tBu})(SPh)] (4)

$C_{54}H_{54}N_4O_2SZn \cdot 2C_4H_8O$, Fw = 1032.65, colourless needle, 0.41 × 0.05 × 0.04 mm^3, monoclinic, $P2_1/n$ (no. 14), *a* = 9.6290(3), *b* = 25.5389(8), *c* = 22.9504(6) Å, β = 101.534(1) °, V = 5529.9(3) Å^3, Z = 4, D_x = 1.240 g/cm^3, μ = 0.53 mm^{-1}. The diffraction experiment was performed on a Bruker Kappa ApexII diffractometer with sealed tube and Triumph monochromator (λ = 0.71073 Å) at a temperature of 150(2) K up to a resolution of $(\sin\theta/\lambda)_{max}$ = 0.65 Å^{-1}. The Eval15 software[1] was used for the intensity integration. A numerical absorption correction and scaling was performed with SADABS[3] (correction range 0.74-1.00). A total of 92199 reflections was measured, 12701 reflections were unique (R_{int} = 0.138), 7559 reflections were observed [I>2σ(I)]. The structure was solved with Patterson superposition methods using SHELXT.[4] Structure refinement was performed with SHELXL-2018[5] on F^2 of all reflections. Non-hydrogen atoms were refined freely with anisotropic displacement parameters. Hydrogen atoms were introduced in calculated positions and refined with a riding model. The co-crystallized THF molecules were refined with a disorder model. 723 Parameters were refined with 310 restraints (distances, angles and displacement parameters in the disordered THF). R1/wR2 [I > 2σ(I)]: 0.0577 / 0.1224. R1/wR2 [all refl.]: 0.1214 / 0.1461. S = 1.021. Residual electron density between -0.69 and 0.63 e/Å^3. Geometry calculations and checking for higher symmetry was performed with the PLATON program.[7]

Crystallographic details for [Zn(Im^{Ph2}NNO^{tBu})(SPh)(py)] (5)

$C_{59}H_{59}N_5O_2SZn \cdot 0.3(C_5H_5N)$, Fw = 991.27, colourless plate, 0.39 × 0.25 × 0.03 mm^3, monoclinic, $P2_1/c$ (no. 14), *a* = 14.0508(5), *b* = 26.6435(11), *c* = 16.9367(6) Å, β = 122.751(2) °, V = 5332.5(4) Å^3, Z = 4, D_x = 1.235 g/cm^3, μ = 0.55 mm^{-1}. The diffraction experiment was performed on a Bruker Kappa ApexII diffractometer with sealed tube and Triumph monochromator (λ = 0.71073 Å) at a temperature of 150(2) K up to a resolution of $(\sin\theta/\lambda)_{max}$ = 0.61 Å^{-1}. The Eval15 software[1] was used for the intensity integration. A large anisotropic mosaicity[2] about *hkl*=(0,0,1) was used for the prediction of the reflection profiles. A numerical absorption correction and scaling was performed with SADABS[3] (correction range 0.76-1.00). A total of 49701 reflections was measured, 9923 reflections were unique (R_{int} = 0.100), 6018 reflections were observed [I>2σ(I)]. The structure was solved with Patterson superposition methods using SHELXT.[4] Structure refinement was performed with SHELXL-2018[5] on F^2 of all reflections. Non-hydrogen atoms were refined freely with anisotropic displacement parameters. Hydrogen atoms were introduced in calculated positions and refined with a riding model. The co-crystallized non-coordinated pyridine molecule was refined with a partial occupancy. 676 Parameters were refined with 105 restraints (distances, angles, displacement parameters and molecular flatness in the partially occupied pyridine). R1/wR2 [I > 2σ(I)]: 0.0621 / 0.1390. R1/wR2 [all refl.]: 0.1235 / 0.1666. S = 1.042. Residual electron density between -0.52 and 1.53 e/Å^3. Geometry calculations and checking for higher symmetry was performed with the PLATON program.[7]

B.2 NMR Data

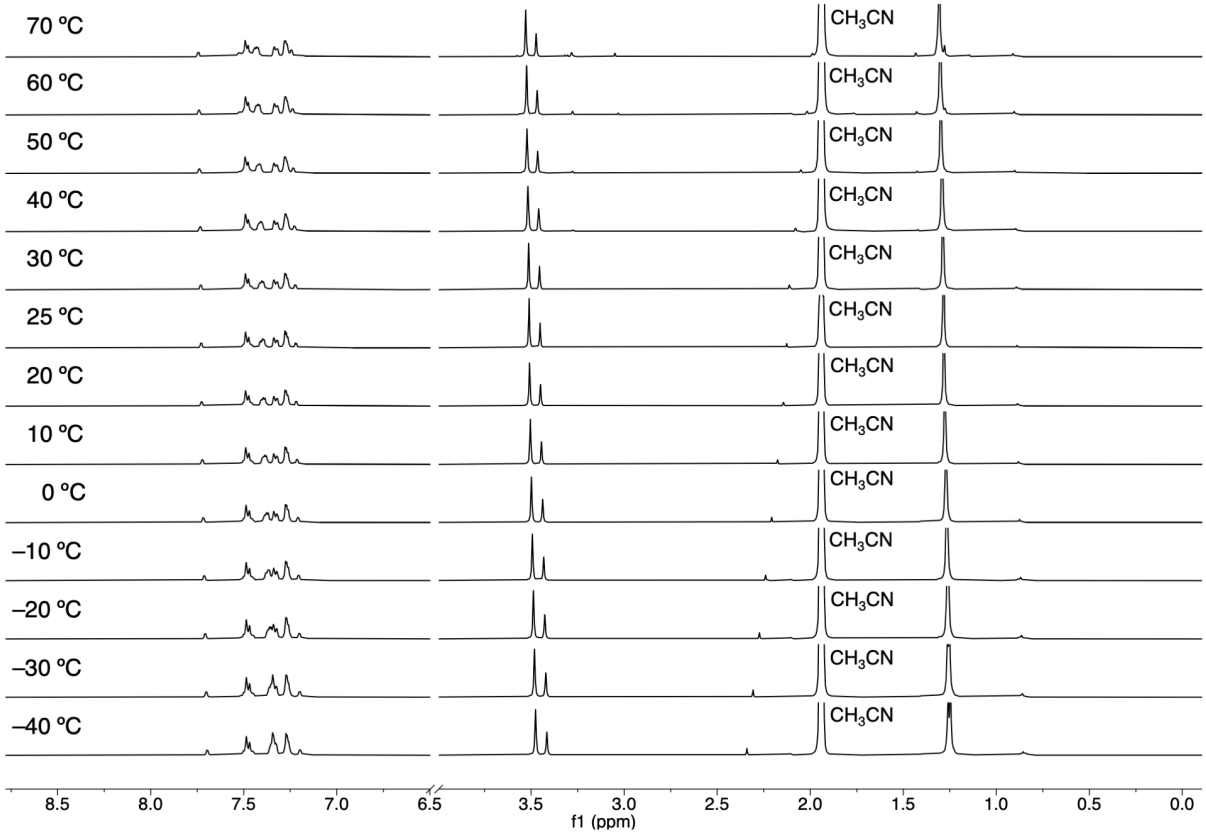

Figure B1. Stacked VT ^{1}H NMR (400 Hz) spectra of **2** in CD_3CN.

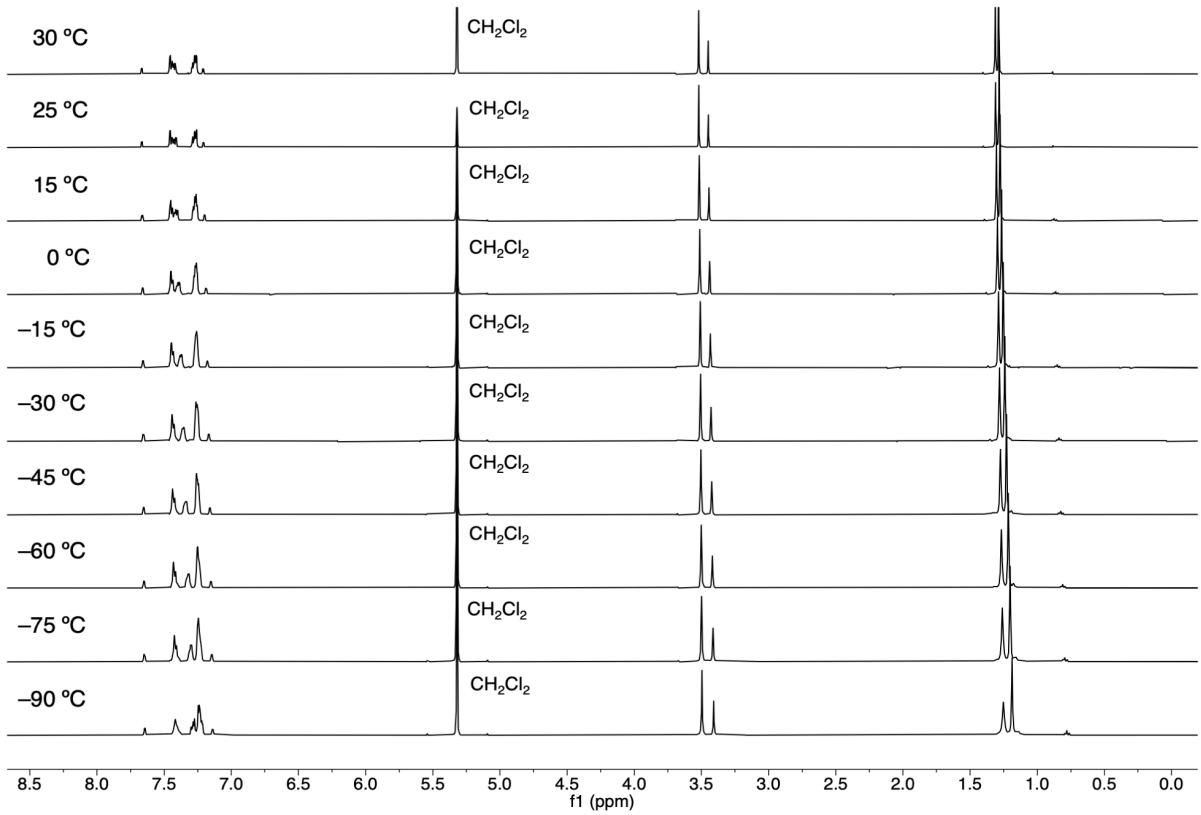

Figure B2. Stacked VT ^{1}H NMR (400 Hz) spectra of **2** in CD_2Cl_2.

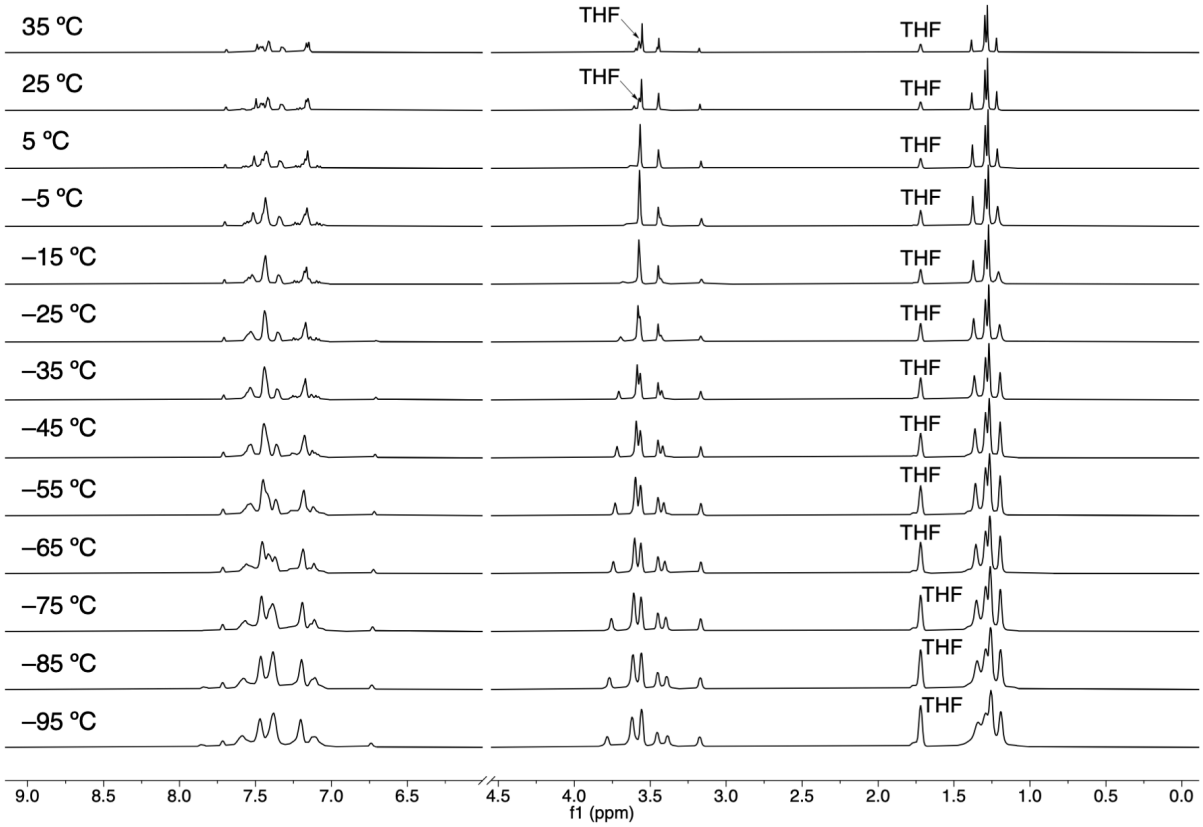

Figure B3. Stacked VT ^{1}H NMR (400 Hz) spectra of **2** in THF-d_8.

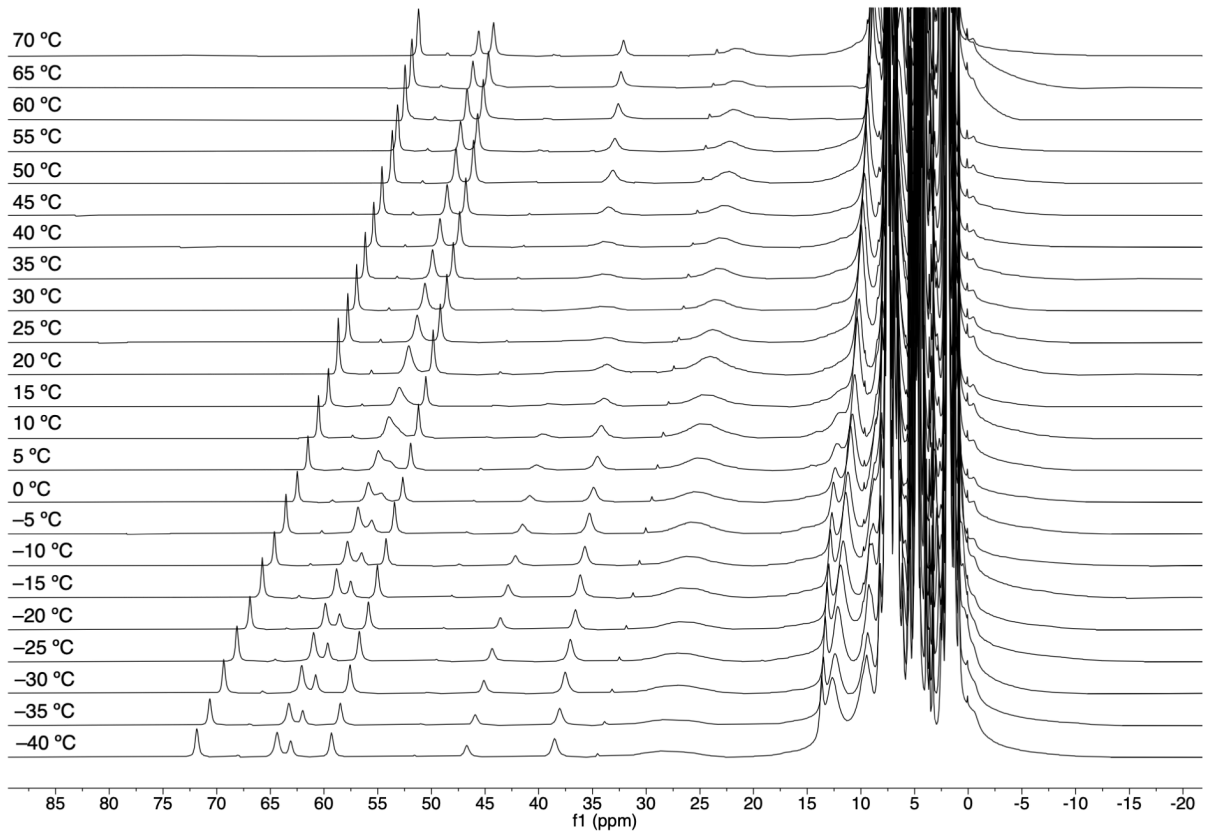

Figure B4. Stacked VT ^{1}H NMR (400 Hz) spectra of **1** in CD_3CN.

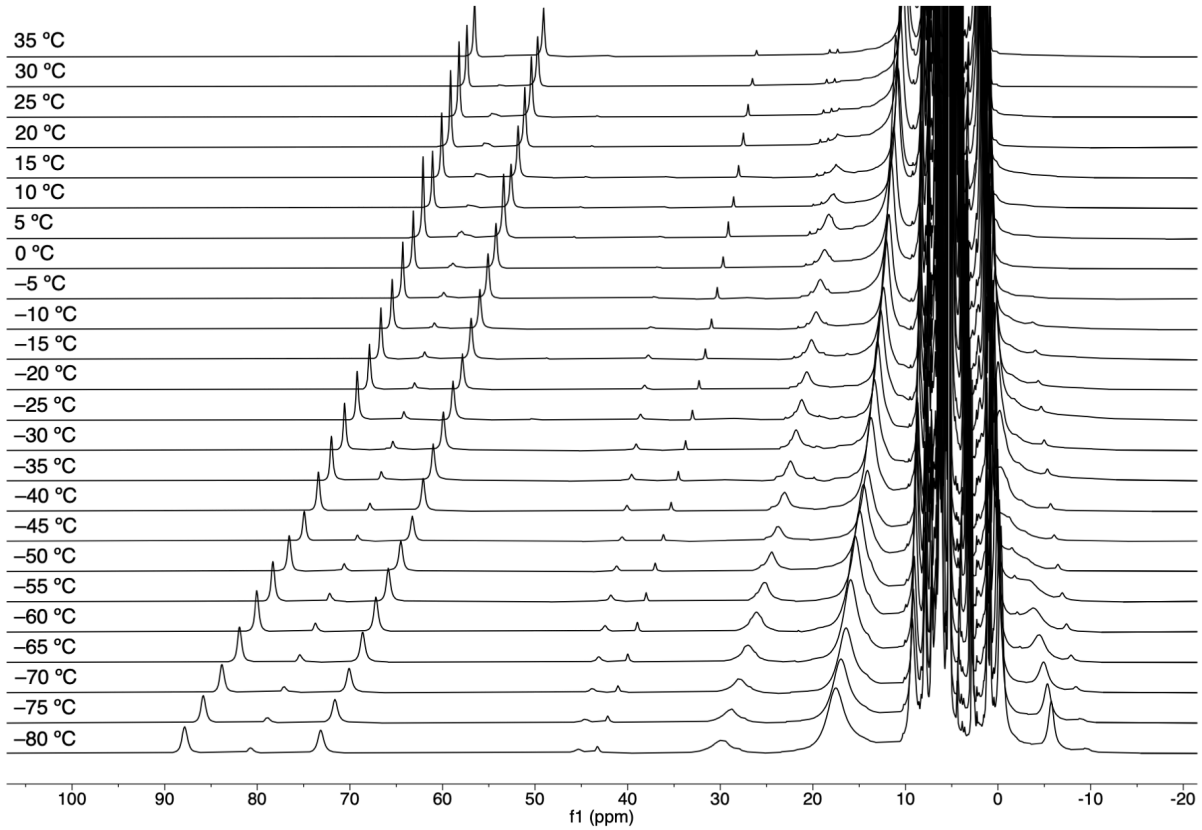

Figure B5. Stacked VT ^{1}H NMR (400 Hz) spectra of **1** in CD_2Cl_2.

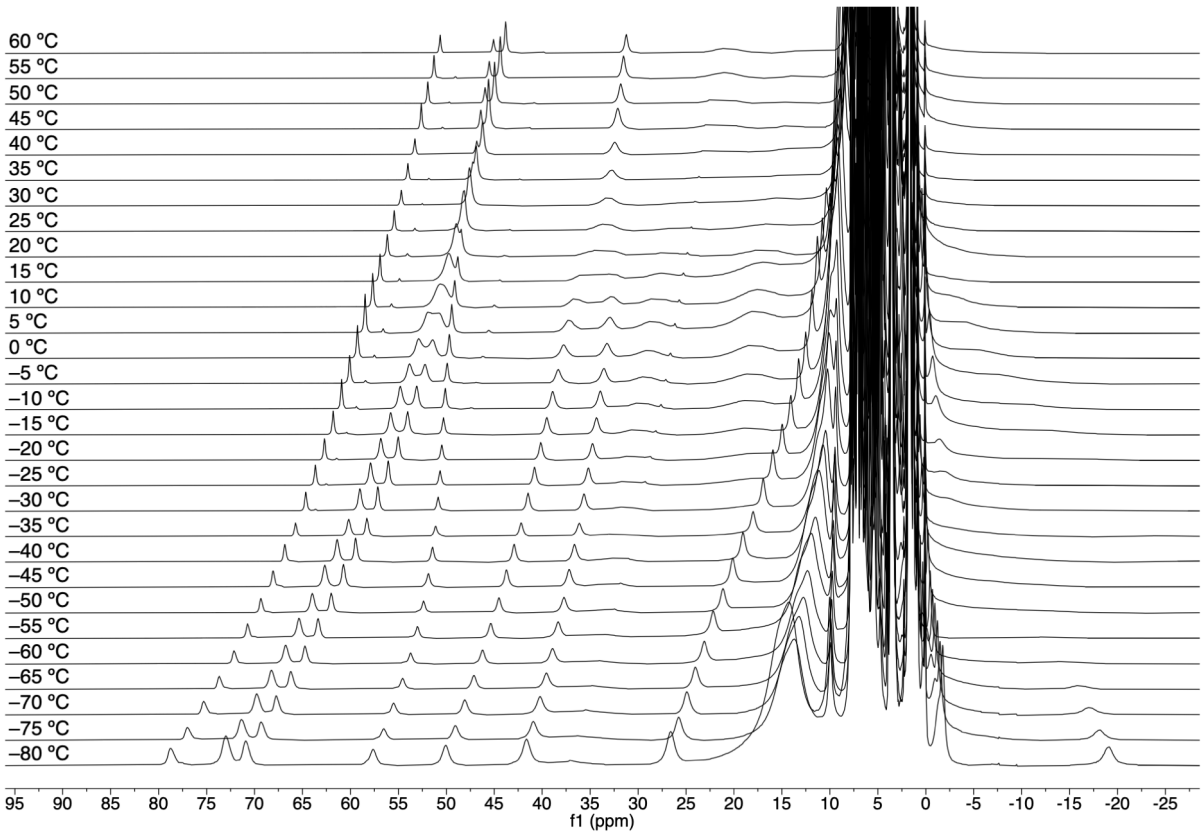

Figure B6. Stacked VT ^{1}H NMR (400 Hz) spectra of **1** in THF-d_8.

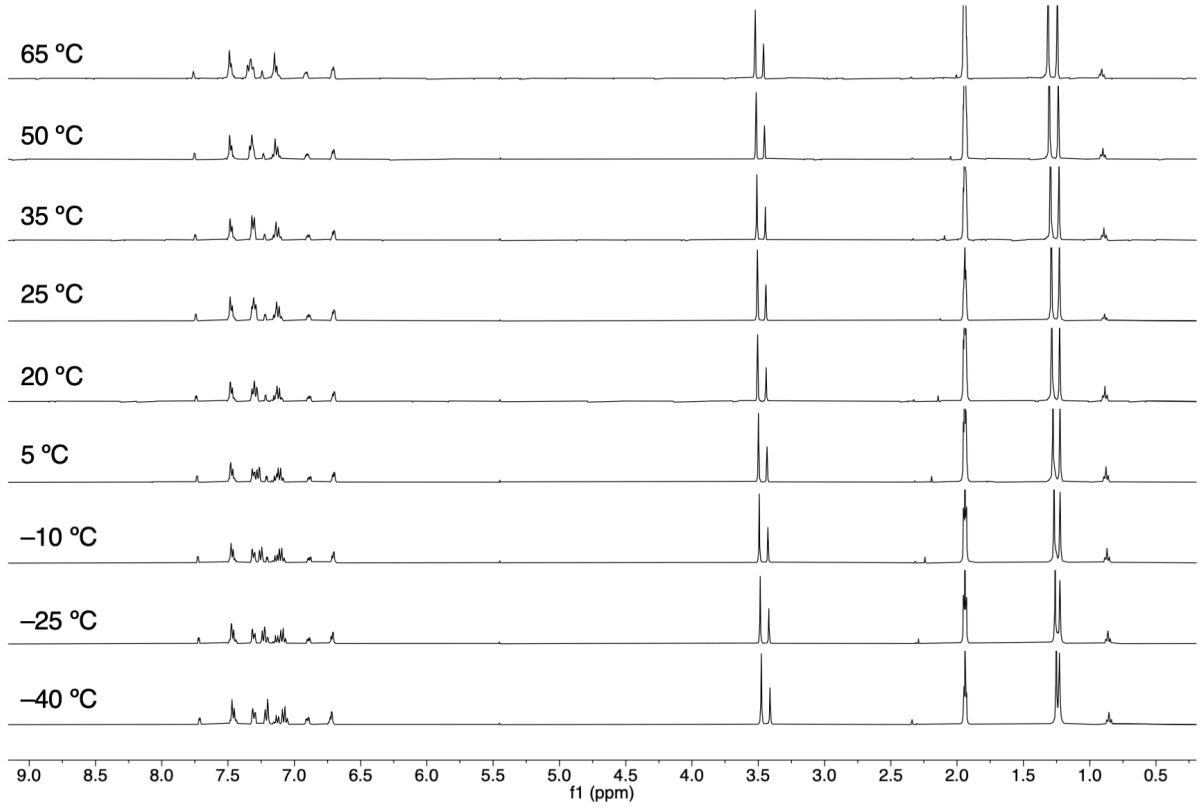

Figure B7. Stacked VT ^{1}H NMR (400 Hz) spectra of **4** in CD_3CN.

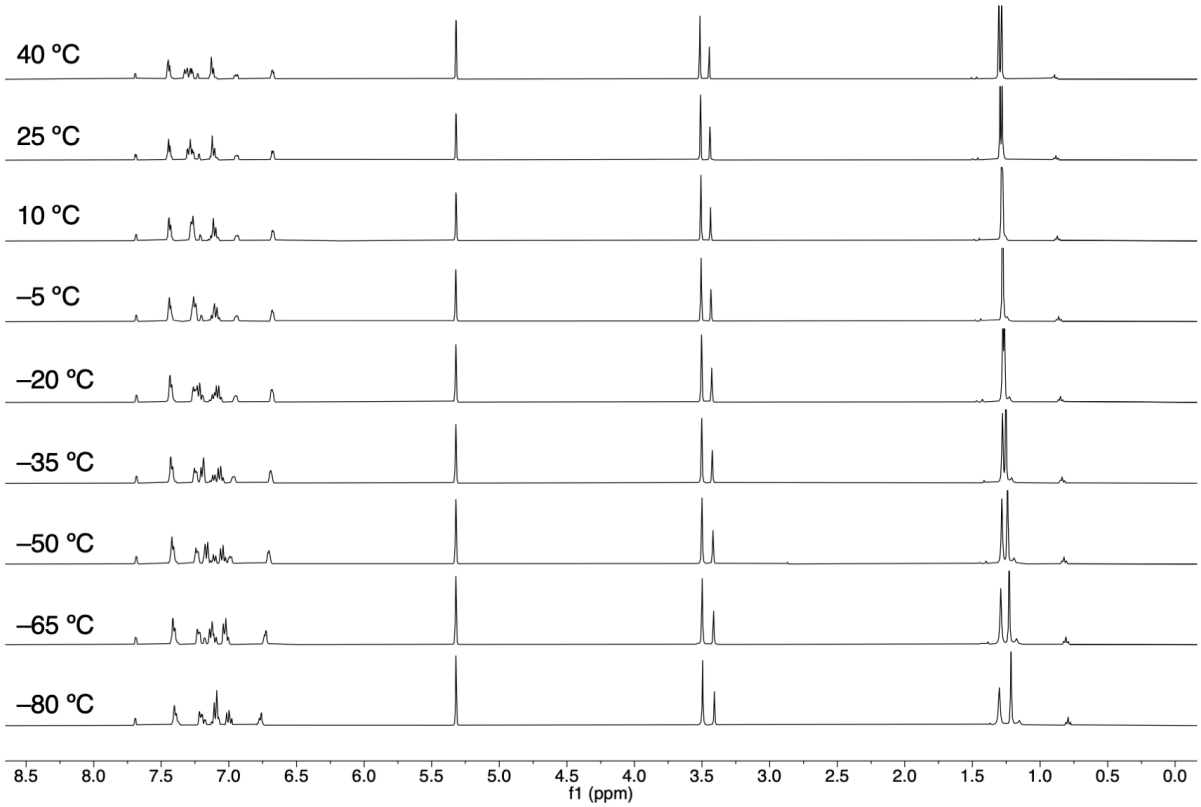

Figure B8. Stacked VT ^{1}H NMR (400 Hz) spectra of **4** in CD_2Cl_2.

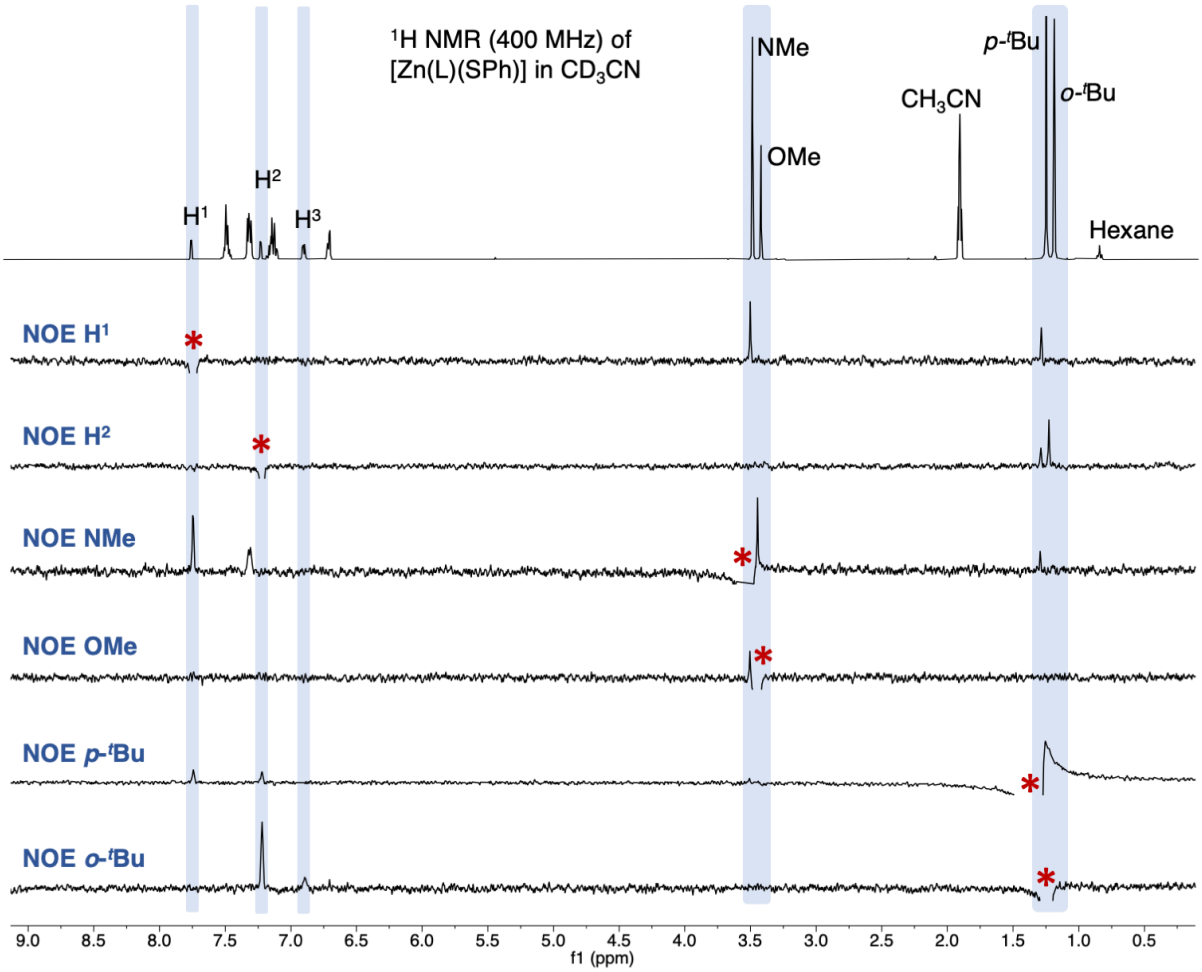

Figure B9. Stacked 1D NOE ^{1}H NMR spectra of **4** in CD_3CN at 25 °C. Selectively excited NMR signals are highlighted with a red asterisk and are in the negative phase (not depicted).

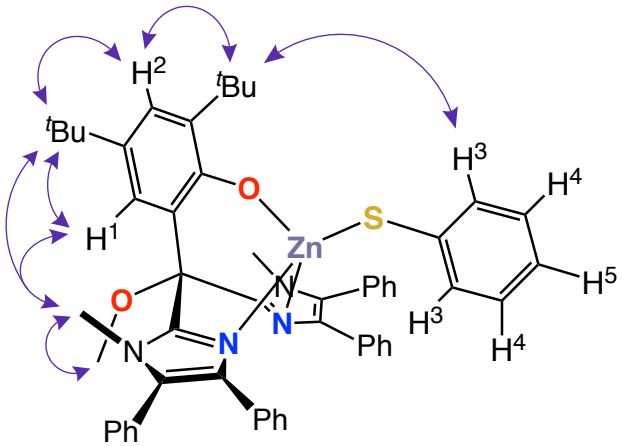

Figure B10. Schematic representation of the through-space correlations in **4** observed by 1D NOE experiments.

B.3 Cyclic Voltammetry

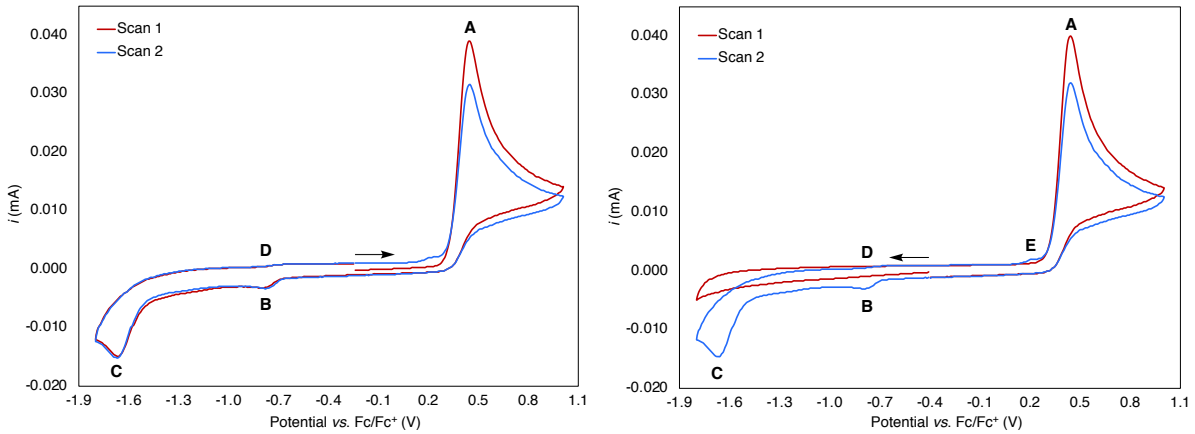

Figure B11. CV of **K-Im^{Ph2}NNO^{tBu}** recorded in an electrolyte solution of 0.1 M [^{n}Bu$_4$N]PF$_6$ in acetonitrile. Left: the CV recorded when scanning in the oxidative direction (2 scans). Right: the CV recorded when scanning in the reductive direction (2 scans).

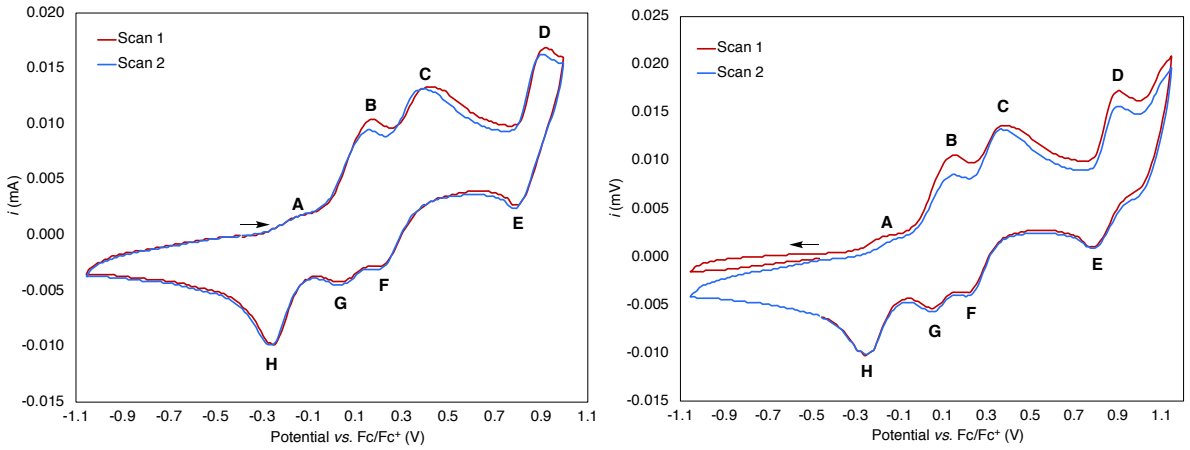

Figure B12. CV of **1** recorded in an electrolyte solution of 0.1 M [^{n}Bu$_4$N]PF$_6$ in acetonitrile. Left: the CV recorded when scanning in the oxidative direction (2 scans). Right: the CV recorded when scanning in the reductive direction (2 scans).

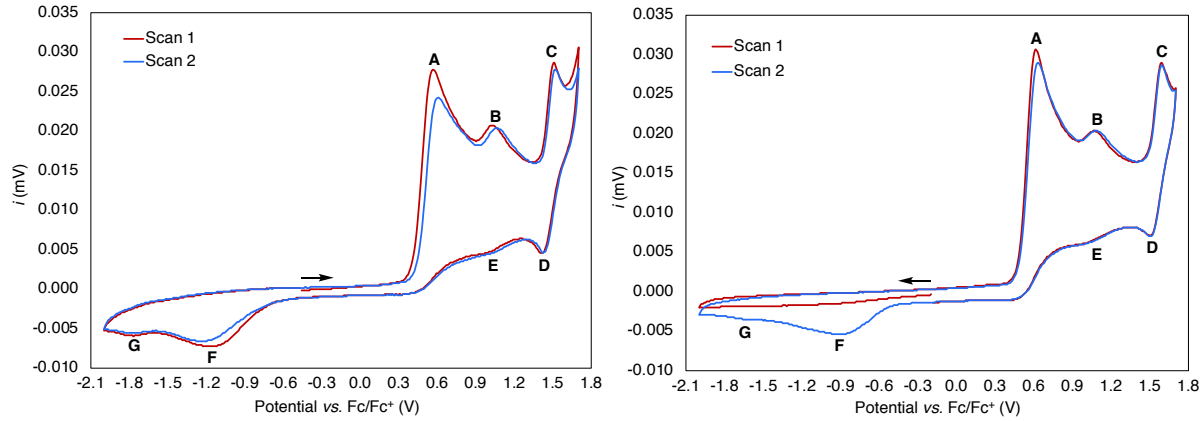

Figure B13. CV of **4** recorded in an electrolyte solution of 0.1 M [^{n}Bu$_4$N]PF$_6$ in acetonitrile. Left: the CV recorded when scanning in the oxidative direction (2 scans). Right: the CV recorded when scanning in the reductive direction (2 scans).

B.4 ^{57}Fe Mössbauer Spectroscopy

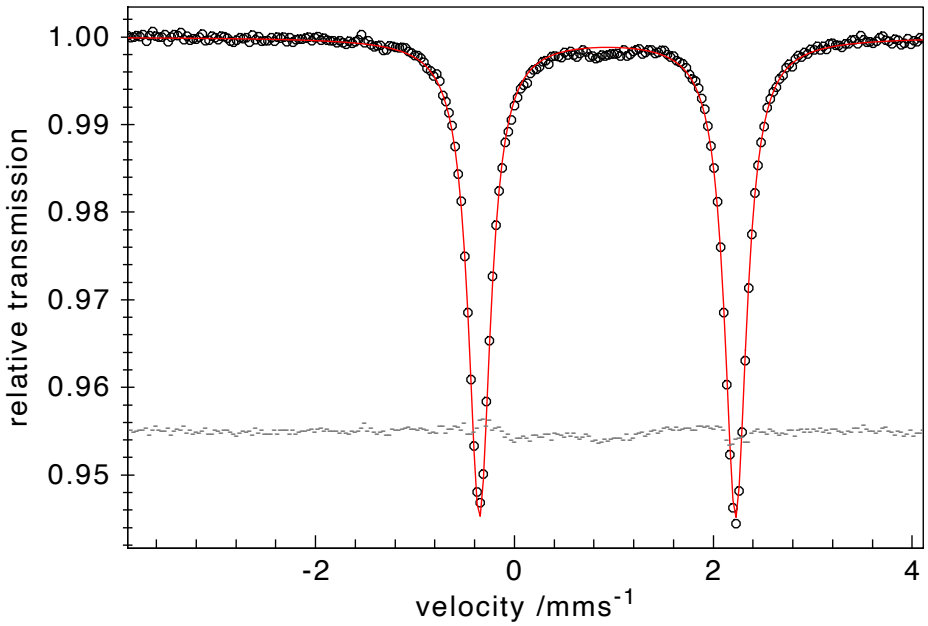

Figure B14. The zero-field ^{57}Fe Mössbauer spectra for **1**, recorded at 80 K. Data points are depicted by black circles and the best fit for **1** (100% relative abundancy) is given by the red trace, where $\delta = 0.94$ mm s^{-1} and $|\Delta E_Q| = 2.58$ mm s^{-1}.

B.5 References and Notes

(1) Schreurs, A. M. M.; Xian, X.; Kroon-Batenburg, L. M. J. *J. Appl. Crystallogr.* **2010**, *43*, 70–82.
(2) Duisenberg, A. J. M. *Acta Crystallogr. Sect. A* **1983**, *39*, 211–216.
(3) Sheldrick, G. M. SADABS and TWINABS, 2014.
(4) Sheldrick, G. M. *Acta Crystallogr. Sect. A Found. Crystallogr.* **2015**, *71*, 3–8.
(5) Sheldrick, G. M. *Acta Crystallogr. Sect. C Struct. Chem.* **2015**, *71*, 3–8.
(6) Spek, A. L. *Acta Crystallogr. Sect. C Struct. Chem.* **2015**, *71*, 9–18.
(7) Spek, A. L. *Acta Crystallogr. Sect. D Biol. Crystallogr.* **2009**, *65*, 148–155.

Appendix C

Supporting Information to Chapter 4

C.1 X-ray Crystal Structure Determinations

Crystallographic details for [Fe(Im^{Ph2}NNO^{tBu})(S^{t}Bu)] (3)

$C_{52}H_{58}FeN_4O_2S \cdot 3C_4H_8O \cdot 0.5C_6H_{14}$, Fw = 1118.33, pale yellow needle, 0.21 × 0.13 × 0.07 mm^3, triclinic, $P\overline{1}$ (no. 2), a = 10.8759(3), b = 14.0250(3), c = 20.9674(6) Å, α = 96.899(1), β = 97.400(1), γ = 102.128(1) °, V = 3064.89(13) Å^3, Z = 2, D_x = 1.212 g/cm^3, μ = 0.33 mm^{-1}. The diffraction experiment was performed on a Bruker Kappa ApexII diffractometer with sealed tube and Triumph monochromator (λ = 0.71073 Å) at a temperature of 150(2) K up to a resolution of $(\sin\theta/\lambda)_{max}$ = 0.65 Å^{-1}. The crystal appeared to be cracked with an angle of 4.02 ° between the two fragments. Consequently, two orientation matrices were used for the integration with the Eval15 software.[1] A multi-scan absorption correction and scaling was performed with TWINABS[2] (correction range 0.67-0.75). A total of 111247 reflections was measured, 14095 reflections were unique (R_{int} = 0.083), 8948 reflections were observed [I>2σ(I)]. The structure was solved with Patterson superposition methods using SHELXT.[3] Structure refinement was performed with SHELXL-2018[4] on F^2 of all reflections based on an HKLF-5 file.[5] Non-hydrogen atoms were refined freely with anisotropic displacement parameters. Hydrogen atoms were introduced in calculated positions and refined with a riding model. One *t*-butyl group at the phenyl moiety, the THF solvent molecules and the *n*-hexane on an inversion center were refined with disorder models. 866 Parameters were refined with 648 restraints (distances, angles and displacement parameters in the disordered groups). R1/wR2 [I > 2σ(I)]: 0.0624 / 0.1477. R1/wR2 [all refl.]: 0.1129 / 0.1739. S = 1.020. Batch scale factor for the two crystal fragments BASF = 0.360(4). Residual electron density between -0.56 and 0.71 e/Å^3. Geometry calculations and checking for higher symmetry was performed with the PLATON program.[6]

Crystallographic details for [Zn(Im^{Ph2}NNO^{tBu})(S^{t}Bu)] (4)

$2C_{52}H_{58}N_4O_2SZn \cdot 3C_4H_8O \cdot 0.5C_6H_{14}$, Fw = 1996.30, colourless needle, 0.45 × 0.22 × 0.18 mm^3, monoclinic, $P2_1/n$ (no. 14), a = 19.9337(3), b = 20.1339(3), c = 27.0442(5) Å, β = 91.503(1) °, V = 10850.3(3) Å^3, Z = 4, D_x = 1.222 g/cm^3, μ = 0.54 mm^{-1}. The diffraction experiment was performed on a Bruker Kappa ApexII diffractometer with sealed tube and Triumph monochromator (λ = 0.71073 Å) at a temperature of 150(2) K up to a resolution of $(\sin\theta/\lambda)_{max}$ = 0.65 Å^{-1}. The Eval15 software[1] was used for the intensity integration. A multi-scan absorption correction and scaling was performed with SADABS[2] (correction range 0.69-0.75). A total of 264823 reflections was measured, 24902 reflections were unique (R_{int} = 0.035), 20959 reflections were observed [I>2σ(I)]. The structure was solved with Patterson superposition methods using SHELXT.[3] Structure refinement was performed with SHELXL-2018[4] on F^2 of all reflections. Non-hydrogen atoms were refined freely with anisotropic displacement parameters. Hydrogen atoms were introduced in calculated positions and refined with a riding model. One *t*-butyl group at the phenyl moiety, the THF solvent molecules and the *n*-hexane on an inversion center were refined with disorder models. 1402 Parameters were refined with 524 restraints (distances, angles and displacement parameters in the disordered groups). R1/wR2 [I > 2σ(I)]: 0.0355 / 0.0957. R1/wR2 [all refl.]: 0.0447 / 0.1022. S = 1.032. Residual electron density between -0.45 and 0.53 e/Å^3. Geometry calculations and checking for higher symmetry was performed with the PLATON program.[6]

Crystallographic details for [Fe(Im^{Ph2}NNO^{tBu})(SBn)] (5)

$C_{55}H_{56}FeN_4O_2S \cdot 2C_4H_8O$, Fw = 1037.15, pale yellow needle, 0.41 × 0.08 × 0.03 mm^3, monoclinic, $P2_1/c$ (no. 14), *a* = 15.5990(8), *b* = 20.7907(8), *c* = 17.2966(9) Å, β = 100.981(3) °, V = 5506.8(4) Å^3, Z = 4, D_x = 1.251 g/cm^3, μ = 0.36 mm^{-1}. The diffraction experiment was performed on a Bruker Kappa ApexII diffractometer with sealed tube and Triumph monochromator (λ = 0.71073 Å) at a temperature of 150(2) K up to a resolution of $(\sin\theta/\lambda)_{max}$ = 0.61 Å^{-1}. The Eval15 software[1] was used for the intensity integration. A multi-scan absorption correction and scaling was performed with SADABS[2] (correction range 0.60-0.75). A total of 45318 reflections was measured, 10250 reflections were unique (R_{int} = 0.110), 5642 reflections were observed [I>2σ(I)]. Initial coordinates were taken from the isostructural Zn compound **6**. Structure refinement was performed with SHELXL-2018[4] on F^2 of all reflections. Non-hydrogen atoms were refined freely with anisotropic displacement parameters. Hydrogen atoms were introduced in calculated positions and refined with a riding model. The THF solvent molecules were refined with disorder models. 723 Parameters were refined with 300 restraints (distances, angles and displacement parameters in the disordered THF). R1/wR2 [I > 2σ(I)]: 0.0633 / 0.1386. R1/wR2 [all refl.]: 0.1383 / 0.1697. S = 1.018. Residual electron density between -0.50 and 0.45 e/Å^3. Geometry calculations and checking for higher symmetry was performed with the PLATON program.[6]

Crystallographic details for [Zn(Im^{Ph2}NNO^{tBu})(SBn)] (6)

$C_{55}H_{56}N_4O_2SZn \cdot 2C_4H_8O$, Fw = 1046.67, colourless plate, 0.24 × 0.08 × 0.03 mm^3, monoclinic, $P2_1/c$ (no. 14), *a* = 15.5805(6), *b* = 20.8217(8), *c* = 17.3347(6) Å, β = 100.540(2) °, V = 5528.7(3) Å^3, Z = 4, D_x = 1.257 g/cm^3, μ = 0.53 mm^{-1}. The diffraction experiment was performed on a Bruker Kappa ApexII diffractometer with sealed tube and Triumph monochromator (λ = 0.71073 Å) at a temperature of 150(2) K up to a resolution of $(\sin\theta/\lambda)_{max}$ = 0.61 Å^{-1}. The Eval15 software[1] was used for the intensity integration. A multi-scan absorption correction and scaling was performed with SADABS[2] (correction range 0.62-0.75). A total of 104219 reflections was measured, 10294 reflections were unique (R_{int} = 0.102), 7161 reflections were observed [I>2σ(I)]. The structure was solved with Patterson superposition methods using SHELXT.[3] Structure refinement was performed with SHELXL-2018[4] on F^2 of all reflections. Non-hydrogen atoms were refined freely with anisotropic displacement parameters. Hydrogen atoms of the metal complex were located in difference Fourier maps. Hydrogen atoms of the THF were introduced in calculated positions. All hydrogen atoms were refined with a riding model. The THF solvent molecules were refined with disorder models. 723 Parameters were refined with 300 restraints (distances, angles and displacement parameters in the disordered THF). R1/wR2 [I > 2σ(I)]: 0.0463 / 0.1029. R1/wR2 [all refl.]: 0.0821 / 0.1192. S = 1.015. Residual electron density between -0.46 and 0.40 e/Å^3. Geometry calculations and checking for higher symmetry was performed with the PLATON program.[6]

Crystallographic details for [Fe(Im^{Ph2}NNO^{tBu})(SPh)] (7)

$C_{54}H_{54}FeN_4O_2S$, Fw = 878.92, colourless block, 0.46 × 0.22 × 0.12 mm^3, monoclinic, $P2_1/c$ (no. 14), *a* = 10.7803(5), *b* = 19.7843(11), *c* = 22.2695(7) Å, β = 96.283(3) °, V = 4721.1(4) Å^3, Z = 4, D_x = 1.237 g/cm^3, μ = 0.41 mm^{-1}. The diffraction experiment was performed on a Bruker Kappa ApexII diffractometer with sealed tube and Triumph monochromator (λ = 0.71073 Å) at a temperature of 150(2) K up to a resolution of $(\sin\theta/\lambda)_{max}$ = 0.65 Å^{-1}. The crystal appeared to be cracked with an angle of 1.52 ° between the two fragments. Consequently, two orientation matrices were used for the integration with the Eval15 software.[1] A multi-scan absorption correction and scaling was performed with TWINABS[2] (correction range 0.55-0.75). A total of 63860 reflections was measured, 12214 reflections were unique (R_{int} = 0.060), 8479 reflections were observed [I>2σ(I)]. The structure was solved with Patterson superposition methods using SHELXT.[3] Structure refinement was performed

with SHELXL-2018[4] on F^2 of all reflections based on an HKLF-5 file.[5] Non-hydrogen atoms were refined freely with anisotropic displacement parameters. Hydrogen atoms were introduced in calculated positions and refined with a riding model. 866 Parameters were refined with no restraints. R1/wR2 [I > 2σ(I)]: 0.0524 / 0.1209. R1/wR2 [all refl.]: 0.0863 / 0.1339. S = 1.039. Batch scale factor for the two crystal fragments BASF = 0.228(4). Residual electron density between -0.49 and 0.82 e/Å^3. Geometry calculations and checking for higher symmetry was performed with the PLATON program.[6]

Crystallographic details for [Fe(Im^{Ph2}NNO^{tBu})(SMes)] (9)

$C_{57}H_{60}FeN_4O_2S \cdot C_4H_8O$ + disordered solvent, Fw = 993.10[*], yellow block, 0.56 × 0.19 × 0.11 mm^3, monoclinic, $P2_1/n$ (no. 14), *a* = 13.9609(4), *b* = 21.6280(6), *c* = 19.0610(6) Å, β = 97.147(1) °, V = 5710.7(3) Å^3, Z = 4, D_x = 1.155 g/cm$^{3[*]}$, μ = 0.35 mm$^{-1[*]}$. The diffraction experiment was performed on a Bruker Kappa ApexII diffractometer with sealed tube and Triumph monochromator (λ = 0.71073 Å) at a temperature of 150(2) K up to a resolution of $(\sin\theta/\lambda)_{max}$ = 0.65 Å^{-1}. The Eval15 software[1] was used for the intensity integration. A multi-scan absorption correction and scaling was performed with SADABS[2] (correction range 0.65-0.75). A total of 92665 reflections was measured, 13118 reflections were unique (R_{int} = 0.058), 9231 reflections were observed [I>2σ(I)]. Initial coordinates were taken from the isostructural Zn compound **10**. Structure refinement was performed with SHELXL-2018[4] on F^2 of all reflections. The crystal structure contains large voids (656 Å^3/unit cell) filled with severely disordered hexane solvent molecules. Their contribution to the structure factors was secured by the SQUEEZE algorithm[7] resulting in 114 electrons / unit cell. Non-hydrogen atoms were refined freely with anisotropic displacement parameters. Hydrogen atoms were introduced in calculated positions and refined with a riding model. One *t*-butyl group at the phenyl moiety was refined with a disorder model. 674 Parameters were refined with 174 restraints (distances, angles and displacement parameters in the *t*-butyl group and the THF solvent). R1/wR2 [I > 2σ(I)]: 0.0452 / 0.1148. R1/wR2 [all refl.]: 0.0723 / 0.1266. S = 1.041. Residual electron density between -0.46 and 0.37 e/Å^3. Geometry calculations and checking for higher symmetry was performed with the PLATON program.[6] [*] Derived values do not contain the contribution of the disordered solvent.

Crystallographic details for [Zn(Im^{Ph2}NNO^{tBu})(SMes)] (10)

$C_{57}H_{60}N_4O_2SZn \cdot CH_2Cl_2$ + disordered solvent, Fw = 1015.44[*], colourless block, 0.37 × 0.30 × 0.25 mm^3, monoclinic, $P2_1/n$ (no. 14), *a* = 13.7731(4), *b* = 21.5877(5), *c* = 19.0611(4) Å, β = 96.740(1) °, V = 5628.3(3) Å^3, Z = 4, D_x = 1.198 g/cm$^{3[*]}$, μ = 0.61 mm$^{-1[*]}$. The diffraction experiment was performed on a Bruker Kappa ApexII diffractometer with sealed tube and Triumph monochromator (λ = 0.71073 Å) at a temperature of 150(2) K up to a resolution of $(\sin\theta/\lambda)_{max}$ = 0.65 Å^{-1}. The Eval15 software[1] was used for the intensity integration. A multi-scan absorption correction and scaling was performed with SADABS[2] (correction range 0.68-0.75). A total of 89623 reflections was measured, 12924 reflections were unique (R_{int} = 0.040), 10111 reflections were observed [I>2σ(I)]. The structure was solved with Patterson superposition methods using SHELXT.[3] Structure refinement was performed with SHELXL-2018[4] on F^2 of all reflections. The crystal structure contains large voids (726 Å^3/unit cell) filled with severely disordered solvent molecules. Their contribution to the structure factors was secured by the SQUEEZE algorithm[7] resulting in 142 electrons / unit cell. Non-hydrogen atoms were refined freely with anisotropic displacement parameters. Hydrogen atoms were introduced in calculated positions and refined with a riding model. 625 Parameters were refined with no restraints. R1/wR2 [I > 2σ(I)]: 0.0351 / 0.0886. R1/wR2 [all refl.]: 0.0495 / 0.0940. S = 1.058. Residual electron density between -0.47 and 0.45 e/Å^3. Geometry calculations and checking for higher symmetry was performed with the PLATON program.[6] [*] Derived values do not contain the contribution of the disordered solvent.

Crystallographic details for [Fe(Im^{Ph2}NNO^{tBu})(SPh^{OMe})] (11)

$C_{55}H_{56}FeN_4O_3S \cdot 2CH_2Cl_2$, Fw = 1078.80, colourless block, 0.54 × 0.40 × 0.13 mm^3, triclinic, $P\overline{1}$ (no. 2), *a* = 11.2472(8), *b* = 15.7749(10), *c* = 16.5564(10) Å, α = 83.594(5), β = 72.109(4), γ = 78.295(4) °, V = 2733.5(3) Å^3, Z = 2, D_x = 1.311 g/cm^3, μ = 0.56 mm^{-1}. The diffraction experiment was performed on a Bruker Kappa ApexII diffractometer with sealed tube and Triumph monochromator (λ = 0.71073 Å) at a temperature of 150(2) K up to a resolution of $(\sin\theta/\lambda)_{max}$ = 0.65 Å^{-1}. The crystal appeared to be cracked into several fragments. Three orientation matrices for the major fragments were used for the integration with the Eval15 software.[1] A multi-scan absorption correction and scaling was performed with TWINABS[2] (correction range 0.49-0.75). A total of 151504 reflections was measured, 12744 reflections were unique (R_{int} = 0.061), 10253 reflections were observed [I>2σ(I)]. The structure was solved with Patterson superposition methods using SHELXT.[3] Structure refinement was performed with SHELXL-2018[4] on F^2 of all reflections based on an HKLF-5 file.[5] Non-hydrogen atoms were refined freely with anisotropic displacement parameters. Hydrogen atoms were introduced in calculated positions and refined with a riding model. 643 Parameters were refined with no restraints. R1/wR2 [I > 2σ(I)]: 0.0587 / 0.1648. R1/wR2 [all refl.]: 0.0728 / 0.1748. S = 1.077. Batch scale factor for the three crystal fragments BASF = 0.255(2), 0.143(2). Residual electron density between -0.92 and 1.09 e/Å^3. Geometry calculations and checking for higher symmetry was performed with the PLATON program.[6]

Crystallographic details for [Zn(Im^{Ph2}NNO^{tBu})(SPh^{OMe})] (12)

$C_{55}H_{56}N_4O_3SZn$ + disordered solvent, Fw = 918.46[*], colourless plate, 0.38 × 0.28 × 0.03 mm^3, triclinic, $P\overline{1}$ (no. 2), *a* = 10.9545(6), *b* = 15.8612(9), *c* = 15.9033(6) Å, α = 91.560(2), β = 104.311(2), γ = 92.977(2) °, V = 2671.6(2) Å^3, Z = 2, D_x = 1.142 g/cm$^{3[*]}$, μ = 0.54 mm$^{-1[*]}$. The diffraction experiment was performed on a Bruker Kappa ApexII diffractometer with sealed tube and Triumph monochromator (λ = 0.71073 Å) at a temperature of 150(2) K up to a resolution of $(\sin\theta/\lambda)_{max}$ = 0.61 Å^{-1}. The Eval15 software[1] was used for the intensity integration. A numerical absorption correction and scaling was performed with SADABS[2] (correction range 0.57-1.00). A total of 49197 reflections was measured, 9969 reflections were unique (R_{int} = 0.067), 7103 reflections were observed [I>2σ(I)]. The structure was solved with Patterson superposition methods using SHELXT.[3] Structure refinement was performed with SHELXL-2018[4] on F^2 of all reflections. The crystal structure contains large voids (457 Å^3/unit cell) filled with severely disordered hexane solvent molecules. Their contribution to the structure factors was secured by the SQUEEZE algorithm[7] resulting in 49 electrons / unit cell. Non-hydrogen atoms were refined freely with anisotropic displacement parameters. Hydrogen atoms were introduced in calculated positions and refined with a riding model. One *t*-butyl group at the phenyl moiety was refined with a disorder model. 618 Parameters were refined with 144 restraints (distances, angles and displacement parameters in the disordered *t*-butyl group). R1/wR2 [I > 2σ(I)]: 0.0476 / 0.1122. R1/wR2 [all refl.]: 0.0762 / 0.1251. S = 1.039. Residual electron density between -0.41 and 1.11 e/Å^3. Geometry calculations and checking for higher symmetry was performed with the PLATON program.[6] [*] Derived values do not contain the contribution of the disordered solvent.

Crystallographic details for [Zn(Im^{Ph2}NNO^{tBu})(SPh^{CF3})] (14)

$C_{55}H_{53}F_3N_4O_2SZn \cdot 2C_4H_8O \cdot C_6H_{14}$, Fw = 1186.82, colourless needle, 0.45 × 0.22 × 0.14 mm^3, triclinic, $P\overline{1}$ (no. 2), *a* = 13.5785(4), *b* = 14.9598(5), *c* = 16.9249(5) Å, α = 68.418(2), β = 84.639(2), γ = 88.737(2) °, V = 3182.68(19) Å^3, Z = 2, D_x = 1.238 g/cm^3, μ = 0.48 mm^{-1}. The diffraction experiment was performed on a Bruker Kappa ApexII diffractometer with sealed tube and Triumph monochromator (λ = 0.71073 Å) at a temperature of 150(2) K up to a resolution of $(\sin\theta/\lambda)_{max}$ = 0.65 Å^{-1}. The Eval15 software[1] was used for the intensity integration. A multi-scan absorption correction

and scaling was performed with TWINABS[2] (correction range 0.63-0.75). A total of 70345 reflections was measured, 14619 reflections were unique (R_{int} = 0.044), 11267 reflections were observed [I>2σ(I)]. The structure was solved with Patterson superposition methods using SHELXT.[3] Structure refinement was performed with SHELXL-2018[4] on F^2 of all reflections. Non-hydrogen atoms were refined freely with anisotropic displacement parameters. H atoms of the metal complex were located in difference Fourier maps. H atoms of the solvent molecules were introduced in calculated positions. All hydrogen atoms were refined with a riding model. The CF_3 group and the THF and *n*-hexane solvent molecules were refined with disorder models. 923 Parameters were refined with 655 restraints (distances, angles and displacement parameters in the disordered groups). R1/wR2 [I > 2σ(I)]: 0.0419 / 0.1058. R1/wR2 [all refl.]: 0.0616 / 0.1148. S = 1.035. Residual electron density between -0.37 and 0.75 e/Å^3. Geometry calculations and checking for higher symmetry was performed with the PLATON program.[6]

Crystallographic details for $[Fe(L\text{-quinone})_2](PF_6)_2$ (15)

$[C_{94}H_{92}FeN_8O_2](PF_6)_2 \cdot 9C_4H_8O$, Fw = 2360.47, red plate, 0.44 × 0.30 × 0.07 mm^3, monoclinic, I2/a (no. 15), *a* = 29.6937(8), *b* = 14.2183(5), *c* = 30.0172(9) Å, β = 99.758(1) °, V = 12489.7(7) Å^3, Z = 4, D_x = 1.255 g/cm^3, μ = 0.33 mm^{-1}. The diffraction experiment was performed on a Bruker Kappa ApexII diffractometer with sealed tube and Triumph monochromator (λ = 0.71073 Å) at a temperature of 150(2) K up to a resolution of $(\sin\theta/\lambda)_{max}$ = 0.61 Å^{-1}. A split-mosaic model was used for the intensity integration with the Eval15 software.[1] A multi-scan absorption correction and scaling was performed with SADABS[2] (correction range 0.63-0.75). A total of 93614 reflections was measured, 11609 reflections were unique (R_{int} = 0.071), 7844 reflections were observed [I>2σ(I)]. The structure was solved with Patterson superposition methods using SHELXT.[3] Structure refinement was performed with SHELXL-2018[4] on F^2 of all reflections. Non-hydrogen atoms were refined freely with anisotropic displacement parameters. Hydrogen atoms were introduced in calculated positions and refined with a riding model. The PF_6 anion and some of the THF solvent molecules were refined with disorder models. 893 Parameters were refined with 1472 restraints (distances, angles and displacement parameters in the disordered groups). R1/wR2 [I > 2σ(I)]: 0.0726 / 0.1945. R1/wR2 [all refl.]: 0.1091 / 0.2275. S = 1.026. Residual electron density between -0.47 and 0.97 e/Å^3. Geometry calculations and checking for higher symmetry was performed with the PLATON program.[6]

Crystallographic details for $[Fe_2(L^*)_2(Cl)_2]$ (16)

$C_{94}H_{92}Cl_2Fe_2N_8O_4 \cdot C_6H_6 \cdot H_2O$, Fw = 1676.47, dark purple plate, 0.27 × 0.26 × 0.06 mm^3, monoclinic, $P2_1/c$ (no. 14), *a* = 23.6538(5), *b* = 14.8689(4), *c* = 26.3368(6) Å, β = 106.168(1) °, V = 8896.5(4) Å^3, Z = 4, D_x = 1.252 g/cm^3, μ = 0.44 mm^{-1}. The diffraction experiment was performed on a Bruker Kappa ApexII diffractometer with sealed tube and Triumph monochromator (λ = 0.71073 Å) at a temperature of 150(2) K up to a resolution of $(\sin\theta/\lambda)_{max}$ = 0.65 Å^{-1}. The intensities were integrated with the Eval15 software.[1] The presence of a small additional crystal fragment was ignored during the integration. A multi-scan absorption correction and scaling was performed with SADABS[2] (correction range 0.67-0.75). A total of 97414 reflections was measured, 20457 reflections were unique (R_{int} = 0.082), 12658 reflections were observed [I>2σ(I)]. The structure was solved with Patterson superposition methods using SHELXT.[3] Structure refinement was performed with SHELXL-2018[4] on F^2 of all reflections. Non-hydrogen atoms were refined freely with anisotropic displacement parameters. Hydrogen atoms were introduced in calculated positions and refined with a riding model. One of the phenyl groups was refined with a disorder model. A peak in the residual electron density was interpreted as water molecule and included in the refinement. 1131 Parameters were refined with 172 restraints (distances, angles, displacement parameters and ring flatness in the disordered group). R1/wR2 [I > 2σ(I)]: 0.0489 / 0.0988. R1/wR2 [all refl.]: 0.1029 / 0.1165. S = 1.013. Residual electron density between –0.38 and 0.64 e/Å^3. Geometry calculations and checking for higher symmetry was performed with PLATON.[6]

C.2 NMR Data

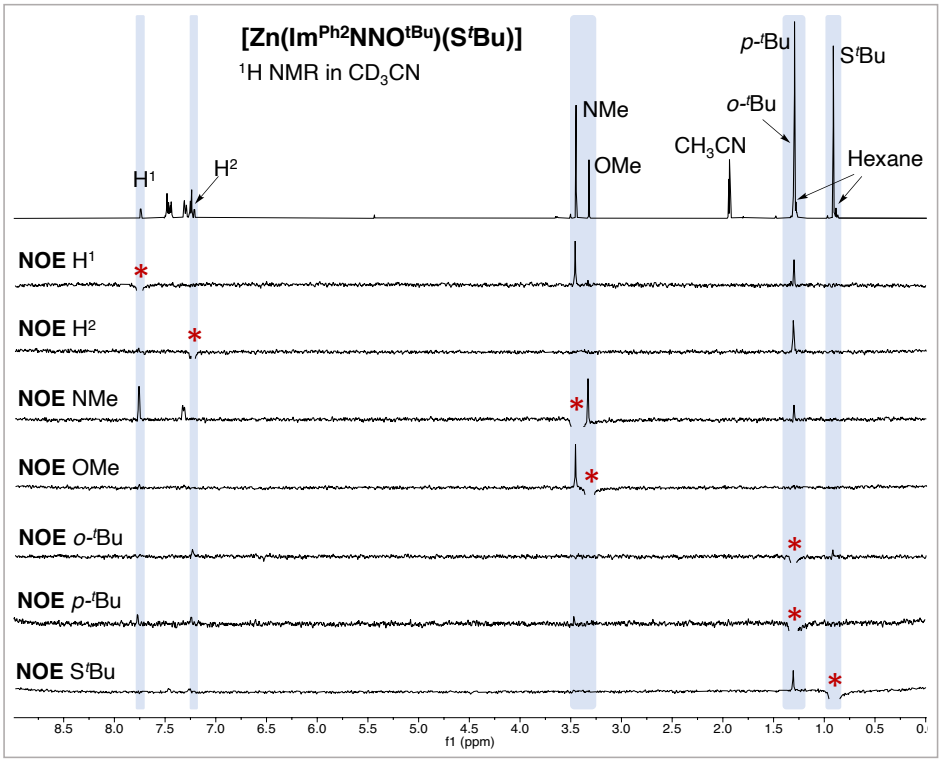

Figure C1. Stacked 1D NOE ^{1}H NMR spectra of **4** in CD_3CN at 25 °C. Selectively excited NMR signals are highlighted with a red asterisk and are in the negative phase (not depicted).

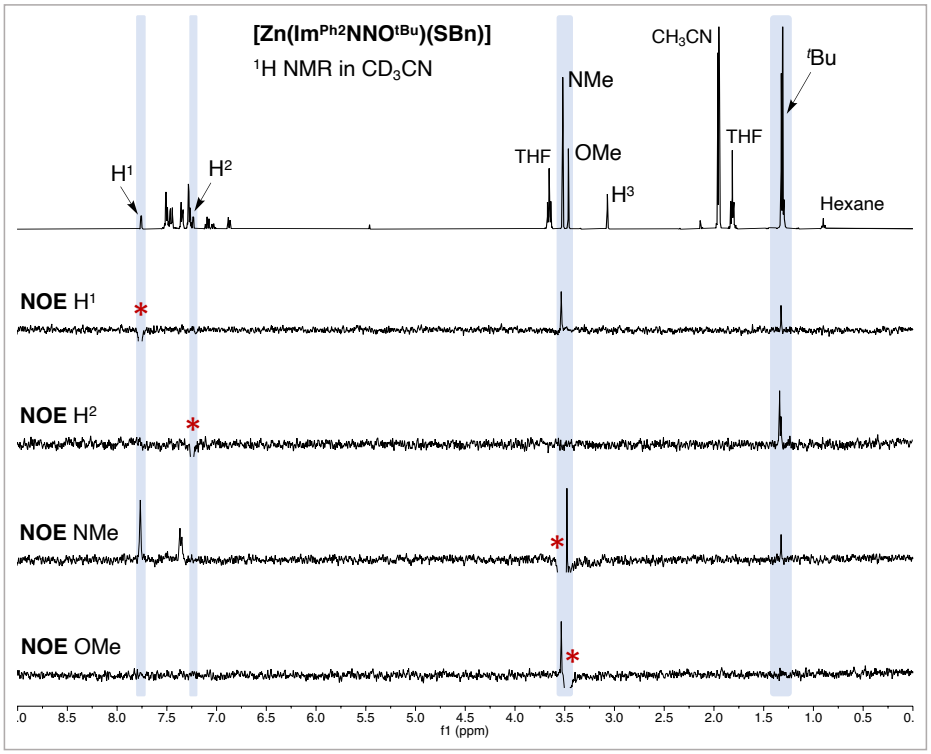

Figure C2. Stacked 1D NOE ^{1}H NMR spectra of **6** in CD_3CN at 25 °C. Selectively excited NMR signals are highlighted with a red asterisk and are in the negative phase (not depicted).

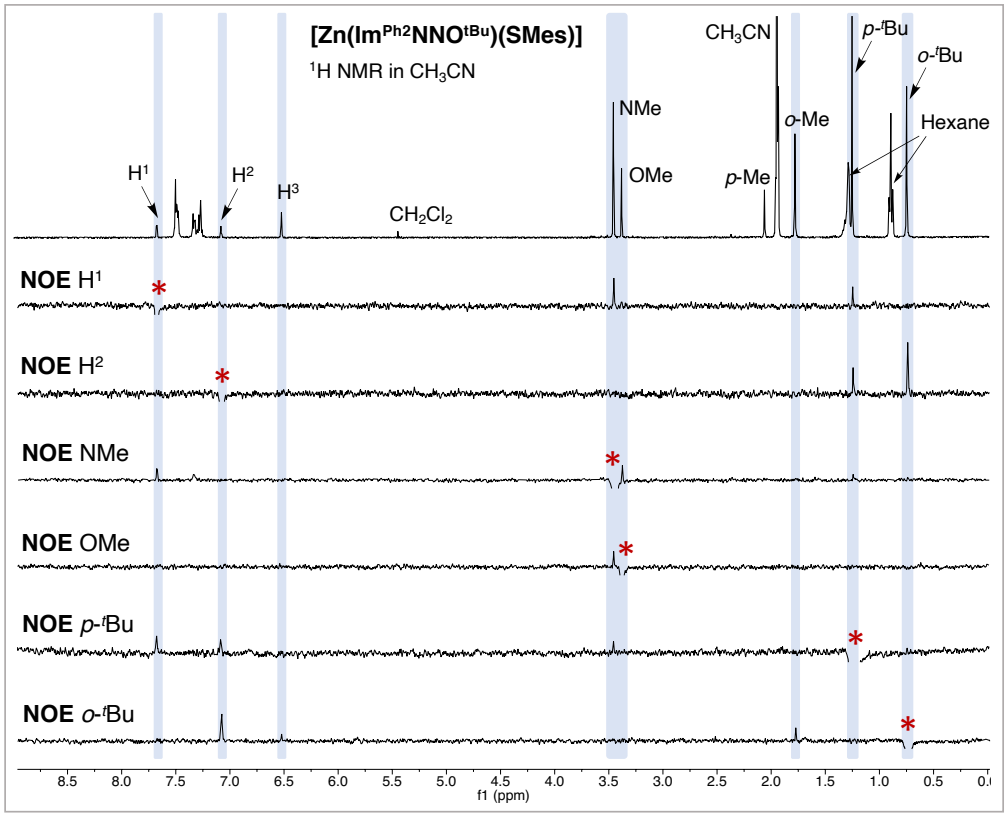

Figure C3. Stacked 1D NOE ^{1}H NMR spectra of **10** in CD_3CN at 25 °C. Selectively excited NMR signals are highlighted with a red asterisk and are in the negative phase (not depicted).

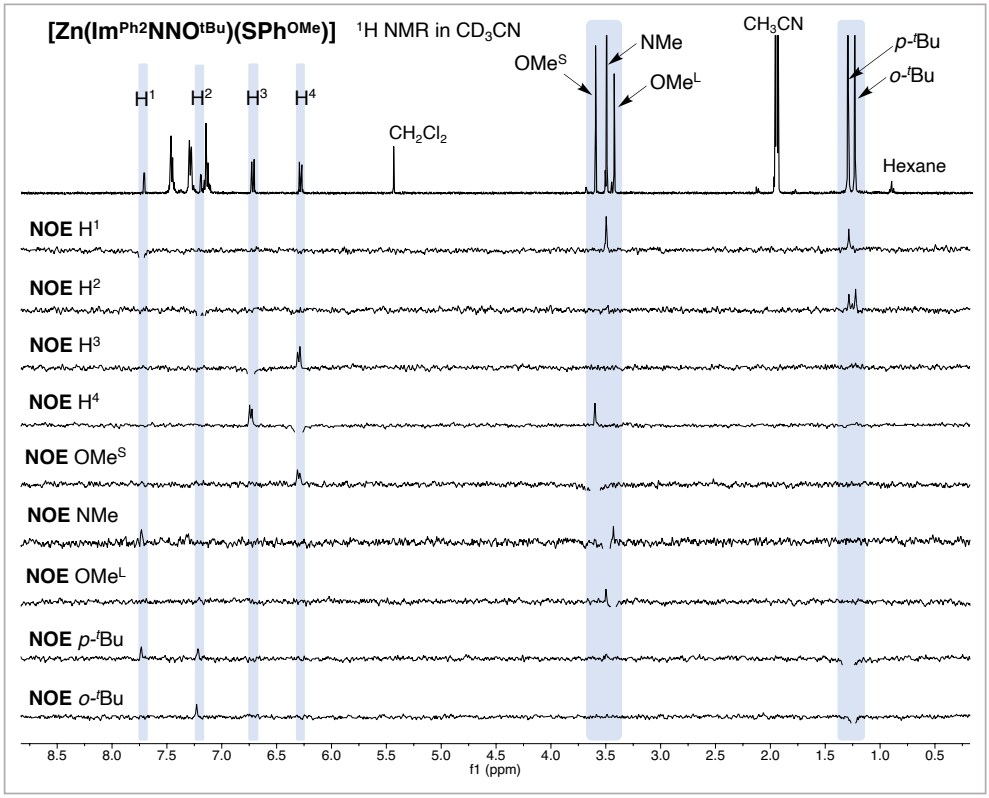

Figure C4. Stacked 1D NOE ^{1}H NMR spectra of **12** in CD_3CN at 25 °C. Selectively excited NMR signals are highlighted with a red asterisk and are in the negative phase (not depicted).

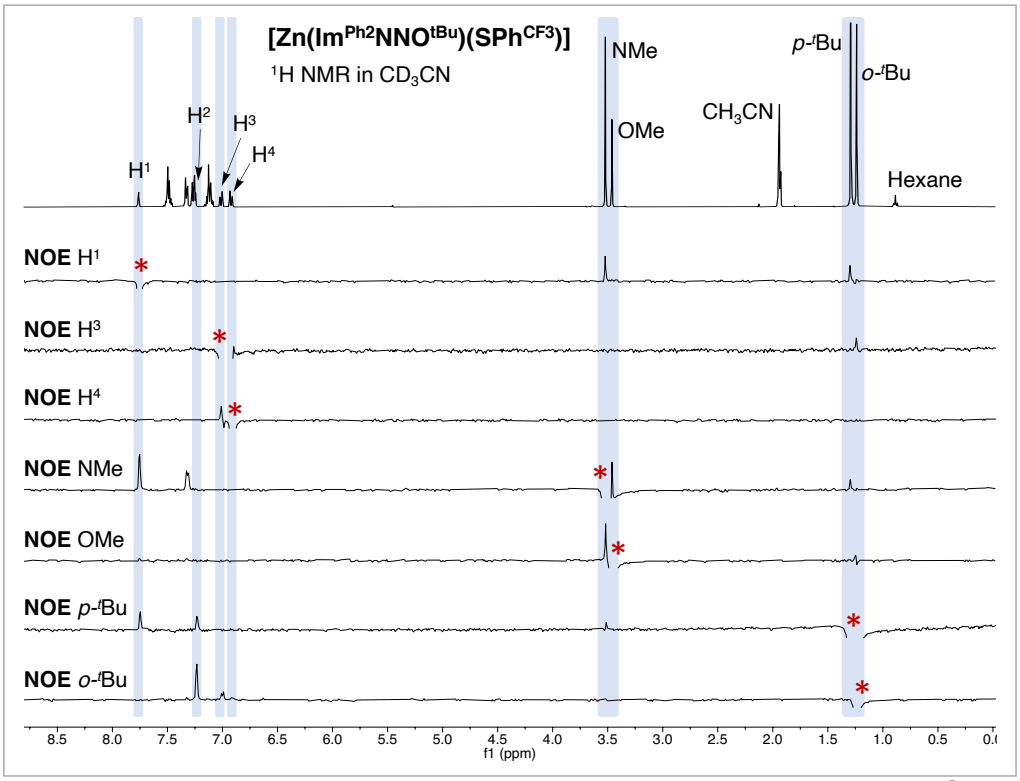

Figure C5. Stacked 1D NOE ^{1}H NMR spectra of **14** in CD_3CN at 25 °C. Selectively excited NMR signals are highlighted with a red asterisk and are in the negative phase (not depicted).

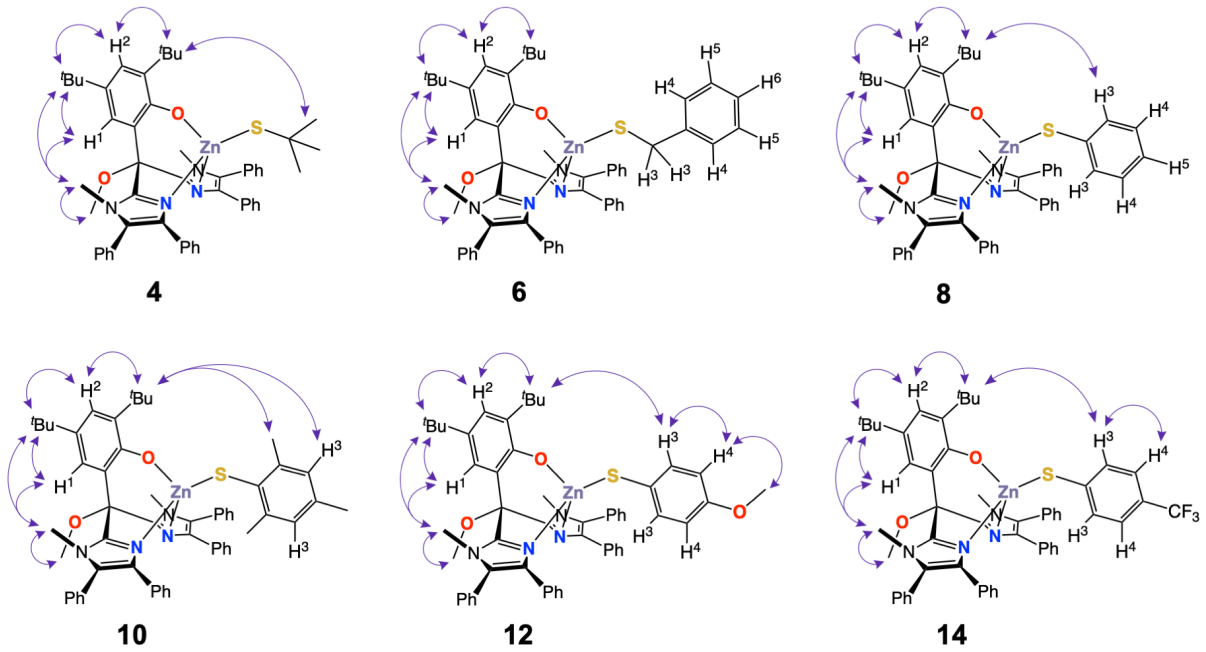

Scheme C1. Schematic depiction of the through-space correlations (purple arrows) observed by 1D NOE NMR experiments for zinc thiolate complexes **4**, **6**, **8**, **10**, **12** and **14**.

C.3 EPR Simulations

EPR simulations were performed using the EasySpin software package (version 5.2.33).[8] Simulations were performed by taking into account two paramagnetic species.

Parameters species 1:
Nucleus Fe, spin $S = {}^3/_2$, $g_x = 1.92$, $g_y = 2.07$, $g_z = 2.01$, $D = 5\ \mathrm{cm}^{-1}$, $E/D = 0.03$, $\sigma(E/D) = 0.06$.

Parameters species 2:
Nucleus Fe, spin $S = {}^1/_2$, $g_{iso} = 2.02$.

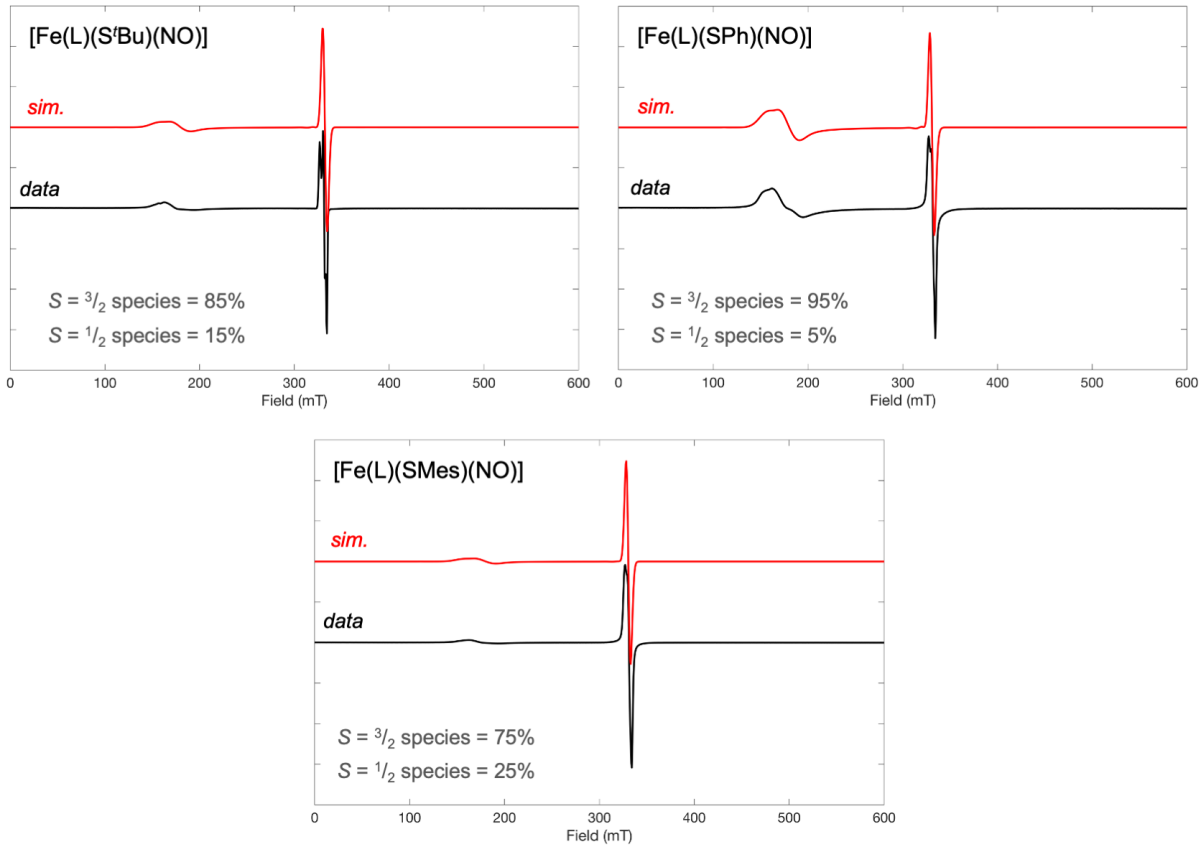

Figure C6. EPR data (black trace) and EasySpin simulations (red trace) obtained for the reaction mixtures containing $\mathbf{3}^{\mathbf{NO}}$ ([Fe(L)(S^{t}Bu)(NO)]), $\mathbf{7}^{\mathbf{NO}}$ ([Fe(L)(SPh)(NO)]), and $\mathbf{9}^{\mathbf{NO}}$ ([Fe(L)(SMes)(NO)]).

C.4 References

(1) Schreurs, A. M. M.; Xian, X.; Kroon-Batenburg, L. M. J. *J. Appl. Crystallogr.* **2010**, *43*, 70–82.
(2) Sheldrick, G. M. SADABS and TWINABS, 2014.
(3) Sheldrick, G. M. *Acta Crystallogr. Sect. A Found. Crystallogr.* **2015**, *71*, 3–8.
(4) Sheldrick, G. M. *Acta Crystallogr. Sect. C Struct. Chem.* **2015**, *71*, 3–8.
(5) Herbst-Irmer, R.; Sheldrick, G. M. *Acta Crystallogr. Sect. B Struct. Sci.* **1998**, *54*, 443–449.
(6) Spek, A. L. *Acta Crystallogr. Sect. D Biol. Crystallogr.* **2009**, *65*, 148–155.
(7) Spek, A. L. *Acta Crystallogr. Sect. C Struct. Chem.* **2015**, *71*, 9–18.
(8) Stoll, S.; Schweiger, A. *J. Magn. Reson.* **2006**, *178*, 42–55.

Appendix D

Supporting Information to Chapter 5

D.1 X-ray Crystal Structure Determination

Crystallographic details for [Fe(Im^{Ph2}NNO^{tBu})(BF)] (2)

$C_{56}H_{54}FeN_4O_5 \cdot 0.378(C_6H_{14}) \cdot 1.244(C_4H_8O)$, Fw = 1041.03, dark brown block, 0.52 × 0.49 × 0.37 mm^3, monoclinic, $P2_1/c$ (no. 14), a = 14.1539(3), b = 19.9835(4), c = 19.7815(4) Å, β = 97.544(1) °, V = 5546.67(19) Å^3, Z = 4, D_x = 1.247 g/cm^3, μ = 0.33 mm^{-1}. The diffraction experiment was performed on a Bruker Kappa ApexII diffractometer with sealed tube and Triumph monochromator (λ = 0.71073 Å) at a temperature of 150(2) K up to a resolution of $(\sin\theta/\lambda)_{max}$ = 0.65 Å^{-1}. The Eval15 software[1] was used for the intensity integration. A multi-scan absorption correction and scaling was performed with SADABS[2] (correction range 0.66-0.75). A total of 113740 reflections was measured, 12752 reflections were unique (R_{int} = 0.037), 10460 reflections were observed [I>2σ(I)]. The structure was solved with Patterson superposition methods using SHELXT.[3] Structure refinement was performed with SHELXL-2018[4] on F^2 of all reflections. Non-hydrogen atoms were refined freely with anisotropic displacement parameters. Partially occupied n-hexane and THF molecules were on the location of the solvent. The disorder in the solvent was not fully resolved. Hydrogen atoms were introduced in calculated positions and refined with a riding model. 749 Parameters were refined with 225 restraints (distances, angles and displacement parameters in the partially occupied solvent). R1/wR2 [I > 2σ(I)]: 0.0461 / 0.1212. R1/wR2 [all refl.]: 0.0581 / 0.1308. S = 1.033. Residual electron density between -0.42 and 1.03 e/Å^3. Geometry calculations and checking for higher symmetry was performed with the PLATON program.[5]

D.2 NMR Data

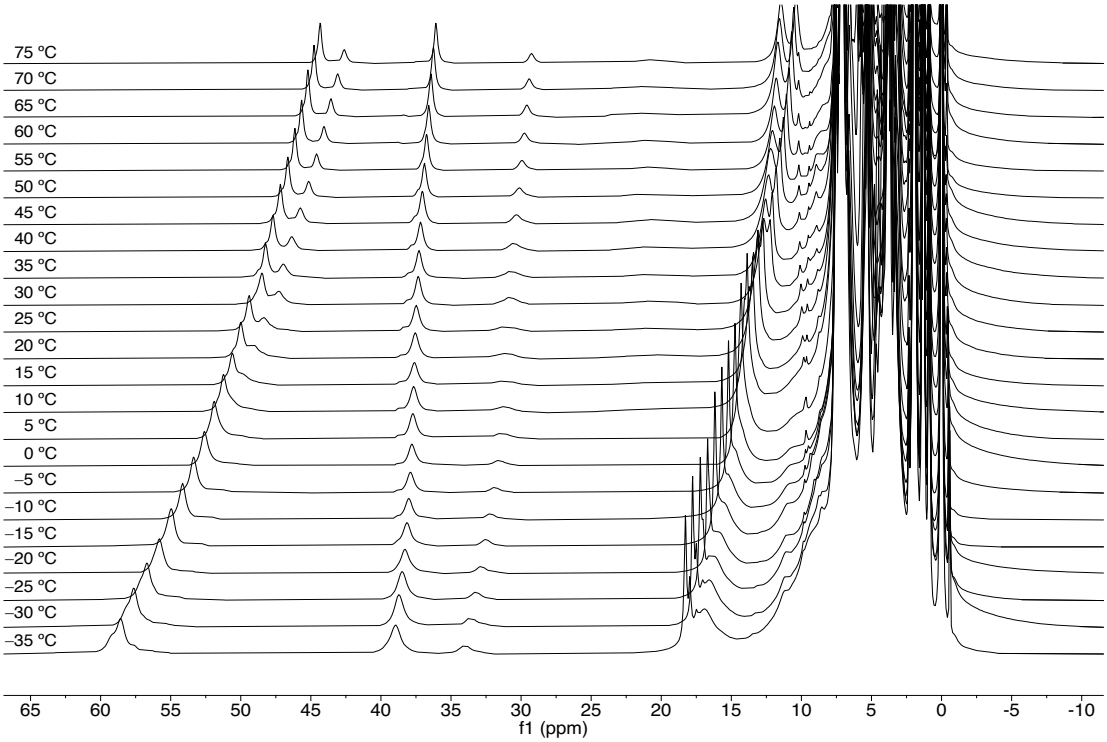

Figure D1. Stacked VT ^{1}H NMR (400 MHz) spectra of **2**, recorded in CD_3CN.

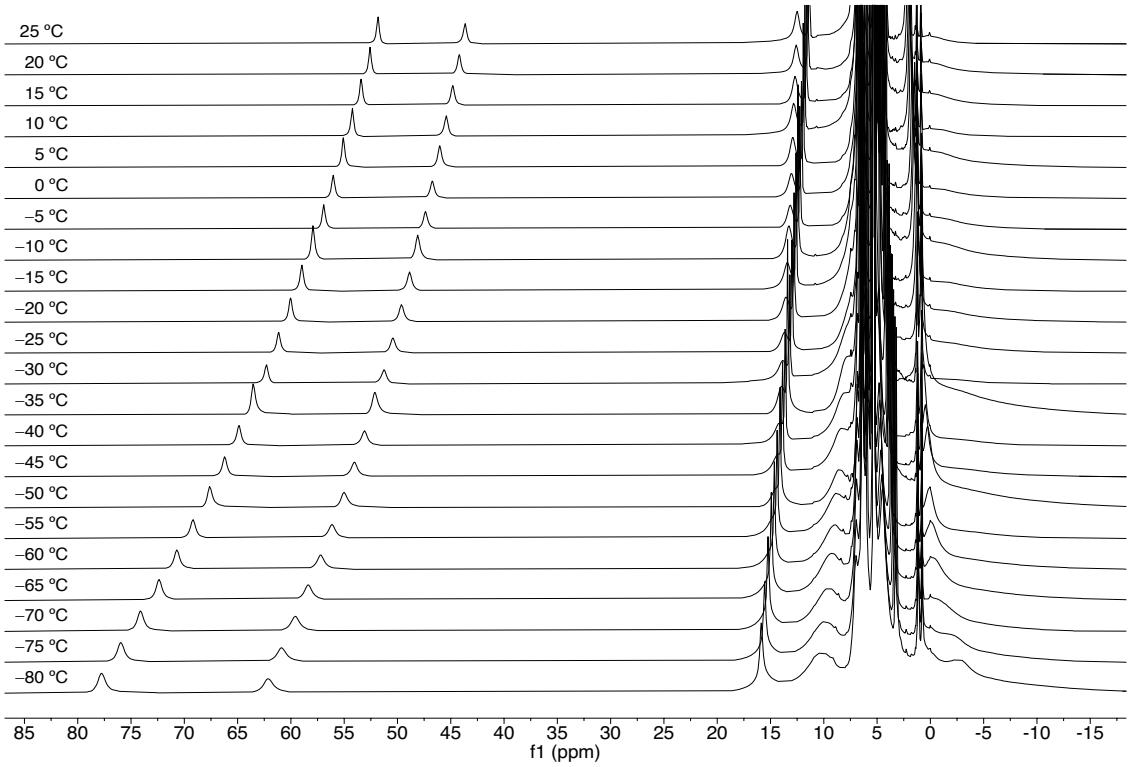

Figure D2. Stacked VT ^{1}H NMR (400 MHz) spectra of **2**, recorded in CD_2Cl_2.

D.3 UV-Vis Data

Table D1. UV-vis data for **2** as well as other previously reported iron(II) benzoylformate complexes.

Complex	Solvent	λ (nm), (ε, M^{-1} cm^{-1})	Colour	Reference
[Fe(Im^{Ph2}NNO^{tBu})(BF)] (**2**)	MeCN CH_2Cl_2	545 (430), 610 (526), 735 (300) 540 (760), 600 (830), 740 (360)	Blue Blue	Chapter 5 of this thesis
[Fe(Tp^{3Me,5Me})(κ$_2$-BF)]	MeCN	555, 610 (λ_{max})	Blue-purple	Ref[6]
[Fe(Tp^{3Ph,5Ph})(κ$_2$-BF)]	CH_2Cl_2	476 (210), 531 (340), 584 (300)	Red-violet	Ref[7,8]
[Fe$_2$(Tp^{3iPr,5iPr})$_2$(μ$_2$-BF)$_2$]	MeCN	553 (510), 610 (610)	Blue	Ref[9]
[Fe(Tp^{3tBu,5iPr})(κ$_2$-BF)]	CH_2Cl_2	558 (30), 565 (148), 621 (130)	Blue-purple	Ref[10]
[Fe(Tp^{3Ph,5Me})(κ$_2$-BF)]	MeCN	537 (315), 580 (300)	Violet	Ref[11]
[Fe(TPA)(κ$_1$-BF)(solv)]$^+$	MeCN CH_2Cl_2	385 (2400) 374 (1300), 550-610 (270)	Yellow Green	Ref[12]
[Fe(5TLA)(κ$_1$-BF)(solv)]$^+$	MeCN CH_2Cl_2	380 (2400) 378 (1700), 560-620 (370)	Yellow Green	Ref[12]
[Fe(6TLA)(κ$_2$-BF)]$^+$	MeCN	385 (2400), 544 (670)	Blue-purple	Ref[12]
[Fe(^{i}Pr$_3$tacn)(κ$_2$-BF)(OTf)]	MeCN	520 (300), 570 (300)	Purple	Ref[13]
[Fe$_2$(Me$_2$HDP)$_2$(μ$_2$-BF)]$^+$	MeCN	450 (1800)	Yellow-orange	Ref[14]

D.4 Cyclic Voltammetry

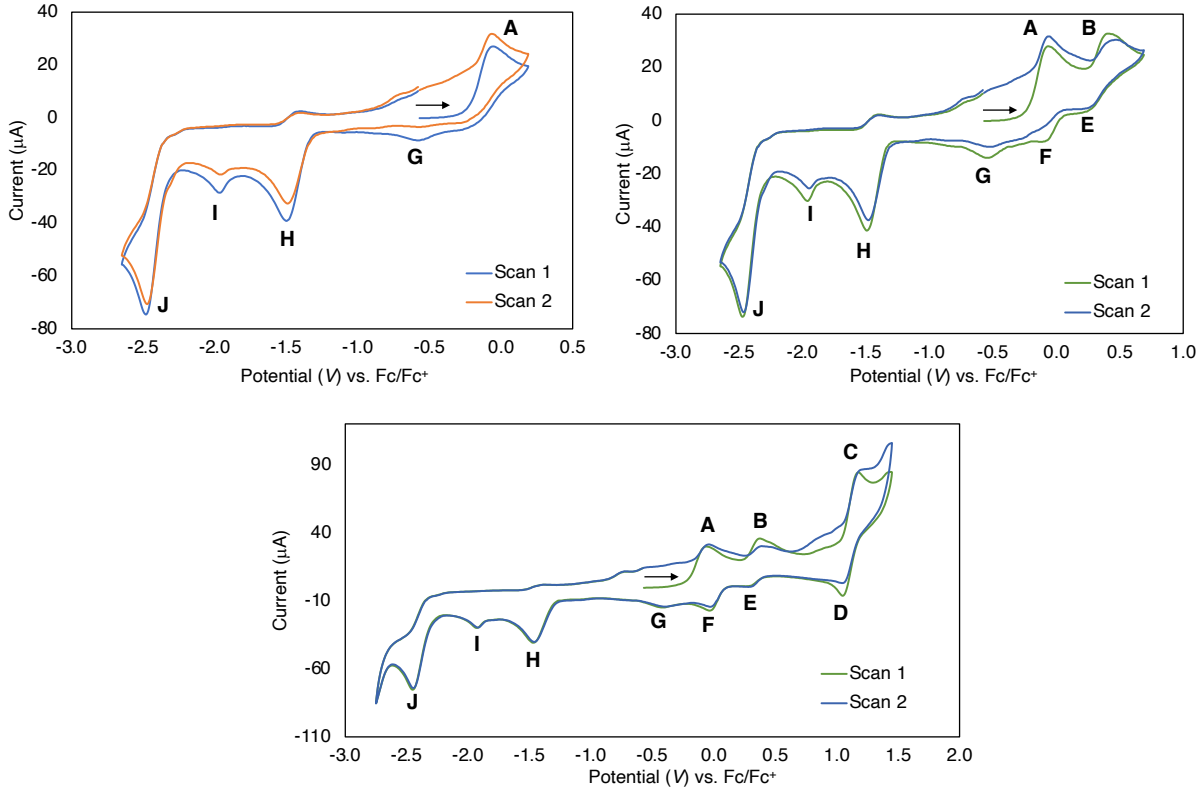

Figure D3. Cyclic voltammograms of **2** showing the degradation of the responses **A**-**G** upon cycling through the reductive responses **H**-**J**. For each voltammogram, 2 scans have been recorded.

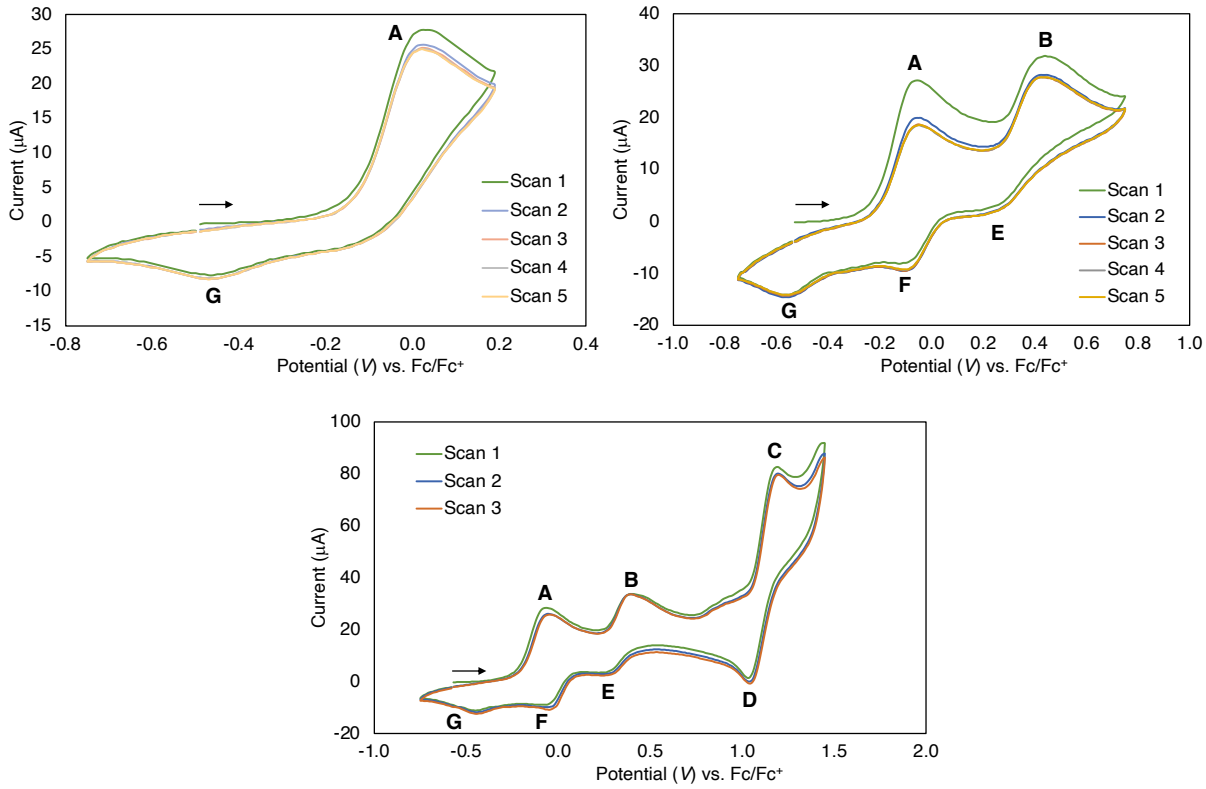

Figure D4. Cyclic voltammograms of **2** showing the reproducibility of events **A**-**G** upon cycling multiple times through the potential window without going through events **H**-**J**.

D.5 HR-ESI-MS

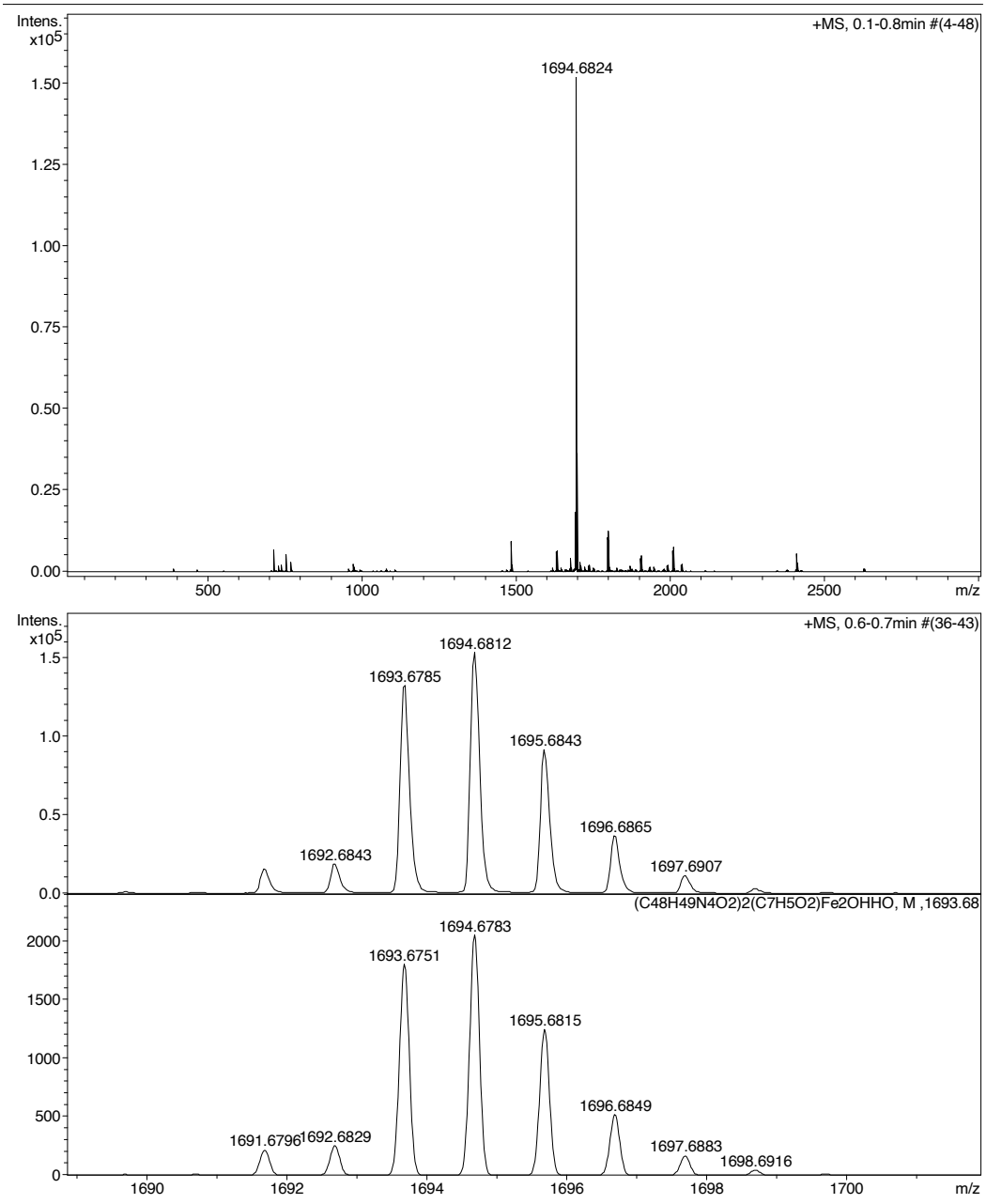

Figure D5. ESI-MS (positive mode) of **2** in MeCN within the first 5 minutes of oxidation with $^{16}O_2$. A zoom of the peak of interest is given in the middle panel, and the corresponding simulation is provided in the bottom panel.

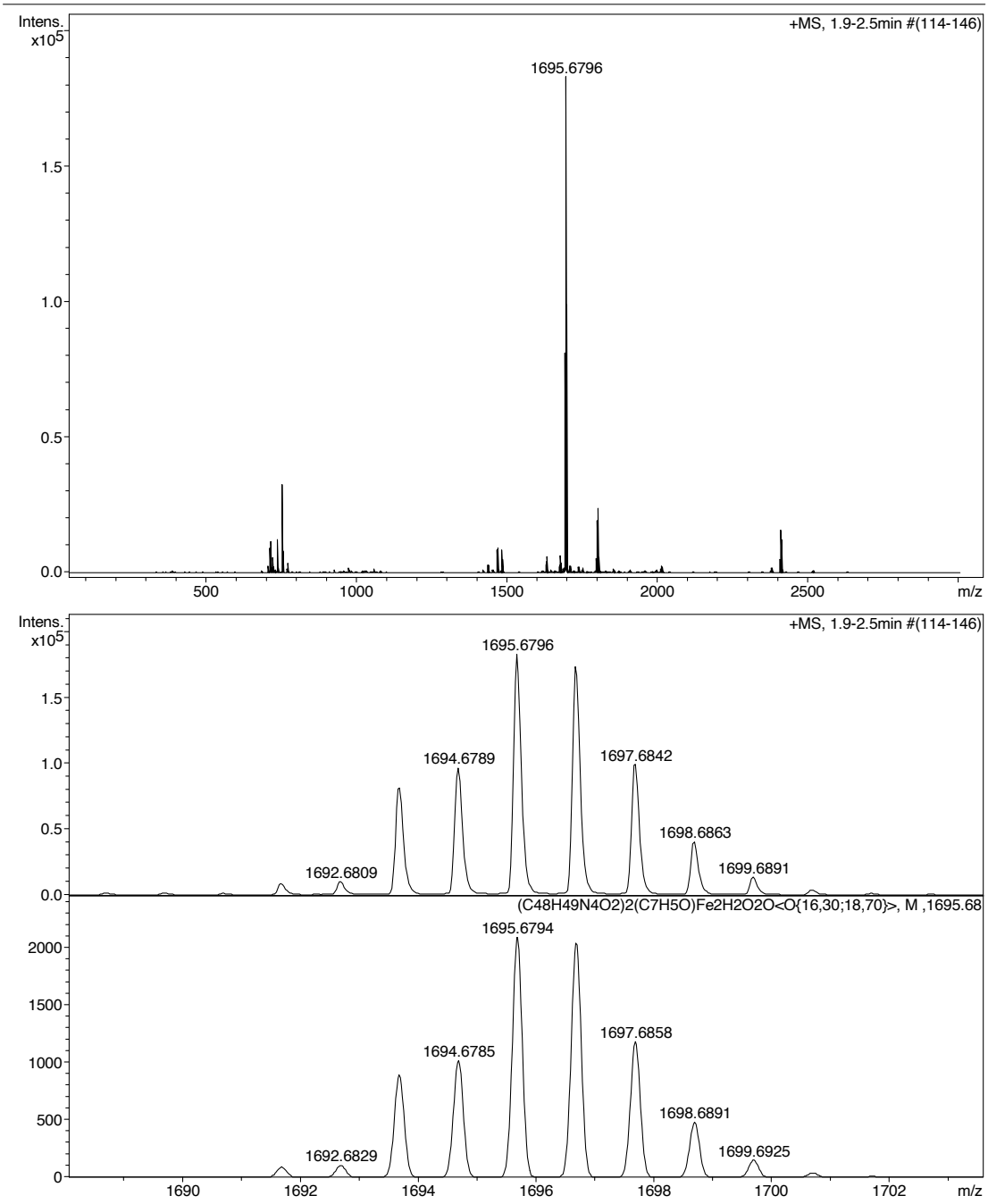

Figure D6. ESI-MS of **2** upon oxidation with $^{18}O_2$, initial oxidation. A zoom of the peak of interest is given in the middle panel, and the corresponding simulation is provided in the bottom panel.

D.6 References and Notes

(1) Schreurs, A. M. M.; Xian, X.; Kroon-Batenburg, L. M. J. *J. Appl. Crystallogr.* **2010**, *43*, 70–82.
(2) Sheldrick, G. M. SADABS and TWINABS, 2014.
(3) Sheldrick, G. M. *Acta Crystallogr. Sect. A Found. Crystallogr.* **2015**, *71*, 3–8.
(4) Sheldrick, G. M. *Acta Crystallogr. Sect. C Struct. Chem.* **2015**, *71*, 3–8.
(5) Spek, A. L. *Acta Crystallogr. Sect. D Biol. Crystallogr.* **2009**, *65*, 148–155.
(6) Ha, E. H.; Ho, R. Y. N.; Kisiel, J. F.; Valentine, J. S. *Inorg. Chem.* **1995**, *34*, 2265–2266.
(7) Hegg, E. L.; Ho, R. Y. N.; Que, L. *J. Am. Chem. Soc.* **1999**, *121*, 1972–1973.

(8) Mukherjee, A.; Martinho, M.; Bominaar, E. L.; Münck, E.; Que, L. *Angew. Chemie Int. Ed.* **2009**, *48*, 1780–1783.
(9) Mukherjee, A.; Cranswick, M. A.; Chakrabarti, M.; Paine, T. K.; Fujisawa, K.; Münck, E.; Que, L. *Inorg. Chem.* **2010**, *49*, 3618–3628.
(10) Hikichi, S.; Ogihara, T.; Fujisawa, K.; Kitajima, N.; Akita, M.; Moro-oka, Y. *Inorg. Chem.* **1997**, *36*, 4539–4547.
(11) Sheet, D.; Paine, T. K. *Chem. Sci.* **2016**, *7*, 5322–5331.
(12) Chiou, Y.-M.; Que, L. *J. Am. Chem. Soc.* **1995**, *117*, 3999–4013.
(13) Sánchez-Eguía, B. N.; Serrano-Plana, J.; Company, A.; Costas, M. *Chem. Commun.* **2020**, *56*, 14369–14372.
(14) Chiou, Y.-M.; Que, L. *Angew. Chemie Int. Ed.* **1994**, *33*, 1886–1888.

Appendix E

Supporting Information to Chapter 6

E.1 X-ray Crystal Structure Determinations

Crystallographic details for $[Fe(L4^{ATol})_2](OTf)_2$ (34)

$[C_{56}H_{58}FeN_{10}O_2](CF_3O_3S)_2 \cdot C_4H_8O$ + disordered solvent, Fw = 1329.21[*], colourless block, 0.37 × 0.20 × 0.12 mm^3, monoclinic, $P2_1/n$ (no. 14), a = 17.1313(9), b = 22.3178(12), c = 17.9415(8) Å, β = 95.848(3) °, V = 6823.9(6) Å^3, Z = 4, D_x = 1.294 g/cm^3 [*], μ = 0.36 mm^{-1} [*]. 78255 Reflections were measured on a Bruker Kappa ApexII diffractometer with sealed tube and Triumph monochromator (λ = 0.71073 Å) at a temperature of 150(2) K up to a resolution of (sin θ/λ) max = 0.65 Å^{-1}. The Eval15 software[1] was used for the integration of the intensities. Multiscan absorption correction and scaling was performed with SADABS[2] (correction range 0.66-0.75). 15644 Reflections were unique (R_{int} = 0.051), of which 10025 were observed *[I>2σ(I)]*. The structure was solved with Patterson superposition methods using SHELXT.[3] Least-squares refinement was performed with SHELXL-2016[4] against F^2 of all reflections. The crystal structure contains voids (868 Å^3/ unit cell) filled with disordered *n*-hexane molecules. Their contribution to the structure factors was secured by back-Fourier transformation using the SQUEEZE algorithm[5] resulting in 181 electrons / unit cell. Non-hydrogen atoms were refined freely with anisotropic displacement parameters. One uncoordinated THF was refined with a disorder model. N–H hydrogen atoms were located in difference Fourier maps and refined freely with isotropic displacement parameters. C–H hydrogen atoms were introduced in calculated positions and refined with a riding model. 839 Parameters were refined with 95 restraints (distances, angles and displacement parameters in the disordered THF). R1/wR2 [I > 2σ(I)]: 0.0517 / 0.1284. R1/wR2 [all refl.]: 0.0907 / 0.1459. S = 1.040. Residual electron density between −0.59 and 0.77 e/Å^3. Geometry calculations and checking for higher symmetry were performed with the PLATON program.[6]

Crystallographic details for $[Fe(L4^{ATol})(Cl)_2]$ (35)

$C_{28}H_{29}Cl_2FeN_5O \cdot CH_3CN$, Fw = 619.36, yellow needle, 0.54 × 0.08 × 0.04 mm^3, orthorhombic, Pbca (no. 61), a = 23.5486(9), b = 9.3808(5), c = 26.3996(13) Å, V = 5831.8(5) Å^3, Z = 8, D_x = 1.411 g/cm^3, μ = 0.74 mm^{-1}. 69946 Reflections were measured on a Bruker Kappa ApexII diffractometer with sealed tube and Triumph monochromator (λ = 0.71073 Å) at a temperature of 150(2) K up to a resolution of (sin θ/λ) max = 0.65 Å^{-1}. The Eval15 software[1] was used for the integration of the intensities. A numerical absorption correction and scaling was performed with SADABS[2] (correction range 0.61-1.00). 6704 Reflections were unique (R_{int} = 0.084), of which 4738 were observed [I>2σ(I)]. The structure was solved with Patterson superposition methods using SHELXT.[3] Least-squares refinement was performed with SHELXL-2016[4] against F^2 of all reflections. Non-hydrogen atoms were refined freely with anisotropic displacement parameters. The N–H hydrogen atom was located in difference Fourier maps and refined freely with an isotropic displacement parameter. C–H hydrogen atoms were introduced in calculated positions and refined with a riding model. 371 Parameters were refined with no restraints. R1/wR2 [I > 2σ(I)]: 0.0484 / 0.1169. R1/wR2 [all refl.]: 0.0811 / 0.1332. S = 1.075. Residual electron density between −0.59 and 1.30 e/Å^3. Geometry calculations and checking for higher symmetry were performed with the PLATON program.[6]

E.2 References and Notes

(1) Schreurs, A. M. M.; Xian, X.; Kroon-Batenburg, L. M. J. *J. Appl. Crystallogr.* **2010**, *43*, 70–82.
(2) Sheldrick, G. M. SADABS and TWINABS, 2014.
(3) Sheldrick, G. M. *Acta Crystallogr. Sect. A Found. Crystallogr.* **2015**, *71*, 3–8.
(4) Sheldrick, G. M. *Acta Crystallogr. Sect. C Struct. Chem.* **2015**, *71*, 3–8.
(5) Spek, A. L. *Acta Crystallogr. Sect. C Struct. Chem.* **2015**, *71*, 9–18.
(6) Spek, A. L. *Acta Crystallogr. Sect. D Biol. Crystallogr.* **2009**, *65*, 148–155.

Appendix F

^{57}Fe Mössbauer Spectroscopy

The recoilless nuclear emission and resonant absorption (fluorescence) of γ-rays, also known as the Mössbauer effect, is a physical phenomenon that was discovered by Rudolf Mössbauer in 1958.[1,2] The spectroscopy method based on this resonance effect is known as Mössbauer spectroscopy. It is a powerful tool for elucidating the local electronic structure of atomic nuclei, the most extensively studied of which is ^{57}Fe. The advantage of Mössbauer spectroscopy is that it measures the "local" electronic structure of an atomic nucleus, and is sensitive only to the first coordination sphere of atoms bound to the Mössbauer-active nucleus. In enzymology, this has been particularly useful in elucidating the electronic structure of iron nuclei contained within the large three-dimensional encasing of a protein scaffold.[3,4]

The γ-source for ^{57}Fe Mössbauer spectroscopy is ^{57}Co, a metastable isotope with a half-life of 270 days. ^{57}Co decays through electron capture to ^{57}Fe ($I = {}^5/_2$), which can either decay directly to its $I = {}^1/_2$ ground state (15%) or can decay by means of an additional nuclear transition to the Mössbauer-active $I = {}^3/_2$ excited state (85%).[2] The decay of the $I = {}^3/_2$ excited state to the $I = {}^1/_2$ ground state releases γ-rays of energy that corresponds to the energy of reabsorption of the γ-rays by ground-state ^{57}Fe atoms contained within a solid-state sample of interest (powder or frozen solution). Due to the chemically distinct nature of the emitter and the absorber, a range of energies must be scanned for resonance absorption to occur. Mössbauer spectroscopy exploits the Doppler effect by moving the source periodically with controlled velocities further from (–υ) or closer to (+υ) the sample, thereby compressing or elongating the wavelength of the emitted γ-radiation (Figure F1). In a Mössbauer spectrum, the source velocity (mm s^{-1}) is displayed on the *x*-axis and the fraction of photons transmitted through the sample is displayed on the *y*-axis.

Figure F1. A schematic depiction of the Mössbauer experiment. The radioactive source on the left can be moved closer to (+υ) or further (–υ) from the absorber (i.e. the sample of interest), thereby exploiting the Doppler effect to create an energy spectrum with which the sample can be analysed. Figure is reproduced from Gütlich, Bill and Trautwein.[2]

The simplest type of Mössbauer spectrum is known as a quadrupole doublet, characterised by two lines corresponding to the transitions from the $I = {}^1/_2$ ^{57}Fe ground state to the $m_I = \pm {}^1/_2$ and $m_I = \pm {}^3/_2$ states of the $I = {}^3/_2$ ^{57}Fe excited nuclear state (Figure F2). Chemical information is extracted from the Mössbauer spectrum using two important parameter: the isomer shift (δ) and the quadrupole splitting ($|\Delta E_Q|$), both measured in mm s^{-1}.

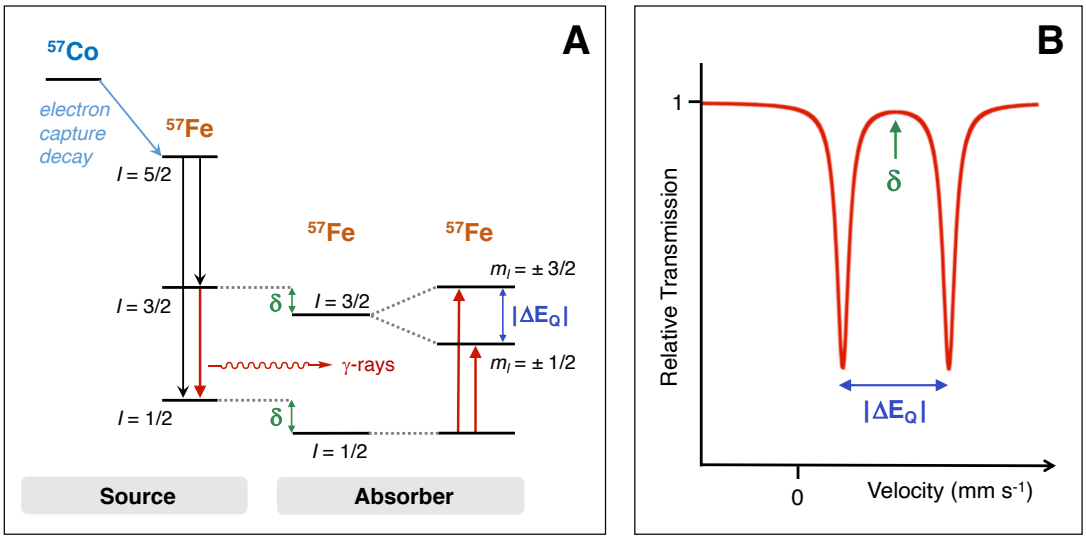

Figure F2. A: Nuclear transition cascade for the radioactive decay of ^{57}Co to ^{57}Fe ($I = {}^{1}/_{2}$). In this process, Mössbauer γ-rays are emitted that can excite the ground state of the iron-containing absorber (sample of interest). **B**: An idealised Mössbauer spectrum (quadrupole doublet) obtained in the absence of an applied magnetic field. Figure adapted from Gütlich *et al.*[2]

Isomer shift (δ) is a measure of the *s*-electron density at the iron nucleus and is strongly affected by the valence 4s orbitals that participate in bonding and the degree of electrostatic shielding they experience from *p* and *d* electrons. The isomer shift therefore changes significantly according to the oxidation state, the spin state and the number and type of ligands. In general, a more positive isomer shift is associated to a lower electron density at the iron nucleus. The following trends help the interpretation of isomer shifts:[5] (i) $\delta(Fe^{IV}) < \delta(Fe^{III}) < \delta(Fe^{II})$, (ii) $\delta(LS) < \delta(HS)$, (iii) soft ligands tend to produce lower isomer shifts by donating more electron density to the iron centre and increasing the covalency of the Fe–L bonds, (iv) low coordinate complexes tend to have more covalent Fe–L bonds and lower isomer shifts than complexes with high coordination numbers.

Quadrupole splitting ($|\Delta E_Q|$) is a hyperfine coupling that arises from the interaction between the non-spherical nuclear charge of the $I = {}^{3}/_{2}$ excited ^{57}Fe state and an external electric field gradient. This results in the splitting of the excited state in two states, the $m_I = \pm{}^{1}/_{2}$ and $m_I = \pm{}^{3}/_{2}$ states, giving rise to the two lines of the Mössbauer spectrum. The peak-to-peak separation is known as the quadrupole splitting, denoted $|\Delta E_Q|$, and is typically proportional to the strength of the electric field gradient. In general, the quadrupole splitting is interpreted as a reflection of spherical (a)symmetry of the coordination sphere and the population of the iron's 3d orbitals.[2]

References

(1) Parak, F. *Nature* **2011**, *478*, 325–325.
(2) Gütlich, P.; Bill, E.; Trautwein, A. *Mossbauer spectroscopy and transition metal chemistry : fundamentals and application*; Springer, 2011.
(3) Johnson, C. E. In *Perspectives in Mössbauer Spectroscopy*; Springer US: Boston, MA, 1973; pp. 79–88.
(4) Garcia-Serres, R.; Clémancey, M.; Latour, J.-M.; Blondin, G. *J. Biol. Inorg. Chem.* **2018**, *23*, 635–644.
(5) Pandelia, M.-E.; Lanz, N. D.; Booker, S. J.; Krebs, C. *Biochim. Biophys. Acta - Mol. Cell Res.* **2015**, *1853*, 1395–1405.

Appendix G

Biorthogonalization

Compounds that contain unpaired electrons, such as the high-spin iron(II) complexes discussed in this thesis, are typically analysed computationally by means of unrestricted open-shell calculations (e.g. unrestricted Hartree-Fock (UHF) or unrestricted Kohn-Sham (UKS) computations). The wavefunctions generated from these calculations produce α and β subsets of molecular orbitals (MOs), required mathematically to account for singly occupied MOs. However, these α and β subsets are often at an energetic mismatch, which makes the MO analysis of the compound of interest difficult since two sets of orbitals must be taken into consideration simultaneously. To circumvent this issue, it is possible to run restricted open-shell calculations (ROHF or ROKS). However, the total electronic energy, orbital energy and electron distribution is not as accurate as unrestricted open-shell calculations.

The *Multiwfn* software package[1] provides a convenient mathematical solution to this problem: the so-called "biorthogonalization" function. This algorithm performs the biorthogonalization between the α and β subset orbitals obtained from unrestricted open-shell wavefunctions with a spin multiplicity greater than 1 (i.e. where $S > 0$). This process generates a new set of orbitals that still comprises an α and a β subset, but whose wavefunctions now match each other almost perfectly such that these can be considered simultaneously. Two conditions must be satisfied in order for biorthogonalization to be successful: 1) for each set of spin orbitals, they are orthonormal with themselves, and 2) the α orbitals are orthonormal with the β orbitals.[2] Without biorthogonalization, the UHF/UKS orbitals only satisfy the first condition.

Biorthogonalization is realised mathematically *via* singular value decomposition (SVD). This means that an overlap integral matrix (**O**) is constructed between the α and β orbitals, and SVD is applied to decompose it such that $\mathbf{O}=\mathbf{U}\Sigma\mathbf{V}^*$, where Σ is a diagonal matrix with non-negative real numbers on the diagonal (also known as singular values). These singular values correspond to the overlap integrals between the α and β orbitals, which, after the biorthogonalization process, should be very close to 1.[2] **U** and **V** are column matrices that correspond to the transformation matrix between the original orbitals and the new biorthogonalized orbitals of α or β spin, respectively. For a more detailed explanation, the reader is referred to the *Multiwfn* manual, available online free of charge.[2]

The biorthogonalized α and β orbitals cannot be considered eigenfunctions of the Fock operator. However, their energies can be evaluated using the Fock matrix generated by natural bonding orbital (NBO) analysis, which orders them energetically as would be expected from the Fock operator. *Multiwfn* orders the biorthogonalized orbitals energetically using the average energy of the α and β counterparts.

References

(1) Lu, T.; Chen, F. *J. Comput. Chem.* **2012**, *33*, 580–592.
(2) Lu, T. Multiwfn manual, version 3.8 http://sobereva.com/multiwfn/misc/Multiwfn_3.8_dev.pdf (accessed Jun 7, 2020).

Summary & Perspectives

Metal sites in biology catalyse some of the most challenging and consequential reactions on Earth, ranging from oxygen transport in animals to photosynthesis in plants and nitrogen-fixation in bacteria. This astounding breadth of reactivity includes attractive features such as small molecule activation and late-stage functionalisation, all of which are achieved under physiological conditions and with exquisite stereo- and regioselectivity. For bioinorganic chemists, the direct deployment, engineering or mimicry of metalloenzymes and metal-containing biomolecules in research and commercial applications holds great potential for improving the green credentials of today's chemical industry.

This thesis describes the development of synthetic, bioinspired iron complexes that model O_2-activating non-heme iron enzymes featuring the 2-His-1-Carboxylate facial triad (2H1C) at their active site. More particularly, this research aims to create iron complexes that model the structure and reactivity of isopenicillin N synthase (IPNS, Figure 1A). This unique iron metalloenzyme catalyses the synthetically challenging bicyclisation of its thiolate substrate, which involves the formation of two new C–X bonds (X = N, S) using O_2 as the oxidant.

Three important objectives define the research described in this thesis. The first is the design of so-called "*N,N,O*" ligand scaffolds that structurally model the 2H1C by providing two neutral N-donors and an anionic O-donor. Together, these should coordinate to a single metal ion by means of a tripodal κ_3-*N,N,O* coordination motif. In this thesis, bis-imidazole phenolate ligands are explored as potential 2H1C mimics since their constituent imidazoles model the naturally occurring histidyl groups of the 2H1C and can also be tuned sterically, while their anionic phenolate O-donor can be tuned both sterically and electronically (Figure 1B). The second objective is to synthesise well-defined mononuclear *N,N,O*-bound iron thiolate complexes that model the substrate-bound IPNS active site.

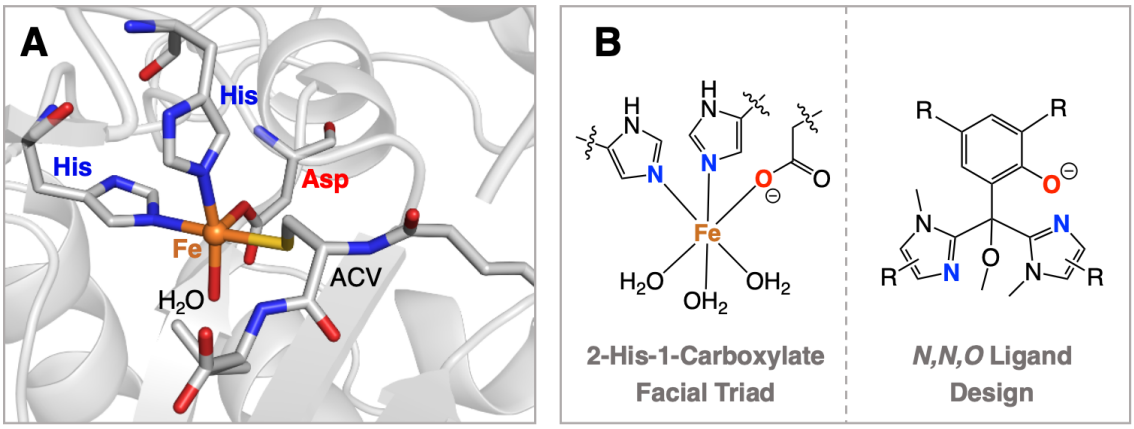

Figure 1. A: The substrate-bound active site of IPNS. B: A schematic depiction of the 2H1C and the bioinspired *N,N,O* bis-imidazole phenolate ligand design.

Biomimetic metal thiolate complexes that incorporate an anionic O-donor are relatively rare, and there is much debate in the literature regarding the influence of the O-donor on the reactivity of IPNS. Finally, the third objective is to explore the reactivity of these unique metal thiolate complexes in the presence of different oxidants, including O_2.

This thesis comprises six chapters. **Chapter 1** discusses the role of iron-sulfur bonds in the structure and function of different sulfur-ligated iron metalloenzymes including IPNS. Bioinspired iron thiolate complexes relevant to each enzyme are highlighted and inter-comparisons are made between complexes designed to model different aspects of these unique sulfur-ligated enzyme active sites. This provides a molecular "tool-kit" with which to better understand and predict the structure and reactivity of iron thiolate complexes.

Chapter 2 presents the synthesis and coordination chemistry of *N,N,O* ligands **BenzImNNO** and **Im^{Ph2}NNO**. The varying steric bulk of their constituent imidazoles is shown to have a significant impact on the coordination mode of the phenolic O-donor and, consequently, on the nuclearity of the complexes. Reacting **BenzImNNO** with 1 equiv. ZnX_2 (X = Cl, OTf) produces dinuclear $[Zn(BenzImNNO)_2ZnX_2]$ complexes (Scheme 1). In these complexes, one of the zinc ions is octahedral, facially capped by two κ_3-*N,N,O* ligand molecules, while the other zinc ion is tetrahedral, bound to both ligands' phenolic O-donors. Reacting **BenzImNNO** with 0.5 equiv. $Zn(OTf)_2$ affords a mixture of products, including a mononuclear bis-ligand complex $[Zn(BenzImNNO)_2]$ and dinuclear complex $[Zn(BenzImNNO)_2Zn(OTf)_2]$ (Scheme 1).

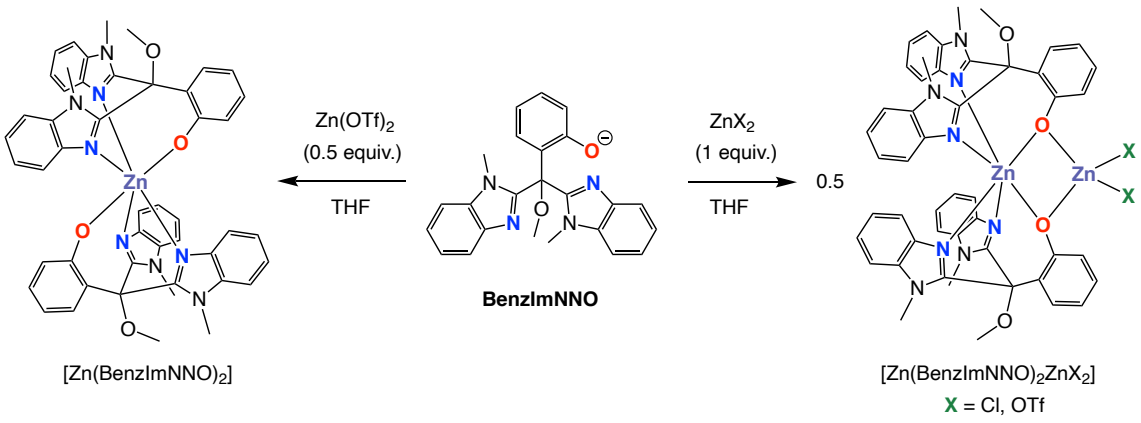

Scheme 1. Synthesis of mono- and dinuclear zinc complexes supported by **BenzImNNO**.

In contrast, the increased steric bulk of **Im^{Ph2}NNO** gives rise to a unique bridging μ_2:κ_2-*N,N*:κ_1-*O* coordination mode, which affords dinuclear complexes $[M_2(Im^{Ph2}NNO)_2(OTf)_2]$ (M = Fe, Zn) with facially opposing metal sites (Scheme 2). We investigate the robustness of the ligand's dinucleating coordination mode during oxidative transformations and demonstrate that its coordination mode is retained upon triflate substitution for a biorelevant thiophenolate co-ligand.

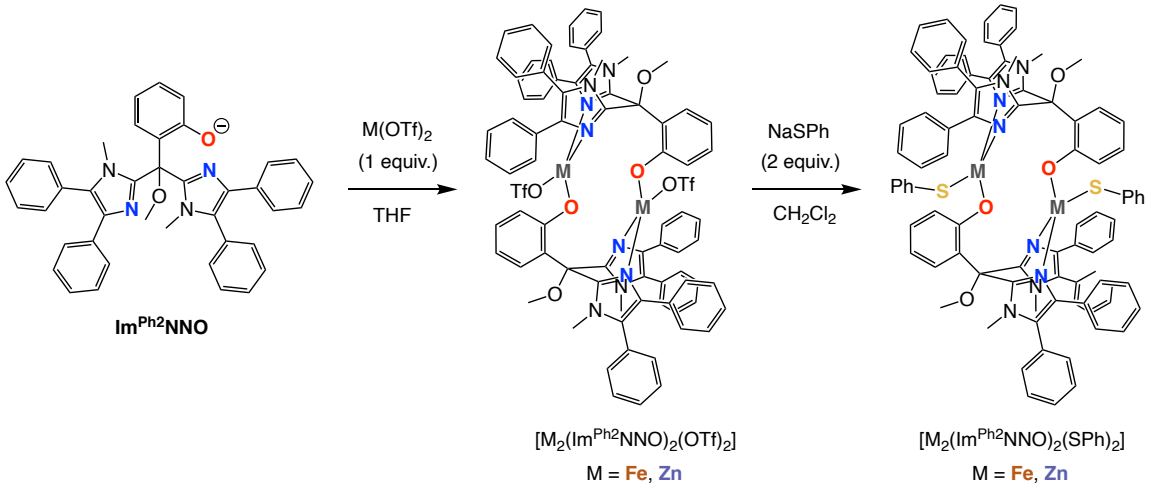

Scheme 2. Synthesis of dinuclear iron and zinc complexes supported by **Im^{Ph2}NNO**.

Chapter 3 describes the synthesis and coordination chemistry of ligand **Im^{Ph2}NNO^{tBu}**, which features *tert*-butyl groups on the *ortho* and *para* positions of its phenolate O-donor. Reacting **Im^{Ph2}NNO^{tBu}** with MCl_2 (M = Fe, Zn) affords mononuclear complexes [M(Im^{Ph2}NNO^{tBu})(Cl)] in high yield (Scheme 3). The tripodal κ$_3$-*N,N,O* ligand coordination observed in their X-ray crystal structures remains intact and well-defined in MeCN and CH_2Cl_2 solution. Consequently, these complexes can be regarded as convenient synthons from which to create a range of different biomimetic complexes, by substituting the chloride ligand for biorelevant co-ligands. This is exemplified by the reaction of [Zn(Im^{Ph2}NNO^{tBu})(Cl)] with NaSPh, which affords a tetrahedral zinc thiolate complex, [Zn(Im^{Ph2}NNO^{tBu})(SPh)], that is relevant to IPNS biomimicry.

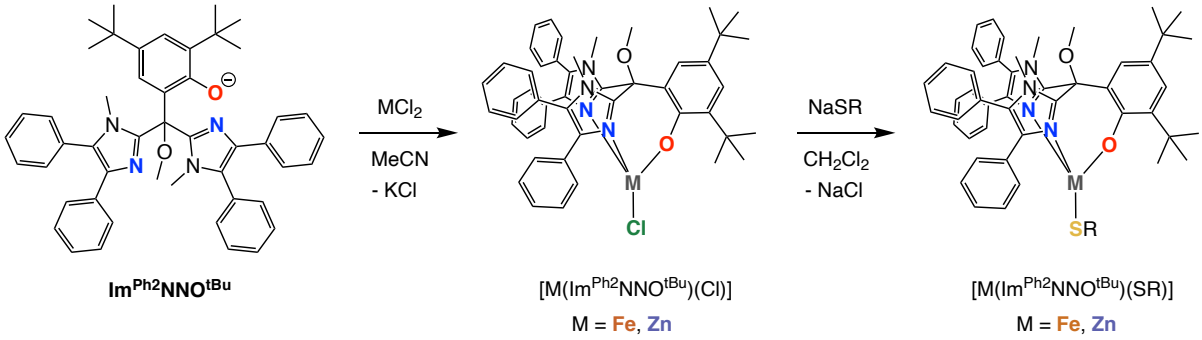

Scheme 3. Synthesis of mononuclear iron and zinc complexes supported by **Im^{Ph2}NNO^{tBu}**. R = ^{t}Bu, Bn, Ph, Mes, 4-OMe-Ph, 4-CF_3-Ph.

Having established the biomimetic potential of the **Im^{Ph2}NNO^{tBu}** ligand, **Chapter 4** expands on the methodology developed in Chapter 3 and presents the synthesis, structure and reactivity of a family of mononuclear iron and zinc thiolate complexes, [M(Im^{Ph2}NNO^{tBu})(SR)] (M = Fe, Zn; R = ^{t}Bu, Bn, Ph, Mes, 4-OMe-Ph, 4-CF_3-Ph) (Scheme 3). Analysis of the complex structures in the solid- and solution state reveals that they are all tetrahedral in geometry, facially capped by the κ$_3$-*N,N,O* donor set of the **Im^{Ph2}NNO^{tBu}** ligand. The M–S bond lengths vary according to the approximate donicity

and steric bulk of the thiolate co-ligand. The modulation in sulfur-to-metal charge transfer is also reflected by the solid-state Mössbauer parameters of the iron thiolate complexes. Cyclic voltammetry (CV) studies show that the first electrochemical oxidation occurs on the iron centre for all iron thiolate complexes, and that its redox potential is tuned by the donicity of the thiolate ligand. We also investigate the reactivity of the iron thiolate complexes to different oxidants, including O_2, NO, PhIO and $[Ph_3C]PF_6$. In all cases, the data suggests that the iron is easily oxidised to its ferric form, with sulfonate formation observed for the reactions with O_2 and PhIO.

Chapter 5 presents a biomimetic study of α-ketoglutarate (αKG) dependent iron enzymes, the largest sub-family of 2H1C-containing non-heme iron enzymes. An iron(II) benzoylformate complex is reported, [Fe(Im^{Ph2}NNO^{tBu})(BF)], whose mononuclear, pentacoordinate structure and tripodal κ$_3$-*N,N,O* supporting ligand qualify it as one of the most structurally faithful models reported to date (Scheme 4). Indeed, its Mössbauer parameters are very close to those reported for αKG-bound enzyme active sites. The X-ray crystal structure of the complex reveals a putative vacant site located *trans* to one of the imidazole groups, which can accommodate NO-binding (as shown by EPR, IR, UV-vis and DFT studies). Exposing the complex to O_2 induces a rapid decarboxylation reaction, producing an interesting diiron(III) benzoate complex, [Fe$_2$(Im^{Ph2}NNO^{tBu})$_2$(μ$_2$-OBz)(μ$_2$-OH)$_2$]$^+$ (Scheme 4). High-resolution ESI-MS measurements and experiments using isotopically-labelled $^{18}O_2$ show that one oxygen atom is incorporated within the benzoate moiety, thus mirroring native αKG-dependent enzyme reactivity.

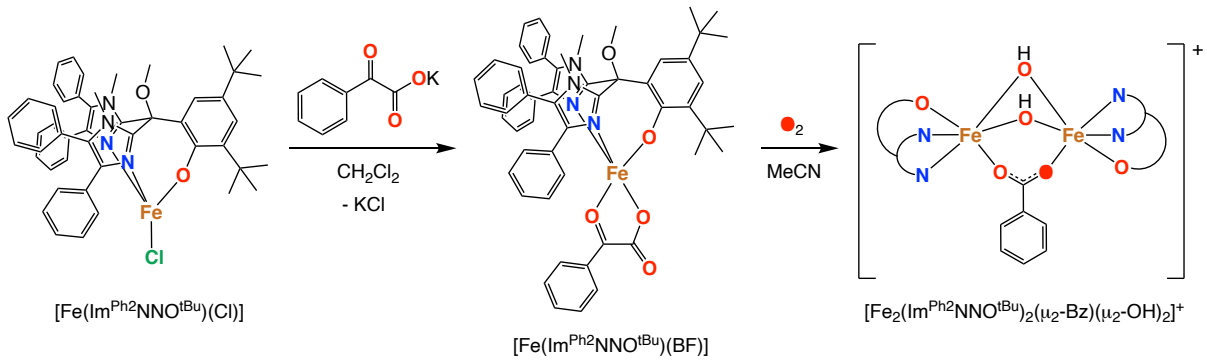

Scheme 4. Synthesis of a mononuclear iron(II) benzoylformate complex, [Fe(Im^{Ph2}NNO^{tBu})(BF)]. Exposure to O_2 leads to the formation of diiron(III) complex [Fe$_2$(Im^{Ph2}NNO^{tBu})$_2$(μ$_2$-OBz)(μ$_2$-OH)$_2$]$^+$.

Finally, **Chapter 6** closes this thesis with a short perspective on the evolution of bioinspired *N,N,O* ligand design for structurally modelling the 2H1C. Particular emphasis is placed on the different families of bis-imidazole-derived *N,N,O* ligands, including those with a carboxylate, ester, amide or phenolate group as an O-donor. The coordination chemistry of these different ligands is discussed in detail, with general trends and the pro's and con's highlighted in all cases.

Importantly, the work described in this thesis also highlights certain vulnerabilities of the bis-imidazole phenolate *N,N,O* ligand design, particularly with respect to the methoxy group of the ligand backbone (Scheme 5). Firstly, it was found that irreversible oxidation of the phenolate moiety to its quinone form is rendered thermodynamically favourable by the triply benzylic nature of the ligand's bridgehead carbon atom, which increases the leaving group ability of the methoxy group. Secondly, it was shown that the terminal methyl group is susceptible to Lewis acid catalysed C–O bond cleavage, which affords an anionic alkoxide group that can bind to the metal centre and disrupt the desired *N,N,O* coordination mode. Nonetheless, given the very limited number of tridentate *N,N,O* ligands available for the synthesis of well-defined mononuclear iron complexes, the bis-imidazole phenolate ligand family presented in this thesis qualifies as a valuable bioinspired platform for further modelling 2H1C-containing non-heme iron enzyme active sites.

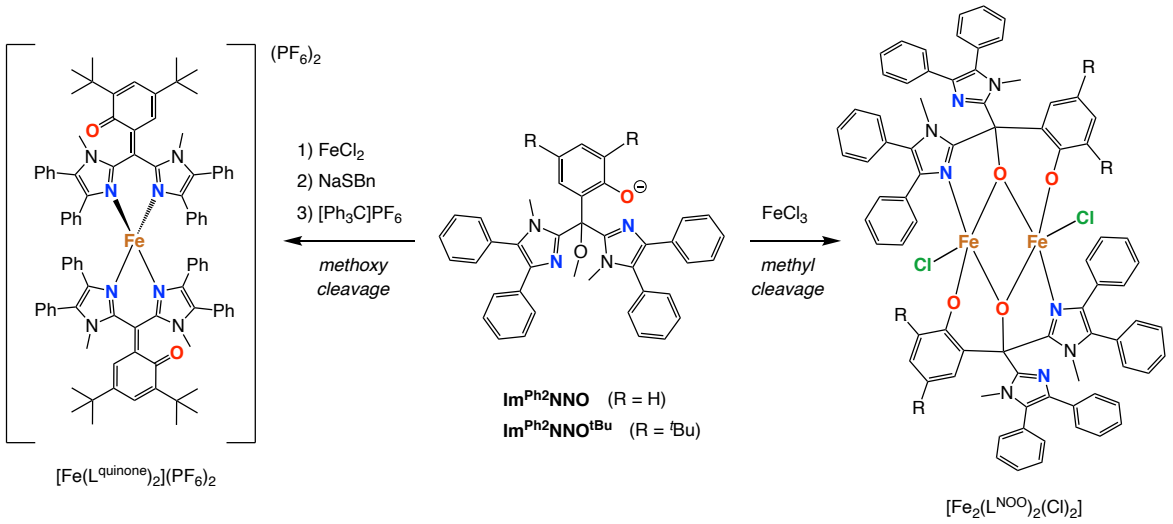

Scheme 5. Products of methyl or methoxy cleavage observed for ligands **Im^{Ph2}NNO** and **Im^{Ph2}NNO^{tBu}** in the presence of $FeCl_3$.

General Conclusions and Perspective

To conclude, this thesis has reported the synthesis and coordination chemistry of three new bioinspired *N,N,O* phenolate ligands (**BenzImNNO**, **Im^{Ph2}NNO** and **Im^{Ph2}NNO^{tBu}**), designed to model the ubiquitous 2-His-1-Carboxylate facial triad found in mononuclear non-heme iron enzymes. The results show that obtaining the desired mononuclear, monoligated, *N,N,O*-bound iron complexes is strongly dependent on two ligand design considerations: the size of the imidazoles and the degree of substitution on the phenolate group. **Im^{Ph2}NNO^{tBu}**, which features bulky substituents on both its imidazole and phenolate groups, was shown to be the most promising ligand scaffold, affording mononuclear, tetra- and pentacoordinate *N,N,O*-bound iron complexes in high yield. Overall, the work described in this thesis illustrates how systematic investigation of the coordination chemistry of structurally related ligands is crucial for establishing the biomimetic potential of a new molecular enzyme modelling platform.

It is important to mention that the *N,N,O* phenolate ligand design diverges from the 2H1C in terms of the redox non-innocence character associated to aromatic phenolate rings. In particular, 2,4-disubstituted phenolates may help stabilise the accumulation of spin density on the ligand scaffold, which could be relevant for biomimetic studies of mononuclear non-heme enzymes such as intradiol cleaving dioxygenases (iron-based) or galactose oxidase (copper-based) that contain a tyrosinate residue at their active site. Nonetheless, the ease with which phenols can be functionalised opens up more possibilities for ligand design and helps avoid certain drawbacks associated to carboxylic acids, such as decarboxylation, poor solubility, or the formation of coordination oligomers.

Finally, the work described in this thesis it but a small drop in an ocean of different approaches and bioinspired ligand designs aimed at modelling mononuclear non-heme iron enzymes. Common to them all is the general recognition that artificially reproducing native enzyme reactivity is extremely challenging. Indeed, metalloenzyme reactivity is governed not only by the first coordination sphere around the metal centre but also by the secondary coordination sphere, the surrounding protein scaffold and a complex network of hydrogen bonding interactions. Modelling IPNS reactivity is no exception to this rule, and its unique C–X bond-forming reactivity has in fact been attributed to specific steric interactions between its substrate and the surrounding protein scaffold. While the iron thiolate complexes reported in this thesis do qualify as some of the most structurally faithful IPNS models reported to date, O_2 reactivity studies have resulted in sulfonate product formation, demonstrating that sulfur oxygenation is possible with this biomimetic system.

Further studies could usefully investigate how these complexes interact with O_2 and how sulfur oxygenation occurs mechanistically. Future investigations with this system could also focus on the use of amide-containing thiolate co-factors that more closely model IPNS' natural substrate. In this vein, it will probably be advantageous to incorporate structural elements that help pre-organise the co-factor in favour of C–X bond forming reactions, thereby mimicking the role of the second coordination sphere in the enzyme.

Samenvatting & Vooruitzicht

Biologisch metaalcentra katalyseren enkele van de meest uitdagende en belangrijke reacties op aarde, variërend van zuurstoftransport bij dieren tot fotosynthese in planten en stikstoffixatie in bacteriën. Deze wonderlijke en brede reactiviteit, welke bereikt wordt onder fysiologische omstandigheden en met een uitstekende stereo- en regioselectiviteit, biedt verschillende aantrekkelijke mogelijkheden voor de synthetisch chemicus, bijvoorbeeld voor de activering van kleine moleculen en in de functionalisering van complexe moleculen. Voor bio-anorganische chemici biedt de directe inzet, optimalisering of nabootsing van metallo-enzymen en metaal-bevattende biomoleculen een scala aan mogelijkheden voor het verbeteren en vergroenen van de hedendaagse chemische industrie.

Dit proefschrift beschrijft de ontwikkeling van synthetische, bio-geïnspireerde ijzercomplexen die O_2-activerende niet-heem-ijzer bevattende enzymen modelleren met een 2-His-1-carboxylaat faciale triade (2H1C) in hun actieve centrum. Meer in het bijzonder streeft dit onderzoek ernaar om ijzercomplexen te creëren die de structuur en reactiviteit van isopenicilline-N-synthase (IPNS, Figuur 1A) modelleren. Dit unieke ijzer-enzym katalyseert de synthetisch uitdagende bicyclisatie van het thiolsubstraat ACV, waarbij twee nieuwe C–X bindingen (X= N, S) worden gevormd met O_2 als oxidator.

Drie belangrijke doelstellingen definiëren het onderzoek dat in dit proefschrift beschreven wordt. De eerste is het ontwerp van een zogenaamde "*N,N,O*"-ligand dat de 2H1C structureel modelleert met twee neutrale N-donoren en een anionische O-donor. Samen moeten deze coördineren aan een enkel metaalion door middel van een drievoudige κ_3-*N,N,*O coördinatie. In dit proefschrift worden bis-imidazool-fenolaatliganden onderzocht als potentiële 2H1C-modellen, aangezien de sterisch te variëren imidazoolgroepen de natuurlijk voorkomende histidyl-groepen van de 2H1C modelleren en de fenolaatgroep een anionische O-donor modelleert die zowel sterisch als elektronisch kan worden

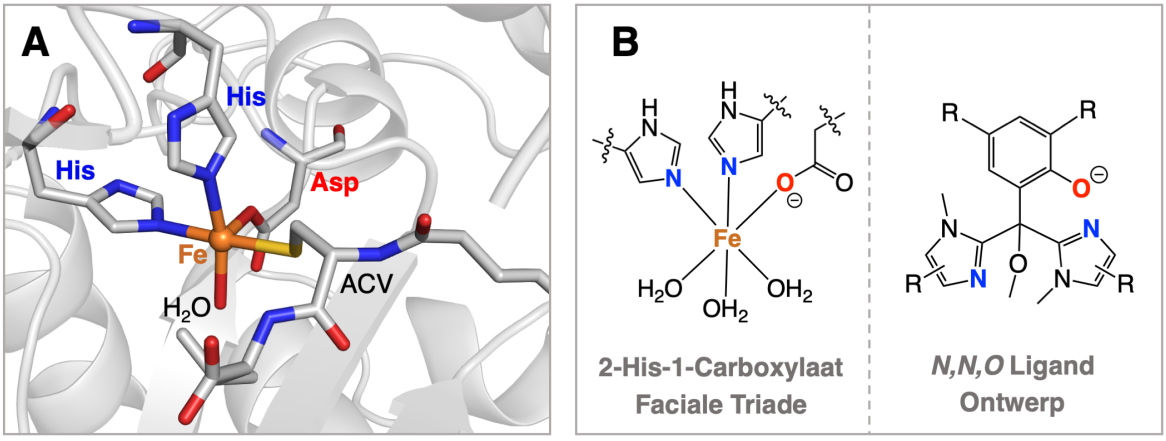

Figuur 1. A: De substraat gebonden actieve plaats van IPNS. B: Een schematische weergave van de 2H1C en het bio-geïnspireerde *N,N,O* bis-imidazool fenolaat ligand ontwerp.

gevarieerd (Figuur 1B). Het tweede onderzoeksdoel is om goed gedefinieerde mononucleaire *N,N,O*-gebonden ijzerthiolaat-complexen te synthetiseren die het substraat-gebonden actieve centrum van IPNS nabootsen. Er bestaan weinig biomimetische ijzerthiolaat-complexen die een anionische donor bevatten, en er is veel discussie in de literatuur over de invloed van de O-donor op de reactiviteit van IPNS. Het derde onderzoeksdoel, tenslotte is het bestuderen van de reactivititeit van deze unieke ijzerthiolaat-complexen in de aanwezigheid van verschillende oxidatoren, waaronder O_2.

Als eerste van de zes hoofstukken bespreekt **Hoofdstuk 1** de rol van ijzer-zwavelbindingen in de structuur en functie van verschillende zwavel-gebonden ijzer-enzymen, waaronder IPNS. De structuur en reactiviteit van relevante synthetische ijzerthiolaat-complexen worden beschreven in vergelijking met het actieve centrum van het betreffende enzym en ten opzichte van elkaar. Dit overzicht levert een moleculaire 'toolbox' op waarmee de structuur en reactiviteit van ijzerthiolaat-complexen beter begrepen en voorspelt kan worden.

Hoofdstuk 2 beschrijft de synthese en coördinatiechemie van de *N,N,O* liganden **BenzImNNO** en **Im^{Ph2}NNO**. Het verschil in sterische bulk van de imidazoolgroepen in deze liganden heeft een grote invloed op de coördinatie van de fenolische O-donor en daarmee op de nuclearitеit van de metaalcomplexen. De reactie van **BenzImNNO** met 1 equiv. ZnX_2 (X = Cl, OTf) geeft dinucleaire [Zn(BenzImNNO)$_2$ZnX$_2$]-complexen (Schema 1). In deze complexen is één van de zinkionen octaëdrisch, faciaal gecoördineerd door twee κ_3-*N,N,O* ligandmoleculen, terwijl het andere zinkion tetraëdrisch is, gebonden aan de fenolische O-donoren van beide liganden. **BenzImNNO** reageert met 0.5 equiv. $Zn(OTf)_2$ tot een mengsel van producten, waaronder het mononucleair bis-ligand complex [Zn(BenzImNNO)$_2$] en dinucleair complex [Zn(BenzImNNO)$_2$Zn(OTf)$_2$] (Schema 1).

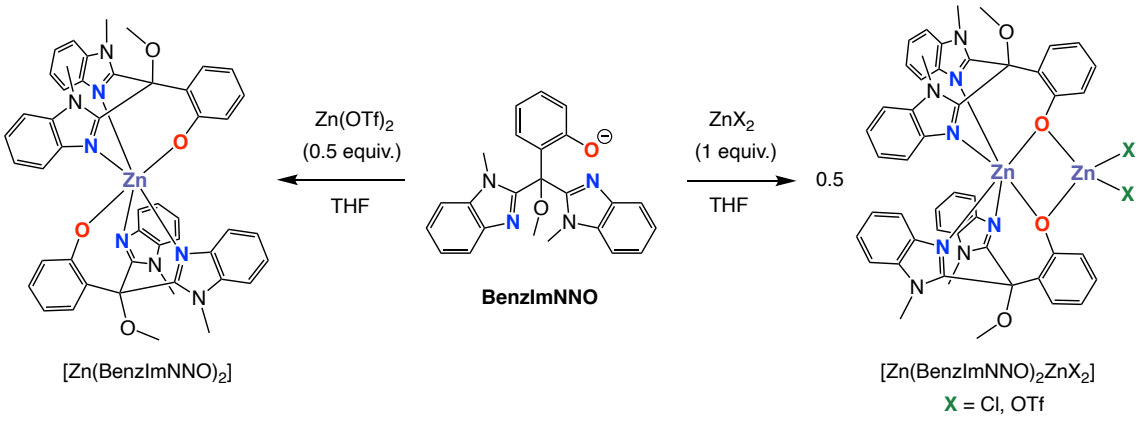

Schema 1. Synthese van mono- en dinucleaire zinkcomplexen op basis van **BenzImNNO**.

Daarentegen geeft de toegenomen sterische bulk van **Im^{Ph2}NNO** aanleiding tot een unieke bruggende μ_2:κ_2-*N,N*:κ_1-*O* coördinatie van het ligand, die dinucleaire complexen [M$_2$(Im^{Ph2}NNO)$_2$(OTf)$_2$] (M = Fe, Zn) met tegenover elkaar liggende metaalcentra geeft

(Schema 2). De unieke dinucleaire structuur van deze complexen blijft behouden bij substitutie van het triflaat-ligand voor een biorelevant thiofenolaat-co-ligand.

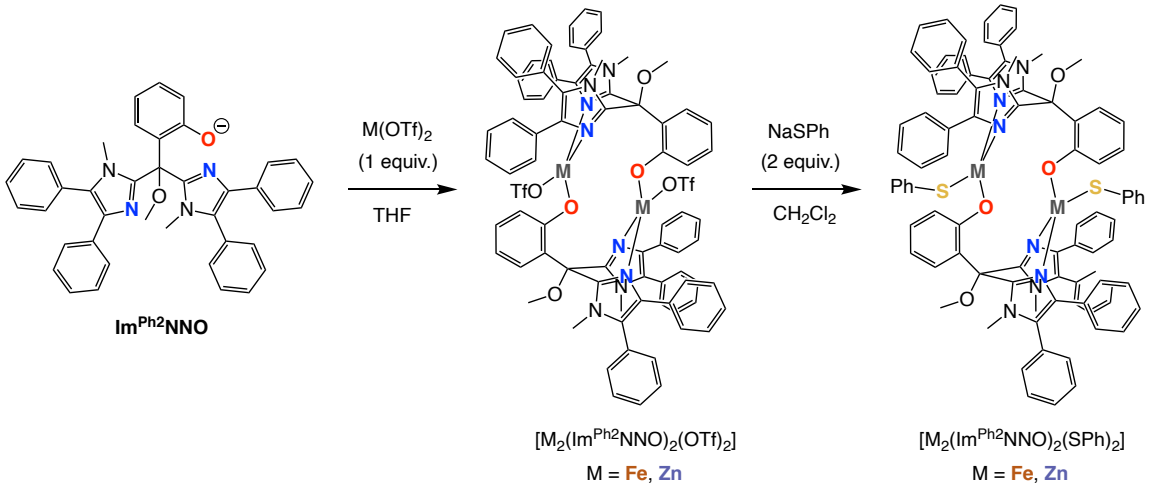

Schema 2. Synthese van dinucleaire ijzer- en zinkcomplexen afgeleid van het **Im^{Ph2}NNO** ligand.

Hoofdstuk 3 beschrijft de synthese en coördinatiechemie van het **Im^{Ph2}NNO^{tBu}** ligand, dat *tert*-butylgroepen bevat op de *ortho*- en *para*-posities van de fenolaatgroep. De reactie van **Im^{Ph2}NNO^{tBu}** met MCl_2 (M = Fe, Zn) geeft mononucleaire complexen [M(Im^{Ph2}NNO^{tBu})(Cl)] in hoge opbrengsten (Schema 3). De tripodale κ_3-*N,N,O*-coördinatie van het ligand zoals waargenomen in de kristalstructuur blijft intact en goed gedefinieerd in oplossing (acetonitril en dichloormethaan). Deze complexen kunnen daarom beschouwd worden als geschikte synthons om een reeks van verschillende biomimetische complexen te synthetiseren, d.m.v. substitutie van het chloride ligand voor biorelevante co-liganden. Dit wordt geïllustreerd door de reactie van [Zn(Im^{Ph2}NNO^{tBu})(Cl)] met NaSPh, wat tetraëdrisch zinkthiolaat-complex [Zn(Im^{Ph2}NNO^{tBu})(SPh)] geeft, dat relevant is voor IPNS-modellering.

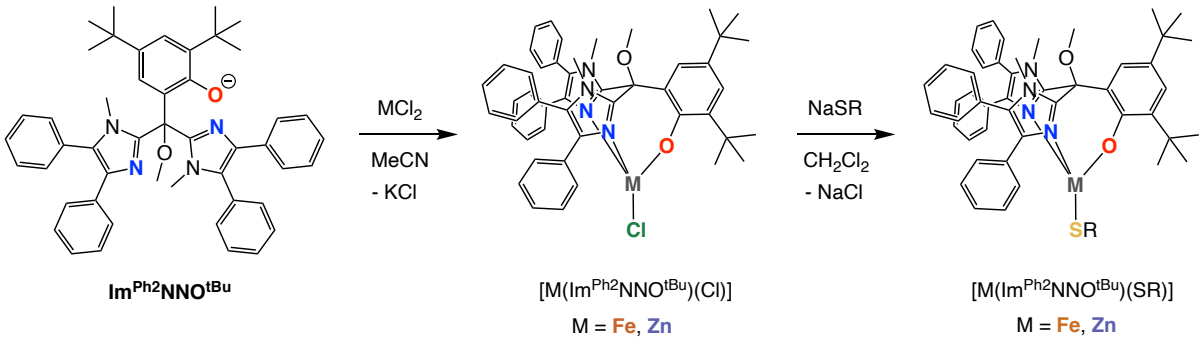

Schema 3. Synthese van mononucleaire ijzer- en zinkcomplexen gebaseerd op **Im^{Ph2}NNO^{tBu}**. R = ^{t}Bu, Bn, Ph, Mes, 4-OMe-Ph, 4-CF_3-Ph.

Hoofdstuk 4 breidt de coördinatiechemie van het in Hoofdstuk 3 ontwikkelde **Im^{Ph2}NNO^{tBu}** ligand uit en beschrijft de synthese, structuur en reactiviteit van een familie van mononucleaire ijzer- en zinkthiolaatcomplexen [M(Im^{Ph2}NNO^{tBu})(SR)] (M = Fe, Zn; R = ^{t}Bu, Bn, Ph, Mes, 4-OMe-Ph, 4-CF_3-Ph) (Schema 3). Analyse van de structuren van

de complexen in de vaste- en opgeloste toestand laat zien dat ze allen een tetraëdrische structuur hebben, faciaal gecoördineerd door de κ_3-*N,N,O* donorset van het **Im^{Ph2}NNO^{tBu}** ligand. De M–S bindingslengtes variëren afhankelijk van de electron-donerende karakter en de sterische bulk van het thiolaat-co-ligand. De variatie in zwavel-naar-metaal ladingsoverdracht wordt ook weerspiegeld door de vaste-stof Mössbauer-parameters van de ijzerthiolaat-complexen. Cyclische voltammetrie toont aan dat de eerste elektrochemische oxidatie plaats vindt op het ijzercentrum bij alle ijzerthiolaat-complexen, en dat de redoxpotentiaal wordt bepaald door de donerende eigenschappen van het thiolaatligand. Een studie naar de reactiviteit van de ijzerthiolaat-complexen met verschillende oxidatoren, waaronder O_2, NO, PhIO en $[Ph_3C]PF_6$, laat zien dat het ijzercentrum gemakkelijk wordt geoxideerd tot de ijzer(III)-toestand, waarbij een sulfonaat wordt gevormd in de reacties met O_2 en PhIO.

Hoofstuk 5 presenteert een biomimetische studie naar α-ketoglutaraat (αKG) afhankelijke ijzerenzymen, de grootste subfamilie van 2H1C-bevattende niet-heem-ijzerenzymen. Er wordt een ijzer(II)-benzoylformiaatcomplex beschreven, [Fe(Im^{Ph2}NNO^{tBu})(BF)], waarvan de mononucleaire, penta-gecoördineerde structuur en het κ_3-*N,N,O* gecoördineerde ligand het kwalificeren als één van de tot nu toe meest structureel-getrouwe modellen voor dergelijke enzymen (Schema 4). De Mössbauerparameters liggen inderdaad zeer dicht bij die gerapporteerd voor de αKG-gebonden enzymen. De kristalstructuur van het complex laat een vacante coördinatieplaats zien, die zich trans tot een van de imidazoolgroepen bevindt en die de binding van een NO-molecuul kan accommoderen (zoals aangetoond met EPR, IR, UV-Vis en DFT-onderzoek). Blootstelling van het complex aan O_2 resulteert in een snelle decarboxyleringsreactie, waarbij een interessant di-ijzer(III)benzoaatcomplex wordt gevormd, $[Fe_2(Im^{Ph2}NNO^{tBu})_2(\mu_2\text{-OBz})(\mu_2\text{-OH})_2]^+$ (Schema 4). Hoge resolutie ESI-MS metingen en experimenten met isotoop-gelabeld $^{18}O_2$ laten zien dat één O_2-zuurstofatoom is opgenomen in de benzoaatgroep, waarmee αKG-afhankelijke enzymreactiviteit wordt nagebootst.

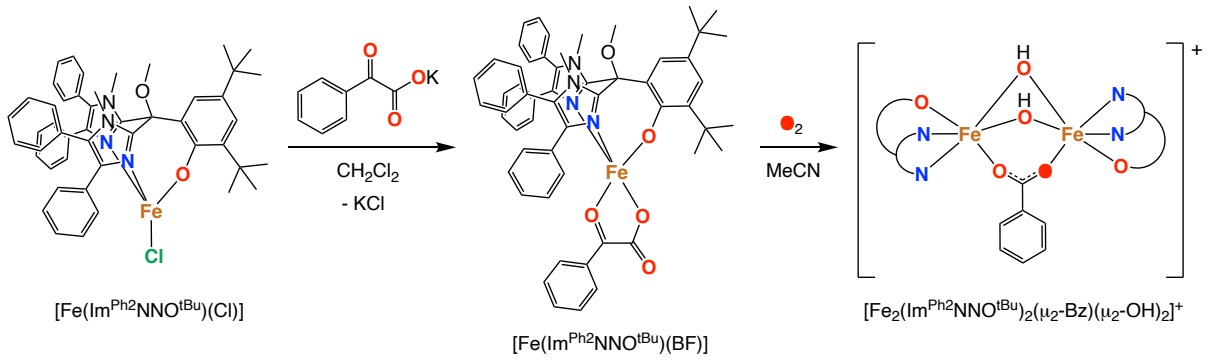

Schema 4. Synthese van een mononucleair iron(II) benzoylformiaat complex, [Fe(Im^{Ph2}NNO^{tBu})(BF)]. Blootstelling aan O_2 leidt tot di-ijzer(III)complex $[Fe_2(Im^{Ph2}NNO^{tBu})_2(\mu_2\text{-OBz})(\mu_2\text{-OH})_2]^+$.

Ten slotte sluit **Hoofdstuk 6** dit proefschrift af met een kort perspectief op de evolutie van bio-geïnspireerde *N,N,O*-ligandontwerp voor het structureel modelleren van de 2H1C.

Bijzondere nadruk wordt gelegd op de verschillende families van *N,N,O*-liganden gebaseerd op imidazool, waaronder die met een carboxylaat-, ester-, amide- of fenolaatgroep als O-donor. De coördinatiechemie van deze verschillende liganden wordt in detail besproken, waarbij algemene trends en de voor- en nadelen worden beschreven.

Belangrijk is dat het werk dat in dit proefschrift wordt beschreven ook bepaalde kwetsbaarheden van het ontwerp van het bis-imidazolfenolaat *N,N,O*-ligand aantoont, in het bijzonder met betrekking tot de methoxygroep aan de 'achterzijde' van het ligand (Schema 5). Ten eerste werd gevonden dat de onomkeerbare oxidatie van de fenolaatgroep tot zijn quinonvorm thermodynamisch gunstig is vanwege de drievoudige benzylische positie in het bruggenhoofd, wat de methoxygroep een betere vertrekkende groep maakt. Ten tweede is aangetoond dat de methylgroep vatbaar is voor Lewis-zuur gekatalyseerde verbreking van de C–O-binding, wat een anionische alkoxidegroep oplevert die aan het metaalcentrum kan binden en de gewenste κ_3-*N,N,O*-coördinatiemodus kan verstoren. Desalniettemin, gezien het zeer beperkte aantal tridentate *N,N,O*-liganden dat beschikbaar is voor de synthese van goed gedefinieerde mononucleaire ijzercomplexen, kwalificeert de in dit proefschrift gepresenteerde bis-imidazoolfenolaat ligandfamilie zich als een waardevol bio-geïnspireerd platform voor verdere modellering van 2H1C-bevattende actieve centra in niet-heem-ijzerenzymen.

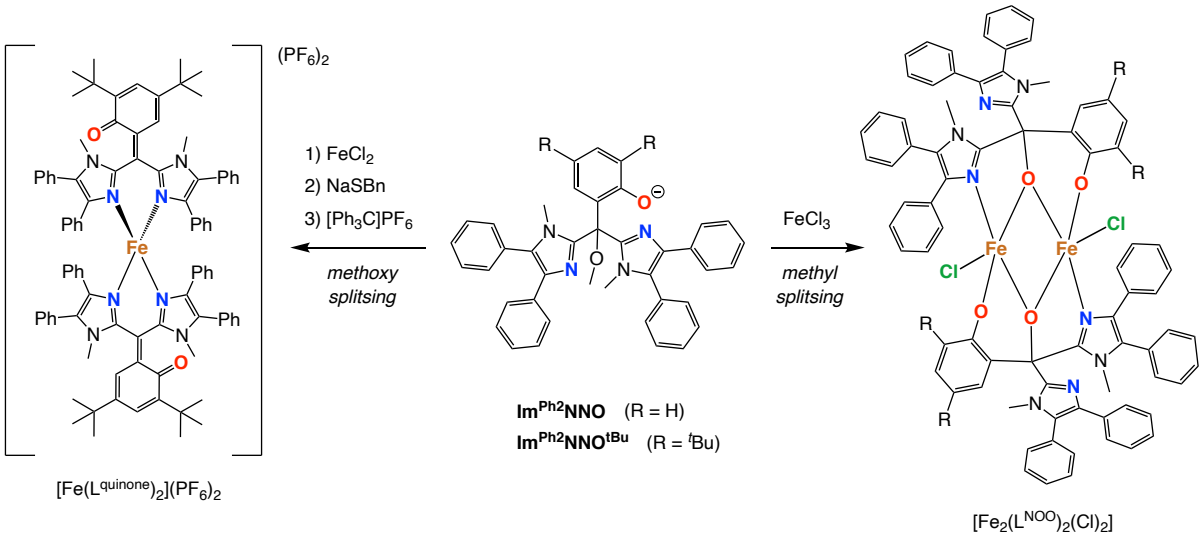

Schema 5. Onverwachte producten van methyl- of methoxy-splitsing waargenomen voor liganden **Im^{Ph2}NNO** en **Im^{Ph2}NNO^{tBu}** in aanwezigheid van $FeCl_3$.

Algemene conclusies en vooruitzicht

Concluderend heeft dit proefschrift de synthese en coördinatiechemie gerapporteerd van drie nieuwe bio-geïnspireerde *N,N,O*-fenolaatliganden (**BenzImNNO**, **Im^{Ph2}NNO** en **Im^{Ph2}NNO^{tBu}**), ontworpen om de alomtegenwoordige 2-His-1-Carboxylaat faciaal triade te modelleren die wordt gevonden in mononucleaire niet-heem ijzer enzymen. Het proefschrift laat zien dat het verkrijgen van de gewenste mononucleaire, monogeligeerde,

N,N,O-gebonden ijzercomplexen sterk afhankelijk is van twee overwegingen bij het ontwerp van liganden: de grootte van de imidazoolgroepen en de mate van substitutie op de fenolaatgroep. **Im^{Ph2}NNO^{tBu}**, dat grote substituenten bevat op zowel de imidazool- als de fenolaatgroepen, bleek het meest veelbelovende ligandraamwerk te zijn, dat in staat is mononucleaire, tetra- en penta-gecoördineerde *N,N,O*-gebonden ijzercomplexen te vormen. Al met al laat dit proefschrift zien hoe systematisch onderzoek van de coördinatiechemie van structureel-verwante liganden cruciaal is voor het vaststellen van het biomimetische potentieel van nieuw moleculaire enzymmodellen.

Het is belangrijk om op te merken dat het ontwerp van de *N,N,O*-fenolaatliganden afwijkt van de 2H1C in termen van het redox-actieve karakter dat typisch is voor aromatische fenolaatringen. Met name het gebruik van 2,4-digesubstitueerde fenolaten kan de accumulatie van spindichtheid op de ligandstructuur stabiliseren en zou relevant kunnen zijn voor biomimetische studies van mononucleaire niet-heem-enzymen zoals intradiol-splitsende dioxygenases (op ijzer gebaseerd) of galactose-oxidase (koper-gebaseerd), die een tyrosinaatresidu in hun actieve centrum bevatten. Desalniettemin opent het gemak waarmee fenolen kunnen worden gefunctionaliseerd veel mogelijkheden voor het ontwerpen van liganden en helpt het bepaalde nadelen van carbonzuren te voorkomen, zoals decarboxylering, slechte oplosbaarheid of de vorming van coördinatie-oligomeren.

Ten slotte is het onderzoek beschreven in dit proefschrift slechts een kleine druppel in een oceaan van verschillende benaderingen en bio-geïnspireerde ligandontwerpen die gericht zijn op het modelleren van mononucleaire niet-heem-ijzerenzymen. Ze hebben gemeen dat het een grote uitdaging is om de reactiviteit van natuurlijke enzymen te reproduceren met synthetische modellen. De reactiviteit van metallo-enzymen wordt niet alleen bepaald door de eerste coördinatiesfeer rond het metaalcentrum, maar ook door de secundaire coördinatiesfeer en de omringende eiwitstructuur. Het modelleren van IPNS-reactiviteit is geen uitzondering op deze regel, en de unieke C–X-bindingsvormende reactiviteit wordt mede toegeschreven aan specifieke sterische interacties tussen het substraat en de omringende eiwitstructuur. Hoewel de ijzerthiolaat-complexen die in dit proefschrift worden beschreven kwalificeren als enkele van de tot nu toe meest structureel getrouwe IPNS-modellen, hebben O_2-reactiviteitstudies geresulteerd in de vorming van sulfonaatproducten, wat aantoont dat zwaveloxygenatie mogelijk is met deze biomimetische systemen.

Verdere studies zouden nuttig kunnen zijn om de details van de interactie van de nieuwe complexen met O_2 en het onderliggende mechanisme van de zwaveloxygenatie te onderzoeken. Toekomstige onderzoeken met dit systeem kunnen zich ook richten op het gebruik van amide-bevattende thiolaat-co-factoren die het natuurlijke substraat van IPNS beter modelleren. Vanuit deze gedachte zou het voordelig kunnen zijn om structurele elementen op te nemen die helpen bij het voor-organiseren van de substraat om C–X-bindingsvormende reacties te bevorderen, waarmee de rol van de tweede coördinatiesfeer in het enzym wordt nagebootst.

Synthèse et perspectives

En biologie, les sites actifs des métalloenzymes catalysent certaines réactions parmi les plus complexes et importantes qui soient, comme le transport de l'oxygène chez les animaux, la photosynthèse des plantes ainsi que la fixation de l'azote chez certaines bactéries. Ces métalloenzymes ont une incroyable capacité à transformer de petites molécules ainsi qu'à fonctionnaliser des molécules plus complexes avec une stéréosélectivité et une régiosélectivité remarquables dans des conditions physiologiques. Pour les chimistes bio-inorganiques, l'utilisation directe, l'ingénierie ou l'imitation des métalloenzymes constitue une voie riche de possibilités pour accroître la durabilité de l'industrie chimique actuelle.

Cette thèse présente de nouveaux complexes de fer qui miment les sites actifs des enzymes à fer non héminique montrant la triade faciale 2-His-1-Carboxylate (2H1C) et pouvant activer le dioxygène. Plus précisément, les travaux se sont focalisés sur la création de complexes de fer reproduisant la structure et la réactivité du site actif de l'isopenicilline N synthase (IPNS, figure 1A). Cette métalloenzyme a la particularité de catalyser la bicyclisation de son substrat thiol en utilisant le dioxygène comme oxydant, créant ainsi deux nouvelles liaisons C–X (X = N, S).

Les travaux menés dans le cadre de la présente thèse poursuivent trois objectifs majeurs. Premièrement, la synthèse de ligands *« N,N,O »* possédant deux imidazoles (donneurs N neutres) et un phénolate (donneur O anionique), qui imitent la structure de la triade 2H1C. Ces ligands sont conçus pour se coordiner à un seul ion métallique de façon tripodale de type κ_3-*N,N,O* (Figure 1B). La structure du ligand permet également d'étudier les variations stériques et électroniques au niveau des groupes imidazoles et phénolate. Le deuxième objectif vise à synthétiser des complexes thiolates de fer mononucléaires bien définis à partir du ligand *N,N,O* afin d'imiter le site actif de l'IPNS lié à son substrat. Les complexes thiolates métalliques bioinspirés qui contiennent un donneur O anionique sont

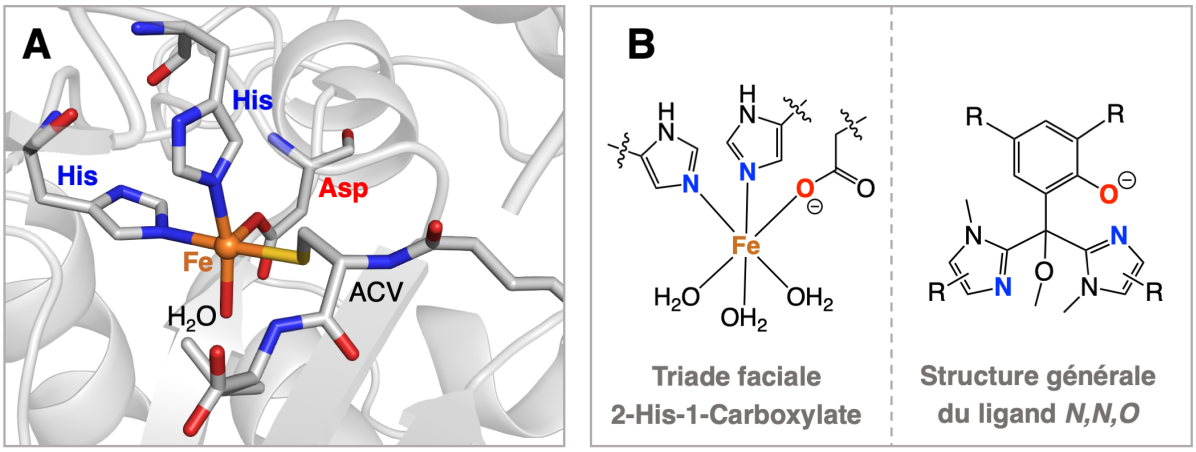

Figure 1. A : Site actif de l'IPNS lié à son substrat thiol. B : Représentation schématique de la triade 2H1C et de la structure générale des ligands *N,N,O* phénolates à motif bis-imidazole bioinspirés.

relativement rares, et le débat se poursuit dans la littérature quant à l'influence du donneur O sur la réactivité de l'IPNS. Enfin, le troisième objectif consiste à étudier la réactivité de ces complexes thiolates métalliques en présence de divers oxydants, dont le dioxygène.

La présente thèse est divisée en 6 chapitres. Le **chapitre 1** décrit le rôle des liaisons fer-soufre dans la structure et le fonctionnement de l'IPNS ainsi que de différentes métalloenzymes à base de fer possédant un ligand thiolate dans leur site actif. Cette analyse est complétée par la description et la comparaison de plusieurs complexes thiolates de fer bioinspirés afin d'obtenir une « boîte à outils » moléculaire permettant de mieux comprendre et prédire la structure et la réactivité de ces complexes .

Le **chapitre 2** présente la synthèse et la chimie de coordination des ligands *N,N,O* **BenzImNNO** et **Im^{Ph2}NNO**. Nous montrons que la variation de l'encombrement stérique des imidazoles a un impact important sur le mode de coordination du donneur O phénolique et sur la nucléarité des complexes. La réaction de **BenzImNNO** avec 1 équiv. ZnX_2 (X = Cl, OTf) conduit à la formation de complexes dinucléaires de formule $[Zn(BenzImNNO)_2ZnX_2]$ (Schéma 1). Dans ces complexes, l'un des ions de zinc est octaédrique et coordiné de manière faciale par deux ligands κ_3-*N,N,O*, tandis que l'autre ion de zinc est tétraédrique et lié au donneur O phénolique des deux ligands. En faisant réagir **BenzImNNO** avec 0.5 équiv. $Zn(OTf)_2$, on obtient un mélange de produits, dont un complexe mononucléaire à deux ligands de formule $[Zn(BenzImNNO)_2]$ et un complexe dinucléaire de formule $[Zn(BenzImNNO)_2Zn(OTf)_2]$ (Schéma 1).

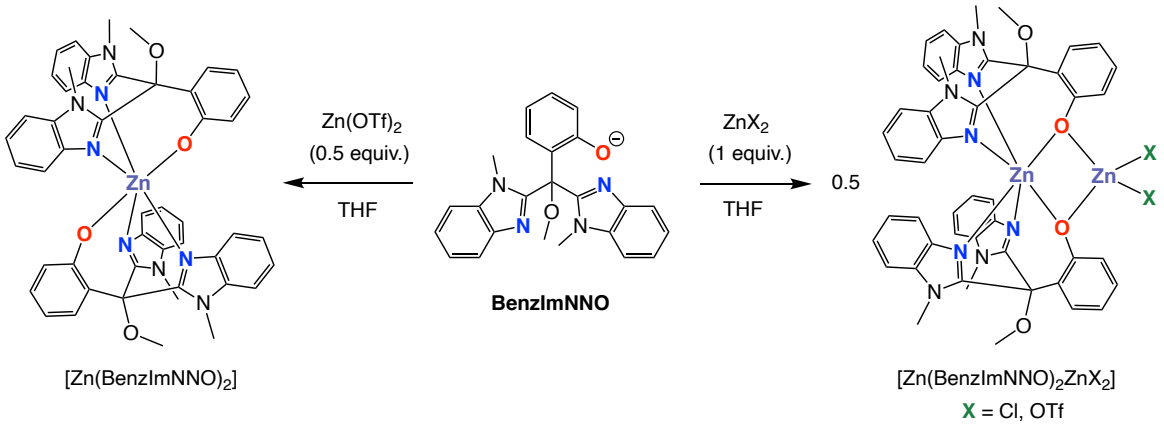

Schéma 1. Synthèse de complexes zinc liés à **BenzImNNO**.

En revanche, l'utilisation du ligand **Im^{Ph2}NNO**, dont l'encombrement stérique est plus important, entraîne un mode unique de coordination μ_2:κ_2-*N,N*:κ_1-*O*, qui conduit à la formation de complexes dinucléaires de formule $[M_2(Im^{Ph2}NNO)_2(OTf)_2]$ (M = Fe, Zn) dotés de sites métalliques à faces opposées (Schéma 2). Nous étudions la robustesse du mode de coordination dinucléaire du ligand pendant des transformations oxydatives, et nous montrons que ce mode de coordination demeure inchangé en cas de substitution du triflate par un co-ligand thiophénolate biologiquement pertinent.

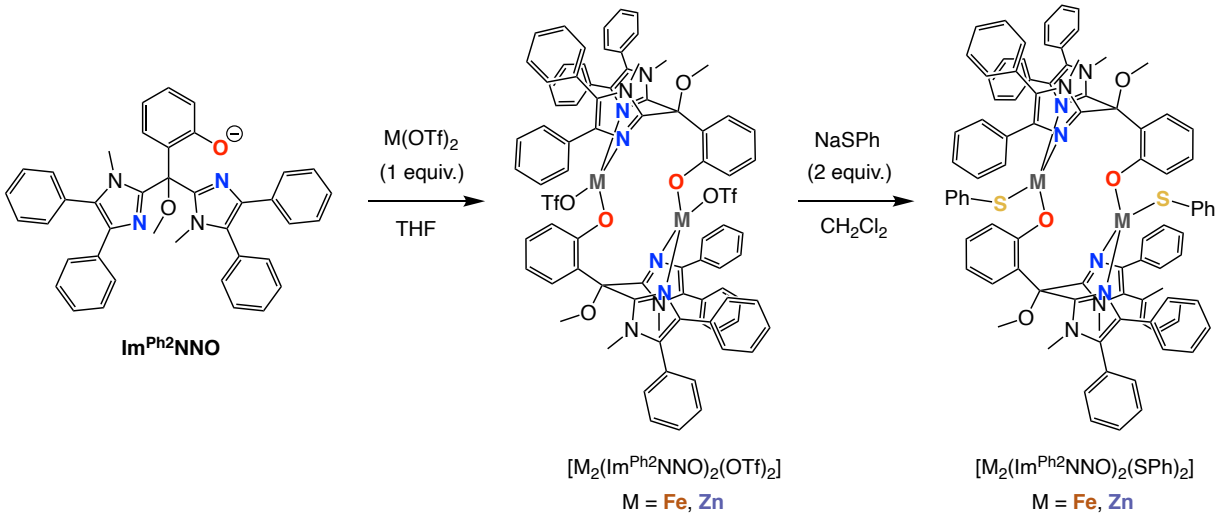

Schéma 2. Synthèse de complexes dinucléaires fer et zinc liés par **Im^{Ph2}NNO**.

Le **chapitre 3** décrit la synthèse et la chimie de coordination du ligand **Im^{Ph2}NNO^{tBu}**, qui présente des groupes *tert*-butyle sur les positions *ortho* et *para* du phénolate. La réaction de **Im^{Ph2}NNO^{tBu}** avec MCl_2 (M = Fe, Zn) conduit à la formation de complexes mononucléaires de formule [M(Im^{Ph2}NNO^{tBu})(Cl)] avec un haut rendement (Schéma 3). La coordination tripodale κ_3-*N,N,O* du ligand observée dans leurs structures cristallines étudiées par diffraction des rayons X demeure intacte et bien définie dans les solutions MeCN et CH_2Cl_2. Ces complexes peuvent donc être considérés comme des synthons importants pour créer un large éventail de complexes bioinspirés, moyennant la substitution du ligand chlore par des co-ligands biologiquement pertinents. Ainsi, la réaction de [Zn(Im^{Ph2}NNO^{tBu})(Cl)] avec NaSPh permet d'obtenir un complexe de zinc thiolate tétraédrique de formule [Zn(Im^{Ph2}NNO^{tBu})(SPh)], utile pour le biomimétisme de l'IPNS.

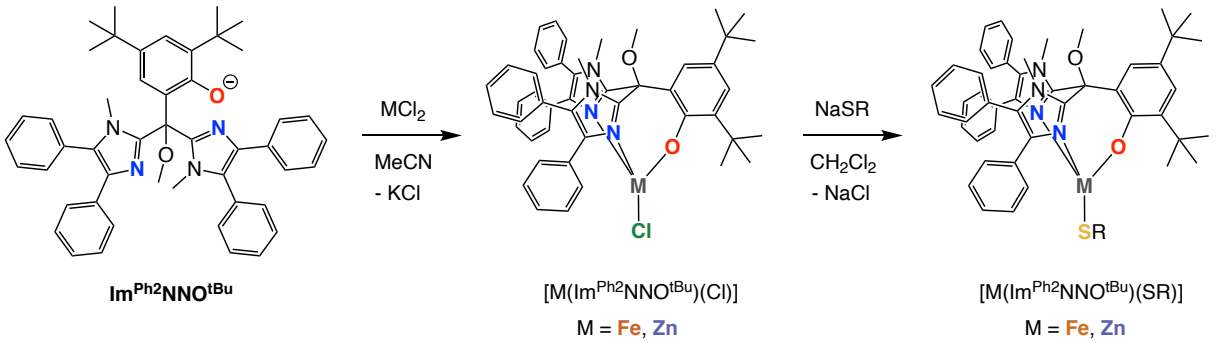

Schéma 3. Synthèse de complexes mononucléaires fer et zinc liés par **Im^{Ph2}NNO^{tBu}**. R = ^{t}Bu, Bn, Ph, Mes, 4-OMe-Ph, 4-CF_3-Ph.

Le potentiel biomimétique du ligand **Im^{Ph2}NNO^{tBu}** ayant été établi, le **chapitre 4** extrapole la méthodologie décrite dans le chapitre 3 et présente la synthèse, la structure et la réactivité d'une famille de complexes thiolates mononucléaires de fer et de zinc de formule [M(Im^{Ph2}NNO^{tBu})(SR)] (M = Fe, Zn; R = ^{t}Bu, Bn, Ph, Mes, 4-OMe-Ph, 4-CF_3-Ph) (Schéma 3). L'analyse des structures de ces complexes à l'état solide et en solution montre que ceux-

ci sont tous de géométrie tétraédrique, coordinés de manière faciale par l'ensemble donneur κ$_3$-*N,N,O* du ligand **Im^{Ph2}NNO^{tBu}**. Les longueurs de la liaison M–S varient selon le pouvoir donneur et l'encombrement stérique du co-ligand thiolate. La variation du transfert de charge entre le soufre et le métal se reflète également dans les paramètres Mössbauer des complexes thiolates de fer à l'état solide. Des études de voltamétrie cyclique montrent que la première oxydation électrochimique se produit sur le fer pour tous les complexes thiolates à base de fer, et que son potentiel redox varie selon le pouvoir donneur du thiolate. Nous étudions aussi la réactivité des complexes thiolates de fer avec divers oxydants, y compris O_2, NO, PhIO et $[Ph_3C]PF_6$. Dans tous les cas, les données indiquent que le fer est facilement oxydé vers sa forme ferrique, la formation de sulfonate étant observée lors des réactions avec O_2 et PhIO.

Le **chapitre 5** présente une étude biomimétique des enzymes à fer dépendantes de l'alpha-cétoglutarate (αKG), la plus grande sous-famille d'enzymes à fer non héminique présentant la triade faciale 2H1C. Nous y décrivons un complexe benzoylformate de fer(II) de formule [Fe(Im^{Ph2}NNO^{tBu})(BF)] qui, par sa structure mononucléaire pentacoordinée et son ligand κ$_3$-*N,N,O,* constitue l'un des modèles les plus structurellement fidèles décrits à ce jour (Schéma 4). En effet, ses paramètres Mössbauer sont très proches de ceux décrits pour les sites actifs d'enzymes liés à l'alpha-cétoglutarate, et sa structure cristalline étudiée par diffraction des rayons X révèle l'existence d'un site de coordination vide situé *trans* par rapport à l'un des groupes imidazoles, qui pourrait accueillir une molécule de NO (comme le montrent les études RPE, IR, UV-vis et DFT). L'exposition du complexe à une atmosphère de O_2 entraîne une rapide réaction de décarboxylation qui conduit à la formation d'un intéressant complexe benzoate diferrique de formule $[Fe_2(Im^{Ph2}NNO^{tBu})_2(\mu_2\text{-}OBz)(\mu_2\text{-}OH)_2]^+$ (Schéma 4). Les mesures ESI-MS à haute résolution et les expériences avec l'oxygène lourd ($^{18}O_2$) montrent qu'un atome d'oxygène est incorporé dans la portion benzoate, reproduisant ainsi la réactivité naturelle des enzymes dépendantes de l'alpha-cétoglutarate.

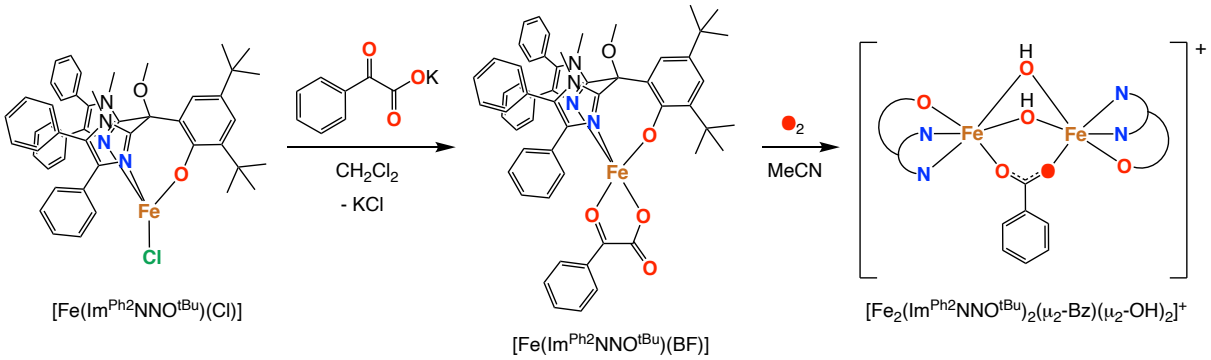

Schéma 4. Synthèse du complexe [Fe(Im^{Ph2}NNO^{tBu})(BF)]. L'exposition à O_2 conduit à la formation d'un complexe diferrique de formule $[Fe_2(Im^{Ph2}NNO^{tBu})_2(\mu_2\text{-}OBz)(\mu_2\text{-}OH)_2]^+$.

Enfin, le **chapitre 6** clôt la présente thèse par un bref aperçu de l'évolution conceptuelle des ligands *N,N,O* bioinspirés pour la modélisation structurelle de la triade faciale 2H1C. Une attention particulière est accordée aux différentes familles de ligands *N,N,O* à motif

bis-imidazole, y compris ceux comportant un groupe carboxylate, ester, amide ou phénolate comme donneur O. Nous étudions en détail la chimie de coordination de ces différents ligands et mettons en avant les tendances générales ainsi que les avantages et inconvénients de chacun d'eux.

Les travaux décrits dans ce manuscrit mettent en lumière certaines fragilités dans la structure des ligands *N,N,O* phénolates à motif bis-imidazole, notamment au niveau du groupe méthoxy de leur « épine dorsale » (Schéma 5). D'abord, il est apparu qu'une oxydation irréversible du phénolate vers sa forme quinonique est rendue thermodynamiquement possible à cause de la triple substitution de la position benzylique du phénol, augmentant ainsi la capacité nucléofuge du groupe méthoxy. Ensuite, il a été montré que la présence d'un acide de Lewis peut conduire au clivage du groupe methyle, ce qui conduit à la formation d'une alcoxyde pouvant se lier au centre métallique et perturber le mode de coordination κ_3-*N,N,O* recherché. Néanmoins, vu le nombre restreint de ligands *N,N,O* tridentés disponibles pour la synthèse de complexes mononucléaires à base de fer, la famille des ligands phénolates à motif bis-imidazole décrite dans la présente thèse constitue une plateforme bioinspirée utile pour explorer davantage la modélisation des sites actifs des enzymes à fer non héminique qui présentent la triade faciale 2H1C.

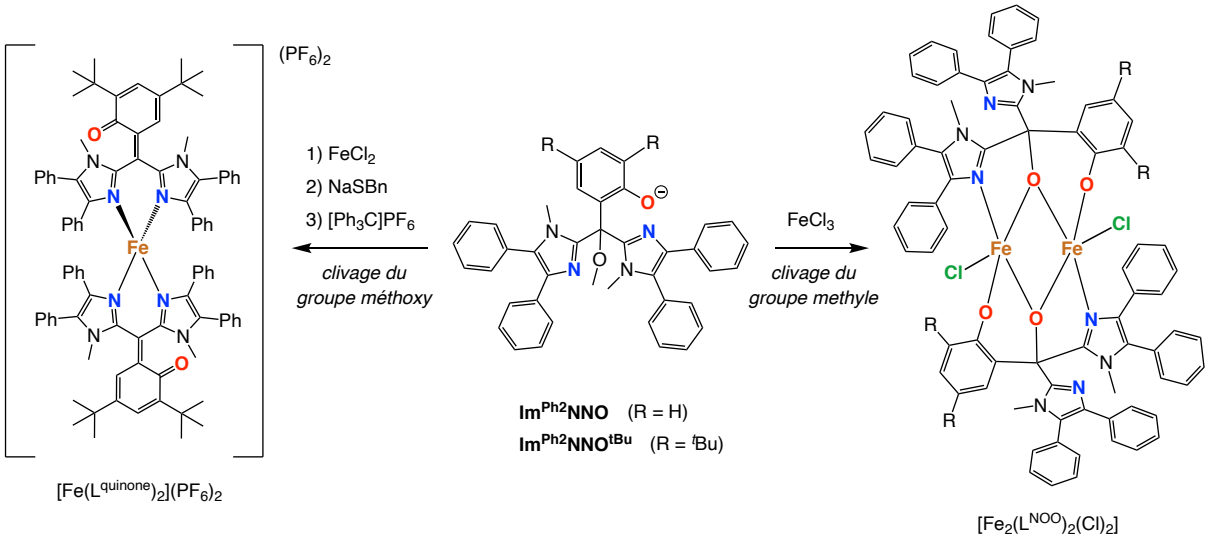

Schéma 5. Clivage du groupe methyle ou methoxy des ligands **Im^{Ph2}NNO** et **Im^{Ph2}NNO^{tBu}** en présence de $FeCl_3$.

Conclusions générales et perspectives

La présente thèse porte sur la synthèse et la chimie de coordination de trois nouveaux ligands phénolates *N,N,O* bioinspirés (**BenzImNNO**, **Im^{Ph2}NNO** et **Im^{Ph2}NNO^{tBu}**), conçus pour reproduire la triade faciale 2-His-1-Carboxylate très courante dans les enzymes à base de monofer non héminique. Les résultats obtenus montrent que la synthèse de complexes mononucléaires à base de fer coordiné à un seul ligand *N,N,O* est largement tributaire de deux facteurs du design du ligand: l'encombrement stérique des groupes imidazoles et le

degré de substitution du groupe phénolate. Le ligand **Im^{Ph2}NNO^{tBu}**, qui comporte des substituants volumineux sur ses groupes imidazoles et phénolate, s'avère le plus prometteur, car il permet la formation à haut rendement de complexes mononucléaires à base de fer tétra-et pentacoordinés présentant une coordination tripodale de type *N,N,O*. D'une manière générale, les travaux décrits dans la présente thèse illustrent l'importance d'étudier de manière systématique la chimie de coordination de ligands structurellement apparentés afin d'établir le potentiel biomimétique d'une nouvelle plateforme de modélisation moléculaire d'enzymes.

Il importe de noter que le ligand phénolate *N,N,O* diverge de la triade faciale 2H1C par le caractère rédox non innocent du groupe phénolate. En particulier, les phénolates 2,4-disubstitués peuvent stabiliser l'accumulation de densité de spin sur le ligand, offrant ainsi des perspectives pour les études biomimétiques d'enzymes mononucléaires non héminiques telles que les intradiol catéchol dioxygénases (à base de fer) ou l'oxydase de galactose (à base de cuivre), qui contiennent un résidu tyrosine dans leur site actif. Néanmoins, la facilité avec laquelle les phénols peuvent être fonctionnalisés ouvre une large gamme de possibilités pour la conception de ligands et permet d'éviter certains inconvénients associés aux acides carboxyliques, tels que la décarboxylation, la faible solubilité, ou la formation d'oligomères de coordination.

Enfin, les travaux décrits dans le présent manuscrit ne constituent que la partie visible de l'iceberg parmi les multiples approches suivies pour la conception de ligands bioinspirés visant à modéliser les enzymes non héminiques mononucléaires à base de fer. Il est toutefois communément reconnu que la reproduction artificielle de la réactivité naturelle des enzymes constitue un défi majeur. En effet, la réactivité des métalloenzymes est gouvernée non seulement par la première sphère de coordination autour du centre métallique mais aussi par la seconde sphère de coordination, le squelette de la protéine et un réseau complexe de liaisons hydrogène. La modélisation de la réactivité de l'IPNS ne constitue pas une exception à la règle. En effet, sa réactivité très particulière de couplage C–X est attribuée à des interactions stériques spécifiques entre son substrat et le squelette de la protéine. Si les complexes thiolates ferreux décrits dans la présente thèse s'inscrivent parmi les modèles IPNS les plus structurellement fidèles à ce jour, les études de réactivité avec O_2 ont néanmoins révélé la formation de sulfonates, montrant ainsi que l'oxygénation du soufre peut avoir lieu avec ce système biomimétique.

Des études ultérieures pourraient utilement explorer les modalités d'interaction de ces complexes avec O_2 ainsi que les aspects mécanistiques de l'oxygénation du soufre. La poursuite de la recherche pourrait également s'axer sur l'utilisation d'un co-ligand thiolate amide reproduisant plus fidèlement le substrat naturel de l'IPNS. A cet effet, il serait probablement bénéfique d'incorporer des éléments structurels qui préorganiseraient le co-ligand de manière à favoriser les réactions de couplage C–X, mimant ainsi le rôle de la seconde sphère de coordination de l'enzyme.

Acknowledgements

Coming to the Netherlands and conducting my PhD in the group of Organic Chemistry and Catalysis (OCC) at Utrecht University has been an amazing adventure. It has shaped me both professionally and personally, and I loved discovering the perks and quirks of life in Utrecht. And after all these years, I cannot help but draw an analogy between the completion of this thesis and the daily cycle through Utrecht city centre. For one thing, the PhD's skyline has never ceased to change, where ideas have come and gone and projects have grown, shrunk or undergone significant renovation. Every day, I found myself navigating through lots of (sometimes unexpected) data, which made me think carefully about the next move. And finally, despite some very blustery or rainy days, there have also been many brilliantly sunny days that enabled me to glide along on a soft, warm breeze. This journey has now come to an end. Along the way, I've had the privilege to gain a peloton of valuable companions, without whose slipstream I would never have been able to complete this thesis and to whom I am greatly indebted.

First and foremost, I would like to express my deepest gratitude to **Prof. Dr. Bert Klein Gebbink**, my supervisor and promotor. Dear Bert, there is so much that I have to thank you for. Thank you for the opportunity you gave me to conduct my PhD in the OCC and for the trust you placed in me to continue with the "*N,N,O*" project, one of the oldest projects in your group. I am also incredibly grateful and honoured that I could be part of the European NoNoMeCat consortium, which opened the door to many interesting collaborations, fun meetings across (remote!) corners of Europe, and exciting new experiences abroad, both in academia and in industry. I also wish to thank you for the financial generosity you have shown me over the past few years, not only for attending scientific courses and conferences, but also for the contract extension that enabled me to continue with both written and practical work when the COVID19 pandemic started. When I first joined the group, you also agreed to sponsor a Dutch language course for me. This became an invaluable means for me to integrate in the Netherlands and learn how to communicate about science (and beyond!) in Dutch. Ultimately, this has been a means for me to expand my own Belgian identity, and has therefore had a huge impact on my own personal development. Thank you so much for this. And finally, thank you for all your support and the valuable input and advice you shared that helped me grow as a scientist, as well as the freedom you gave me to explore and determine the course of the project. I hope that you are happy with this thesis and everything we have been able to achieve together. Hartelijk dank voor alles, Bert!

I also wish to thank past and present members of OCC staff, whose relentless work has kept the OCC infrastructure running smoothly over the years. To **Danny Broere**, thank you so much for the opportunity you gave me to continue in the OCC as a "pre-doc" post-doc within your sub-group. I learned a tremendous amount during this time, and it was a very valuable experience. Thank you for always promoting such open discussion in the OCC about science and lab safety, and for your enthusiasm during lab outings and group events. I wish you the very best for the continuation of your research and your academic career. Pour **Marc-Etienne Moret**, merci pour toute ton aide à travers ces dernières années, pour toutes tes suggestions utiles concernant ma recherche et pour l'aide avec la DFT et l'interprétation des spectres EPR. Tes explications pédagogiques m'ont toujours aidé à mieux cibler mes questions scientifiques. Merci également pour les discussions intéressantes lors des déjeuners à l'UMC, les borrels et les cookie breaks. Je te souhaite tout le bonheur au monde à Maartensdijk et une très bonne continuation de carrière à Utrecht ! **Pieter Bruijnincx**, als allereerste lid van het "*N,N,O* team" is jouw proefschrift altijd een belangrijke inspiratie voor mij geweest tijdens mijn aioschap. Dank je wel dat je nu lid van mijn leescommissie wil zijn. Ook bedankt voor de uitnodiging om ToC graphics en journal covers te maken voor jouw mooie publicaties! Ik wens je nog veel succes met je spannende

onderzoek naar circulaire en duurzame chemie. **Arnaud Thevenon**, merci pour tout, et je te souhaite plein de succès et une très bonne continuation à Utrecht! **Gerard van Koten**, bedankt voor ons leuke gesprek in Bazel, en ook voor de bemoedigende woorden in het begin van mijn PhD. **Johann Jastrzebski**, hartelijk dank voor alle hulp de afgelopen jaren! Jij bent een enorme steun geweest voor mij en iedereen op de OCC dankzij al je aandacht voor detail, je waardevolle NMR-expertise en je ICT kennis. Zonder jou was het NoNoMeCat consortium ook niet gelukt, en ik ben zeer dankbaar voor alle administratie, organisatie en moeite die je daarvoor gedaan hebt. Ik ben blij dat ik je laatste jaren op de OCC heb mee kunnen maken en ik wens je heel veel plezier met je welverdiende pensioen en met je groeiende familie! **Matthias Otte**, I am grateful for all your help and suggestions in the beginning of my PhD, and the interesting discussions we had during our "rotovap dates". Thank you for the many great times and delicious schnitzels in Göttingen! Good that we talked about it! **Léon Witteman**, wat fijn dat je weer op de OCC bent komen werken! Dank je wel voor al je hulp, ook tijdens de jaren dat je nog promovendus was. Jouw behulpzaamheid, creativiteit en enthousiasme zorgen voor een fijne werkomgeving. Ook bedankt, jij en Sharon, voor alle leuke momenten samen tijdens het boulderen. **Thomas Ran**, "mercikes" voor alle steun en gezelligheid op het lab de afgelopen jaren. Jij weet goed hoe je alle OCC-ers kan binden met een goede sfeer, en dat waardeer ik heel erg. Zonder jou had ik mijn nieuwe woning op de Gruttersdijk niet gevonden, dus hartelijk dank voor je hulp daarmee! **Jord van Schaik**, dank je wel voor alle advies en technische assistentie toen ik op het lab begon. Ik ben heel dankbaar dat je deur altijd open stond voor allerlei vragen. **Henk Kleijn**, bedankt voor je geduld en voor alles dat je mij geleerd hebt tijdens mijn start op de OCC, inclusief de training op de heilige ESI-MS machine! **Richard Naastepad**, bedankt voor alle hulp, creativiteit en gezelligheid op het lab toen wij samen amide liganden aan het maken waren aan het begin van mijn promotietraject! **Silvia Benschop**, hartelijk dank voor al je hulp met het inplannen van de verschillende meetings en evenementen in de drukke OCC kalender! Ook bedankt voor je hulp met alle administratie aan het einde van mijn PhD en mijn tijdelijke ICT/GV-overeenkomst. **Milka Westbeek**, bedankt voor je hulp met alle administratie in het begin van mijn PhD, en voor alle leuke gesprekken naast het koffieapparaat of bij jou op kantoor. Jouw aandacht voor de gezondheid van iedereen op de OCC is zeer waardevol!

To **Martin Lutz**. Dear Martin, thank you for all the time you took to "elutzidate" the X-ray crystal structures in this thesis and for the many times you fought for that one good crystal lurking in a murky sea of (sometimes smelly!) compound solution. Your analyses, which feature prominently in all chapters, have been invaluable for me to understand the structure of my iron complexes, and receiving your invitation to come to the *Kruytgebouw* for a measurement was often the highlight of that particular day for me and my students. Thanks as well for the interesting courses and the lively conversations during our NoNoMeCat trip to Brest. I wish you all the best with the continuation of your time at Utrecht University and in your new lab in the *David de Wiedgebouw*!

To **Miquel Costas**, my second supervisor within the NoNoMeCat consortium. Thank you so much for all the valuable input you gave me during our Skype sessions in the beginning of my PhD and, later on, for the help in completing Chapter 5 of this thesis. Your positive and encouraging feedback always reinvigorated my motivation and drive. I also wish to thank you for the kind hospitality during my secondment at the University of Girona. I learned a lot about catalysis and was blown away by your variable temperature UV-Vis equipment! It was also a pleasure to discover the beauties of Girona and the surrounding region of Catalonia. A big thank you also to **Brenda Sánchez-Eguía** and **Laura Gómez Martín** for the kind help in the lab and the valuable ESI-MS measurements, all of which feature prominently in Chapter 5 of this thesis.

To **Andrew Edmunds**, my industrial supervisor within the NoNoMeCat consortium. Dear Andy, you have become such an integral part of my NoNoMeCat experience. Thank you so much not only for having been present at every single consortium meeting, but also for your kind, insightful and friendly input to everyone after our presentations. I also wish to thank you for having made my industrial placement at Syngenta and in Basel such a pleasant one. I learned a lot, and I appreciate you having taken the time to explain the fundamentals in lead compound design. Thanks to **Dorothée**, **Guillaume** and **Julia** for all the help in the lab! Aux autres stagiaires, **Timothée**, **Clément**, **Aidan** et **Mickael**, merci d'avoir partagé vos pauses midi avec moi et pour les baignades rafraichissantes dans le Rhin !

To **Eckhard Bill** and **Shengfa Ye**, my collaborators from the Max Planck Institutes for Chemical Energy Conversion (MPI-CEC) and for Kohlenforschung (MPI-KOFO). Thank you both for the kind hospitality during my secondment and my many day-trips to your spectroscopy lab. Thanks as well for all the measurement time you dedicated to my numerous samples, the results of which can be seen in all chapters of this thesis. I greatly value the open discussions and scientific input you shared with me, thanks to which I learned a lot. To **Bernd Mienert** and **Andreas Göbels**, thank you both for your technical assistance and for taking the time to explain some of the theory behind the Mössbauer and SQUID equipment! **Casey van Stappen**, it was a pleasure getting to know you, thank you for your kindness and for sending elaborate and insightful answers to my very basic DFT or spectroscopy questions! Thanks also for the TD-DFT analysis of my iron thiolate complexes that you did for me. I wish you all the best with your new adventures in Texas! To **Maxime**, **Ola**, **Nico**, **Albert**, **Zac** and **Romain**, thank you for including me in all your extra-curricular culinary and artistic activities! You made me feel extremely welcome and I greatly appreciate your kindness.

To **Jana Roithová** and **Guilherme Tripodi**, my collaborators at the Radboud University in Nijmegen, thank you for welcoming me into your lab and for running some ESI-MS measurements and discussing interesting mechanistic possibilities.

A big thank you to the professors and industrial scientists that took part in the NoNoMeCat consortium and who helped organise the many scientific and social events in different locations: **Martin Albrecht**, **Miquel Costas**, **Jeremy Harvey**, **Philippe Schollmeyer**, **Xile Hu**, **Henrik Junge**, **Shengfa Ye**, **James Douglas**, **Andrew Edmunds**, **Peter Sponholz**, and **Kevin Mahoney**. I would also like to thank all the other PhD candidates from the consortium, the NoNoMeKittens that grew up to become NoNoMeCats with me: **Maxime**, **Christoph**, **Marco**, **Wei**, **Runze**, **Marten**, **Andrea D.**, **Andrea M.**, **Valeria**, **Simone**, **Eduard** and **Serhii**. It's been a pleasure watching your chemistry evolve and seeing you each year for a catch-up. Thank you all for making the meetings such a pleasant experience and for making me laugh every time. I wish you all the utmost happiness and success in your careers ahead!

To the wonderful DAC crew, **Nynke**, **Silvia**, **Doug, Sophie**, **Fuqiang**, **Annelies**, **Jeroen**, and **Faranaaz**, thank you for making the DAC such a fun and pleasant team to be a part of. I enjoyed our meetings and admire the creativity you brought to the table when planning the next Do-Days or games nights. I wish you all the best with the end of your PhDs and the start of your respective careers!

The results described in this thesis would never have been achieved without the valuable help of some very talented students whom I had the pleasure to work with. **Hidde**, mijn allereerste masterstudent, wat heb ik zo veel van jou geleerd! Je creativiteit en je enthousiasme hebben altijd een sterke indruk op mij gemaakt. Jouw project was zeker niet makkelijk, maar dankzij je harde werk, je slimme vragen en je talent op het lab, heb je schitterende resultaten behaald die nu gepubliceerd zijn (Hoofdstuk 2). Bovendien hebben jouw resultaten veel nieuwe projecten in mijn PhD gestimuleerd, wat alleen maar

jouw sterke kwaliteiten als wetenschapper bevestigen. Dank je wel voor alles! **Daniël**, ik ben zeer dankbaar dat ik jouw onderzoeksstage begeleider mocht zijn. Dankzij je vele werk heb je grote stappen in ons project kunnen maken, inclusief het synthetiseren van de eerste mononucleaire, *N,N,O*-verbonden ijzer en zink complexen die het startpunt van zo veel nieuwe onderzoekslijnen zijn geworden. Ook hebben je zes "erg fraaie" kristalstructuren je de bijnaam *The Nucleator* opgeleverd. Je was nooit bang om vragen te stellen en om te leren van alle mensen rondom je. Hierdoor ben je ontzettend creatief geweest en heb je uitstekende resultaten geleverd die nu gepubliceerd zijn (Hoofdstuk 3). Ik heb superveel genoten van onze gesprekken over chemie, over gekke Britse gewoontes, over muziek, en over onze persoonlijke vooruitzichten in het leven. Dank je wel! **Annemiek**, lieve iron sister en paranimf, de zwavelbruggen in je mooie krullende haar waren al een voorbode in ons eerste gesprek voor een prachtige samenwerking. Jij bent op de OCC begonnen zonder veel organometaal synthese ervaring, maar bent daarna vertrokken als koningin van de "crystal structure league". Jouw bijzondere groeiproces en je ontzettend harde werk zijn een grote inspiratie voor mij geweest, en ik ben erg dankbaar dat wij samen hebben kunnen werken. Wat hebben we ook heerlijk gekletst en gelachen tijdens onze roadtrips naar het Max-Planck-Institut in Duitsland, en ik waardeer het feit dat ik met jou over alles kon praten. Al je mooie werk is te zien in Hoofdstukken 3 en 4, dank je wel voor alles! **Noortje** en **Nora**, onderzoek naar paramagnetische ijzer en koper complexen is niet makkelijk om uit te voeren, zeker niet als je alles moet leren en toepassen in een bachelorproject van korte duur. Jullie hebben ontzettend goed gewerkt, en ik ben heel trots op alles wat jullie hebben bereikt! **Stella** en **Iris**, dank jullie wel voor de mooie literatuurverslagen die jullie geschreven hebben! Ik heb er veel van geleerd en ben blij dat we samen hebben kunnen werken.

I would like to send a massive thanks to the past and present PhD/postdoc researchers of the OCC. I arrived in the Netherlands alone, and you became a "second family" to me, making me feel at home and helping me develop as a scientist, as a colleague and as a person. **Emma**, dank je wel voor alle hulp en steun in het begin van mijn promotie, en ook voor alle bemoedigende woorden! **Peter J.**, bedankt voor de gezelligheid en alle AFM tip en basement grapjes door de jaren. Ik kijk uit naar de volgende keer dat we samen kunnen gaan karten! **Jianming**, you are one of the coolest people I know and I miss hearing you burst out in laughter when you sat at the desk behind me. Thank you for always sharing your good spirits and for projecting such a beautiful vision of the world through your photography. **Pradip**, I'm grateful for all the help and advice you gave me when I started my PhD. Thank you for training me to use the CV, a technique that features prominently throughout this thesis. It was a pleasure getting to know you, and I hope we will meet again soon either in Europe or in India. **Alessio**, le *Swiss Express*, j'admire énormément ton intégrité et je te remercie de tout cœur pour tout ce que tu as fait pour le groupe pendant tes années à Utrecht. Merci pour tous les petits « cadeaux » qu'on trouvait cachés sur nos bureaux, dans nos sacs ou dans nos capuchons. Merci aussi pour tous les Kings Nights de dingue chez toi! Ne t'inquiètes pas, je tiens toujours ta poche pour ma protection. **Jing**, it was an absolute honour getting to know you and standing next to you as your paranymph. I admire your strength, your hard-working ethic and your unfailing kindness and helpfulness to everyone around you. **Eduard**, fellow NoNoMeKitten, thank you for sharing your catalysis expertise with me and for all the great times in and outside the lab! You are a great guy and I'm glad we could share and discuss so much over the course of our PhDs, especially in the final stages. **María**, ¿qué onda? Thank you for being my desk neighbour all these years, for your hilarious stories about dramatic Mexican life and also for introducing me to the delicious "fresitas" sweets! **Pamela**, gorgeous curlygirl, thank you for always being so open to discussion, for sharing the same OCD for glovebox cleanliness and, most importantly, for bringing your fiery rhythm and dance to the group! **Pablo**, merci pour ta gentillesse, pour ton amitié, pour toute ton aide et toutes les conversations intéressantes ces dernières années. Je suis vraiment heureuse d'avoir partagé ces années avec toi dans l'OCC. **Fanshi**, you are a wonderful guy and it's been a pleasure working with you and getting to know you. Thank you so much for your helpfulness, your kindness

and your legendary comments! **Cody**, lieve krullenbol, bedankt voor alle gezelligheid op het lab, voor de geweldige woordgrapjes, voor de Codybrouw, de Feringa selfies, en voor alle positiviteit door de jaren heen! Jouw oog voor detail en jouw vermogen om belangrijke onderzoekvragen te stellen hebben altijd een sterke indruk op mij gemaakt. Lieve **Jochem**, mon chouchou, zullen we nog een koffietje doen? Jij brengt zo een leuke sfeer op de OCC en ik waardeer het feit dat je zo makkelijk iedereen kan binden. Dank je wel voor alle Broodje Ben en UMC-dates, voor je enthousiasme om samen te gaan squashen of fietsen, en alle gezellige uitjes naar Micks. **Roel**, super bedankt voor je proactieve aanpak van allerlei zaken op de OCC en je behulpzaamheid. Zonder jou (pyromania) waren de OCC campingtrips ook niet zo legendary geweest, dank je wel voor alle enthousiasme en gezelligheid! **Razvan**, thank you for being such an inspiring colleague, for always being so open about lab safety and for the high standards of lab etiquette you set as an example. I think the group was incredibly lucky to have had you these last few years, and it was a pleasure to work creatively with you for your scientific illustrations! **Luke**, I enjoyed being able to share memories of life in Britain with you. Thanks for all the laughs, for your enthusiasm during the Belgian beer borrels, and also for always listening when I needed to talk things through. **Lars**, van 2e jaar practicum student tot superslimme collega, ik ben dankbaar dat ik jou heb leren kennen en dat wij zo veel mooie tijden op het lab hebben kunnen delen. Ik wens je nog veel succes met je spannende onderzoek! **Joel**, your chill and helpful character is as epic as your hair, thanks for being such a great colleague! To **Charl**, **Tharun**, **Agneev**, **Fuqiang**, **Mou**, **Angshuk**, **Stanislav** thanks for the great atmosphere you brought to the group, and I wish you all the best with the completion of your projects in the OCC and your future careers!

To the wonderful 90's NOW crew. **Bas**, fellow "barnacle", wat kan ik altijd zo hard lachen met jou! Dank je wel voor je vriendschap, voor je steun, voor de oversized knuffels, voor alle leuke borrels en etentjes samen, voor onze fietstochten (soms door de sneeuw!), voor onze dierenpark uitjes, en ook voor alle enthousiasme tijdens de camping trips. **Dide**, bedankt voor alles wat je mij geleerd hebt over de jaren, op het lab en ook in het leven. Ik bewonder je passie voor chemie, je oog voor detail en je aandacht voor de gezondheid van de groep. Dank je wel voor alle ski, Pinkpop en Paaspop avonturen en voor de inspirerende gesprekken! **Manuel**, thank you for sharing your incredible love of life and your positive energy! You have the gift of seeing value in everything and everyone around you, and you inspire me to be the best version of myself. I am grateful for your friendship and all your generosity over the years.

Special thanks go to the "social bubble" that kept me sane during the pandemic lockdowns as well as the final stages of my thesis writing. **Martine**, zonnestraaltje van de groep, samen hebben we de kunst van improvisatie geperfectioneerd en ik ben dankbaar dat we zo veel mooie momenten hebben kunnen delen, bij de Ikea, de Intratuin, het Maximapark, in de jacuzzi, en nog veel meer (allemaal via Breukelen, natuurlijk). Jouw lach is echt een superpower, en ik werd er altijd blij van als ik met jou was. Lieve **Maartje**, wat ben ik blij dat je al sinds je pre-master binnen de OCC bent komen werken, dat ik als gevolg jarenlang heb kunnen genieten van je teamwork, je creativiteit, je positiviteit, je passie en je energie. Dank je wel voor alles en dat we altijd zo makkelijk over alles konden praten! Yamasssss! **Errikos**, jouw komst op de OCC is voor mij synoniem met de Golden Days. Samen hebben we zo veel spannend onderzoek en leuke glovebox sessies meegemaakt, en jij maakte ieder dag mooier met je grote glimlach en je uitbarstende enthousiasme. Super bedankt voor je onsterfelijke steun en vriendschap door de jaren, met jou weet ik dat het voor altijd *l'Amour Toujours* zal zijn! **Sander**, paranimf, collega, vriend. Al vanaf dag één stond je altijd klaar om iedereen te helpen, en ik heb enorm respect voor je pragmatisch en proactieve manier om oplossingen te bedenken. Als (bijna)tegenoverburen door al die jaren hebben we veel van onze verschillende projecten meegemaakt, en dankzij een ondeugend twinkeling in je ogen wist ik meteen dat het tijd was om koffie te halen en even bij te kletsen en onze "expertise" delen. Bij jou kon ik altijd terecht om advies te vragen, en je wist altijd precies hoe je me aan het lachen kreeg. Ik ben zeer dankbaar dat wij elkaar hebben leren kennen en dat je op deze dag naast mij staat.

Dear **Serhii**, I don't even know where to start in thanking you. I am so, so grateful for the fact that we crossed paths at the OCC and that we were able to spend these important years together, supporting each other during the ups and downs of PhD/PD life. I deeply admire your passion for chemistry and your never-ending thirst for knowledge, as well as your determination and persistence in the face of challenging research and impossible circumstances. You set a high standard on many levels that pushed me to demand more of myself, and I believe I became a better scientist because of you. Thank you for all your help, whether it be in the form of DFT trouble-shooting, tips and tricks for glovebox usage, or explaining how to do elaborate NMR experiments, as well as countless other times that I don't have space to list out here. Thank you for your friendship that I hold so dear and all the wonderful moments we shared outside the lab, cycling home sometimes late at night, walking along the river Vecht, cycling to Kasteel de Haar, Peking duck dates, photographing the tulip fields, and, of course, the endless supply of internet "memes" you shared online. I wish you all the best for your new adventures in Groningen and beyond! Thank you.

Numerous students have come and gone from the OCC over the years: **Laurens B.**, **Cecilia**, **Richt**, **Annet**, **Joost**, **Maxime**, **Jitse**, **Sam H.**, **Raoul**, **Laurens V.**, **Yuri**, **Elena H.**, **Yoni**, **Bram**, **Arthur**, **Lada**, **Jelle**, **Jesse**, **Sam v.d. L.**, **Max**, **Tom**, **Alex**, **Thomas D.**, **Sjoerd**, **Yang**, **Chick**, **Tú**, **Bauke**, **Jasmijn**, **Elena R.**, **Eva**, **Kasper**, **Abdullah**, **Erkay**, **Koen**, **Luuk**, **Marieke**, **Minka**, **Dylan**, **Janneke**, **Floris**, **Lisanne**, **Vito**, **Matthijs** and all other students past and present. To all of you, thank you for your contributions to the group, whether it be in the form of crystal structure cake, birthday cake, cookies, Easter egg hunts, Greek dinners at Sirtaki, bursts of infectious laughter, the Friday Eurodance playlist, canoeing along the new Utrechtse Singel, the *gezelligheid* during the camping trips or simply a good old chat during a coffee break. You made the OCC a colourful and warm place to be, and I'm so grateful to you all for that. **Marc**, merci tellement pour ta toute ta gentillesse et les discussions intéressantes et passionnées ! **Andrea**, *grazie mille* for always making me smile and for your high spirits and incredible generosity! It was truly a pleasure working with you.

To my friends from London, **Layla**, **Joel**, **Sam**, **Chris, Alice**, **Janice**, **Alex**, **Dongwhi** and, of course, **Tristan**. Although I chose to leave London, I have by no means forgotten our wonderful student years and the impact you had on shaping me both as a person and as a chemist. Thank you for your continued friendship despite the distance and for always making me laugh during our online chats. Dearest **Jemima**, thank you for your kind visits to the Netherlands and for such a lovely catch-up each time! Those moments meant a lot to me. Much love to **Nikki**, **Alec**, **Richard**, **Ed**, **Stephanie** and **Marcie** too. I look forward to seeing you all again in London or in Scotland.

Dear **Junshuai,** dear Jeremy. You are my oldest fiend in Utrecht and I have spent so many happy years living with you at the Cervanteslaan. I loved coming back home and being able to share a Belgian beer or a "Mannenliefde" with you, looking out over the Amsterdam-Rijnkanaal to the magical sunsets of Oog in Al. Thank you for always having been there to listen to me, and for always finding the perfect Chinese proverb for every situation. We've seen each other grow a lot over the past few years and, in many respects, we crossed some important personal milestones at the same time. I am deeply grateful for the comfort and happiness you have given me in your friendship. Thank you.

Cher **Sébastien**, depuis qu'on s'est connu lors de mon stage à Solvay tu as toujours été tellement gentil et ouvert avec moi. Tu m'as encouragé à tenter plein de nouvelles activités sportives, et grâce à toi j'ai appris à moins hésiter et à foncer davantage. Merci pour tout, pour ton soutien moral et pour ton amitié constante ! Chère **Christine**, « tante Titine », merci pour ton encouragement, ton soutien et toute ta gentillesse depuis que je suis toute petite ! Chers **Anne** et **Daniel**, je vous remercie de tout cœur pour votre gentillesse et votre générosité non seulement envers moi mais aussi envers toute ma famille. Merci

pour tout le soutien moral et aussi d'être venus me rendre visite à Bâle pendant mon petit stage industriel ! Chers **Marianne** et **Gilbert**, je suis tellement heureuse quand je suis avec vous, merci pour toute votre gentillesse et tous les beaux moments en famille, en France et en Belgique.

To my girlfriends in Belgium, **Miloni**, **Kelly**, **Kristina** and **Melanie**. Your continued friendship and support all these years mean the world to me. You anchored me in moments that I felt lost, and I am so grateful that I could always come back home and blow off some steam with you, discovering lots of interesting, quirky and beautiful new places in Belgium in the process. **Kris**, thank you for having come to visit me in Utrecht and in Basel, for your wise words, for your unfailing support and for never being afraid to be critical where I was afraid to be so myself. **Melanie**, you talked me through many intense, happy and challenging moments the last few years and I honestly don't know where I would be without you. Thank you for being you, for always being there and for the comfort of your friendship.

Lieve **Jacco**. Wij zijn begonnen als collega's maar snel ben je een van de belangrijkste personen in mijn leven geworden. Jij leerde me altijd perspectief te blijven zien, en dat het allerbelangrijkste wat na dit promotietraject overblijft mijn persoonlijke ontwikkeling is en mijn band met de mensen om me heen. Dank je wel voor je liefde, je vriendschap, je gezelschap, voor de bemoedigende woorden, en voor alle steun de afgelopen jaren. Dankzij jou, heb ik ook veel nieuwe dingen in Nederland ontdekt, inclusief carnaval in Eindhoven, Disco Snolly op Paaspop, Pinkpop met de Joske fanclub, de tulpenroute in de Noordoostpolder, happy-hardcore muziek, en nog veel meer. Ik ben zeer dankbaar dat dit allemaal met jou heb kunnen beleven, en ik kijk uit naar alle mooie avonturen dat we nog samen zullen delen. **Anne**, **Hans**, **Martine**, **Stijn** en **Silvie**, dank jullie wel voor alle steun en voor de warme ontvangst binnen jullie familie. Tot slot, een dikke knuffel voor **Pim**, **Lieke**, **Rens**, **Bram** en **Lars**, ik wens jullie heel veel succes in de toekomst!

To **Sarah**, my lovely sister, thank you for all your support and advice these last few years, for having come to visit me (and now live with me!) in Utrecht, and for your kind messages that always make me smile. I look forward to all the things we'll do together now as our new adventures unfold! Enfin, je tiens à remercier de tout cœur mes très chers parents, **David** et **Catherine**, pour l'amour qu'ils m'ont toujours donné, leur soutien et toute l'aide qu'ils m'ont apporté durant mes études. The completion of this thesis is a testament to the constant encouragement you gave me in all aspects of life, as well as the curiosity that you instilled and nurtured in me from a very young age. You have always been my biggest inspiration, and I dedicate this thesis to you both.

Mercikes!

Emily

About the Author

Emily C. Monkcom was born on 17th March 1992 in Brussels, Belgium. She completed her school education at the European School of Brussels in 2010 and began her undergraduate chemistry studies at Imperial College London that same year. From 2013 to 2014, she spent a year in industry at Solvay in Brussels, preparing heterogenous Pd/Al_2O_3 catalysts for the continuous production of H_2O_2 in the anthraquinone auto-oxidation process. Her final master project, conducted between 2014 and 2015 at Imperial College, was focused on the study of copper(I) alkylamide intermediates in the modified Ullmann reaction.

In 2016, she began her PhD under the supervision of Prof. Dr. Bert Klein Gebbink in the group of Organic Chemistry and Catalysis (OCC), at Utrecht University. The most important results of this research are presented in this thesis. The project was financially supported by the European Union "Horizon 2020" funding programme, and forms part of the "Non-Noble Metal Catalysis" (NoNoMeCat) Marie-Curie ITN consortium. Parts of this thesis have been presented at national and international conferences, including the Netherlands Conference for Chemistry and Catalysis (NCCC 2017, 2018 and 2019, Noordwijkerhout, The Netherlands), the 22nd European Conference on Organometallic Chemistry (EuCOMC 2017, Amsterdam, The Netherlands), the Girona Seminar on Predictive Catalysis (GS2018, Girona, Spain), and the 19th International Conference on Biological Inorganic Chemistry (ICBIC 2019, Interlaken, Switzerland).

In 2021, she undertook a 1-year post-doc in the group of Dr. Ing. Danny Broere (in the OCC), working on the development of dinuclear first-row transition metal complexes as novel, bioinspired catalysts for the oxidation of aromatic substrates.

List of Publications

A Family of Mononuclear *N,N,O*-Bound Iron and Zinc Thiolate Complexes that Structurally Model IPNS; E. C. Monkcom, A. J. de Vries, D. de Bruin, M. Lutz, G. Tripodi, J. Roithová, S. Ye, E. Bill, R. J. M. Klein Gebbink, *manuscript in preparation.*

Synthesis, Structure and Reactivity of a Mononuclear *N,N,O*-Bound Fe(II) α-Keto-Acid Complex; E. C. Monkcom, L. Gómez Martín, M. Lutz, S. Ye, E. Bill, M. Costas, R. J. M. Klein Gebbink, *manuscript in preparation.*

2H1C Mimicry: Bioinspired Iron and Zinc Complexes Supported by *N,N,O* Phenolate Ligands; E. C. Monkcom, H. A. Negenman, E. Masferrer-Rius, M. Lutz, S. Ye, E. Bill, R. J. M. Klein Gebbink, *European Journal of Inorganic Chemistry*, **2022**, 9, e202101046, 1-14.
doi: 10.1002/ejic.202101046

Structurally Modelling the 2-His-1-Carboxylate Facial Triad with a Bulky *N,N,O* Phenolate Ligand; E. C. Monkcom, D. de Bruin, A. J. de Vries, M. Lutz, S. Ye, R. J. M. Klein Gebbink, *Chemistry – A European Journal*, **2021**, 27, 16, 5191–5204.
doi: 10.1002/chem.202004633

Bioinspired Non-Heme Iron Complexes: The Evolution of Facial *N,N,O* Ligand Design; E. C. Monkcom, P. Ghosh, E. Folkertsma, H. A. Negenman, M. Lutz, R. J. M. Klein Gebbink, *Chimia International Journal for Chemistry*, **2020**, 74, 6, 450–466.
doi: 10.2533/chimia.2020.450

Crystal Structure of tetrakis(tetrahydrofuran-κ_O)bis(trifluoromethanesulfonato-κ_O)iron(II); C. F. Riemersma, E. C. Monkcom, R. J. M. Klein Gebbink, M. Lutz, *Acta Crystallographica E75, Crystallographic Communications,* **2019**, 1548–1551.
doi: 10.1107/S2056989019013094